Super-resolution ultrasound imaging with microbubbles

Christensen-Jeffries, Kirsten Mia

Awarding institution:
King's College London

SUPER-RESOLUTION ULTRASOUND IMAGING WITH MICROBUBBLES

Kirsten Mia Christensen-Jeffries

Submitted in fulfillment of the requirements for the degree of

Doctor of Philosophy

Division of Imaging Sciences and Biomedical Engineering

School of Medicine

Kings College London

May 2016

CONTENTS

ACKNOWLEDGEMENTS

I am hugely thankful to my primary supervisor, Dr. Robert Eckersley. I owe much to his enthusiasm, guidance and unwavering support, his probing questions, and the freedom with which he allowed me to become an independent researcher and explore this exciting and multifaceted project. I am immensely grateful to my co-supervisors, Dr. Mengxing Tang and Dr. Christopher Dunsby, whose individual expertise has provided me with immeasurable gains in knowledge throughout the years, and whose insightful comments have maintained a clear purpose for the progression of this work; Dr. Mengxing Tang for his invaluable feedback, advice and guidance at weekly group meetings, and Dr. Christopher Dunsby, whose fundamental input in the initial concept instigated such a fascinating project. I would also very much like to thank Prof. Peter Wells and Dr. Jeffrey Bamber for their time and commitment in examining my thesis.

One of the most rewarding aspects of this project has been the opportunity to work alongside many talented colleagues. The ultrasound research group at Imperial College London and Kings College London has provided the opportunity to share research ideas in a stimulating, yet relaxed, environment. In particular, I would like to thank Dr David Cosgrove for his invaluable expertise and guidance. I thank Olivia Veissman for providing the initial groundwork in this interesting and exciting new project, and Dr. Richard Browning, whose skills and hard work resulted in a productive and enjoyable collaboration. I am grateful to Dr. Markus Schirmer for his hard work, continual reassurance and positivity. I thank Dr Katherine Wiliams, Dr. Brahman Dharmarajah and Prof. Alun Davies at the Section of Surgery, Charing Cross Hospital and Mr. Tony Young at Imperial College London for sharing their time, knowledge and hard work. I would like to also acknowledge Prof. Piero Tortoli, Dr. Francesco Guidi, and Dr. Alessandro Ramalli for their selfless sharing of expertise during our collaboration.

Thanks also to my friends and colleagues in the KCL Biomedical Engineering Department, who brightened everyday with interesting lunchtime chats and indispensible tea breaks.

Above all I would like to thank my parents. None of this could have been done without their unconditional love, reassurance, and understanding. Their optimism and encouragement have kept me going.

This thesis is dedicated to my brother, Nils Christensen-Jeffries, whose positivity, unapologetic sense of humour, and love for life will forever inspire me, and who has always believed in me more than I have myself.

ABSTRACT

Ultrasound imaging is one of the most widely used clinical imaging methods offering safe, real-time imaging at low cost with excellent accessibility. However, the structure and flow of deep microvasculature, which can serve as a marker of pathological or dysfunctional tissue, cannot be adequately resolved using standard clinical ultrasound imaging frequencies due to diffraction. Conventional ultrasound imaging resolution is related to the wavelength employed, however, high frequency approaches used to improve resolutions are limited in penetration depth. Therefore, there is a crucial clinical need for the development of new techniques that can fill this 'resolution gap'.

This work develops a technique to generate super-resolved images of the vasculature using accumulated localisations of spatially isolated microbubble contrast signals. Furthermore, a temporal tracking algorithm is introduced, enabling the extraction of fluid flow velocities. Using this approach, *in vitro* flow phantoms are visualised to a depth of 7 cm at sub-diffraction scale using standard clinical ultrasound equipment. In subsequent work, super-resolution imaging and velocity mapping are demonstrated *in vivo*, providing quantitative estimates of blood flow velocities at a super-resolved spatial scale. The algorithm is then extended to acquire quantitative measures for the clinical evaluation of human lower limb perfusion, where super-resolution localisation measures are able to identify differences in the microcirculation between patients and healthy volunteers following exercise.

Super-resolution imaging relies on the correct identification of spatially isolated bubble signals, while user defined thresholding limits its clinical translation. To address this challenge, machine learning techniques for foreground detection and signal classification are investigated. It is shown that support vector machines provide promising results for super-resolved imaging, whereas the unsupervised approaches investigated appear unsuitable.

In addition, the 2D acquisition strategy employed limits the application of the technique to structures with limited 3D complexity. This work concludes by developing a fast,

multi-probe approach, which allows 3D super-resolution imaging and flow detection *in vitro*.

1 INTRODUCTION

1.1 MOTIVATION

The structure and flow of the microcirculation reflects the requirements and conditions of local cells and tissue. This assertion underscores the importance of visualising the presence, structure and function of blood vessels. A lack of blood flow can be a marker of pathological, damaged or dysfunctional tissue, such as ischaemia [1], peripheral arterial disease (PAD) [2]–[5], and coronary heart disease [6], while an increase can indicate rapid and uncontrollable cell growth or proliferation caused by cancer and metastasis [7]–[10],[11].

Identification and evaluation of angiogenesis and other such microvascular conditions requires the assessment of morphological parameters, such as vessel density, size and branching patterns, as well as functional parameters such as blood flow rate [8], [12] that can benefit from non-invasive high-resolution imaging. Detecting such microscopic changes using non-invasive *in vivo* assessment would allow early clinical intervention and would provide a means of closely monitoring the treatment of such diseases. Furthermore, recent findings suggest that targeting sites of angiogenesis may be critical for therapeutic cancer treatment [9], [10]. However, small vessel sizes and low blood flows make assessing the microcirculation challenging [11]. Current clinical imaging modalities such as MRI, PET, CT and Ultrasound (US) allow non-invasive examination. However, these approaches cannot adequately resolve microvasculature, and are mainly used to determine functional indicators such as blood flow velocity.

Optical light microscopy can resolve microscopic structures and offer profound insights into microvascular physiological changes, but cannot be applied *in vivo* at clinically useful depths.

Through the development of microbubbles as US contrast agents [13], [14], and the advent of advanced techniques to exploit their nonlinear response, US imaging specificity and sensitivity has improved [15]. Visualisation of the vasculature using contrast agents has progressed with techniques such as maximum intensity persistence (MIP) imaging [9], where the pixel maximum intensity over time is displayed in the image, and power Doppler sonography [11], which allows estimation of blood flow from frequency shifts caused by blood motion. However, diffraction of the transmitted and received waves means US resolution is limited, thus imaging at the micrometre scale is still required. High frequency US methods have been developed as a means of obtaining high-resolution imaging [11], however these techniques have limited application due to the inherent compromise between higher frequencies and limited penetration depth. Thus, there is a crucial clinical need to develop new imaging techniques that can fill this 'resolution gap' [8].

This thesis examines and develops the technique of acoustic super-resolution US imaging. This acoustic analogue of established super-resolution optical microscopy techniques aims to reconstruct super-resolved maps of fine microvessels by imaging spatially isolated microbubble signals. The ability to accurately resolve complex microvascular structures containing microbubbles could be a vital step to tackle this resolution challenge. An understanding of the method and its inherent challenges is presented, along with initial practical investigation into the fundamental issue concerning the accuracy with which the position of a single scatterer can be determined using US. A technique for the estimation of microvascular blood velocity is also developed. Demonstration of the use of this technique *in vitro* is first performed and analysed, before the technique is further developed for *in vivo* implementation. The imaging technique is extended with the goal of generating quantitative measures for the clinical evaluation of tissue perfusion. The use of machine learning based post-processing tools for foreground detection and single bubble identification is then explored, with first demonstration of some of the potential benefits and challenges for

the aim of progressing towards viable clinical implementation. Finally, limitations arising from the 2D US acquisition process highlighted throughout the project guided the development and implementation of a compounding 3D strategy for the exploration and demonstration of 3D bubble localisation. It is hoped that the aforementioned developments presented in this thesis will aid the progression of super-resolution imaging towards clinical implementation.

There are several excellent general reviews of vascular imaging [12], [16]–[19], which illustrate the pace of development and breadth of research in this field. The following review presents the current requirements and challenges associated with microvascular imaging for the general field of medical imaging, before focusing on challenges and opportunities within US imaging and, more specifically, within contrast enhanced US imaging (CEUS). In addition, aforementioned well established techniques for high resolution imaging within the optical field will be discussed in relation to the acoustic analogue.

1.2 Significance and Clinical Need

Improvements in microvascular imaging will benefit wide ranging areas of healthcare that rely on the monitoring of microvascular structure and blood flow, such as those associated with cancer, diabetes, ischemia, peripheral arterial disease (PAD), and regenerative treatments. Such conditions affect a large proportion of the patient population, where around 8 million people are diagnosed with cancer around the world each year, with around 1 in 3 people diagnosed with the condition at some point in their lifetime [20]. Population studies have estimated that PAD affects more than 10 % of people aged over 55 years [2], [21], [22] where recent studies have found the majority of individuals diagnosed with PAD also exhibit cardiovascular disease risk factors [23]. PAD and Diabetic Foot Disease resulted in approximately 12 000 lower limb amputations in 2012-2013 in England alone [24]. In view of the importance of techniques to examine microcirculation for the diagnosis and prognosis and monitoring of such disease states [4]–[7], [25], [26], the development of new qualitative and quantitative techniques to fulfil this requirement is crucial.

1.2.1 THE CIRCULATORY SYSTEM

The human circulatory system comprises a dynamic network of blood vessels responsible for the transport of nutrients, oxygen and hormones, while facilitating the removal of waste products and toxins [27]. Blood comprises a liquid matrix (plasma), denser and more viscous than water, in which a composition of specialised cells serve individual functions [28]. Approximately 45% of the blood volume is formed of red blood cells, whose primary function is to transport oxygen; however the actual concentration of red blood cells in blood decreases with reduced vessel size and varies across the vessel diameter [29]. Vessels transport blood around the body at wide ranging velocities and flow conditions, where mean vessel diameters range from a few centimetres, down to only a few micrometres in size at the peripheral capillary beds (see Table 1.1).

Vessel	Vessel Function	Total Area (cm^2)	Internal Diameter	Mean Flow Velocity
Aorta	Feeding channel	5	2.5 cm	30 cm/s
Arteries		20	3 – 10 mm	20 mm/s
Arterioles		40	30 µm	
Capillaries	Exchange	2500	5 µm	0.3 mm/s
Venules	Draining channel	250	70 µm	3 mm/s
Veins		80	0.5 cm	10 mm/s
Vena Cava		8	1.2 cm	

Table 1.1. Average blood vessel parameters within the human circulation. Adapted from [28], data from [25] [29].

Blood vessel sizes and characteristics are attune to their function within the network. Thicker, conduit vessels are composed of impermeable layered walls composed of muscle and elastic fibres, whereas capillaries are characterised by thin walled vessels, allowing permeation of nutrients and oxygen across the membrane (Figure 1.1). Blood is pumped at high pressure through larger blood vessels from the heart's ventricles, where the volume of blood disperses throughout the body with fractions dependent upon metabolic requirements. Vessels such as the aorta and major arteries branch and proliferate into smaller arterioles which taper into a fine vascular network where the capillary bed tends to the metabolic needs of individual organs and cells, before the

venous system (venules and veins) permits the transport of deoxygenated blood back to the heart [27], [28], [30].

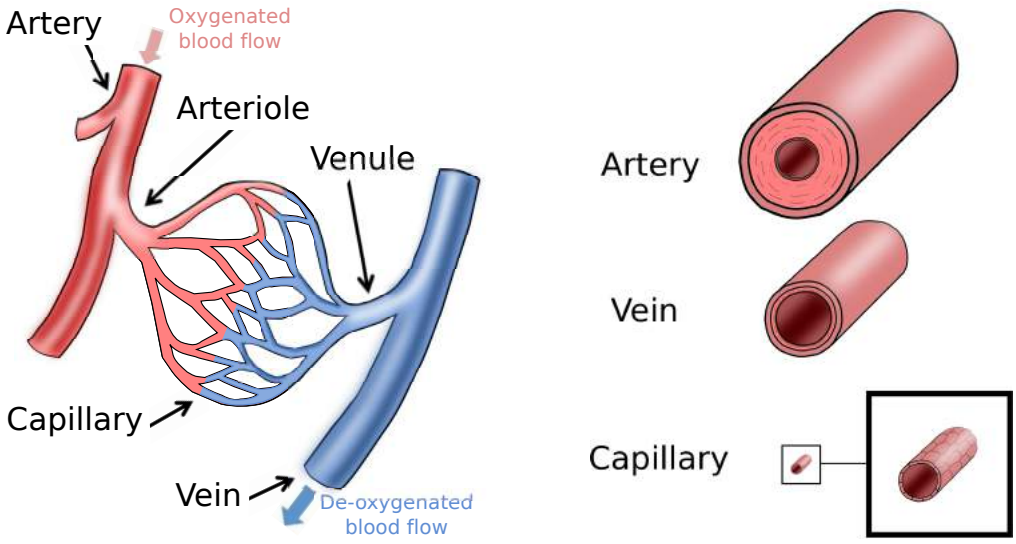

Figure 1.1. Vessels of the microcirculation. The circulatory system features arteries which branch into smaller arterioles into a network of capillary vessels before venules deliver the deoxygenated blood into veins for return to the heart. Arteries comprise thick muscular walls for pumping blood away from the body, while veins are thin walled, large lumen, low pressure channels for transporting blood back to the heart. Capillaries have a single endothelial cell layer wall for nutrient and gas exchange. Microcirculation figure adapted with permission courtesy of Encyclopaedia Britannica, Inc., copyright 2006; microvessel figure inspired by [31].

1.2.2 The Human Microcirculation

The microcirculation comprises the largest total vascular area of the entire circulatory system (see Table 1.1 – arterioles, venules and capillaries). This encompasses a network of vessels typically under 100 μm in diameter [27]. Respiratory gas exchange, the transferal of vital nutrients and filtration occur in the microcirculation [27], [28]. Blood flow velocities must therefore be low enough to allow respiratory gas exchange, but high enough to maintain shear rates that inhibit clot formation. Typical blood velocities and shear rates in human capillaries range from around 0 to 1500 μm/s and 100 to 500 s^{-1} and depend on numerous factors, including the organ physiology, and metabolic demand [27], [30], [32], [33]. Vessels and organs have the ability to control local flow

rates in response to variations in metabolic activity through contraction and dilation of the vessel lumen, often arterioles [34].

1.2.2.1 ARTERIOLES AND VENULES

Each small artery branches into several arterioles as its diameter decreases toward the periphery. Arterioles are generally less than 500 μm in diameter, with a thick, smooth muscle wall and narrow lumen (approximately 30 μm in diameter) which branches into approximately 10 - 100 capillaries [27]. Pre-capillary arterioles have an internal diameter of around 15 to 20 μm and are surrounded by only one layer of smooth muscle cells. Arterioles are considered a major site for total vascular resistance which performs a dominant role in the regulation of blood flow to tissues and organs. Blood flow is controlled by the alteration of the arteriole radius, where arteriole wall muscles can respond to the local metabolic activity in a tissue or organ [27], [35]–[37]. These vascular flow variations can indicate conditions which require increased energy expenditure, such as angiogenesis for malignant tumour growth and metastasis, or ischaemia caused by the restriction of the blood supply [7], [38], [39].

The organisation of the venular network is similar to that of the arterioles except that venules are more prevalent than the arterioles and are thin walled with a larger lumen (Figure 1.1). Capillaries drain into these larger vessels; the passive, distensible nature of the post-capillary venules accounts for the ability of these microvessels to store and mobilise significant quantities of blood in certain organs [35]–[37].

1.2.2.2 CAPILLARIES

Arterioles give rise to capillaries. Capillaries have an average diameter of around 5 μm lined by a single layer of endothelial cells and a thin membrane of around 1 μm [27]. The structure and wall thickness of capillaries vary considerably between and within organs depending on the specific tissue function. The capillary network, with its large surface area, slow flow, and highly permeable endothelial wall, is well suited for the exchange of gases and nutrients between the bloodstream and tissues [27], [35]–[37].

1.2.2.3 DISEASE CHARACTERISTICS

ANGIOGENESIS

Angiogensis is the growth of new blood vessels from the existing vasculature and can

occur as a result of natural processes involving tissue repair and remodelling and is usually self-limiting in time (such as wound healing by coagulation) [40], [41]. This is controlled by a range of angiogenic factors and inhibitors.

Tumour angiogenesis refers to the sprouting of new vessels towards a solid tumour [35], [36]. Without recruitment of new dedicated blood vessels, tumour cell growth depletes the local oxygen supply causing nutritive deficiency and a hypoxic microenvironment [40]–[42]. Growth of tumours beyond a few millimetres in diameter and the spread from the primary tumour site are therefore unlikely without angiogenic growth [41]. This hypoxic state instigates biological events that create vascular growth and allow rapid cell proliferation, which ultimately form a dedicated tumour microvasculature [40]. In contrast to the self-limiting process occurring in standard angiogenesis, tumour angiogenesis is uncontrollable and can last for years [40].

Tumour vasculature contains morphological abnormalities such as tortuous vessels with loops, shunts, dead ends, high microvessel densities, and vascular elongation, which combine to form a chaotic vascular network [34], [41]. Alongside these architectural differences, regional blood flow is often heterogeneously distributed in space, and irregular in time. These sometimes include variable and even reverse flow patterns. Tumours of different type and grade additionally demonstrate a wide range of flow rates [34]. As treatments and non-surgical forms of cancer therapy (chemotherapy, radiation therapy) become more specialised and targeted, so too must the methods to diagnose, as well as monitor and assess their clinical response. Detailed knowledge of *in vivo* blood flow could also be useful for the optimisation of these therapies. The importance of accurate assessment of the microvasculature is highlighted in oncological applications with more recent emphasis on tumour vasculature, angiogenic processes and developments of anti-angiogenic therapies since its approval in 2004 in combating cancer [43]–[45]. Furthermore, angiogenesis is not just characteristic of cancerous disease, it is also common to other forms of pathology including Psoriasis, Diabetic retinopathy and rheumatoid arthritis [40].

PAD

Peripheral arterial disease (PAD) is a condition characterised by a build-up of fatty deposits called atheroma in the arterial walls [46]. This accumulation narrows the

arteries and causes obstruction to blood flow in the extremities [46], [47]. Measuring changes in musculoskeletal perfusion are important in the management of PAD, however these remain difficult to measure. This application will be discussed in more detail in Chapter 5.

1.2.3 MEDICAL IMAGING

The importance of early diagnostic indicators is well recognised in the field of health care and medical research, with efficacy of treatment and survival rates shown to increase with early detection and intervention [24], [48], [49]. With significant recent advances in genomic technologies, and molecular genetics, the development of new therapies and targeted drugs means that treatments are able to pinpoint specific regions associated with early disease progression such as angiogenic growth, inflammation or reduced peripheral blood flow [50]. Providing accepted biomarkers to monitor and assess disease progression and therapeutic treatments is therefore crucial. Imaging based biomarkers provide benefits such as non-invasive assessment and repeated imaging over time for comparative measurements (for example for a longitudinal study, or as an individualised control in baseline vs. post treatment). Furthermore images can often be provided fast, or in close to real-time, depending on the imaging modality. As such, medical imaging provides a desirable and crucial role in the detection, diagnosis and assessment of therapeutic efficacy and monitoring of disease states.

Currently there exist a number of clinical imaging technologies that can be used to assess features of the microvasculature; a brief summary of the most relevant is presented in the following section.

1.2.4 EXISTING TECHNIQUES TO IMAGE THE MICROVASCULATURE

Significant advances have been made in the development of techniques to image microvascular structure and circulation. Each imaging modality provides their own distinct advantages and limitations in this regard; Table 1.2 defines these characteristics for some of the main imaging modalities in current clinical use, such as magnetic resonance imaging (MRI), positron emission tomography (PET), optics, and X-ray computed tomography (CT).

Current developments in microvascular imaging techniques within these fields are on-going, and indeed some of the resolutions included in Table 1.2 are being succeeded with continually advancing and specialised methods. Some of the most relevant are discussed below.

Modality	Resolution	Advantages	Limitations
MRI	~ 100 µm	- Non-ionising - Good soft tissue contrast - Diffusible contrast agent - No penetration limit	- Expensive - Long acquisition time - Diffusible contrast agent
CT	~ 200 µm	- Simple quantification - Diffusible contrast agent - No penetration limit	- Ionising radiation - Toxic contrast agent - Diffusible contrast agent
Optics (OCT)	~ 5 µm	- Real time - Non-ionising	- Limited penetration (mm)
PET	~ 3 mm	- Good sensitivity - No penetration limit	- Ionising radiation - Lack of anatomical Information - Limited availability
US	~ 100 µm	- Real time - Non-ionising - Cheap - Intravascular contrast agent	- Limited penetration (cm) - Intravascular contrast agent

Table 1.2. Features of clinical imaging modalities for imaging the microvasculature.

1.2.4.1 OPTICS

Optical techniques provide the highest resolution of the commonly available imaging modalities, and are used effectively to characterise superficial vascular anatomy and function. Optical Coherence Tomography (OCT), and more recently phase variance

(PV) and speckle variance (SV) OCT have been able to provide high-resolution *in vivo* mapping of the microvasculature with the advantage of being non-invasive and providing localisation at high spatial and temporal resolution [51], [52]. Doppler OCT (DOCT, also known as optical Doppler tomography), has become an established tool for flow measurements and mapping blood vessels in the skin and retina [53]–[55]. This uses the phase changes or Doppler frequency shifts caused by the motion of particles to reconstruct images. These techniques are able to generate excellent 3D renderings of vasculature with micrometre scale resolution, and sub-millimetre per second blood flow sensitivity for complete assessment of microvascular structures *in vivo* [56]. There is, however, a major limitation with optical techniques caused by a spatial resolution that degrades rapidly with depth due to extensive scattering. It is therefore limited to 1-3 mm, and in some cases depth penetration only extends in the order of hundreds of microns, and hence application is limited to that of superficial vasculature.

1.2.4.2 MAGNETIC RESONANCE IMAGING

Magnetic resonance imaging (MRI) imaging uses no ionizing radiation and no intra-arterial puncture. It provides excellent soft tissue contrast enabling tissue segregation and volume quantification. Dynamic contrast enhanced MRI (DCE-MRI) uses the tissue distribution of paramagnetic contrast agents such as Gadolinium to estimate physiological characteristics such as perfusion pressure and blood flow [57]. DCE-MRI has been demonstrated to be able to quantify surrogate markers of tumour angiogenesis, such as fractional plasma volume and trans-endothelial permeability [58], [59]. High-field MRI and contrast enhanced MR angiography have shown resolutions of ~100 μm [60]–[62], but this is not sufficient for microvascular imaging [59], and there are some concerns regarding the safety of MR contrast agents [63], [64]. Furthermore, MRI is costly, requires long acquisition times, is not capable of real-time imaging, and is non-portable.

1.2.4.3 X-RAY COMPUTED TOMOGRAPHY

Contrast enhanced micro-CT enables imaging of small animals and organ biopsies with a resolution of 1 μm [65]–[67], however is not applicable to human imaging. High resolution CT has been able to visualise structures within the human lung equal to approximately 200 μm, said to be on the resolution limit of the technique [68],[69]. CT

has the advantage of a lower cost compared to MRI, with the ability to produce images of high resolution and excellent quality, but is limited by a high ionizing radiation exposure and contrast agent toxicity.

1.2.4.4 ULTRASOUND

While a variety of medical imaging modalities such as these have been developed for blood flow imaging in the body, none can directly image microvascular blood flow in intact tissues at depth. By comparison, US is the least expensive, the most portable, and has the potential for fast, real time acquisition, which are some of the reasons why it currently accounts for about one in four of all imaging procedures worldwide [70]. Furthermore, US does not expose the patient to ionising radiation and clinical US systems are designed to keep bio-effects negligible [71], [72], [73]. This makes US a powerful tool for medical diagnosis.

1.3 ULTRASOUND IMAGING

US is a wide ranging and continually advancing field, where innovations through the application of physics and engineering is paving the way for new and improved imaging technologies for diagnosis, treatment assessment and guidance of therapy [13], [70], [74]. Some excellent reviews provide an insight into developments in the extensive field of US imaging [70], [75], [76]. The following review focuses on the general characteristics and physics of US imaging, the achievable spatial resolution, and more specifically, contrast enhanced US (CEUS) for imaging the microvasculature.

1.3.1 TRANSDUCERS AND BASIC CONCEPTS

A transducer typically consists of many piezoelectric elements that convert electrical energy into mechanical vibrations in the form of sound waves, and conversely change mechanical vibrations from received echoes into electrical signals [77]. This mechanical energy propagates typically in the form of a pulsed wave from the surface of the transducer into soft tissue through the compression and rarefaction of particles of the medium. Sound waves are absorbed in part by tissue, but are also reflected, or scattered, back to the transducer where they are detected [78]. Acoustic impedance, defined as the product of the speed of sound of the medium and its density, is important in the determination of acoustic transmission and reflection at the boundary of two materials

having different acoustic impedances. The larger the difference in acoustic impedance, the larger the amount of sound reflected from a surface [77]. Standard Brightness mode (B-mode) grey scale images are constructed by the amplitude of the envelope detected received echo [79]. The amplitude and reception time of the received backscattered signals provide information about the acoustic properties of the medium at different depths in the sample. Resulting US images are generated from the combination of many acoustic radio frequency (RF) lines of pulse echo data, each representing the time record of scattered waves from different depths, which together form an image of the target structure. The processing capabilities of US scanners allow for the creation of real-time images for diagnostic use.

US systems vary considerably from low-end systems, to high-end, and from one manufacturer to another [79]. As such, on-board processing design and features vary considerably amongst clinical systems and it is often difficult to gather information on the exact processing performed on data prior to image generation. A schematic overview of a typical US processing pipeline can be found in Figure 1.2, and specific examples of processing features are discussed further in the following section.

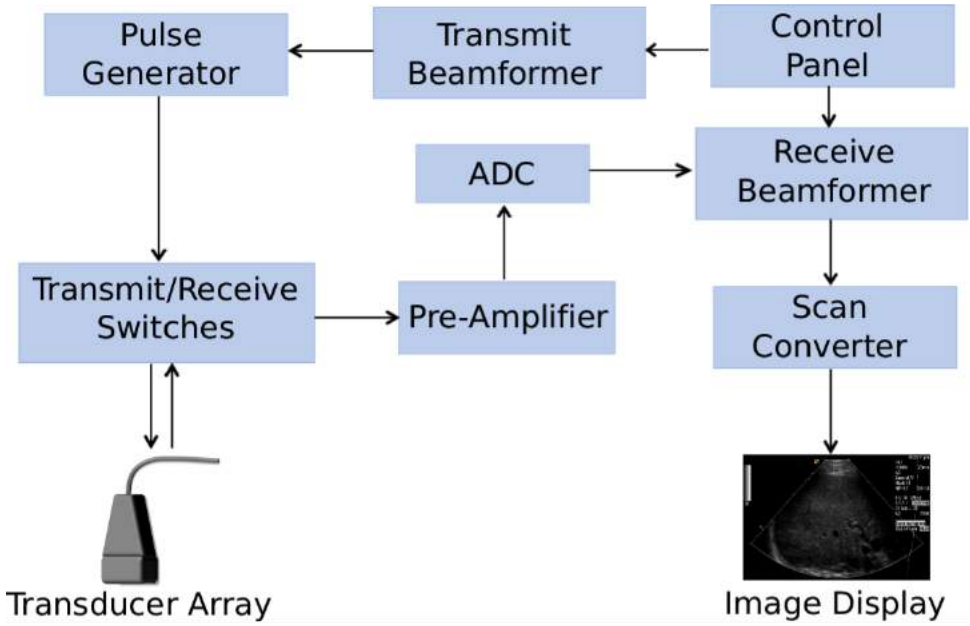

Figure 1.2. A typical US system pipeline showing an outline of US transmission, reception and processing. The arrows indicate the pathway of the US data through the system components. The beamformers generate electronic delays in an array to achieve transmit and receive focusing. In phased arrays it can also perform beam steering.

1.3.2 TRANSMISSION

1.3.2.1 TRANSDUCER AND BEAMFORMER

A single element or group of simultaneously fired elements in an array have a focal distance which is a function of the transducer aperture, the operating frequency, and the presence of any lenses on the element surface [80]. Transducer arrays, however, provide flexibility not available with a solid aperture, such as beam focusing and steering through the delay and weighting of individual elements [79]. Phased array and many linear array transducers of piezoelectric elements are able to transmit acoustic pressure waves with a waveform focused at a selectable focal distance in the field of view (see Figure 1.3). This is performed by the beamformer, which generates electronic time delays in an array to achieve transmit and receive focusing. Conventional imaging acquires data line-by-line by either varying the phase delays of all transducer elements to sweep the beam across the imaging region (phased array), or by activating a subset of adjacent elements sequentially to sweep across the region (linear array) [77]. A digital beamformer is often included in modern, high-end systems and would require the addition of a digital to analogue converter (DAC) [80],[81].

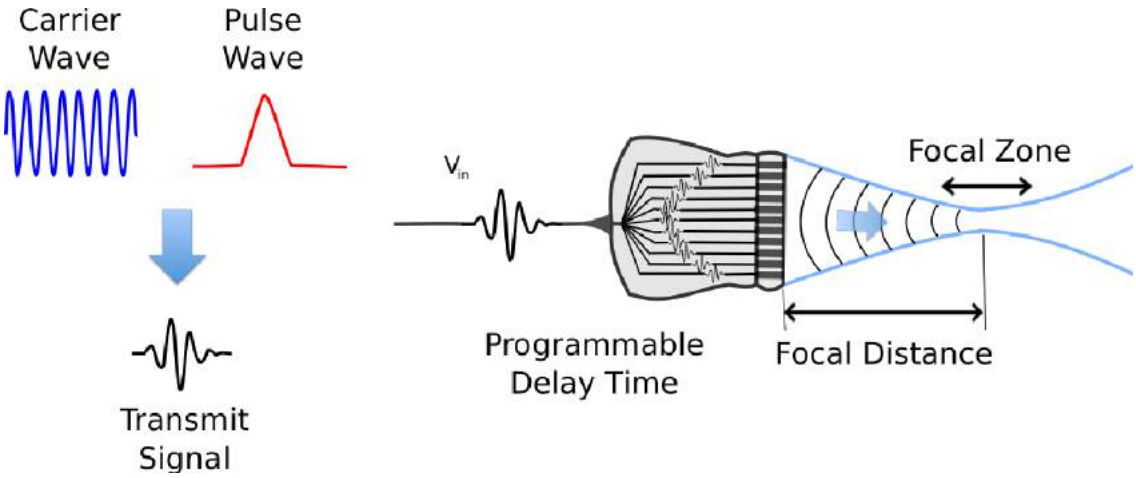

Figure 1.3. Illustration of transmission from phased array transducer. The transmission pulse is created from a modulated carrier wave. Focussing is achieved using programmable time delays of individual adjacent transducer elements. The minimum beam diameter occurs at the focal depth.

1.3.2.2 PULSE GENERATOR

Pulse generators provide the electronic signal designed to excite the piezoelectric elements to produce and transmit sound waves of specific frequency, pulse duration and pulse repetition frequency (PRF). Adjustment of the applied voltage controls the output amplitude of the signal. This must be carefully controlled; a high power will generate high intensity waves able to penetrate into the body and improve echo detection from deeper structures, however, the resulting power deposition in the body must be considered. Therefore, increasing the gain (see section 1.3.3.1), and lowering the frequency to increase penetration depth (see section 1.3.4.1) may be performed instead of increasing the output power [81].

1.3.2.3 TRANSMIT/RECEIVE SWITCH

Echo signals received at the transducer are considerably lower than those transmitted. Therefore the high voltages associated with transmit, and the sensitive receive electronics must be isolated from each other to some extent. The transmit/receive switch is synchronised with the pulse generator and switches to receive electronics once the vibrations associated with sound transmission has stopped.

1.3.3 RECEPTION

1.3.3.1 RECEIVE ELECTRONICS AND BEAMFORMER

Resulting echoes from scattering are received by multiple elements, however processing is first performed at the individual element level. Due to low voltage receive echoes, amplifiers are needed to strengthen signals to facilitate subsequent processing. Thus, the initial step following detection in processing is often time gain compensation (TGC). TGC amplifiers aim to compensate for the loss in signal caused by tissue absorption and attenuation with depth; this is performed by amplifying echoes received later in time to correct for the larger attenuation of signals traveling deeper into the medium [79]. Signals are then sampled by analogue-to-digital converters (ADCs) and processing such as the application of apodisation functions are applied. These apply different amplitude weightings to each of the elements in order to alter the shape of the beam. Receive beamforming is then applied: the signals received from individual elements are appropriately delayed to permit a coherent summation of the signals through fixed delay and sum beamforming, illustrated in Figure 1.4.

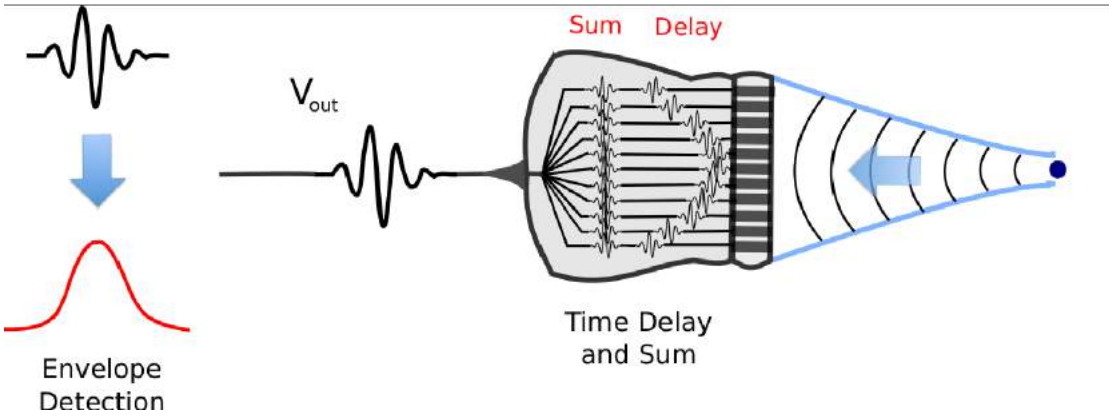

Figure 1.4. Illustration of reception and fixed delay and sum beamforming of pulse-echoes. The pulse received by transducer elements are individually delayed, then summed. Other processing may also be applied including time gain compensation (TGC), analogue-to-digital conversion (ADC) and band pass filtering, before being envelope detected.

Alternatively, dynamic beamforming can be implemented which uses continuously changing delays on received signals which track the received echo depth as they come from progressively deeper tissue. Beamformer operations are typically performed in application-specific integrated circuit (ASIC) or field-programmable gate array (FPGA) among others. FPGAs will be referred to again in Chapter 7.

1.3.3.2 POST-PROCESSING

Once the data is beamformed, depending on the imaging modes and US system, various processing is then carried out. Typically, the beamformed data is subject to various filtering operations such as band-pass filtering to reduce noise outside of the frequencies of interest [82]. In B-Mode, the most common practice is demodulation of the signals, which extracts the original signal from the modulated carrier wave. This can be performed using a number of methods, including IQ demodulation, which converts signals to real (I) and quadrature (Q) components, referred to as In-phase and Quadrature (IQ) data, and these can be combined to obtain the analytic envelope of the signal. This is often followed by log compression. This is performed for each scan line independently. Since the magnitude of the resulting complex signal is used for imaging, this processing discards the phase information contained within the signal [82].

DYNAMIC RANGE

The dynamic range is the ratio of the largest to the smallest signal that can be visualised. The maximum dynamic range of the human eye is in the order of 30 dB [79]. The range of received echo amplitudes falls under a large intensity range due to the need to image near-field strong echoes simultaneously with deep weak echoes. The attenuation of the signal with depth can be somewhat compensated by the amplification of signals using TGC. The actual dynamic range the system can observe (i.e. the ratio of the largest signal, to the to smallest discernable signal that can be processed by the scanner) depends on the ADC bits, and fundamentally the electronic noise level [82]. A user controlled dynamic range parameter on US scanners allows adjustment of this intensity range for display [79].

MECHANICAL INDEX (MI)

Another important system parameter is the user defined Mechanical Index (MI), which is directly related to the peak negative transmit acoustic pressure, p_N in kPa, and the frequency, f, in MHz, of the transducer, and is defined by

$$MI = \frac{p_N}{\sqrt{f}} \tag{1.1}$$

MI is an indication of the potential for mechanical bio-effects created by the US insonation; therefore in the U.S. the Food and Drug Administration (FDA) specifies a maximum MI of 1.9 $MPaMHz^{-1/2}$ for clinical investigations [83]. However, it must be noted that the value of MI given by Equation (1.1) is only an approximation, and the real MI value is spatially variant since the acoustic wave will be subject to attenuation and diffraction during propagation

1.3.3.3 SCAN CONVERTER

A variety of processing operations including several 2D noise reduction and image enhancement functions are often performed on the data before being displayed for human observation. The exact processing and their order depend on the system configuration and the processing already performed in other system components. These may include image smoothing, speckle reduction, and histogram equalization for improved image contrast [82]. The scan converter additionally interpolates the raw data

for generation of 2D output images to fit the desired display system for real-time video display [79], [81].

It is important to be aware of the various modifications applied to the original backscattered RF data in the image formation process when processing and analysing the image output data available from a clinical scanner. To analyse the images, the application of logarithmic decompression can be applied to attempt to obtain information relating to the original data prior to scan conversion. Additionally, the storage of the image typically involves an image compression procedure, such as JPEG compression, which uses perceptual coding for more efficient transmission and storage of images. Lossy compression techniques such as this are not 'bit-preserving' and some of the original data information is lost in the output image [84].

1.3.4 Spatial Resolution of Ultrasound Imaging

One major limitation in imaging the vasculature with US is the spatial resolution achievable using conventional systems, which currently lies in the range of hundreds of microns, to a few millimetres [81]. The ability of an US system to distinguish between two points at a particular depth in tissue, the resolution, is determined predominantly by the transducer, the wave properties, and system settings.

A fundamental physical property of a wave is diffraction. As the US transducer and receiver are of finite size, this phenomenon poses a limit to the achievable resolution of standard US imaging. For typical human scanning frequencies using contrast agents (~1-6 MHz, see section 1.3.6), the achievable in plane resolution is typically in the order of hundreds of microns. The overall beam shape is the product of the transmit and receive beams [79].

The acoustic pulse is a three dimensional object, where a resolution cell can be defined by the lateral and axial resolution, along with the elevational beam thickness, as illustrated in Figure 1.5. As can be observed, the beam width and pulse shape will vary across the acoustic field.

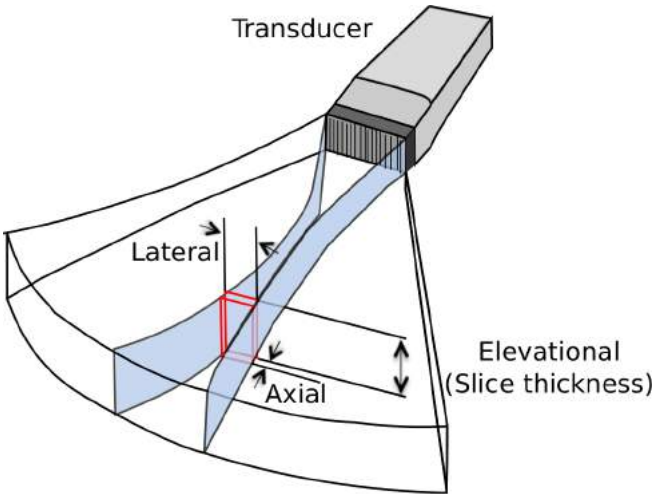

Figure 1.5 The axial, lateral and elevational components of resolution in three dimensions for a phased array transducer. The axial resolution in the propagation direction is dependent upon the US SPL. The lateral resolution is dependent upon the geometry and focussing of the transducer, and the elevational resolution is determined by the height of the transducer elements, along with the focussing of the focal lens. The minimal beam width occurs at the focus of the transducer. Both the elevational and lateral resolutions vary considerably with depth. Figure edited from [80].

1.3.4.1 AXIAL RESOLUTION

The axial resolution is the minimum distance that can be differentiated between two reflectors located in the direction of propagation. This requires that returning echoes are distinct from one another. The minimum required separation distance is equal to half the spatial pulse length (SPL), given by

$$Axial\ Resolution = \frac{SPL}{2} = \frac{N_c \lambda}{2} \tag{1.2}$$

$$= \frac{c t_p}{2}, \tag{1.3}$$

to avoid overlap in the returning echoes, where λ is the US wavelength, N_c is the number of cycles in the imaging pulse, t_p is the pulse duration, and c is the speed of sound in the insonified medium. The axial resolution thus increases with shorter spatial pulse length. Typical US imaging pulses consist of around two or three cycles, the number of which is determined by damping of piezoelectric elements after excitation. High damping reduces the number of cycles in a pulse, hence shortening the spatial

pulse length. The wavelength of a pulse is determined by the operating frequency of the transducer. Higher resolution can therefore be achieved by increasing the frequency and broadening the bandwidth, however, this is accompanied by a resulting loss in penetration distance and sensitivity due to attenuation [79], [81].

ATTENUATION EFFECTS AND RESOLUTION

Attenuation, the loss of acoustic energy with propagation distance, is caused primarily by scattering and tissue absorption. As the US beam travels through tissue layers, the amplitude of the original signal reduces as the depth of penetration increases and is dependent upon the attenuation coefficient of the specific tissue type. Attenuation hence limits penetration depth. This has significant effects on the resolution achievable using US. Firstly, during wave propagation, attenuation of the propagating wave energy effectively lowers the centre frequency of the propagating wave as it travels, and hence lowering the achievable resolution. Furthermore, higher centre frequency pulses are more strongly attenuated; this reduces the backscatter amplitude with depth, and thus penetration depth decreases correspondingly. As a consequence, high resolution is difficult to achieve at larger depths [79].

At a particular frequency, increasing attenuation with depth from the transducer is minimised by progressive amplification of the reflected pulses through TGC. Axial resolution of deep structures is thus comparatively low since a transducer of lower frequency is required. In these situations, excessive attenuation would preclude the use of high-frequency transducers, even after amplification of reflected US by TGC [78]. As an alternative, transducers which are able to get close to the structure of interest have been developed so that a high-frequency transducer can be used with high axial resolution. Examples of this practice are trans-oesophageal probes, as well high frequency endoscopic probes for colorectal tumour staging [85], [86]. The requirement for achieving high resolution at clinically useful imaging depths is however still required for many disease conditions which occur in deep tissues and organs.

1.3.4.2 LATERAL RESOLUTION

The lateral resolution reflects the ability to distinguish two objects in the lateral direction. The achievable lateral spatial resolution in an US system is inherently limited

by diffraction of the transmitted and received waves from a finite transducer aperture. This spatially variant resolution depends upon the wavelength and bandwidth of the US wave employed, the finite size of the transducer aperture, and the ~~transmit~~ focal depth [79]. Different geometries and focusing abilities will therefore result in variations in lateral resolution among transducer models and parameter settings. The lateral resolution for a flat, linear transducer is given by the -6 dB pulse-echo beam diameter at the focus [87], [88], given by

$$Lateral\ Resolution\ = 1.02\ \frac{F\ c}{fD}, \tag{1.4}$$

where F is the distance from the transducer to the focal point, D is the length of the aperture (i.e. the width of the elements used in the transducer) and f is the transmitted frequency [89]. Equation (1.4) shows that improvement in lateral resolution be achieved by increasing the aperture, but this will limit its suitability for use in the clinic, for example the practicality of patient imaging, in addition to the passing of the US beam through bone structures such as the ribs for cardiac imaging [89]. Increased frequency will also improve the lateral resolution, however this will come with inherent penetration limitations as discussed in the previous section. Other factors will also influence the achievable resolution in a target region. Phase aberration caused by tissue inhomogeneities destroys the focusing of the US beam, leading to a reduction in both the spatial and contrast resolution [90].

Lateral resolution is greatly enhanced by focusing using phased array transducers. For typical imaging frequencies between 1 – 15 MHz, the lateral resolution typically ranges between 3 mm to 0.3 mm [79]. Figure 1.5 illustrates the lateral and elevational planes of the US beam and their variation with depth and focus.

1.3.4.3 ELEVATIONAL RESOLUTION

The elevational width of the beam defines the slice thickness of the sampled volume perpendicular to the image plane and typically possesses the poorest resolution. The slice thickness has a significant effect on the image resolution, where volume averaging of acoustic features in the elevational direction can occur, particularly in the far field,

and in regions close to the transducer. Similarly to the lateral beam width, the elevational beam width depends on aperture geometry; however, here the dependency is on element height rather than width. A fixed focal distance is achieved by the use of a fixed focal lens across the surface of the array (no dynamic electronic focusing) [81].

1.3.4.4 POINT SPREAD FUNCTION (PSF)

The image of a stationary scatterer smaller than the size of the spatial resolution of the system can be estimated by the point spread function (PSF) of the system, and this characterises the spatial resolution of an imaging system [40], [79]. It should be noted however that the two dimensional image PSF is effectively a slice though the three dimensional response.

If it is assumed that the US imaging system has a linear and spatially invariant PSF, H, then the image of a point scatterer can be considered as the convolution of the point source, estimated as a Dirac Delta function, $\delta(x, y)$, with H. Since the PSF is not spherically symmetric as discussed in previous sections, it can be separated into the lateral, $H_2(x)$, and axial $H_1(y)$ component. The appearance of the point in the US image, $I(x, y)$, can then be described by the two stage convolution [91] given by

$$I(x, y) = H_2(x) \otimes H_1(y) \otimes \delta(x, y) \tag{1.5}$$

The PSF therefore describes how a point in the sampled space is blurred in the final image. Since the beam thickness and the axial resolution are spatially variant, they will, in reality, depend on the position of the point scatterer within the acoustic field. The displayed image is a projection of scattered signals along the elevational direction into the axial-lateral plane. The elevational beam width will thus be important in this thesis when considering scattering objects within the sampling volume of the transducer.

Figure 1.6 provides an illustration of the stages involved in the formation of a standard B-mode image of a point scatterer. Here, the point scatterer is convolved with the acoustic PSF as given in Equation (1.5), first in the axial direction, Figure 1.6B, and then by the lateral beam width, Figure 1.6C. This signal is then envelope detected using the Hilbert transform for image display, Figure 1.6D.

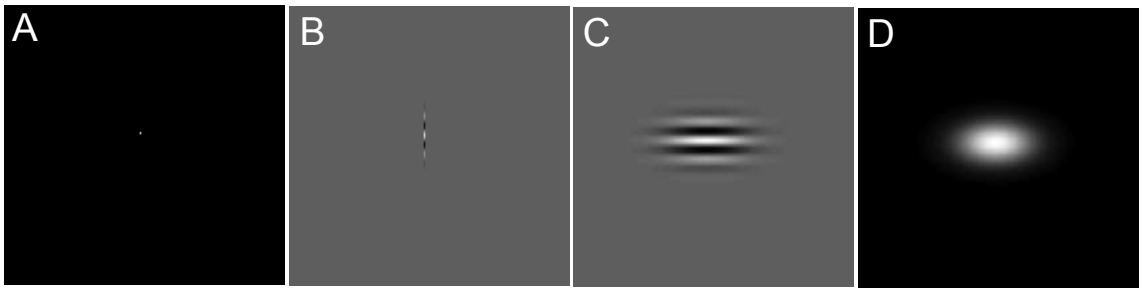

Figure 1.6. Illustration of the formation of the image of a point scatterer. Part (A) illustrates a point scatterer. Figure (B) and (C) show the convolution of the point scatterer with the axial pulse shape and the lateral beam width. Figure (D) shows the result following envelope detection using the Hilbert transform of (C). Figure inspired by [91].

An object that is significantly smaller than the spatial resolution of the system can be considered as a point scatterer. When detected, such objects appear larger than their true dimension due to the PSF [40], [79]. When two or more scatterers occur within the resolution limit, their signals interfere, and they become indistinguishable.

As discussed previously, visualisation of the microcirculation requires the resolution of structures under 100 μm in size, where the smallest vessels are under 10 μm (Table 1.1). As is evident in the approximate values of resolution discussed here, typical US imaging resolutions are not able to resolve microscopic structures within the microvascular bed. One such example of a sub-resolution sized object is the US contrast agent used to enhance visualisation of the vascular bed, the microbubble. The properties and application of microbubbles are discussed further in the following section.

1.3.5 MICROBUBBLE CONTRAST AGENTS

Visualisation of the vasculature in clinical US has been greatly enhanced with the development of microbubbles as contrast agents [13], [14], [92]. Microbubbles are micrometre sized gas encapsulated spheres, typically 1-7 μm in size, which exhibit a large backscatter signal as their resonance frequency matches the 1 to 15 MHz range of clinical US, which makes them an ideal contrast agent [12], [13]. Most modern microbubbles are composed of high molecular weight gases surrounded by a thin, biocompatible shell that inhibits diffusion into the surroundings, provides stability and prevents coalescence [93].

Microbubbles are used to enhance the signal from microvascular flow as the backscattered echo from red blood cells is much smaller in amplitude than the echo of the surrounding tissue [14]. Microbubbles are similar in size to red blood cells, and hence remain within the vascular space, allowing multiple passages through the lungs [13]. They therefore act as microvascular markers. Having the ability to resolve the structures containing these point scatterers would be an important step in the assessment of tumour microvasculature and other angiogenic diseases using clinical US [7], [12], [25].

When sound hits the microbubble, the bubble undergoes compression and expansion resulting in a volume pulsation causing the surrounding medium to oscillate, as illustrated in Figure 1.7 for SonoVue^{TM} (*Bracco* UK Limited) microbubbles. The returning echo is much stronger than that from similar sized red blood cells since the compressibility of gas inside the bubble allows large volumetric ~~bubble~~ oscillation~~,~~; furthermore, microbubbles of this size have a resonance frequency which falls within the medical US frequency range [76].

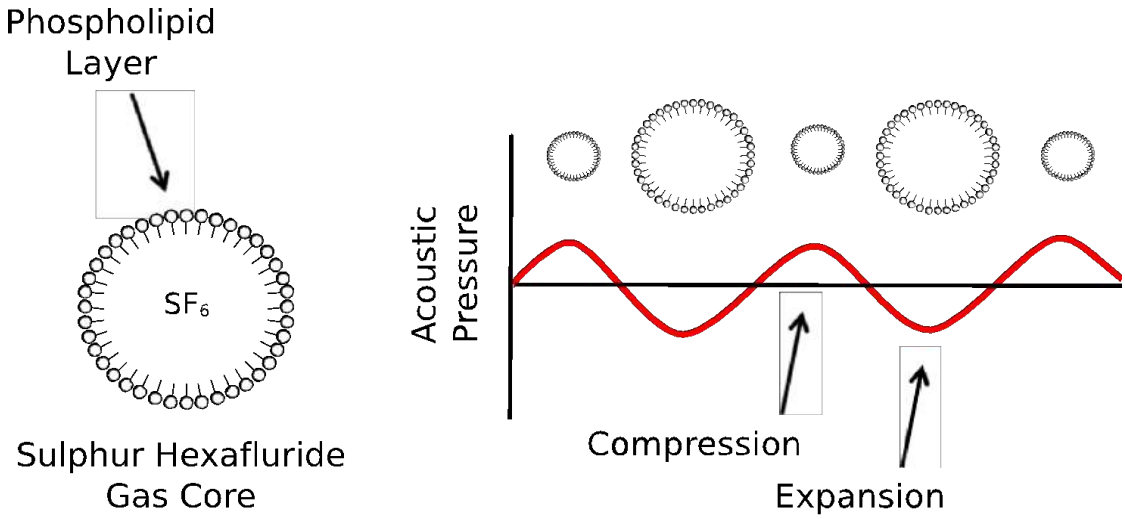

Figure 1.7. SonoVue^{TM} microbubble and its response to a sound wave. Microbubbles are comprised of a phospholipid monolayer, and a sulphur hexafluoride (SF_6) gas core. When insonated with a acoustic wave, the bubble undergoes compression and expansion phases, resulting in the creation of a backscatter echo.

At low acoustic pressures, the microbubbles oscillate linearly resulting in symmetrical scattered signals with the same frequency as the transmitted pulse. At higher pressures,

the microbubble vibrates with asymmetrical oscillations, where the expansion and compression amplitudes become unequal [94], [95]. This 'non-linear' response to the acoustic pressure wave generates a broad spectrum of radiated energy at multiples and integer sub-multiples of the insonating frequency, termed harmonics and subharmonics [76]. The nonlinear response of microbubbles lends itself to being used with selective detection strategies which can distinguish the nonlinear bubble echo from the predominantly linear signal of the surrounding tissue. There have been many signal processing techniques developed and these will be discussed in the following section.

At even higher acoustic pressures, the microbubble shell is compromised at a threshold negative pressure, and the microbubbles are disrupted which releases the contained gas, and dissolution occurs. CEUS therefore commonly uses a considerably lower MI than the FDA approved level stated above of between 0.05–0.4 $MPaMHz^{-1/2}$ to minimise bubble disruption [83]; however, the system-displayed MI in itself has been shown not to directly predict the amount of microbubble destruction, with other factors related to scanner and transducer settings also contributing to the outcome [96]. This phenomenon, although unfavourable in many imaging strategies, can however be advantageous in certain situations. Techniques such as destruction-replenishment allow the estimation of dynamic blood flow and volume information following the disruption and subsequent monitoring in real time of microbubble replenishment into a tissue region of interest [97]. This will be discussed further in Section 1.4.1.1.

In this thesis, microbubbles are used as a marker for the presence of vasculature, and are used to track the flow within the target microstructures. The beneficial properties of microbubbles for this work are summarised below:

- Similar in size to red blood cells so can emulate the same transit kinetics through the circulation.
- Remain within the vascular space so act as a marker.
- Nonlinear behaviour allows the use of bubble specific imaging techniques, which selectively detect nonlinearity from bubbles, while suppressing linear signals predominantly from background.
- Since this is an exogenous contrast agent, its concentration can be controlled.

Both the advancement in microbubble engineering [98] and the improved understanding of microbubble behaviour [94], has facilitated the progress of CEUS into a routine diagnostic procedure [99]. Great reviews of the mechanical properties, acoustic response, application, challenges, and future directions of microbubbles have been published [94], [99], [100] which demonstrates the wide recognition of these contrast agents as a valuable diagnostic tool. In this thesis, I will provide a summary of the use of microbubbles in CEUS, and specifically their role in imaging the microvasculature.

1.3.6 CONTRAST ENHANCED ULTRASOUND IMAGING (CEUS)

Through the development of microbubbles as US contrast agents, and the advent of advanced techniques to exploit the unique nonlinear response of microbubbles, US imaging specificity and sensitivity has improved. Multi-pulse imaging procedures such as Pulse Inversion (PI) and Amplitude Modulation (AM) [8] have provided improved resolution and signal-to-noise ratios (SNR) and have been shown to provide enhanced lesion visibility and diagnostic confidence [15], [39]. These techniques exploit the nonlinear signature of microbubble scattering in order to detect contrast agent in the blood, while suppressing linear signals. This can provide enhanced visualisation of perfusion; an example abdominal contrast enhanced image is shown alongside a simultaneously acquired B-mode scan of the same region in Figure 1.8. Here, visualisation of a liver lesion is greatly enhanced with the use of CEUS.

In order to increase the sensitivity of the detecting system for the microbubble signal, so-called harmonic imaging can be used. The probe receives at the double of the fundamental transmit frequency, where a low pass filter removes the fundamental signals [76]. Thereby, echoes at the fundamental frequency, produced by linear scatterers, are not detected. The second harmonic signal component of the bubble echo experiences higher attenuation, since these occur at higher frequencies, however, since they are generated by the bubbles, the received echo is enough to produce a substantial signal [81]. This technique, however, is not in itself ideal since the use of a low pass filter reduces the bandwidth, and hence reduces the resulting spatial resolution [81]. The development of techniques such as pulse inversion have been significant in improving this spatial resolution through the retention of wide band pulses [101], [102].

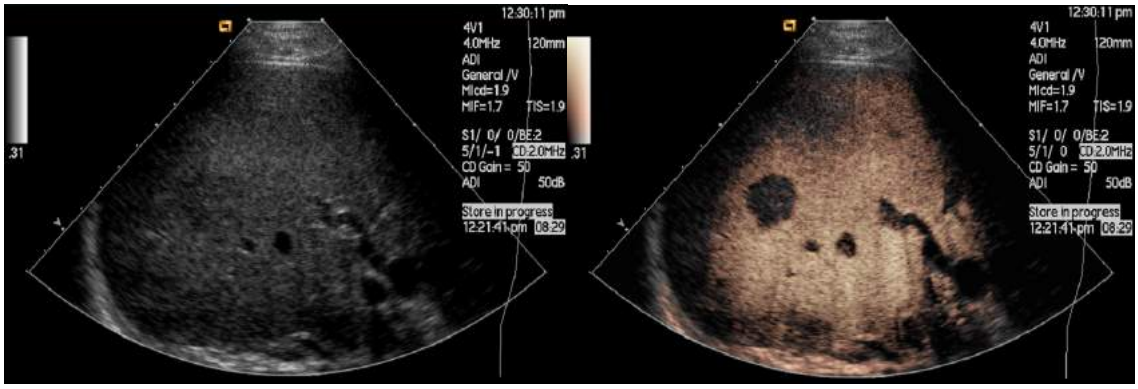

Figure 1.8. Abdominal US B-mode scan alongside sequentially acquired CEUS imaging, where a weakly perfused region corresponding to a liver lesion can be clearly visualised with the introduction of microbubble contrast agents. Figure acquired from Hammersmith Hospital courtesy of Prof. Cosgrove.

1.3.6.1 PULSE INVERSION (PI)

Pulse Inversion (PI), also known as pulse subtraction or phase inversion mode, involves the transmission of two successive pulses along each scan line, 180° phase shifted with respect to one another [101], [102]. When reflected by a linear scatterer, the two received echoes cancel each other when summed since they are out of phase. In the case of a nonlinear scatterer, however, the sum of the two echoes is non-zero as the initial phase difference of 180° is not conserved [103]. Figure 1.9A illustrates this schematically. As a result, the fundamental component of the echo cancels, but the harmonic component adds, doubling the magnitude of the harmonic level of a single echo [104].

1.3.6.2 AMPLITUDE MODULATION (AM)

In amplitude modulation (AM) [8], instead of inverting the polarity between the two pulses, the pulses are modified in amplitude. When the echoes are received, the amplitude difference will be compensated using a scaling factor before subtracting the signals, to remove the linear scattering. This is illustrated in Figure 1.9B. Alternatively, three consecutive pulses can be sent with amplitudes (½, 1, ½), and the scattered response from the half amplitude pulses are subtracted from the full amplitude response [105]. This results in echoes both having nonlinear signal at the fundamental and the 2nd harmonic frequency, however the 2nd harmonic part is lower than in PI [79]. This leads to conserving of the odd harmonic components in the processed echo signal. This holds some advantages over PI such as the ability to detect pressure dependent

nonlinear effects and increased sensitivity since the fundamental component contains the most energy and is least attenuated due to its lower frequency [106].

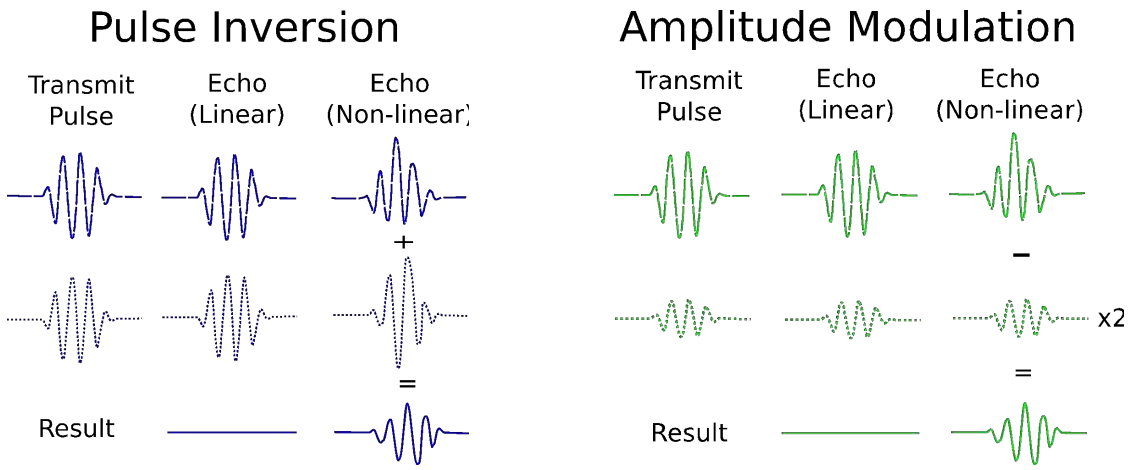

Figure 1.9. Principles of pulse inversion (PI) and amplitude modulation (AM). (A) PI: A positive (dashed line) and inverted (dotted line) pulses are transmitted sequentially along one scan line. Linear targets produce symmetric scattered echoes, while non-linear targets produce asymmetric echoes to those transmitted. Linear targets thus cancel upon summation, whereas residual signal remains for non-linear echoes. (B) AM: A full amplitude (dashed line) and scaled down version of the same pulse (dotted line) are transmitted as successive pulses, here shown for a scaling factor of 2. The amplitude difference will be compensated using a scaling factor before subtracting the signals, to remove the linear scattering. Alternatively, three consecutive pulses can be sent with amplitudes (½, 1, ½), and the scattered response from the half amplitude pulses are subtracted from the full amplitude response.

1.3.6.3 Alternative Multi-Pulse Sequences

Multi-pulse sequences where the amplitude of the pulses is modified, as well as inverting the phase, such as pulse inversion amplitude modulation (PIAM), have the advantage of both gaining a stronger second harmonic component than AM and a fundamental component which is not present in PI, while also maintaining the suppression of the linear signals [106]. Contrast pulse sequencing (CPS) refers to a more general strategy involving the transmission of a number of amplitude and phase modified pulses along each scan line, with corresponding weighting factors. By summing echoes from a suitable choice of transmission pulses and with appropriate weighting factors, detection or suppression of specific harmonics is possible [104], [107]. Typically only two pulse amplitudes are used, one being half that of the other,

and phase shifts of either 0 or 180 degrees, although variations of these do exist. A mode known as Cadence™ CPS will be implemented in some parts of this thesis, and involves the transmission of three pulses with amplitudes (½, -1, ½) and weightings (1,1,1); this is illustrated in Figure 1.10. This has been shown to have high microbubble sensitivity since echoes generated have a large second harmonic component [97].

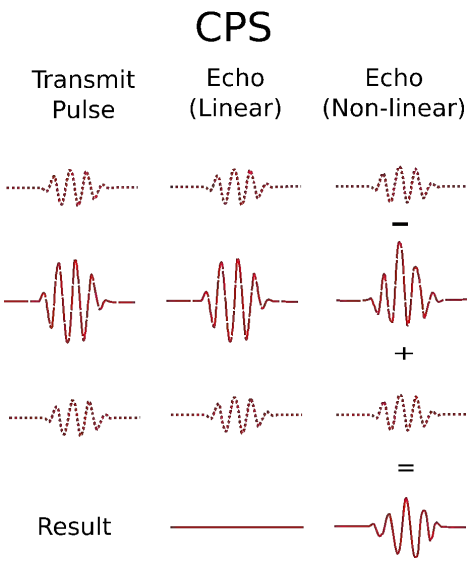

Figure 1.10. Principles of Cadence CPS pulse sequencing. Transmission pulses consist of multiple pulses varying in amplitude and phase. The illustration here is shown for 3 pulses: one half-amplitude pulse, followed by a full amplitude pulse, followed by a half amplitude pulse. When the pulses are scattered by a linear target they cancel, while generating residual signal when the scattered signals contain harmonic components from non-linear scatterers.

1.3.6.4 CEUS Summary

Disadvantages of multi-pulse schemes like these include a reduction in frame rate, as well as sensitivity to motion of single bubbles and bubble clouds [108]. However, through these methods, microbubbles allow a much improved visualisation of the vasculature [79], [104]. Despite this, the previously discussed resolution limitations mean that inadequate visualisation of discrete microscopic structures remains. Furthermore, the bubble size is far below the resolution limit of conventional US and their corresponding image is blurred.

CEUS has been applied to study wide ranging vascular conditions such as myocardial microcirculation and detection of abnormal blood perfusion of myocardium, renal and

hepatic blood flow and skeletal muscle flow responses to exercise [38], [97], [109]–[111]. As previously mentioned, characteristics of the capillary bed include slow flow velocity (around 300 μm/s), and minute vessel structures (often under 10 μm) with very low flow rates. These make imaging and quantifying the microcirculation very challenging [27], [112]. Currently, given the resolution limits of conventional clinical US imaging discussed previously, visualisation the microvasculature in detail is not possible, therefore functional and physiological surrogates are often estimated which monitor the kinetics of contrast agent distribution within tissue.

1.4 Literature Review

1.4.1 Current US Angiogenic and Microvascular Imaging Techniques

Several techniques have been applied in the US field to attempt to identify microvascular and angiogenic vessels. Advances in microbubble contrast agent imaging [76], [100], [113] and power Doppler [114], [115] are particularly significant in this regard.

1.4.1.1 Dynamic Contrast Enhanced Ultrasound

A well developed CEUS technique involves the generation of time intensity curves (TICs) following the passage of an intravenous bolus injection through a tissue of interest. These can be quantified to provide measurements for angiogenic assessment [116], where quantitative measurements aim to supplement anatomical or qualitative features with markers of vascular function [42] and provide an easy and direct measurement [117]. Many functional indices can be derived from these curves, including bolus arrival time, wash in/out curves, as well as more complex indices of blood flow and blood volume within malignant tissue. Furthermore, many existing CEUS approaches for perfusion quantification are based on features of the temporal and spatial distribution of the contrast agent during perfusion within tissue. Blood flow analysis and perfusion imaging has, however, been subject to a significant level of variability in imaging results [118], [119]. Flow analysis has been shown to be significantly affected by US system settings and imaging conditions such as insonation power, physical differences relating to individual patients, and target depth. Amplitude-

based parameters have been shown to be more influenced by system changes than time-related measures [83], [120]. These factors have resulted in diagnostic uncertainty and have impeded the clinical translation of some techniques. Further discussion of these approaches are included in Chapter 5.

1.4.1.2 DOPPLER US

Doppler US is the most widely used clinical imaging modality for accessing vessel flow, often used in imaging larger vessels such as the carotid artery, where typically a parametric map of blood speed is overlaid upon the corresponding B-Mode image. One significant benefit of Doppler US is that displays are dynamic in nature, often with real-time visualisation not available to all medical imaging modalities. These aid in conveying characteristics of tissue blood flow such as velocity, pulsatility, intermittency, and variations in time. As such, dynamic imaging can provide valuable additions to the static images reported in publications. The use of Power Doppler US along with quantitative image processing has been applied for the *in vivo* assessment of tumour angiogenesis, where differences in derived vascular indices were found when comparing early and advanced stage ovarian cancer [115].

Despite its wide clinical acceptance, active research in Doppler US continues. In particular, the extension of the velocity sensitivity and spatial resolution is important in the imaging and assessment of slower flows in smaller blood vessels of the microcirculation. In practice, the use of Doppler US at clinical frequencies to detect blood flow slower than a centimetre per second *in vivo* is challenging but possible [121]; velocities in the order of millimetres per second have been demonstrated using 40-60 MHz US frequencies, however will be limited in depth due to attenuation [11], [122].

Detection of angiogenesis using high frequency Doppler has been explored by several groups where the use of frequencies of around 50 MHz allows the assessment of flow dynamics in vessels as small as 15 μm [123]–[125]. By increasing the US frequency to the 40–100 MHz range, high-frequency US, or US biomicroscopy (UBM) [126], has been used to image tumour models in animal studies at high resolution [122]. Blood flow velocity on the order of a few millimetres per second in vessels as small as 20 μm

in diameter has been detected [127]. Velocities in the range of capillary flow (under 1 mm/s) have been detected in *in vitro* phantoms [124], [125]. One practical difficulty for this technique *in vivo* up until recently has been the lack of high-frequency multi-element transducer arrays, however, these have now become commercially available [128], [129]. While the use of high frequency US does allow improved resolution and the ability to map and measure microvascular morphology and flow, it is inherently limited due to the aforementioned compromise between frequency and imaging depth. US at 40 MHz range will provide resolution of approximately 60 μm, but will be limited to a penetration depth of around 5-6 mm, and therefore possesses a major limitation for clinical implementation [74], [126].

1.4.1.3 US ACOUSTIC ANGIOGRAPHY

High frequency US methods traditionally used for obtaining high resolution images have limited application due to the inherent compromise between higher frequencies and limited penetration depth [54]. Thus a new US imaging technique designed to limit the effect of this enhanced attenuation, while maintaining high resolution of contrast enhanced vasculature is acoustic angiography.

The potential of US acoustic angiography was first demonstrated by Kruse and Ferrara, where it was observed that microbubbles excited with short pulses at 2.25 MHz produced a transient response with frequency content that far exceeded 10 MHz [130]. Acoustic angiography has since demonstrated high resolution microvascular imaging by using dual-frequency transducers allowing excitation of microbubbles at low frequency close to their resonance using the low frequency element (often around 4 MHz), while the high frequency element (~30 MHz) is able to detect high frequency content from the microbubble echoes in the 15–45 MHz bandwidth. Since the high frequency is only present in receive, attenuation effects are reduced. The resulting images illustrate high resolution depictions of the microvasculature, with suppressed background tissue. This was able to provide similar level of resolution to that of photoacoustic tomography (see following section), and has been shown to be able to provide a resolution of approximately 150 μm down to approximately 5 mm depth with the expected potential for a greater depth of penetration of a few centimetres [131], [132].

The main challenge of this approach is the requirement for transducers which consist of both low and high frequency confocal elements, not common to standard US imaging transducers typically operating within a single frequency range. Such transducers are currently in the prototype stage and would require new designated equipment in the clinic. Furthermore, the technique has notable limitations; the likely need for bubble destruction to obtain the best signal, and more significantly, despite the reduction in attenuation effects owing to only using high frequency in receive, the resolution/attenuation trade-off still remains, and this will limit the achievable penetration depth.

1.4.1.4 PHOTOACOUSTICS

A recent hybrid US imaging technique called photoacoustic tomography (PAT) has been developed which detects the acoustic waves generated from an object by optical absorption after being irradiated with pulsed or intensity modulated optical waves [133]. This technique, and embodiments of it such as photoacoustic microscopy (PAM), photoacoustic computed tomography (PACT) and photoacoustic endoscopy (PAE) have shown impressive 3D renderings of microvascular structures *in vivo* [134]. This technique can provide sub-100 μm spatial resolution images of the microvasculature when using >10 MHz acoustic frequencies as well as additional functional data [135]. This technique, however, as with all standard US imaging techniques, suffers from the inherent trade-off between achievable spatial resolution and depth penetration, with estimated resolutions for optical resolution PAM (OR-PAM) of 5 μm laterally and 15 μm axially, but with a limit of 0.7 mm penetration depth [136]. This can be improved to a depth of 50 mm with ultrasound array based PACT (UA-PACT), but with a considerable reduction in the achievable resolution to 800 μm laterally and 300 μm axially [134], [137], [138].

In general, the majority of techniques developed for microvascular imaging do not have sufficient penetration depth to reach many structures of interest within the body, and have limited sensitivity to slow blood flows of the capillary. Additionally, many of these techniques require the development or implementation of specialised equipment for translation to the clinic. There is therefore clinical demand for a non-invasive, high resolution imaging technique able to resolve microvascular structures and

microcirculatory blood flow at depth.

1.4.2 SUPER-RESOLUTION OPTICAL IMAGING

In the last decade, localisation techniques which surpass the diffraction limit have revolutionised optical microscopy [139]–[142]. This has provoked widespread attention, including most notably the Nobel Prize in Chemistry 2014 being jointly awarded to Eric Betzig, Stefan W. Hell and William E. Moerner for the development of super-resolved fluorescence microscopy.

Conventionally, the spatial resolution of such a coherent imaging technique is derived from the wavelength used. This diffraction limit, about 200–300 nm in the lateral direction and 500–700 nm in the axial direction for conventional fluorescence microscopy, is comparable to or larger than many subcellular structures, leaving them too small to be observed in detail [143]. Sub-diffraction optical imaging is now a well-developed and continually advancing field, where three research groups independently developed and implemented the first methods of this kind, photoactivated localisation microscopy (PALM) [139], fluorescence photoactivation localisation microscopy (F-PALM) [142] and stochastic reconstruction microscopy (STORM) [140], which have been able to image live cell structures at nanometre scales [143].

The optical super-resolution field is continually advancing and as such, a snapshot of the current techniques and applications are discussed here. These methods use photoswitchable fluorophores to label biological samples. Randomly distributed fluorescent sources that are too close to resolve can be activated a subset at a time. Controlling the number of visible fluorophores in the imaging volume enables optically active molecules to be separated by much more than the width of the point spread function. The theoretically achievable localisation precision for a single fluorophore is therefore not diffraction-limited, and is now only restricted by the statistical (shot) noise [141], [144]. This allows individual protein positions to be estimated with high precision (the localisation precision can be as much as 10-times better than the diffraction-limited resolution) from the centroid of each spatially isolated fluorescent molecule [142]. After a series of acquisitions, a super resolved image of the structure is

then constructed by overlaying all the localisations, where structures on length scales shorter than the classical diffraction limit can then be visualised.

In STORM, two lasers and photo-switchable dyes attached to proteins of interest are imaged with a total internal reflection microscope (TIRF). Individual fluorescent molecules are switched on or off by using light of different colours (different in wavelength to the imaging light). Repeating imaging with different colour illuminations, where each causes a stochastically different subset of fluorophores to be turned on, enables the positions of many fluorophores to be determined and thus an overall image to be reconstructed. These have been demonstrated to provide imaging resolutions of approximately 20 nm, an order of magnitude higher than conventional light microscopy [140], [143]. PALM and FPALM implement the use of photoactivatable protein fluorophores and image using a TIRF and traditional confocal microscope respectively. For these photoactivatable molecules, the activation rate is controlled by the activation illumination intensity; the number of active fluorophores can be controlled photophysically by changing the rates of photoactivation and photobleaching by the illumination intensity of the laser used to excite the fluorescence. The fluorescence is imaged by a CCD camera, and then the molecules are either reversibly inactivated or irreversibly photobleached to remove them from the field of view [142].

The key feature of these techniques is that the number of point sources within an image must be sufficiently sparse that each individual fluorophore is spatially isolated so that it can be identified by an appropriate detection algorithm. The theoretically achievable localisation precision for single fluorophore scales with the inverse square root of the number of photons emitted by the protein. In practice, background and readout noise reduce the precision, however accuracies are still in the nanometre range. Furthermore, 3D imaging has been realised with various 3D single-particle localisation methods, including astigmatic imaging, which uses a lens to introduce depth dependent features in the two-dimensional image [145].

The requirement for multiple excitations of fluorophore subsets would imply that extended acquisition times are required to generate PALM and STORM images.

However, both STORM and PALM have demonstrated the ability to perform live cell imaging to record dynamic processes in living cells at the nanometre scale [146], [147]. The applicability of live cell imaging depends predominantly on the photo-physical limitations of the probe, its sensitivity, as well as the speed of the process to be imaged.

These sub-diffraction imaging techniques overcome the same fundamental physics seen in US due to diffraction, and have been able to provide previously unseen details of biological structures and processes in optics.

1.4.3 SUPER-RESOLUTION ULTRASOUND IMAGING

The successful implementation of sub-diffraction imaging in optical microscopy provides robust example methods from which underlying principles can be adapted to provide powerful sub-diffraction imaging in US, where depths of more than 10 cm are possible. Super-resolution techniques are a relatively new venture within US imaging. These draw upon significant gains seen within optical super-resolution in the aim of emulating a similar relative improvement in resolution for US.

The acoustic technique draws on the use of microbubbles to provide single detection events. Attributes of microbubbles discussed in Section 1.3.5 make them an ideal candidate for this use. Most importantly, their size means they not only create large backscatter signals, but they also remain within the circulatory system, and are significantly smaller than the spatial resolution of the US system, thus their image will be blurred by the point spread function (PSF) of the imaging system. This provides an opportunity to map microvessels at a sub-diffraction scale. Individual microbubbles densely packed within the resolution limit of the imaging system, cannot be resolved from each other. By spatially and temporally separating microbubble excitations, isolated signals can be obtained, where each bubble can then be localised to a much higher precision by determining its centre of mass. Thus, by combining the localisations of many bubbles flowing through a vessel, a super-resolved image of the vessel structure smaller than the diffraction limited resolution cell can be generated.

During the beginning of the work presented in this thesis, our group proposed and demonstrated the potential for super-resolution imaging using microbubbles. In our

initial study in 2013, [148], two adjacent 200 μm tube phantoms were resolved in super-resolved images, corresponding to a size 5.7 to 2.3 times smaller than the PSF of the imaging system. Here, a low concentration of microbubbles was passed through the microvessel structures in order to improve the probability of imaging spatially isolated bubbles, while reducing the chance of imaging multiple bubbles within one resolution sized area. Images were constructed by localising many spatially isolated microbubble signals over a series of image frames. This was performed at a low frequency of 2 MHz and at a depth of 4 cm; high frequency US imaging is generally limited to a depth of under 1 cm. This approach was achieved using image data from an unmodified clinical US system in a standard contrast enhanced mode and thus is directly transferable to the clinic. Following this work, the technique was demonstrated *in vivo*, where super-resolved images were able to visualise the microvasculature in a mouse ear, and furthermore, the development of a bubble tracking algorithm enabled the generation of velocity maps with super-resolved spatial detail [149].

To our knowledge, only three other groups worldwide work on similar ideas. Siepmann et al. demonstrated a similar idea by localising microbubbles using their centre of mass. This was performed using hard shelled microbubbles, Polybutyl cyanoacrylate (PBCA), at high frequencies of 40 MHz and using a linear B-Mode imaging strategy for molecular imaging [150]. An improvement was demonstrated in the vessel resolution compared to MIP at the same frequency in a mouse tumour xenograft. Due to the high imaging frequencies employed, gains in depth penetration were not demonstrated.

O'Reilly *et al.* 2013 [151] performed high-resolution vascular mapping of a tube phantom through an *ex vivo* human skull using a similar low microbubble concentration technique for the application of transcranial imaging. A sparse hemispherical receiver array and a passive beamforming algorithm were used to create a 3D image by scanning the transmit focus through a target volume. Phase and amplitude correction were applied to compensate for the aberrating effects of the skull bone. Results showed 70% of the localisations were found to lie within the expected tube diameter of around 255 μm. This transcranial imaging study showed the potential of this super-resolution technique to achieve high resolution imaging at depth in a challenging target area, and thus may also be able to enhance US imaging in other anatomical regions with suitable

array geometries and frequencies. Transcranial imaging such as this would, however, require specialised imaging equipment similar to those used in this study.

Independently, a study by Desailly *et al.* 2013 [152] demonstrated a super-resolution technique *in vitro* which used low frequency, high-frame-rate plane wave imaging and a high microbubble dilution (between 10^4 and 10^5 microbubbles per ml) to obtain high resolution images of microfluidic channels. The technique is based on the principle that when imaging a polydispersed microbubble distribution at an appropriate acoustic transmit pressure, microbubbles can be moved, destroyed or experience stochastic changes in their scattering characteristics over millisecond time scales. These changes are considered to be stochastic depending on the bubble's size and environment. In this way, the sources are said to be 'acoustically activated' and can then be localised beyond the diffraction limit. This approach uses frame rates above 100 Hz to visualise events occurring on the microsecond scale and was able to visualise the separation of channel structures below the imaging wavelength which were separated by between 50 – 200 μm. The efficiency of this technique is also dependent upon the number of scattering events identified in each frame, where in the reported values, approximately one localisation occurred in every 3 frames. Thus, with high frame rates such as this, acquisition time may predominantly be determined by the number of transient events occurring in each frame acquisition.

1.4.3.1 IS IT TRULY SUPER-RESOLUTION?

The term 'super-resolution' is well established in the field of optics [141], [143]–[145], [147], where 'super-resolution techniques' typically comprise those which can provide images with a higher resolution than the diffraction limit. The debate regarding whether 'super-resolution' is the correct term for our technique stems from the distinction between resolving objects within the sub-diffraction limit instantaneously to obtain the resulting image, compared to achieving images which resolve structures within the sub-diffraction limit without ever separating two objects within the diffraction limit at the same time.

In some parts of the literature, optical super-resolution techniques have been separated into two broad categories: those that are 'true' super-resolution techniques, and those

that are ‘functional’ techniques [153], [154]. These have been used to distinguish techniques which capture information contained within evanescent waves to break the Abbe limit (the diffraction limit of light), and those which use experimental techniques to reconstruct super-resolution images without separating any two objects within the resolution limit at any instantaneous point [154]. Functional super-resolution optical techniques, which include stochastic super-resolution techniques discussed previously (PALM, FPALM, and STORM), have far succeeded true techniques due to their low expense, simplicity and high resolution results [153].

In this sense, imaging in this project may be termed ‘functional’ super-resolution, in that microbubble signals are spatially isolated and localised over time in order to visualise vascular detail on a sub-diffraction scale. The name of the technique in this project is somewhat inconsequential, since the result is certainly achieved not by localising two microbubbles within the diffraction limit at any one instance, but the resulting image aims to be on a super-resolution scale. It is for ease and simplicity that the technique is termed super-resolution for the remainder of this thesis.

1.4.4 Critique and Current Challenges

Before the use of an acoustic super-resolution technique is accepted as a reliable tool for high resolution assessment of the microvasculature, a number of challenges must be addressed:

1. High resolution techniques tend to degrade considerably beyond a few millimetres in depth: In most of the established US (or hybrid) techniques discussed here, high resolutions are achievable at depths which are typically under 1 cm, and more often limited to approximately 5 mm for very high resolutions. Ideally, clinical techniques would be able to exceed these depths, and preferably image down to tens of centimetres.
2. High resolution techniques often require specialised or expensive equipment: Ideally, techniques would be easily implementable in conventional clinical scanners, and require limited extra cost to the healthcare system.
3. Techniques able to detect slow blood flows of the microcirculation are limited: The majority of imaging techniques are limited to detecting blood flow speeds of many

millimetres per second due to tissue/transducer motion which obscures the detection of low blood flow. High frequency Doppler US has demonstrated improved slow flow detection, but is currently limited in penetration depth.

4. Extraction of quantitative information: The opportunity to extract quantitative information is important to provide effective assessment of the microvascular environment. These may include structural quantitative measures such as microvessel density, tortuosity and diameter, or perfusion features and flow related clinical markers.
5. Ultrasound measures a 3D volume using 2D image acquisition: resolution is poorest in the elevational direction (slice thickness). Developing high resolution in three dimensions is important for complete microvascular assessment.

1.5 OUTLINE OF THESIS

The overall objective of this project is to develop and demonstrate acoustic super-resolution imaging with the goal of progressing towards resolving microvascular structures *in vivo* in humans.

1.5.1 AIM & OBJECTIVES

In order to effectively reach this global aim, a number of key objectives were identified.

1. Investigation of the achievable localisation precision using super-resolution imaging.

   The localisation precision is crucial in estimating the resolution improvement achievable using super-resolution US imaging, and therefore is required in the initial stage to assess the value and potential of the method.
2. Investigation and development of computer assisted analysis algorithms for single bubble signal detection.

   Algorithm development is critical to the identification and subsequent localisation of isolated, single bubble signals. Without accurate methods to identify these signals, interference, speckle and noise could jeopardise the method.
3. Implementation and analysis of the super-resolution technique on *in vitro* phantoms.

Initial implementation and demonstration of the technique in the first instance is required using *in vitro* phantoms; here, the underlying structure is known, and can be specially designed to assess its performance, in addition to highlighting associated challenges. This would provide an important transition from its theoretical basis, to practical demonstration of its potential resolution improvement.

4. Development and demonstration of *in vivo* super-resolution imaging.
   To enable translation into the clinical environment, challenges associated with *in vivo* imaging not present *in vitro* will need to be introduced, such as target motion, pulsatile blood flow, and more complex, branching vascular structures.
5. Exploration of the quantification of microvascular blood flow.
   The extraction of quantitative measures of blood flow in addition to qualitative images could aid clinical diagnosis, and thus presents a major opportunity for investigation.
6. Exploration of the translation of super-resolution imaging to 3D.
   The requirement for 3D implementation of super-resolution imaging is evident given the 3D nature of the majority of *in vivo* target structures. Thus, the transition from 2D to 3D imaging is an important step towards clinically valuable implementation.'

These have been defined as the objectives for this project, however, there are other equally plausible objectives to consider such as localisation accuracy and quantification. These have not been overlooked, they will be discussed in some detail in this project, but their full investigation should be performed within future work in this field.

1.5.2 SUMMARY OF THESIS

This thesis consists of 7 further main chapters. Chapter 2 introduces the theory of acoustic scattering, fast plane wave imaging and the principle and methodology behind acoustic super-resolution imaging. Chapter 3 consists of three distinct primary investigations: the estimation and investigation of the localisation precision available using a conventional clinical US scanner, initial *in vitro* validation and analysis, along with Poisson statistical predictions. Within this chapter, a bubble tracking technique is developed to allow estimation of flow velocities within the structures. In Chapter 4, the

technique is implemented *in vivo*, producing highly resolved images of the mouse ear vasculature. The algorithm is then extended to acquire quantitative measures for the assessment of microcirculatory changes in a clinical study of human lower limb perfusion in Chapter 5. Chapter 6 introduces machine learning techniques with the aim of investigating the use of automated and semi-automated post-processing algorithms for signal detection and differentiation. Finally, in Chapter 7 a fast, multi-probe approach is developed, which allows 3D super-resolution imaging and flow detection *in vitro*. The final conclusion will summarise results and provide an outlook on the challenges still facing acoustic super-resolution imaging. This overview provides the basis for the proposed future work presented within the conclusion of this thesis.

2 BACKGROUND AND THEORY

2.1 INTRODUCTION

In this chapter, the theoretical models used to describe the acoustic signal from a single bubble are presented, along with discussion on effects brought on by physical conditions such as their proximity to vessel boundaries or neighbouring bubbles, in light of their possible implications for super-resolution US imaging.

Models used to describe microbubble behaviour have developed alongside advances in US technology. One such advancement is the use of plane waves for fast US imaging. The acquisition and image generation procedures involved in plane wave imaging are outlined in comparison to conventional imaging discussed in Chapter 1; these plane wave procedures will be implemented in Chapter 7.

Lastly, the principle and method of acoustic super-resolution is outlined, and the key localisation techniques implemented in the study are described.

2.2 ACOUSTIC BEHAVIOUR OF SINGLE MICROBUBBLES IN ACOUSTIC FIELDS

2.2.1 SCATTERING FROM SMALL PARTICLES

The simplest mathematical description of the scattering of sound waves from a particle whose diameter is much smaller than the incident wavelength,

$$d \ll \lambda \text{ or } ka \ll 1, \tag{2.1}$$

is Rayleigh scattering [155], proposed in 1871 by Lord Rayleigh where d is the particle diameter, λ is the wavelength of the incident acoustic wave, $k = 2\pi/\lambda$ is the acoustic wavenumber and $a = \frac{1}{2}d$ is the particle radius [155]. The scattering cross-section of this model is given by

$$\sigma_s = 4\pi a^2 (ka)^4 \left[\left(\frac{K - K_0}{3K} \right)^2 + \frac{1}{3} \left(\frac{\rho - \rho_0}{2\rho + \rho_0} \right)^2 \right], \tag{2.2}$$

$$\sigma_s = \frac{\pi^5 d^6 f^4}{v^4} \left[\left(\frac{K - K_0}{3K} \right)^2 + \frac{1}{3} \left(\frac{\rho - \rho_0}{2\rho + \rho_0} \right)^2 \right], \tag{2.3}$$

[156] where v is the speed of sound in the medium. Rayleigh scattering therefore depends on the 4th power of the frequency, and 6th power of particle diameter. The bracketed term describes the dependence of scattering on the particle material parameters, given by the density,

$$\rho = \frac{m}{V}, \tag{2.4}$$

where m is the mass and V is the volume of the scatterer, and the bulk modulus, K, defined by

$$K = -V \frac{\Delta p}{\Delta V}, \tag{2.5}$$

where Δp is the change in pressure and ΔV is the change in volume, and thus is a measure of the compressional stiffness. Gas filled, elastic-shelled microbubbles are inherently compressible. If the bulk modulus of the scatterer is different to that of the surrounding fluid, K_0, then the particle will experience volumetric oscillations under acoustic insonation, and will act as a monopole scatterer where the scattered intensity is spherically symmetric [156], [157]. If the scatterer density is different to that of the surrounding fluid, ρ_0, the particle will experience translatory motion as it oscillates forward and backward within the acoustic field, and will subsequently radiate sound in a dipole pattern, where directionality is proportional to the cosine of the angle to the incident sound wave [156]. Therefore with a compressible sphere, the angle at which the Rayleigh scattering intensity vanishes depends upon the ratio between the density and compressibility of the particle and the surrounding medium [157].

The emitted sound pressure $P_s(r,t)$ from a compressible body capable of volume oscillations such as a bubble, insonated by an incident wave with pressure $P(t)$, can be separated into two main contributions. These are the contribution from the active emission of sound caused by bubble oscillations, and the passive contribution due to the perturbation of the density field in surrounding fluid caused by the presence of the bubble in the path of the sound wave [159]. In general for the case of diagnostic microbubbles, it has been shown that the passive contribution to the scattering cross-section is negligible; instead, it is almost entirely caused by the active component [159], and therefore is assumed to be spherically symmetric.

2.2.2 Development of Bubble Models

Following this discovery, in the mid 1900s, much research was conducted on the scattering of sound from gas filled objects, where an important theory applied was the resonance scattering theory. This aims to predict the frequencies of sound that are resonant with a particular size, core or shell [160]. As discussed in Chapter 1, microbubbles are highly compressible and therefore capable of volumetric oscillations. Furthermore, bubbles between 1-7 μm in diameter have a resonance frequency which falls within the frequency range conventionally used in diagnostic US imaging [76]. Thus, microbubbles return considerably stronger echoes than similar sized tissue

scatterers such as red blood cells, and making them extremely effective US contrast agents.

These relations are true for a linear scatterer, however, it is important to appreciate that the response of microbubbles is significantly more complicated, particularly at higher acoustic powers where bubble responses are non-linear. Furthermore, this model ignores both resonance effects and sound absorption by microbubbles in an acoustic field. The Rayleigh–Plesset equation is an ordinary differential equation derived from the Navier–Stokes equations under the assumption of spherical symmetry which governs the oscillatory behaviour of the radius of a spherical gas bubble in an infinite body of liquid [161]–[163]. Its general form is given by

$$\frac{P_B(t) - P_\infty(t)}{\rho_L} = R\frac{d^2R}{dt^2} + \frac{3}{2}\left(\frac{dR}{dt}\right)^2 + \frac{4\vartheta_L}{R}\frac{dR}{dt} + \frac{2S}{\rho_L R} \tag{2.6}$$

where, $P_B(t)$ is the pressure within the bubble, assumed to be uniform, $P_\infty(t)$ is the external pressure infinitely far from the bubble, ρ_L is the density of the surrounding liquid, assumed to be constant, $R(t)$ is the radius of the bubble at time t, ϑ_L is the kinematic viscosity of the surrounding liquid, assumed to be constant and S is the surface tension of the bubble. Provided that $P_B(t)$ and $P_\infty(t)$ are known, the Rayleigh–Plesset equation can be used to solve for the time-varying bubble radius $R(t)$. Many variants of this equation have been presented for studying the dynamics of encapsulated microbubble contrast agents in the conventional frequency range of 1–10 MHz, incorporating various microbubble encapsulations, shell parameters and surrounding liquids [5], [11]–[15], [156]. In this project, SonoVue™ microbubble contrast agents were employed. These are commercially available phospholipid shelled microbubbles with a perflurocarbon gas core (see Figure 1.7). The following section discusses some of the models relevant to this particular contrast agent.

2.2.3 Acoustic Scattering from SonoVue™

Encapsulated microbubbles were initially modelled by De Jong et al. (1992) and De Jong and Hoff (1993) by incorporating elasticity and friction into the established Rayleigh-Plesset model [169]–[171]. A recently developed model based on a modified

Herring model presented by Morgan et al. (2000) [172] includes shell parameters such as shell elasticity, χ, shell viscosity, μ_{sh}, and shell thickness ε, and is given by

$$\begin{aligned}\rho_L R\ddot{R} + \frac{3}{2}\rho_L \dot{R}^2 = \left(p_0 + \frac{2\sigma}{R_0} + \frac{2\chi}{R_0}\right)\left(\frac{R_0}{R}\right)^{3\gamma}\left(1 - \frac{3\gamma}{c}\dot{R}\right) \\ -\frac{4\mu_L \dot{R}}{R} - \frac{2\sigma}{R_0}\left(1 - \frac{1}{c}\dot{R}\right) - \frac{2\chi}{R}\left(\frac{R_0}{R}\right)^2\left(1 - \frac{3}{\mathrm{c}}\dot{R}\right) \\ -12\mu_{sh}\varepsilon\frac{\dot{R}}{R(R-\varepsilon)} - \left(p_0 + P(t)\right),\end{aligned} \tag{2.7}$$

where R_0 is the initial bubble radius, γ is the polytropic gas exponent, P is the pressure, in the surrounding fluid, and p_0 is the ambient pressure. Here, $\dot{R} = \frac{dR}{dt}$ and $\ddot{R} = \frac{d^2R}{dt^2}$, representing the velocity and acceleration of the bubble wall. The bubble resonance frequency, f_0, can be analytically derived from equation (2.7), and is given by [171],

$$f_0 = \sqrt{\left(\frac{1}{\rho {R_0}^2}3\gamma p_0 + \frac{1}{\rho {R_0}^2}(3\gamma - 1)\frac{2\sigma}{R_0} + \frac{1}{\rho {R_0}^2}(\gamma - 1)\frac{6\chi}{R_0}\right)}. \tag{2.8}$$

This model has been shown to correlate with experimental results for SonoVue™ microbubbles using high speed optical imaging [171], and places the range of resonance frequencies for bubbles of diameter between 2-4 μm, at 4 – 1.5 MHz.

2.2.4 MICROBUBBLES IN SMALL VESSELS

As previously discussed, modelling the dynamics of microbubbles has principally been focused on modifications of Rayleigh-Plesset bubble dynamics equations, using the assumption that a single microbubble is surrounded by an infinite fluid, and remains spherical until it collapses [173]. These have been demonstrated to work well in predicting experimental results for free bubbles or bubbles in large vessels [174]–[176].

In the body, microbubble dynamics within small vessels may not be well approximated by this assumption since the proximity of a tube wall or boundary to a single microbubble is known to affect microbubble oscillations [177] and has also been shown

to induce non-spherical shape deformations [178]. The investigation of the effect of a rigid tube boundary on gas bubble natural frequency predicted that the natural frequency of a bubble in a rigid tube decreases with decreasing tube radius and with increasing bubble radius [179]–[181]. Caskey et al. 2006 recently studied the oscillation of microbubbles using high speed camera images in capillary-sized tube phantoms (diameters: 12, 25, and 195 μm), where the bubble's expansion ratio in a rigid capillary phantom was found to be substantially decreased as compared to the prediction of the Rayleigh-Plesset model for microbubbles within an infinite liquid [182]. In an experimental study performed at 50 kPa, the amplitude of oscillations of microbubbles in tubes with inner diameter 25 μm were 50 % lower than those in a 160 μm tube using an ultra-high-speed camera [183]. Furthermore, the number of microbubbles that did not oscillate above the noise level of the system increased by 48% in the smaller tubes, indicating increased oscillation damping. However in this study, no difference was observed between the microbubble resonance frequency curves between the tube sizes [183]. Single microbubble acoustic measurements were also performed in narrow tubing, where increased harmonic scattering was found for Definity™ (Bristol-Myers-Squibb) and biSphere™ (Point Biomedical) microbubbles oscillating within smaller tubes of 50 μm diameter and higher rigidity, compared to 200 μm tubes [184], [185]. However, the different tube materials (of varying rigidity) may have affected the acoustic field within these experiments.

True capillaries, however, are not rigid structures. These effects were therefore further investigated in models of compliable vessels [173], [186]. It was found that the resonance frequency of oscillation of a bubble in a compliable vessel increases with decreasing vessel size, while decreasing with increasing values of vessel rigidity. The natural frequency of a bubble in the unbounded field was found to be the lower limit of the bubble natural frequency in the compliable vessel. For a bubble with the same initial radius, when the vessel size approaches the bubble size, the effect of the compliable vessel is enhanced. In small vessels (diameter ≤ 40 μm) the compliable vessel boundary had a noticeable effect on the bubble oscillation frequency, while for larger vessels, the resonance frequency could be approximated by the Rayleigh-Plesset equation [186]. In a study by Garbin et al. (2007), it was hypothesised that an effective pressure-dependent threshold microbubble diameter exists, above which single polymer-shelled agents

respond to acoustic interrogation close to a boundary [187]. Although capillary walls are typically formed of a single layer of endothelial cells, their compliance is not only dependent upon the rigidity of the vessel, but in addition, that of the surrounding tissue [173].

Each organ has a unique capillary network. Microbubble behaviour will therefore be influenced by the characteristics of their microvascular environment. Additionally, it has been shown that the presence of a neighbouring bubble considerably suppresses bubble oscillations while retaining the spherical symmetry of both bubbles; this result has been attributed to a shift in resonance frequency [177].

These models and experimental results suggest that microbubble size, blood vessel size distribution, and the type and surroundings of vasculature are crucial in the response of microbubbles to the transmitted frequency in CEUS [185], [186].

2.3 IMAGE ACQUISITION

2.3.1 DEVELOPMENT OF US IMAGING

Microbubble behaviour has been investigated alongside continual developments in US technology to image these contrast agents. One advancement aimed at providing considerably enhanced frame rates is the use of plane wave US imaging as opposed to 'conventional' US scanning.

2.3.2 CONVENTIONAL CLINICAL US IMAGING

Conventional clinical US scanners and linear array probes are employed within Chapters 3-6. These acquire data line-by-line using focused pulses by activating a subset of adjacent elements sequentially to sweep across the region as described in Chapter 1. Image output data available from a clinical scanner is thus utilised in the aforementioned chapters.

2.3.3 FAST PLANE WAVE US IMAGING

Conventional US imaging with line-by-line focused pulses (Figure 2.1A), however, limits the highest achievable time resolution. Ultrasonic plane-waves are generated instead by transmitting from all (or a large set) of transducer elements without focusing

delays and allow insonification of a large field of view with each transmission (Figure 2.1B) enabling fast frame rates often over 1000 frames per second [188]–[191]. If one wave is sufficient to create an image frame, then the frame rate is equal to the PRF.

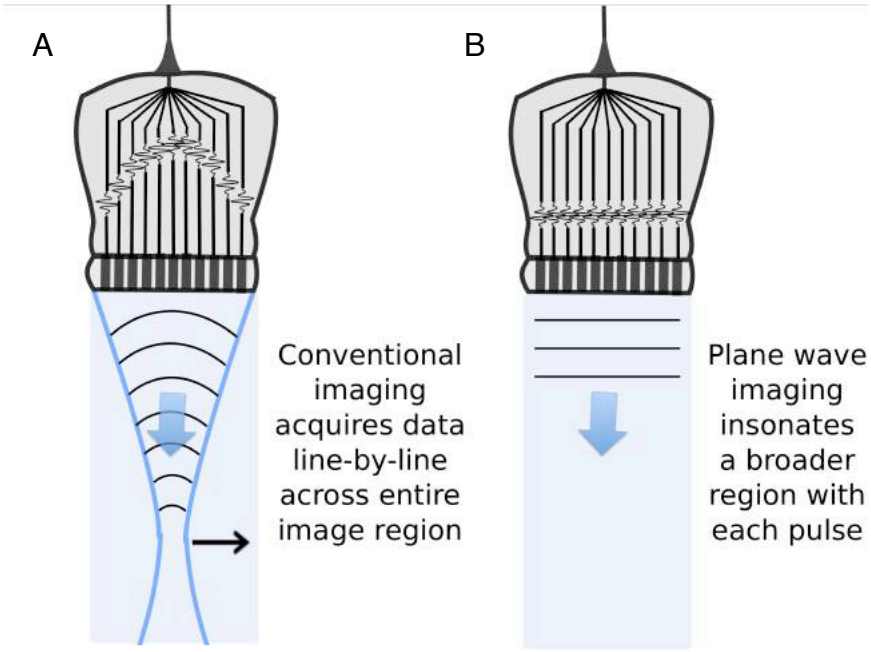

Figure 2.1. Illustration of conventional US phased array imaging and plane wave imaging. Conventional imaging acquires data line-by-line by either varying the phase delays of all transducer elements to sweep the focus across the imaging region as shown here (phased array), or by activating a subset of adjacent elements sequentially to sweep across the region (linear array). Plane wave imaging uses unfocused pulses to insonate a broad region in one insonation offering higher frame rates, however, post-processing methods must be implemented to restore image quality.

2.3.3.1 BEAMFORMING

As discussed previously, when a small scatterer is insonified by a plane wave, it can be assumed to emit a spherical wave. This is detected by each of the individual parallel linear array elements subject to delay arrival times depending on the absolute distance from the scattering object. Coherent plane-wave compounding is the coherent addition of echoes from several successive plane waves transmissions, which can be tilted at different angles. This technique was first proposed in 2004 [192]. Beamforming techniques to improve the spatial resolution of plane wave imaging have been increasingly studied with the emergence and proliferation of fast plane wave imaging

techniques in recent years [189], [193]–[196]. In this work, a technique proposed by Montaldo et al. 2009 [189] was implemented to create a whole image frame from the simple case of a single angle acoustic plane wave; the basic principle is illustrated in Figure 2.2.

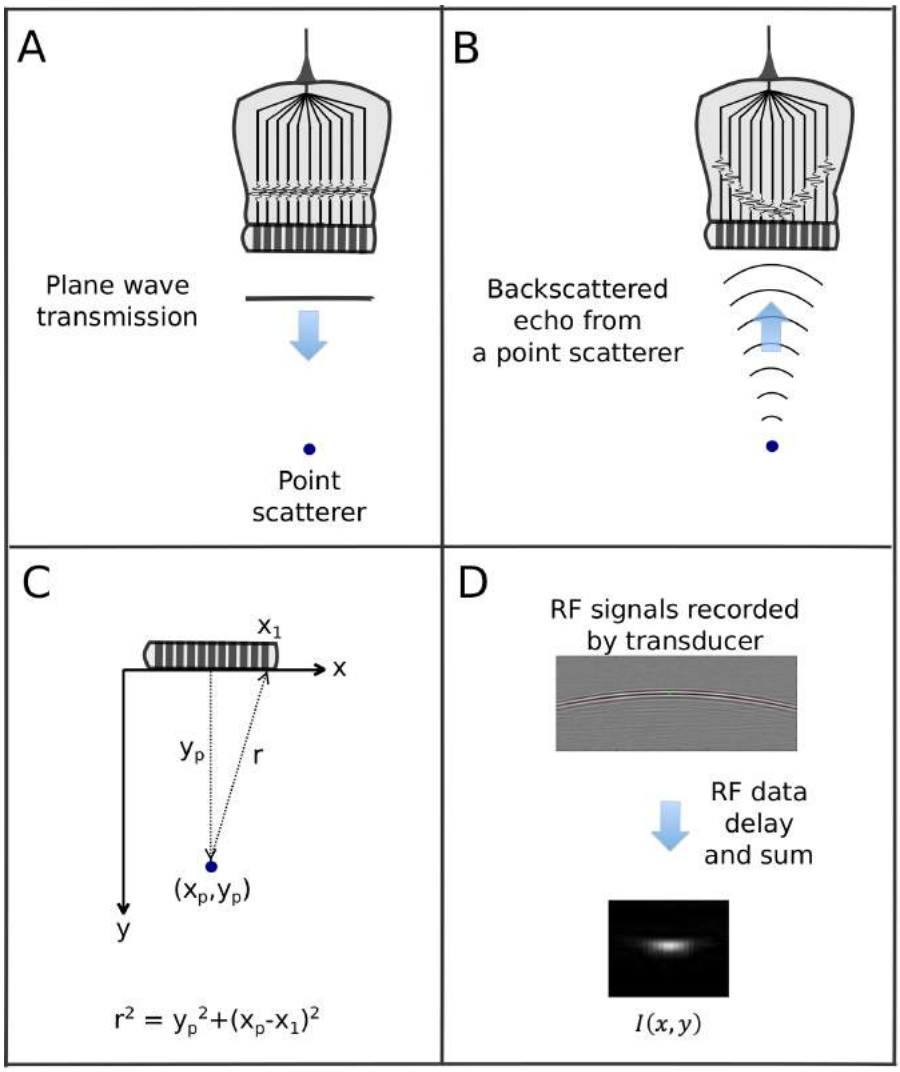

Figure 2.2. (A) Plane wave transmission. (B) Backscattered echo from a point scatterer. (C) Geometry of echo signal from plane wave provides time delays. (D) RF signals received at the transducer are delayed and coherently summed using Equation (2.10) to produce image $I(x, y)$. Figure inspired by [189].

In this method, since there is no transmit focussing, image resolution is attained during reception using parallel processing in the following way. Transmitted plane waves from the entire transducer aperture, of size $2a$, insonate a broad field of view (see Figure

2.2A) [189]. Echoes originating from a specific point within the region, (x_p, y_p), are received at individual transducer elements, subject to a time delay, $\tau(x_1, x_p, y_p)$, equal to

$$\tau(x_1, x_p, y_p) = \frac{y_p + \sqrt{{y_p}^2 + (x_1 - x_p)^2}}{c}, \tag{2.9}$$

where c is the speed of sound in the medium and $x_1$is the transducer element (see Figure 2.2B and C). After applying these delays to the received RF signals, $RF(x_1, t)$, the echoes from scatterers can be coherently summed. Thus, each point (x_p, y_p) of the image, I, is obtained by adding coherently the contribution of each scatterer in the array direction x_1, given by

$$I(x_p, y_p) = \int_{x_p - a}^{x_p + a} RF\left(x_1, \tau(x_1, x_p, y_p)\right) dx_1, \tag{2.10}$$

[189]. The source of the echo can then be estimated by fitting these arrival times with a time-of-flight model assuming a homogeneous medium. A reconstructed image of the scatterer is thus obtained (Figure 2.2D). Nevertheless, since the beamforming process is restricted to the receive mode, the US images obtained from plane wave transmission suffer from a compromise in image quality without techniques such as coherent compounding of many angled plane waves which has been shown to improve the resolution and contrast while still improving frame rates to standard scanning techniques [189]–[191], [197].

2.4 Super-Resolution Acoustic Imaging with Microbubbles

As with all wave-based imaging techniques, US faces a resolution limit due to the diffraction of waves as they travel from a finite source, and thus two objects are indistinguishable from one another if they are located within a distance proportional to the US transmit wavelength (Equation (1.2) and (1.4), Chapter 1). This distance typically falls between 100 μm and 1 mm in clinical applications.

At common clinical concentrations, a cloud of microbubbles can be considered as a random distribution of Rayleigh scatterers. However, although the image of a point scatterer is a finite sized blur represented by the PSF, the precision at which an isolated scatterer position can be determined from its image can be significantly higher than the diffraction limit [139], [140], [198], [199]. The lumen of a vessel can ultimately be defined by all the spatial positions existing within its vascular walls. It is thus conceivable that acoustic super-resolution can be achieved by determining, to very high precision, the position of objects that flow solely within the vessel structure, and generating a US image using these spatial coordinates.

The acoustic super-resolution imaging procedure proposed is illustrated in Figure 2.3. This involves the injection or infusion of a low microbubble concentration; a low concentration in this application is one which provides a high probability of imaging spatially isolated bubble signals in the target of interest (Figure 2.3A). Each of the bubble positions can then be estimated using methods to deconvolve the scatterer signal (Figure 2.3B - D), with a localisation precision determined by characteristics of the US system, image acquisition parameters and processing methods. Approaches which can be employed to obtain this high precision localisation are discussed in Section 2.4.1. By acquiring a series of image frames (Figure 2.3E), these signals can be individually separated in space and time; an image of the confining structure can then be generated by superimposing the localised bubble positions from the series of frames, (Figure 2.3F), onto a single map, (Figure 2.3G). This should provide an image where the resolution is no longer limited by diffraction, but visualisation of structures is now dictated by the localisation precision and the density of localisations in the final image.

The use of low concentrations of microbubbles creates several key advantages. Firstly, as mentioned above, the dilution allows for the detection of spatially and temporally isolated microbubble excitations within the imaging field of view, enabling the deconvolution of the microbubble signal and consequential microbubble localisation over many image frames. Secondly, the spatiotemporal observation of microbubbles allows for the measurement of bubble velocity, and hence the measurement of local haemodynamic information due to their similarity to red blood cells [200], [201]. Thirdly, by employing a low bubble concentration, the majority of sources have a

separation distance between them, which is expected to reduce the likelihood of bubble-bubble interactions which could change each individual bubble signal and/or signals from both bubbles will not be separable, and hence potentially reduce the accuracy of the localisation.

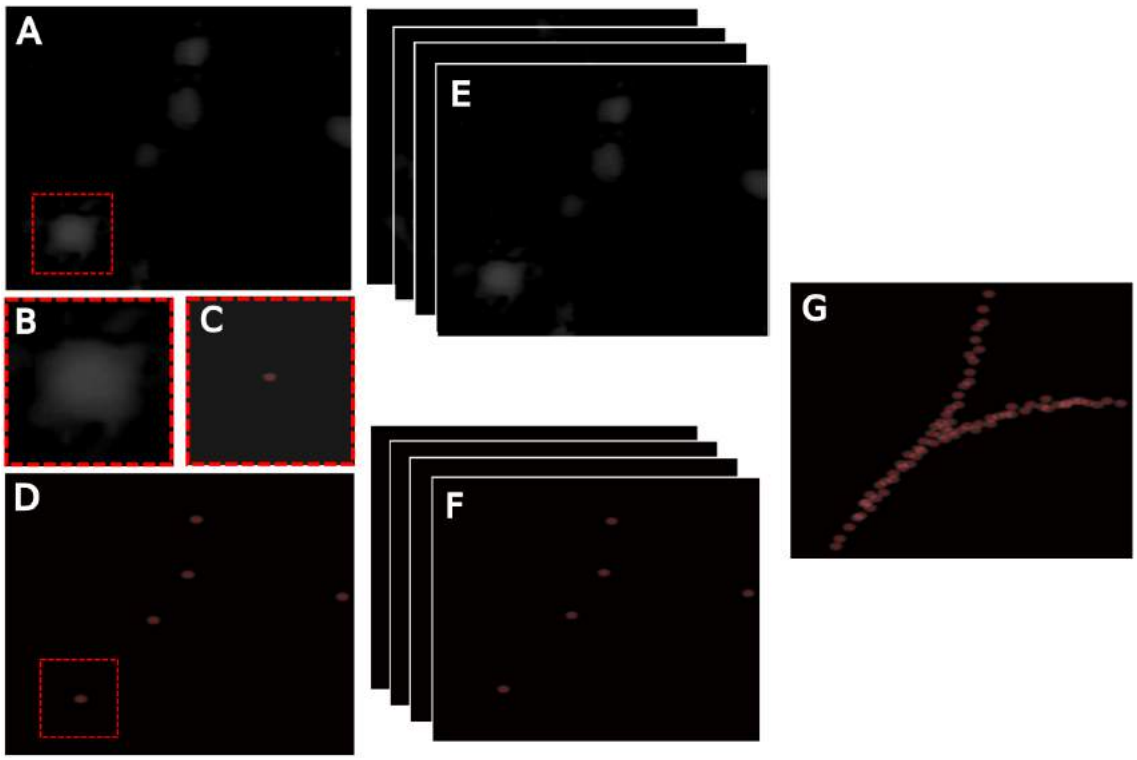

Figure 2.3. Acoustic super-resolution imaging outline. (A) Image frame containing spatially isolated bubble signals, such as that enlarged in (B). Localisation of the isolated signal is shown in (C), where each signal provides a localisation within the field of view. Acquisition of multiple frames containing bubble flow, such as that shown in (E), allows superposition of all detected localisations, (F), in a final image map revealing the structure of the underlying vessel structure, as demonstrated in (G).

The major challenge of acoustic super-resolution is to detect a sufficient number of separable sources in each frame to achieve super-resolved maps of vessels within a practically useful acquisition time. Another crucial factor in the success of this technique is the method of obtaining bubble localisations.

2.4.1 Localisation Techniques

So far in optical microscopy, super-resolution techniques have mainly implemented variations on Gaussian model PSF fitting to obtain localisations due to its simplicity and

computational efficiency, despite the lack of physical foundation [139], [141], [143], [199], [202], [203]. Differences were found in its suitability dependent upon whether or not the dipole was freely rotating or possessed a fixed orientation and, as such, the achievable localisation accuracy is affected by the suitability of the PSF model [202]. The issue of how to precisely model the PSF in agreement with the laws of optics has been addressed by a number of groups and remains under investigation. The simplest alternative to fitting is calculating the centre of mass, or centroid. A number of super-resolution microscopy analysis methods use centroiding estimates [204], [205] and it has been shown to have advantages when performing localisation of moving fluorophores and single particle tracking [206], mainly due to the requirement for minimal assumptions about the image shape.

2.4.1.1 CENTRE OF MASS

If it is assumed that the microbubble undergoes spherical oscillations under US insonation, and that a microbubble is unaffected by interactions with neighbouring bubbles and boundary walls, then its image would be blurred by the PSF of the imaging system, and the location of an individual bubble can be estimated by the centre of mass of the spatially isolated bubble signal. The centre of mass of a signal distribution is the unique point where the weighted relative position of the distributed signal pixels sums to zero. The distribution of the signal is thus balanced around the centre of mass. The calculation of the intensity weighted centre of mass, or 'centroid', $[C_x, C_y]$, of the scatter signal in the image, can be given by the average of the weighted position coordinates of the distribution,

$$[\mathrm{C_x}, \mathrm{C_y}] = \frac{\sum_\mathrm{i} \mathrm{I}(\mathrm{x_i}, \mathrm{y_i})[\mathrm{x_i}, \mathrm{y_i}]}{\sum_\mathrm{i} \mathrm{I}(\mathrm{x_i}, \mathrm{y_i})} \tag{2.11}$$

where i are the pixel indices in the region, $I(x_i, y_i)$ is the intensity of the pixel located at (x_i, y_i), and $[x_i, y_i]$ represents the coordinates at the pixel i. Here, the assumption is that the geometric centre of the signal region represents the location of the underlying scatterer. An illustration of the centre of mass algorithm is shown in Figure 2.4. The coordinates of the centre of mass are at a sub-pixel scale and thus can be plotted in super-resolution images with micrometre scale pixel sizes.

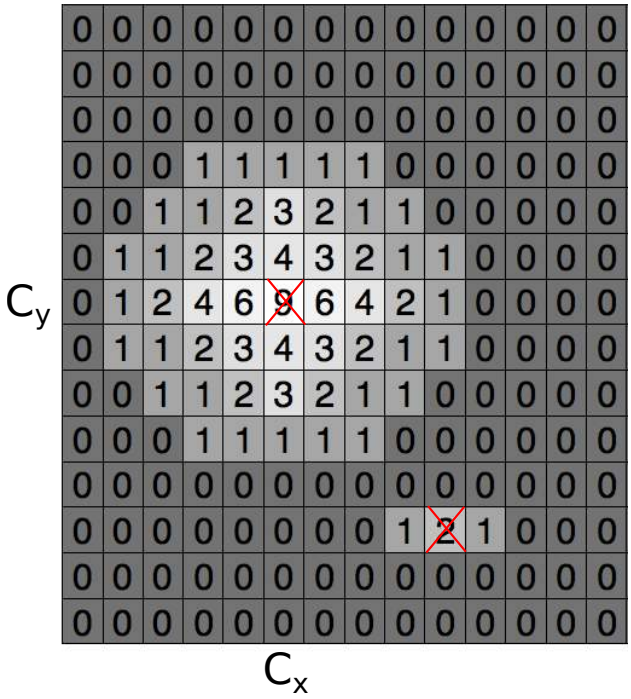

Figure 2.4. Illustration of the centre of mass algorithm. All connected regions of non-zero pixels within the binary image represent foreground regions. The centre of mass algorithm is applied to foreground regions, where $I(x_i, y_i)$ is the intensity value at the pixel located at (x_i, y_i), and C_x, C_y are the coordinates of the centre of mass of the regions represented by the red crosses. The smaller region represents a non-bubble signal which may be removed with rejection criteria.

2.4.1.2 Model Fitting

An alternative method of estimating the position of a point scatterer relies on fitting a model PSF to the measured pixel data and determining the position of its peak. For an image based analysis, this will be a 2D PSF model. This PSF is the impulse response of the imaging system and is assumed to be close to that of a Gaussian profile, given by

$$f(x,y) = \mathrm{A}\exp\left(-\left(\frac{(x-x_0)^2}{2\sigma_x^2}+\frac{(y-y_0)^2}{2\sigma_y^2}\right)\right)+B, \tag{2.12}$$

using an iterative least squares fitting algorithm in MATLAB, where A is the amplitude, B is the expected background level, x_0, y_0 is the centre of the Gaussian function, σ_x and σ_y are the standard deviations in x and y respectively. The spatial coordinates of the

microbubble position are then found by deconvolving the Gaussian fit. The Gaussian function was chosen as an initial approximation of the PSF signal with all parameters free to vary. Since the US resolution in the lateral and axial planes often differ from one another, an elliptical Gaussian profile can be defined and modified based on the axial and lateral components of the resolution as described above via parameters σ_x and σ_y. This model also allows for variation in the background level and amplitude of signals. Furthermore, this function is simple and easy to implement as a PSF model for fitting the position of scatterers for localisation.

3 TWO-DIMENSIONAL SUPER-RESOLUTION ULTRASOUND IMAGING *IN VITRO*

3.1 INTRODUCTION AND MOTIVATION

This chapter aims to demonstrate the potential of super-resolution using microbubbles to achieve image resolution beyond the diffraction limit. In order to achieve this objective, super-resolution imaging must first be demonstrated and explored in a controlled environment using *in vitro* phantoms.

A fundamental issue in the quantitative analysis of single bubble localisation concerns the accuracy with which the position of a single scatterer can be estimated. Determining this precision is not only of importance to be able to characterise the level of accuracy achievable, but this also has impact on the choice of imaging target that can be accurately studied using this technique.

Aspects of this work were presented at The 19th European Symposium on Ultrasound Contrast Imaging 2014 in Rotterdam, under the title: 'Super-Resolution using Single Bubble Acoustics and Ultrasound.'

Thus, in the first stage, the resolution and localisation precision that can be achieved with the conventional clinical imaging system is investigated under varying scanning settings. Thereafter, 2D *in vitro* super-resolution methods are developed and evaluated using capillary tube flow phantoms designed and constructed to enable assessment of imaging performance at depths of 7 cm using dilute suspensions of microbubble contrast agents. Post-processing algorithms are subsequently developed to visualise microvascular structures and flow. Qualitative and quantitative analysis of the data is performed in order to better understand the origin of the underlying signals for progression of the technique towards imaging more realistic structures. Additionally, Poisson statistical analysis is applied to experimental data to evaluate the performance of post-processing algorithms.

The work presented in this chapter is separated into three distinct investigations and is organised as follows. Section 3.2i involves the characterisation of the US imaging system and its localisation precision, Section 3.2ii describes *in vitro* US imaging, localisation and velocity tracking performed using microbubble flow phantoms. Lastly, Poisson statistics is introduced in Section 3.2iii as a tool to analyse the imaging of single bubbles in acoustic super-resolution.

3.2i ULTRASOUND SYSTEM CHARACTERISATION

3.2i.1 AIM

To estimate the diffraction limited resolution and investigate the localisation precision achievable with the conventional clinical imaging system employed.

3.2i.2 INTRODUCTION

As discussed in Chapter 2, PSF models and centroiding techniques have typically been used for super-resolution optical imaging techniques. In this chapter, the effect of the method of localisation, as well as variations in US system scanning parameters (such as MI and image compression techniques) on the accuracy of the super-resolution technique are investigated. An unmodified clinical system was used in order to demonstrate the benefits that can be achieved in the current clinical environment where typically only image data is accessible. In addition, using this scanner rather than a

custom built system/research device should demonstrate the benefits of super-resolution even in the most restricted conditions with limited data access; availability of data prior to image output could improve the technique even further. Results are discussed in relation to the following *in vitro* work and will form the basis for parameter settings for the proceeding experiments.

3.2i.3 METHOD

3.2i.3.1 ULTRASOUND EQUIPMENT AND ACQUISITION SETTINGS

Experimental data was acquired using a standard, unmodified Siemens Acuson Sequoia clinical US scanning system (Siemens, Issaquah, WA) using Cadence™ CPS mode [107], a multi-pulse technique discussed in Chapter 1, Section 1.3.6.3, that is sensitive and specific to contrast agents. Imaging was performed with a 4C1 abdominal convex probe and targets were scanned down to a depth of 7 cm in water where the variable focus of the imaging system was fixed at 6 cm depth. An ROI was defined around the target at the focus with pixel size m x n, where $m = 42\,\mu m$ and $n = 38\,\mu m$. All images were acquired using the maximum dynamic range available of 100 dB so that the widest range of echo intensities were displayed in the image data. The inbuilt TGC enhancement may not be linear and therefore was minimised at -20 dB (equivalent to no depth gain compensation) to reduce the chance that image intensities were ~~not~~ altered by additional unknown signal processing within the scanner. A central transmit frequency of 2 MHz and a maximum frame capture rate of 25 fps were used. The remaining acquisition settings were investigated in the following sections in relation to their affect on the system resolution and localisation precision.

3.2i.3.2 MEASUREMENT OF ELEVATIONAL RESOLUTION

The elevational resolution of the system was estimated at the transmit focus of 6 cm by imaging a 100 μm diameter brass wire which spanned the lateral direction. The wire was used to emulate the signal received from a scatterer smaller than the in plane resolution of the system. This target resulted in strong backscatter signals and provided an easily implementable target for experimental studies. In CPS, the signal is predominantly governed by nonlinear propagation. The wire was moved in 200 μm steps over the entire elevational field of view, where again 50 image frames were acquired at each step. The total intensity of a region of interest (ROI) defined around the

wire signal was calculated at each step. The elevational resolution was measured as the FWHM of the intensity profile. To account for the finite size of the wire, the measured full-width at half-maximum ($FWHM_{measured}$) value was de-convolved by the finite size of the wire, ($FWHM_{true}$), to obtain the values of the PSF FWHM, ($FWHM_{PSF}$), given by:

$$FWHM_{measured}^{\ 2} = FWHM_{true}^{\ 2} + FWHM_{PSF}^{\ 2} \tag{3.1}$$

$$FWHM_{PSF} = \sqrt{FWHM_{measured}^{\ 2} - FWHM_{true}^{\ 2}} \tag{3.2}$$

3.2i.3.3 Measurement of In Plane Diffraction Limited Resolution and Localisation Precision

A 100 μm diameter brass wire was secured tightly between two needles and placed in a gas equilibrated water bath. The wire was positioned such that its cross-section was in the imaging plane and 50 image frames were acquired at each variable parameter setting. The cross-section of the wire was estimated to be smaller than the diffraction limited resolution of the scanner and was used to mimic a point scatterer. Perpendicular alignment of the transducer and wire was performed by visual inspection. Ranges of parameter settings investigated are displayed in Table 3.1, where all measurements were performed at the focus of 60 mm unless otherwise specified. The system is able to store image data in the form of video files with JPEG compression, where the 'Compression Factor' parameter, defined by either 'Low' or 'High' compression, determines the image storage quality on the clinical system. The effect of changing a parameter defined as 'SpaceTime Resolution' is also explored; this is stated to emphasise temporal resolution (T1 or T2) or spatial resolution (S1 or S2). Unless otherwise specified, the default settings were: Compression Factor: Low, MI: 0.07 $MPaMHz^{-1/2}$, and Space/Time Parameter: S1.

Parameter Tested	Parameter Ranges
Compression Factor	Low/High
Mechanical Index (MI)	0.07-0.45 $MPaMHz^{-1/2}$
Space/Time Parameter	S1/S2/T1/T2
Depth	60-70 mm

Table 3.1. Parameter ranges investigated for system characterisation.

3.2i.3.4 IMAGE PROCESSING

All data were processed on a standard PC using MATLAB (The MathWorks, Inc., Natick, MA). Firstly, recorded video sequences consisting of colour images (3D numeric array of red, green and blue colour planes) were converted to 8 bit grey scale images using MATLAB's inbuilt 'rgb2gray' function to retain the luminence of each pixel which was expected to retain signal amplitude information. As discussed in Chapter 1, it is likely that echo amplitudes were logarithmically compressed prior to image display within the scanner. To recover the estimated intensity of the acoustic signal, I, the following relation is applied to remove logarithmic compression based on the user defined dynamic range, $d = 100\ dB$, given by,

$$\frac{I}{I_0} = 20^{\frac{p \cdot d}{n \cdot 10}} \tag{3.3}$$

where p is the integer pixel value from the stored image, and $n = 255$ is the number of quantisation levels in a standard 8 bit grey scale image.

Characterisation of the noise in the system was performed on 50 control frames. These were acquired with no imaging target and were assumed to be representative of background noise. The background intensity level for each frame was defined as the 99th percentile of the pixel values; the 99th percentile provides the intensity value below which 99 % of the pixel values exist, and is employed here to ensure the threshold is above the large majority of intensities represented by noise, but is not affected by any outlier pixels within the background frames. The mean of all background intensity levels determined for each frame was used as an intensity threshold to eliminate background noise in the data frames.

3.2i.3.5 In plane Diffraction Limited Resolution

The FWHM of the wire signal after background subtraction was measured in each frame. The imaging resolution of the US system was estimated by calculating the average FWHM in the lateral and axial directions over all frames. To account for the finite size of the wire in the measurement of the PSF the measured full-width at half-maximum ($FWHM_{measured}$) value was de-convolved by the finite size of the wire as shown in Equation (3.2).

3.2i.3.6 Localisation Precision

Two methods of single scatterer localisation were compared. The first method involved the calculation of the intensity weighted centre of mass, or 'centroid' coordinates, $[\boldsymbol{C_x}, \boldsymbol{C_y}]$, of the scatter signal in the image, using Equation (2.11) in Chapter 2, and reproduced here

$$[C_x, C_y] = \frac{\sum_i I(x_i, y_i)[x_i, y_i]}{\sum_i I(x_i, y_i)},$$

where i are the pixel indices in the region, $I(x_i, y_i)$ is the intensity of pixel located at (x_i, y_i) and $[x_i, y_i]$ represents the coordinates at the pixel i. Here, the assumption is that the geometric center of the signal region represents the location of the underlying scatterer.

The second technique involved fitting a 2D Gaussian PSF model to the signal and defining the location of the underlying scatterer as the position of the peak of that function. This is given by Equation (2.12) in Chapter 2, and provided again here,

$$\mathrm{f(x,y)} = \mathrm{A}\exp\left(-\left(\frac{(\mathrm{x}-\mathrm{x_0})^2}{2\sigma_\mathrm{x}^2} + \frac{(\mathrm{y}-\mathrm{y_0})^2}{2\sigma_\mathrm{y}^2}\right)\right) + \mathrm{B},$$

using a least squares fitting algorithm with all fit parameters left free to vary, where A is the amplitude, B is the expected background level, x_0, y_0 is the centre of the Gaussian function, σ_x and σ_y are the standard deviations in x and y respectively. This was applied due to its common use as an estimation of the PSF of imaging systems, and its widespread use in optical super-resolution techniques. For each frame, the localisation

was obtained by calculating the position (x_0, y_0) of the peak of this Gaussian profile, where the amplitude and standard deviation in x and y were unknown variables.

By calculating the variation in the estimated location of the PSF from a point scatterer over a large number of frames, an estimate of the potential error in the localisation can be acquired. In this work, the estimated localisation precision was calculated as the standard deviation of the localisation position over all frames.

3.2i.4 RESULTS

3.2i.4.1 ELEVATIONAL RESOLUTION

Figure 3.1 shows results from the elevational resolution measurement where the calculated FWHM of the entire profile was 1100 μm following deconvolution (1105 μm prior to deconvolution). This defines the slice thickness of the imaging volume at the transmit focus. Each image frame will be the weighted projection of echoes along the elevational direction into the axial-lateral plane.

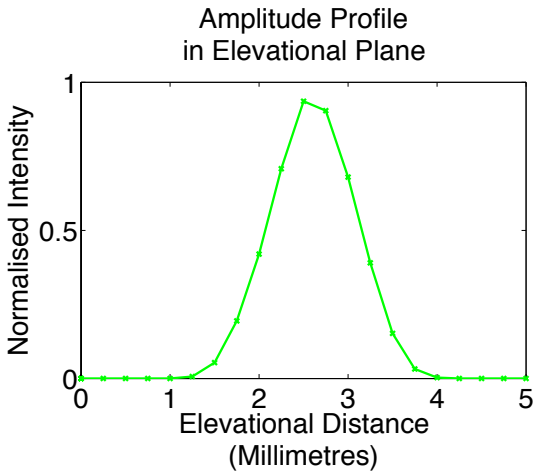

Figure 3.1. Amplitude profile of the signal from a brass wire in the elevational direction. This shows the log decompressed plot of total echo amplitude in each frame when moving a brass wire across the elevational plane of the imaging system. The FWHM of the elevational profile was estimated to be 1.1 mm.

3.2i.4.2 IN PLANE DIFFRACTION LIMITED RESOLUTION

Figure 3.2 shows an example contrast enhanced US image of the wire target cross-section at the focus, where the cross represents the centroid of the signal, along with axial and lateral normalised intensity profiles intersecting the centroid in Figure 3.2B

and C. The FWHMs of the PSF in this example were measured to be 239 μm and 336 μm (Figure 3.2C) in the axial and lateral directions respectively, giving an estimate of the diffraction limited resolution of the scanner under the settings used here.

The FWHMs estimated over varying MI at high and low JPEG compression levels are shown in Figure 3.3, where error bars display the standard deviation. Axial FWHMs using high JPEG compression are smaller in 16 out of 17 measurements over varying MI, with an average axial FWHM of 269 μm, compared to 331 μm with low compression. Axial FWHMs shows a moderate positive Pearson cross-correlation (PCC) with increasing MI of 0.84 using low compression, whereas lateral FWHMs show moderate correlation (PCC = 0.69 for low compression). Insonation with high MI may give rise to wire vibrations, and thus emitting energy after the original pulse has been reflected and would mean that the axial extent of signal becomes larger, while the lateral width remains largely the same.

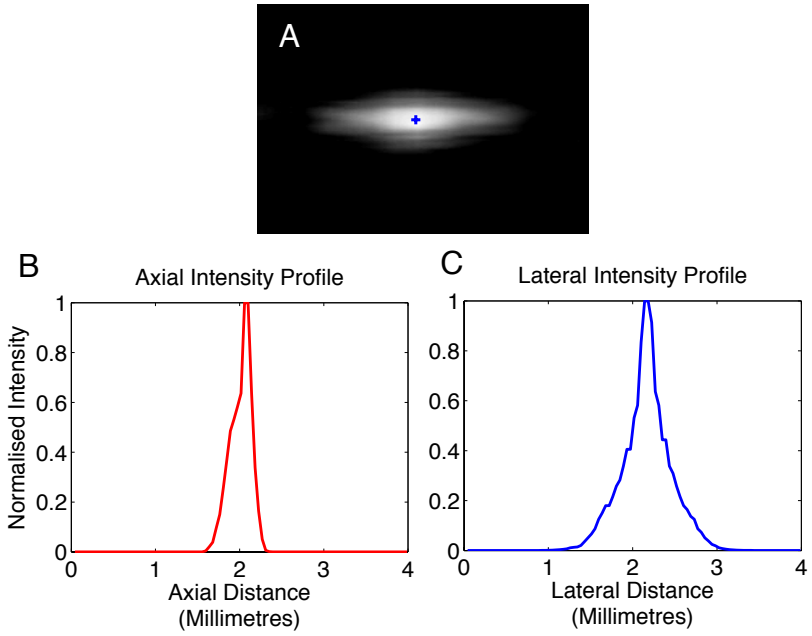

Figure 3.2. Imaging a point scatterer. (A) Example log-compressed CEUS image of the wire target cross-section at the focus, where the cross represents the centroid, along with example axial and lateral normalised intensity profiles of log-decompressed data intersecting the centroid in (B) and (C). The average FWHMs over 50 frames were measured to be 239 μm and 336 μm in the axial and lateral directions respectively, giving an estimate of the diffraction limited resolution of the scanner under the settings used here. The acquired images have pixel size m x n, where $m = 42\ \mu m$ and $n = 38\ \mu m$.

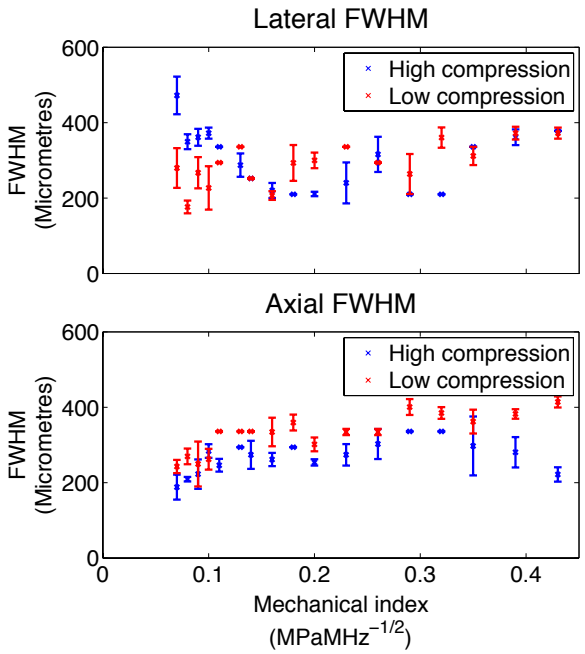

Figure 3.3. FWHMs of the wire signal for varying MI. Measurements were performed at two compression levels defined by the clinical system. Compression levels show most significant effect on the axial FWHM of the signal, where the mean axial FWHMs are 351 μm and 269 μm for low and high compression respectively.

3.2i.4.3 Localisation Precision

The localisation precisions estimated over varying mechanical index (MI) at high and low compression levels are shown in Figure 3.4, where Figure 3.4A and B show results using the centre of mass localisation algorithm and Gaussian fitting respectively. Using the former algorithm, low compression data yields a mean localisation precision over all MI of 1.6 μm and 1.9 μm in the lateral and axial directions respectively, compared to 1.7 and 2.2 μm for high compression. Low compression rates additionally provide an enhanced signal-to-noise (SNR) compared to high compression using the same MI (Figure 3.5) which may indicate a reason for this increased precision. Furthermore, results shown in Figure 3.4A suggest that the lateral localisation precision using centre of mass localisation may be affected by noise; this is shown in the gradual increase in standard deviation at lower acoustic powers, with a moderate negative PCC of -0.52 (high compression) and -0.56 (low compression), where SNR also decreases with lowering MI (Figure 3.5). The axial localisation precision, however, shows a weak positive correlation (PCC = 0.31, 0.49 for high and low compression respectively), which could be due to wire vibrations as discussed previously.

The standard deviations vary between approximately 0.2 μm and 5.9 μm in both spatial directions for all centroid measurements performed here. At the lowest MI of 0.07, and using a low compression, the error is low at under 1.5 μm in both axial and lateral directions. Localisation precisions using the Gaussian fitting algorithm have a similar range in the axial direction (0.1 - 5.6 μm), however are considerably lower in the lateral plane, ranging from 0.1 to 1.8 μm. PCC values between localisation precision values and MI are under 0.2 for both compression levels, indicating no evident relationship between acoustic amplitude and errors in fitting localisations.

Using the poorest localisation precisions found here of 5.9 μm and 5.6 μm laterally and axially, and FWHM values of FWHMx ≈ 336 μm and FWHMy ≈ 239 μm as reference values for the diffraction limited resolution of the scanner, the localisation precision is a factor of between 43-57 higher.

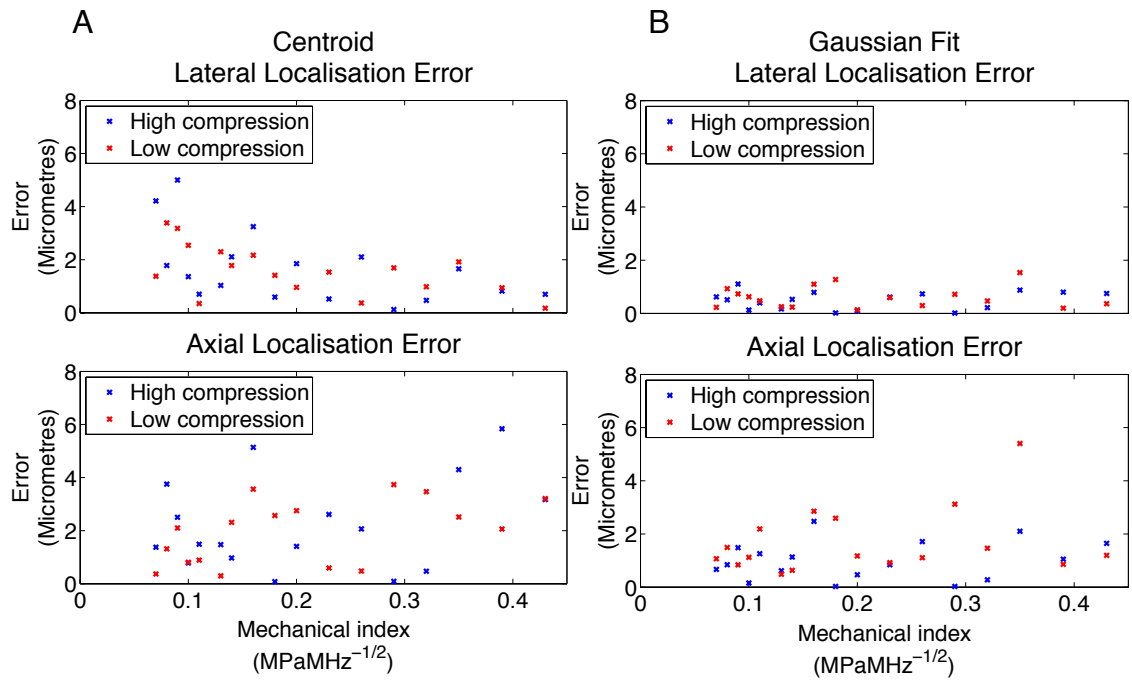

Figure 3.4. Localisation errors, estimated by calculating the variation in the scatterer localisation over 50 frames, where each localisation position was found using (A) centroiding algorithm and (B) Gaussian fitting of the wire signal for varying Mechanical Index (MI). Measurements were performed at two compression levels defined by the clinical system.

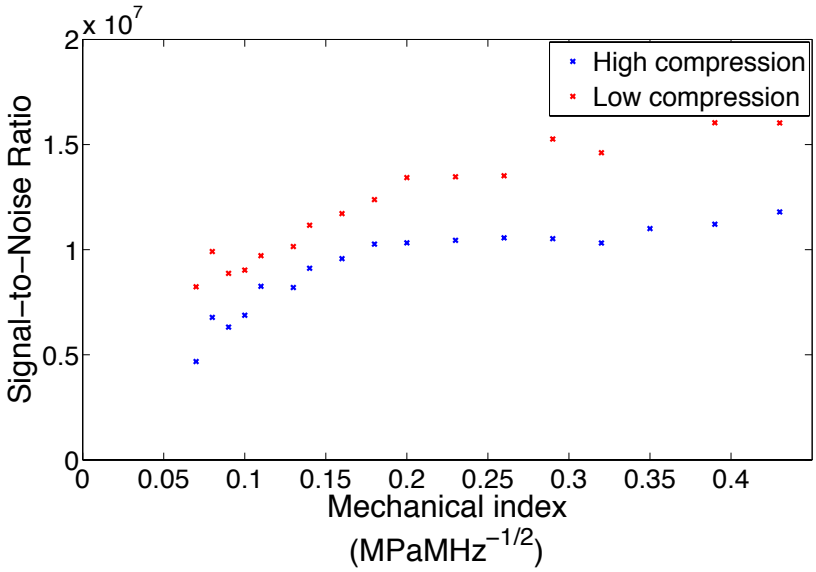

Figure 3.5. Signal-to-noise (SNR) of the scattered signal for varying Mechanical Index (MI) with high and low compression. The results show a trend in increased SNR with increasing MI. Low compression rates provide an enhanced SNR compared to high compression using the same MI.

Figure 3.6 displays the effect of changing the 'SpaceTime Resolution' parameter, as defined on the scanner, on localisation error at a fixed depth of 60 mm. Results indicate that S1 provides the highest localisation precision of 0.76 μm and 1.06 μm laterally and axially using centroiding, and even smaller at 0.14 μm and 0.39 μm using fitting. Measurements of localisation precision at various depths in Figure 3.6 demonstrate the highest localisation precision at the focus of 60 mm, with a centroiding localisation precision of 0.3 and 0.6 in the axial and lateral directions respectively. The reduction in precision seen with increasing depth away from the focus in Figure 3.6 may be due to attenuation of the signal with depth, as well as reduced focusing ~~in the far field~~. Again here, Gaussian fitting in most cases localises the PSF with higher precision compared to the centroiding algorithm, where at the focus the errors are 0.18 μm and 0.4 μm in the axial and lateral directions respectively.

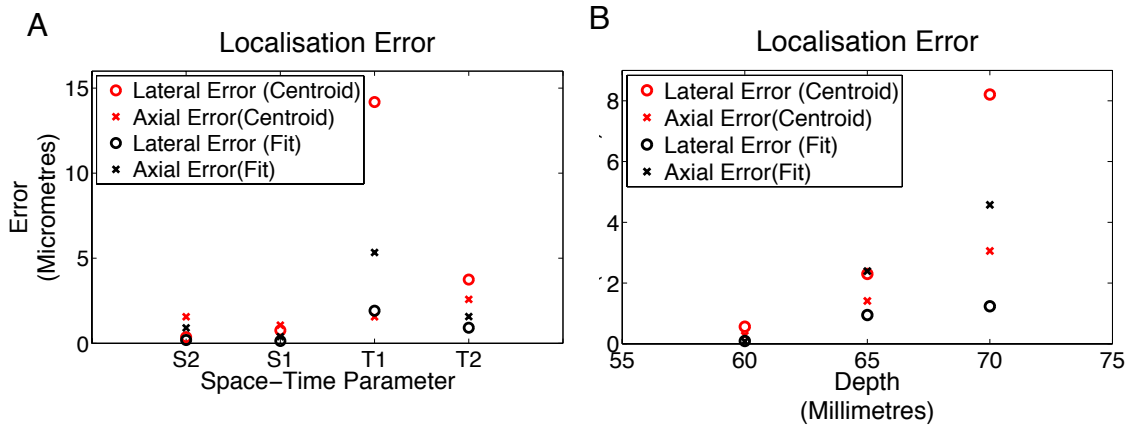

Figure 3.6. Effect of 'SpaceTime Resolution' scanner parameter and depth on localisation error. (A) Results indicate that S1 provides the highest localisation precision using the centroiding algorithm. (B) Graphs show the lateral and axial localisation precision at varying depths, where the transducer focus is set to 60 mm. Data shown in red depict results using the centroiding algorithm, whereas data shown in black is the result of using 2D Gaussian fitting.

3.2i.4.4 Gaussian Fitting

The goodness of fit using a 2D Gaussian PSF model on an example wire signal at the focus (low compression, MI 0.35) is shown in Figure 3.7, where Figure 3.7A displays the original wire signal (blue scatter graph) overlaid upon the Gaussian model (multi-coloured surface) with R-squared value equal to 0.8738. Figure 3.7B displays R-squared values over a range of MI, where the mean value was 0.9120.

3.2i.4.5 Summary of Findings

Scanning parameters for future *in vitro* experiments were chosen based on results shown in this section, and are displayed in Table 3.2. Low compression levels provided a higher SNR in comparison to equivalent signals using high compression. A low MI of 0.07 was used for succeeding experiments since a high localisation precision was demonstrated when using low compression, and in addition the use of low MI should reduce the chance of bubble destruction over long acquisition times; this was confirmed by monitoring the motion of a number of single bubbles over the entire field of view. The mean localisation precision at these settings was found to be 0.6 μm and 0.9 μm in the axial and lateral directions respectively.

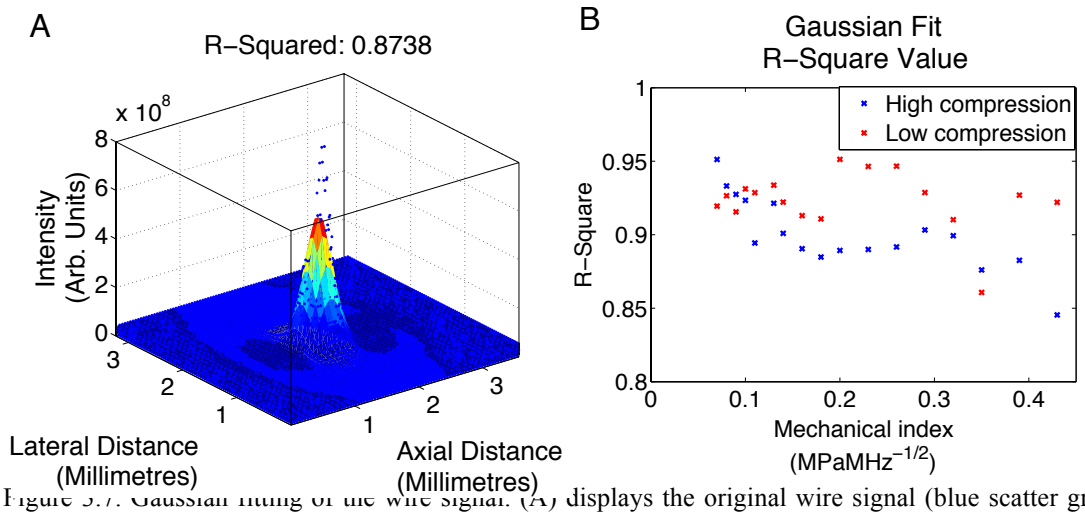

Figure 3.7. Gaussian fitting of the wire signal. (A) displays the original wire signal (blue scatter graph) overlayed upon the Gaussian fit (multi-coloured surface) where the R-squared value is 0.8738. (B) displays R-square values over the range of MI investigated.

Parameter Name	Parameter Setting
Compression Factor	Low
Frame Rate	25 Hz
MI	0.07 $MPaMHz^{-1/2}$
Frequency	2 MHz
Space/Time Parameter	S1
Dynamic Range	100 dB
Time Gain Compensation	-20 dB

Table 3.2. Parameter settings for *in vitro* experiments.

Additionally, the mean and standard deviation of a range of features of the PSF signals measured over the range of parameter settings tested in Table 3.2 are shown in Table 3.3 and will be referred to in Section 3.2ii.4.2. These characteristics were calculated in MATLAB using the 'regionprops' function. Signal characteristics include: the total signal area, the total signal intensity, the average signal intensity per square millimetre, the diameter of a circle with the same area as the region, the perimeter, the circularity of the signal, the major and minor axis lengths, and the eccentricity of the signal. Circularity here is defined as a measure of compactness, given by the ratio of area to

perimeter, and eccentricity measures the amount the signal deviates from being a circle (the ratio of the distance between the foci of the ellipse and its major axis length).

Signal Characteristic	Mean	Standard deviation	Units
Area	7	0.1	mm^2
Total Intensity	4×10^{10}	8×10^{7}	AU
Circularity	0.33	0.02	-
Eccentricity	0.93	0.005	-
Minor Axis Length	2.0	0.05	mm
Major Axis Length	4.8	0.08	mm
Equivalent Diameter	3.0	0.02	mm
Perimeter	16.1	0.5	mm

Table 3.3. Mean and standard deviation of a range of features of wire signals measured at the focus using parameter settings as defined in Table 3.2. Signal characteristics include: the total signal area, the total intensity of the signal (in arbitrary units (AU)), the average signal intensity per square millimetre, the diameter of a circle with the same area as the region, the perimeter of the signal, the circularity of the signal, the major and minor axis lengths, and the eccentricity of the signal.

3.2i.5 DISCUSSION

3.2i.5.1 IN PLANE DIFFRACTION LIMITED RESOLUTION

The average estimated FWHM of the wire signal at the focus was 336 μm and 239 μm in the lateral and axial directions respectively. The signal acquired in these experiments provides an indication of the appearance of a point scatterer in the US image, and thus the FWHMs provide an estimate of the system's in plane diffraction limited resolution.

3.2i.5.2 DIFFERENCE TO MICROBUBBLE IMAGES

Microbubbles are oscillating, coated gas spheres significantly smaller in size than the wire, and therefore will likely give rise to a different backscattered signal to that observed here. In the case of CPS imaging, images are created based on the nonlinearity of received signals, rather than the fundamental signal as in B-Mode. The nonlinear PSF measured from a wire using CPS is likely to come predominantly from nonlinear propagation of US in water, while that measured from a bubble originates from their

nonlinear oscillatory behaviour. Furthermore, these backscatter signals may vary amongst the bubble population, where bubble signal characteristics have previously been observed to depend on many factors including the microbubble size, compressibility, shell properties, the US insonating frequency, among many more bubble characteristics and experimental conditions [207]–[210].

The use of a wire target meant that the image was effectively a representation of the line spread function. However, this provided a simple and easily implementable experiment to estimate the image of a scatterer which did not exceed the size of the US resolution in plane, and thus is assumed to have a similar representation to a point scatterer in this instance.

An alternative method to estimate the diffraction limited resolution of the scanning system would be to simulate the acoustic field for arbitrary shaped transducers using the concept of spatial impulse responses (using software such as Field 2 [211]). However, imaging parameters within the clinical imaging system, such as the number of active elements, the element pitch, as well as on-board post-processing procedures are unknown. Furthermore, many of the existing simulation software packages can only evaluate the system resolution for linear imaging and not for contrast imaging mode used in this work. Nevertheless, the method performed provides an experimental estimate of the diffraction limited image of a point scatterer for use in comparison to the super-resolution approach.

3.2i.5.3 Experimental Errors

The occurrence of motion while insonating the wire may affect localisation estimations. Since only 50 image frames were analysed, the limited time frame reduces the chance of significant motion occurring. Additionally, the use of an optical bench reduced external motion effects. Error in the perpendicular alignment of the wire target may cause elongation of the scatterer signal in the image, which could cause a bias in the localisation position with respect to the wire location. This however would remain the same throughout consecutive frames.

3.2i.5.4 METHOD OF LOCALISATION

One crucial factor in the success of acoustic super-resolution is the method of obtaining localisations. Gaussian fitting yielded a generally greater precision over varying depth, MI, and image compression levels compared to calculating the centre of mass. This may be due to the increased sensitivity of the centre of mass calculation to intensity outliers and noise; this calculation makes an estimate of the centroid using the intensities of every individual pixel comprising the signal, and therefore the final localisation will be sensitive to signal variations. The fitting approach can be more robust to noise since it considers the overall shape and amplitude of the signal assuming a characteristic signal model.

Surface fitting in general is reliant on the definition of a suitable PSF model and initialisation estimations for the fit to succeed. Although this model has been used extensively in single molecule optical microscopy [139], [141], [143], [199], [202], [212], the use of the Gaussian model PSF for the optical case has been questioned, and in some cases its use has been deemed unsuitable [202] due to its lack of physical foundation [199], [202], [203]. Furthermore, it has been shown that Gaussian functions decay more rapidly than many typical PSFs, which causes significant discrepancies between the model and image data at the signal tail [213], [214].

It may additionally be questionable to assume that single bubble signals are Gaussian distributed. The Gaussian approximation may be useful in certain cases where bubble signals maintain a smooth circular or elliptical profile, or similar signals to that observed from the wire scatterer, where on average R-squared = 0.8738. However, despite the precision shown in localisation results, signals observed in contrast agent experiments have been observed to vary considerably in size and intensity [207]–[210], and therefore the Gaussian approximation may not be suitable as a model for the entire microbubble distribution. This will be investigated further in Section 3.2ii.4.2.

Conversely, centroid estimations require no prior information about the shape or size of the tracked particle image. Furthermore, non-iterative techniques such as the centre of mass algorithm which use only simple arithmetic operations are computationally less expensive than implementing a surface fitting algorithm which typically requires the

comparison of a model with data on a pixel-by-pixel basis using an iterative least squares function fitting approach. In the implementation used in this section, the centroiding method was measured to be more than two orders of magnitude faster than 2D Gaussian fitting, indicating its potential for real-time applications [204].

In light of its computational ease and speed, and due to the expectation that bubble signals will be highly variable in the following experiments, centroiding by calculating the centre of mass will be implemented in the following experiments.

3.2i.5.5 LOCALISATION PRECISION

The resolution of this approach is limited ultimately by the achievable localisation precision. Measurements on the fixed brass wire suggest that for this system this can be in the range of 0.1 to 6.5 μm using centroiding.

Scanners incorporate various levels of integrated signal and image processing components in order to manage the rich amount of data acquired in each scan and to present the image information for human observation; these include band-pass filtering, beamforming, envelope detection, log compression and image enhancement processing such as image smoothing, among other unknown onboard system post-processing procedures. Measurements of the localisation precision were performed on image data acquired from the scanner and therefore will be influenced by the inbuilt scanner post-processing it has been subjected to. Each of these processes could reduce the available precision. Localisation precisions using centre of mass centroiding shown in Figure 3.4 indicate a marginally lower accuracy is typically obtained with high JPEG compression, which could be caused by the loss of data information involved in this lossy compression technique [215]. Further, the results suggest that the lateral localisation precision is affected by SNR, shown by a general increase in error with decreasing acoustic power and corresponding decreasing SNR (Figure 3.5). If the unprocessed data was available, then the localisation precision would be fundamentally limited by the read-out noise of the US system.

These results show that the precision at which a stationary scatterer can be localised is affected by experimental conditions such as noise, image compression procedures, and the method of localisation.

3.2i.6 Summary and Consequences for Future Work

The FWHM of the PSF at the focus is measured to be 239 μm in the axial direction and 336 μm in the lateral direction, giving an estimate of the diffraction limited resolution size of the scanner. Parameter settings defined in Table 3.2 are used for future microbubble experiments in this chapter. The mean estimated localisation precision of the point scatterer for the following experiments, 0.6 μm and 0.9 μm in the axial and lateral directions, is significantly smaller by two orders of magnitude, giving rise to the possibility of visualising sub-diffraction structures using single bubble localisation. The level of precision estimated using parameter settings defined in Table 3.2 indicates that imaging targets in the range of a few microns may be able to be accurately studied under these conditions. As ultrasonic waves are able to penetrate >10 cm of tissue, extracting bubble localisations using this technique could thus lead to the reconstruction of deep vessel structures.

3.2ii *In Vitro* Super-Resolution Imaging

3.2ii.1 Aim

To develop acoustic super-resolution imaging to enable visualisation of sub-diffraction sized capillary structures *in vitro* using low frequency US.

3.2ii.2 Introduction

In the following section, the construction of flow phantoms comprising sub-diffraction sized structures is described. The imaging procedure, illustrated in Figure 3.8, is presented, involving the acquisition of multiple frames of microbubble flow through capillary tubes. Post-processing procedures used to detect and localise scatter events, and generate super-resolution images are then described.

3.2ii.3 METHOD

3.2ii.3.1 EXPERIMENTAL EQUIPMENT AND SETTINGS

Experimental data was acquired identically to that in preceding characterisation experiments (section 3.2i), in addition to those newly defined parameters shown in Table 3.2.

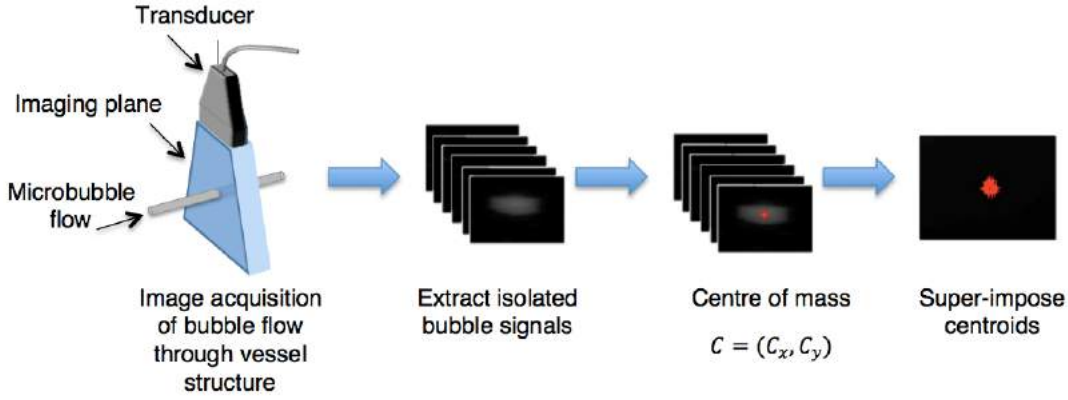

Figure 3.8. Outline of imaging procedure for cross-sectional imaging. A low concentration of microbubbles are introduced into a flow system such that there is a high probability of imaging spatially isolated bubble signals. Centroiding algorithms are applied to these signals, and resulting localisations allow an image of the underlying structure to be generated. Relative sizes shown are not to scale.

3.2ii.3.2 PHANTOM DEVELOPMENT

Super-resolution imaging was demonstrated using thin walled cellulose capillary tubes (Hemophan®, Membrana) of internal diameter 200 μm ± 15 μm, a wall thickness of 8 ± 1 μm in the dry state and a length change under wet conditions of ± 1% (specifications provided by the manufacturer). The ends of the tube were threaded into butterfly needles and sealed with commercially available epoxy-resin before being placed in a gas equilibrated water bath, see Figure 3.9. One end of the butterfly needle tubing was placed in a beaker of dilute microbubble solution, and the other was attached to a syringe pump.

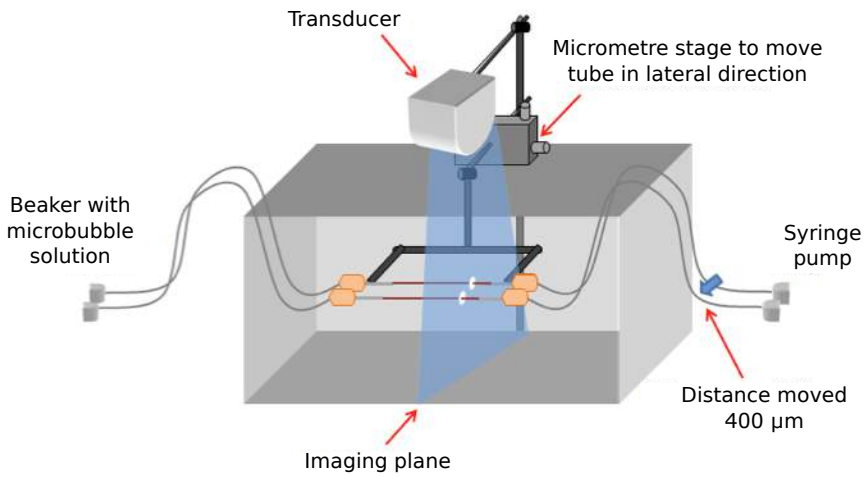

Figure 3.9. Imaging set-up for the cross-sectional 'double tube' experiment. A single cellulose tube was imaged before and after moving the structure 400 µm in the lateral direction using a micrometre stage.

In the first *in vitro* phantom, a single capillary tube was positioned parallel to the transducer's elevational plane such that its cross-section was within the imaging plane of the transducer; this set-up is illustrated in the schematic shown in Figure 3.9. During microbubble flow through the system, video data was acquired, before the tube was displaced by 400 µm in the lateral direction using a 3-axis translational micrometre screw stage (Newport M-562, CA, USA). Imaging was subsequently repeated in this new location. The careful positioning of a single tube in two locations enabled precise control over the distance between the tube centres. Subsequently, the transducer was rotated such that the length of the tube spanned across the lateral direction in the imaging plane, termed 'lateral' imaging for the remainder of this thesis. This enabled imaging of a larger structure within the transducer field of view. Moreover, temporal observation of the same microbubbles allowed measurement and analysis of microbubble flow. Additionally, 'crossed tube' phantom configurations were constructed. In this set-up, two cellulose tubes were positioned diagonally with their centres touching, as shown in Figure 3.10.

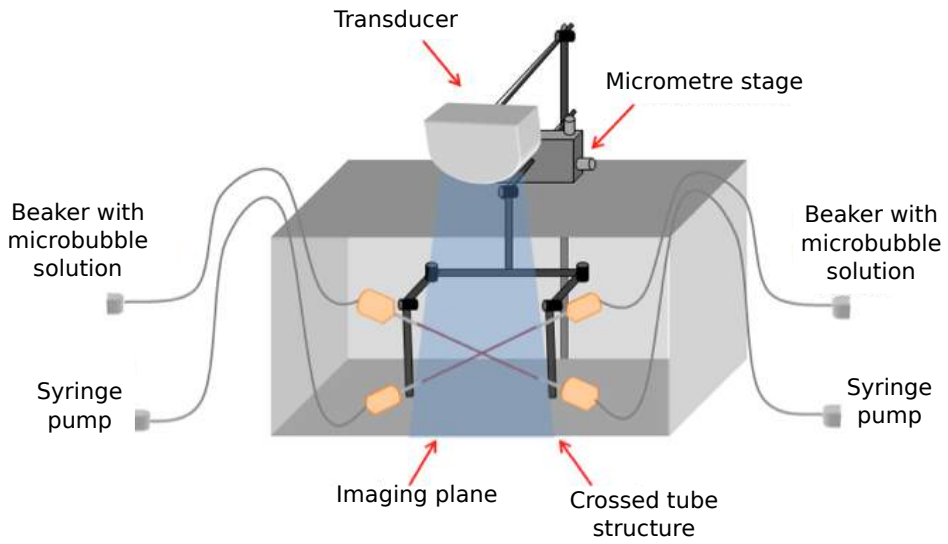

Figure 3.10. Ultrasound imaging set-up for crossed tube experiments. Both tubes were connected to separate syringes within the same syringe pump; hence the flow rate was kept approximately equal in both systems.

Each tube was connected to separate syringes, where the flow rate of both tubes was controlled using the same syringe pump. The opposing tube endings were placed in the same beaker containing a dilute microbubble suspension. Therefore, the flow rate and concentration in both tubes were assumed to be approximately equal. *In vitro* targets were at a depth of approximately 6 - 7 cm and were positioned on an optical bench (Nexus™, Thorlabs) to dampen possible table vibrations due to human or external factors.

3.2ii.3.3 MICROBUBBLE SOLUTION

Given the size of the capillary tubes used in comparison to conventional diffraction limited US image resolution (see section 3.2i), for the cross-sectional phantom experiments, a maximum of one microbubble should be imaged in any given frame to ensure spatial and temporal separation of individual microbubble signals as discussed in Chapter 2. Thus, the concentration was calculated prior to experiments based on the desired microbubble concentration and sample volume size.

The imaging of a 3D structure using a 1D array transducer creates an US image, $I(x, y)$, which is a 2D projection of the echoes originating within the slice volume along the elevational dimension,

$$\mathrm{I}(x,y) = \int_{\Delta z} I(x,y,z')\,dz', \tag{3.4}$$

where here the beam width, Δz, is assumed to be constant across the region of interest. When imaging a cross-sectional slice of a tube, if any angle exists in the tube position relative to the angle parallel to the transducer face, an elliptical cylinder of the target is effectively sampled. Figure 3.11 illustrates this scenario and the effect on the resulting image. The elongation in the image can then be given by

$$\mathrm{L_E} = \frac{\mathrm{d}}{\cos\theta} + \Delta z \sin\theta \tag{3.5}$$

The sampling volume is then given by

$$Vs = \pi ab\Delta z = \frac{\pi r^2 \Delta z}{\cos\theta}. \tag{3.6}$$

where a and b are the major- and minor-semi axes of the ellipse, r the inner radius of the tube, Δz is the elevational width, and θ the angle of the transducer with respect to the normal of the tube, as indicated in Figure 3.11.

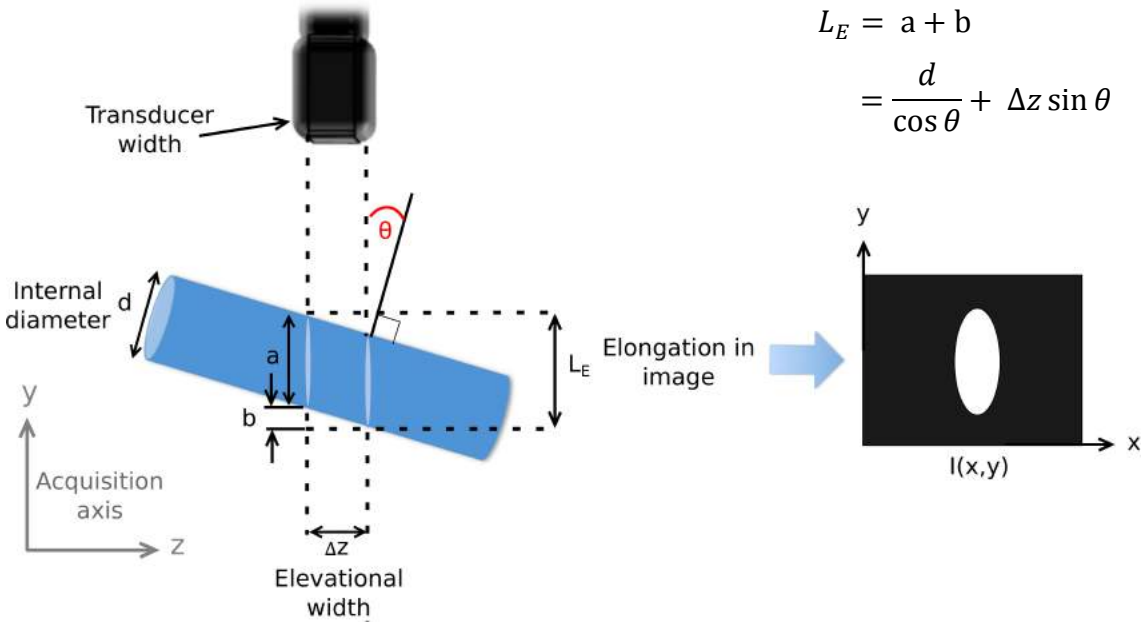

Figure 3.11. Schematic representation of the sampling volume. The transducer is put at an oblique angle θ to reduce the backscattered signal from the tube. The sampling volume is contained in the elliptical cylinder of width Δz. Objects not shown to scale.

In all microbubble experiments in this project SonoVue™ microbubbles (Bracco Diagnostics Inc., Princeton, NJ) are used. SonoVue™ agents are filled with sulfur hexafluoride with a thin lipid shell coating. A 5 ml vial of SonoVue contrast agent typically contains in the order of 10^8 microbubbles/ml suspension [216]. An estimation of the microbubble concentration required in the beaker dilution was performed by firstly defining a desired bubble per sample volume per frame. For cross-sectional imaging, in order to image one bubble per sample volume, V_s, per frame, the following relation should hold for the concentration within the beaker dilution,

$$\frac{1}{\mathrm{V_s}} = \frac{\mathrm{V_i C}}{\mathrm{V_{Total}}} \tag{3.7}$$

$$\frac{1}{V_s} = \frac{V_i C}{V_i + V_w} \tag{3.8}$$

$$V_i = \frac{V_w}{\mathrm{C}V_s - 1} \tag{3.9}$$

where V_i is the injection volume of SonoVue™ from the vial, C is the original bubble concentration in the vial, V_w is the volume of water add to the beaker, and $V_{Total} = V_i + V_w$ is the total volume of the beaker dilution. The original concentration C is determined using an optical bubble counting program (see following Section 3.2ii.3.4).

3.2ii.3.4 Optical Bubble Counting and Sizing

A sample of SonoVue™ microbubble suspension was injected onto a haemocytometer and 40 images were acquired using a light microscope. A MATLAB program written by Dr. Robert Eckersley (Department of Biomedical Engineering, King's College London) and Dr. Charles Sennoga (Department of Chemistry, Imperial College London) was used to compute the concentration and size distribution of the microbubbles [217]. An example frame is shown in Figure 3.12. The cumulative size distribution and histogram computed over all image frames are shown in Figure 3.13A and B. Figure 3.13 indicates that 100 % of the bubbles within the sample were within 7.27 μm in diameter, and approximately 80% were below 3 μm. The mean microbubble diameter was 2.21 μm.

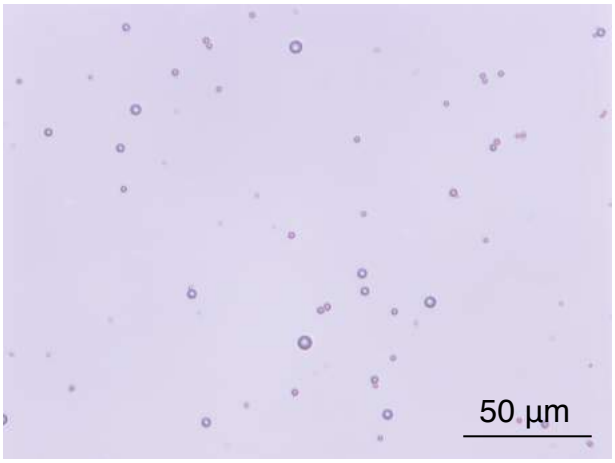

Figure 3.12. Example optical image of a sample of SonoVue™ contrast agent prior to performing *in vitro* flow phantom experiments.

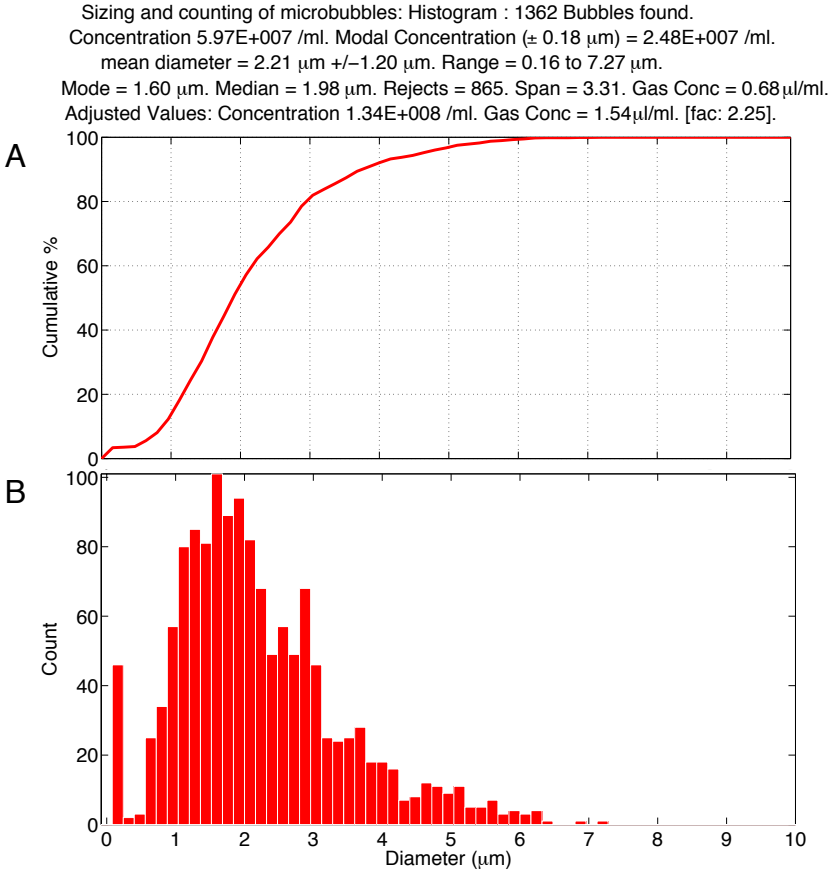

Figure 3.13. Sizing and counting of microbubbles. Part (A) displays the cumulative size distribution of microbubble sizes and (B) displays the corresponding microbubble size count histogram.

This yields the optically visible bubble concentration. The concentration observed acoustically is determined by the ability of the US imaging system to generate and receive backscattered signals from these bubbles. Given that the resonance frequency of a microbubble is directly related to its size (Chapter 2, Section 2.2.3), and US systems have limited frequency bandwidth, the imaging system is optimised only for a subset of the polydispersed microbubble population. If the microbubble resonance is outside the bandwidth, the backscattered signal may be too weak to be detected. The bandwidth therefore creates a size interval over which bubbles are resonant. The resonance frequencies for SonoVue™ microbubbles can be modeled with a modified Herring model presented by Morgan et al. [172] for coated bubbles incorporating shell parameters as discussed in Chapter 2 (shell elasticity was taken as $\chi = 0.26$ N/m, surface tension $\sigma_s = 0.051$ N/m and the polytropic gas exponent $\gamma = 1.07$) which has been shown to correlate to experimental results [171] Thus, the effective concentration of resonant bubbles can be calculated using Equation (2.8).

.

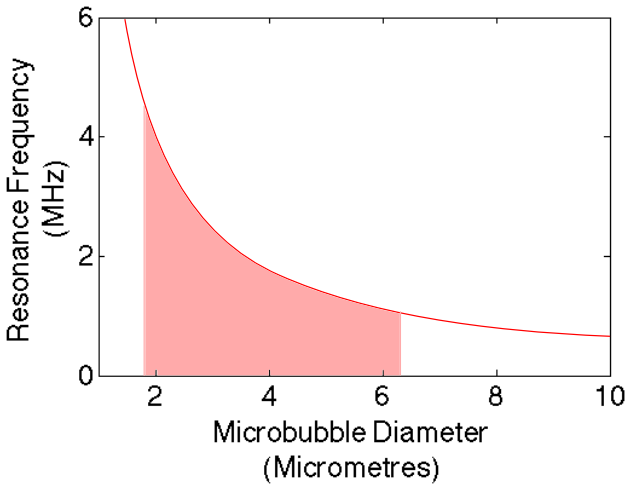

Figure 3.14. Resonance frequency of microbubbles as a function of diameter according to Equation (2.8) [172]. The bandwidth of the transducer ranges from 1 to 4.5 MHz which is used to define the size range of resonant bubbles (indicated in green). Bubbles with a diameter between approximately 1.8 and 6.3 μm have a resonance frequency that lies within the bandwidth (shaded area).

The bandwidth of the transducer ranges from 1 to 4.5 MHz which indicates that the diameter range of resonant bubbles is between approximately 1.8 and 6.3 μm [218], indicated by the shaded area in the graph. Together with the cumulative size distribution

in Figure 3.13A, the effective concentration of resonant bubbles was then estimated to be 56% of the original concentration. The sample volume is calculated according to Equation (3.6), as

$$\mathrm{V_s} = \frac{\pi \mathrm{r}^2 \Delta \mathrm{z}}{\cos\theta} = 0.035 \text{ ml}, \tag{3.10}$$

where $r = 0.1$ mm, and $\theta = 5°$ is the estimated tilt in transducer positioning in order to minimise reflection from the tube wall. The elevational width Δz at the focus was measured to be 1.1 mm (Section 3.2i.4.1) using settings consistent with *in vitro* microbubble experiments as shown in Table 3.2. The effective concentration, C_E, is given by

$$\mathrm{C_E} = 0.56 \cdot \mathrm{C} \tag{3.11}$$

$$= 0.56 \cdot 1.34 \cdot 10^8$$

$$= 7.5 \cdot 10^7 \, microbubbles/ml$$

The SonoVue™ injection volume can then be calculated using Equation (3.9) using instead the effective concentration ($C_i = C_E$), and choosing a water volume of V_w = 600 ml,

$$V_i = \frac{V_w}{C_E V_s - 1} \tag{3.12}$$

$$= \frac{600}{7.5 \cdot 10^7 \cdot 0.035 - 1} \tag{3.13}$$

$$= 2.3 \cdot 10^{-4} \, ml$$

During imaging, this concentration was found to be considerably lower than required, where bubbles occurred approximately every few hundred frames. The concentration was thus adjusted empirically by monitoring the bubble per frame density during image acquisition in an attempt to provide microbubble signals approximately every few

frames. The empirically determined volume, V_i = 100 µl, was used for subsequent phantom experiments. Possible reasons for the discrepancy in the estimated bubble concentration required are discussed in Section 3.2ii.5.3.

Since there exists a polydispersed microbubble population, and the scattering from microbubbles has high dependency on the microbubble size and mechanical properties, a large variation in the echoes received at the transducer is likely. Providing each individual microbubble exhibits similar scattering properties during the duration of imaging, there exists an opportunity to identify signals originating from the same microbubble across multiple frames, and distinguishing those which are from different bubbles. The similarity of bubble signals occurring in consecutive frames, and the dissimilarity between individual bubbles can be visualised in Results Section 3.2ii.4.4, Figure 3.37. This assumption will be implemented in a tracking algorithm described in Section 3.2ii.3.6.

3.2ii.3.5 Flow Phantom Imaging Procedure

The apparatus shown in Figure 3.9 was attached to a micrometre stage which enabled precise positioning of the tube within the US focus (at a depth of 6 cm). A dilute suspension of Sonovue™ was drawn through the tube using the syringe pump withdrawing at a rate of 100 µl per minute. Video clips were taken on the US scanner using Cadence™ CPS mode imaging mode as in the characterisation experiments. The microbubble suspension was stirred to ensure a uniform distribution of microbubbles within the suspension.

3.2ii.3.6 Image Processing

Super-resolution Algorithm

Firstly, video sequences were processed according to that described in post-processing Section 3.2i.3.4. *In vitro* frames which potentially contained a microbubble signal were then identified by comparing the total intensity of each frame to the maximum total intensity of 50 background frames acquired prior to microbubble injection which were assumed to be representative of background noise. Frames below the threshold deemed not to contain bubble signals were added to a rolling background average, while frames above the threshold had the rolling background average subtracted from them; the

resulting images were referred to as potential bubble images. The rolling average was taken over n = 10 frames in order to remove the unwanted background signals due to static structures such as the echo from the tube wall and other unwanted noise, without removing weak signals from slow moving bubbles.

Potential bubble frames were then segmented according to whether the pixel values were above the background intensity level defined previously. Characteristics of each connected region in the segmented image, including size, intensity, and perimeter, were then calculated for analysis. In initial results, the size of the connected regions were compared to the expected PSF based on characterisation experiments in order to reject signals coming from noise. An empirically determined upper threshold attempted to reject multiple bubble signals which are not spatially separated, or unexpectedly large signals which may be due to unknown bubble interactions. This is because it cannot be assumed that the centre of mass of signals from multiple unresolved microbubbles within a PSF sized volume is representative of the bubble location. Empirically determined thresholds could also be chosen to reject regions based on other signal properties; this will be discussed further in Results Section 3.2ii.4. Regions meeting these criteria were classified as bubbles and the intensity weighted centre of mass of the region was calculated using Equation (2.11). Centroid positions from each frame are then superimposed onto a single map to form an image of the underlying structure containing the microbubbles using the image generation procedure described in Section 3.2ii.3.7.

MICROBUBBLE TRACKING ALGORITHM

A microbubble tracking algorithm was developed in MATLAB to estimate the flow velocity within the phantoms. Firstly, for each frame n, individual microbubble signals were identified as described in the previous section. Each bubble signal in frame n and each of the bubble signals found in frame $n+1$ within a search window were then identified. The search window size was defined to reject bubbles which far exceeded the expected flow velocity in the target. The pairwise Pearson's linear correlation coefficient was calculated between images consisting of each of the bubble signals, centred at their center of mass. If no prior information is known about the target, the search window size can be defined as the whole frame, however this has a compromise

of increased computation time, and may additionally result in increased false positive detections. In these experiments, the search window was defined to be the size of the entire field of view since the expected velocity was presumed to be unknown. A pair of signals were considered to originate from the same bubble if the maximum cross correlation exceeded an empirically determined threshold of 0.8. For each pair, a velocity vector was then calculated between C_x^n, C_y^n and C_x^{n+1}, C_y^{n+1} and assigned to the centroid location C_x^{n+1}, C_y^{n+1} in frame $n+1$. Velocity maps were then generated using the method described in the following section 3.2ii.3.7.

Assessment of speeds during the entire acquisition employed the use of track identities. A track identity number k_i was assigned to each individual tracking event such as this, where $i = 1, ...,$ m is the microbubble track index and m is the tracked number of microbubbles over the entire acquisition. If a bubble is subsequently identified in frame $n+2$, and exceeds the cross correlation threshold with the bubble signal in frame $n+1$, it will then be assigned the same track identity, k_i. Assigning track identities allowed monitoring of the same bubble over its trajectory within the field of view. This allows the calculation of average bubble velocities within the vessel for better velocity estimation, and furthermore, enabled assessment of the number of occurrences of bubble velocities without biasing the representation of slower moving bubbles which are likely to be sampled more times within the target volume.

3.2ii.3.7 Image Rendering

Pixelated image generation

Results were visualised through the generation of image maps containing pixels of size $m \times n$, chosen to equal that of the acquired image frames, where $m = 42\ \mu m$ and $n = 38\ \mu m$. Each pixel value equalled the sum of all localisations occurring within the pixel area.

Super-resolution image generation

An improved image rendering technique was written for generation of the final super-resolution images, where the new pixel size was chosen to be below the localisation precision of the system. In this chapter, each pixel was $0.3 \times 0.3\ \mu m$ and each individual bubble localisation was represented by a 2D Gaussian profile centred at

$C = (C_x, C_y)$ with standard deviations, σ_x and σ_y, given by the average lateral and axial localisation uncertainty of the PSF (equal to 0.6 μm axially and 0.9 μm laterally at the focus). The super-resolution map resulting from the sum of all the individual centroid localisation distributions across all frames creates an image in which the displayed value is proportional to the chance of detecting a microbubble positioned at that location.

FLOW VELOCITY IMAGE GENERATION

To generate smooth flow velocity images, the neighbouring velocity vectors v_i associated with each localised bubble position C are combined using a weighted spatial averaging approach. This was required in order to reduce the influence of outliers in the final visualisation. A Gaussian function was used in order to weight velocity vectors from scatterers localised close to the bubble position higher than those found far away. Furthermore, the function should degrade significantly at distances beyond a neighbourhood radius, in order to reduce the impact of localisations of scatterers which exist in separate vessels. Firstly, for each velocity vector v_c at C, all $i = 1, \dots j$ centroids which exist within a neighbourhood of radius $r = 40$ μm are identified, where r is defined based on the underlying target vessel sizes and the noise. A weighting w_i is then applied to each v_i, given by

$$\mathrm{w_i} = \mathrm{e}^{-\left(\frac{\mathrm{d_i}}{\mathrm{r}}\right)^2}, \tag{3.14}$$

where d_i is the distance from C to centroid C_i, and $i = 1, \dots j$. The velocity v_c is then given by the weighted sum of all neighbourhood velocity distributions

$$\mathrm{v_c} = \frac{1}{\mathrm{Z}} \sum_{\mathrm{i=1}}^{\mathrm{j}} \mathrm{w_i v_i}, \tag{3.15}$$

where Z is the normalisation factor given by

$$\mathrm{Z} = \sum_{\mathrm{i=1}}^{\mathrm{j}} \mathrm{w_i}. \tag{3.16}$$

The speed and direction components of velocity are then presented in separate images. Velocity vector components for each localisation were displayed on the 95% confidence interval of the 2D Gaussian profile used to generate the super-resolved images.

3.2ii.4 RESULTS

3.2ii.4.1 CROSS-SECTIONAL IMAGING

During the cross-sectional experiment, 3814 scattering events were detected and localised from 12376 acquired frames. Figure 3.15A shows a 2D map of the resulting localisation distribution, with a pixel size equal to that of the acquired image data of 38 x 42 μm. Here, approximately 5 pixels in the distribution map corresponds to the 200 μm tube diameter. Figure 3.15B displays the lateral line profile of the two count distributions taken through the pixel of maximum count. Two distinct regions of high centroid counts can be observed that can be attributed to the positions of the tubes within the image and successfully demonstrates the ability of the technique to visualise the objects. The distance between the two peaks in the lateral bar profile shown in Figure 3.15B is measured to be 329 ± 29 μm. Additionally evident is a significant elongation in the axial direction. This elongation may be due to the transducer being slightly tilted in relation to the tube (Figure 3.11). The possible factors influencing the count distribution seen here will be discussed further in Section 3.2ii.5.1.

Figure 3.16 shows the summation of the acquired diffraction limited image data used for this measurement in red where the two tube regions cannot be distinguished, with the super-resolution map overlaid in green.

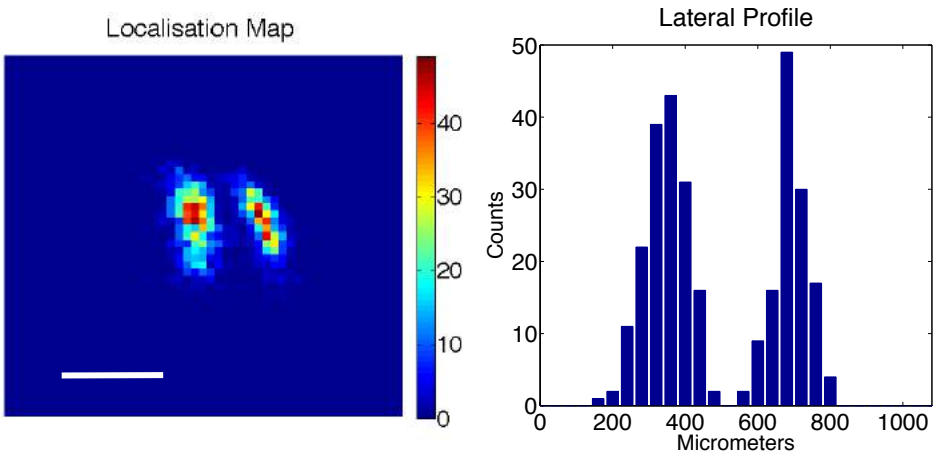

Figure 3.15. Localisation map and profile for cross-sectional imaging. (A) Location map obtained for the 200 μm internal diameter cellulose tube moved 400 μm from original position. Pixel size 38 x 42 μm. (B) Corresponding lateral bar profile showing the localisation counts per pixel across the maximum intensity value. Scale bar 500 μm.

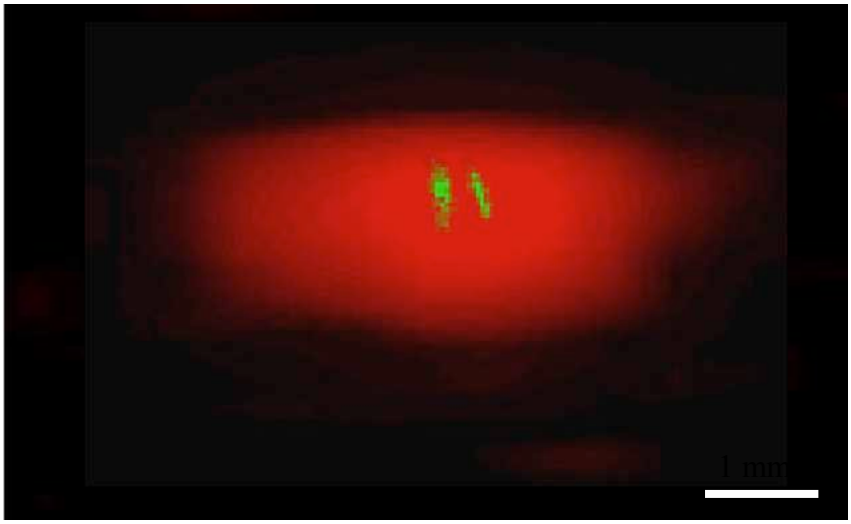

Figure 3.16. Overlay of the localisation map (green) on the summed diffraction limited image data (red). Scale bar 1 mm.

Figure 3.17 displays the same localisation results as that in Figure 3.15A, however here each localisation is represented as a 2D Gaussian profile centred at $C = (C_x, C_y)$ with standard deviations, σ_x and σ_y, given by the average lateral and axial localisation uncertainty measured in Section 3.2i. The resulting map from the sum of all the individual localisations across all frames creates an image in which the displayed intensity value is proportional to the chance of finding a microbubble positioned at that

location. Providing the image pixel size is smaller than the localisation error of the imaging system such that a relatively smooth Gaussian profile can be generated, the resulting visualisation is largely unaffected by an arbitrary choice of pixel size. Instead, visualisation in the final image depends upon the localisation precision of the system and the density of detected localisations. The lateral intensity profile across the approximated centre of the vessels is shown in Figure 3.17, where both the raw data (red), and a smoothed version of the data (blue) are displayed. Smoothing was performed by convolving a sliding averaging window across the raw profile data, where the window size was chosen to be 75 μm. By visual assessment this was considered to smooth the data without removing the overall shape and amplitude of the underlying signal. The FWHM of the smoothed vessel profiles are 150 μm and 122 μm for each vessel respectively (raw: 146 μm and 91 μm).

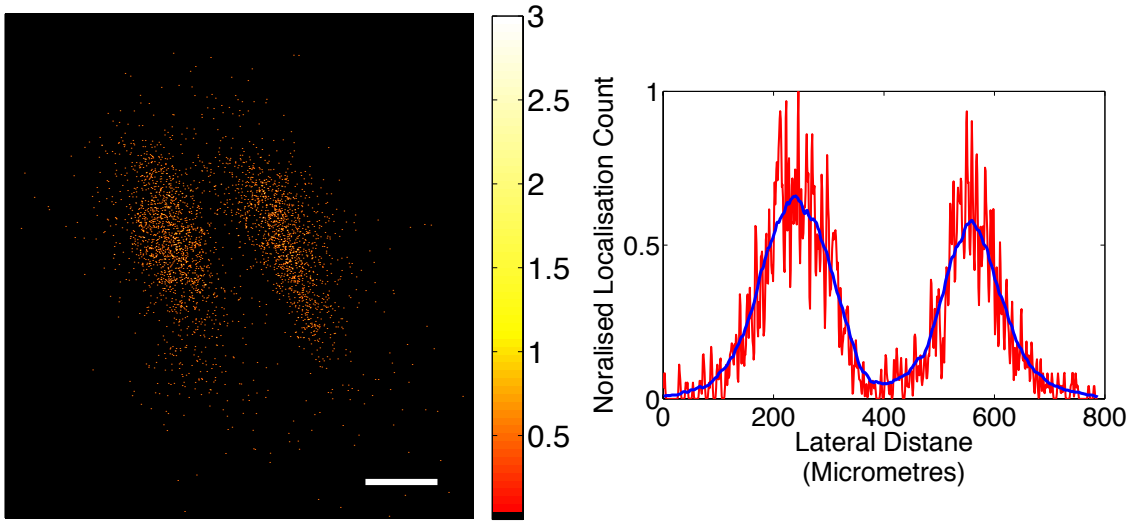

Figure 3.17. Localisation map where each localisation is represented as a 2D Gaussian profile centred at $C = (C_x, C_y)$ with standard deviations, σ_x and σ_y, given by the average lateral and axial localisation uncertainty. The resulting map from the superposition of all the individual localisations across all frames creates an image in which the displayed intensity value is proportional to the chance of finding a microbubble positioned at that location. Also shown is the lateral intensity profile across the approximated centre of the vessels where both a line plot through the raw data (red), and a smoothed version of the data (blue) are displayed. Scale bar, 200 μm.

The spatial maps in Figure 3.18 are colour-coded to display some of the underlying features of each candidate bubble signal at their estimated localisation position. Features

displayed are (A) the total signal area, (B) the total intensity of the signal, (C) the average signal intensity per square millimetre, (D) the diameter of a circle with the same area as the region, (E), the perimeter of the signal, (F) the circularity of the signal, (G) and (H) show the major and minor axis lengths, and (I) shows the eccentricity of the signal. The estimated area of candidate bubble regions generally increases with depth in both tubes (A), as is also seen for the total signal intensity of the signal regions in (B). This intensity increase can be seen to be at least in part due to an increase in intensity per square millimetre, in addition to an increased region size. The equivalent diameters, perimeters and major and minor axis lengths shown in Figure 3.18D, E, G and H respectively follow a similar trend in spatial distribution to that shown in Figure 3.18A, B and C. Possible causes of this are further investigated in Section 3.2ii.4.2 and discussed in Section 3.2ii.5.2.

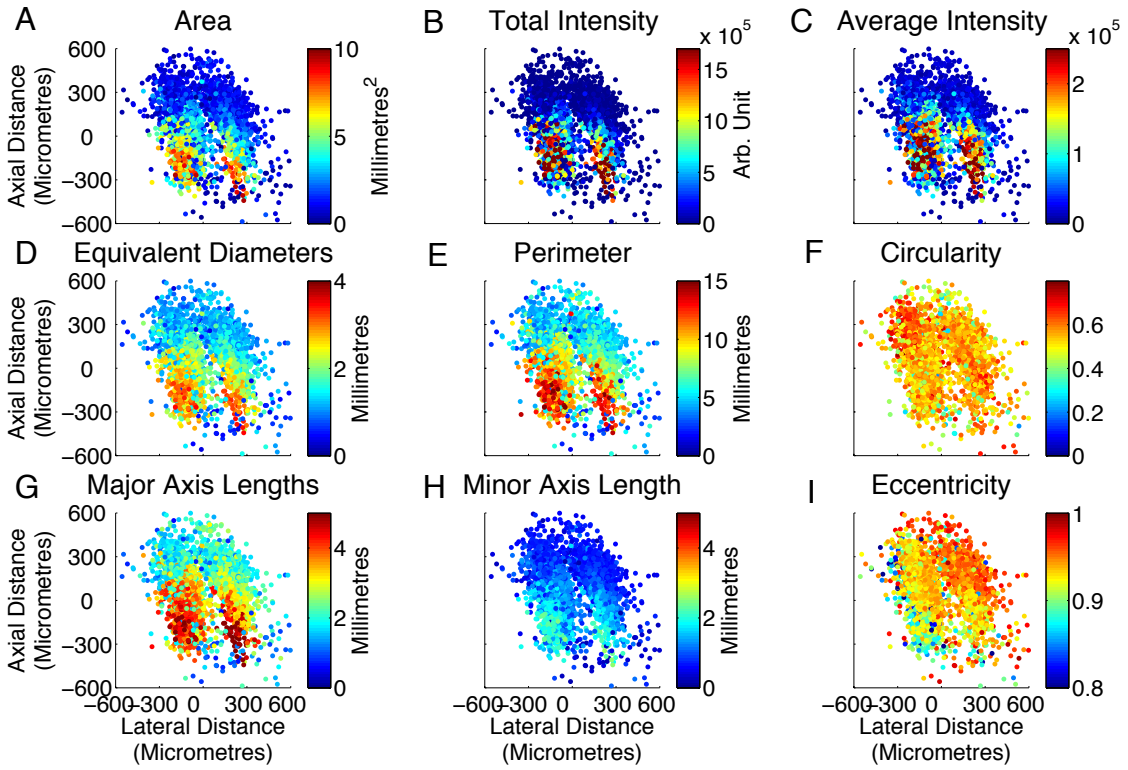

Figure 3.18. Spatial maps of signal characteristics from cross-sectional tube imaging and their corresponding spatial location. Plots display (A) the total signal area, (B) the total intensity of the signal, (C) the average signal intensity per square millimetre, (D) the diameter of a circle with the same area as the region, (E), the perimeter of the signal, (F) the circularity of the signal, (G) and (H) show the major and minor axis lengths, and (I) shows the eccentricity of the signal.

The eccentricity and circularity shown in Figure 3.18F and I respectively indicate that signals become less elliptical and more circular in lower regions. These same measurements were performed on wire signals in characterisation experiments (shown in Table 3.3, Section 3.2i.4.5); the average values found for the wire fall within those found for the double tube data, excluding the total intensity and perimeter of candidate regions, seen above in Figure 3.18B and E. Microbubble signals are demonstrated to be considerably weaker than the wire; the wire signal intensity is over 4 orders of magnitude higher than those found for microbubbles, while the average perimeter is 1 mm larger (Table 3.3) than the largest detected in bubble data (Figure 3.18E).

By examining histograms of the detected signal areas, it may be possible to identify distributions which correspond to noise. Figure 3.19A displays the original localisation map shown in Figure 3.17 displayed alongside its corresponding histogram of signal area, in addition to the lateral intensity profile across the approximated centre of the vessels where line plots through both the raw data (red), and a smoothed version of the data (blue) are displayed. The FWHMs for both data types are displayed in Table 3.4 for comparison. The smallest signal regions found in the data exhibit a separated distribution in the histogram, which may indicate a division between signals originating from bubbles and those from noise. In the second example in Figure 3.19B, bubble signals below the first minimum in the histogram are thus rejected. Both localisation maps and lateral profiles display only minor changes.

Estimated FWHMs in the axial direction are significantly larger than those measured laterally in all cases. This elongation may be due to the tilt described previously, where a 5° angle from the normal to the tube would cause an apparent elongated length, L_E, given by (3.5), of

$$\mathrm{L_E} = \frac{200}{\cos 5^\circ} + 1100 \cdot \sin 5^\circ \tag{3.17}$$

$$= 297\ \mu\mathrm{m}.$$

By also rejecting large signals corresponding to those present predominantly in lower regions of the tube, approximately 7 mm^2 and above (see Figure 3.18), a small reduction in the FWHM of the axial profiles is seen Table 3.4.

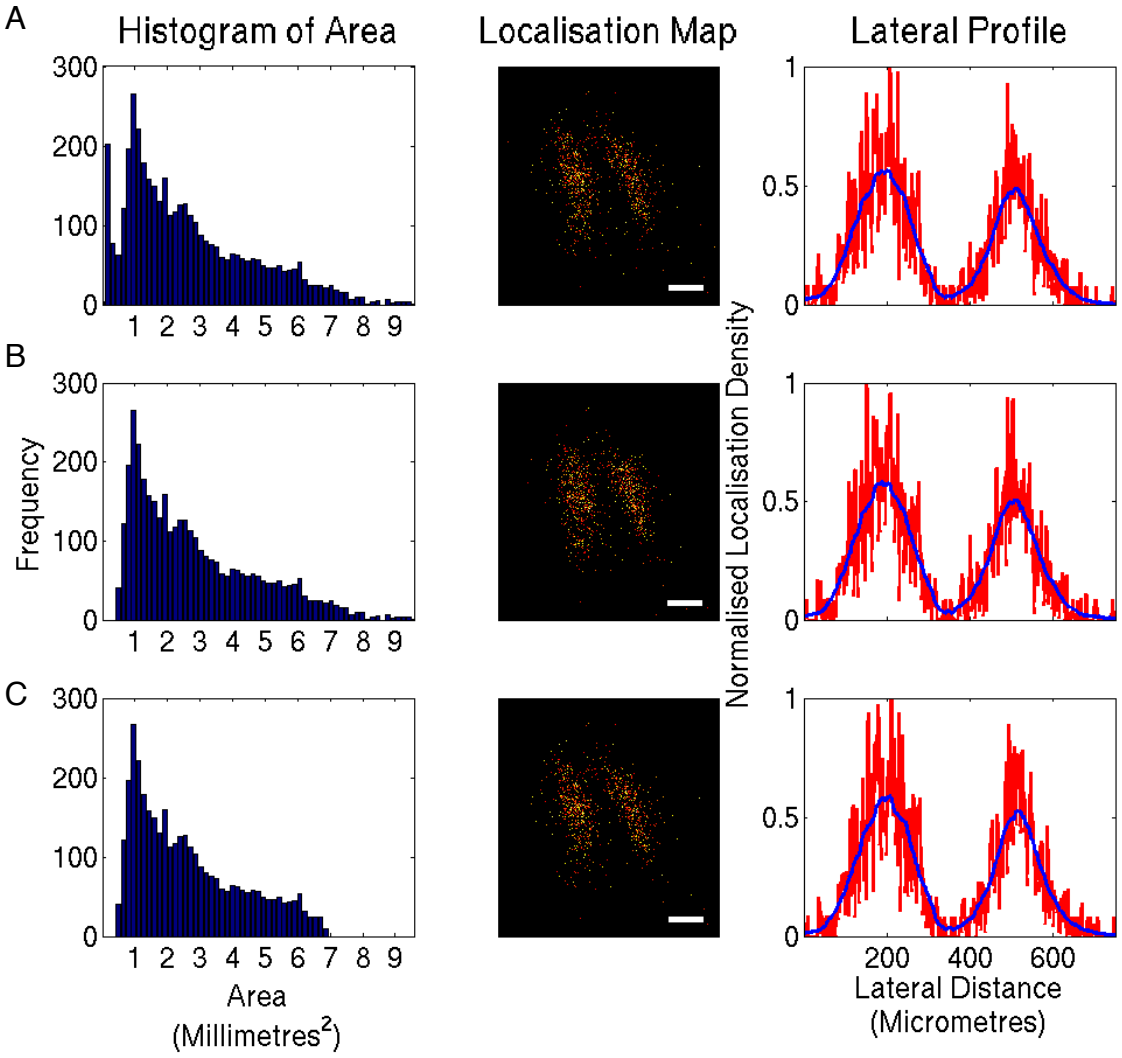

Figure 3.19. Localisation maps displayed alongside corresponding histograms of signal area, in addition to lateral intensity profiles across the approximated centre of the vessels. Part (A) shows results when accepting all signal regions. (B) displays results when rejecting signals with the smallest sizes illustrated by the first histogram peak in (A), and (C) shows results when additionally rejecting signals above 7mm^2. Scale bars, 200 μm.

Data Type		FWHMx (μm)		FWHMy (μm)	
		Tube 1	Tube 2	Tube 1	Tube 2
A	Raw	146	91	281	281
	Smoothed	150	122	311	280
B	Raw	145	92	271	278
	Smoothed	150	122	307	278
C	Raw	147	96	261	270
	Smoothed	151	123	301	270

Table 3.4. FWHM results measured on raw and smoothed lateral and axial image profiles across the approximated centres of the tube cross-sections for (A), (B) and (C) in Figure 3.19. Results are rounded to the nearest micrometre.

3.2ii.4.2 Lateral Imaging

Figure 3.20 displays the localisation map results from lateral imaging of a single capillary tube. Figure 3.21 shows the corresponding average axial count profile across the entire length of the tube. The FWHM of the interpolated tube profile is 212 μm. This is slightly larger than the nominal diameter of the capillary tube, however if the tube is not completely horizontal across the image, there will be an error in this estimate. Here, the ability of this technique to visualise the vessel structure across a larger area is demonstrated, where the ends of the tube are approximately 6.5 mm away from the focal point; the ability of the super-resolution technique ~~to~~ does not visibly degrade over the full 12 mm tube length.

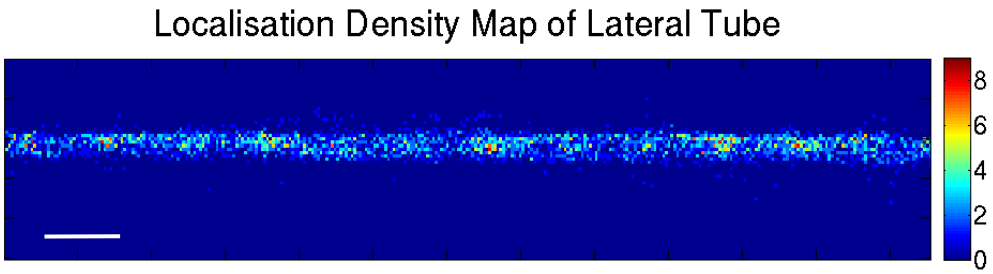

Figure 3.20. Localisation map obtained for lateral imaging of the capillary tube. The colour bar shows the localisation counts per pixel. Pixel size 38 x 42 μm, scale bar, 1 mm.

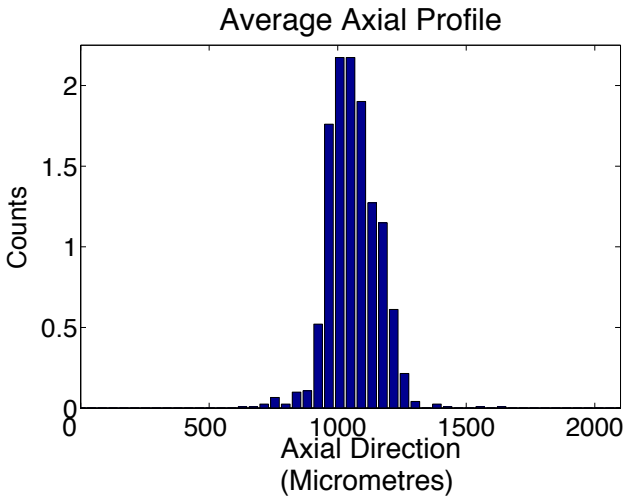

Figure 3.21. Average axial bar profile across the lateral direction for lateral imaging of the capillary tube.

Figure 3.22 displays the same results as that in Figure 3.20, this time using 2D Gaussian localisation profiles. To reduce the influence of a possible tilt in the tube over the lateral extent, average localisation profiles were measured at three points along the lateral extent of the tube, each with a window size of 3 mm. These are shown in Figure 3.23, and corresponding FWHM values for raw and smoothed data are presented in Table 3.5 (smoothing was consistent with that applied in Figure 3.17).

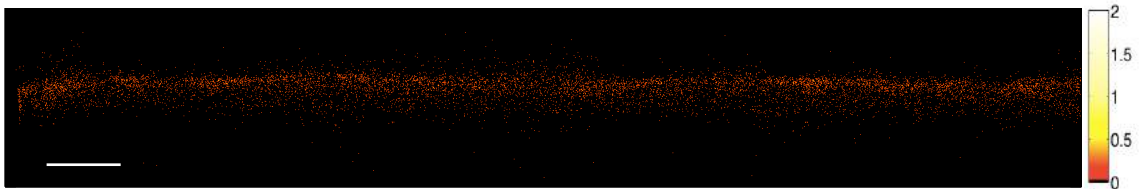

Figure 3.22. Lateral tube localisation map where each localisation is represented as a 2D Gaussian profile centred at $C = (C_x, C_y)$ with standard deviations, σ_x and σ_y, given by the average lateral and axial localisation uncertainty of the PSF. The resulting map from the sum of all the individual localisations across all frames creates an image in which the displayed intensity value is proportional to the chance of finding a microbubble positioned at that location. Scale bar 1 mm.

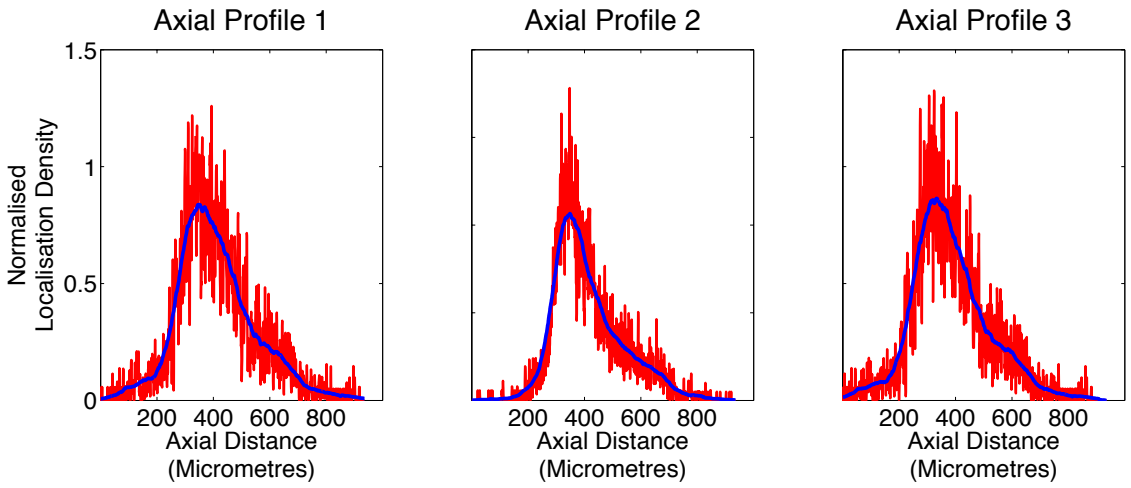

Figure 3.23. Localisation profiles through three sections of the lateral tube profile. Each profile displays the average over a 5 mm length of the tube. A line plot through the raw data is shown in red, and smoothed data using a sliding window of length 75 μm is shown in blue.

Data Type	Profile 1	Profile 2	Profile 3
Raw	254	123	233
Smoothed	232	178	220

Table 3.5. Table displaying FWHM measured on raw and smoothed axial image profiles across the three 5 mm sections of the lateral tube. Results are rounded to the nearest micrometre.

Corresponding colour spatial maps as seen in Figure 3.18 are displayed for lateral tube imaging in Figure 3.24, showing a small section of the tube length. Spatial patterns in signal features seen in cross-sectional data are further corroborated here, where the uppermost centroids predominantly have a smaller area and lower intensity which increases with depth, and only few low intensity signals are observed at the bottom of the tube.

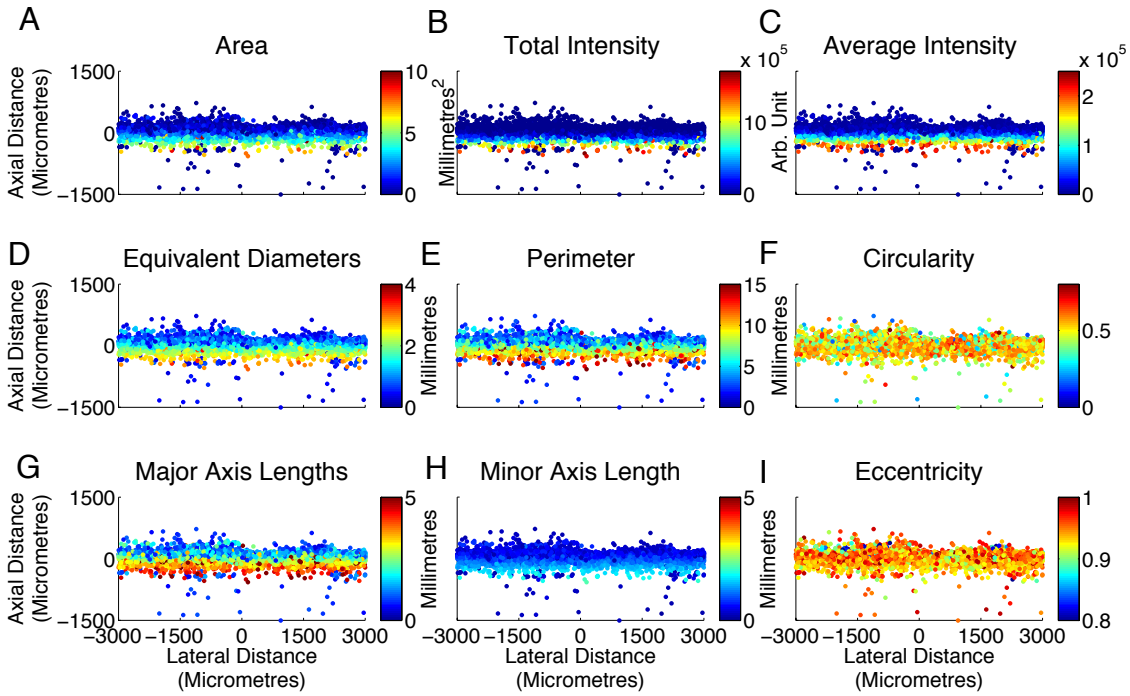

Figure 3.24. Colour spatial maps showing a small section of the lateral tube profile, where the colour bar displays the following signal characteristics: (A) the total signal area, (B) the total intensity of the signal, (C) the average signal intensity per square millimetre, (D) the diameter of a circle with the same area as the region, (E), the perimeter of the signal, (F) the circularity of the signal, (G) and (H) show the major and minor axis lengths, and (I) shows the eccentricity of the signal.

Comparison to Visual Assessment

Providing the frame and microbubble flow rate are such that the trajectory of bubbles can be captured a number of times through the field of view, visual assessment can be performed to identify the nature of each signal source. Acquiring a set of signals from known sources (e.g. a single microbubble) through visual assessment will allow measurement of common signal features corresponding to that source, and hence may aid in their identification in post-processing algorithms. Around 300 signals identified to be single bubbles were manually selected from 160 frames in the lateral tube flow data through dynamic visualisation. These 300 bubble signals are assumed to representative of those occurring within the entire dataset. Measured features of these signals are displayed in histograms in Figure 3.25. Differences in these feature measurements to those shown in Figure 3.24 may indicate signals originating from single bubbles and those that may instead result from multiple bubbles or noise. As an example, the total intensity of all single bubble signals identified did not exceed

$10 \cdot 10^5$ AU, which would exclude localisations positioned in the lower regions of Figure 3.24B.

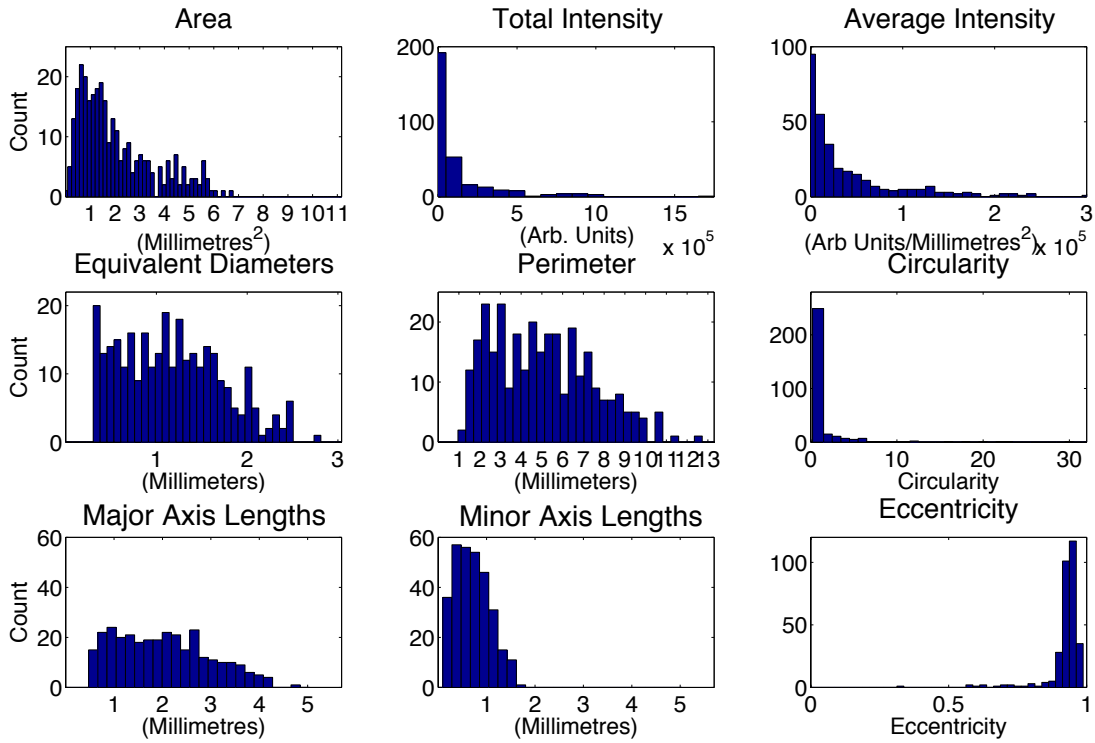

Figure 3.25. Histograms of signal features from 300 single bubbles found within the lateral image data.

Figure 3.26 shows six examples of single bubble signal profiles in the axial (Figure 3.26A) and lateral (Figure 3.26B) directions. A large variation in both shape, signal amplitude, and spatial extent across detected bubbles is evident. Thus, defining a 2D surface to fit to these signals for single bubble identification and high precision localisation may be difficult.

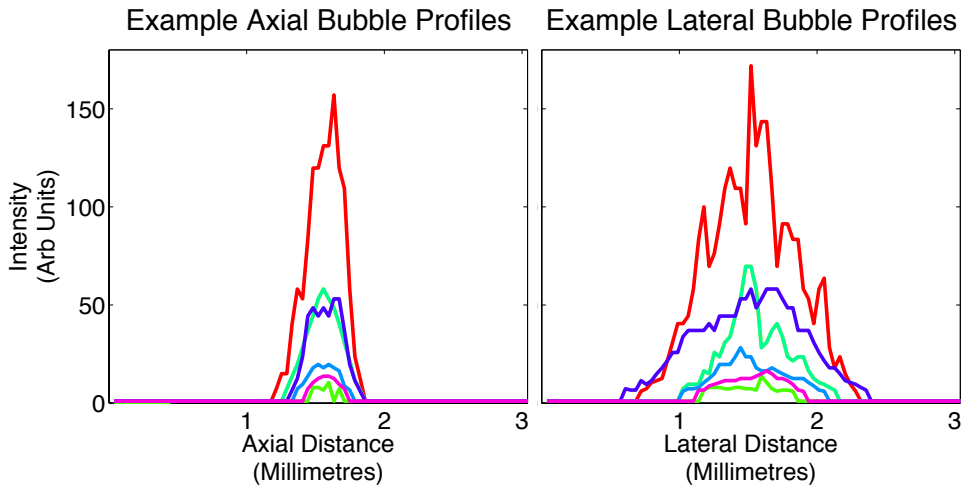

Figure 3.26. Example single bubble signal line profiles in the axial (A) and lateral (B) directions. Profiles show a large variation in both shape and signal amplitude.

Two example single bubble signals (blue scatter graph) and their corresponding Gaussian fit (multi-coloured surface) are shown in Figure 3.27, where the R-squared values are 0.7954 and 0.8817 respectively. The mean R-squared value resulting from fitting 300 candidate bubble signals to the Gaussian model was 0.8032 (c.f. mean R-squared = 0.9120 for wire signal), whereas the mean R-squared value was found to be lower at 0.7843 for 300 single bubble signals. This indicates that rejecting signals based on Gaussian fit error measurements such as R-squared may not be effective at determining those coming from single bubbles. If a fitting algorithm were to be implemented, a more representative 2D surface model would be required.

Without implementing fitting algorithms in the post-processing procedure, signals from unknown sources must be subjected to rejection criteria in order to remove unwanted signals before applying the centroiding algorithm; the range of signal features measured for the isolated single bubble signals identified within the lateral data could instead be used. In the following results, detected backscatter signals from the double tube experiment were processed again. By applying the ranges shown in Figure 3.25 to restrict bubble signals, a new localisation map for the double tube experiment was created. Figure 3.28 displays the resulting localisation map, signal area histogram, and corresponding lateral and axial profiles through the left and right tube respectively. The FWHMs of both the raw data shown in red, and a smoothed version of the data are displayed in Table 3.6 (smoothing was again consistent with that applied in Figure

3.17). FWHMs shown in Table 3.6 indicate a shorter axial distribution of scatterers in both tubes, while the width of the profiles is marginally wider to those values shown in Table 3.4.

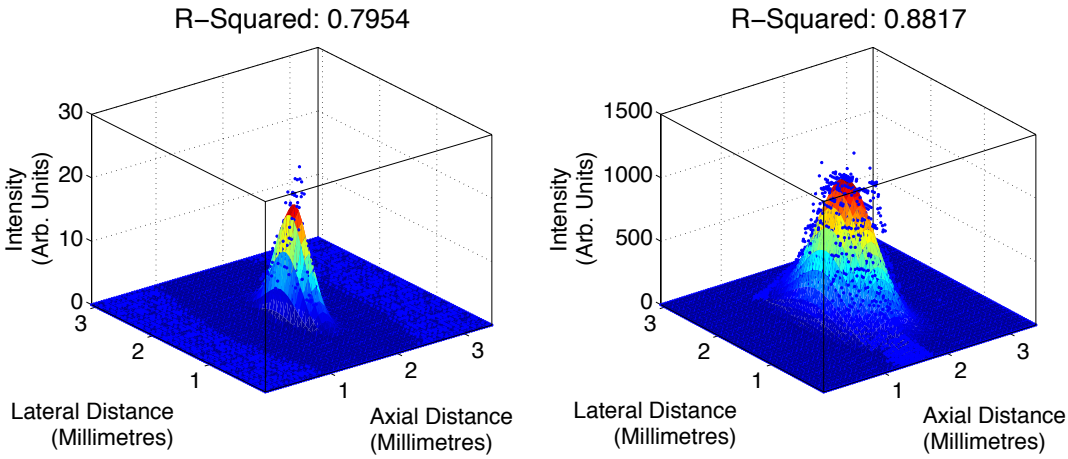

Figure 3.27. Two example single bubble signals (shown in blue) and their corresponding Gaussian fit (shown in jet colour map), where the RMSE calculated are 2.0, and 104.1 respectively.

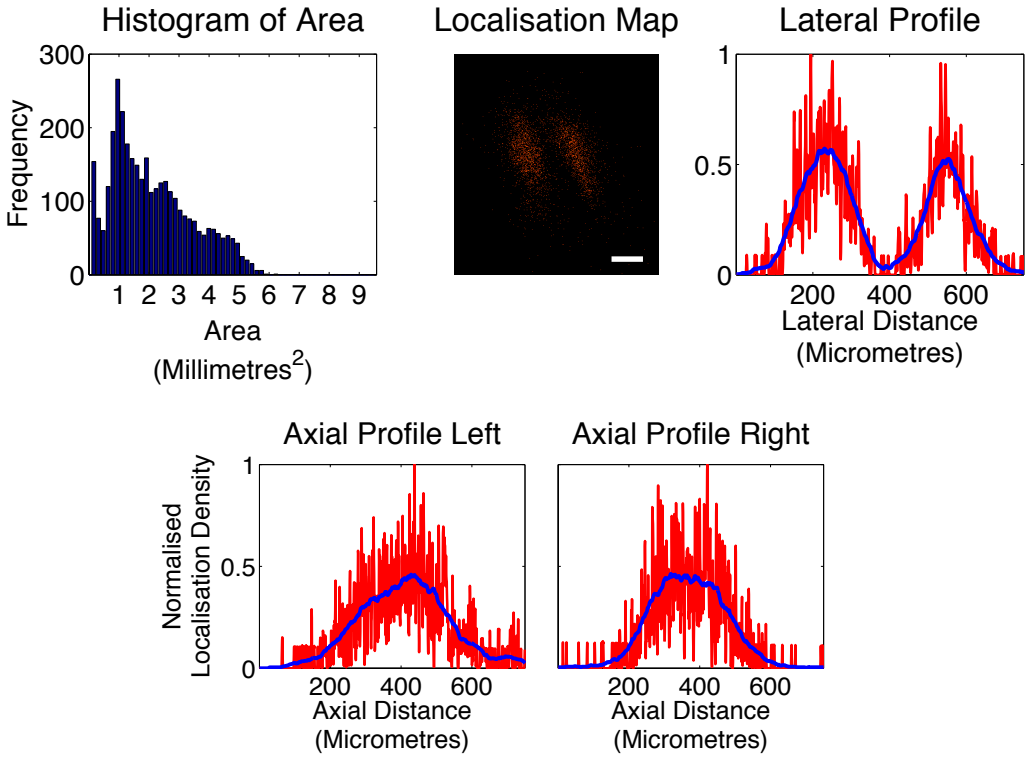

Figure 3.28. Localisation map, histogram of signal area, and corresponding lateral and axial profiles through the left and right tube respectively are displayed where bubble signals are restricted to within the range found for single bubbles as shown in Figure 3.25. The line plot through the raw data are shown in red, where the blue shows the result after applying a sliding smoothing window of length 75 μm.

Data Type	FWHMx (μm)		FWHMy (μm)	
	Tube 1	Tube 2	Tube 1	Tube 2
Raw	167	111	249	257
Smoothed	165	134	291	257

Table 3.6. FWHM results measured on raw and smoothed lateral and axial image profiles across the approximated centres of the tube cross-sections. Results are rounded to the nearest micrometre.

Figure 3.29 shows the performance of the algorithm over 4 frames of the lateral tube video data. It can be observed that two bubble signals are travelling at different speeds to each other and thus these 4 frames document different stages of the point at which one overtakes the other. As can be seen, the algorithm identifies the presence of two bubble signals when signals are separated in Figure 3.29A and B. However, while these multiple bubble signals fully or partially overlap, in Figure 3.29C and D, the algorithm detects a position in the centre as if they were an individual bubble.

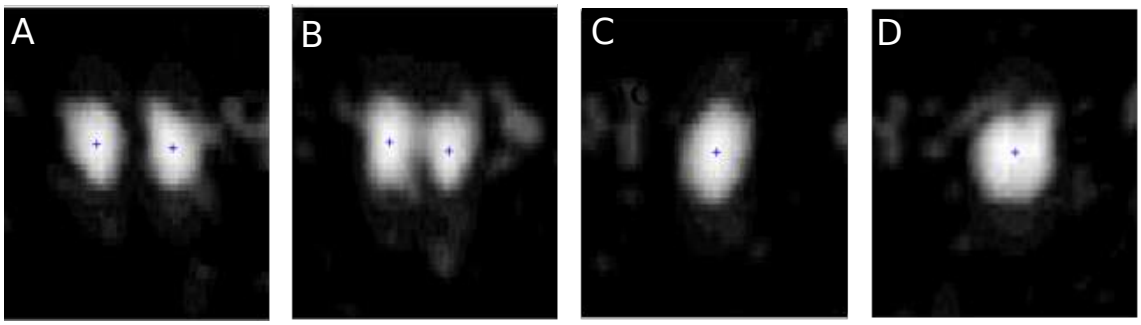

Figure 3.29. Four consecutive frames of lateral tube data. This shows two spatially separated bubbles flowing at different speeds in (A) and (B), (C), the point of overlap, and (D) the bubbles signals beginning to separate. The blue crosses indicate the centre of mass localisation. Contrast in these images has~~ve~~ been enhanced for visualisation.

In this instance, this false detection does not present a problem since the localisation remains within the lumen of the vessel being imaged. However, it is desirable that the localisation algorithm should reject objects such as those in Figure 3.29D as they are indistinguishable from multiple spatially separated but unresolved microbubbles. As a simple example, if two parallel vessel stuctures exist within the resolution size of the

imaging system, a single bubble present in each of the tubes may provide overlapping or partially overlapping backscatter signals. Centroiding algorithms may then find a localisation position between the two tubes. Furthermore, possible interference patterns caused by the presence of clusters of microbubbles within the resolution may result in speckle that could have peaks outside the vessel lumen. The following cross-tube phantom design provides examples of these incidents, as shown in the next section 3.2ii.4.3.

3.2ii.4.3 Crossed Tube Imaging

The crossed phantom design allows assessment of the effects of overlapping or interfering bubble signals in separated vessel structures, giving rise to localisations outside of the vessel structure. Figure 3.30A shows an example image frame consisting of spatially isolated bubble signals, while Figure 3.30B, C and D show examples where multiple bubble signals are interfering.

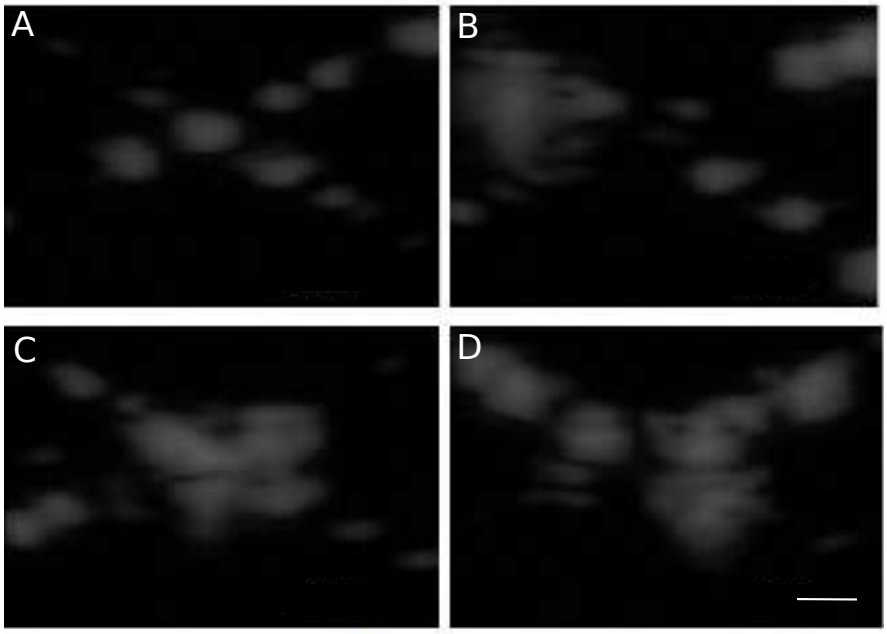

Figure 3.30. (A) Example of spatially isolated bubble signals in crossed tube phantom. Parts (B),(C) and (D) show examples where bubble signals are interfering or overlapping.

Resulting localisations using super-resolution algorithms with thresholding are shown in Figure 3.31, alongside optical images of the centre section of the crossed tube phantom. Figure 3.32 shows the corresponding localisation map overlaid upon the summed

diffraction limited image data. Effects of the system elevational resolution can then be analysed if the angle of the target structure is known. The angle between the crossed tubes was estimated using both optical and super-resolution images for comparison. Linear fits to the super-resolution localisation positions found an angle of 65.8 ± 1°; similarly, an angle of 65.8 ± 0.8° was found by performing line fits on four optical images of the crossed tube phantoms.

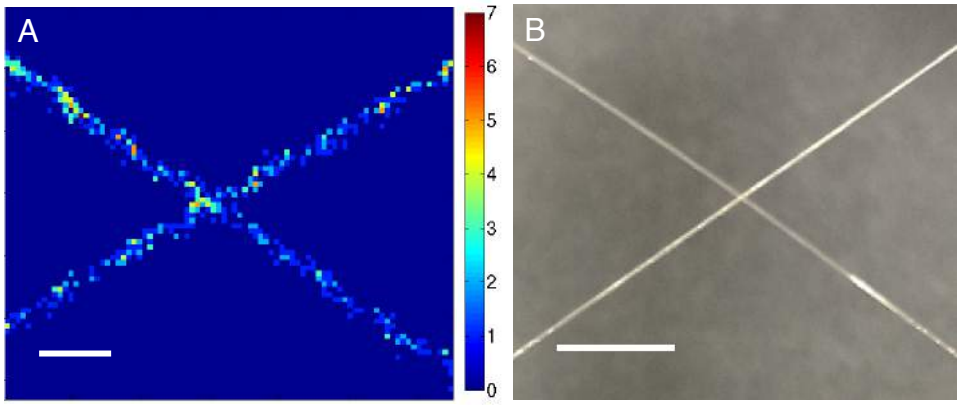

Figure 3.31. (A) Localisation map of crossed tube experiment, scale bar 500 μm. The colour bar shows the localisation counts per pixel. (B) Optical image of the crossed tubes, scale bar 5 mm.

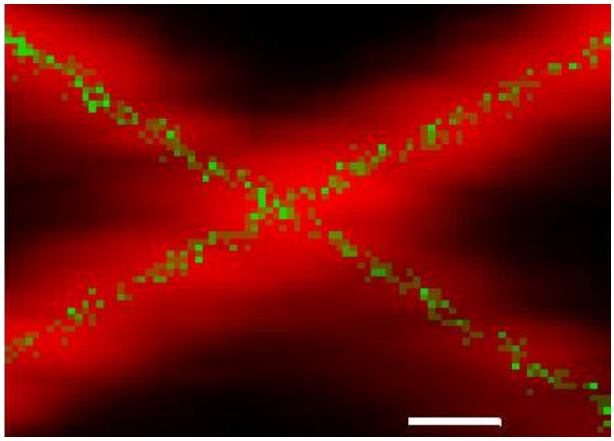

Figure 3.32. Overlay of the centroid density map (green) on the summed diffraction limited image data (red). Scale bar 500 μm.

These angles can then be used to calculate the expected elongation, L_E, in the localisation distribution when imaging the cross-section of this phantom. Equation (3.5) becomes,

$$L_E = \frac{200}{\cos 65.8} + 1100 \cdot \sin 65.8 \tag{3.18}$$

$$= 1491.2\ \mu m$$

Figure 3.33 displays the resulting localisation maps of cross-sectional imaging of the crossed tube structure at three slice positions: the centre (Figure 3.33A), and incremental distances equal to the elevational width, 1100 µm, (Figure 3.33B) and 2200 µm (Figure 3.33C). The lower localisation count in the image at the centre of the tubes may be due to the rejection of a large number of signals deemed to come from overlapping or interfering signals. A larger count can be seen in both vessel profiles in Figure 3.33B, where 2 distinct profiles can be resolved. The results of imaging a slice further from the centre, (Figure 3.33C), displays a clear separation in the two localisation profiles. Corresponding FWHM values are considerably elongated compared to the 200 µm tube diameter (Figure 3.33F). The FWHMs of the image structures in Figure 3.33B are in good agreement to the expected elongation calculated in Equation (3.18).

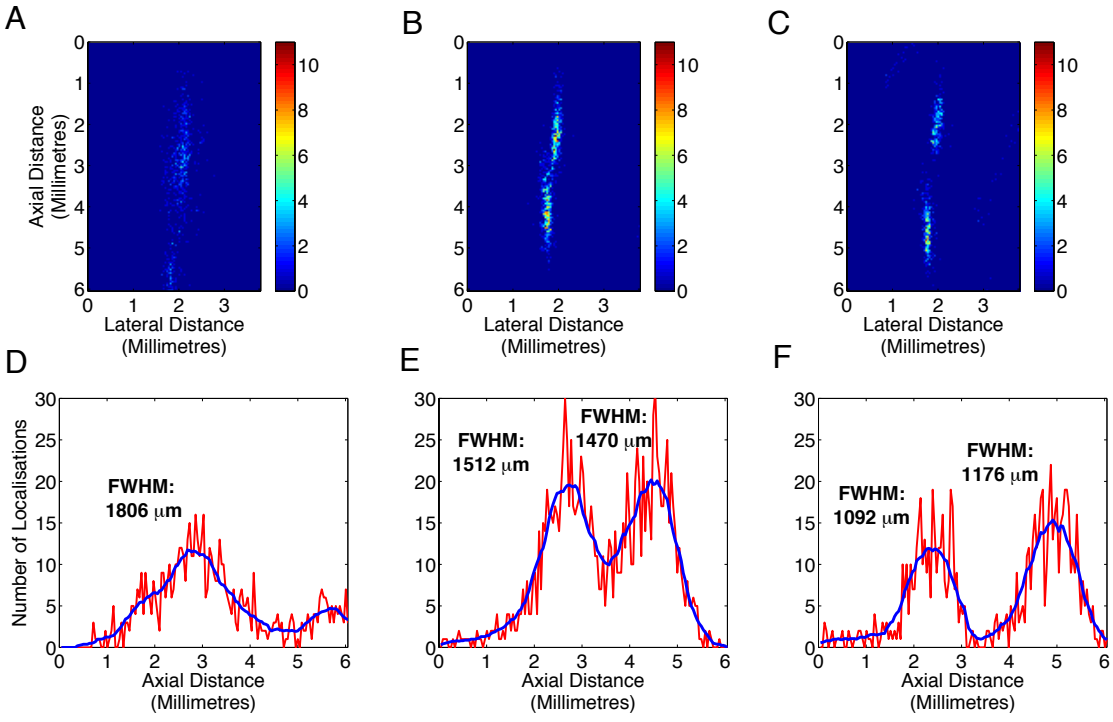

Figure 3.33. Localisation maps of cross-sectional imaging of the crossed structure at three slice positions, displaying localisations at (A) the centre, (B) 1100 µm from the centre, and (C) 2200 µm from the centre. The colour bar shows the localisation counts per pixel. Corresponding average axial line profiles through raw (red) and smoothed (blue) data are shown in (D), (E) and (F).

The profile shown in Figure 3.33D is approximately 300 μm larger than that expected, and additionally a large amount of signals are evident below the expected tube diameter. This may be due to the occurrence of large, multiple, or interfering bubble signals at the centre similar to those seen in Figure 3.30. Based on the estimated tube angles, and the elevational distance moved, the estimated tube separation can be calculated using trigonometry to be 1.4 mm and 2.8 mm at 1100 μm and 2200 μm respectively. The distances calculated from smoothed data in Figure 3.33 are 1710 μm and 2450 μm respectively.

Figure 3.34 shows a similar spatial distribution of bubble signal features as observed for both the double and lateral tube data, where the largest and most intense signals, likely to be similar to those seen in Figure 3.30B, C and D, lead to localisation points outside of the tube diameter, for example those located in the space between the two vessels.

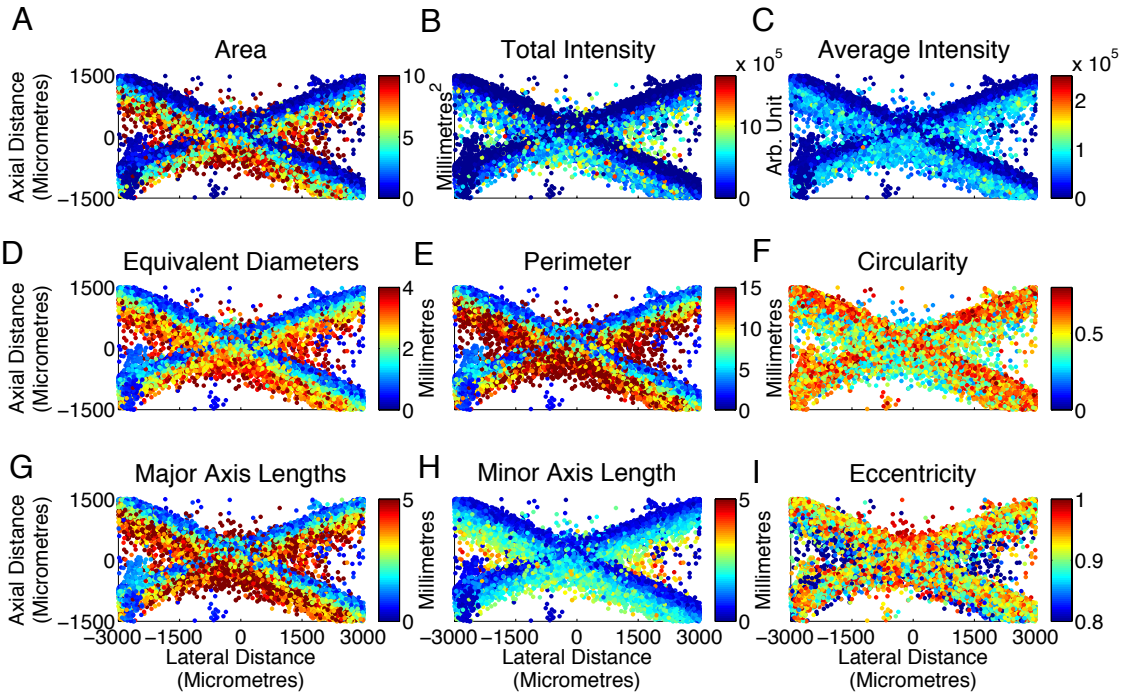

Figure 3.34. Colour spatial maps showing a small section of the crossed tube profile, where the colour bar displays the following signal features: (A) the total signal area, (B) the total intensity of the signal, (C) the average signal intensity per square millimetre, (D) the diameter of a circle with the same area as the region, (E), the perimeter of the signal, (F) the circularity of the signal, (G) and (H) show the major and minor axis lengths, and (I) shows the eccentricity of the signal.

The corresponding localisation density map using Gaussian rendering is shown in Figure 3.35, where some blurring can be observed at the centre of the structure, as well as in areas below the tube diameter.

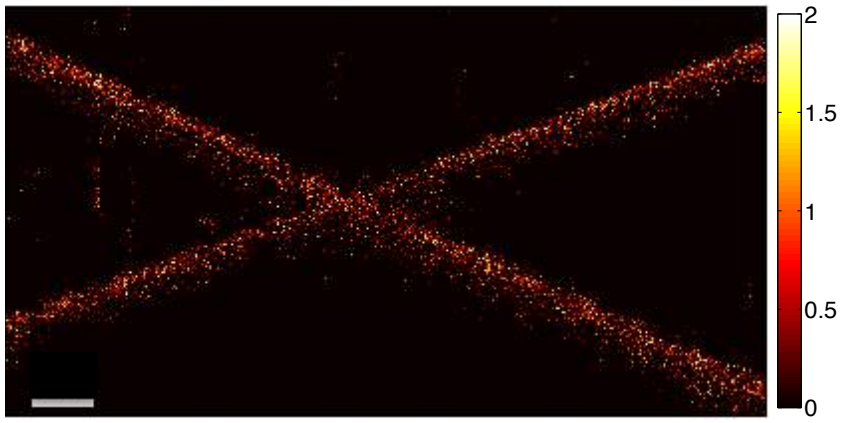

Figure 3.35. Crossed tube localisation density map using Gaussian rendering, where the displayed intensity value is proportional to the chance of finding a microbubble positioned at that location. Scale bar 1 mm.

3.2ii.4.4 In Vitro Velcocity Tracking

Velocity tracking was tested in lateral and crossed tube phantoms; examples of tracks found in lateral tube data are shown in Figure 3.36, and crossed tube data in Figure 3.37. The number of localisations over the field of view depends on the speed of flow and the US imaging frame rate. Here the flow rate was set to 200 µl/min, corresponding to a mean speed of 106 mm/s flowing through a 200 µm tube (Appendix Section 9.2). To confirm whether this lies in the range of laminar flow, Reynolds number can be calculated by

$$Re = \frac{\rho v d}{\mu}, \tag{3.19}$$

where the density of water is $\rho = 1000\ \mathrm{kg/m^3}$, the diameter is $d = 2 \cdot 10^{-4}\ m$, and the dynamic viscosity of water at 20° is $1.002 \cdot 10^{-4}\ Ns/m^2$. Since $Re = 212 \ll 2100$, this suggests flow will be laminar within the tube [219].

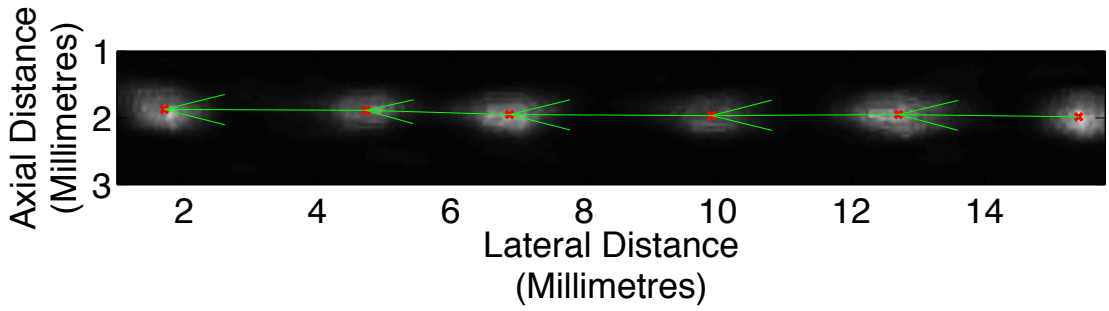

Figure 3.36. Example of single bubble tracking in lateral tube vessel, where the tracked bubble speed was estimated to be 65.2 mm/s.

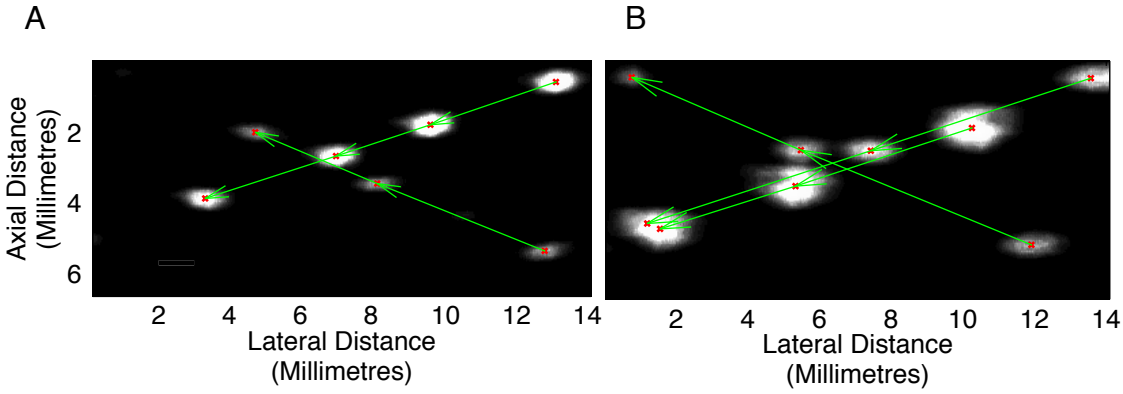

Figure 3.37. Velocity tracks and bubble signals over seven consecutive frames within the crossed tube phantom, with (A) a lower concentration, and (B) a higher concentration.

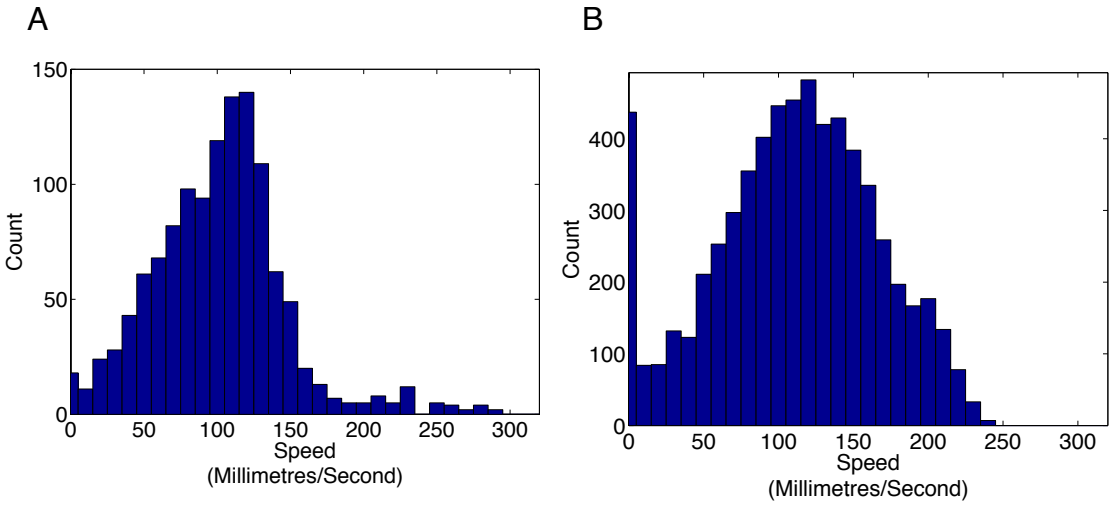

Figure 3.38. Speed histogram using single bubble tracking in (A) lateral tube image data, and (B) crossed tube image data, at a flow rate of 200 ul/min (106 mm/s). The mean and median speeds tracked are 101.2 mm/s and 103.1 mm/s respectively for the lateral tube, and 110.2 mm/s and 113.1 mm/s for the crossed tube.

Tracked speed histograms are shown in Figure 3.38 displaying a peak count at a velocity of 120 mm/s. The mean and median speeds tracked are 101.2 mm/s and 103.1 mm/s respectively. If we assume a laminar flow within the tube, the parabolic flow profile will mean speeds will range from 0 to V_{max}, where the average speed is expected to be $V_{max}/2$. V_{max} in the lateral tube experiments was found to be 287.8 mm/s which is faster than the expected maximum velocity based on the mean speeds demonstrated here. The search window was defined to be the size of the entire field of view since the expected velocity was presumed to be unknown. This may lead to increased false positive detections if the number of signals in the field of view is large or if the SNR is low. The mean of tracked speeds within the crossed tube were 110.2 mm/s and 113.1 mm/s respectively. Figure 3.39 shows the directional component of velocity, where the different flow directions are evident.

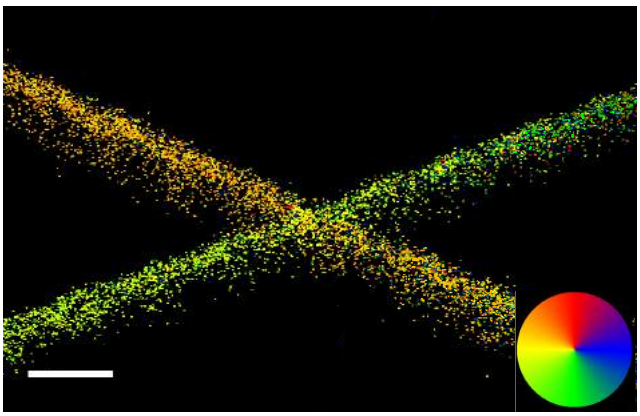

Figure 3.39. Directional velocity map of the crossed tube structure shows different flow directions of the two tube structures. Scale bar 1 mm.

3.2ii.5 Discussion

By localising isolated US signals from microbubbles flowing within vessels, capillary structures smaller than the estimated diffraction limited resolution of the imaging system have been visualised. Additionally, the development of a microbubble tracking technique allows visualisation of the flow at a super-resolution scale.

3.2ii.5.1 Analysis of super-resolution Images

As can be observed in the cross-sectional double tube results, the centroid count distribution reduces towards the edges of the tube cross-section, instead of that of a

uniform distribution as would be expected assuming a uniform bubble concentration across the tube. Furthermore, the FWHMs of the double tube profiles in the lateral direction were measured to be narrower than the nominal tube diameter. The same microbubble can be clearly observed to flow along the entire tube length in the lateral data and therefore it is unlikely that slower flowing bubbles travelling at the edge due to a parabolic flow profile are being destroyed during imaging. A possible explanation for this distribution is that there may be damping of the microbubble backscatter signals due to reduced bubble oscillations close to vessel boundaries [220]. The presence of a wall has been shown to suppress bubble oscillation amplitudes and mean backscattered pressures [183], [184]. Furthermore, the amplitude of single bubble oscillations has been found to decrease with decreasing distance to a wall with fixed frequency [177]. This damping has been attributed to a number of issues including dissipation introduced by the viscous boundary layer at the wall, thermal diffusion, re-radiation of sound in addition to asymmetric oscillations which may arise in the vicinity of a wall [207]. Furthermore, the vicinity of a rigid wall has been demonstrated to cause a shift in the resonance frequency of the bubble. Since experiments in this chapter were carried out at a fixed insonation frequency of 2 MHz, it is possible that the occurrence of weaker signals close to the wall due to a this shift may not be detected, or may be misclassified as noise and thus rejected.

Furthermore, assuming that the localisation corresponds to the position at the centre of each microbubble, the diameter of the vessel will be underestimated by at least the diameter of the microbubble, which is likely to be in the range of 1-7 μm. Furthermore, the distribution of red blood cells is not homogeneous in flowing blood due to the Fåhræus effect. This effect occurs due to the fact that at high shear rates, the disc-shaped red blood cells rotate as a result of the velocity gradient. This results in cell migration towards the centre of the vessel, resulting in a lower viscosity region (a few micrometres thick) next to the boundary wall [29], [221], the size of which depends on the shear rate [222]. Since microbubbles have an intravascular rheology similar to that of red blood cells [201], [223], [224], it may be possible that a microbubble-free layer may exist at the vessel boundary, causing a further underestimation of the vessel size depending on the shear rate within the vessel [225].

There are a number of key factors which influence the visualisation of the vasculature in the final super-resolution images. Firstly, the spatial resolution is limited by the localisation uncertainties σ_x and σ_y of the system, since these determine the size of each Gaussian localisation profile in the image. Secondly, the density of these localisations determines the SNR in the rendered image. A reduced localisation density gives less complete information about the spatial distribution of the bubble flow inside the structure. A fundamental compromise therefore exists between the exclusion criteria of bubble signals and the density of localisations in the final image. The strict inclusion of bubbles with only a narrow spectrum of sizes and intensities similar to that of our expected PSF should result in a sharper image with a higher resolution. However, the spatial distribution of localisations will be more sparse unless acquisition time or frame rate is increased. The size of each Gaussian localisation in the image compared to the target vessel area gives an indication of the number of localisations required to create adequate visualisation in the image; in the work shown here, with the 2D localisation precision under 1 μm in size and the cross-sectional area of each vessel structure at 31400 μm^2, providing full spatial coverage of both tubes in the final image would require over 62800 localisations. Since the diffraction limited resolution of the system requires that at most a single microbubble should be imaged in any one frame, a significantly long acquisition time would be required. The relationship between the localisation precision, the diffraction limited resolution, the microbubble concentration, and the density of localisations in the final image are therefore key factors for optimising the performance of this technique. These are implemented in a Poission statistical model included in Section Appendix 9.1.

3.2ii.5.2 FEATURES OF BUBBLE SIGNALS

The colour encoded spatial maps display some of the underlying features of each candidate bubble signal at their estimated localisation position. A clear dominance of smaller, lower signals from the uppermost centroids is evident. Furthermore, the equivalent diameters, perimeters and major and minor axis lengths follow a similar trend in spatial distribution.

In the event of a tilted tube, smaller, lower intensity bubble regions may be caused by the bubble position within the elevational plane; if bubbles are located on the edge of

the elevational field of view, their signal will be reduced due to the amplitude profile displayed in Section 3.2i.4.1. However, if this were the case, low amplitude signals would be evident in the top and bottom of the image as the tube extends out of the transducer field of view; the significant dominance of low amplitude signals near the top of the tube compared to the bottom implies that there may be alternative factors causing this.

As can be visualised in Figure 3.30, the sizes of multiple interacting signals appear in general larger than those of single bubble signals. In addition, they appear to exhibit more complex perimeter and intensity patterns. One approach to eliminating the possibility of these signals degrading the final image, as is implemented in this chapter, is to attempt to identify and reject these signals based on shape and intensity; this is additionally performed in a number of optical microscopy methods [140], [226], [227]. Centroids from larger, brighter signals evident in the lower regions of the tubes (as seen in Figure 3.18, Figure 3.24 and Figure 3.34) may be caused by similar multiple bubble interactions, where the centre of mass of interacting bubble signals no longer represents the location of the underlying source, and a mis-localisation thus occurs outside of the nominal tube diameter. This may contribute to a proportion of the localisations outside the tube diameter, however, the significant dominance of signals below the nominal tube diameter, and not above or around, implies that there may be other contributing factors.

Due to their thin shell and gas core, microbubbles are substantially less dense than water, and thus float. The degree and rate of floatation is primarily determined by the microbubble size, density and viscosity of liquid in the vessel, and density of the gas within the microbubbles [228]. Buoyancy of gas filled microbubbles may contribute to the spatial distribution of microbubbles in the tube even with mixing of microbubbles prior to imaging [229]. Weaker bubble signals in upper regions could instead be attributed to a damped response from bubbles floating up against the upper tube wall [183], [208]. The damping effect would thus be less significant at the lower edge due to the presence of fewer bubbles, and furthermore these bubbles would be less likely to be forced against the lower wall.

Furthermore, increased floatation of larger bubbles may mean that signals coming from lower regions are predominantly from smaller bubbles. The insonating frequency of 2 MHz corresponds to the resonance frequency of bubbles approximately 3.2 μm in size [171], [172]. In previous microbubble sizing and counting experiments, approximately 80% of the bubbles were below 3 μm, with a mean microbubble diameter of 2.21 μm, but ranged up to 7.27 μm in diameter. If bubble signals present in the lower regions of the tube correspond to the resonance frequency of the insonating sound of around 3.2 μm, then this could result in significantly enhanced backscatter signals in a particular region. Resonant or ringing bubbles will have a strong scattered signal, where continuing ringing oscillations after the forced oscillation due to insonation has terminated [104] will spread the signal in the axial direction and could lead to a localisation at a position deeper than that of the scatterer. In these cases, the correspondence between centre of mass and scatterer position may not hold. Asymmetrical lateral profiles through super-resolution images could be observed in Figure 3.23, where higher localisation counts were present below (i.e. at larger axial distance) rather than above the tube position, which could be a result of inaccuracies in the localisation process. The accuracy of the centre of mass assumption is therefore an important topic for investigation in the future.

The flow within the tubes was running from right to left in both tubes (Figure 3.37) with the axial distance representative of distance towards the ground. Radiation force only acts when the acoustic field is present, and thus its magnitude was not expected to cause significant displacements at these diagnostic pressures and over such short pulse durations [11][12]. Furthermore, radiation force would cause an increased downward movement of bubbles, which would increase with increased US exposure. Since all the bubbles enter the field of view on the right hand side of the image, an increase in bubble motion would be expected with distance across the US field – this was not evident in the results. Increases in pulse duration, pulse repetition frequency (PRF), pressure and proximity to microbubble resonance may increase this effect. [13]. Secondary radiation force is not expected to be significant when using such a low bubble concentration.

Thresholds were based on the characterisation of signals considered to originate from single bubble signals, however the centroiding algorithm showed an inability to identify

signals which overlapped significantly. This may be a cause of some localisations existing outside the tube structures, particularly the increasing number of localisations that can be observed as the two crossed tube vessels gain proximity, as shown in Figure 3.34. Thresholds were determined empirically in these experiments; in the future, an automatic means of differentiating these signals is required.

In optical super-resolution microscopy, multiple model PSFs can be fit to partially overlapping signals using the DAOSTORM algorithm [230] created for high density data. At higher concentrations than those used here, identification and accurate localisation of individual bubble sources within some partially overlapping signals may be possible, however, in the occurrence of speckle, the accurate localisation of each underlying scatterer using this technique is not possible. Furthermore, the development of a model PSF function for microbubbles which is more suited than the 2D Gaussian model must be identified before approaches such as these are implemented. Additionally, complex underlying physical interactions of the multiple bubbles and US wave may limit the accuracy of such an approach. Without tested approaches specialised for localisation of high density data, and further investigation into the effects of nearby or interacting bubbles on the resulting image, it remains important for this approach to ensure the microbubble concentration is at a level where multiple microbubble events are isolated.

3.2ii.5.3 MICROBUBBLE CONCENTRATION

Prior to imaging, the microbubble concentration needed to ensure a high probability of imaging single bubbles in each frame in the cross-sectional experiments was calculated. During initial testing, this estimated concentration was found to be considerably lower than that required for efficient acquisition, where bubbles initially occurred approximately every 100 frames. The concentration in the beaker was consequently empirically adjusted to achieve a higher microbubble detection rate. The disparity between the calculated concentration and that observed experimentally may be due to a number of experimental uncertainties. The initial estimated concentration was based on the assumption that the microbubble size distribution gives rise to a frequency range over which bubbles strongly oscillate, and that the percentage of the bubble population with resonant frequencies which fall within the 50% bandwidth will be detected [231].

In reality, however this may not be the case. Differences in the transmit and receive bandwidths will affect the overall detection of bubble signals. The transmit bandwidth defines the frequency range that could excite the microbubbles, however, signals from excited bubbles may not be present in the resulting data if its frequency lies beyond the receive bandwidth of the transducer. Furthermore, a reduction in microbubble concentration over time due to dissolution in the water will mean a higher initial injection concentration will be required for sufficient bubble per frame density at the target location. Microbubbles may also be destroyed within the flow system, which contained long lengths of larger tubing. Additionally, bubble floatation within the beaker suspension may mean only a fraction of the bubbles within the dilution were introduced into the flow system.

3.2ii.5.4 US FREQUENCY

The resolution of conventional US can of course be improved by using higher frequency US. However, as discussed in Chapter 1, an inherent compromise exists that a higher frequency also results in a lower penetration depth. For any given US frequency, implementing localisation approaches such as this should be able to improve the spatial resolution.

3.2ii.5.5 ASSESSMENT OF ELONGATION

The resolution of the US scanner in the elevational direction was measured to be approximately 1.1 mm, see Figure 3.1. In cross-sectional experiments, in order to minimise the reflection of the surface of the tube, the transducer was set at a small angle. The tilt of the transducer with respect to the line perpendicular to the tube was estimated to be around 5°. The 2D image displayed on the scanner is a projection of the sampled slice along the elevational direction z, and therefore imaging the tube at a slight tilt will elongate its appearance in the super-resolution image. When elongation due to the tilt of the tube is combined with the size of the tube, the effective shape over which localisation events are expected to occur is an ellipse with major axis length of approximately 300 μm. The angle, however, is purely an estimation; at these small angles, an increase or decrease of 1° will change the expected FWHM diameter by as much as 19 μm using this system. Centroids detected outside of this elongated region in the image could be attributed to reflections at the tube wall that can interfere with the

reflections from the microbubble, or to the presence of multiple bubbles in the resolution cell as previously discussed.

3.2ii.5.6 LOCALISATION PRECISION

The resolution of super-resolution imaging by single bubble localisation is limited ultimately by the achievable localisation precision which is estimated to be in the range of 0.1 to 6.5 μm for this unmodified clinical system using compressed image data and centroiding. For acoustic super-resolution, it is necessary that the microbubbles are flowing through the target volume. In these experiments, the distance moved by a fast moving microbubble during the time taken to scan one PSF sized area for speeds of 200 μm/min is estimated to be approximately 47 μm in the lateral direction perpendicular to the plane of imaging (Appendix Section 9.3). In this imaging set-up, this corresponds to a distance just under two image pixels in size. Since the bubbles remain within the 200 μm internal diameter, the signal localisation is still likely to be positioned within the vessel structure, however this may be a problem if the bubble motion involves a change in direction. Additionally, flow speed may have implications on microbubble signal features. The spatial extent of the signal may change depending on the relationship between the scan direction and the flow direction. Slower flows characteristic of the microvasculature, however, will have considerably less motion and thus this may be more of an issue for larger vessels. In future, the use of faster US scanners capable of receiving on all, or a large number of detector elements in parallel will allow the motion of the microbubbles to become negligible compared to the localisation precision.

3.2ii.5.7 VELOCITY MAPPING

The bubble tracking algorithm was able to generate velocity maps where speed histogram distributions of two *in vitro* phantoms demonstrated mean and median speeds which correlated well to flow rate settings with assumed laminar flow. The extension of this technique to extract flow velocity data has the significant advantage of providing flow information at a super-resolution scale. Furthermore, it enables the detection of bubble velocities for 360° in plane, in contrast to conventional US Doppler imaging, which is sensitive mostly to flow towards or away from the transducer and is unable to resolve speeds at micrometre scale.

The accuracy of velocity tracking using single bubble localisation depends on the precision of localisation measurements in each frame. The velocities in the lateral and axial direction are given by,

$$v_x = \frac{(C_x^2 - C_x^1)}{\Delta t}, \tag{3.20}$$

$$v_y = \frac{(C_y^2 - C_y^1)}{\Delta t}, \tag{3.21}$$

where C_x^1, C_y^1 and C_x^2, C_y^2 are the lateral and axial localisation positions of a bubble detected in frame 1 and frame 2 respectively, and Δt is the time interval between frames. The error in the velocity calculation assuming that the frame time interval is known without error, is then given by the following relation, (shown for the lateral component as an example),

$$\sigma_{vx} = \sqrt{\left(\left(\frac{1}{\Delta t}\right)^2 \cdot {\sigma_x}^2 + \left(-\frac{1}{\Delta t}\right)^2 \cdot {\sigma_x}^2\right)} = \frac{\sqrt{2}}{\Delta t}\sigma_x \tag{3.22}$$

$$= \pm\sqrt{2}\,\sigma_x \cdot frame\ rate. \tag{3.23}$$

With localisation precisions given by σ_x= 0.9 μm and σ_y = 0.6 μm in the lateral and axial directions respectively, the errors on the velocity measurements are given by

$$\sigma_{vx} = \pm 32\ \mu m/s$$

and

$$\sigma_{vy} = \pm 21\ \mu m/s.$$

Thus, this sets a lower limit on the slow flows that can be estimated using this approach. With a different imaging system or data format, higher SNR, or modified frequency and depth, the localisation precision, and hence the velocity precision will vary.

3.2ii.5.8 Overall Resolution

Factors discussed here make it difficult to determine the overall resolution of the super-resolution US imaging system presented. However, it is clear from the results in Figure 3.15 that two 200 μm inner diameter cellulose tubes can be visualised beyond that of the diffraction limited image data, and where the whole 12 mm length of this tube in the field of view can be observed at high resolution. These experiments were performed at depths of 6-7 cm, far beyond the depths achievable with many other high resolution techniques (such as photoacoustic tomography and acoustic angiography). Since this was performed in water, the effects of intervening tissue will however need to be addressed. The limit on the localisation precision is dependent on many system characteristics as demonstrated and discussed in Section 3.2i.

3.2iii Poisson Statistical Assessment of Algorithm

3.2iii.1 Aim

To model the occurrence of bubbles in image frames using Poisson statistics to assess the performance of the super-resolution algorithm for single bubble detection.

3.2iii.2 Introduction

A controllable bubble concentration is crucial to ensuring the imaging of isolated bubbles. Furthermore, in the occurrence of multiple bubbles within the resolution of the imaging system, an effective algorithm is needed to reject these signals. The use of a statistical model to predict the occurrence and number of bubble signals is explored.

3.2iii.3 Theory

Poisson statistics can be used to express the probability of a given number of events occurring in a fixed interval of time or space, if these events are independent and discrete, and occur with a known average rate [232], [233]. In this work, an event is defined as the presence of a bubble, and the fixed spatiotemporal interval of observation is an image frame, where it is assumed that the bubbles do not cluster, and therefore bubble events can be defined for a finite set of values of k. The imaging of microbubble flow within the vessels is assumed to be stochastic and discrete, such that it involves a

randomly determined set of observations, where each observation, or image frame, can be considered as a sample from a probability distribution. In this case, the probability P of having k bubbles in an image frame can be given by the following relation

$$P(k) = \frac{\mu^k e^{-\mu}}{k!}, \tag{3.24}$$

where μ is the Poisson expectation value, found using the known number of events occurring in one sample volume, V_S, given by

$$\mu = C \cdot V_S, \tag{3.25}$$

where C is the microbubble concentration [232], [233].

3.2iii.4 METHOD AND RESULTS

Using the lateral data, bubble signals can be observed spatially and temporally. This aids in establishing the identity of single or multiple bubble signals as discussed in the previous *in vitro* experimental Section 3.2ii.4.2. Moreover, comparison of Poisson statistical predictions with experimental results allows assessment of the performance of the super-resolution algorithm, as well as analysis of microbubble concentration to reduce acquisition time, while maintaining a high probability of imaging spatially isolated microbubble signals.

In order to implement Poisson statistics, one known parameter is required: the average microbubble occurrence rate. This can be determined using one experimental measurement; the number of non-bubble frames, $k = 0$, can be measured from the initial post-processing step in which non-bubble frames are determined by applying a threshold based on the characterisation of the noise of the scanner. The Poisson expectation value can thus be calculated as follows, and predictions for the total number of frames containing k numbers of bubbles can be made, where here $k = 1$ or > 1 for the lateral tube data.

$$P(0) = \frac{Non - bubble\ Frames}{Total\ Frames}, \tag{3.26}$$

$$= \frac{6627}{10948} = 0.605$$

The expectation value can then be given by

$$\mu = -\ln[P(0)] = 0.502 \tag{3.27}$$

Thus, Poisson predictions can be formed for $k = 1$ and $k > 1$ as follows

$$P(1) = \frac{\mu^1 e^{-\mu}}{1!} = 0.304 \tag{3.28}$$

and

$$P(>1) = 1 - \big(P(0) + P(1)\big) \approx 0.091 \tag{3.29}$$

According to Poisson predictions, 30.4% and 9.1% of total frames should contain single bubbles and more than one bubble respectively. These figures are displayed in Table 3.7, alongside experimental results measured using post-processing procedures described in this chapter. Following single bubble localisation, 29.4% of the signals were determined to be single bubbles, while 10.1% were considered to come from multiple bubbles. This corresponds well to predictions using Poisson statistics. Visual assessment of 200 frames of data identified a higher number of both single and multiple bubble signals than both Poisson predicted values, and experimental estimations.

Number of Bubbles in Frame	Poisson Predicted Values (%)	Experimental Measurement (%)	Visual Assessment (%)
0	-	60.5	54.5
1	30.4	29.4	33.0
>1	9.1	10.1	12.5

Table 3.7. Shows the Poisson predicted percentage of frames containing no bubbles, single bubbles, and multiple bubbles in the lateral tube data set. These are compared to experimental values following single bubble localisation, where 29.4% of the signals were determined to be single bubbles, while 10.1% were

considered to come from multiple bubbles. Visual assessment of 200 frames of data identified a higher number of both single and multiple bubble signals of 33.0% and 13.5% respectively.

Poisson statistics were then employed to assess the algorithm in the cross-sectional experiments. Predictions were calculated as follows

$$P(0) = \frac{Non - bubble\ Frames}{Total\ Frames}, \tag{3.30}$$

$$= \frac{10234}{12376}$$

$$= 0.8269$$

The expectation value is then calculated by

$$\mu = -\ln[P(0)] = 0.1901 \tag{3.31}$$

Thus, Poisson predictions can be formed for $k = 1$ and $k > 1$ as follows

$$P(1) = \frac{\mu^1 e^{-\mu}}{1!} \tag{3.32}$$

$$= 0.1571$$

and

$$P(> 1) = 1 - \big(P(0) + P(1)\big) \tag{3.33}$$

$$= 0.0160$$

Results from Poisson predictions are compared to experimental estimations in Table 3.8. In this case, visual assessment could not be performed since the tube diameter is within the spatial resolution of the imaging system thus visual differentiation between multiple and single bubble signals was not possible. A strong correspondence between predicted and measured results is evident here.

Number of Bubbles in Frame	Poisson Predicted Values (%)	Experimental Measurement (%)
0	-	82.7
1	15.7	15.0
>1	1.6	2.3

Table 3.8. Shows the Poisson predicted percentage of frames containing no bubbles, a single bubble, and multiple bubbles in the cross-sectional data set. These are compared to experimental values following single bubble localisation. The third and fourth columns display the number of frames corresponding to these values.

3.2iii.5 DISCUSSION

Both cross-sectional and lateral Poisson predicted values agree (within 1%) with experimental measurements. Assuming that the statistics employed work well to describe the imaging process, results suggest that the super-resolution algorithm achieves reasonable accuracy in detecting the correct quantity of single bubble signals, noise, and signals from multiple sources. In addition, visual assessment in the lateral tube analysis correlates well to the values seen for Poisson predictions with percentages differing by at most 6% in all cases. Comparison to the number of bubble events found through visual assessment indicated a slight under-detection of single bubble signals using the algorithm. This may be indicative of a harsh noise rejection threshold causing low amplitude bubble scattering events to be rejected at the initial post-processing stage. This may contribute to the lower localisation count observed at the edge of the cross-sectional tubes in Section 3.2ii.4.1.

By employing Poisson statistics to maximise $P(1)$, microbubble concentrations may be adjusted for efficient data acquisition (Appendix Section 9.1). Since it has been seen in Section 3.2ii.3.4 that estimations of the required microbubble concentration prior to experimentation can be inaccurate, a more appropriate approach could involve monitoring the bubble per frame density during acquisition.

There are a number of assumptions involved in the application of Poisson statistics which would lead to discrepancies between predicted and experimental findings. For example, the assumption that events are independent may not always hold; if clustering of microbubbles occurs [234], or if the frame rate is high enough that the volume of blood imaged in previous observations is present in those subsequent, the same microbubble will be imaged consecutively. Furthermore, Poisson statistical predictions are based on the non-bubble frame criteria implemented in the initial post-processing step, and thus inaccuracies in the characterisation of the system noise could alter the overall results. For more detailed discussion on the implementation of Poisson statistics for this application see Appendix Section 9.1.

3.3 SUMMARY AND COMMENTS

These results demonstrate that single bubble localisation can produce acoustic super-resolution and super-resolved flow velocity images *in vitro* from standard image data acquired by an unmodified clinical US system. There are a number of potential challenges that will have to be addressed to progress towards *in vivo* implementation, including the development of motion correction techniques which are sensitive enough to retain the gain in resolution achieved. Furthermore, using the current acquisition method, the image obtained is a projection of all echoes in the 3D sample volume along the elevational direction. In this work, the orientation of the imaging phantom was known and thus attempts could be made to estimate the elongations obtained due to the tilt of the transducer. In a more realistic application, however, the orientation of the structure is not known and will vary across the field of view, for example the spread of a complex microvascular network. Thus, the elevational resolution may have a significant affect on the success of the technique *in vivo*.

4 In Vivo Acoustic Super-Resolution and Super-Resolved Velocity Mapping

4.1 Introduction and Motivation

So far in this project, acoustic super-resolution has been explored in a controlled environment using *in vitro* phantoms, where results have demonstrated its potential to achieve image resolution beyond that of the conventional clinical imaging system. However, many aspects of clinical imaging cannot be easily recreated *in vitro*, including

---

Aspects of this work were presented at the IEEE International Ultrasonics Symposium 2014, Chicago under the title: 'Acoustic Single Bubble Tracking at Super-Resolution.'

An overview of this work was presented at the 2015 Artimino Conference on Medical Ultrasound, under the title 'Super-resolution ultrasound imaging.'

Parts of this work are also published in IEEE Transactions on Medical Imaging: K. Christensen-Jeffries, R. J. Browning, M.-X. Tang, C. Dunsby, and R. J. Eckersley, "In Vivo Acoustic Super-Resolution and Super-Resolved Velocity Mapping Using Microbubbles," *IEEE Trans. Med. Imaging*, 2015.

effects of tissue motion and realistic dynamics of blood flow through complex branching vessel structures. In order to develop such a technique for the imaging of tumour vasculature and microvascular diseases in humans, it is necessary to study the limitations and possible improvements of various processing techniques in as realistic a situation as possible, without introducing too many confounding factors simultaneously. The aim of this chapter is, therefore, to demonstrate and test the capabilities of the developed technique in a more challenging, *in vivo* environment.

In this work, the first practical demonstration of the potential and limitations of acoustic super-resolution and super-resolved velocity tracking *in vivo* is presented. The experimental design utilises a relatively superficial structure in the mouse, the vasculature in the ear, which enables comparison of the technique to optical images of the same region. This work incorporates three important new influences on the technique: (1) the effect of motion and motion correction techniques on the final image resolution, (2) the sensitivity of velocity tracking algorithms to slow flow in the microvasculature, and (3) the challenges for imaging when the exact structure, complexity and blood flow velocities of the target are unknown. This is therefore an important systematic step towards translating this technique to humans. It is therefore likely to demonstrate where improvements in both image acquisition and data processing are most required.

This chapter is organised as follows. Firstly, the US imaging system and methods for estimating the diffraction limited resolution are described. In addition, the choice of the *in vivo* model, the ear of a mouse, is motivated, before the materials and methods for performing *in vivo* US and optical imaging are discussed. Post-processing algorithms to estimate and correct for motion, the development of localisation and velocity tracking algorithms, as well as image generation procedures are then described. Super-resolution and super-resolved velocity mapping results are subsequently presented.

4.2 MATERIALS AND METHODS

4.2.1 ULTRASOUND EQUIPMENT AND ACQUISITION SETTINGS

All data were acquired using a standard, unmodified Siemens Acuson Sequoia clinical US scanning system (Siemens, Issaquah, WA) using Cadence™ CPS mode [20]. A 15L8 linear array transducer was chosen for use in this experiment due to the suitability of a small probe size to the *in vivo* mouse ear model. The frequency was set to 7 MHz on the scanner, which corresponded to a measured transmit frequency of 6.5 MHz after performing characterisation experiments (see Results Section 4.3.1, Figure 4.2B) with a hydrophone (0.2 mm Needle hydrophone SN:1893, Precision Acoustics Ltd). A low transmit power equivalent to an MI of 0.16 was used to ensure minimal bubble disruption, while maintaining a good visual SNR. Data were acquired using the maximum frame rate and dynamic range available for this system at these image settings of 25 Hz and 100 dB respectively, along with a TGC of -20 dB and a focus set to 8.5 mm.

4.2.2 ULTRASOUND SYSTEM CHARACTERISATION

4.2.2.1 IN PLANE RESOLUTION AND LOCALISATION PRECISION

Firstly, measurements of the transmit pulse SPL and frequency were performed using the aforementioned hydrophone and measurements of voltage were converted to acoustic pressure using the calibrated frequency response of the hydrophone. Experimental characterisation of the PSF was then performed to assess the diffraction limited resolution and localisation precision of the US imaging system. Similarly to characterisation experiments performed in Chapter 3, a 100 μm diameter brass wire was held horizontally between two fixings in a gas equilibrated water bath. The wire was positioned normal to the US image plane so that the cross-section of the wire was imaged to imitate a point scatterer. This was performed at depths of 0.5 cm, 0.75 cm, 1 cm and 1.25 cm from the transducer face to test the PSF over the range of depths imaged *in vivo*. Firstly, each frame was de-compressed using the method described in Chapter 3, Equation (3.3). The centre of mass of the wire signal was then calculated for each frame, as well as the FWHM of the signal in the lateral and axial directions. The resolution of the US system was measured as the average FWHM over 50 frames in lateral and axial directions. The localisation precision was measured to be the standard

deviation of the measured centre of mass over the same number of frames, as described in Chapter 3, Section 0. To account for the finite size of the wire in the measurement of the PSF we de-convolved the measured FWHM value by the finite size of the wire using Equation (3.2) to obtain new values of the PSF FWHM.

4.2.2.2 ELEVATIONAL RESOLUTION

The elevational resolution of the system was estimated by measuring the acoustic signal from the transducer over the elevational plane. This was performed by translating a hydrophone in 0.125 mm steps across the field of view and measuring the peak-to-peak acoustic pressure. This step size was estimated to be far below the resolution in the elevational direction.

4.2.3 IN VIVO MODEL

4.2.3.1 JUSTIFICATION OF MODEL

The mouse ear model (albino, CD1 strain of mice) was chosen for *in vivo* demonstration of the 2D super-resolution technique for a number of reasons. Firstly, the mouse ear circulation consists of microvessels similar in diameter and blood flow velocity to those in a human capillary network [30], [32], [235], [236]. Furthermore, the mouse ear contains well defined, branching structures which have limited complexity in the third (elevational) dimension. The benefits to this are twofold. Firstly, since the localisation map is a superposition of bubbles travelling through the entire image slice, complexity within the elevational plane could degrade the final image quality. With the ear thickness at under 1 mm [237], the target structure is comparable to the elevational slice thickness which was estimated to be approximately 1 mm (see Section 4.3.1, Figure 4.5). Secondly, the thickness and transparency of the albino CD1 mouse ear meant that optical validation of the technique was possible without histology or surgical procedures. Furthermore, since the ear is a surface structure, motion was primarily limited to that of head movement caused by respiration; thus motion was estimated to be predominantly rigid in nature and less complex than that of deep tissue structures. In addition, mice can be maintained in an in-house minimal disease facility.

This *in vivo* model provides an intermediate and logical step between *in vitro* experiments, and complex 3D *in vivo* structure. It allows development and refinement

of practical and post-processing procedures, before proceeding to situations where more dense and complex data will be likely.

4.2.3.2 IN VIVO ETHICS

All animal work was conducted under the authority of the UK Home Office project license as required by the Animals (Scientific Procedures) Act 1986. Mice were maintained in a minimal disease facility fully compliant with Home Office guidelines with food and water *ad libitum*. Three 27-28 g, 8-week-old, female, CD1 mice were anaesthetized using 5% isofluorane gas, before being reduced to between 1-2% after catheter placement and monitored constantly. The mice were not mechanically ventilated and therefore were naturally breathing.

4.2.4 OPTICAL IMAGING

One ear of the mouse was depilated by shaving and depilatory cream was applied to ensure visibility of the vascular structure for optical microscopy. The mouse was positioned on a light diffusing stage such that the ear was relatively flat against the surface of the stage (Figure 4.1A). Optical images of the vascular structure were then acquired using a Wild Heerbrugg M650 (Switzerland) microscope and a SONY Handycam HDR SR12E (Japan) camera. It is important to note that optical and US imaging were performed separately and with adjusted mouse positions.

4.2.5 ULTRASOUND IMAGING

The anaesthetised mouse was transferred to a heat mat and positioned with the prepared ear vertical to the surface, as shown in Figure 4.1B. The transducer was positioned above the ear such that the entire width of the ear was within the lateral field of view and the length of the ear extended in the axial imaging direction. Acoustic gel was applied around the ear to cover the entire elevational imaging plane as well as to flatten the ear within the plane, and was applied above the ear in order to couple to the imaging device. The gel was centrifuged prior to use to minimise the presence of air bubbles.

A 29G catheter flushed with heparin for anticoagulation was placed in the mouse tail vein. A suspension of SonoVue™ microbubbles at 2.5× the original concentration of the original vial was administered. The original concentration was increased prior to

administration due to the restriction on total injection volume which should not exceed 200 μl; this meant that a higher concentration infusion, spread over a longer time period, was more suitable for super-resolution imaging. Adminstration was performed using a syringe pump with an infusion rate of between 0.2-5.0 μl per minute The infusion rate was varied in response to visual inspection of the images in real time, to provide a bubble per frame density which ensured that a high proportion of the bubble signals in each frame were spatially isolated. An estimate suggests that the resulting bubble infusion rate per unit blood volume is in the range of ~ 1-10 times that used in conventional human contrast imaging [21] - [22]. The region around the mouse ear was defined on the US system at a depth of 0.6-1.5 cm and video data of microbubbles flowing through branching blood vessels in the mouse ear was captured directly to PC from the S-Video out via an analogue to digital capture device (Intensity Shuttle, Blackmagic Design). The storage capacity was therefore not restricted by the limited on-board hardware of the ultrasound system. Upon reaching the maximum injection volume, the anaesthetised mouse was culled. After acquiring a single dataset, the *in vivo* imaging procedure was modified to incorporate a longer acquisition time (up to 1 hour) to investigate the effect of imaging duration on the resulting images.

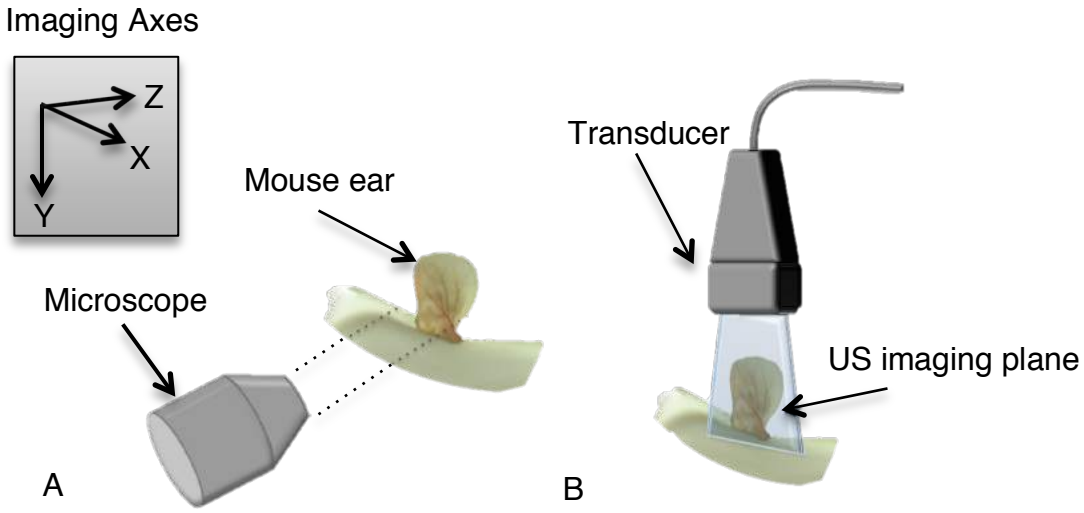

Figure 4.1. Schematic diagram of imaging set-up. (A) Optical set-up where microscopic imaging was performed across the surface of the mouse ear. (B) US set-up consisting of the transducer positioned above the mouse ear such that the entire width was within the US lateral field of view.

4.2.6 POST-PROCESSING ALGORITHMS

Algorithms were written in MATLAB to process the acquired video data as follows. Firstly, all image frames were logarithmically decompressed before a motion estimation algorithm was applied, as described in the following section.

4.2.6.1 MOTION ESTIMATION

The anaesthetised mouse was secured in position within the stationary transducer's field of view in order to limit non-respiratory motion effects as much as possible, however despite this, motion effects were still observed. Algorithms were written for a 2D rigid, sub-pixel cross-correlation procedure as follows. Firstly, a reference frame, which was considered to exist between inhalations when motion was at its lowest, was identified manually before processing, within which an observation region of interest (ROI) was defined. This was subsequently compared with different candidate ROIs within a pre-defined search range from all other frames of US data. These regions were up-sampled using bicubic interpolation from the original pixel scale (30 x 30 μm for mouse 1 and 23 x 23 μm for mouse 2 and 3) to a 1 x 1 μm pixel scale, where the output pixel value is a weighted average of pixels in the nearest 4-by-4 neighbourhood [238]. This approach has been demonstrated to be more accurate than other techniques such as linear or nearest neighbour interpolation, while remaining more computationally efficient than techniques such as cubic spline [238]. The motion is estimated from the spatial shift between the reference ROI and the best-match comparison region using the normalised cross-correlation function, with the quality factor defined by the value of the cross-correlation function at this point. Normalised cross-correlation techniques are commonly used for US tissue motion estimation techniques [239], [240], [241]. Since access is restricted to image data here, upsampling was performed in order to enable motion estimations at sub-pixel scales.

4.2.6.2 SIMULATION TESTING

Simulated test images were constructed to assess the accuracy of the motion estimation algorithms. Each simulated image consisted of a random distribution of point scatterers on a micrometre-sized pixel grid. These scatterers were convolved with a 2D Gaussian function equal in size to the measured axial and lateral FWHMs of the US imaging system PSF. An identical image was then shifted by a randomly specified micrometre

distance in the lateral and axial directions. Subsequently, zero-mean Gaussian noise, statistical noise with a Gaussian probability density function, was generated independently and added to each image individually in the frequency domain. A range of SNR values from 0.0001 to 1 were applied to each image, where SNR is defined here as

$$SNR = \frac{s^2}{{\sigma_N}^2}, \tag{4.1}$$

where s is the signal amplitude, ${\sigma_N}^2$ is the variance of the noise. Band-pass filtering was then performed in the frequency domain based on the bandwidth of the transducer. Images were then down-sampled by averaging non-overlapping blocks in the image to create larger pixels with a scale equal to that of the original experimental image data (this was defined as the largest pixel size over all data sets equal to 30 x 30 μm). Sub-pixel motion estimation procedures were then performed on the resulting images as described above. The image generation, random shift and motion estimation procedure was repeated 500 times at each noise level, using two different sized ROIs (35 x 35 pixels and 70 x 70 pixels). The padding region was equal in size to that used for *in vivo* data described below. The average error and variance over all images was then calculated.

4.2.6.3 *IN VIVO* ESTIMATION

In mouse experiment 1, motion estimation algorithms were performed on CEUS images, while for mouse experiments 2 and 3 B-mode images were used due to lack of strong stationary scatterers within the CEUS data. The target had limited motion over the duration of imaging, i.e. the ear stayed in the approximate centre of the field of view for the duration of acquisition. De-correlations were observed which were regular and well defined in time and were considered to be caused by respiratory motion (see Results Section 4.3.2.2). This regular motion was estimated from preliminary investigations to be between 0-200 μm. The pre-defined search range was defined as approximately 600 μm in order to detect all minor movements, while limiting computation time.

Removal of breathing induced motion artefacts was attempted by excluding frames with an empirically determined cross-correlation value of less than 0.979 deemed to contain motion based on results presented in Section 4.3.2.2. In this way, data were 'gated' such that images were assumed to be from consistent phases of the respiratory cycle. Undoubtedly, the rejection of acquired frames is not ideal for efficiency of the technique. These results are shown alongside those generated from the entire dataset, with and without 2D rigid motion correction, allowing for comparison of the three approaches.

4.2.7 MICROBUBBLE LOCALISATION AND TRACKING

The frames were then processed based on algorithms described in Chapter 3, Section 3.2ii.3.6, where firstly frames potentially containing a microbubble signal were identified by comparing the total intensity of each frame to an empirically determined threshold; this was calculated from the maximum total intensity of 50 background frames acquired prior to microbubble injection which were assumed to be representative of background noise. 'Empty' frames were added to a rolling background average, while potential bubble frames had the rolling background average subtracted from them. The rolling average was again taken over n = 10 frames in order to remove unwanted background signals from static structures without removing slow moving weak signals from bubbles. Potential bubble frames were then segmented according to whether the pixel values were above the background intensity level over 50 background frames as described previously. The size of any connected regions in the image in which pixel values were above this background intensity threshold were compared to the expected PSF based on our initial characterisation experiments in order to reject signals coming from noise or from multiple bubbles. The intensity-weighted centre of mass of each spatially isolated microbubble signal was then calculated to obtain coordinates for the localised bubble position C_x, C_y.

Tracking algorithms developed in Chapter 3 (Section 3.2ii.3.6) were then applied in order to create super-resolved velocity maps. In this work, the individual intensity cross correlations between each bubble signal in frame n and each of the bubble signals found in frame $n+1$ within a 400 micrometre search window were calculated and the maximum cross correlation was found for each signal in frame n. The search window

size was defined to reject bubbles which far exceeded the expected red blood cell velocity in the ear of a few millimetres per second . A pair of signals were deemed to come from the same bubble if the maximum cross correlation between the signal images exceeded an empirically determined threshold of 0.8. For each pair, a velocity vector was then calculated between C_x^n, C_y^n and C_x^{n+1}, C_y^{n+1} and assigned to the centroid location C_x^{n+1}, C_y^{n+1} in frame $n+1$ and was assigned a track identity number k_i, as described in Chapter 3. If a bubble is identified in frame $n+2$, and exceeds the cross correlation threshold with a bubble signal in frame $n+1$, it will then be assigned the same track identity, k_i.

4.2.8 IMAGE RENDERING

Images were generated using scripts described in Chapter 3, Section 3.2ii.3.7, where each individual bubble localisation was represented by a 2-D Gaussian profile centered at C_x, C_y with standard deviations, σ_x and σ_y, given by the average lateral and axial localisation uncertainty of the estimated diffraction limited resolution. The super-resolution map resulting from the sum of all the individual centroid localisation distributions across all frames creates an image in which the displayed value is proportional to the chance of detecting a microbubble positioned at that location. Velocity images were generated used the method described in Section 3.2ii.3.7.

4.3 RESULTS

4.3.1 ULTRASOUND SYSTEM CHARACTERISATION

A hydrophone measurement performed at the focus of the 15L8 transducer with a frequency setting of 7 MHz is displayed in Figure 4.2A for an individual pulse within the CPS sequence, where a lower average measured transmit frequency of 6.5 MHz was found (Figure 4.2B), with a peak negative pressure of 460 kPa and FWHM of 376 ns.

As discussed in Chapter 1, the axial resolution is limited by one half of the spatial pulse length (SPL) of the acoustic echo response. Since the acoustic echo is proportional to the square of the acoustic pressure transmit wave, the SPL is taken as the FWHM of the squared acoustic signal at the transducer focus, however, it must be noted that this measure does not include receive signal processing and therefore is likely to differ from

that observed in the US image. From the hydrophone measurements, and assuming the speed of sound in soft tissue is given by $c = 1540$ m/s, we have

$$Axial\ Resolution\ = \frac{Spatial\ Pulse\ Length\ (SPL)}{2}. \tag{4.2}$$

$$= \frac{244 \times 10^{-9} s\ \cdot 1540\ \mathrm{m/s}}{2} = 188\ \mu m. \tag{4.3}$$

Given that we are using CPS imaging, the effective US frequency is approximated as the mean of the fundamental and second harmonic, i.e. 9.75 MHz, thus the FWHM of the spatial pulse length reduces to

$$\frac{SPL}{2} = \frac{\left(\frac{2 \cdot 244 \times 10^{-9} s}{3}\right)\ \cdot 1540\ \mathrm{m/s}}{2} = 125\ \mu m. \tag{4.4}$$

The expected lateral resolution is harder to estimate in the absence of proprietary knowledge of the exact transducer design - assuming a F/1 aperture at 9.75 MHz gives a FWHM of 160 µm, and 237 µm at 6.5 MHz.

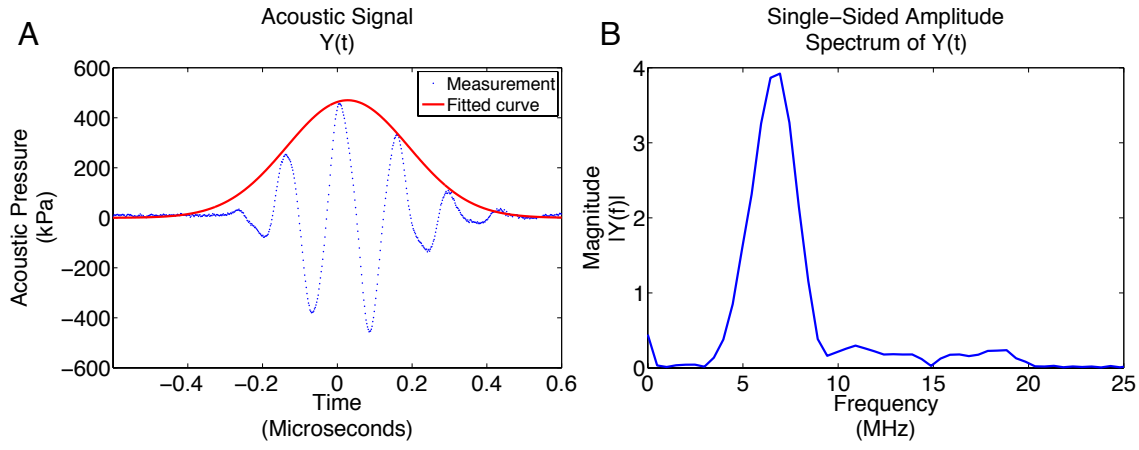

Figure 4.2. Hydrophone measurement at transducer 15L8 focus (8.5 mm), where (A) displayes the measured acoustic response (blue) with envelope detection (red), and (B) shows the magnitude frequency spectrum, with peak at 6.5 MHz.

To estimate the diffraction limited resolution experimentally, a stationary point scatterer was used to measure the FWHM over the depth range 0.5-1.25 cm. Results across the depth range are shown in Figure 4.3 and Table 4.1, along with estimations derived from hydrophone measurements. Figure 4.4A shows an example image of the wire cross-section at a depth of 1.25 cm, which provides the highest measured resolution for CPS imaging over the range investigated, measured to be a FWHM of 112 μm in the lateral and 94 μm in the axial direction as shown in Figure 4.4C and D.

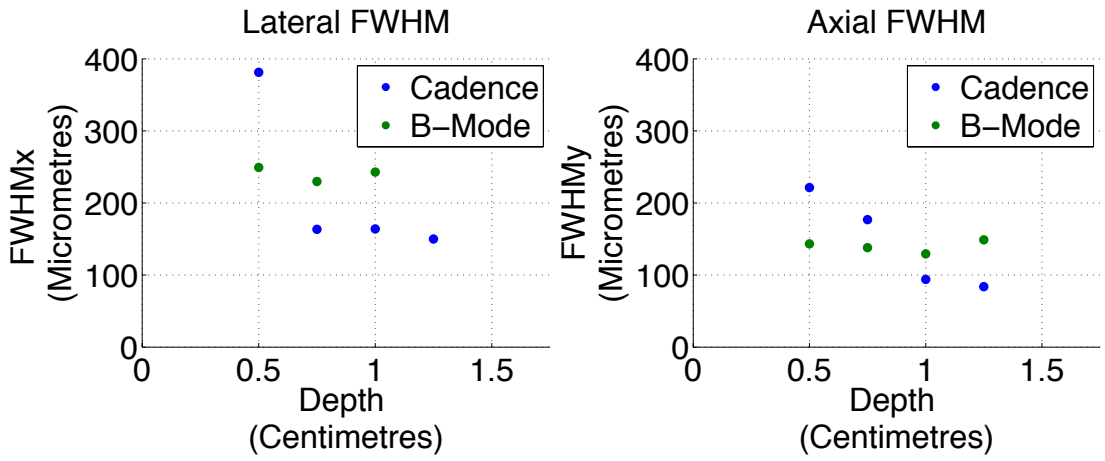

Figure 4.3. Lateral and axial FWHM measurements at depths between 0.5 -1.25 cm at 0.25 cm intervals using CPS and B-Mode.

Depth (cm)	**CPS Mode**		**B-Mode**	
	Lateral FWHM (μm)	**Axial FWHM** (μm)	**Lateral FWHM** (μm)	**Axial FWHM** (μm)
0.5	368	221	228	143
0.75	130	177	207	138
1	130	94	221	129
1.25	112	94	368	149
Mean	185	146	256	140
Minimum	112	94	207	129
Estimate at 0.9 cm	160	125	237	188

Table 4.1. Experimental measurements of FWHM of the PSF at varying depths using both CPS Mode and B-Mode. This is compared to estimations of the system resolution based on hydrophone measurements, where axial estimations are shown in Equations (4.3) and (4.4).

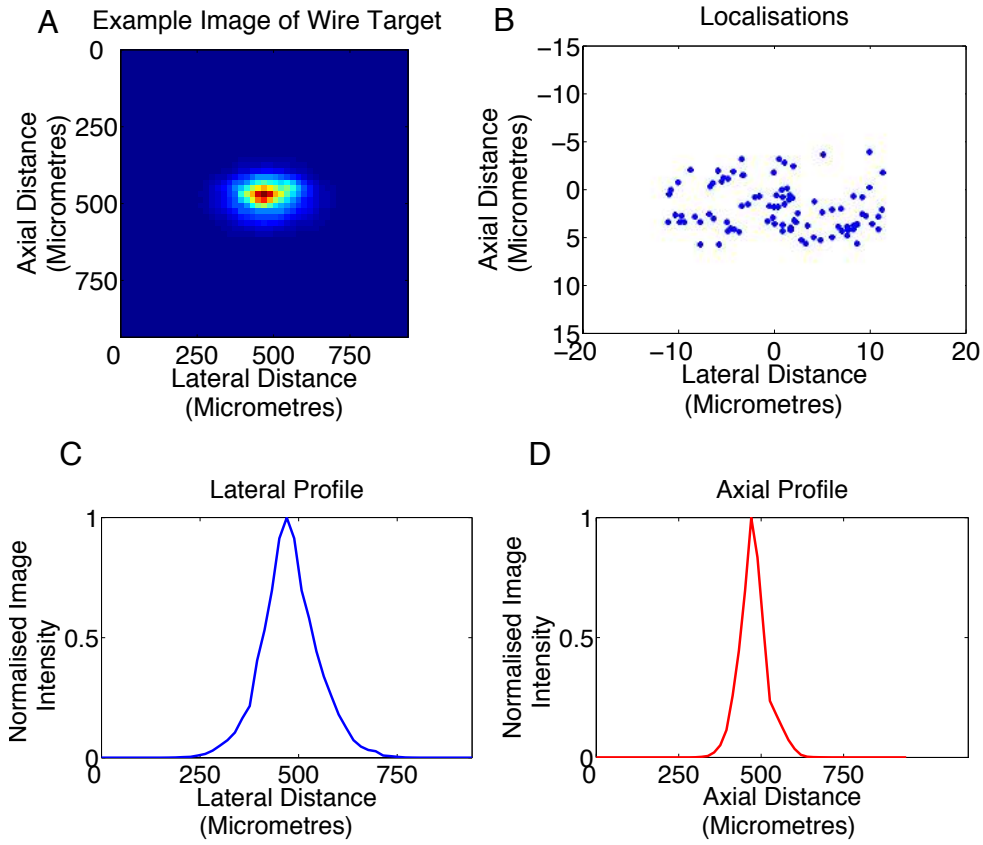

Figure 4.4. Characterisation of US imaging system. (A) shows an example logarithmically decompressed image of 100 μm diameter wire target cross-section at 1.25 cm. (B) displays the localisations of the point scatterer over 100 frames, and (C) and (D) display the PSF profiles in the lateral and axial directions respectively.

The measured axial FWHMs in B-Mode are lower than those predicted using the SPL calculated from hydrophone measurements. A significant difference between predicted and measured values are also seen using CPS imaging mode. Possible reasons for these differences are discussed further in Section 4.4. Since there is a large variation in the estimated and experimental values of diffraction limited resolution, the smallest measurements of the wire PSF are used as an indication of the highest diffraction limited resolution possible. The localisation precision of this point scatterer in the lateral and axial directions was estimated by calculating the standard deviation of localisations over 50 frames, as shown in Figure 4.4B, and was found to be 6 and 2 μm respectively. Figure 4.5 displays the measurement of the elevational field of view which was found to have a FWHM of 994 μm.

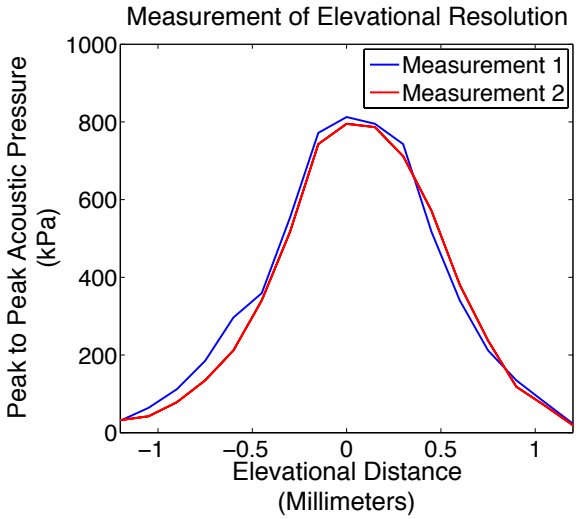

Figure 4.5. Measurement of peak-to-peak acoustic pressure across the transducer's elevational plane using a hydrophone. The FWHM of the profile is 994 μm.

4.3.2 Motion Estimation

4.3.2.1 Simulated Motion Estimation

An example micrometre-grid sized simulated image used to test the motion estimation algorithm is displayed in Figure 4.6A. Down-sampling of this image results in pixelated images as shown in (B) and (C) where ROI 1 and ROI 2 are displayed with sizes 35 x 35 pixels and 70 x 70 pixels respectively. Figure 4.6D, E and F display the simulated images with added Gaussian noise with SNR of 0.15, 0.01, and 0.001 respectively. Figure 4.6G and H show the resulting average error in motion estimations over 500 images for each ROI where error bars equal the variance. Figure 4.6I and J display the lateral and axial variance over the 500 images for small and large ROIs respectively. This recovered the displacement on a micrometre scale with 100% accuracy for motion within the padding region for both ROI sizes at SNR values above 0.15. The average variance increased with simulated noise; at the lowest SNR of 0.0001 variance was a maximum of 5.07 μm and 9.23 μm axially and laterally for ROI 1, and 4.76 μm and 9.19 μm correspondingly for ROI 2. Maximum absolute errors were found to be 4 μm axially and 6 μm laterally at the lowest SNR.

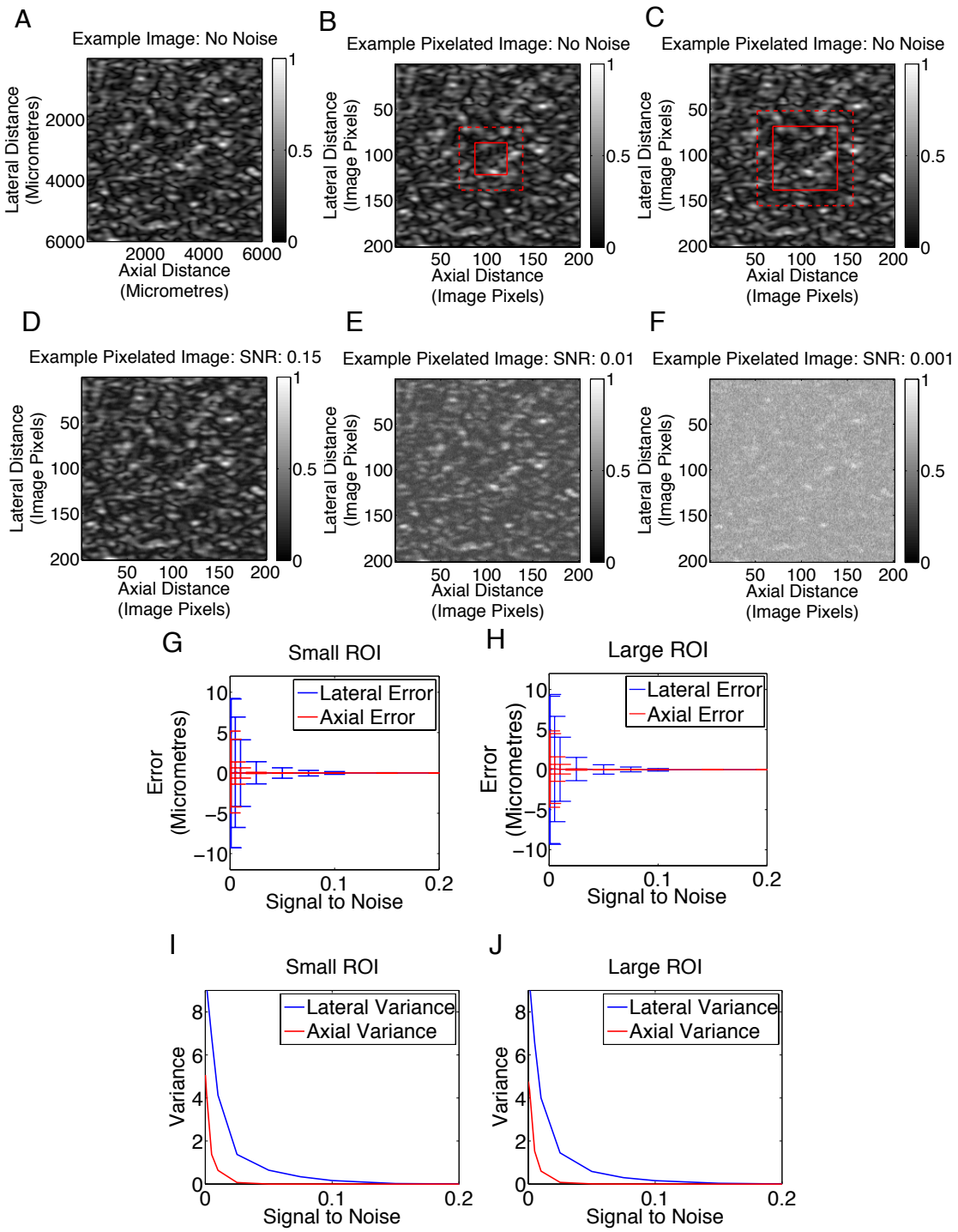

Figure 4.6. Example simulated images for motion estimation algorithm testing. (A) shows a simulated image on a micrometre scale, before down-sampling into pixelated images as shown in (B) and (C) where ROI 1 and ROI 2 are displayed with sizes 35 x 35 pixels and 70 x 70 pixels respectively. Figures (D), (E) and (F) display the simulated images with added Gaussian noise with SNR of 0.15, 0.01, and 0.001 respectively. (G) and (H) show the average error in motion estimations over 500 images for each ROI where error bars equal the variance. (I) and (J) display the lateral and axial variance over the 500 images for small and large ROIs respectively. Note: average error and variance values for SNR above 0.2 were equal to zero and are not presented.

4.3.2.2 IN VIVO MOTION ESTIMATION

De-correlations were observed using the motion estimation algorithm in the *in vivo* data. These can be observed in Figure 4.7, and enlarged in Figure 4.7B, which shows a subset of the frames analysed for mouse 1. Here we can see two forms of periodic motion. These motion effects can be observed in both cross-correlation values and in motion estimations for all of the mouse data analysed in this chapter, where motion was most evident in lateral estimation values. Figure 4.8 shows the estimated lateral and axial motion detected for mouse 2.

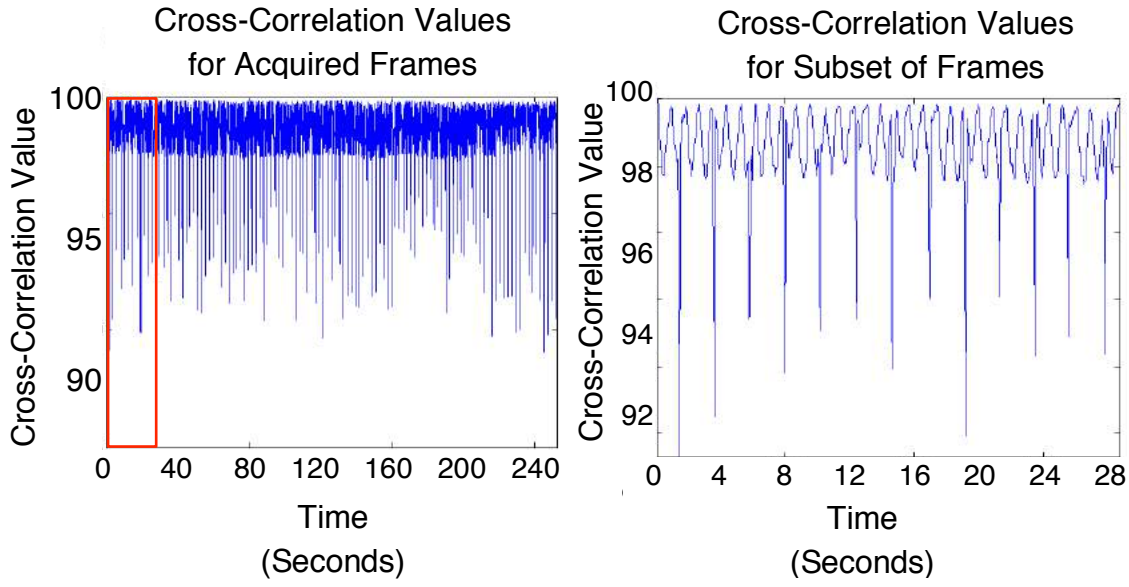

Figure 4.7. Cross correlation values for motion estimation algorithms showing a low frequency and high frequency characteristic pattern within the *in vivo* data.

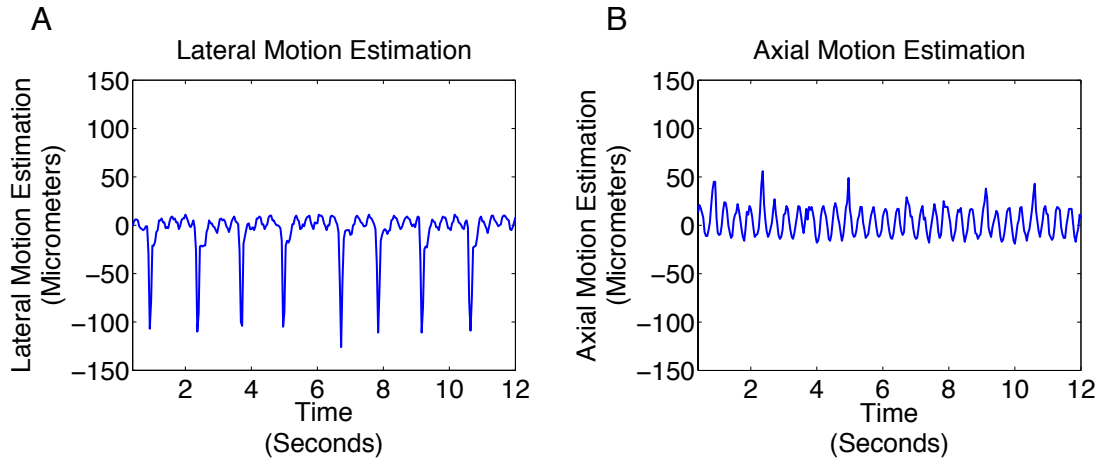

Figure 4.8. Lateral (A) and axial (B) estimations of motion across a subsection of acquired frames.

The frequency of these effects was measured across three sections of the lateral motion estimation values in each data set; these are displayed in Table 4.2. The lower frequency, higher amplitude motion has a characteristic frequency of approximately 0.74 Hz for mouse 2 and 3, and 0.48 Hz for mouse 1. This motion was occasionally violent and erratic, as displayed in Figure 4.9 (note the different y-axis scale in Figure 4.9 compared to Figure 4.8), however the two motion effects remained in general relatively regular in time. Respiration rates for sedated mice stated in the literature appear to be highly dependent on the concentration and type of anaesthesia used, where breathing rates can vary between 0.73 Hz (2% isoflurane) – 1.73 Hz (1.25% isoflurane) [242]. Thus, the measured rates fall within the normal range for the breathing rate of CD1 mice under isoflurane anaesthesia at our isoflurane concentration for mouse 2 and 3. A considerably lower rate was measured for mouse 1, which may be due to a higher concentration of anaethesia being used in the initial experiment which can cause further lowering of respiratory rates.

	Periodic Motion A (Hz)			**Periodic Motion B (Hz)**		
Measurement	Mouse 1	Mouse 2	Mouse 3	Mouse 1	Mouse 2	Mouse 3
1	0.483	0.676	0.772	1.44	2.993	2.800
2	0.386	0.869	0.676	1.35	2.897	2.993
3	0.579	0.676	0.772	2.31	2.800	2.800
Mean	0.48	0.74	0.74	1.7	2.90	2.86

Table 4.2. Frequency estimations for two types of periodic motion (A and B) for three CD1 mice, given by the average frequency over 300 frames from three separate sections of lateral motion estimations.

The higher frequency motion evident has low amplitude; the peak to peak amplitude of these motion estimations are within one imaging pixel in size (less than approximately 20 μm). Through visual assessment of video data, these variations did not appear to be due to bulk motion of the mouse ear, but instead from rippling signal intensity fluctuations across the image frame. This visual assessment is supported by images seen in Figure 4.10, which displays the difference image between four example frames with the reference frame. Figure 4.10B, with estimated low amplitude motion of 16 μm, demonstrated similar differences to that shown in Figure 4.10A where no motion was detected. This can be compared to difference images for presumed breathing motion

frames shown in Figure 4.10C and D (estimated motion of more than 100 μm). Heart rates of anaesthetised mice have been documented at between 7.3-9 beats per second using 1-2% isoflurane; this is considerably higher than the frequency observed in these data and as such this has been eliminated as a possible cause for this variation [235], [7]. The fluctuations are periodic in nature and therefore were not attributed to errors in the motion estimation algorithm. It is therefore expected that this variation may be a result of electrical oscillations or mechanical vibrations caused by the active motor within the anaesthesia scavenger unit which had to be kept close to the mouse during imaging.

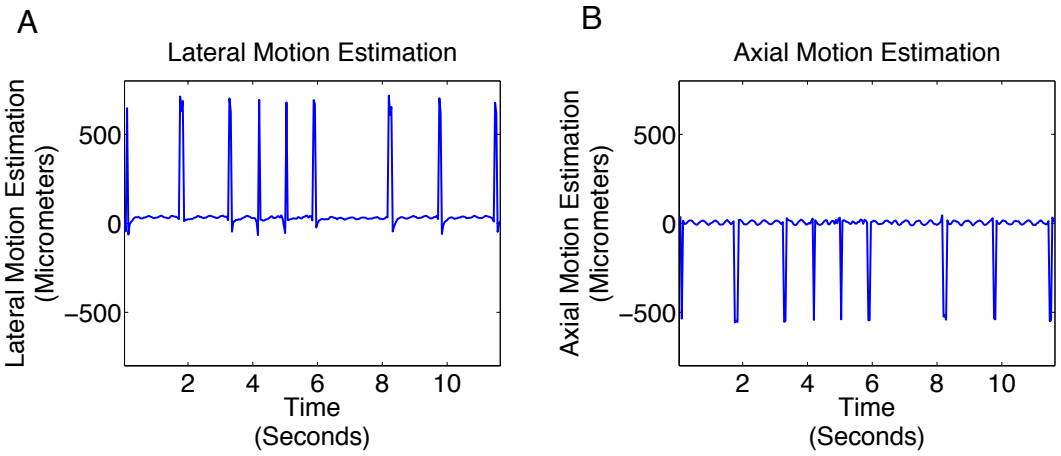

Figure 4.9. Lateral (A) and axial (B) motion estimations across a subsection of frames where breathing appears violent and erratic.

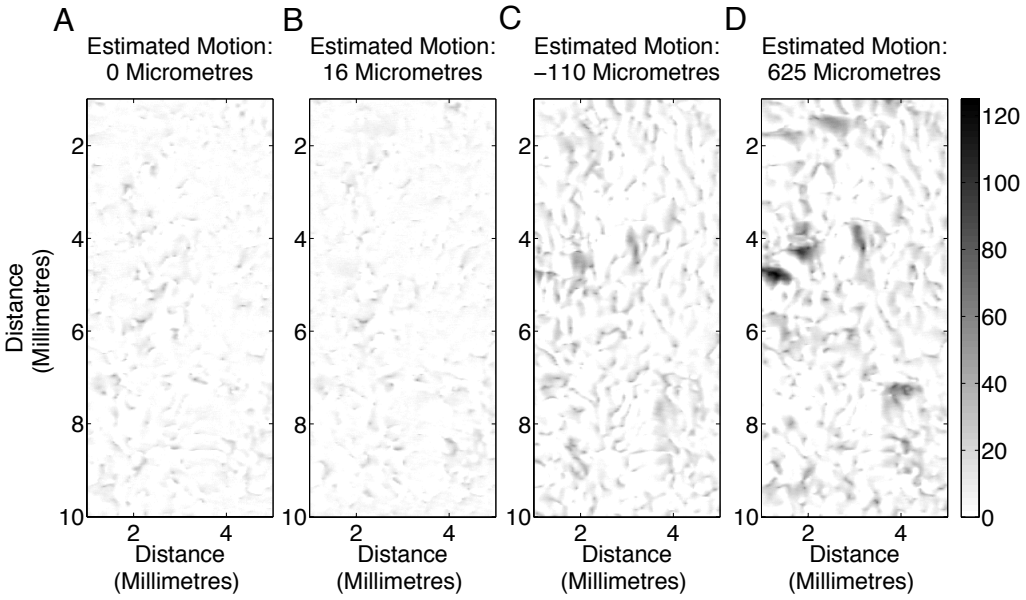

Figure 4.10. Difference images between four example frames with the reference frame, with estimated motion of 0 μm (A), 16 μm (B), -110 μm (C), and 625 μm (D).

4.3.3 *IN VIVO* SUPER-RESOLUTION

Figure 4.11A shows a typical CPS image frame of the mouse ear vasculature containing multiple bubble signals which are not spatially isolated – leading to an image that is similar to conventional contrast imaging. Here, diffraction limits visibility of the underlying structure and makes size estimation of the vessels impossible; the bubble concentration is too high to allow individual bubbles to be localised. Figure 4.11B displays the super-resolved *in vivo* image produced using single bubble localisation, where the branching vessel structures in the mouse ear are clearly visible. An optical image of the vascular structure in the mouse ear is shown in Figure 4.11C. Here, motion rejection was used to remove frames considered to have respiratory motion as described in Section 4.2.6.3.

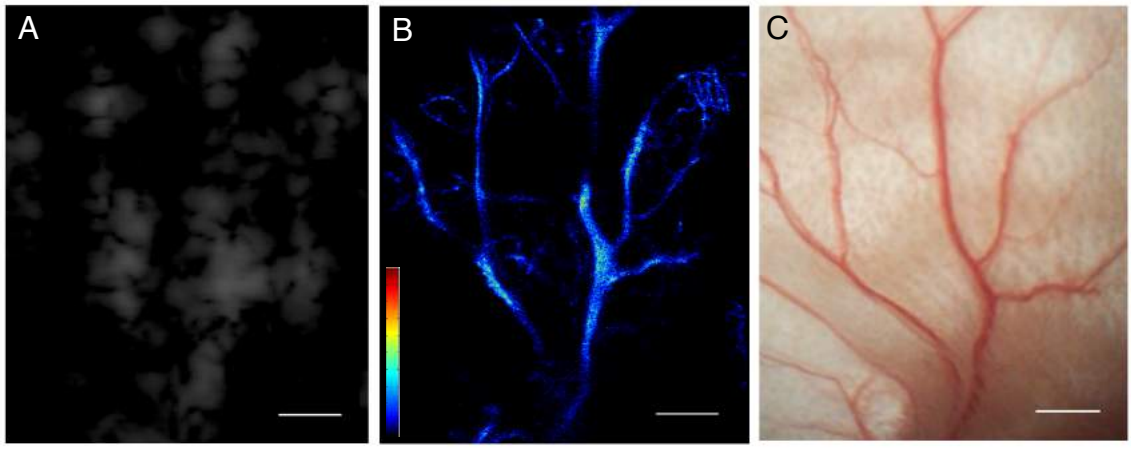

Figure 4.11. Comparative images of mouse ear microvasculature using standard contrast enhanced US, single bubble localisation method, and optical microscopy obtained using a surgical microscope. (A) A single high microbubble concentration image frame acquired using conventional Cadence™ CPS imaging mode. (B) Super-resolution image created as a probability density map where the colour scale represents the number of bubbles localised in a given location (colour bar scale, 0 - 20). (C) Corresponding optical image of the vasculature within the same mouse ear acquired *in vivo*. Scale bars, 1 mm.

Two vessels identified in the super-resolution image (Figure 4.12A), are shown at higher magnification in Figure 4.12B and C. Average vessel diameters of 19 ± 2.8 μm (Figure 4.12D), and 39 ± 1.4 μm (Figure 4.12E) were measured at a depth of 0.8 cm and 0.9 cm respectively, compared to the measured diffraction limited lateral and axial resolutions of 112 μm and 94 μm. Corresponding measurements from an optical image for the vessel analysed in Figure 4.12D give an average vessel diameter of 24.4 ± 4.8 μm (Figure 4.13).

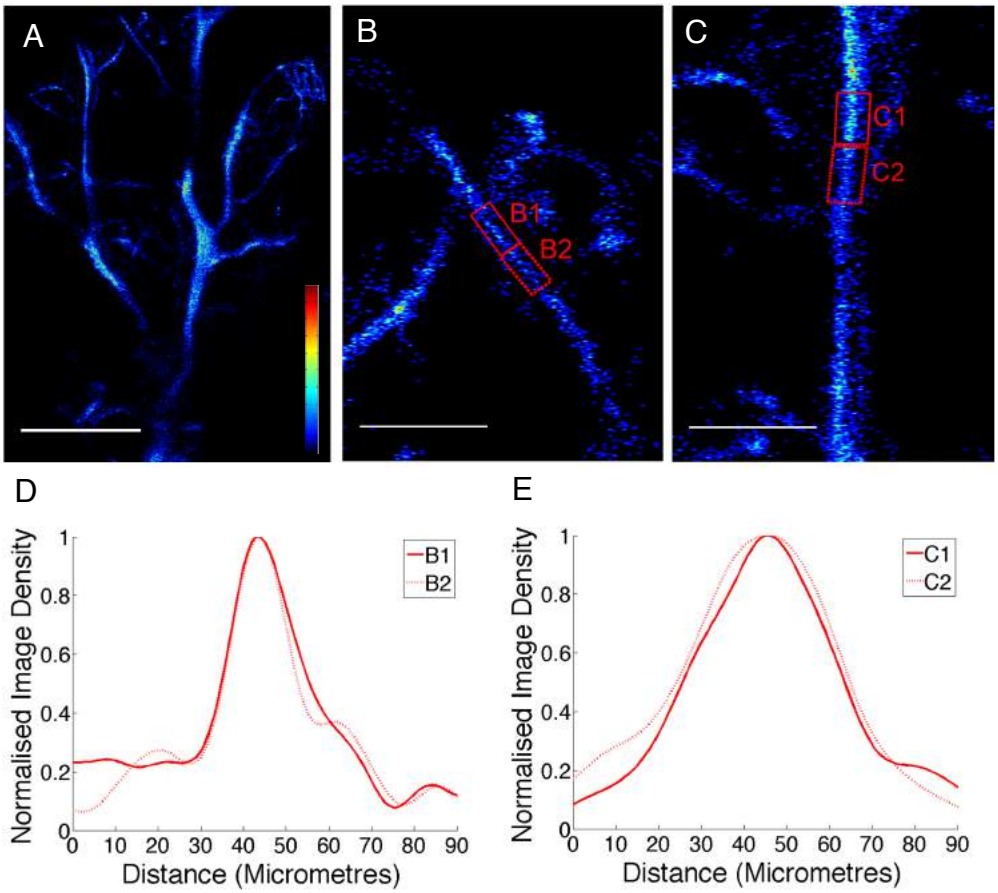

Figure 4.12. Super-resolved vessel measurements. (A) Super-resolution image as shown in Figure 4.11B, where the white boxes identify two vessels of interest, shown at higher magnification (B) and (C). (D) and (E) show two average normalised line profiles across regions of 200 µm length (B1-B2 and C1-C2), as outlined in (B) and (C). The mean profile FWHM was 19 ± 2.8 µm and 39 ± 1.4 µm for the curves shown in (D) and (E) respectively. Colour bar scale, 0 – 20. Scale bars, 2 mm (A), 500 µm (B, C).

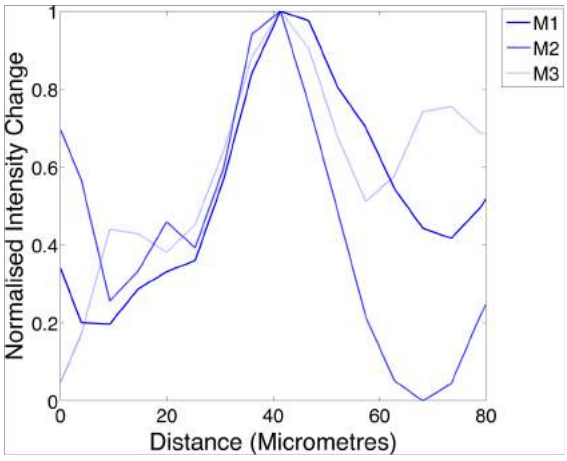

Figure 4.13. Optical image profiles at 3 locations (M1-M3) across vessel shown in Figure 4.12B and corresponding profiles in Figure 4.12D, where each profile spans 200 µm of the length of the vessel. The mean FWHM of the optical profiles is 24.4 ± 4.8 µm. The pixel size of the optical images is 5.4 µm.

Figure 4.14 demonstrates the impact of post-processing thresholding constraints applied to detected signals, and how these affect visualisation of targets in the final image. Four localisation maps can be seen which are created using the same initial set of localisations, using increasingly stringent size constraints. Initially this results in a sharper image, but further increase creates increasingly incomplete information on the spatial distribution of the target and thus degrades the final visualisation.

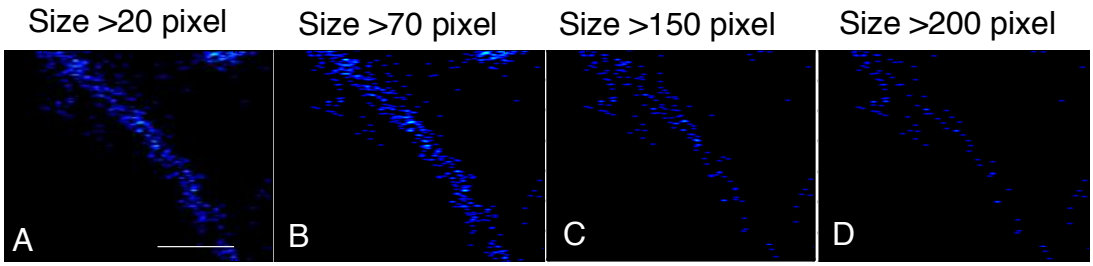

Figure 4.14. Localisation maps created using the same localised bubbles from a section of the ear in Mouse1, using increasingly stringent constraints on the size of signals allowed in the final image. Increasing this constraint initially results in a crisper image, but further increase in thresholds creates increasingly incomplete information on the spatial distribution of the target. Colour bar equivalent to that displayed in Figure 4.11B. Scale bar, 200 μm.

As introduced briefly in the methodology section, in an attempt to retain localisation accuracy, breathing induced motion artefacts were removed by excluding frames with an empirically determined cross-correlation value of less than 0.979 in order to 'gate' data from consistent phases of the respiratory cycle. Comparative super-resolved images created using all frames, with and without motion correction are shown in Figure 4.15 for mouse 1. Figure 4.15A displays the resulting images after motion rejection as previously seen. Figure 4.15B shows the localisation map generated using all frames with no motion correction, and Figure 4.15C shows the result using all frames with sub-pixel motion correction. Corresponding graphs in Figure 4.15D, E and F display the average number of localisations over a 200 μm section of the profile indicated in red in Figure 4.15A. Motion rejection shows the narrowest profile for the arteriole vessel, however the localisation density in the neighbouring vessel is low. Without motion correction or rejection, the localisations from all frames are spread and the two vessels are unresolved. Motion corrected results show preservation of a narrow vessel profile with higher SNR, particularly evident in the left hand vessel profile.

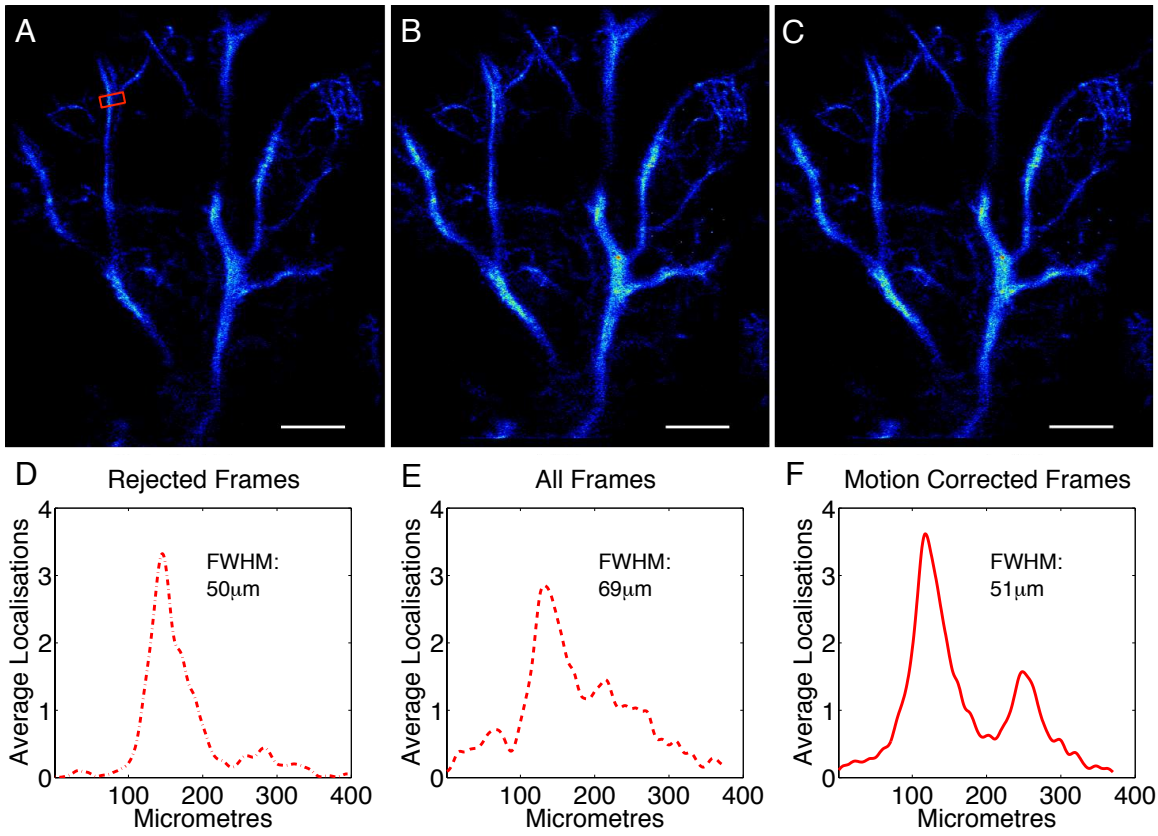

Figure 4.15. Super-resolved images. Part (A) displays the resulting localisation map using a frame rejection strategy for values less than 0.979, part (B) displays resulting localisation maps after processing all acquired frames with no motion correction, and (C) displays results using 2D rigid motion correction. Profiles displayed below in (D), (E) and (F) show the average localisations across the 200 μm section of the profile shown in red in (A). Colour bar equivalent to that displayed in Figure 4.13. Scale bars, 1 mm.

Figure 4.16 shows comparative optical profiles of this and two additional vessel structures through the same area. In almost all cases, motion rejection profiles demonstrate lower average localisations compared to comparative super-resolution methods. The distance measured between the two peaks observed in Figure 4.16A and those in motion corrected super-resolution profiles in Figure 4.16B are 121 μm and 130 μm respectively. The FWHM of the optical vessel profile in Figure 4.16E (157 μm) matched well to that measured for motion corrected and non-corrected profiles in Figure 4.16F (155 μm and 154 μm).

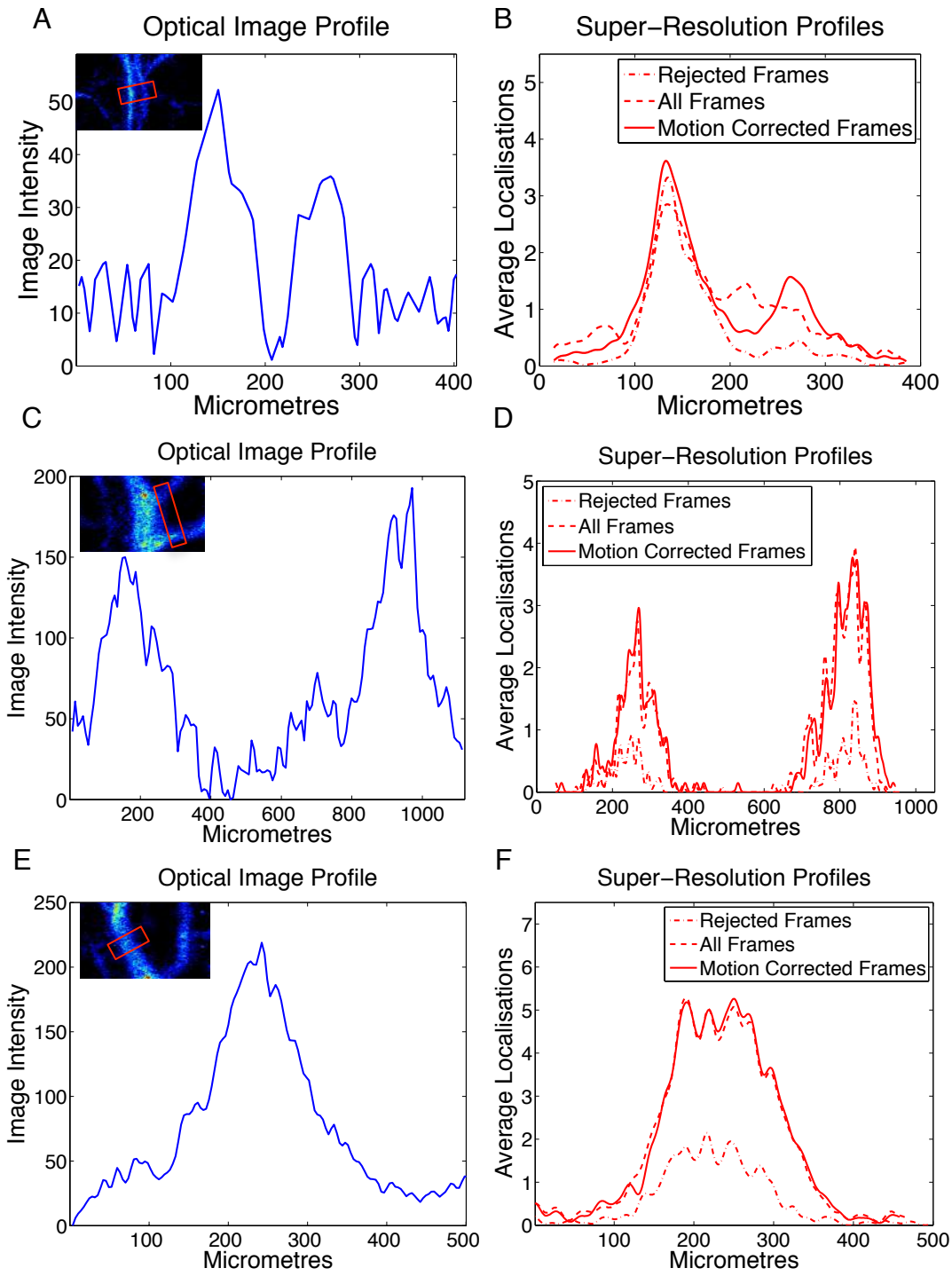

Figure 4.16. Comparison between optical (A,C,E) and corresponding super-resolution (B,D,F) profiles of structures indicated in inset images. In most cases, motion rejection profiles demonstrate lower average localisations compared to using all frames with and without motion correction. Colour bar equivalent to that displayed in Figure 4.13.

4.3.3.1 In Vivo Velocity Mapping

Figure 4.17A shows the original super-resolution image, alongside colour-encoded flow images of the vascular structure attained at super-resolution in Figure 4.17B and C. Figure 4.17B displays the directional component of velocity over 360° and Figure 4.17C shows the speed variation for bubble flow within the vessels. Differentiation between flow direction and speed can separate the opposing blood flow into arteries and veins, and therefore enhance the visualisation of objects within the image which are not otherwise spatially separable. Figure 4.18 shows one such example in more detail, where opposing flow directions (Figure 4.18A) can be seen to correlate with two distinct speed distributions (Figure 4.18B). This is shown in the speed profile along a 400 μm section of the vessel structure (Figure 4.18C), which reveals a high speed at the vessel centres with decreasing speeds toward the vessel walls (Figure 4.18C). The peak average velocity in the artery is 3080 μm/s, and only 1850 μm/s in the vein. This higher speed arterial flow and slower flow present in veins can be observed throughout the vasculature (Figure 4.19).

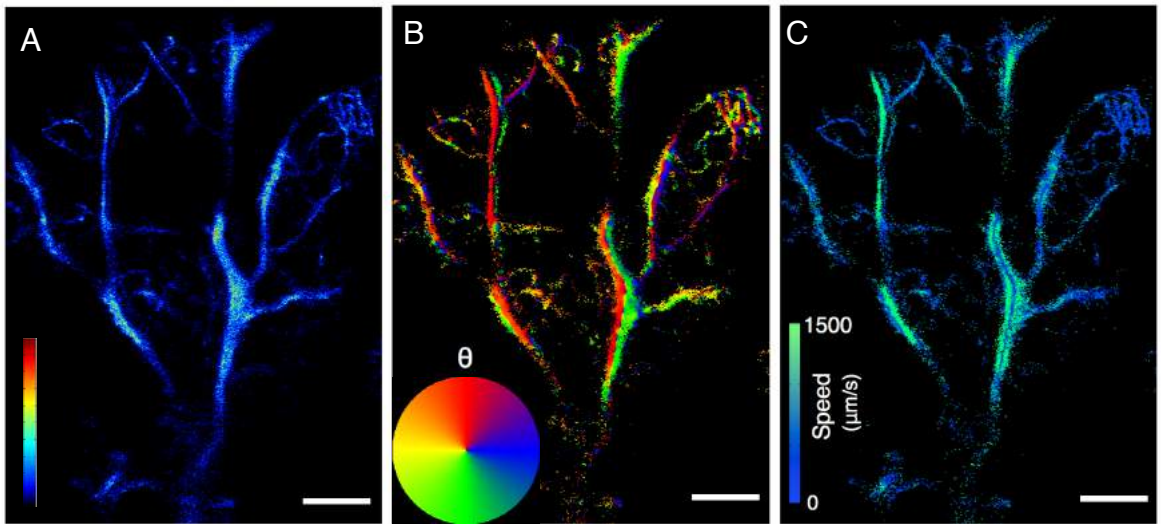

Figure 4.17. Super-resolution velocity maps. (A) Super-resolution image as shown in Figure 4.11B and the corresponding image displaying the direction of blood flow in (B). (C) shows the corresponding speed of flow through the vessels, where speeds above 1500 μm/s are set to the maximum on the colour bar. Colour bar for (A) 0-20, equivalent to that displayed in Figure 4.11B,. Scale bars, 1 mm.

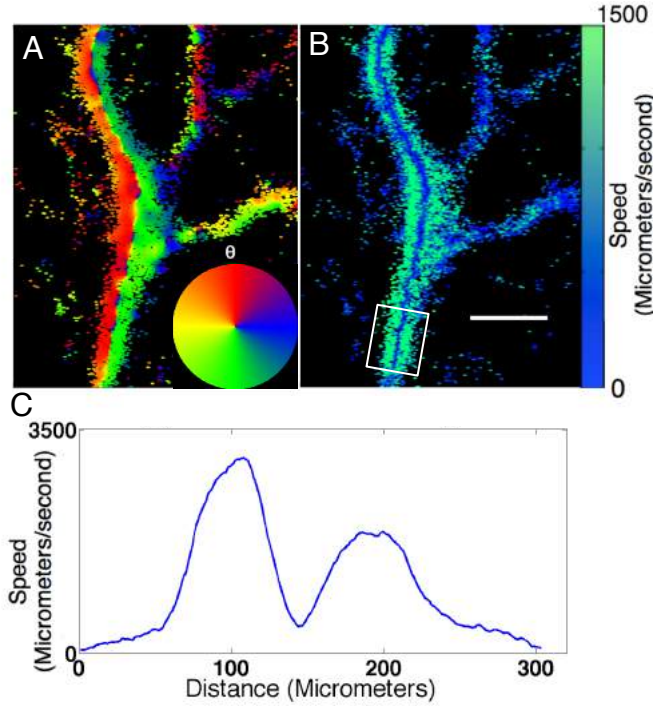

Figure 4.18. Regional velocity maps. (A) Magnified image sections from Figure 4.17B and C, where structures that appeared initially to be one vessel can be differentiated into an adjacent artery and vein with opposing flows. (B) shows the corresponding speed of flow through the vessels, where speeds above 1500 μm /s are set to the maximum on the colour bar. The corresponding average flow profile over 400 μm (white box) is shown in (C). In both, two vessel profiles can be clearly identified by a distinct slow flow separation, where faster flow is apparent in the centres of the vessels. Scale bar, 500 μm.

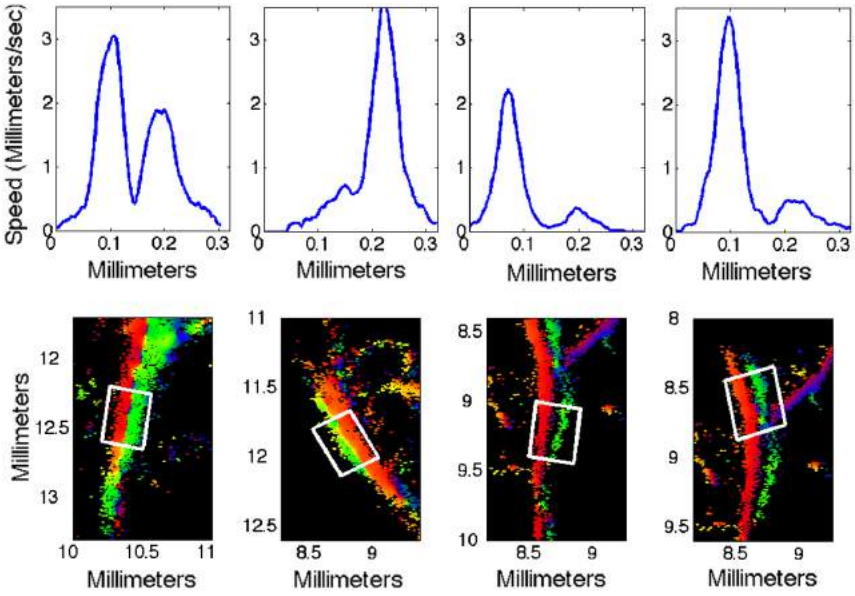

Figure 4.19. Magnified image sections taken throughout the microvasculature from Figure 4.17B, showing vessels with opposing flow directions, and their corresponding average flow speed profiles across 400 μm (indicated by the white boxes).

Super-resolution maps accumulated after two minute time intervals $t_1 - t_5$ are displayed in Figure 4.20, where t_5 contains the combined centroids detected after 10 minutes of acquisition. The super-resolution image created after two minutes (t_1) contains 28027 centroids from 3000 frames, an average of just over 9 localisations per frame, where many vessel structures can already be observed. After four minutes, additional vessel structures appear in the image, and existing ones gain contrast to the background. Further increase in time adds further detail, and enhances the localisation count in vessel structures in the final image.

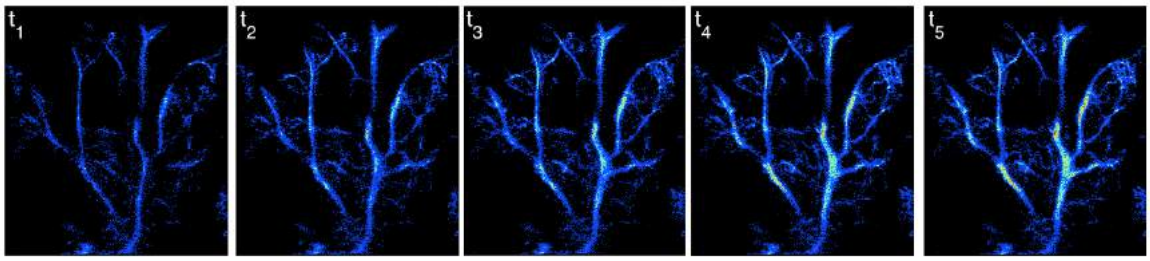

Figure 4.20. Super-resolution maps generated at two minute time intervals $t_1 - t_5$, up to a total time of 10 minutes (colour map limit = 20). Colour bar equivalent to that displayed in Figure 4.11B.

4.3.3.2 Extending the Imaging Acquisition

The following mouse experiments had extended imaging duration of up to 50 minutes. Figure 4.21A and Figure 4.22A show the super-resolved velocity maps for mouse 2 and 3 respectively, with enlarged versions displayed in Figure 4.21B and Figure 4.22B, where FWHM of vessel profiles over 200 μm sections are measured down to 47 μm. Additionally, two vessel structures can be seen to be resolved within a 350 μm lateral distance in Figure 4.21C, ROI 4. Super-resolved velocity maps in Figure 4.23 and Figure 4.25 again show the enhancement of vessel differentiation from velocity tracking. Higher speeds can be seen to correlate to larger vessel structures, likely to be part of the primary level branching structures extending from the base of the mouse ear due to their location and structural appearance. Vessel structures measured in Figure 4.24 display many double vessel structures where arterioles and venules pair together and appear as a single structure in the original localisation map. In Figure 4.26, five adjacent vessel structures are visible with opposing flow directions. Corresponding speed profiles show 4 distinct speed profiles, where the vessel on the far right is unresolved.

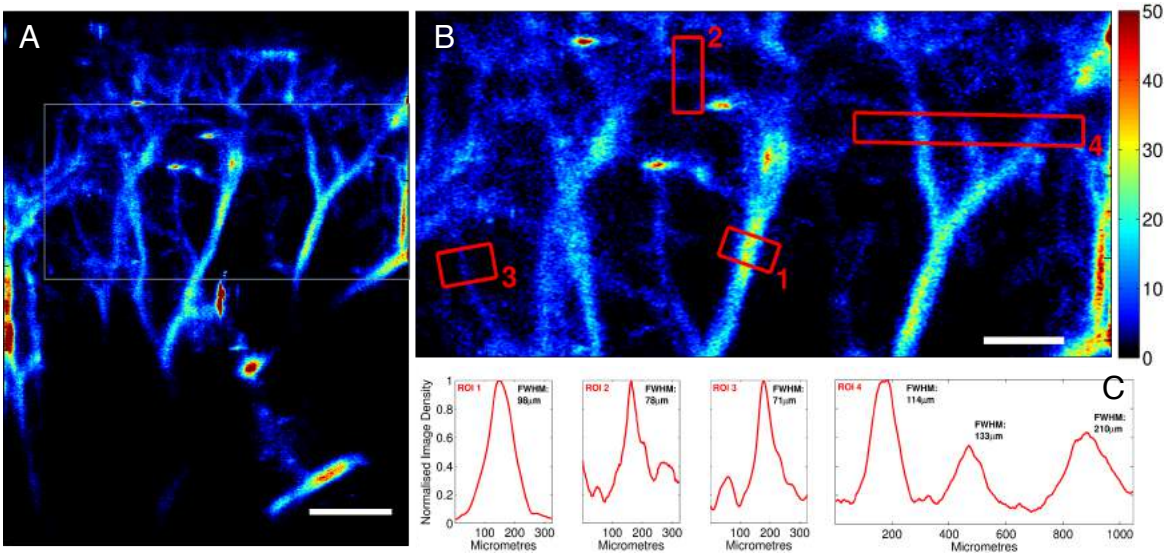

Figure 4.21. Super-resolution images for mouse 2. (A) Super-resolution image, (B) enlarged section shown in white in (A), and (C) the profiles through 4 structures. Scale bar in (A), 1 mm, and (B), 500 μm.

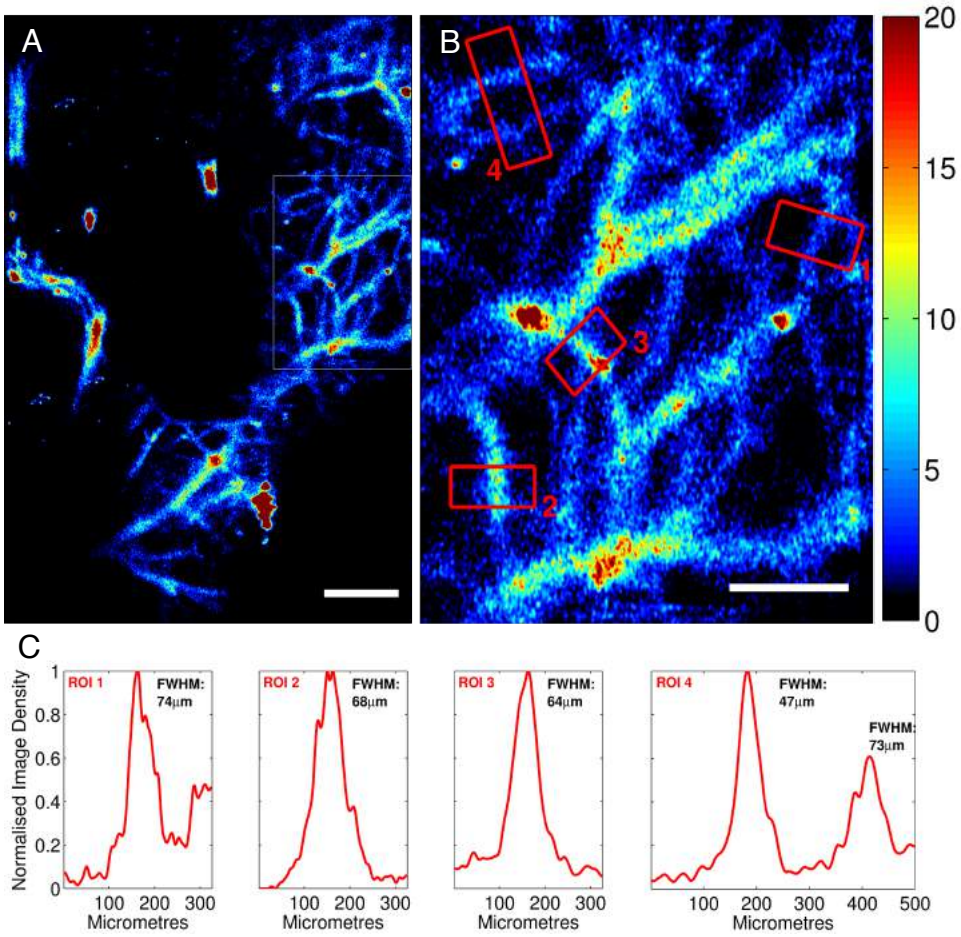

Figure 4.22. Super-resolution images for mouse 3. (A) Super-resolution image, (B) an enlarged image of the section shown in white in (A), and (C) displays the corresponding average profiles through 4 vessel structures. Scale bar in (A), 1 mm, and in (B), 500 μm.

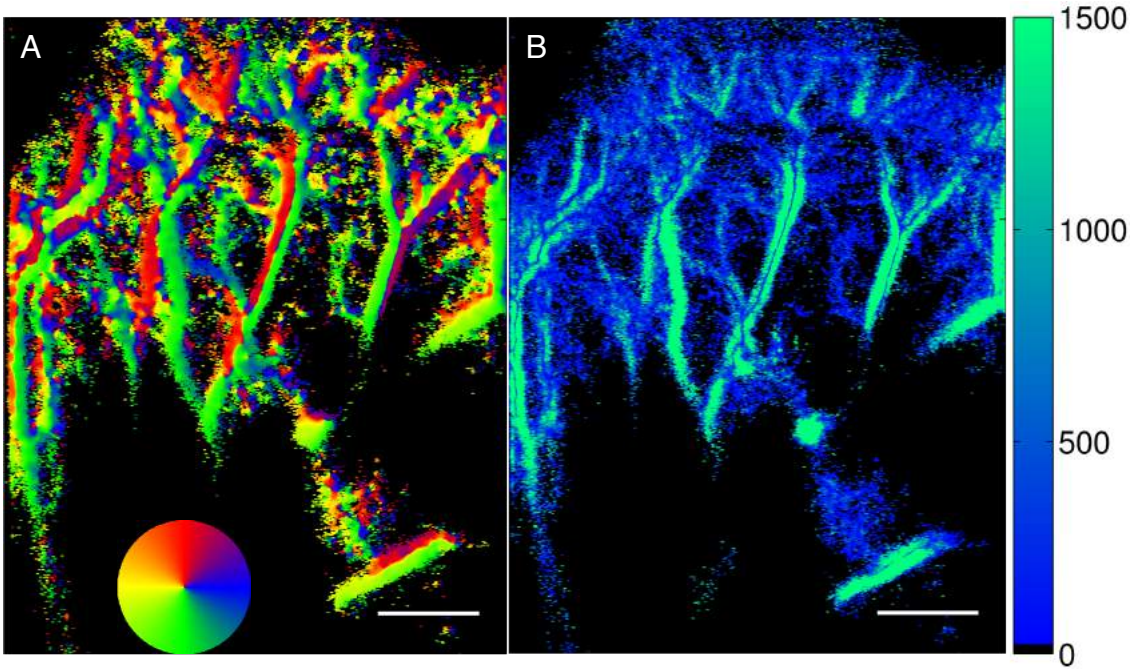

Figure 4.23. Super-resolved velocity maps for mouse 2. (A) and (B) display the direction and speed of blood flow, where speeds above 1500 µm/s are set to the maximum on the colour bar. Scale bars, 1 mm.

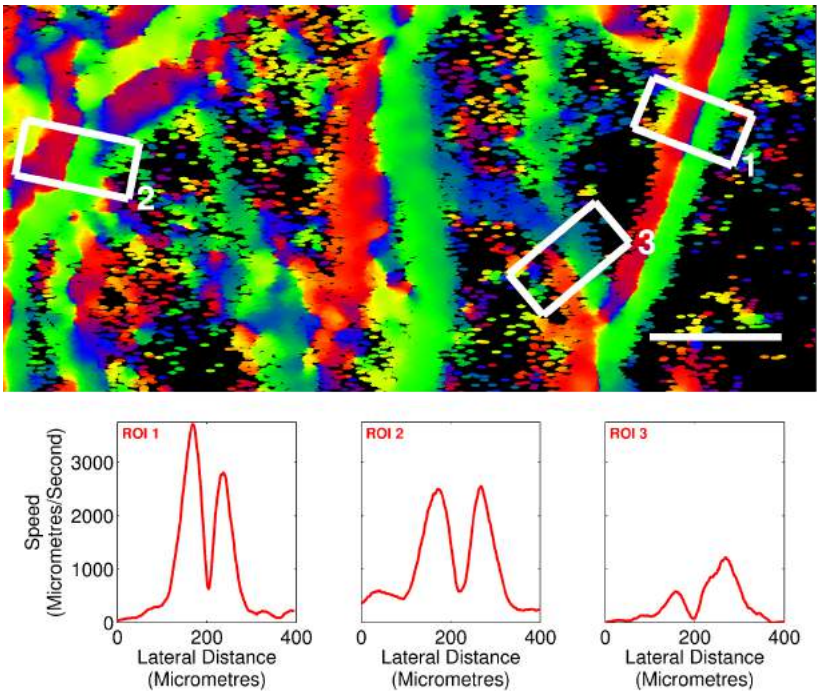

Figure 4.24. Enlarged section of map of directional component of velocity shown in Figure 4.23D, where three corresponding average speed profile over 200 µm are displayed below.

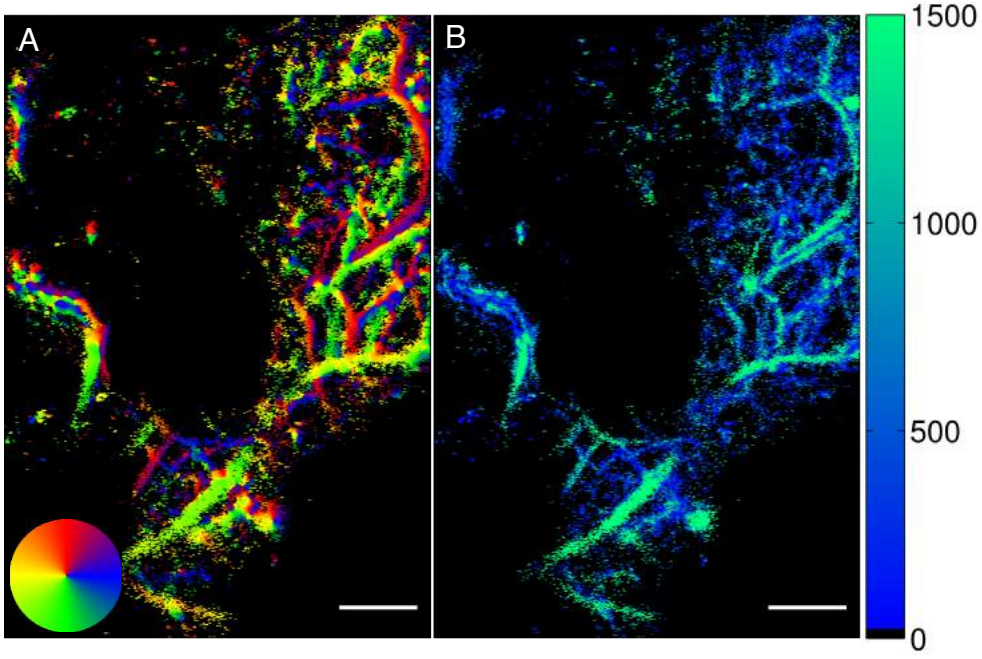

Figure 4.25. Super-resolved velocity maps for mouse 3. (A) and (B) display the direction and speed of blood flow, where speeds above 1500 µm/s are set to the maximum on the colourbar. Scale bars, 1 mm.

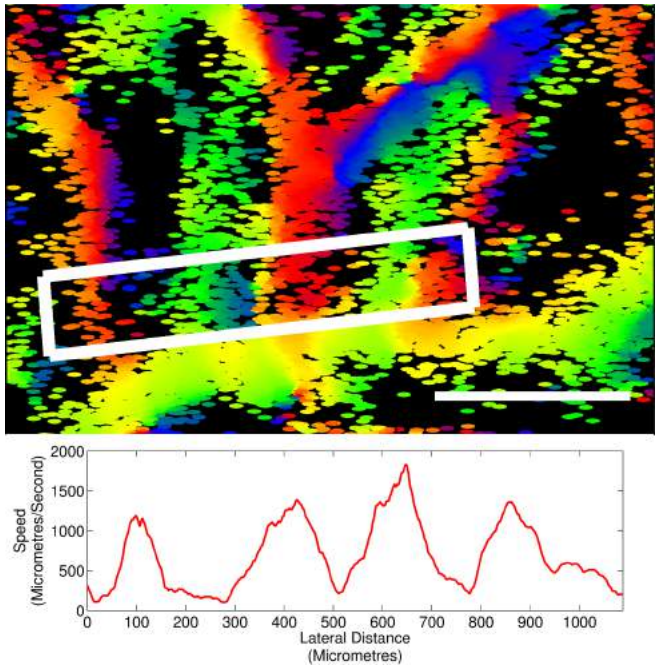

Figure 4.26. Enlarged section of map of directional component of velocity shown in Figure 4.25D, where the corresponding average speed profile over 200 µm is displayed below.

Figure 4.27 displays super-resolution localisation maps at ten minute time intervals for mouse 1 and 2 respectively, where again vessel structures become more well defined and gaining contrast to the background over the course of image acquisition. In earlier time intervals, vessels stemming from the base of the ear are larger with more localisations; as scan time increases, networks of smaller vessels existing between the larger vessels begin to emerge. In both cases there is an increased spread of localisations in areas between the larger vessels, which may imply the increased presence of capillaries in this region, compared to that imaged in mouse 1.

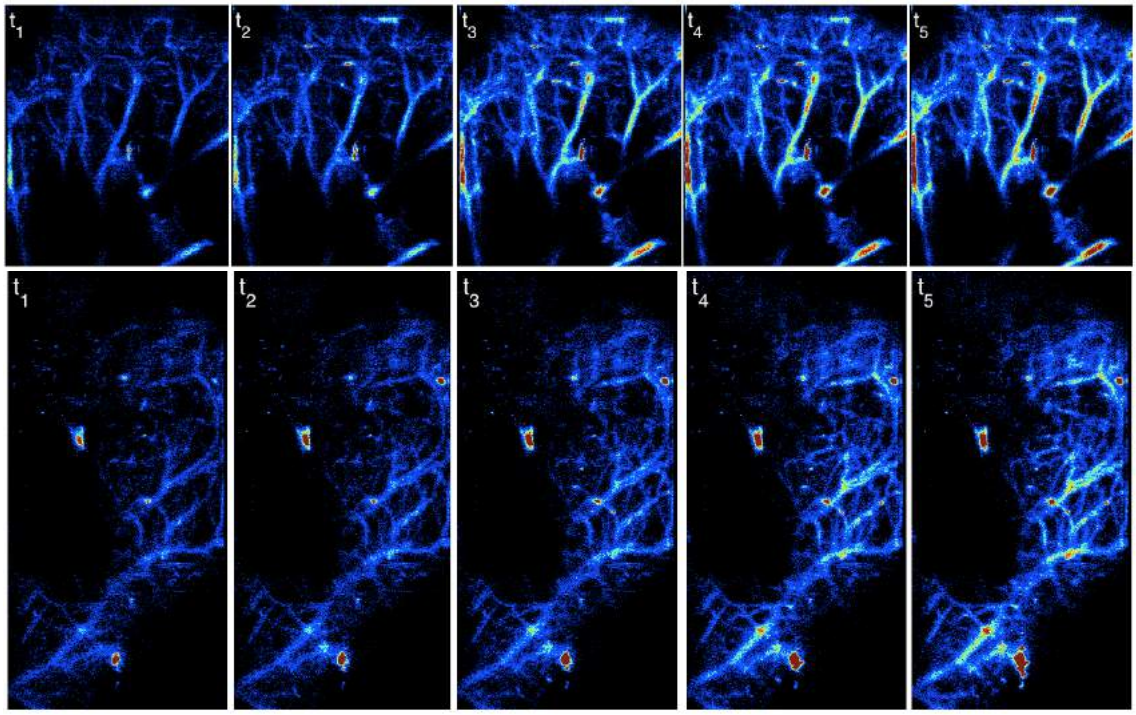

Figure 4.27. Super-resolution maps generated at ten minute time intervals $t_1 - t_5$, up to a total time of 50 minutes (colour map limit = 20). Colour bars equivalent to those displayed in Figure 4.21 (top) and Figure 4.22 (bottom).

Figure 4.28 displays speed histograms for the three *in vivo* data sets. Speeds of 700 μm/s, 748 μm/s and 760 μm/s are most frequently tracked within the three *in vivo* data sets respectively which falls within the range of speeds of mouse ear, from the principal vessels branching from the base of the ear at an average of 3.5 mm/s, down to capillary vessels at arterioles and venules at around 60 μm. Note that mouse 2 and 3 have considerably higher localisation counts due to longer imaging duration.

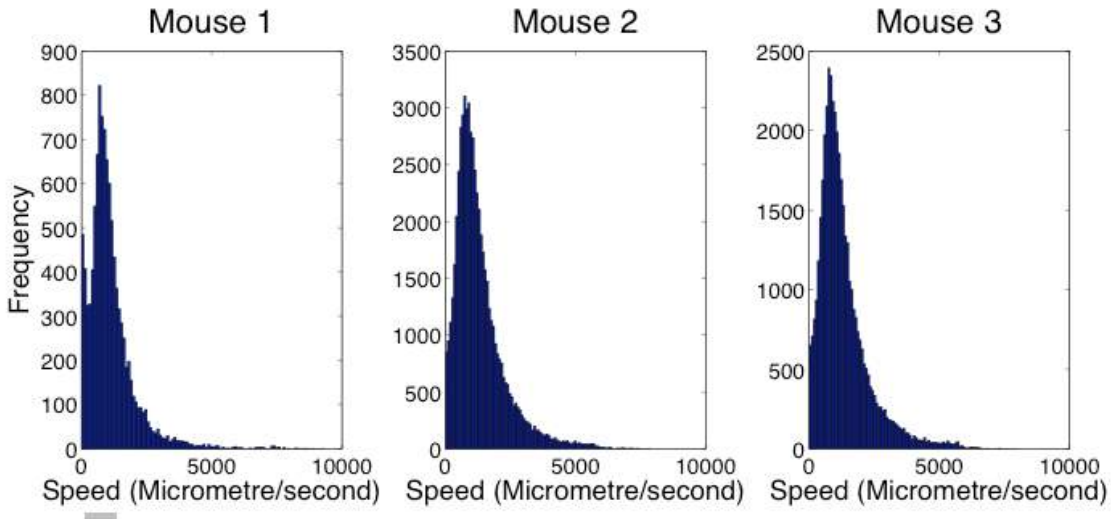

Figure 4.28. Speed histograms for the three *in vivo* data sets. Speeds of 700 μm/s, 748 μm/s and 760 μm/s respectively are most frequently tracked.

4.4 DISCUSSION

In this chapter, a method for performing acoustic super-resolution imaging *in vivo* has been developed and presented; this allowed visualisation of microvessels at the scale of tens of micrometres *in vivo* in 2D, far beyond the diffraction limit of conventional CPS imaging where branching structures within the mouse vasculature cannot be observed. This was then validated using optical imaging of the same area. Furthermore, by performing and examining three different *in vivo* data sets, repeatability of the technique was verified, and the effects of longer acquisition times were explored.

4.4.1 DIFFRACTION LIMITED RESOLUTION

The measured axial PSF FWHM for depths beyond 0.75 cm in B-Mode are approximately half that predicted using SPL calculations from hydrophone measurements. A significant difference in predicted and measured values is also seen using CPS imaging mode. This could be due to a number of reasons. Firstly, measurements of the PSF were performed on image data generated from the scanner, thus processing performed on RF data within the US system prior to the point of image data access is unknown. This could have involved onboard scanner processing such as RF receive amplification, band-pass filtering, beamforming, and temporal and spatial smoothing, which will modify the signal in an unknown manner before being observed in the final image (Chapter 1). Additionally, as discussed in Chapter 3, CPS images are

generated from the nonlinearity of receive signals rather than the fundamental as in B-Mode. The nonlinear PSF measured from a wire using CPS is generated predominantly from nonlinear propagation of US in water. This could result in lower SNR close to the transducer surface where limited propagation has occurred. Lower SNR values may result in a less well defined signal which may have a larger FWHM in shallower regions which becomes stronger and more well defined with depth.

4.4.2 SUPER-RESOLUTION IN VIVO IMAGING

Simulation results of motion correction algorithms using the same ROI size as that used in *in vivo* data estimated errors of up to 6 μm for all noise levels investigated. Motion which exceeded around 20 μm was assumed to originate from a sharp respiratory movement, which can be clearly visualised in video data. Since a simple rigid translational motion correction was used here, any more complex motion such as rotational or non-rigid motion cannot be dealt with using the developed motion correction algorithms and would degrade the accuracy of the resulting localisations. Vessel structures in mouse 2 and 3 were measured to be slightly larger in size to those in mouse 1; this may have been due to an increase in overall motion over considerably longer acquisition times, or due to incomplete correction which could contribute to the broadening of the appearance of vessel structures. More complex motion registration strategies which incorporate non-rigid and rotational motion will be required for data efficiency for long *in vivo* imaging scans in the future, which has attracted a wealth of research due to its importance in real time US imaging[243], [244] [245], [246][247], however out of plane motion will remain ~~a~~ more challenging for 2D imaging.

Vascular structures in mouse 2 and 3 appear more complex and dense than mouse 1, even after the same imaging duration (10 minutes) which may suggest the field of view in the former experiments were predominantly incident on secondary or tertiary branching structures such as arterioles, venules and pre- and post-capillary structures [235], whereas a principal vessel stemming and branching from the base of the mouse ear is dominant in mouse 1 results. The longer imaging duration also uncovered more detail of more dense, vascular structures between the larger vessels within mouse 2 and 3 experiments.

The use of a surgical microscope provided non-invasive optical visualisation of vessel structures within the *in vivo* model. However, this procedure was performed prior to US image acquisition under a different set-up and therefore co-identifying the same region in both acquisitions was challenging particularly considering the incomplete field of view observed in some US images. Without adequate ground truth data for mouse 2 and 3, analysis of the accuracy and resolution of these images is limited. Furthermore, a number of vessels appear more clearly in the super-resolution US image than in the optical image for mouse 1, and vice versa. This may be due to the distinction between the origin of the contrast for each imaging modality. The number of detected microbubbles flowing through a region over the imaging time interval dictates the visualisation of vessels in the final super-resolution image, which, when assuming all the vessels are within the field of view, should be related to the blood volume in the vessels. In the optical image, the image should be representative of the visible contrast of the vessel structures against the rest of the ear, likely to be related to the concentration of oxygenated (bright red) or de-oxygenated (dark red/purple) haemoglobin [28].

While the mouse ear was kept as flat as possible for both the optical and US imaging, the inherent differences between the two modalities mean that there will inevitably be some discrepancies between the two, i.e. small vessels on the far side of the ear from the surgical microscope will not be clearly resolved in optical images. In addition, variations in the mouse ear position in the elevational direction may cause some vessels to be outside of the plane imaged by the US system given the similarity between the width of the mouse ear and the estimated elevational slice thickness (Section 4.3.1) [235]. This is particularly evident in results from mouse 2 and 3, where large regions of the vascular structure are out of the field of view. The visualisation of some structures could be improved with the widening of thresholds within which signals are accepted since signals on the edge of the elevational slice thickness will be in general be lower in amplitude; this however causes the inclusion of more potential noise into the final image. In the final processing a compromise must be found in order to ensure a high enough SNR in the final image; this is again discussed later on in this section. This is a limitation of the 2-D acquisition process and in the future, a 3D implementation of this technique could allow complex structures to be super-resolved in the elevational plane.

The use of a validation technique which is less superficial will additionally enable better visualisation and measurement of underlying vessel structures and would provide a more effective and rigorous validation technique.

Two other main factors which influence the visualisation of the vasculature in the final super-resolution images were discussed in Chapter 3, Section 3.2ii; these are the localisation uncertainties σ_x and σ_y of the system, and the density of these localisations in the rendered image. Furthermore, the approach requires that the microbubbles sample the entire microvascular structure to generate complete information about the underlying structure. Increasing the detection frame rate will increase the microbubble localisation density per second. However, if the flow rate in a particular vessel is sufficiently slow that a microbubble moves by less than the localisation precision between frames, then no additional spatial information is gained by further increasing the frame rate. Therefore, for efficient data collection, the US frame rate should be chosen according to the localisation precision and the microbubble velocities expected within a given sample. This will be discussed further in the Chapter 7.

Currently, processing algorithms developed in this work can process up to 13 frames per second. In the future, optimisation of the current algorithms could enable localisations to be plotted in each frame, and thus the final image to be built up in real time at higher frame rates. This technique would benefit from the development of automated or semi-automated processing which is consistent across patients. This will be investigated further in this thesis.

The concentration of microbubbles used in this work was estimated to be larger than that used clinically. Although the injected bubble concentration was high, the infusion rate was very slow and by monitoring the bubble per frame density, adjustment of the infusion speed allowed for a high number of spatially isolated bubbles in each frame. Furthermore, the number of microbubbles reaching the mouse ear will be considerably lower than that injected due to bubble destruction and dissolution. Moreover, at a frequency of 6.5 MHz, US is less sensitive to bubbles, and furthermore, it is likely that only a small subset of the bubble population are resonant [231].

The resolution of super-resolution images is fundamentally limited by the achievable localisation precision; characterisation measurements suggest that this is 2 to 6 μm for the system used. The data acquired to achieve this super-resolution is the processed image output from a standard, unmodified clinical ultrasound system; as mentioned previously, this has been processed, digitally and logarithmically compressed, as well as envelope detected by the system. Each of these processes could reduce the achievable precision. Using raw data, the read-out noise of the system would be the fundamental limit on localisation precision of the US system.

4.4.3 VELOCITY MAPPING

The extension of this technique to extract flow velocity data from bubble localisations widens the application of the technique to include those of conventional Doppler imaging of microvasculature, with the significant advantage of having flow information with super-resolved spatial detail. Direction and speed images provide a higher level of information to the already super-resolved structures, enabling visualisation of even smaller structures and dynamics within the vessels. Super-resolved velocity mapping enabled the detection of slow blood velocities (in the range of μm/s) and for 360° in plane, in contrast to conventional US Doppler imaging, which is sensitive mostly to flow towards or away from the transducer and is unable to resolve speeds at micrometre scale.

Similar speed histogram distributions were observed in the three *in vivo* data sets. The peak of the histograms fell between 700-760 μm/s which correlates well to microvascular velocity flow values of a mouse ear found in the literature, where red blood cell velocity is stated to range from 60 ± 30 μm/s in the capillaries, to 3500 ± 320 μm/s in the principal vessels [235]. Higher speeds have been detected in this data which may be a result of inaccuracies in the bubble detection algorithm while motion is occurring, or a result of uncorrected motion within frames. To demonstrate the extent to which speed correlates with vessel size, an analysis of estimated vessel diameter versus corresponding average vessel speed would be a possibility for future work.

The distribution of microbubble localisation events in super-resolution images is indicative of the concentration of microbubbles throughout the vessel, regardless of the

flow profile. Coupled arteries and veins that are touching or overlapping will have no spatial separation in super-resolved localisation density maps, but may be able to be distinguished by mapping the velocity. This has been shown in Figure 4.17, where both speed profiles and bubble direction maps display a clear distinction between coupled vessels, with a clear dip in speed between vessels with opposing flow. This speed does not reduce to zero in any of the cases analysed here. Speed and velocity vectors were associated with the 95% confidence interval around their localised position. The spatial averaging of the velocity vectors means that unless the bubbles in opposing vessels were travelling at exactly the opposite velocity in magnitude and direction, the overall average speed component will be non-zero. For example, the two vessels may not run precisely in parallel.

The 2D acquisition strategy and image rendering however, reduces the accuracy of the velocity mapping technique in two main ways. Firstly, the velocity estimation is a projection of the bubble's 3D velocity vector in the 2D imaging plane, thus the out-of-plane velocity component is lost and the in plane components are affected by an unrecoverable error, which will be dependent on the elevational resolution of the system. In this demonstration, this error can be largely neglected due to the limited extension of the vessel structure in the third dimension; the main flow field will be along the length of the vessel in the x-y plane and thus it still allows interpretation of the instantaneous flow field and its structures. Unfortunately, this is not the case when studying highly three dimensional flows, where the only way to avoid the uncertainty error is to measure all three components of the velocity vectors using 3D acquisition strategies.

Furthermore, the 2D acquisition strategy combined with 2D image generation causes an underestimation of the velocity due to spatial averaging. Assuming the tube is straight with a circular cross section and the velocity is kept at a rate where the viscous forces dominate inertial forces, we assume the fluid motion will be laminar within the vessel. This can be validated through visual assessment of the bubble flow, which is consistent with a low Reynolds number ($Re = \frac{\rho v D_H}{\mu} < 1$). The size of the microvessels, estimated to be between 5 – 400 μm are well within the elevational resolution of the system. Using a 1D transducer array, the entire width of many of the vessels could be contained

within one imaging slice. The concentration of microbubbles will be constant across the vessel diameter as discussed above, however the signals visible in the centre of the vessel will originate from bubbles flowing across the entire imaging width of the vessel in the elevational direction ($\sum_{j=1}^{n} j$ in Figure 4.29). The estimation of velocity will be averaged over all those visible at a particular point in the x-y plane, and therefore will likely be underestimated most in the vessel centre, and decreasing towards the vessel wall boundary where the velocity drops to zero, as illustrated in Figure 4.29.

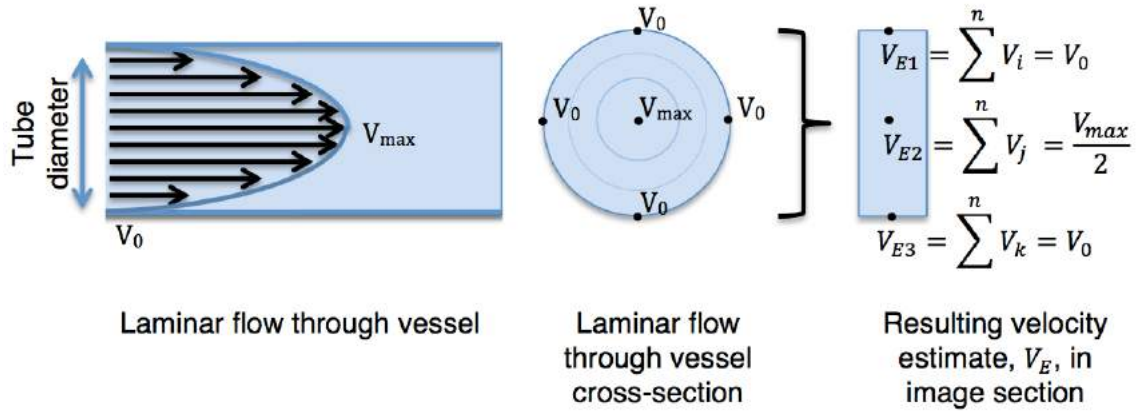

Figure 4.29. Illustration of underestimation of bubble velocity throughout the vessel diameter.

Crucially, to image microvascular flow, the technique employed must be sensitive to slow blood flow in the capillaries. With localisation precisions given by σ_x= 2 μm and σ_y = 6 μm in the axial and lateral directions respectively, the error on axial and lateral velocity measurements are given by $\sigma_{vy} = \pm 71\ \mu m/s$ and $\sigma_{vx} = \pm 212\ \mu m/s$ (Equation (3.23)) using this imaging system and frame rate. Slow flow travelling at speeds below these velocities do not cause a problem for super-resolution maps as they remain within the lumen of the vessel, however the movement of bubbles may not be well estimated in the final measurement.

4.5 CONCLUSION

These results demonstrate that single bubble localisation can produce acoustic super-resolution and super-resolved flow velocity images *in vivo* from standard image data

acquired by an unmodified clinical US system using post-processing localisation algorithms. Vessel structures with a FWHM over 5-times smaller than the diffraction limited resolution were visualised. Achieving a high level of resolution at greater depth and with overlying tissue will be required to demonstrate the potential of the technique to image the vasculature of deep organs.

5 Quantitative Measures for Clinical Imaging of Lower Limb Perfusion

5.1 Introduction

In this work the previously described single bubble localisation techniques presented in Chapters 3-4, were extended with the goal of generating quantitative measures for the clinical evaluation of tissue perfusion.

CEUS provides a valuable tool for visualising and quantifying tissue perfusion, and has been applied to study wide ranging clinical conditions such as cardiovascular disease, cancer and microvascular diseases [74], [109], [111], [248]–[250]. Quantitative measurements aim to supplement anatomical or qualitative features with markers of vascular function [42]. Many existing CEUS approaches for perfusion quantification are based on calculations of image intensities to measure features of the temporal and spatial distribution of the contrast agents as they flow within tissues. One such example is the use of destruction replenishment techniques which aim to extract a number of physiological features of the microcirculation from time intensity curves (TICs) of bubble replenishment [117]. Blood flow analysis and perfusion imaging has, however, been subject to a significant level of variability in imaging results [118], [119] and poor reproducibility has impeded the clinical translation of some techniques. An accurate and

automated technique for quantification of tissue perfusion is desirable for a wide-range of clinical applications including cardiovascular diseases and cancer.

It is hypothesised that by reducing infusion rates, or injecting lower bubble concentrations, the application of super-resolution algorithms could not only facilitate enhanced visualisation, but also enable the extraction of quantitative information from clinical CEUS imaging. The counting and tracking of isolated bubble events over CEUS acquisition aims to estimate changes in the active microcirculation using three parameters derived from estimated perfused blood volume, blood velocity, and perfused microvascular density, as well as offering visual assessment through super-resolved spatial maps of microbubble distribution.

Quantitative algorithms are first validated on *in vitro* phantoms, and are subsequently applied in a clinical study to assess changes in the microcirculation in human lower limbs. Differences in microvascular musculoskeletal perfusion in subjects before and after physical exercise can be indicative of the presence of Peripheral Arterial Disease (PAD). Thus in this work, CEUS imaging of lower limb skeletal muscle pre- and post-exercise is implemented to assess changes in microvascular perfusion, and quantitative results are compared to the existing and well accepted approach for perfusion imaging of destruction replenishment TIC analysis. Assessment of changes in perfusion using US may provide important information into the aetiology of such diseases and a non-invasive means of monitoring the treatment of such diseases [111].

The chapter therefore consists of the following sections: (1) clinical background, motivation, and study outline, (2) the development of clinically relevant quantitative measures, (3) *in vitro* validation, and (4) *in vivo* implementation.

5.2 Clinical Background

5.2.1 Peripheral Arterial Disease (PAD)

Peripheral arterial disease (PAD) is a condition characterised by a build-up of fatty deposits called atheroma in the arterial walls of the legs [46]. The accumulation of

atheroma, a process called atherosclerosis, narrows the arteries and causes obstruction to blood flow in the lower extremities [46], [47].

The most frequent symptom of PAD is intermittent claudication, defined as pain or cramping in the muscles of the leg that reoccurs with exercise and is relieved by rest. More severe symptoms include rest pain, tissue loss, or gangrene [47] and these can result in an increased risk of lower-extremity amputation, especially in patients with diabetes. PAD can also indicate an increased likelihood of systemic vascular disease, with an associated increased risk of myocardial infarction, stroke, and death [3], [47]. The assessment and management of PAD in those with diabetes is more complex and poses some specific issues; conventional non-invasive tests have been shown to be less predictive of the severity of symptoms [3], [47]. This will be discussed in more detail in the following section.

Many medical and surgical therapies to treat PAD aim to increase the circulation in the lower limbs through interventions such as balloon angioplasty, stenting, or surgical re-vascularisation. Impaired lower extremity function is an important predictor of patient outlook in relation to potential functional disability, loss of mobility and loss of limbs [15],[16]. Measuring changes in musculoskeletal perfusion are important in the management of diabetes and PAD, however these remain difficult to measure.

5.2.2 Current Assessment of PAD and Clinical Need

There is an emerging clinical need for the development of a new technique for the assessment of PAD. Non-invasive methods typically used for diagnosing PAD include measuring pressure gradients in the patient's arms and legs, such as the ankle-brachial index (ABI), and colour Doppler flow velocity, or measuring abnormal blood pulse volumes caused by stenosis [111]. These methods have been adequate for detecting more advanced disease in symptomatic patients, however, they also have a number of limitations. Resting pressure gradients and reduced resting flow, such as those measured by ABI, only arise after progression of vessel stenosis in relatively advanced cases of disease [111], [252], [253] and are not ideal for detecting mild to moderate disease which may present only with abnormal microvascular responses to exercise [111]. Moreover, 'normal' ABI values are commonly found in patients with symptomatic PAD

[254]. Therefore, quantifying the functional response related to limb ischemia by assessment of musculoskeletal perfusion following exercise could be a valuable tool for PAD diagnosis. This could also play an important role in the development and assessment of treatments and preventive strategies designed to improve limb perfusion and delay disease progression [111].

5.2.3 ASSESSMENT OF PAD USING CEUS

Destruction-replenishment approaches typically employ the use of a short burst of high power US to destroy microbubbles within the imaging plane during a constant infusion of contrast agent and deduce subsequent physiological features from the dynamics of contrast agent replenishment within the tissue.

Various features directly related to the vascular characteristics of the tissue can then be estimated in order to quantify the spatial extent and magnitude of the flow through the region of interest. These include conducting TIC analysis to extract a number of physiological features such as peak intensity, the rate constant of the refill curves, and time to peak (TTP) of contrast enhancement after an intravenous contrast injection or microbubble destruction. Recent studies have shown great promise in evaluating musculoskeletal microcirculation in lower limb [110], [111], [255]–[259]. A contrast US method for skeletal muscle perfusion has been developed in which measurements of perfusion parameters such as TTP were able to distinguish differences in perfusion in patients with severe PAD from control subjects [110], where a significantly longer TTP was found in PAD patients than control subjects. This is a simple and easily implementable technique, however, TTP values may be influenced by factors relating to the individual patient and experimental variations, for example differences in patient cardiac output, variations in body blood volume and therefore blood distribution, and microbubble injection rate.

In a study by Lindner et al, 2008 [111], skeletal muscle blood flow and flow reserve was measured using stress-rest CEUS perfusion imaging. Relative microvascular blood volume and blood velocity rate were estimated by measuring the peak video intensity and rate constant of the refill curves respectively. Patients with PAD were estimated to have a significantly smaller increase in relative microvascular blood volume and

microvascular blood velocity in response to exercise [111], which were demonstrated to correlate to the presence and severity of PAD in symptomatic patients. This technique may be able to detect more modest or early stage disease than conventional diagnostic techniques.

CEUS has shown great potential in imaging perfusion, however quantitative CEUS has been affected by a number of factors causing variability in imaging results [83], [120]. Many existing CEUS approaches as discussed here are based on the quantification of image intensity or temporally derived measures during perfusion of contrast agents within tissue. Flow analysis has been shown to be significantly affected by US system settings and imaging conditions such as insonation power, physical differences relating to individual patients, and target depth. Amplitude-based parameters have been shown to be more influenced by system changes than time-related measures [83], [120]. Additionally, flow measurements are further complicated by the spatial heterogeneity of tissue blood flow. Large vessels within the tissue typically dominate and can increase the variability of flow measurements. These can mask the influence of the microcirculation, which may preferentially respond to vessel-targeted therapies [260].

These factors have resulted in diagnostic uncertainty and have impeded the clinical translation of some techniques; therefore, qualitative visual assessment remains a standard procedure for some diagnoses. An accurate and automated technique for quantification of tissue perfusion is desirable for a wide-range of clinical applications including cardiovascular diseases and cancer.

5.3 STUDY OUTLINE

Patients exhibiting symptomatic PAD have previously been shown to have a significantly smaller increase in relative microvascular blood volume and microvascular blood velocity in response to exercise compared to healthy individuals. The clinical study therefore involved the participation of healthy subjects and subjects with symptomatic PAD. The aims of the study involved the following:

1. Validation of CEUS and single bubble localisation as a method of estimating changes in muscle microcirculation through *in vitro* and *in vivo* repeatability

studies, given that there is a significant increase in muscle micro-perfusion between rest and post-exercise in healthy individuals.

2. Visualisation and quantification of the microcirculatory differences in patients with symptomatic pathology.
3. Discrimination between healthy subjects and those with microvascular disease via quantitative imaging analysis.

5.3.1 PROPOSED TECHNIQUE

Three new quantitative measures derived from single-bubble localisation to estimate lower limb musculoskeletal microcirculation are proposed: these are the number of single microbubble localisations, the tracked microbubble density, and the microvascular blood speed. For the first measure, it is assumed that variations in the quantity of microbubbles in a volume of tissue will be representative of changes in blood volume within the target area, providing a uniform microbubble concentration, and that this holds up to a limit where the microbubble concentration begins to saturate the image. For the second, it is assumed that the image area covered by microbubble localisations is representative of the area of perfused vasculature, and hence comparison of localisation coverage before and after exercise is indicative of the change in perfused microvessel density, i.e. the density of vessels which sustain blood circulation. Lastly, the average velocity of individual microbubbles tracked within microvessels is assumed to reveal the microvascular blood velocity since microbubbles have an intravascular rheology similar to that of red blood cells [109], [200], [201], [224]. The derivation of these measures is described in further detail in the following section.

5.4 IN VITRO VALIDATION

5.4.1 AIM

To test the performance of algorithms for the assessment of contrast agent volume, tracked microbubble density (TMD), and changes in contrast agent speed using *in vitro* experiments.

5.4.2 METHOD

5.4.2.1 ULTRASOUND IMAGING EQUIPMENT AND SET-UP

CEUS imaging was performed using a clinical Philips iU22 clinical US scanner (Philips Medical Systems, Bothell, WA, USA) with a 3-9 MHz broadband linear array transducer. Imaging was performed using a low mechanical index of 0.06, a frame rate of 13 Hz, gain of 69%, and a dynamic range of 50 dB. Imaging was performed to a depth of 4 cm with a focal zone between 2-3 cm, consistent with clinical imaging protocol. Simultaneous B-Mode image acquisition was also performed.

5.4.2.2 ULTRASOUND SYSTEM CHARACTERISATION

MEASUREMENT OF IN PLANE RESOLUTION AND LOCALISATION PRECISION

The initial step of this work involved characterisation of the diffraction limited resolution of the system and assessment of the potential localisation precision. Characterisation experiments using a 100 μm diameter brass wire performed in Chapters 3-4 were replicated in this chapter using the Philips iU22 clinical scanner operating with settings as defined above. This allowed estimation of the diffraction limited US system resolution and localisation precision.

5.4.2.3 CONCENTRATION EXPERIMENT

FLOW GENERATION

A tank containing 600 ml of gas equilibrated water was prepared. Acoustic absorbers were used to reduce reflections from the container walls, ensuring no scattering artefacts appeared in the image. A magnetic stirrer was used to mix the microbubble suspension, with a rate of just over 1 revolution/second, chosen in order to resemble a typical 60-70 beats per minute resting heart rate [261]. An illustration of the set-up is displayed in Figure 5.1.

CONTRAST AGENT PREPARATION

Five concentrations of microbubble suspension were tested. These were created by mixing the following quantities of SonoVue^{TM} (Bracco, Milan) microbubbles in 600 ml of room temperature gas equilibrated water: 0.05 μl, 0.1 μl, 0.15 μl, 0.2 μl, 0.25 μl. This concentration range was chosen to mimic those visualised in test clinical scans performed on the lower limb of healthy subjects.

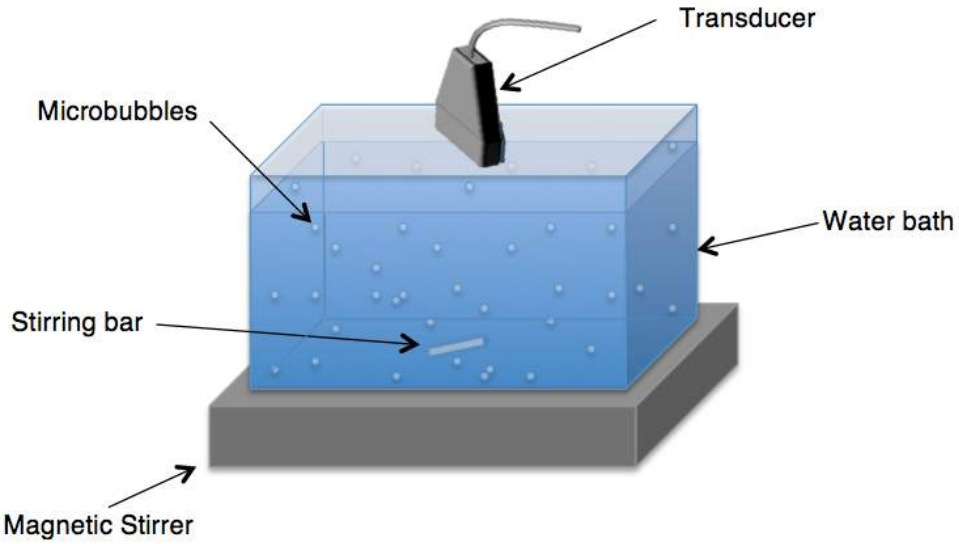

Figure 5.1. *In vitro* set-up for concentration based experiment. A water bath is prepared with a magnetic stirrer.

SEQUENCE ACQUISITION

Each volume of microbubble suspension was extracted using a micropipette and inserted into the water tank. CEUS scanning was then performed and video data was acquired over 30 seconds. Following each data collection, a high MI was applied while stirring continuously to destroy the microbubbles present in the water tank for approximately 1 minute, or sufficient time that no remaining bubbles could be seen in the display. This sequence was repeated for each concentration.

5.4.2.4 SINGLE TUBE EXPERIMENT

Super-resolution imaging was demonstrated using capillary tube flow phantoms similar to those used in Chapter 3. This involved the use of a thin walled cellulose tube of 200 μm internal diameter which was threaded into butterfly needles and sealed before being placed in a gas equilibrated water bath. The length of the tube spanned across the lateral direction in the transducer's imaging plane. This enabled measurement and analysis of fluid flow. A concentration of 0.15 μl SonoVue^{TM}/600 ml water suspension was prepared in a reservoir. One of the tube endings was placed in the reservoir, while the other was attached to a syringe pump. The syringe pump was adjusted to withdraw at five varying speeds: 10 μl/min, 20 μl/min, 50 μl/min and 100 μl/min. Flow rates chosen corresponded to mean speeds of 5.3 mm/s, 10.6 mm/s, 26.5 mm/s and 53.0 mm/s. These speeds were chosen to mimic the range of velocities within the vessels of the lower limb

muscle such as the Dorsalis pedis artery (associated with PAD) [262][33] up to the faster flow in the common femoral artery [263], [264]. CEUS imaging was acquired for 180 seconds at each speed setting.

5.4.2.5 POST PROCESSING

All AVI data files were processed on a standard PC using MATLAB. Firstly, video sequences were converted to grey scale images, and log decompressed as described in Chapter 3. Acquired image frames were then processed using algorithms described in the following sections.

BACKGROUND SUBTRACTION

Image frames displayed spatially variable background noise, which increased considerably with depth, predominantly in the central region of the image (this can be seen in Figure 5.3B in the results section). The average intensity level in an arbitrary sized 15 x 15 pixel region at 3.5 cm depth in 10 background images was a factor of 1.24 higher than the same sized region at 1 cm. This intensity difference is also evident in clinical image data (see Figure 5.13 in clinical results section), where lower regions were on average 1.8 times higher in intensity than in the equivalent upper region. Since this spatial variation was not linear with depth, and changed in shape and amplitude for different patients and different scans, an adaptive, automated background removal technique was devised.

Background estimations were performed by median filtering N background frames using a symmetric median filter of size $m \times m$, before averaging over all frames to generate a representation of the underlying spatially varying background noise. The size of the median filter was chosen by performing a test over a range of sizes for $1 < m < S/2$, where S is the size of the smallest dimension of each frame. The average sum of absolute differences ($S\hat{A}D$) between the median filtered background, x_m, and each contributing background frame, x_b, was calculated by

$$S\hat{A}D(x_m, x_b) = \frac{\sum_{j=1}^{N} \left\| x_m - x_{bj} \right\|_1}{N} \tag{5.1}$$

where

$$\left\|x_{mj} - x_{bj}\right\|_1 = \sum_{i=1}^{M} \left|x_{mi} - x_{bji}\right|, \tag{5.2}$$

and M is the number of pixels in each image. The value of m for which $S\hat{A}D$ is a minimum was assumed to indicate the image most representative of the original background and was then subtracted from data frames as an initial processing step. For each dataset, the 99th percentile of the set of pixels given by $p = \left\{\left|x_{bji} - x_{mi}\right| \middle| j = 1, \ldots, N, i = 1, \ldots, M\right\}$ was used as the intensity threshold on the data frames in order to ensure the threshold is above the large majority of intensities represented by noise, but to avoid affects of outliers within the background frames. For all datasets, $N = 100$, since this corresponded to the approximate number of frames acquired prior to the start of contrast agent infusion in the clinical study. The resulting image then provided candidate bubble regions for further analysis.

BUBBLE LOCALISATION

In vitro data were then processed using an altered version of the single bubble localisation code as introduced in Chapter 3, whereby potential bubble regions were rejected if they were smaller than the size of the measured point spread function, presented in the following Results Section 5.4.3.1; signals below this size were assumed to be representative of noise. Assessment of the size of a small set of multiple bubble signals (identified by visual assessment) provided an upper limit for single bubble classification. The intensity weighted centre of mass of these regions was then calculated as described in Chapter 3.

5.4.2.6 DERIVATION OF QUANTITATIVE MEASURES

For all parameters, measurements must be performed over the same imaging duration, and over the same time-period following the start of the microbubble infusion for clinical studies. Quantitative measures generated by the proposed method are compared with the known microbubble suspension concentrations.

NUMBER OF LOCALISATIONS

The number of microbubbles imaged throughout the acquisition was estimated by performing single bubble localisation. The number of single bubble detections, N_S, was

assumed to correlate with the number of bubbles present in the imaged blood volume, V, by

$$N_S = \alpha CV, \tag{5.3}$$

where C is the microbubble concentration, and α is a parameter relating to the combined effect of the microbubble size distribution, the imaging frequency and bandwidth, effects of bubble dissolution, and other factors which affect the overall proportion of microbubbles detected using CEUS. Thus, this can be used to generate a measure proportional to the volume of fluid within the tissue, provided (1) the concentration of microbubbles in the fluid is constant, and (2) factors comprising α are constant within the imaging time-frame, (3) the probability of imaging multiple overlapping bubbles is negligible and (4) the algorithm is able to detect bubble signals and differentiate these from noise. If the concentration exceeds condition (3), the loss of spatially isolated microbubble signals breaks down the assumptions of this technique. If the dissolution of bubbles occurs over the time-frame of acquisition, this will cause inaccuracies in the estimation of microvascular blood volume, but should not effect the relative measure between patient scans over the same imaging duration.

Tracked Microbubble Density Measure (a surrogate for Active Microvasular Density)

A measure devised to assess the active microvascular density is the tracked microbubble density (TMD). This estimates the area of which tissue is perfused in an ROI. It aims to provide an enhanced measure of perfused vascular density to that provided by MIP since the diffraction limited resolution inherent to this technique may mask subtle yet crucial microvascular detail and differences associated with PAD. TMD is defined by the following calculation,

$$TMD = \frac{Tracked\ Microbuble\ Area}{ROI\ Area}, \tag{5.4}$$

where the tracked microbubble area is the number of pixels in the resulting super-resolution map which have a value of more than a localisation threshold; this threshold was used as a criterion to determine the presence of a microvessel. A localisation threshold (LT) of one means that every pixel which contains at least one bubble

localisation, or the combination of Gaussian profiles contributions in the image sums to more than one, will be considered a component of the microvasculature. This can be chosen so that false or noisy localisations do not contribute to the final estimation, however, capillary structures may contain only single localisations and therefore could be excluded in this final measurement. Choosing LT >= 0.5 (equal to the FWHM of the Gaussian profile), means areas within the localisation precision of a single bubble localisation will be considered as perfused vascular structures. In this work TMD values were investigated with the use of a criterion of LT >1 and LT >= 0.5; these will be compared in the final results. The conditions stated in the previous section are also relevant here.

MICROVASCULAR BLOOD VELOCITY

Patients with PAD are estimated to have a significantly smaller increase in relative microvascular blood velocity in response to exercise [111], hence another measure derived for quantitative assessment using CEUS is the speed of detected microbubble signals. Since this technique utilises microbubble contrast agents that remain within the vascular space, and have flow dynamics similar to that of red blood cells [109], [200], [201], [224], it is hypothesised that measurements of individual bubble tracks could be used to quantify the change in microvascular blood flow and map blood velocity at super-resolution.

5.4.2.7 IN VITRO VELOCITY VALIDATION

Bubbles localised in each frame using the single bubble localisation method were tracked using an adapted version of the algorithm developed in Chapter 3. Modifications included the search window size, which was set to 8 mm for all speed settings since prior knowledge of the target structure or flow was assumed to be limited. This setting exceeds the maximum expected velocity for blood flow in the lower limbs, where the common femoral artery has a velocity of around 350 ml/min in healthy patients [263], [264], corresponding to a mean speed of approximately 9.2 cm/s (7 mm/frame) assuming a 9 mm vessel diameter [265]. The main vessels of interest in this study are smaller with lower blood flow so this defines the largest expected rates that should be detectable with the technique. Additionally, a constant stirring rate was used during the concentration based *in vitro* experiments enabling the effect of concentration on the estimation of speed to be investigated.

5.4.3 RESULTS

5.4.3.1 ULTRASOUND SYSTEM CHARACTERISATION

The average FWHM of the wire scatterer across the field of view was measured to be 305 ± 39 μm laterally, and 349 ± 25 μm axially, providing an indication of the effect of diffraction on point scatterers. The localisation precision was measured to be 94.6 μm in the lateral direction and 107.3 μm in the axial direction.

5.4.3.2 CONCENTRATION EXPERIMENT

Example CEUS image frames with SonoVue™ microbubble volumes equal to 0.1 and 0.2 μl in 600 ml water are shown in Figure 5.2. Bubbles are at a low concentration where the occurrence of multiple overlapping bubbles is low.

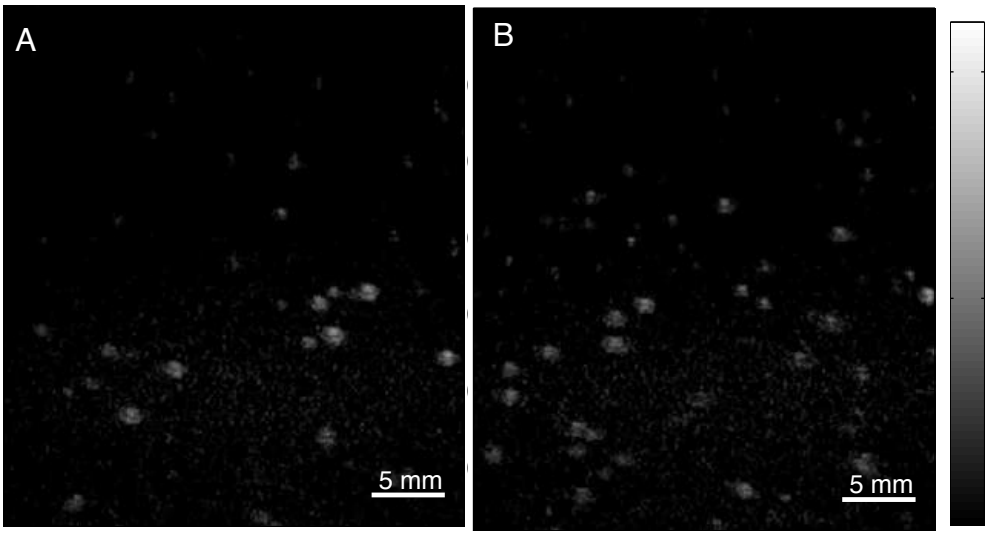

Figure 5.2. Example log-compressed image frames taken from *in vitro* concentration quantification experiment using a volume of (A) 0.1 μl, and (B) 0.2 μl of SonoVue™. Grey scale bar displays intensity 0 – 140 in arbitrary units.

Results displaying the average $S\hat{A}D$ values between median filtered background images and 50 background frames for varying symmetric median filter size are displayed in Figure 5.3A. Figure 5.3B displays the log-decompressed average median filtered background image. In this example, minimisation of the $S\hat{A}D$ occurred at a median filter size of 21×21 pixels, thus this was used to create the background image for subtraction from the subsequent *in vitro* data. The intensity noise threshold applied to

the frames was equal to the 99th percentile of the set of pixels given by $p = \{|x_{bji} - x_{mi}| \; | j = 1, \ldots, N, i = 1, \ldots, M\}$ at this minimum. This image represents an estimate of the spatially varying background signal present in the images, and does not aim to replicate the noise present across the image that can be observed in Figure 5.2.

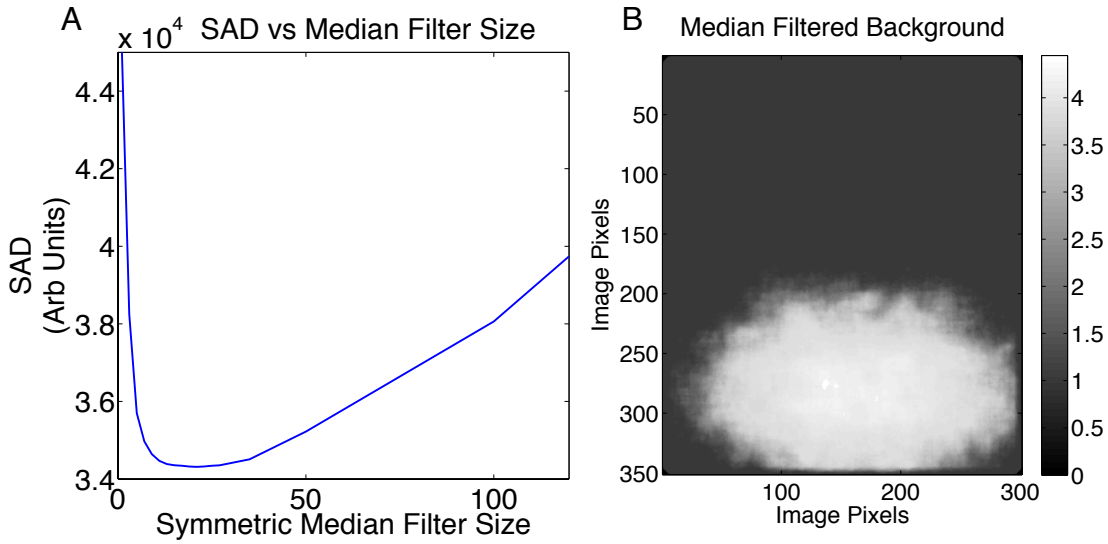

Figure 5.3. (A) Average SAD values between average median filtered background images and 50 background frames for varying symmetric median filter size. Minimisation of the SAD occurred at a median filter size of 21 × 21. Part (B) shows the log-decompressed average median filtered background image.

Quantification of Concentration

Localisation estimations are shown in Figure 5.4 where error bars show the standard deviations over 3 measurements. Average bubble localisation measurements showed a good correlation with the known microbubble volume with an R-squared value of 0.9942. Results for TMD estimations shown in Figure 5.5 display a good correlation using TMD measurements for LT >= 0.5 (Figure 5.5B), where the R-squared was at a similarly high value of 0.9912. A slightly lower R-squared value of 0.9307 was found for measurements made using the TMD with LT > 1, (Figure 5.5A).

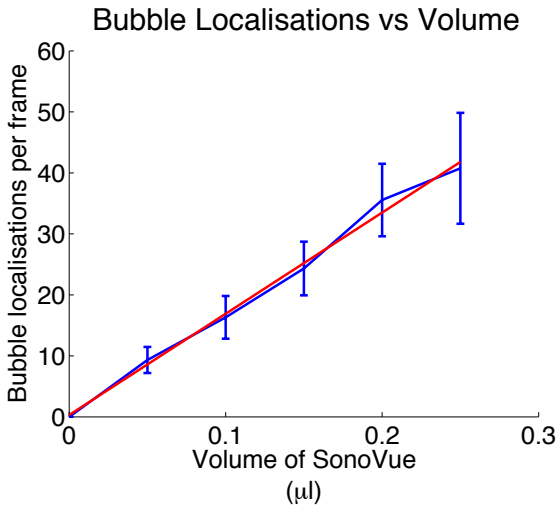

Figure 5.4. Number of bubble localisations per frame for *in vitro* SonoVue™ volumes between 0 and 0.25 µl diluted in 600 ml water. Red line indicates linear fit.

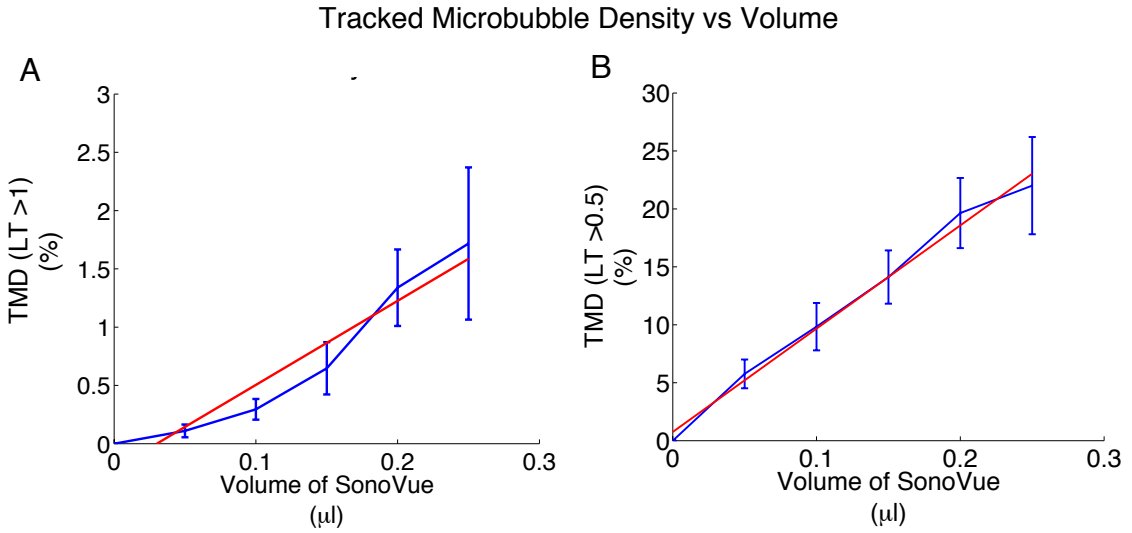

Figure 5.5. TMD as a function of varying microbubble concentrations, where the volume of SonoVue™ was diluted in volumes between 0 and 0.25 µl in 600 ml water. Part (A) displays the result using LT > 1, and (B) LT >= 0.5. Red lines indicate linear fit.

Figure 5.6 displays the tracked bubble speeds within each concentration experiment. This displays a similar shaped profile at each concentration, which is consistent with an assumed equal speed, since the magnetic stirrer remained at a constant revolution rate throughout all experiments. The mean and standard deviation of speeds found within each concentration experiment are shown in Figure 5.7 and Table 5.1. The number of localisation counts is representative of the bubble concentration. The mean tracked

bubble speeds are relatively stable across bubble concentrations tested here, however, there is a moderate increase in estimated mean speed and standard deviation with higher concentrations.

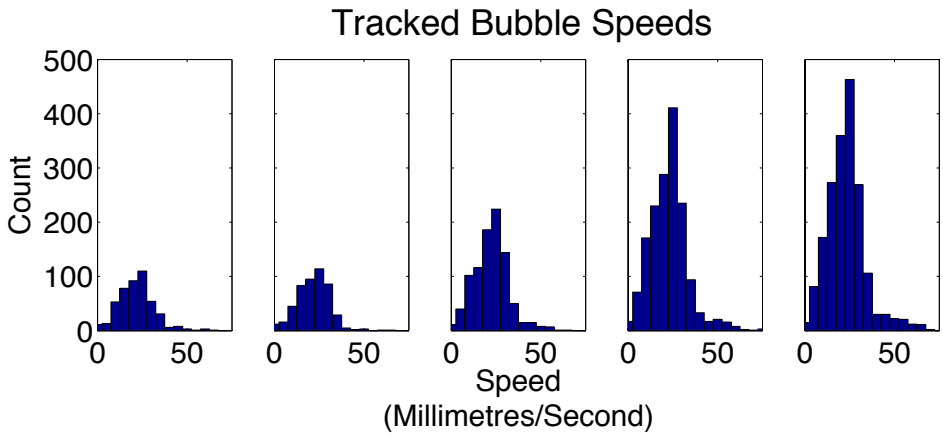

Figure 5.6. Histogram of tracked bubble speeds throughout the concentration experiments, where the stirring rate was kept constant throughout.

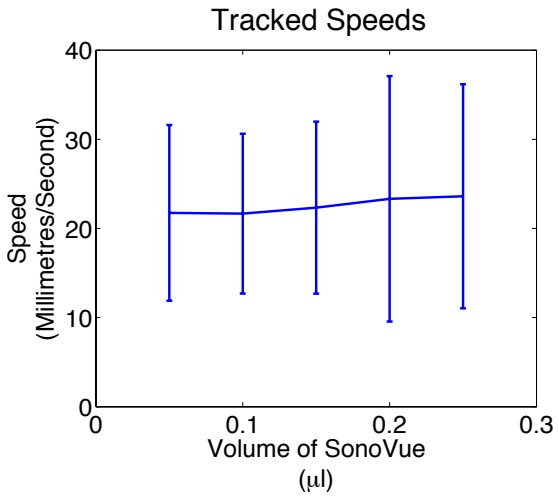

Figure 5.7. Mean tracked bubble speeds within each concentration experiment, where errorbars show the standard deviation. This displays a similar shaped profile at each concentration, which is consistent with an assumed equal speed, since the magnetic stirrer remained at a constant revolution rate throughout all experiments.

Concentration (µl SonoVue in 0.6 l water)	Tracked Speeds (mm/s)	
	Mean	Standard Deviation
0.05	21.8	9.8
0.1	21.7	9.0
0.15	22.3	9.7

0.2	23.3	13.8
0.25	23.6	12.6

Table 5.1. Mean tracked speeds within *in vitro* concentration based experiments. Each measurement was performed with the same stirring rate with varying concentrations of microbubble suspension. The algorithm detection showed consistent estimation of speeds with higher concentrations, while standard deviation increased.

5.4.3.3 SINGLE TUBE EXPERIMENT

Results from *in vitro* velocity investigations displayed in Figure 5.8 show 4 histogram profiles for each flow rate corresponding to mean speeds of 5.3 mm/s, 10.6 mm/s, 26.5 mm/s, and 53.0 mm/s. The mean and standard deviation of the tracked speeds using single bubble localisation are 6.3 ± 11 mm/s, 12.5 ± 6 mm/s, 32.0 ± 15 mm/s and 50.6 ± 23 mm/s, which show a good correlation to experimental speed settings (Figure 5.9).

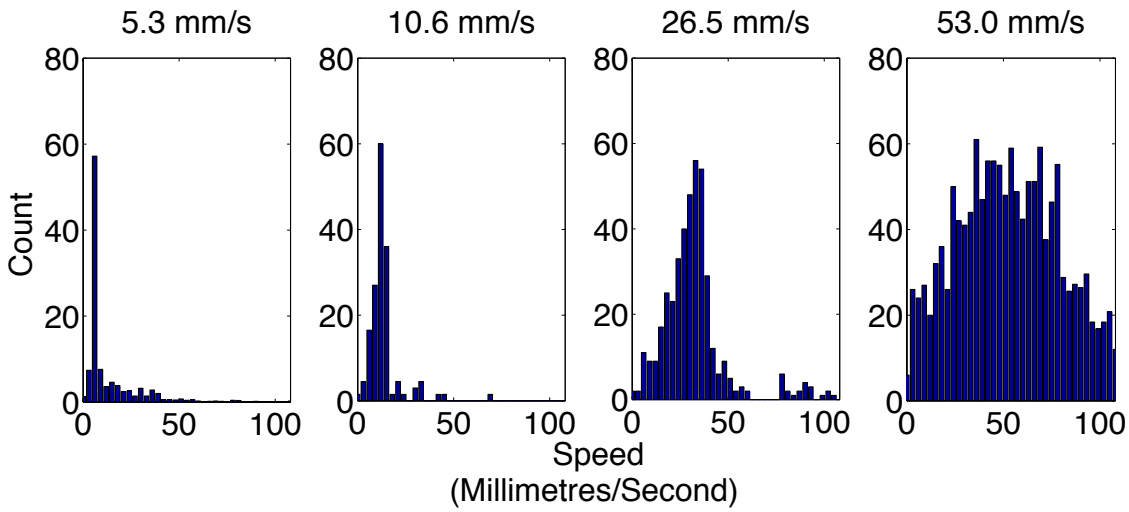

Figure 5.8. Results from *in vitro* velocity investigations show that 4 histogram profiles can be seen for each flow rate corresponding to mean speeds of 5.3 mm/s, 10.6 mm/s, 26.5 mm/s, and 53.0 mm/s. The mean and standard deviation of the tracked speeds using single bubble localisation are 6.3 ± 11 mm/s, 12.5 ± 6 mm/s, 32.0 ± 15 mm/s and 50.6 ± 23 mm/s.

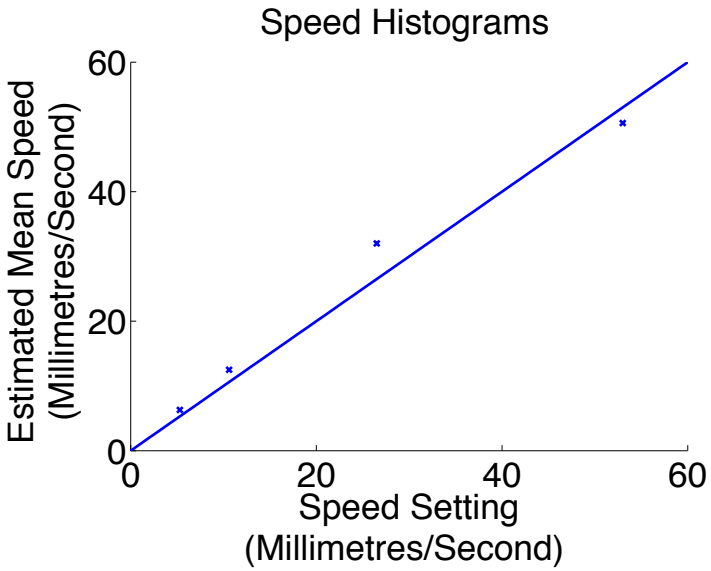

Figure 5.9. Comparison between estimated mean speeds of tracked microbubbles flowing through a 200 µm cellulose tube for experimental speed settings using a syringe pump of 5.3 mm/s, 10.6 mm/s, 26.5 mm/s, and 53.0 mm/s.

5.4.4 Discussion

5.4.4.1 Concentration

Concentration experiments showed the highest R-squared value for bubble localisation, closely followed by TMD (LT >= 0.5). The slightly reduced R-squared value for TMD (LT > 1) may be due to the low bubble concentration, in combination with a short acquisition time. This would mean the likelihood of overlapping localisations, which is necessary to exceed the LT, was small, and thus may not be fully representative of bubble concentration. Estimations of TMD using a localisation condition of more than or equal to 0.5 generated results which were more representative of bubble concentration. Over longer acquisition times, or higher microbubble concentrations, the use of LT > 1 would become more relevant.

The standard deviation is observed to increase with concentration for all quantitative measures; this may be caused by a number of factors including the decay of the microbubble concentration over time, which would lead to greater variation with increasing microbubble concentration. There could additionally be a possible degradation of the accuracy in the measurements with higher concentrations due to the

occurrence of multiple bubble signals which should be rejected in post-processing algorithms.

5.4.4.2 VELOCITY TRACKING

Mean tracked bubble speeds within each concentration experiment were estimated to within 1.8 mm/s across various concentrations while the magnetic stirrer remained at a constant revolution rate throughout. There was a moderate increase in estimated mean speed and standard deviation with increased concentrations. The precise velocities of the microbubbles are likely to be influenced by a number of factors such as the position of the bubble within the container, in relation to the size and shape of the tank, and the distance between the scatterer and the stirrer. Since the velocity of the bubbles could not be more carefully controlled in the concentration-based experiment, validation of the bubble velocities was therefore performed in tube based *in vitro* phantoms.

The total number of tracked bubble localisations was higher for increased speed settings since a larger number of microbubbles will travel through the field of view over the imaging duration. From visual assessment, bubbles often disappeared during flow through the vessel at the slowest speed of 5.3 mm/s, and was also noticeable at a speed of 10.6 mm/s. This could be attributed to the destruction of bubbles within the field of view for slower flowing bubbles due to repeated insonation. This may have an impact for future experiments, where fewer slower moving bubbles may be tracked if they are travelling within the US field of view for considerable time. The amount of microbubble destruction is likely to be dependent on the US insonating pressure, frequency and characteristics of the microbubbles being imaged, for example their resting diameter [266], [267].

A large imaging field of view was chosen to replicate that used in the clinical imaging protocol, and thus pixelation becomes a limiting factor in the achievable localisation precision. The large field of view and low spatial sampling means that each bubble signal covers only a few pixels in the image (note: FWHM of the point scatterer is 349 μm axially, while pixel size is 104 μm). The resulting sensitivity of the velocity measurement is dependent upon the precision of the localisations found in each frame. With this low signal sampling in the image, localisation precision is estimated to be

107.3 μm axially; this means that velocity measurements have an error associated with each measurement of $107\ \mu m\ \cdot\ 13\ Hz \cdot \sqrt{2} = \pm 1967\ \mu m/s$ or just under 2 mm/s in the axial direction using Equation (3.23). This will be discussed in relation to clinical results in Section 5.7.1.6.

5.5 CLINICAL METHODOLOGY

5.5.1 ETHICS AND PATIENT PARTICIPATION

Ethical approval for this clinical study was provided from the National Research Ethics Service (13/LO/0943), and research sponsorship was granted from the Imperial College NHS Trust Research and Development Department. Independent review by Imperial College Peer Review Office deemed the trial to be of significant scientific merit.

5.5.2 CLINICAL ULTRASOUND IMAGING

Four healthy volunteers were screened for absence of vascular disease and diabetes mellitus. All participants provided written informed consent. CEUS was then performed to evaluate the microcirculation in the tibialis anterior muscle, a narrow muscle in the anterior compartment of the lower limb, and the gastrocnemius, a muscle located on the back portion of the lower leg. SonoVue™ was diluted using normal saline (25mg in 20ml) and was administered as an intravenous infusion (VueJect™, Bracco, Milan) at a rate of 4 ml/min via an 18G cannula placed in an antecubital vein. Subjects were scanned on an examination couch in the left-lateral position. Image scans were performed from the medial head of the gastroctrocnemius muscle in the trans-axial plane to a depth of 4 cm with a focal zone between 2-3 cm. Data saving started approximately 10 seconds prior to infusion and captured the full infusion period which lasted approximately 5 minutes. The skin was marked for repeat scanning purposes. The volunteers then performed a timed exercise using a treadmill incline test for 30 minutes, before the imaging sequence was repeated, as illustrated in Figure 5.10. Effort was taken to minimise the interval between termination of exercise and commencement of the scanning procedure. Destruction-replenishment imaging was additionally performed 4 minutes after initiation of the microbubble infusion for comparison using a short burst of high power US with MI 0.77. This entire procedure was repeated on two consecutive days for each healthy volunteer. CEUS sequences acquired both before and after

physical exercise for each subject were analysed to assess features relating to the relative change in microvascular perfusion. This was additionally performed a single time on four patients with diagnosed symptomatic PAD (intermittent claudication).

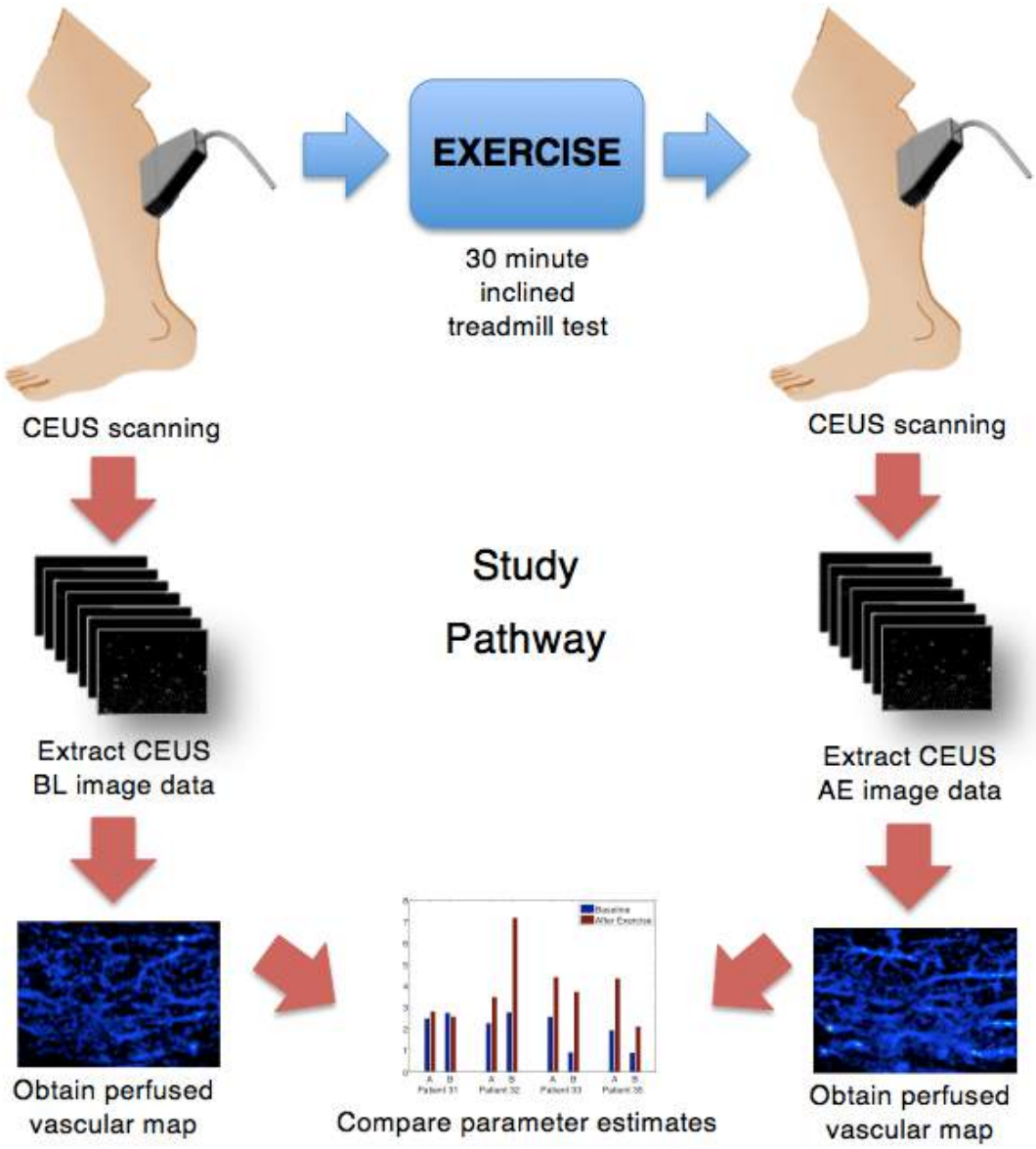

Figure 5.10. Clinical study pathway. A CEUS baseline (BL) scan is firstly performed to evaluate the microcirculation in the lower limb using an intravenous infusion of SonoVue^{TM} microbubbles at a rate of 1 ml/min over 5 minutes. The volunteers then performed a timed exercise using a treadmill incline test for 30 minutes. A repeat CEUS sequence was performed after exercise (AE) and quantitative estimations were analysed. This was repeated on two separate occasions for each healthy patient.

5.5.3 POST PROCESSING

5.5.3.1 DESTRUCTION- REPLENISHMENT ANALYSIS

In vivo flow quantification was estimated using destruction-replenishment time intensity data for each of the subjects. Destruction-replenishment TICs calculated over the entire ROI (shown in Figure 5.14 in the following section) were fitted with a log-normal perfusion model using a non-linear least squares fitting algorithm in MATLAB developed by Hudson et al. [268]. This model describes the replenishment of microbubble contrast agents through the US imaging plane under consideration of certain physical elements of the measurement, including the morphology of the vascular system, the US field, and microbubble properties. A frame obtained 1 second after the destruction pulse is subtracted from subsequent frames to reduce the signal coming from non-capillary vessels [269], [270]. The curve was analysed over 50 seconds following microbubble destruction. Peak intensity, flow rate, and time to peak (TTP) over this period were calculated from this model and compared with results obtained from the microbubble localisation algorithm. It should be noted that the peak intensity denotes the highest intensity reached by the model fit, and the TTP is the first time this intensity occurs.

5.5.3.2 SINGLE BUBBLE LOCALISATION

An example clinical data frame during CEUS imaging of the lower limb of a healthy volunteer is shown in Figure 5.11. The initial processing of clinical AVI files was consistent with the *in vitro* experiments previously described in 5.4.2.5. CEUS clinical image sequences were then processed using the bubble detection algorithm consisting of three steps. Firstly, a rigid motion correction algorithm (see Chapter 4) is applied using simultaneously acquired B-Mode images to correct bulk motion effects. Secondly, background subtraction and super-resolution algorithms are applied to the data. These will be described in more detail in the following section. Lastly, quantitative measures described previously are calculated from the resulting data.

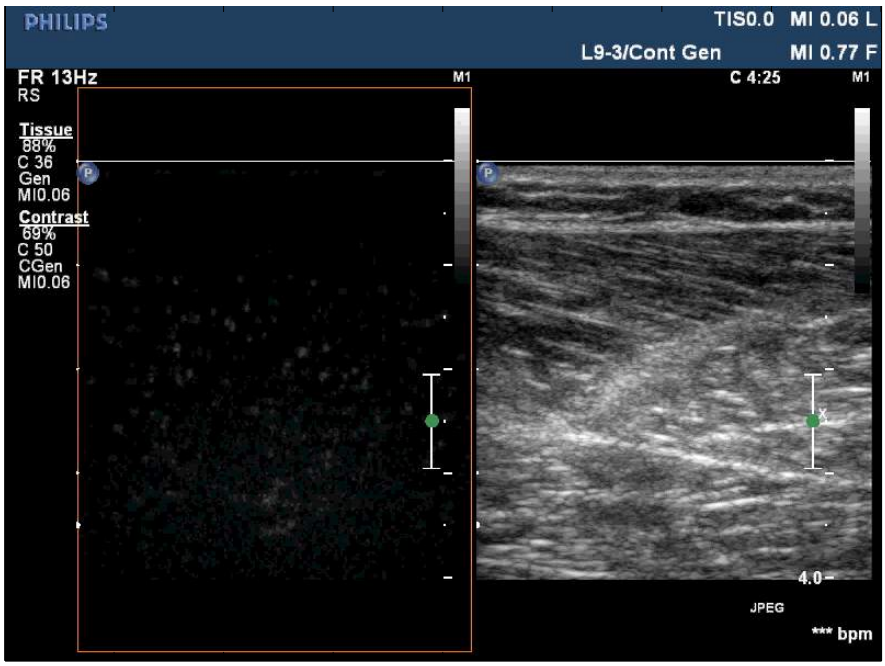

Figure 5.11. An example clinical data frame during CEUS imaging of the lower limb of a healthy volunteer. Microbubble signals can be seen flowing within the microvasculature in the CEUS image in the left, with the simultaneously acquired B-Mode Image is displayed on the right.

5.5.3.2.1 Background Subtraction

Results displaying the average $S\hat{A}D$ values between average median filtered background images and 50 background frames for varying symmetric median filter size for repeated scans on the same healthy subject are displayed in Figure 5.12. Minimisation of the $S\hat{A}D$ occurred at a median filter size of 27×27, thus this was used to create the background image to subtract from the subsequent *in vivo* data. The intensity noise threshold applied to the frames was equal to the 99th percentile of $S\hat{A}D$ at this minimum, here equal to a value of 0.99 x10^{5}. Bubble localisations were then found using the method described in *in vitro* methodology to process potential regions. Examples of background subtraction for two different subject scans are shown in Figure 5.13.

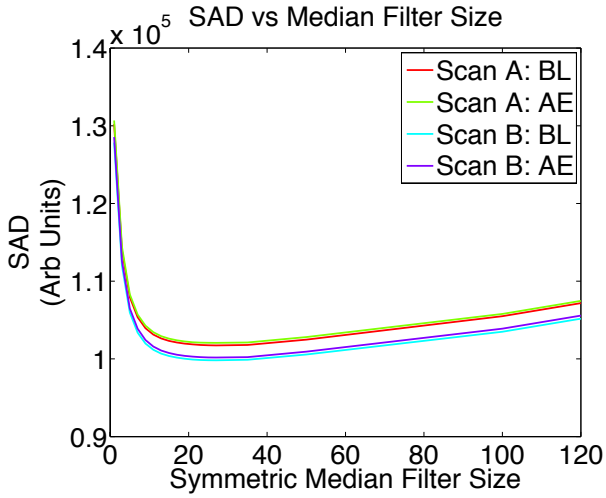

Figure 5.12. Average $S\hat{A}D$ values between average median filtered background images and 50 background frames for varying symmetric median filter size for a healthy subject. The graph shows results for two repeat scans on the same subject, with each scan involving both baseline (BL) scans before exercise, and after-exercise (AE).

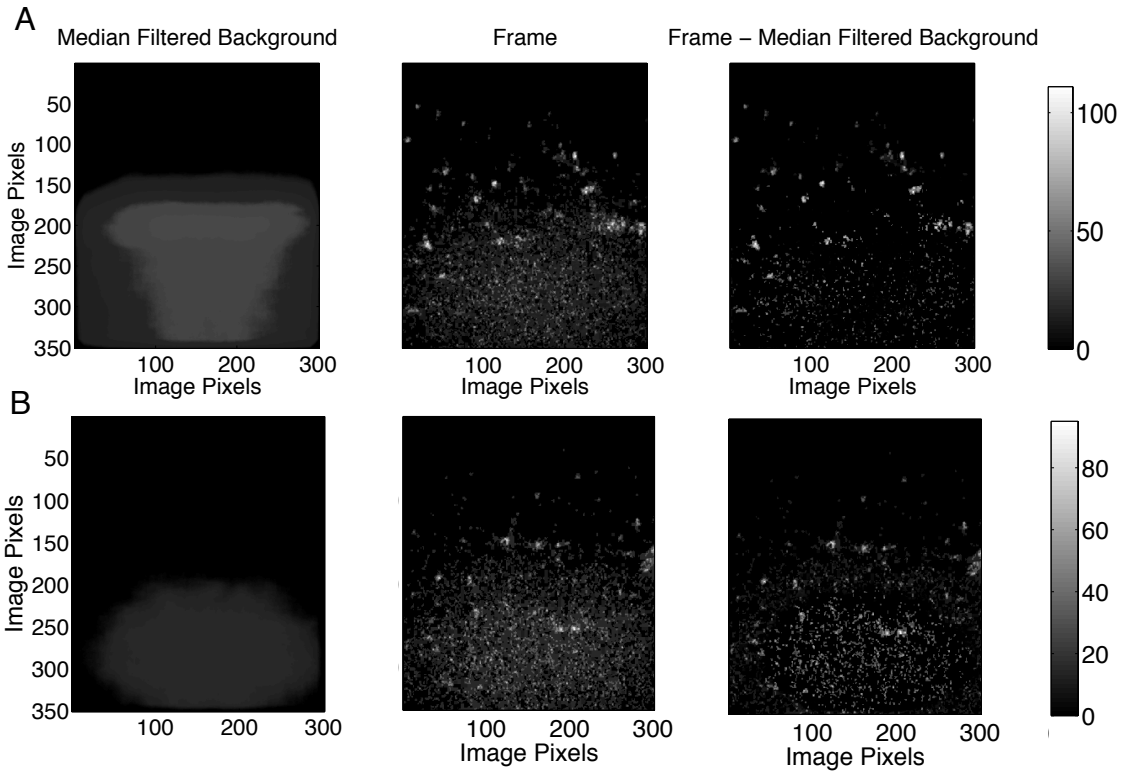

Figure 5.13. Example images showing the log-compressed median filtered background image used to subtract from image frames, alongside an example frame, and the resulting frame after subtraction of the background frame. Grey scale bar displays intensity in arbitrary units. (A) and (B) show examples for two different subject scans.

5.5.3.3 QUANTITATIVE ANALYSIS

Five equal sized regions of interest (ROIs) were defined across the resulting images, as shown in reference to the corresponding B-Mode image frame in Figure 5.14. These allowed variance in quantitative measurements throughout the field of view in the muscle region to be assessed.

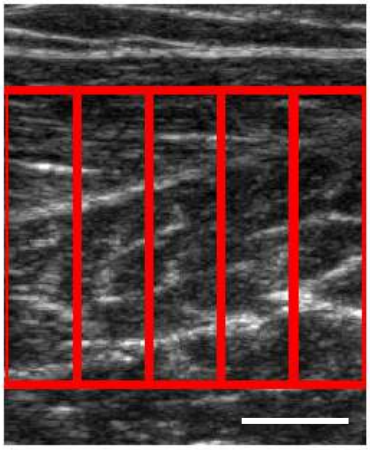

Figure 5.14. Example B-Mode image frame of clinical US data, where 5 uniform ROIs have been defined across the lower limb muscle in red. Destruction replenishment TIC curves were calculated across the entire ROI (outer edges). Scale bar 1 cm.

Lower limb vein diameters range from approximately 6 to 10 mm in diameter [271], with the superficial femoral artery approximately 8 - 9 mm in diameter [265]. This is the main artery of the lower limb and is therefore critical in the supply of oxygenated blood to the leg. To assess PAD, quantification of the microvascular flow after occlusion or vessel narrowing is important. Therefore, vessels deemed to be macro-vessels were removed from the final analysis to discard the contribution of flow from larger arteries. Diameters between 6 - 10 mm correspond to approximately 58 – 96 pixels of the US image. If we assume this will affect results if over 5 mm of vessel length is visible within the image, this would correspond to an area of more than 2800 – 4608 pixels. If the cross-section of such a vessel is imaged it will cover between 2642 - 7238 pixels. Thus, areas in the final image which had connected components corresponding to areas larger than 2642 pixels were removed from final data analysis. This assumes that image acquisition is sufficient to generate spatially distinct macro-vessel structures within the image, and that microvessels are sufficiently disconnected from macro-vessel structures. It is also assumed that microvessels will cover an area

significantly smaller than this, and that the number of localisations covering the capillary area is not sufficient to cover a large area since the acquisition time and concentration would prevent sufficient localisations at this level. From visual assessment, the flow of microbubbles within the larger vessels is significantly higher than those in the microvasculature, which is expected to enable differentiation of these vessel structures from one another. Quantitative measures described in Section 5.4.2.6 were calculated within ROIs and compared before and after exercise. A two tailed paired sample t-test was performed to assess the significance of changes observed between pre- and post-exercise scans, where the significance level was taken as 0.05. Repeatability was measured using the intra-class correlation coefficient (ICC) [272] given by

$$ICC = \frac{S_A^2}{S_A^2 + S_W^2} \tag{5.5}$$

where S_A^2 is the variance between a subject group, and S_W^2 is the variance within groups.

5.6 CLINICAL RESULTS

Figure 5.15 and Figure 5.16 display the destruction-replenishment TIC curves for each healthy subject (V1-V4) and PAD subject (P1-P4) in the following 50 seconds after bubble destruction respectively. Figure 5.17 shows one such patient TIC curve with a log-normal perfusion fit (see Appendix Section 9.4 for remaining volunteer data fits) used to extract perfusion parameters. Table 5.2 summarises the results for both healthy and PAD subjects. Destruction-replenishment analysis provided a mean peak intensity of 1.5 ± 0.6 AU before exercise, and 2.8 ± 1.2 AU after exercise. The mean relative change in peak intensity over all ROIs in all patients was 105.9 ± 121.5%. Volunteers 2, 3 and 4 display higher mean intensities following exercise compared to before exercise, as shown in Figure 5.18. Volunteer 1, however, shows a decrease in peak intensity following exercise in scan B. The ICC was calculated to be 0.4117 for peak intensity measurements. The increase in the peak intensity is statistically significant (paired *t* test; p = 0.0207). TTP results showed variable results (Figure 5.18B and D), where the mean relative change was found to be -8.4 ± 24.6% and changes were found to be insignificant (p = 0.2979). Significance results are summarised in Table 5.3.

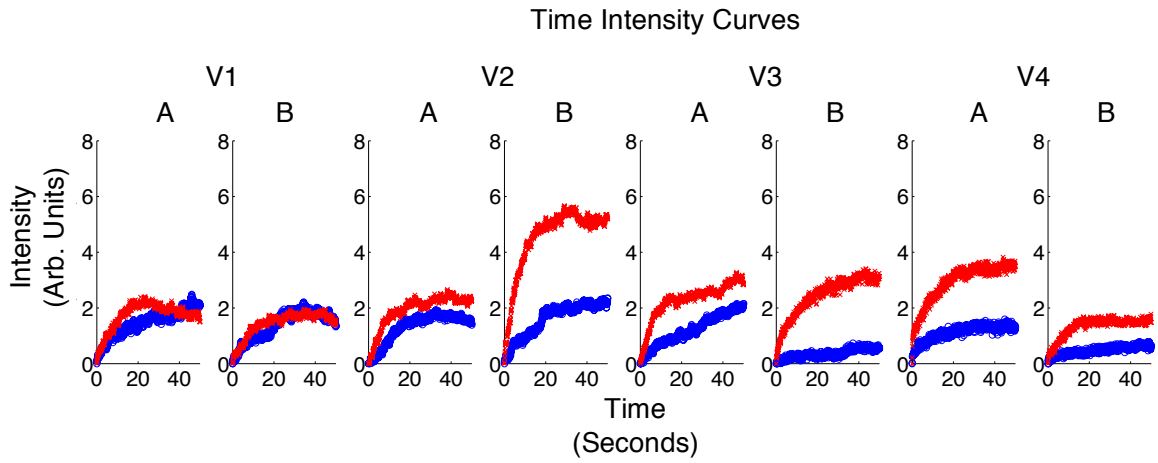

Figure 5.15. Destruction-replenishment TIC curves for each healthy subject in the following 50 seconds after bubble destruction at baseline (blue) and after exercise (red) for repeated scans on consecutive days, A and B.

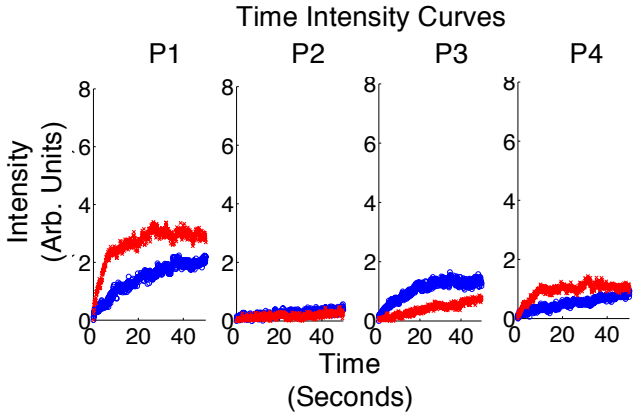

Figure 5.16. Destruction-replenishment TIC curves for each patient with PAD in the following 50 seconds after bubble destruction at baseline (blue) and after exercise (red).

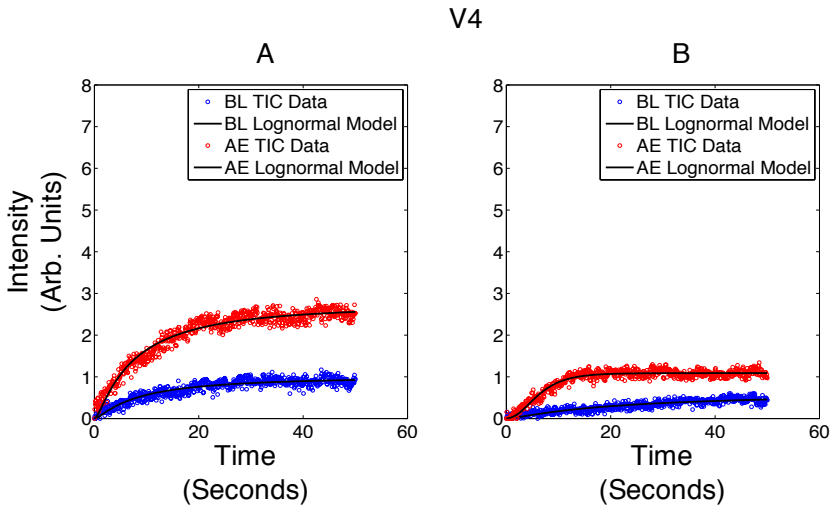

Figure 5.17. Destruction-replenishment TIC curves for example patient 35 in the following 50 seconds after bubble destruction at baseline (blue) and after exercise (red), with log-normal perfusion model fit.

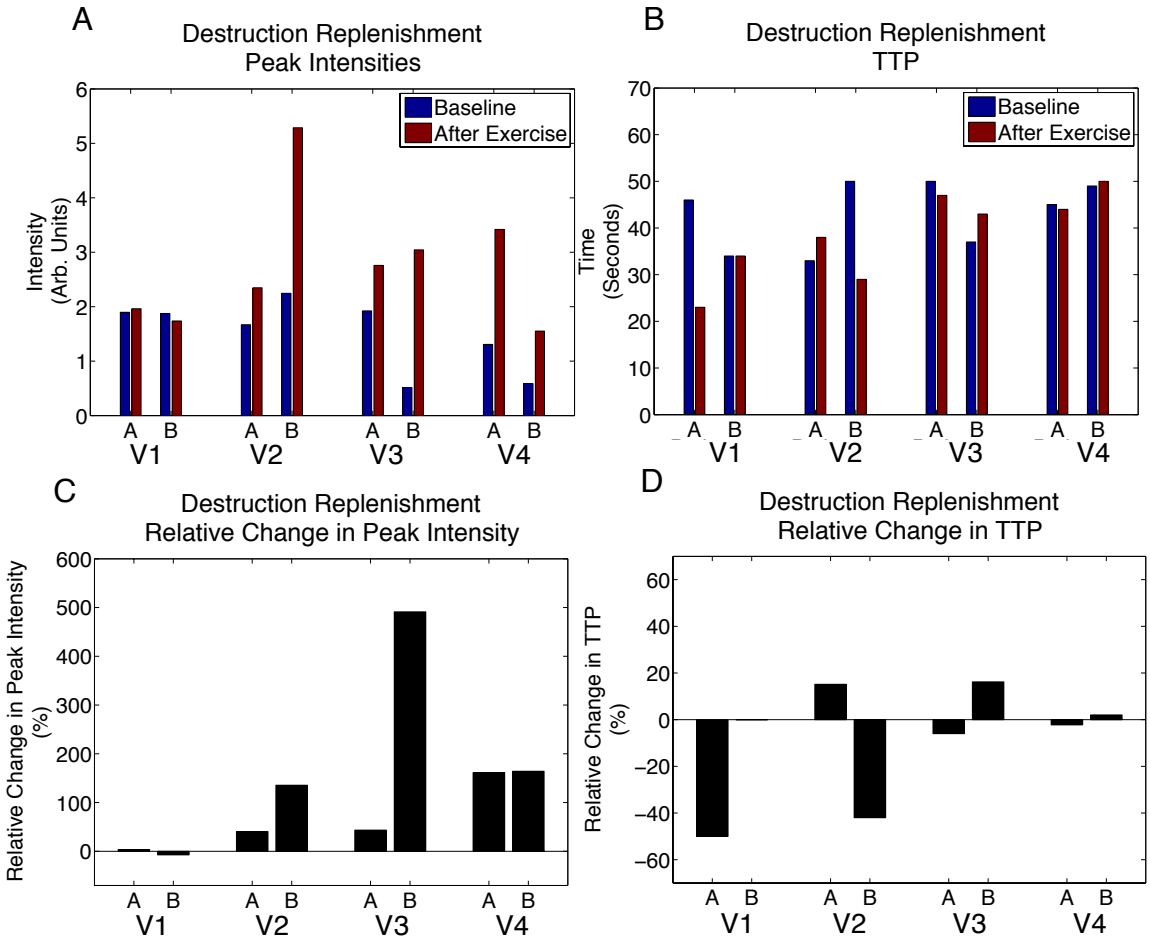

Figure 5.18. (A) Peak intensities estimated before and after exercise using destruction-replenishment TIC curve analysis for healthy volunteers (V1-V4), alongside the relative change shown in (C). (B) Time-to-peak (TTP) values estimated before and after exercise using destruction-replenishment TIC curve analysis for healthy subjects, alongside the relative change shown in (D).

Destruction replenishment mean flow rates are shown in Figure 5.19, given in relative perfusion units (RPU) [273]. This shows a large mean relative increase, however additionally displayed a large standard deviation (351.2 ± 399.9%). This measured the highest ICC value of 0.7284. The increase in the estimated flow rate is statistically significant when directly applying a paired t-test with p = 0.0137. However, the full dataset of the repeatability investigation includes two samples per subject for each scan point. In order to ensure that the correlation between the two samples does not influence the results, the significance values for all repeatability data were recalculated using subsets of the data. Each subset consists of one data point per subject and scan, resulting in $N^R = 16$ subsets, where N is the number of subjects, and R is the number of repeats. The results are summarised in Table 5.3, where for each subject the maximum p-value from all 16 calculations is given. If the hypothesis holds ($p < 0.05$), the approach demonstrates that the results stay significant, independent of any particular scan. Table 5.3 shows that flow rate significance found in the paired t-test may be dependent on particular data results, (p = 0.4192 following stability test), for example, the large change in flow rate found for volunteer 3, scan B. In addition, stability tests showed that p values calculated for destruction-replenishment derived peak intensity changes were no longer significant and were highly dependent upon individual scans within the data.

Equivalent peak intensity results for subjects with PAD using destruction-replenishment TIC curve analysis are shown in Figure 5.20. In these results, 50% of the subjects show an increase in peak intensity, and the remaining present a negative change. The average peak intensities were considerably lower than those for healthy subjects, where peak intensities increased from an average of 1.4 ± 0.7 AU to 1.6 ± 1.3 AU following exercise. The mean relative change of peak intensity with exercise is 5.5 ± 52.5 %, considerably lower than that found for healthy volunteers (105.9 ± 121.5%). A negative average relative change in TTP of -7.7 ± 34.9% was found. Flow rates on average increased by 163.2 ± 293.5%; the large variability in subject results can be observed in Figure 5.21, where a large increase is seen for 50% of the subjects (528% and 272%), and a small decrease can be observed for the remaining subjects (-87% and -61%). A paired t-test revealed the changes following exercise were insignificant for destruction-

replenishment measurements using peak intensity, TTP and flow rate for symptomatic patients (results are summarised in Table 5.3).

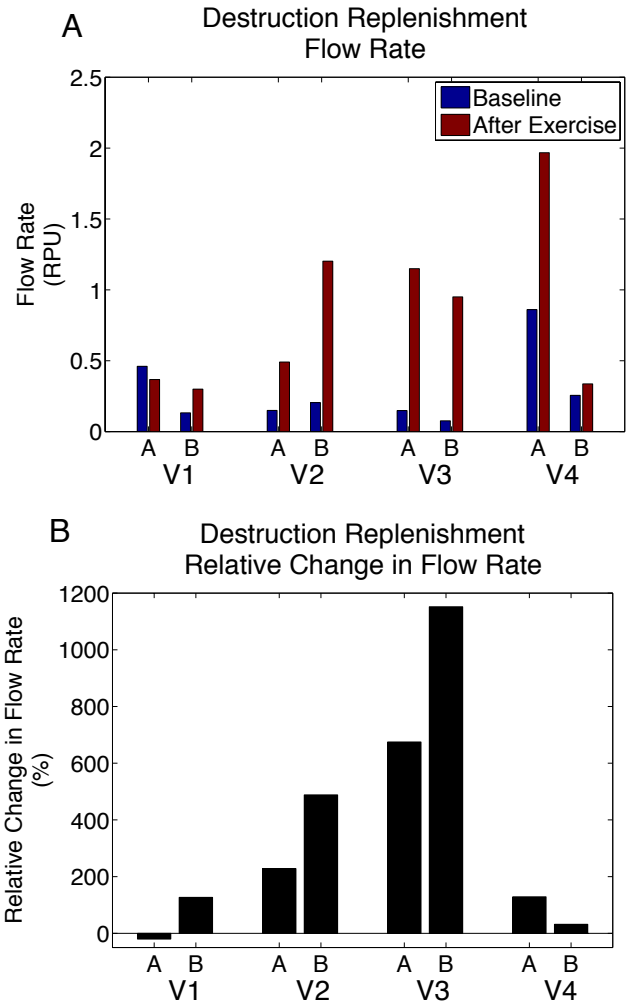

Figure 5.19(A) Flow rate estimated before and after exercise using destruction-replenishment TIC curve analysis for healthy volunteers (V1-V4), alongside the relative change shown in (B).

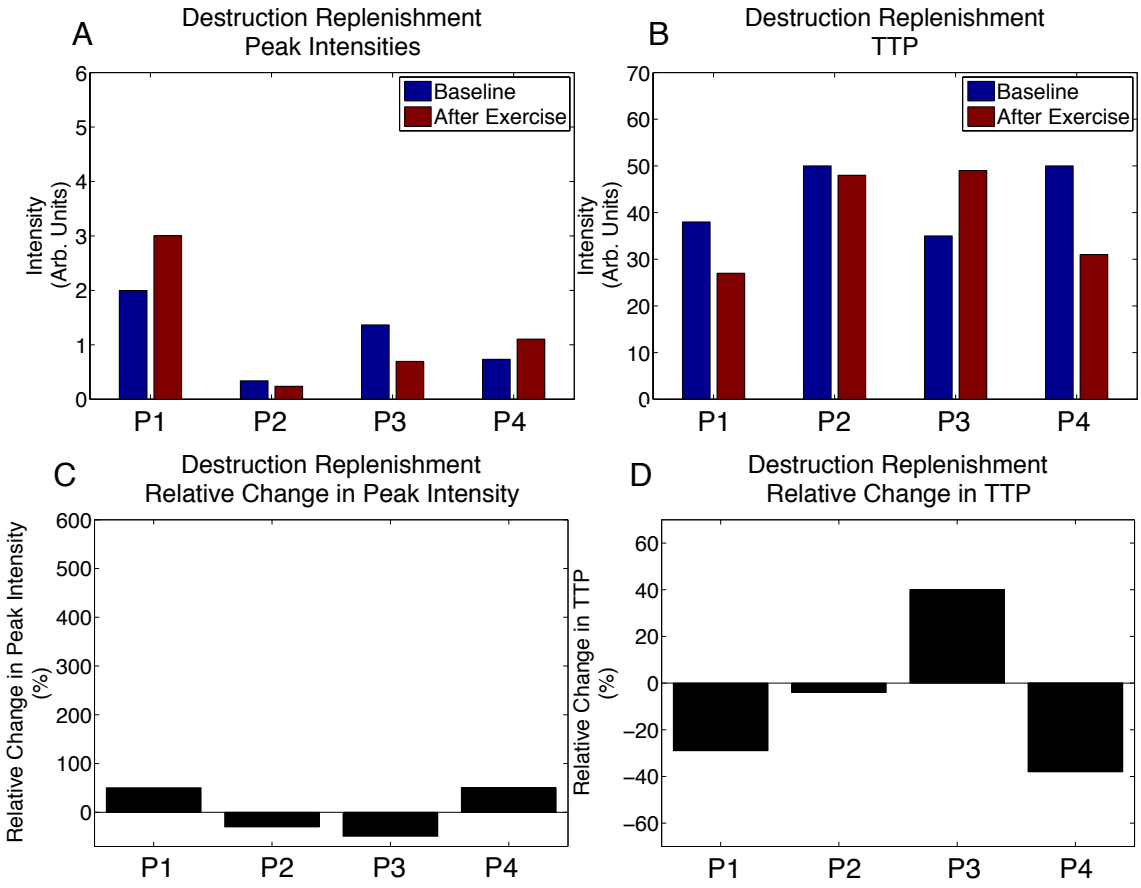

Figure 5.20. (A) Peak intensities estimated before and after exercise using destruction-replenishment TIC curve analysis for subjects with PAD (P1-P4), alongside the relative change shown in (C). (B) Time-to-peak (TTP) estimated before and after exercise using destruction-replenishment TIC curve analysis for subjects with PAD, alongside the relative change shown in (D).

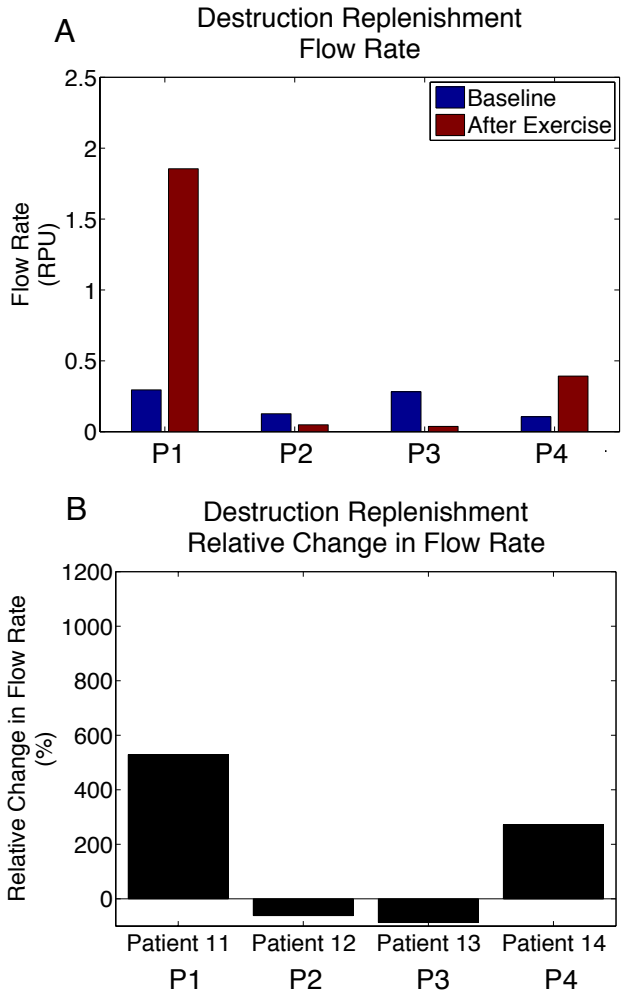

Figure 5.21. (A) Flow rate estimated before and after exercise using destruction-replenishment TIC curve analysis for symptomatic PAD subjects, alongside the relative change shown in (B).

5.6.1 SUPER-RESOLUTION IMAGING

5.6.1.1 BACKGROUND SUBTRACTION

Figure 5.22 shows the effect of pre-processing background subtraction in example localisation images. Figure 5.22A displays the resulting localisation map without median filtered background subtraction, where lower regions can be seen to have a large number of localisations compared to upper regions in the image, presumed to be caused by noise, while localisations appear more uniformly distributed in Figure 5.22B following background subtraction. This can be observed more clearly in enlarged sections in the lower portion of the images shown in Figure 5.22C and D, which exhibit a considerably larger number of background localisations found without using background subtraction (Figure 5.22C). Average profiles over 100 μm taken through the

line indicated in Figure 5.22C and D are shown in Figure 5.22E and F, where two distinct localisation distributions become visible following background subtraction.

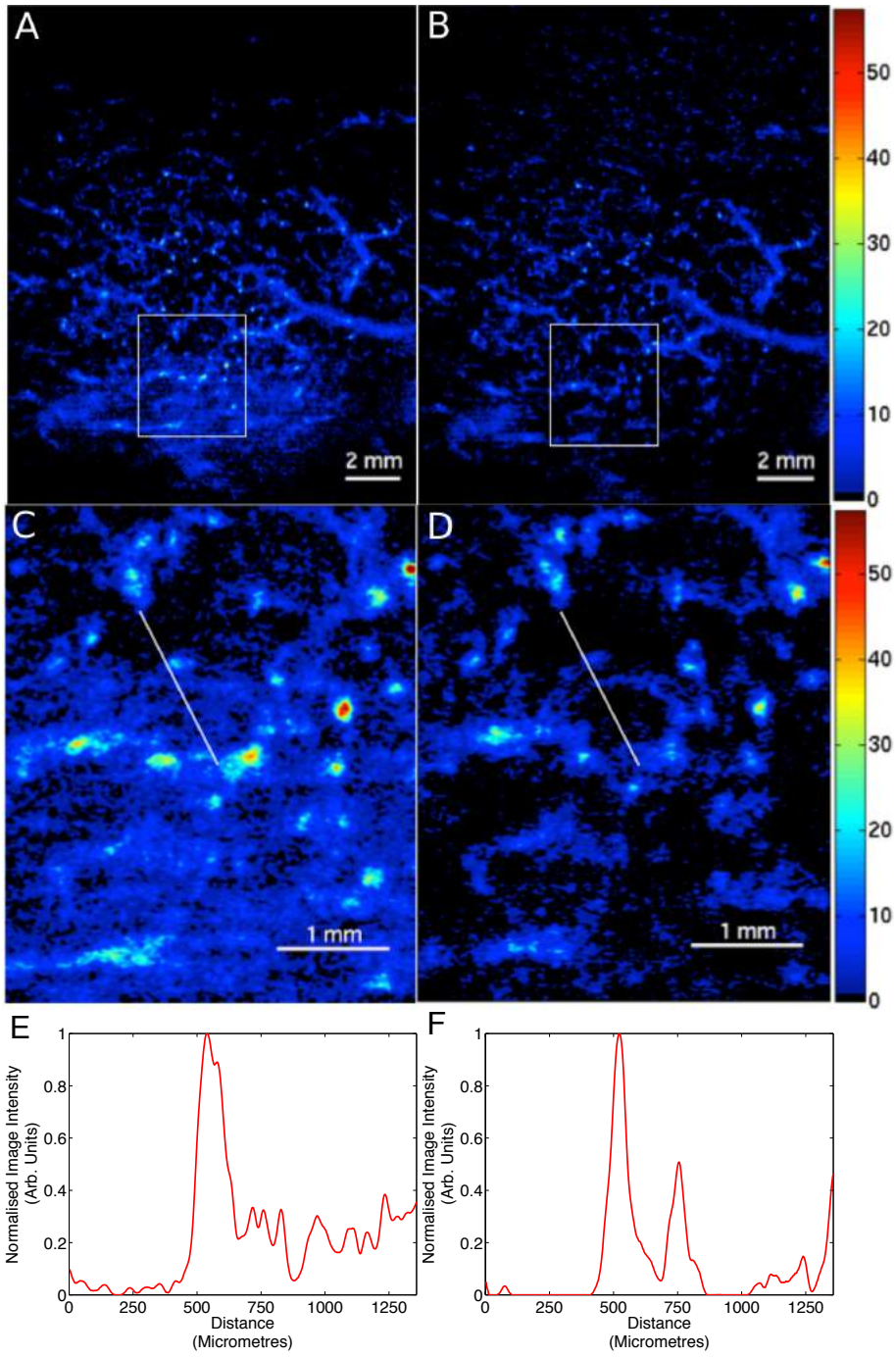

Figure 5.22. The effect of background subtraction in pre-processing steps. (A) Localisation map without median filtered background subtraction, where lower regions can be seen to have a large number of localisations. (B) Localisation map using background subtraction. Enlarged sections of the images indicated with the white box are shown in (C) and (D), where average profiles taken through the line indicated in (C) and (D) over 100 μm are shown in (E) and (F) respectively, where two distinct localisation distributions become visible following background subtraction. Colour scale is proportional to the chance of detecting a bubble at that location.

5.6.1.2 IMAGE RENDERING

Example localisation maps from two healthy volunteers are shown in Figure 5.23, at baseline (Figure 5.23A and C) and after exercise (Figure 5.23B and D) without vessel removal. For demonstration of the improvement in resolution in the final images, Figure 5.24 shows an example vessel structure found within a healthy subject, where a maximum intensity persistence CEUS image created by displaying image pixels at their maximum brightness over the imaging duration [92], [274] is shown alongside a super-resolution image of the same region in grey scale. Visualisation of a sub-millimetre sized structure can be seen in super-resolution images compared to the diffraction limited persistence image, presumed to be of a section of microvasculature.

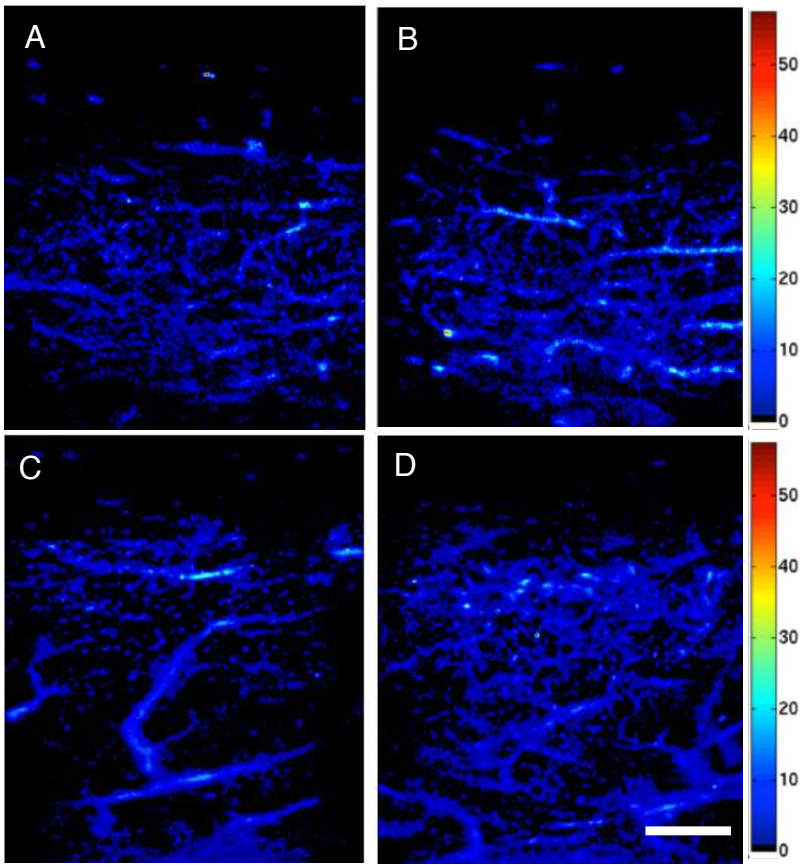

Figure 5.23. Example super-resolution images for two healthy patients before (A) and (C). and after (B) and (D) exercise. Scale bar 4 mm.

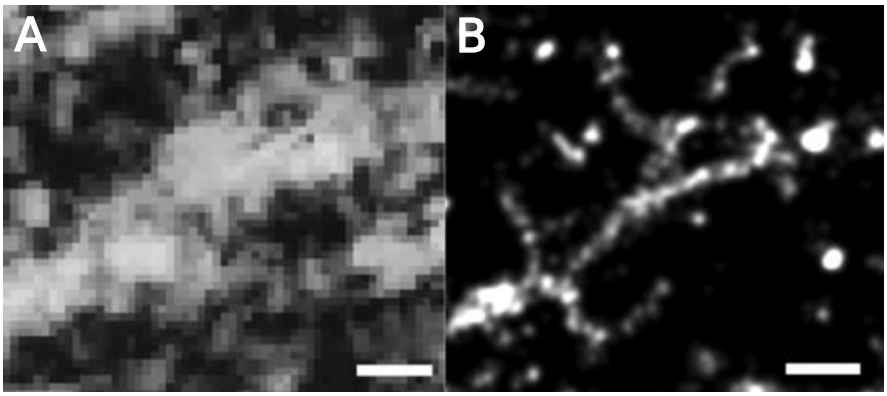

Figure 5.24. Comparative images of vessel structures in the lower limb of healthy human volunteer: (A) Persistence image, (B) super-resolution image. Colour scale is shown in grey for comparison. Scale bar 1 mm.

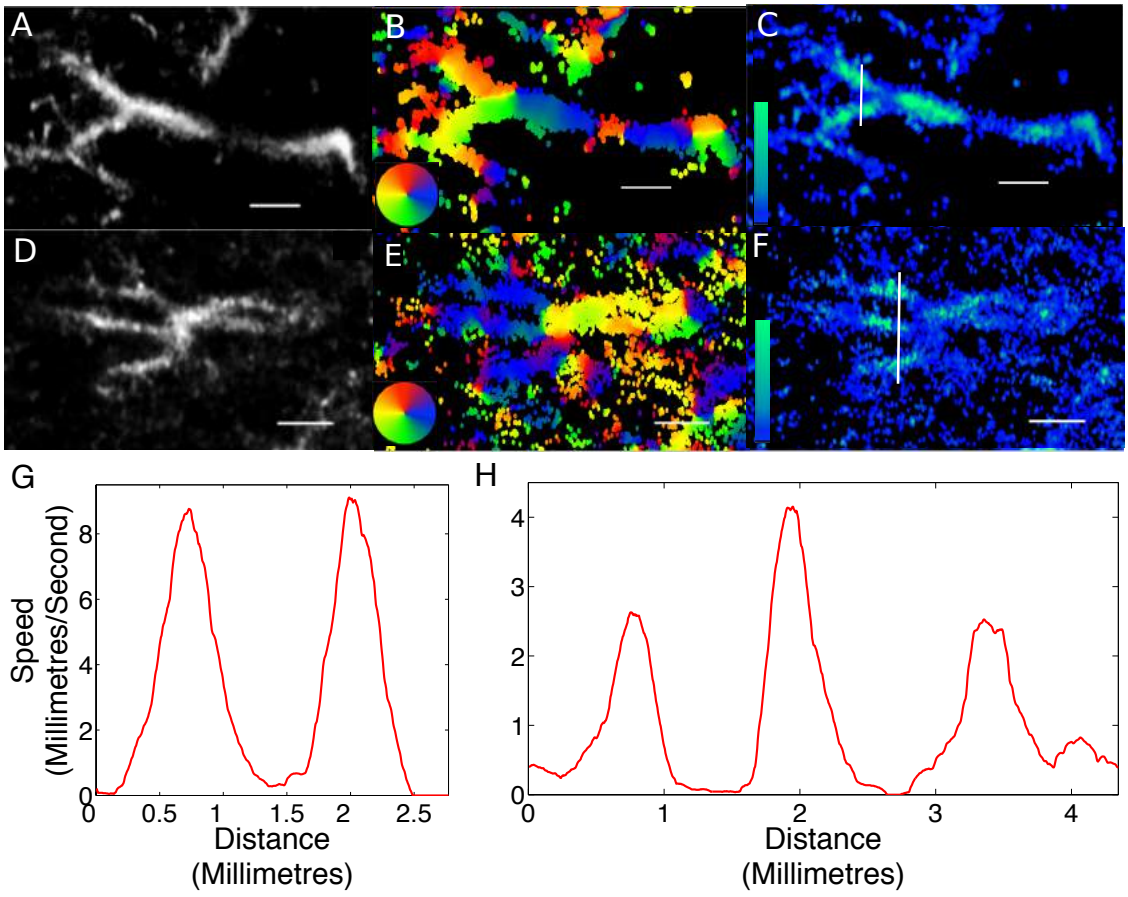

Figure 5.25. Velocity tracking results for volunteer 3. (A) and (D) display localisation maps of vessel structures shown in grey scale, (B) and (E) display directional components of velocity, and (C) and (F) show the speed of blood flow. Average speed profiles taken across 200 μm sections (illustrated by the white lines in (C) and (F)) are displayed in (G) and (H), where the maximum on the scalebar is 2.5 mm/s. Scale bars, 2 mm.

Figure 5.25 displays velocity tracking image results for a healthy subject (V3). Figure 5.25A and D display localisation maps of vessel structures shown in grey scale, Figure 5.25B and E display directional components of velocity, and Figure 5.25C and F show the speed of tracked blood flow. Average speed profiles taken across 200 μm sections (illustrated by the white lines in Figure 5.25C and F) are displayed in Figure 5.25G and H. Two vessel profiles can be seen within a 2.5 mm length in Figure 5.25G, and three within approximately 4 mm in Figure 5.25H.

5.6.1.3 RESULTS FOR HEALTHY SUBJECTS (REPEATABILITY RESULTS)

Figure 5.26 displays measurements of single bubble localisations for each healthy subject, where error bars display the variation over 5 ROIs. The mean and standard deviations of the calculated number of localisations per square millimetre before and after exercise were 49.0 ± 9.0 and 93.4 ± 18.9 respectively. The relative change of each measure pre- and post- exercise is displayed as a percentage value in Figure 5.26B. An increase of at least 80.8% is seen for every subject, where there is an average relative increase of 107.5 ± 24.7% across all subjects and repeats. The ICC calculated for the number of localisations is 0.6469 for the repeatability study. Table 5.2 summarises the results across all patients and parameter measures.

Figure 5.27 and Figure 5.28 display corresponding results for TMD and speed, where two measures of TMD are presented (LT >= 0.5 and LT > 1). The estimated TMD (LT > 1) had an average of 28.0 ± 9.0% before exercise, and 52.5 ± 12.0% after exercise, with a mean relative change of 105.8%. A smaller change was evident using TMD of LT >= 0.5, where the mean and standard deviations were 52.4 ± 13.0% (before exercise) and 76.4 ± 11.0% (after-exercise), with a corresponding average relative increase of 56.5 ± 22.6%. ICC results for TMD show lower repeatability values compared to localisation number, of 0.3379 (LT > 1) and 0.3141 (LT >= 0.5). Relative changes in speed (Figure 5.28) showed increases in tracked speed following exercise with the exception of a single subject (V1) exhibiting a small decrease in tracked speed. A relative change of only 7.7 ± 7.0% was observed on average. Results showed a higher ICC value (0.4257) compared to those using TMD.

The relative change in the estimated TMD is statistically significant when directly applying a paired t-test where $p \ll 0.05$. Furthermore, Table 5.3 shows that p-values are below 0.05 for localisation number and TMD parameters after stability tests, indicating that the results stay significant, independent of any particular scan. This suggests that the approach is stable when varying the scans used.

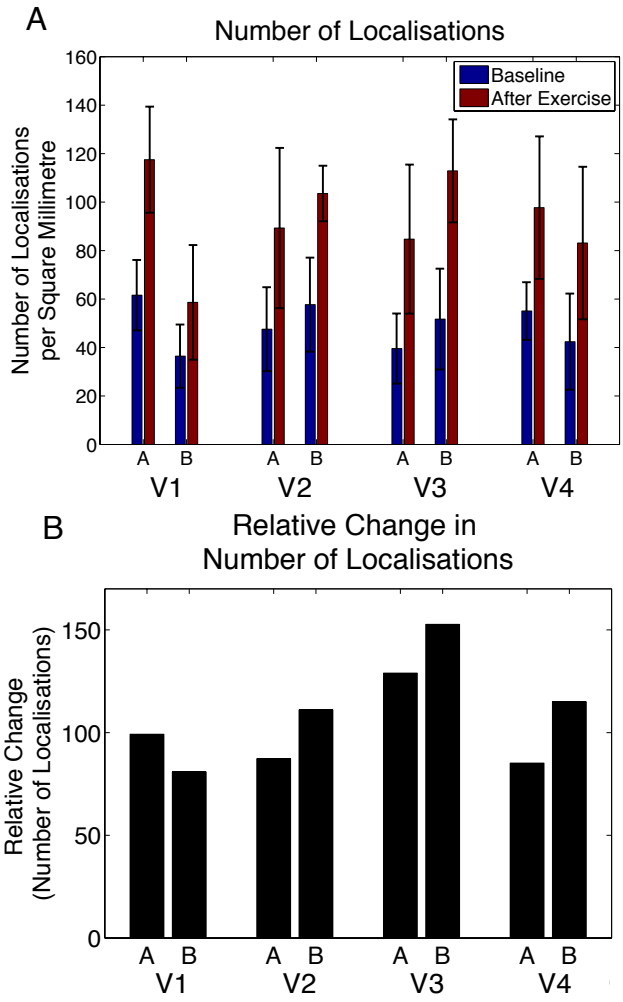

Figure 5.26. Estimated number of bubble localisations found for repeatability data for four healthy volunteers (V1-V4), each scanned on two consecutive days, corresponding to scan A and B displayed in (A). Error bars represent the standard deviation over 5 ROIs. Average relative change following exercise is displayed in (B).

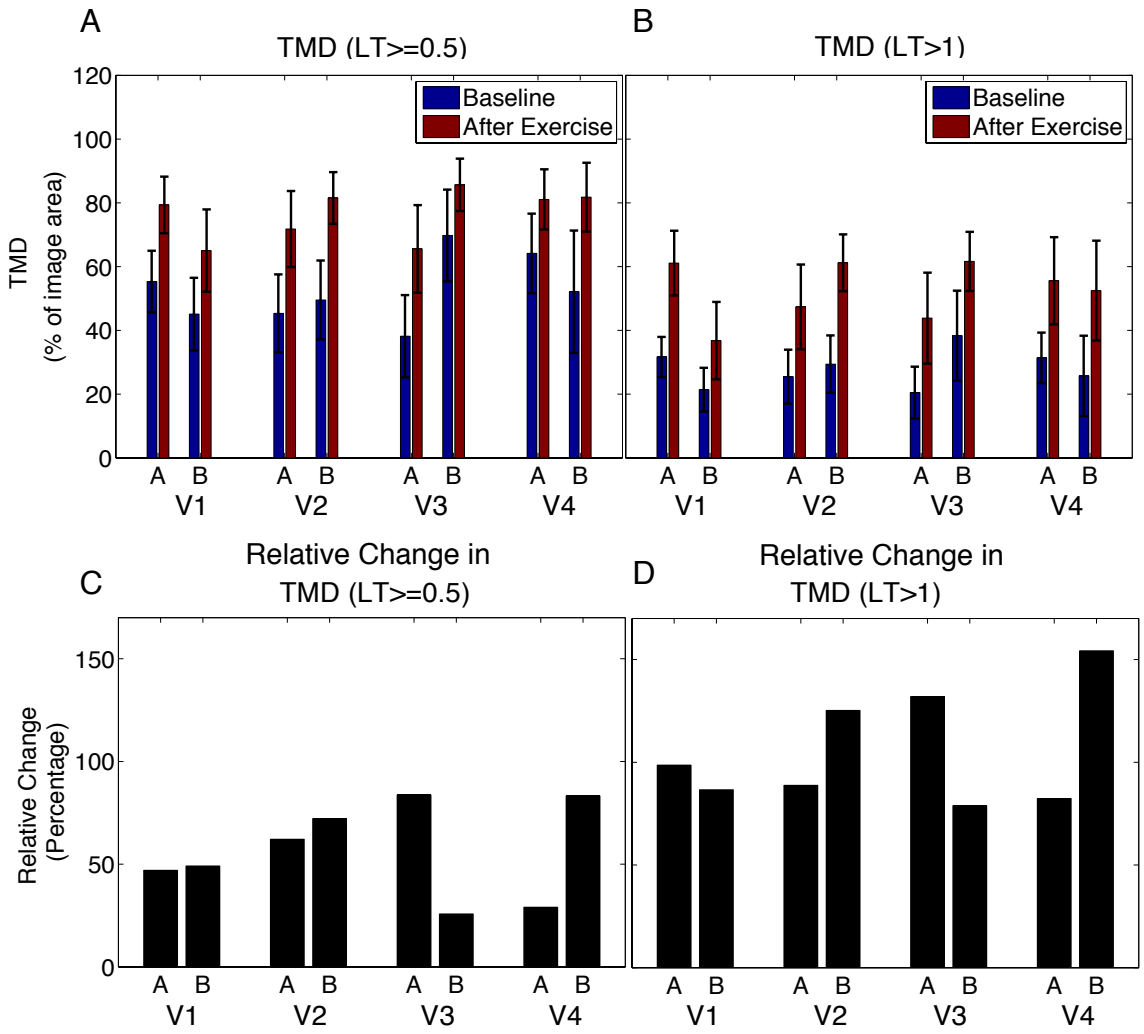

Figure 5.27. Estimated measures of TMD (A) LT >= 0.5 and (B) LT > 1, for repeatability data for four healthy volunteers (V1-V4), with average relative changes shown in (C) and (D). Error bars represent the standard deviation over 5 ROIs.

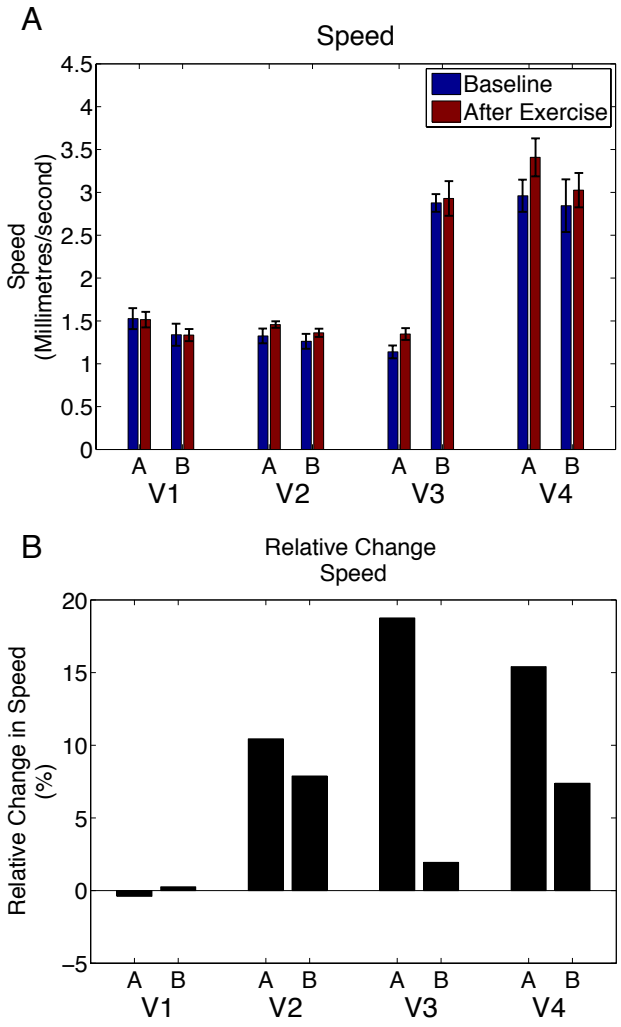

Figure 5.28. Estimated measures of speed for repeatability data for four healthy volunteers (V1-V4) shown in (A), with average relative changes shown in (B). Error bars represent the standard deviation over 5 ROIs.

5.6.1.4 RESULTS FOR SUBJECTS WITH SYMPTOMATIC PAD

Corresponding measurements performed on four subjects diagnosed with symptomatic PAD (P1-P4) are shown in Figure 5.29, Figure 5.30, and Figure 5.31. The mean relative change in the measured number of localisations was 12.7 ± 38.9%, considerably lower than that found for healthy subjects (107.5 ± 24.7%). For TMD measures the mean relative changes were 10.9 ± 27.1% (LT >= 0.5) and 33.1 ± 53.8% (LT > 1). A negative change was observed for P3 for measures of localisation number, and both TMD measures. Relative speed increased for all PAD subjects, where on average the relative speed change was 8.8 ± 3.3%. Relative changes were found to be insignificant ($p > 0.05$) for all measures on PAD patient data (Table 5.3). Overall, relative changes of localisation number and TMD measures showed significance for healthy subjects, while relative changes were insignificant for patients diagnosed with PAD.

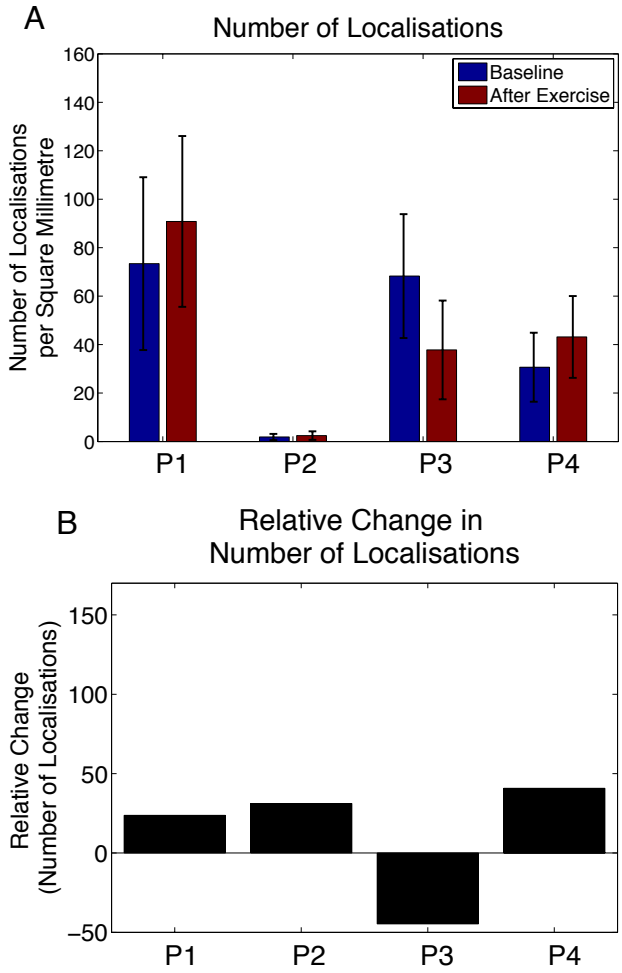

Figure 5.29. (A) Estimated number of bubble localisations found for patients with diagnosed PAD (P1-P4), with corresponding average relative change (B). Error bars represent the standard deviation over 5 ROIs.

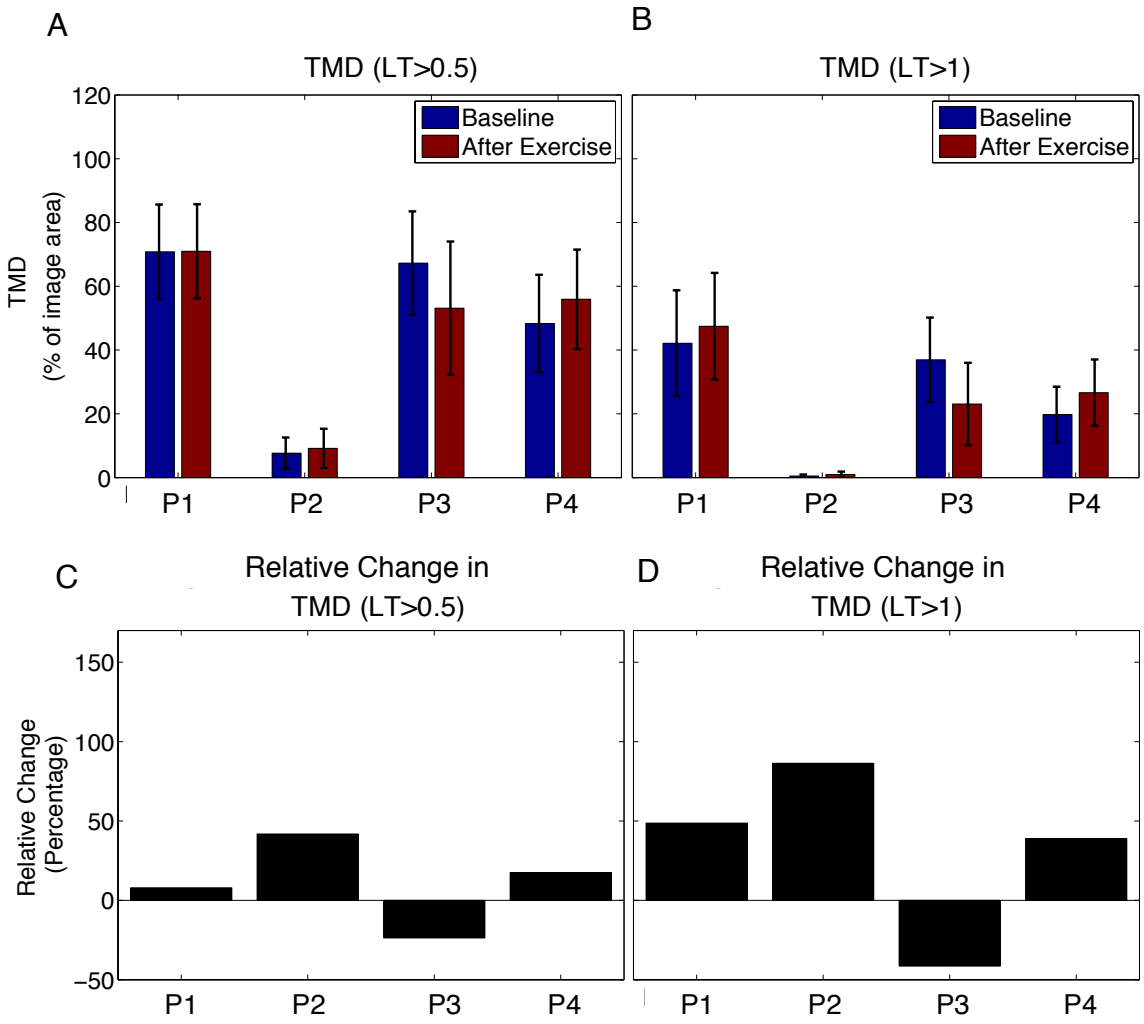

Figure 5.30. Estimated measures of perfused microvascular density (LT>=0.5) and (LT>1), for patients with diagnosed PAD (P1-P4), with average relative changes shown in (C) and (D). Error bars represent the standard deviation over 5 ROIs.

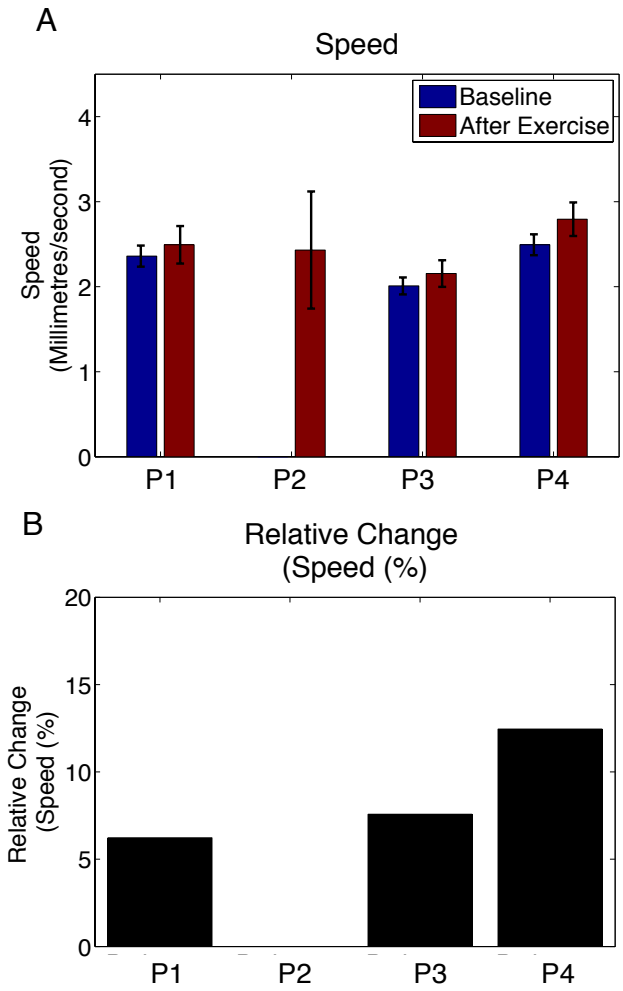

Figure 5.31. Estimated measures of speed for patients with diagnosed PAD (P1-P4) shown in (A), with average relative changes shown in (B). Error bars represent the standard deviation over 5 ROIs. Note: no bubbles were tracked successfully for P2 prior to exercise, and thus P2 is excluded from corresponding results.

Subject Group	Measure	BL	AE	Relative Change (%)	ICC
Healthy (Repeat.)	DR (Peak)	1.5 ± 0.6	2.8 ± 1.2	105.9±121.5	0.4117
	DR (TTP)	43.0 ± 7.2	38.5 ± 9.3	-8.4 ± 24.6	0.3692
	DR (Flow Rate)	0.3 ± 0.3	0.8 ± 0.6	351.2 ± 399.9	0.7284
	Localisations	49.0 ± 9.0	93.4 ± 18.9	107.5 ± 24.7	0.6469
	TMD(LT>=0.5)	28.0 ± 9.0	52.5 ± 12.0	105.8 ± 27.8	0.3141
	TMD (LT>1)	52.4 ± 13.0	76.4 ± 11.0	56.5 ± 22.6	0.3379
	Speed	1.9 ± 0.8	2.0 ± 0.9	7.7 ± 7.0	0.4257
PAD	DR (Peak)	1.4 ± 0.7	1.6 ± 1.3	5.5 ± 52.5	
	DR (TTP)	43.3 ± 7.9	38.8 ± 11.4	-7.7 ± 34.9	N/A
	DR (Flow Rate)	0.2 ± 0.1	0.6 ± 0.9	163.2 ± 293.5	
	Localisations	43.6 ± 33.7	43.6 ± 36.3	12.7 ± 38.9	
	TMD(LT>=0.5)	48.5 ± 28.9	47.3 ± 26.6	10.9 ± 27.1	N/A
	TMD (LT > 1)	24.8 ± 18.8	24.5 ± 19.0	33.1 ± 53.8	
	Speed*	2.3 ± 0.3	2.5 ± 0.3	8.8 ± 3.3	

Table 5.2. Results for healthy (repeatability study) subjects and patients with symptomatic PAD using destruction replenishment (DR) measures, and super-resolution quantitative measures. *Average speed calculations were performed omitting subject P2.

Subject Group	Measure	Normal Test		Stability Test	
		Sig.	p	Sig.	p
Healthy (Repeat.)	DR (Peak)	1	0.0207	0	0.2548
	DR (TTP)	0	0.2979	0	0.9625
	DR (Flow Rate)	1	0.0137	0	0.2604
	Localisations	1	0.000012	1	0.0138
	TMD (LT >= 0.5)	1	0.000009	1	0.0106
	TMD (LT > 1)	1	0.000002	1	0.0059
	Speed	0	0.0722	0	0.4263
PAD	DR (Peak)	0	0.8376	N/A	N/A
	DR (TTP)	0	0.5399		
	DR (Flow Rate)	0	0.4192		
	Localisations	0	0.9999	N/A	N/A
	TMD (LT >= 0.5)	0	0.8090		
	TMD (LT > 1)	0	0.9541		
	Speed*	0	0.0697		

Table 5.3. Results from paired t-tests performed on destruction replenishment (DR) measures, and super-resolution quantitative measures before and after exercise. For stability test, t-tests were performed on 16 subsets of the repeatability data, indicating that the results stay significant, independent of any particular scan. *Speed calculations were performed omitting subject P2. 'Sig' – Significance.

5.7 DISCUSSION

Acoustic super-resolution has shown potential in providing a means of visualising enhanced detail of perfusion in lower-limb tissue compared to that of MIP. The use of bubble localisation number and TMD measures were able to quantify significant differences between pre- and post exercise scans for healthy volunteers, and a considerably reduced, insignificant relative change for patients with symptomatic PAD. Mean relative changes for healthy volunteers were 107.5% compared to 12.7% for subjects with symptomatic PAD. Results demonstrated relative changes in localisation number and TMD parameters for repeatability investigation using super-resolution were significant and suggested that this significance was not highly dependent on any individual scan result. Stability tests showed that p values calculated for destruction-replenishment derived peak intensity and flow rate changes were no longer significant when recalculated using subsets of the data, indicating that this significance was dependent upon individual scans within the data. Furthermore, these destruction-replenishment results were found to have considerably higher standard deviations of calculated relative change across patients, where the mean ± standard deviation was 105.9 ± 121.5% and 351.2 ± 399.9% respectively, compared to standard deviations of under 28% for all super-resolution measures. Localisation number was calculated to provide slightly lower repeatability (ICC = 0.6469) to that of flow rate derived from the lognormal perfusion model of the same patient scans (ICC = 0.7284), and improved repeatability when compared to destruction-replenishment techniques of peak intensity and TTP (0.4117 and 0.3692 respectively).

5.7.1.1 EXPERIMENTAL OBSERVATIONS

Bubble signals were observed to be considerably brighter with a larger spatial extent in the *in vitro* concentration experiment than *in vivo* (comparison of Figure 5.2 and Figure 5.11). This may be due to damping in small vessels [183]–[185]. Furthermore, attenuation of the insonating US wave through overlaying layered skin, fat and muscle tissue *in vivo* may reduce the final amplitude of the wave. Furthermore, the echo structure from the microbubbles appeared to consist of a ‘ripple’ or low intensity streak close to the centre (see Figure 5.2). This may have been caused by JPEG compression, or alternatively due to ringing. These may cause inaccuracies in localisation positions.

The use of RF or IQ data prior to scan conversion and image compression could eliminate this issue in the future.

5.7.1.2 POTENTIAL FOR VARIABILITY

Variation in the combined factors contributing to α betweeen scans will provide inaccuracies in the estimated relative change of detected localistion number. If the microbubble concentration exceeds condition (3) in Section 5.4.2.6, the loss of spatially isolated microbubble signals breaks down the assumptions of this technique. Additionally, if the dissolution of bubbles varies over the time-frame of acquisition, this will cause inaccuracies in the estimation of perfused volume, but should not affect the relative measure between patient scans of the same imaging duration. If the subset of resonant microbubbles varies between pre- and post exercise scans, for example due to a different microbubble size distribution, the measure of microbubble localisation number and microvascular area may be affected. Effort was made to ensure bubbles were kept in the same condition by opening a new vial immediately before imaging and shaking for an equal time period. This technique will be susceptible to changes in scanner parameters such as gain and dynamic range between pre-and post-exercise scans. A scan protocol should therefore be pre-set.

ICC results indicated that localisation number provided the most repeatable results for healthy subject scans using super-resolution. ICC values still may be improved through better methods of repeat scanning. In this study, legs were marked for reference, however image results show differences in vascular structures between scans owing to the slight differences in the imaging field of view and the heterogeneity of the vascularity that exists in the tissue being examined. The results should not be significantly influenced by this if PAD affects the vasculature uniformly, however, disease can be more pronounced in specific regions. Scanning a number of different planes in the elevational direction for each scan would provide a more comprehensive view of the vasculature.

Destruction-replenishment peak intensity and TTP measures showed lower ICC values which may have been caused by affects of macro-vessels within the data. For example, the presence of a large vessel in a low perfused pre-exercise scan, may create peak

intensities which surpass those of highly perfused microvessels in a post-exercise scan. The presence of large vessels within a region of interest could also contribute to a reduced TTP since large vessels and fast flow velocities dominate the early stages of the replenishment TIC, while small vessels and slow flow velocities contribute more at the latter stages [275], [276].

The destruction-replenishment model does not incorporate a decay factor, and instead plateaus after reaching peak intensity. The infusion is assumed to be constant. As can be seen in the TIC curves in Figure 5.15, some subjects exhibit a decaying peak intensity following the highest intensity value, while others follow a gradually increasing intensity.

Localisation number can be affected by noise detections; background subtraction aimed to limit the spatially variant background noise in data. The parameter TMD (LT > 1) is less affected by noise since single localisations distributed in the images will be excluded, however this measure is thus more susceptible to the loss of capillary data. TMD (LT >= 0.5) is more influenced by noise since every localisation is counted, but the parameter may be more indicative of capillary vessel presence where flow volume is low and velocity is slow. Acquisition time and concentration will influence the performance of these parameters, and will require that the image does not saturate with localisations.

In vitro validation experiments show that under concentration and acquisition time constraints, where the concentration is not spatially saturating the image, the measure of TMD (LT >= 0.5) is proportional to concentration. However, the TMD (LT > 1) only becomes representative of concentration once there are significant numbers of localisations i.e. if concentration is high enough, or the acquisition time is long enough that the spatial distribution of localisations begin to build up. The longer the acquisition, the more likely an image pixel will have of containing a localisation value > 0, and thus the threshold for defining the presence of a capillary or macrovessel will require consideration of time. This is a limitation of the technique.

In the beaker, the concentration is presumed to be uniformly distributed and is stirred to ensure a well mixed microbubble solution. *In vivo* however, the heterogeneity of the vasculature will mean that the distribution of microbubbles imaged will not be uniform. Since the imaged sample volume of the transducer will cause projection of scattering events within the 3D volume along the elevational direction, the presence of larger arteries and veins within the imaging volume will create a higher likelihood of observing multiple bubbles within the resolution of the system compared to imaging a single capillary vessel within the elevational slice. The occurrence of many overlapping bubble signals in this case will mean signal rejections are more probable, and hence may result in fewer final localisations. At this point, the number of localisations would no longer be representative of the perfused blood volume.

5.7.1.3 VISUALISATION

Accurate mapping of the vascular network for qualitative evaluation may help to provide indication of abnormalities or heterogeneities of the circulation within the leg. Qualitative assessment aims to provide visual assessment and indication as to the orientation of diseased states. The site and severity of any narrowing of the vessel and the location of blockages of the main vessels causing critical restrictions to blood flow would be useful clinical information for clinicians to make more informed decisions for intervention such as angioplasty or graft insertion. Here, the implementation of 3D super-resolution imaging using a clinical 2D matrix array transducer would be valuable in providing more comprehensive mapping of the lower limb vasculature.

5.7.1.4 BACKGROUND/NOISE REMOVAL

Since the technique aims to measure flow in capillaries that are likely to have low localisation number, background removal must be adequate. Large regions of high image intensity occurring in lower regions within the image were assumed to occur as a result of breakthrough of non linear propagation using a contrast specific imaging mode, due to its presence at depth after significant propagation has occurred. When present, this background makes it difficult to identify bubble signals correctly, for example, noise present in lower regions where high background is present may appear similar to bubble signals occurring close to the transducer. Median filtered background subtraction aimed to remove this spatially varying background signal, however does not remove

noise, as can be seen in Figure 5.13. The subsequent size thresholding step then makes it possible to discriminate between noise and bubble echoes. Qualitative evaluation of the median filtered background subtraction technique showed extraction of localisation distributions assumed to be representative of vessel structures, from background, compared to maps resulting from intensity thresholding only, where the second distribution was not visible amongst the background. This provided automated processing with no subject-dependent user-defined parameters. However, without ground truth validation, judgement of its success is limited. Further investigation needs to be performed for assessment of the approach across different scanners and system settings with appropriate validation.

5.7.1.5 LACK OF GOLD STANDARD

A limitation of this study was the lack of a gold standard for evaluating the degree of severity of vascular impairments. Established destruction-replenishment analysis using peak intensities, TTP and flow rates has been implemented for the evaluation of musculoskeletal microcirculation in lower limb [110], [111], [255]–[258],[273]. This provided a technique with which super-resolution quantitative analysis could be compared. However, the study of healthy subjects using destruction replenishment demonstrated large variability in relative changes using all measures. Furthermore, the involvement of subjects with known disease severity would be of interest to test whether this technique is able to provide additional diagnostic value for detecting the severity of symptomatic PAD. ABIs and abnormal blood pulse volumes would have provided reduced resting flow and pressure gradients indicative of patients with more severe PAD, however are not ideal for detecting mild to moderate disease which may present only with abnormal microvascular responses to exercise [111], [252], [253]. This exploratory study could be followed with future studies which incorporate extra non-invasive measures for indicating disease severity such as the time to claudication (reported by subjects during the treadmill test), and obtaining angiographic severity scores from assessment by an experienced vascular surgeon [111].

5.7.1.6 PIXELATION

With such a large imaging field of view, pixelation becomes a limiting factor in the achievable localisation precision. Uncertainty in localisation position is introduced by

pixelation noise - the increase in error due to the finite size of the pixels in the image [212]. Pixelation noise arises from the spatial uncertainty of the arrival of the US signal in the pixel, and is a result of the system's on-board envelope detection and subsequent image generation procedure. The pixel scale of image data for *in vivo* mouse data acquired in Chapter 4 was 30×30 μm, compared to 104×104 μm in this work. A large 12 cm^2 field of view was imaged to enable the assessment of a large area of lower limb microvasculature. The coarse spatial sampling of the data results in a localisation precision within the same order of magnitude as the original system resolution since any noise or changes in intensity can cause a considerable change in the centre of mass calculation. This does not present a problem for quantitative measures developed in this chapter since these are less reliant upon the overall resolution of the super-resolution imaging technique, but limits the improvement in resolution seen within the resulting images. The evaluation of clinical conditions such as angiogenesis may require a higher reliance upon the localisation precision in order to characterise and quantify accurate clinical measures such as tumour vascular density and tortuosity. In such cases, a more well defined ROI around the object of interest will allow greater spatial sampling of the signals and hence the potential of achieving precision comparable to that seen *in vivo* in Chapter 4. Furthermore, the use of unprocessed RF data will eliminate the affect of pixelation.

This large field of view and low spatial sampling means that each bubble signal covers only a few pixels in the image (note: FWHM of point scatterer is 349 μm axially, while pixel size is 104 μm). This causes two main issues in regards to velocity tracking; the first is that intensity based cross correlations between bubble signals may not be accurate in identifying similarities or differences between bubbles due to their small spatial scale. Secondly, the sensitivity of the velocity measurement is dependent upon the precision of the localisations found in each frame, as discussed in Section 5.4.4, and thus may not be sensitive enough to detect changes in the microvasculature with this spatial sampling. Furthermore, in the event of incomplete large vessel removal in some patients, significantly higher velocities will be detected and included in the overall calculations. These may explain the poor performance of the speed estimations within the quantitative analysis.

5.7.1.7 POTENTIAL ADJUSTMENTS TO TECHNIQUE

Because of the intrinsic trade-off between time and spatial information in the final images, super-resolution imaging is in general slower than conventional US imaging techniques. Nevertheless, limiting the acquisition time may still provide enough information to extract quantitative measures (such as number of localisations), even though the spatial distribution of information in final image may not be sufficient for adequate qualitative analysis. The technique therefore becomes less concerned with high resolution, but remains dependent upon accurate identification of single, spatially isolated microbubble signals. Quantitative measures may then be able to be performed over a short time period following infusion, or a destruction pulse, which will ensure an initial low concentration of incoming microbubbles, and will also allow evaluation of quantitative measures as a function of time following bubble inflow/destruction (e.g. number of localisations vs. time) and may be less susceptible to confounding factors affecting purely intensity-based techniques such as signal attenuation, and nonlinear imaging artefacts [277], [278]. This would provide dynamic information regarding the inflow/reperfusion of bubbles into the tissue, however, the removal of effects caused by large vessels may prove more challenging. This is because the time-period used for analysis following destruction (usually a period long enough to return to steady state concentration within the vasculature) may not be enough to adequately delineate macro-vessels within the image. Instead, bubble flow from macro-vessels and microvessels could be differentiated in time if it is assumed that the majority of the initial inflow is dominated by large vessels.

Furthermore, the differentiation of different vessel sizes and types in super-resolution images could be performed through spatial localisation density, average bubble speeds, or spatial coverage, which may be able to draw out information related to different vessel branch levels. For example, higher speeds generally correlated to vessels with high localisation number in the final maps *in vivo* in Chapter 4 which may indicate primary vessel structures [235]. This would rely on out of plane motion being negligible. Alternatively, the extraction of different levels of branching structure could be achieved through the use of a range of increasing LT values, up to the point at which no spatial regions above the localisation threshold remain. This should provide patient specific information on the branching levels and volume of blood flow imaged.

Additionally, more advanced tracking may be required for *in vivo* data such as this where a high level of noise, complex vasculature, and bubble flow into and out of plane need consideration, such as Monte Carlo data association algorithms as used for tracking in Ackermann et al. 2013 [279].

5.7.1.8 CONTINUATION OF CLINICAL STUDY

With such a small subject sample size, limited diagnostic validation can be gained as yet. An increased number of both control and symptomatic subjects is required for subsequent investigations, and would benefit from the inclusion of a third subject group with diagnosed type-2 diabetes mellitus. Diabetic patients constitute an increasing proportion of patients with PAD [111] and have been shown to have poorer lower extremity function than those with PAD alone [3]. The diagnostic performance of conventional diagnostic techniques is reduced in diabetics [111], [3], [280]–[282]. [46]. For this reason, for a given reduction in ABI, diabetic patients tend to have more impaired lower extremity function than those without diabetes [3], [46] and thus are an important subject group for future tests. This, along with measures of disease grading, would further evaluate the use of super-resolution quantification to provide information regarding PAD severity which would be particularly useful in the diabetic population in whom conventional non-invasive tests were less predictive of the severity of symptoms.

5.8 SUMMARY AND KEY FINDINGS

This technique aimed to enable assessment of changes in the microcirculation of musculoskeletal tissue in the lower limb to quantify obstruction of vascular flow in the lower extremities which could indicate the presence of disease, or response to treatment in diseased subjects. The derived quantitative measure of bubble localisation number provided the most promising and repeatable super-resolution estimates investigated here, where an excellent correlation was found with known bubble concentration in *in vitro* experiments. Developments, however, are required to improve estimations of blood velocity; measurements on a smaller field of view of the lower limb could considerably improve the precision of bubble localisation precision and thus speed estimations, and would also provide improved resolution in the final images. Further investigation into the most suitable acquisition time and concentration is required if this is to be optimised for clinical implementation.

In the future, techniques such as this may be able to improve quantitation of CEUS imaging procedures in both macro- and microvessel imaging. By reducing infusion rates or injecting lower bubble concentrations and applying localisation algorithms, the technique has the potential to enhance the extraction of information from existing CEUS imaging, where estimates of blood volume, perfused vascular density, and blood velocity could be useful clinical measures.

6 LEARNING ALGORITHMS FOR SIGNAL DIFFERENTIATION

6.1 INTRODUCTION AND MOTIVATION

Clinical implementation of super-resolution requires accurate single bubble detection, and would benefit from automated or close to automated processing in order to minimise processing time and user dependence. In previous chapters, differentiation of single bubble events from the image background and from signals originating from multiple bubbles was performed using empirically determined thresholding methods based on features such as intensity or spatial extent, making their clinical implementation challenging (Chapters 3-5). The purpose of this chapter is to explore the use of machine learning based post-processing tools for single bubble identification and

---

Initial work conducted in this chapter in collaboration with Schirmer, M. D. was presented at the IEEE Micro and Nanotechnology in Medicine Conference, Hawaii and published in conference proceedings: Super-Resolved Micro-Vascular Imaging Using Microbubbles and Machine Learning, Christensen-Jeffries, K., Schirmer, M. D., Browning, R., Tang, M-X., Dunsby, C., Aljabar, P., Eckersley, R. Dec 2014 IEEE Micro and Nanotechnology in Medicine Conference, Hawaii.

to provide first demonstration of their potential on newly acquired *in vitro* data, and *in vivo* data acquired in Chapter 4.

In this work, a new pre-processing step is introduced to identify candidate bubble regions by segmenting foreground and background. The analysis of acquired images begins with the differentiation of regions of interest from the background. This is a crucial step for image processing and forms the basis for further signal analysis, such as extraction of shape and boundary features. This has been done using a machine learning algorithm which segments an image into units called superpixels [283], which are regions of a digital image, larger than the original pixel size; this aims to group image pixels into perceptually meaningful segments. Humans are remarkable good at identifying signals of interest and subsequently do very well at differentiating foreground from background information. For computers on the other hand, the differentiation of such can prove to be challenging. By using groupings of perceptually meaningful segments, superpixels try to emulate the strengths of human segmentation, while maintaining reproducibility and feasibility for processing large datasets [284]. In the process, superpixel methods are assumed to learn the structure necessary for segmentation at the scale of interest [283].

Further machine learning approaches are investigated to subsequently classify the segmented foreground. These aim to distinguish individual microbubble signals from those of noise, and those created from more than one bubble, in order to overcome the challenge of reproducible signal classification. Three learning-based methods are examined; these are based on k-means classification [285], Gaussian mixture models (GMMs) [286]–[288], and support vector machines (SVMs) [289]. Such algorithms make data-driven decisions by building a model from the data itself or, in the case of SVMs, from training sets: small sets of manually labelled signals. This is in contrast to obeying a fixed criteria or thresholds as in former processing methods (for example those in Chapters 3 and 4). By learning the characteristics of object features, these approaches allow for classification of large amounts of data with limited user intervention [287], [290], [291]. Such learning techniques have been used in a wide range of applications including tumour detection and classification [292], [293], real-time object tracking [288], [294], [295], and disease classification [296]. These

automated/semi-automated frameworks aim to improve overall reproducibility through limited (or no) user input, which would increase the clinical viability of the technique.

The chapter is organised as follows. Firstly, superpixelation used in the initial processing step is described. Next, the three learning algorithms for signal classification are introduced, and implementation methods and algorithm specific parameters are explained. Qualitative and quantitative evaluation of these approaches is presented for comparison to previous methods (see Chapters 3 and 4).

6.2 BACKGROUND

6.2.1 SUPERPIXELS

Conventional approaches to region segmentation are often based on intensity thresholding [297]–[299] (see chapter 3 and 4). These threshold-based techniques can be unsuitable for images with non-homogeneous objects of interest or a significant amount of noise, where the intensity level of pixels cannot always differentiate regions of interest [300].

Superpixelation is a grouping process designed to capture perceptually important groupings or regions in an image [283]. Applying superpixel segmentation, for example, to the photograph shown in Figure 6.1, the algorithm was able to detect and segment the foreground (leaf), while also attempting to separate different areas of background (stone tiles). While background separation between coloured tiles is not ideal, this approach performs well at separating the foreground from the complex image. Perceptually important groupings can be described as ones which are organised or arranged similar to how the human visual system would interpret or perceive a scene [301]. Principles of groupings have been developed by classical Gestalt theory, which attempts to describe how humans tend to organise visual elements into groups based on features such as similarity and proximity [301], [302], and include features such as intra-region similarity of brightness, texture, and smooth boundaries [283], [301]. Similarly, superpixel algorithms may use clustering techniques to group pixels based on features, such as colour similarity, proximity in the image plane and texture coherence [284], [303]–[306]. To modulate the emphasis on spatial adjacency or intensity

similarity, some superpixel implementations employ a compactness ratio, which will be discussed in Section 6.5.1.

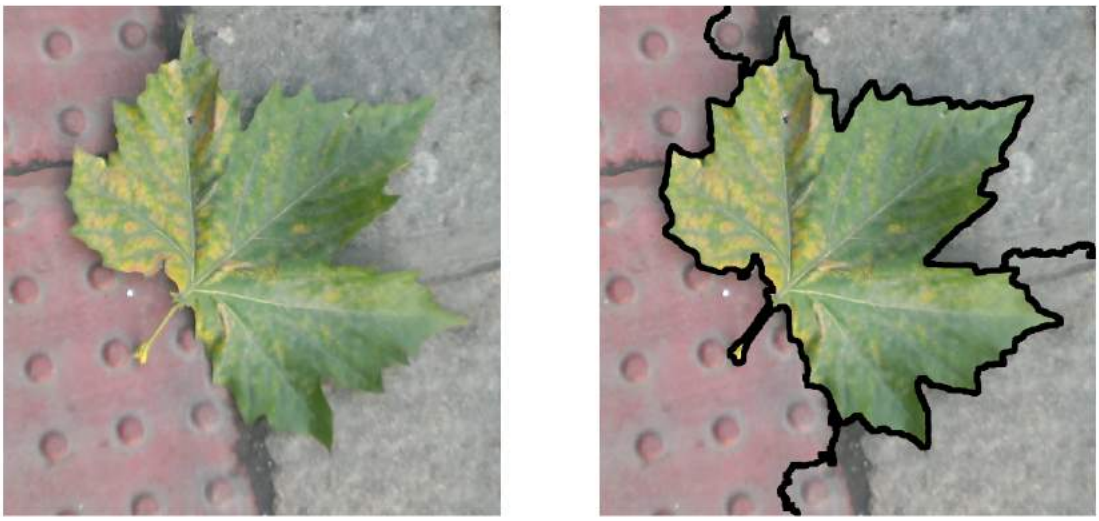

Figure 6.1. Superpixel segmentation results on example image using simple linear iterative clustering (SLIC) [303].

Superpixels have been shown to increase performance over pixel-based methods by preserving 'natural' object boundaries, while capturing redundancy of information in the data [283], [307], [308], often reducing the complexity for subsequent processing tasks. Superpixels have proven valuable in wide ranging applications including image segmentation [309]–[311], object localisation [308] and human body model estimations [312].

6.2.2 Classification using Learning Algorithms

Resulting foreground superpixels require subsequent classification to differentiate signals originating from single bubbles, from those of multiple scatterers and noise. Supervised and unsupervised learning algorithms implemented for this purpose, which learn structure from labelled and unlabelled data respectively, are described in the following sections.

6.2.2.1 K-Means (Unsupervised)

The first method implemented for signal classification is a variance-based clustering technique called k-means clustering [285]. Cluster analysis intends to classify objects into subsets that have meaning in the context of a particular problem [313]. In

particular, k-means clustering aims to partition *n* observations in a *d*-dimensional metric space $\mathbf{R}^d$, into *k* clusters. This is done using a clustering criterion, so as to minimise the average overall squared distances between each data point and it's nearest assigned centre. This unsupervised technique uses the inherent structures in data to organise it into groups of maximum commonality, that is to say, groups of data that share features or attributes. For example, these could include features such as pixel intensity, region size or shape characteristics. K-means clustering uses an iterative refinement technique as illustrated in Figure 6.2.

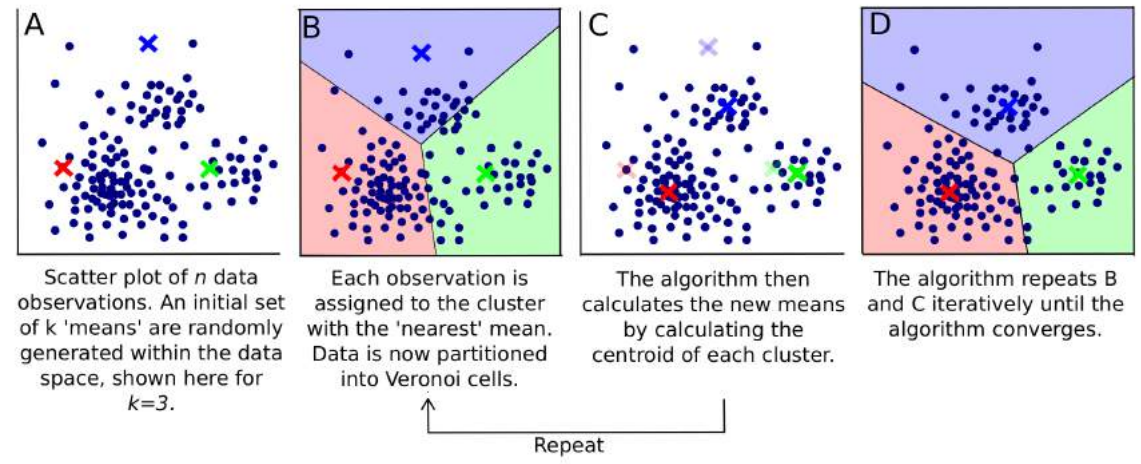

Figure 6.2. Principle of k-means clustering algorithm.

Firstly, an initial set of *k* points are either randomly selected within the data space (Figure 6.2A), or initialised randomly as data points. These are referred to as centres or 'means'. Each observation is then assigned to the cluster with the smallest Euclidean distance, or nearest mean (Figure 6.2B), resulting in a partitioning of the data space into so called Voronoi cells [314]. The centroid of all observations assigned to each cell is then calculated to produce a new cluster mean, μ_i, or centre (Figure 6.2C), given by,

$$\mu_i = \frac{1}{n_i} \sum_{x_j \in S_i} \boldsymbol{x_j}, \tag{6.1}$$

where $\boldsymbol{x_j} \in S_i$ are the set of data points within cluster i, and n_i is the number of data points in S_i. The algorithm repeats step *B* and *C* in Figure 6.2 iteratively until the

assignments no longer change, and the algorithm converges. Each observation now belongs to the cluster of its nearest mean. This means that the within-cluster sum of squared distances, given by

$$V = \sum_{i=1}^{k} \sum_{x_j \in S_i} \left(\left\| \boldsymbol{x_j} - \boldsymbol{\mu_i} \right\| \right)^2, \tag{6.2}$$

is minimised (Figure 6.2D), allowing classification of all observations into *k* clusters.

Advantages of k-means lie in its unsupervised nature and processing speed, however the found solution may not represent the global optimum of the minimisation process. In addition, the algorithm requires the number of clusters as an input parameter necessitating some prior knowledge of the underlying data. In this application, however, data can be thought to consist, for example, of noise, single bubbles and signals from more than one bubble, giving an estimation of three centres for classification.

6.2.2.2 GAUSSIAN MIXTURE MODEL (UNSUPERVISED)

K-means executes a hard partitioning or strict assignment, however, sometimes the boundaries are not clearly defined (or are blurred by noise) and therefore a softer definition may be beneficial. In contrast Gaussian mixture models (GMMs) incorporate uncertainty into cluster assignments and therefore provide a model for the distribution of data where each data observation has some probability of belonging to each cluster. This algorithm is an unsupervised, probability density function which assumes all data points are generated from a mixture of a finite number of Gaussian distributions with unknown parameters [315]. Gaussian mixture modelling may therefore be more effective than *k*-means clustering, for example, when data have different sized structures within them.

Similar to the k-means approach, Gaussian mixture modelling uses an iterative algorithm until the model parameters converge, i.e. that the change in parameters between iterations is below a certain threshold. Mixture models incorporate information about the covariance structure of the data as well as the centres of the underlying Gaussians [286],[33].

The model is a weighted sum of M Gaussian densities, $g(\boldsymbol{x}|\boldsymbol{\mu_i}, \Sigma_i)$, each given by

$$g(\boldsymbol{x}|\boldsymbol{\mu_i}, \Sigma_i) = \frac{1}{(2\pi)^{d/2}\,|\Sigma_i|^{1/2}}\, exp\left\{-\frac{1}{2}(\boldsymbol{x}-\boldsymbol{\mu_i})'\Sigma_i^{-1}(\boldsymbol{x}-\boldsymbol{\mu_i})\right\}, \qquad (6.3)$$

where $\boldsymbol{x}$ is a d-dimensional data observation, $\boldsymbol{\mu_i}$ is the mean vector and Σ_i is the covariance matrix of cluster i, with $i = 1, \ldots, M$. It is assumed that the data is generated by the mixture of multiple Gaussian densities, which can be represented by [315]

$$p(\boldsymbol{x}|\boldsymbol{\mu_i}, w_i, \Sigma_i) = \sum_{i=1}^{M} w_i\, g(\boldsymbol{x}|\boldsymbol{\mu_i}, \Sigma_i), \qquad (6.4)$$

where w_i are the relative weights, with $\sum_{i=1}^{M} w_i = 1$. GMM parameters are estimated from the data using an iterative Expectation-Maximisation (EM) algorithm estimation [286], a method for finding the maximum-likelihood estimate of the parameters of the underlying distribution from a given (incomplete) data set [315]. An illustration of the method is shown in Figure 6.3 using a three-component GMM.

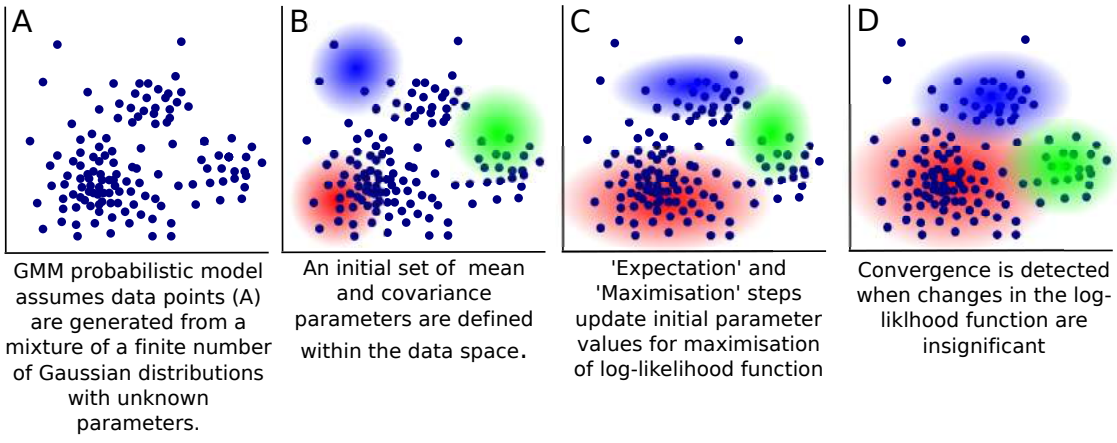

Figure 6.3. Illustration of a three-component GMM using the Expectation-Maximisation (EM) algorithm in two dimensions.

The initial Gaussian parameters or weights can be chosen randomly, or set to an application specific expected value, where the term λ is used to represent the current combined parameters given by $\lambda = \{\mu_i, w_i, \Sigma_i\}$. Each EM iteration then updates the current estimate of λ using expectation (E) and maximisation (M) steps until

convergence is reached [286], [315]. The E step estimates a function for the *expectation* of the GMM likelihood, and the M step updates λ to estimate a new model by computing the resulting parameters through maximising the expected log-likelihood function found in the previous step. Convergence is typically detected when the value of the log-likelihood appears not to change significantly from one iteration to the next.

6.2.2.3 SUPPORT VECTOR MACHINES (SUPERVISED)

The third learning technique implemented is a support vector machine (SVM) approach. SVMs are a group of supervised learning methods which use a training set, along with learning algorithms, to build a model that can map new data onto the model space [317]–[319]. Training sets are a series of data that have been pre-classified (or labelled) either by an expert, or by other means. These are subsequently used to train a classifier that can be used to label new data instances [317].

SVMs are a modified form of the logistic regression model, which describes the relationship between a dependent variable and a set of independent variables using a logistic function [318]. Logistic regressions are often used to predict a binary response based on one or more independent variables, and are widely used for classification problems when observations belong to one of two mutually exclusive categories [318][320]. One of the disadvantages of logistic regression is that it is unable to identify nonlinear structures within data [321]. SVMs, however, are able to generate more complex decision boundaries which may generate better classification results [289][321].

In the case of two classes and given a set of data points $\boldsymbol{x} = \{\mathbf{x}_i\}$ in n-dimensional space, where the labelled classes are given by $\{\mathrm{y}_i : \mathrm{y}_i \in \{-1, 1\}\}$, the SVM training algorithm aims to place a decision boundary between the points classified as $\mathrm{y}_i = 1$ and $\mathrm{y}_i = -1$. In the case of linearly separable data (Figure 6.4A), the optimal boundary (or hyperplane) is the unique boundary that separates the training data with a maximum margin, given by

$$\mathbf{w} \cdot \mathbf{x} + \mathrm{b} = 0, \tag{6.5}$$

where $\mathbf{w}$ is the vector normal to the boundary, and b is constant.

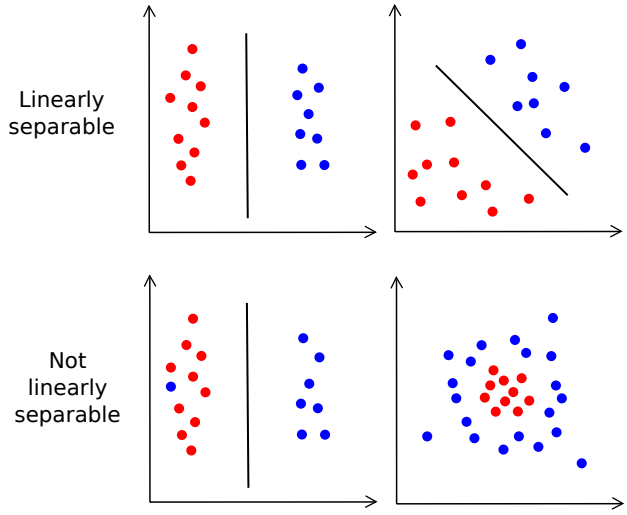

Figure 6.4. Examples of data classification using SVMs: Linearly separable case and non-linearly separable case.

The SVM decision boundary is chosen through the minimisation of the squared norm of $\mathbf{w}$. If the training data are linearly separable, hyperplanes can be defined that separate the classes of data with the maximum distance possible. The region bounded by these hyperplanes is known as the margin, as shown for example in Figure 6.5. If there are two classes, the hyperplanes that define the margin can be described by the equations

$$H_1: \mathbf{w} \cdot \mathbf{x_i} + b = 1 \quad \text{and} \quad H_2: \mathbf{w} \cdot \mathbf{x_i} + b = -1. \tag{6.6}$$

Points $\mathbf{x_i}$ for which the equalities in (6.6) hold are given by the planes H_1 and H_2 and are referred to as support vectors. The term 'support vector' corresponds to the data points that lie closest to the decision surface, as illustrated in Figure 6.5, and are the most 'difficult' to classify. Support vectors have direct impact on the optimum location of the decision boundary. SVMs find the boundary that separates the feature space based on maximising the margin, such that the data can be classified based on the training data. For many datasets, however, linear SVMs may not be able to find a separating boundary due to the presence of misclassified data points [317]. In this case, the use of a 'soft margin' which accepts some instances of misclassification can be beneficial [25],[323].

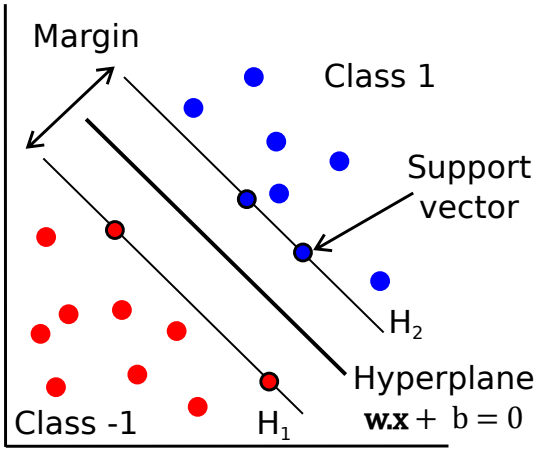

Figure 6.5. An illustration of a SVM model for two groups. Figure inspired by [324].

If the boundary is a plane, the classes are linearly separable, and this is termed linear classification. If the data is non-linearly separable (see Figure 6.4), SVMs can also perform non-linear classification using a kernel function, which indirectly maps data into high-dimensional feature spaces. A linear separating boundary may be found in this higher-dimensional feature space; by using such kernels, SVMs may be more effective at differentiating clusters or classes [289], [317], [319], [322]. Some classification or regression problems are easier to model in high dimensional space, as illustrated in Figure 6.6. By mapping data points to a sufficiently high dimensional space, the linear SVM training algorithm as described above can be used to find the optimal separating hyperplane.

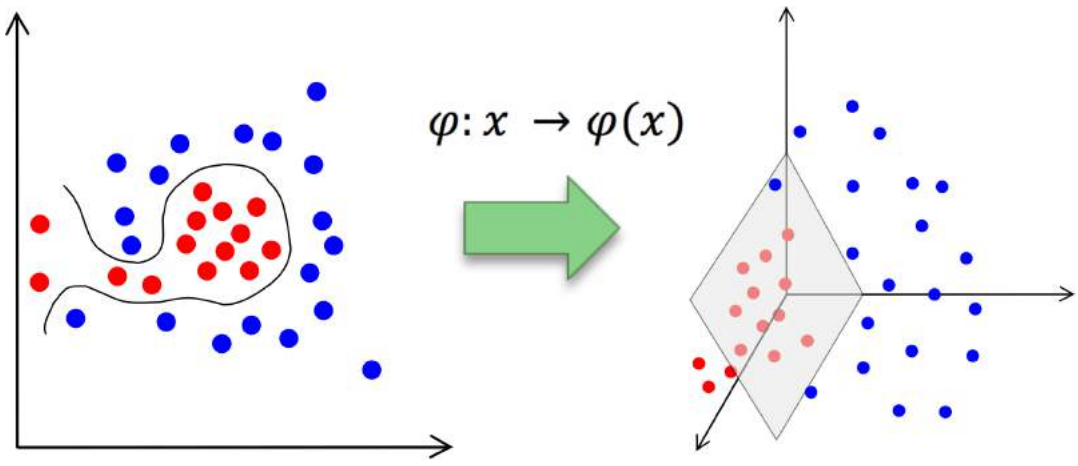

Figure 6.6. The function ϕ can be used to map the data points from n-dimensional space to m-dimensional space where $m > n$. SVM finds a linear separating hyperplane with a maximal margin in this higher dimensional space.

SVMs have demonstrated improvement in classification over logistic regression models [325], and has provided promising results for classification of clinical data, for example in the diagnosis of malignant tumours in breast ultrasonography [326].

6.3 METHOD

An outline of the complete framework used in this chapter is illustrated in Figure 6.7. Following US acquisition, image frames are firstly segmented into foreground and background using superpixels. Candidate regions are then classified using one of the three described learning algorithms. For k-means and GMM models, d properties of the candidate regions (d_k and d_G, respectively) are extracted and used to create a d-dimensional feature space for classification. In case of SVM, two users were tasked to identify 25 occurrences of each signal type. This set was subsequently used to train the classifier, which was then used to label the remaining data.

6.4 ULTRASOUND ACQUISITION

Experimental data was acquired using a standard Siemens Acuson Sequoia clinical US scanning system in Cadence™ contrast pulse sequencing (CPS) mode [107]. Imaging was performed on a crossed tube phantom (details presented in Chapter 3) with a 4C1 abdominal convex probe at a target depth of 6 cm. Imaging parameters were as follows: dynamic range: 100 dB, TGC -20 dB, transmit frequency: 2 MHz, frame rate: 25 fps, MI: 0.07. Three microbubble concentrations were tested; a water volume of 600 ml was prepared in a beaker with each of the following microbubble injection volumes: V_{MB} = 25 µl (C1), 100 µl (C2), and 400 µl (C3) and video data was acquired for 6 minutes at each concentration. Machine learning approaches were first tested on this *in vitro* experimental dataset, and were subsequently applied to *in vivo* data (mouse 1) acquired within Chapter 4. Since the same system settings were implemented here, the characterised diffraction limited resolution of the system for *in vitro* data is 336 µm laterally and 239 µm axially, and for *in vivo* data is given by 316 µm laterally and 209 µm axially (see Chapter 3 and Chapter 4 for details).

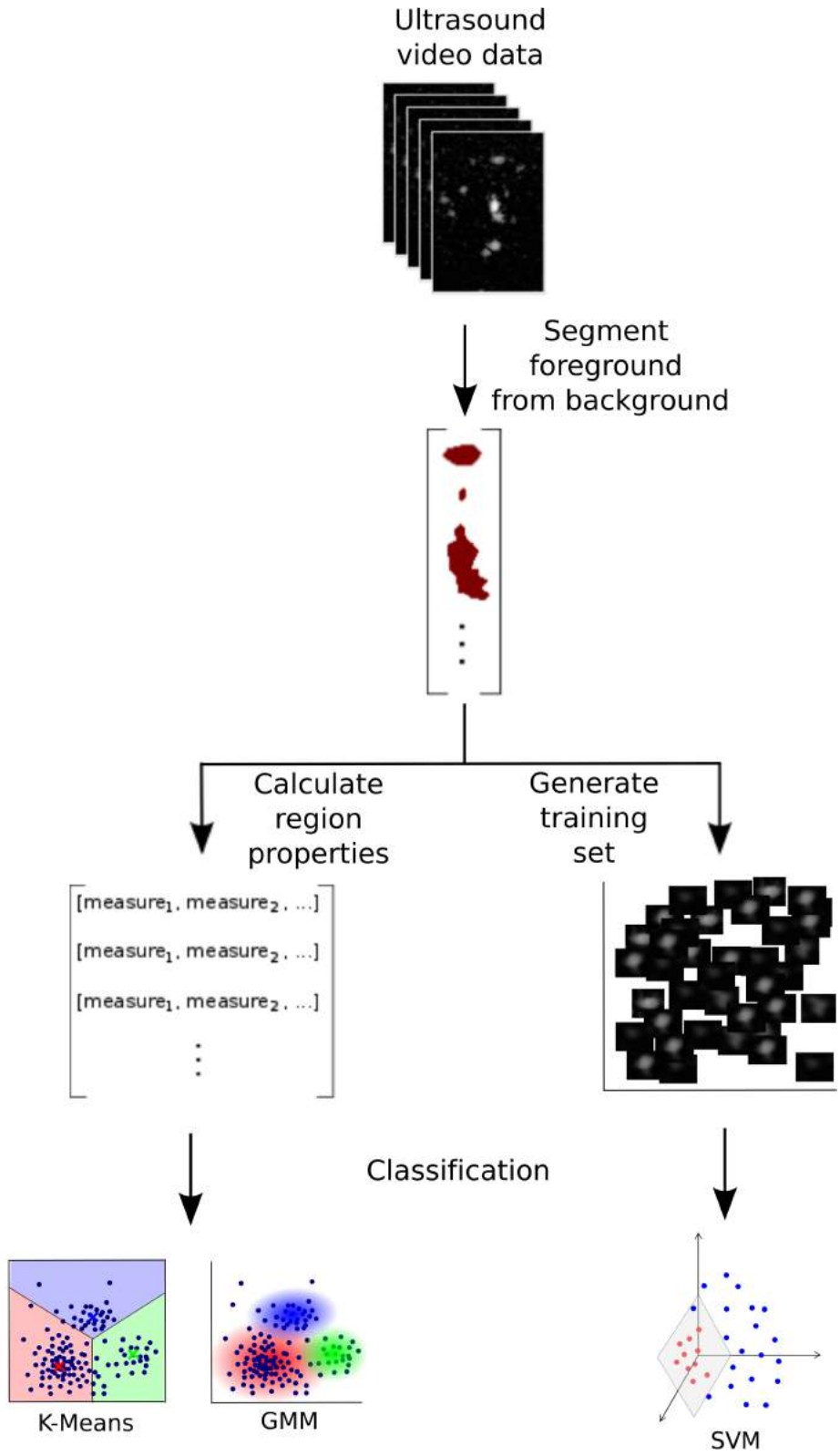

Figure 6.7. Processing pipeline for the acquired video data. Image frames are firstly segmented into foreground and background using superpixels, before candidate regions are classified using one of three learning algorithms. For k-means and GMM models, region properties are used for classification. In addition, two users were tasked to identify 25 occurrences of each signal type. This set was subsequently used to train SVMs, which were then used for classification.

6.5 IMAGE PROCESSING

Foreground/background separation was performed using superpixels. Subsequently, identified foreground signals were classified using the three learning algorithms described in Section 6.5.2. Centroiding was performed on the final classified image regions and plotted using image generation procedures described in Chapter 3. Centroids belonging to the same cluster are displayed as accumulative images to provide information about the (spatial) signal distributions.

6.5.1 FOREGROUND/BACKGROUND SEGMENTATION (SUPERPIXEL)

Superpixel segmentation is performed in order to extract candidate regions from the data. A number of algorithms have been developed for superpixel segmentation [283], [284], [327]–[329]. In this work, superpixel segmentation is implemented using Simple Linear Iterative Clustering (SLIC) [284] (scikit-learn, Python [330]). This algorithm adapts a spatially localised version of k-means clustering to group pixels in the combined colour (or signal intensity) and image space [2], [21] to generate n superpixels. In this application n is set to two, corresponding to foreground and background, and the algorithm is applied to signal intensity images. Another parameter that needs to be defined is the compactness ratio. The compactness ratio, given by

$$Compactness = \frac{Spatial\ Adjacency\ weighting}{Intensity\ weighting}, \tag{6.7}$$

is used to define a relative weighting between the relative "spatial" distance of two pixels, and the similarity of their intensities. A high spatial adjacency weighting (large compactness) will generate segmentation which groups primarily neighbouring pixels. A higher intensity weighting, corresponding to $Compactness < 1$, will place emphasis on intensity similarities rather than their respective distance. A range of values of compactness were tested where a value of 0.1 was deemed to provide stable result, i.e. that variation in compactness ratio did not yield large differences. Individual microbubble signals in the foreground are likely to be spatially compact and distributed across the image. The effect of variations in compactness ratios is investigated in Section 6.6.1.

Since data in this work includes dynamic sequences of the target objects, foreground/background segmentation was performed by including dynamic information. This was done by classifying stacks of consecutive images. In particular, empty frames can be regarded as outliers, where some clusters or classes are missing, i.e. only background information. This may pose a challenge for machine learning algorithms, which classify data into a given number of clusters. By including the previous and following frame to that being segmented, more data was used to learn which pixels belong to foreground or background. This was found to help reduce the effect of empty frames.

6.5.2 DATA CLASSIFICATION

Features, such as shape, intensity and size, are then extracted from candidate regions within the foreground superpixel for the unsupervised post-processing procedures described below. SVMs require training data sets for the classification procedure. When multiple bubbles are present in close proximity, their signals can overlap; as discussed in previous chapters these signals can cause a problem for super-resolution imaging due to the increase in uncertainty in the location of individual scatterers, and the potential for interference effects. The differentiation of single and multiple bubbles therefore becomes important in super-resolution imaging. Thus, classification procedures involved the identification of signals originating from three different sources: noise, single bubbles and multiple bubbles.

6.5.2.1 THRESHOLDING

User defined size and intensity thresholding was applied to the foreground candidate regions following superpixel segmentation. The lower size threshold value was chosen based on the estimated diffraction limited resolution, with an empirically derived upper threshold value, as described in Chapter 3 and 4 for *in vitro* and *in vivo* data respectively. These results will act as a baseline for comparison between the previous and the proposed classification approaches.

6.5.2.2 K-MEANS

This algorithm uses k-means clustering to identify these three sources within the data. Firstly, the features are 'whitened'; this procedure rescales each feature (bubble characteristic) by dividing it by the standard deviation across all observations. This

normalisation gives the data unit variance. The initial cluster centres are initialised as randomly selected data points. As the result of the k-means algorithm may not be unique due to local optima, ten iterations are performed with varying starting points. The final result constitutes the consensus vote of all iterations, providing a more stable estimate of the cluster definition. Features used in the method were based on three properties of the signals, maximum intensity and inertia tensor eigenvalues. The inertia tensor eigenvalues are directly related to the moment of inertia, since eigenvectors are the intrinsic axes of the object and provide information on the spread, and the eigenvalues give information about the distribution of the intensities.

6.5.2.3 GMM

This algorithm implements GMM for clustering of observations, which allows maximum-likelihood estimation of the parameters of a GMM distribution. In this application, the number of mixture components is set to three and the parameters used are the same as those used for K-means described previously. All Gaussians are initialised as standard normal distributions (zero mean and identity covariance). One hundred EM iterations were performed and the process was terminated when the average gain in log-likelihood was below a threshold of 0.001. Weights, means and covariances are updated within the training process.

6.5.2.4 SVM

Two users of similar expertise were tasked to identify 25 occurrences of each signal type. SVM classifiers were trained on these data to recognise and distinguish the appearance of superpixels belonging to each of the signal categories. The commonly used radial basis function (RBF) kernel was used (Gaussian function). The duration of the manual labelling was approximately 45 minutes per dataset.

6.5.2.5 JUDGEMENT OF RESULTS

Phantom data provides the opportunity to qualitatively assess the processing techniques with a known underlying structure and size. This aims to test the ability of the approaches to selectively detect isolated bubble signals, which are assumed to provide localisations only within the tube diameter, while non-spatially separated signals may be localised outside the tube width. If approaches were deemed to have potential for super-resolution imaging, determined by qualitative assessment of both *in vitro* and *in*

vivo experiments, results were subsequently assessed quantitatively, where image intensity profiles were taken close to the centre of the crossed tube structure. In this area, the likelihood of multiple bubble signals increases due to the proximity of the tubes to one another.

6.6 RESULTS

6.6.1 FOREGROUND/BACKGROUND SEGMENTATION (SUPERPIXELS)

Superpixel segmentation results, such as that shown for an example *in vivo* frame in Figure 6.8, separate the image into two superpixels, where the foreground (Figure 6.8B, white) consists of many small separate regions that preserve most of the apparent boundaries that can be visualised in the original image. Figure 6.9 shows the investigation of varying compactness ratio. At a compactness ratio of 1000, the spatial adjacency of pixels is prioritised over the similarity in pixel intensities. For a compactness ratio equal to 1, these factors are weighted equally, and the segmentation of microbubbles from the background can be seen. Ratios below this have weighting favoured towards pixel intensity similarities.

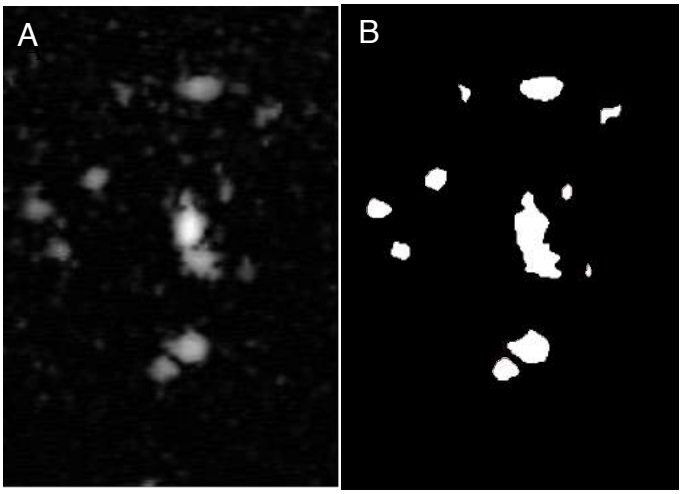

Figure 6.8. Example log-compressed *in vivo* data frame (A) and corresponding superpixel image (B).

Qualitative investigation of the compactness parameter found that a ratio between 1 and 0.5 provides stable results and was not sensitive to variations. The remainder of this work therefore uses a compactness ratio of 0.1. This parameter setting was used in the superpixel processing step for both *in vitro* and *in vivo* datasets. These were performed

with different US scanner with widely varying scanning parameters (see Chapter 4), however, visual assessment of the superpixellation results indicate independence of the algorithm to changes in scanning parameters.

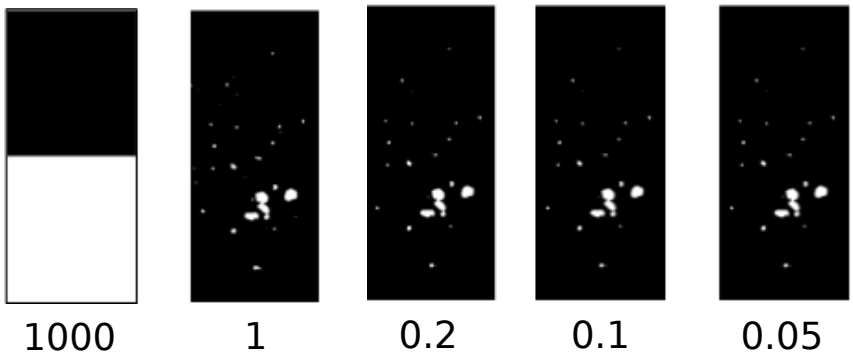

Figure 6.9. Results of foreground segmentation using superpixels with varying compactness ratio.

6.6.2 THRESHOLDING

Figure 6.10 shows *in vitro* results from user defined thresholding of foreground data resulting from superpixelation. Here, localisations from connected regions below an empirically defined size and intensity threshold were assumed to be predominantly from noise. Regions whose properties fell above the upper threshold were expected to be from multiple, unseparated bubbles, and those within were expected to originate from spatially isolated single bubbles. These graphs can be used to compare to machine learning methods in the next sections.

The corresponding thresholded *in vivo* results shown in Figure 6.11 demonstrate a differentiation of a large degree of noise below the threshold, while the main structure of the ear vasculature appears within the thresholds. Above the upper threshold, localisations exist within specific regions of the vascular structure. From work performed in Chapter 4, these regions correspond predominantly to vessel 'junctions', where blood flow faces a change in direction, or branches into two continuing vessels. These junctions are also seen in previous velocity maps to consist of coupled vessel structures with opposing flow directions. In these areas, the likelihood of multiple bubbles coinciding within the resolution of the system is higher, and may therefore represent locations at which multiple bubble signals have occurred.

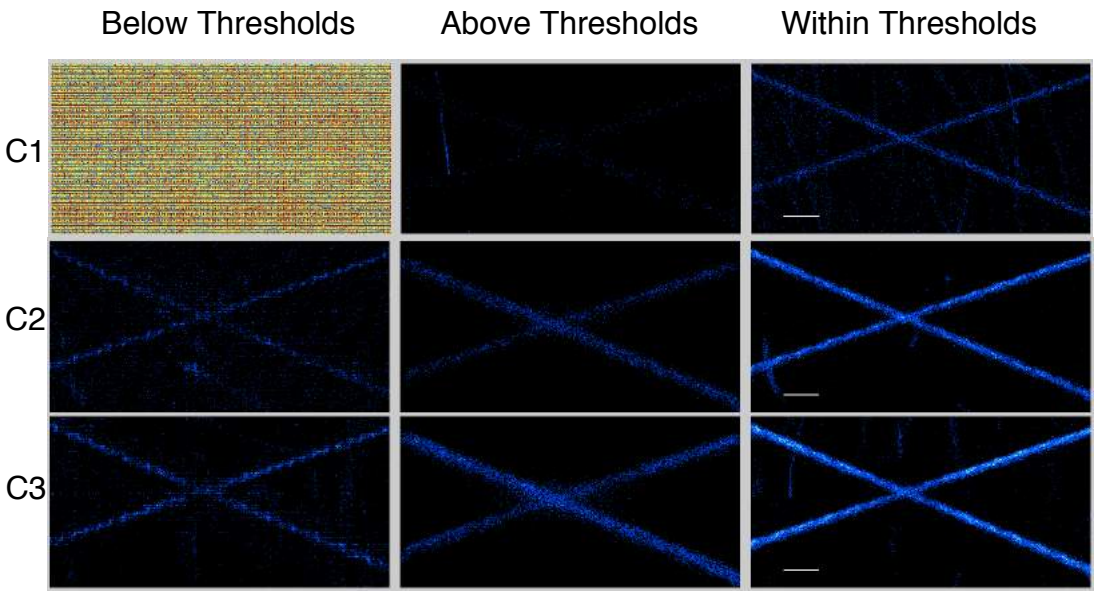

Figure 6.10. *In vitro* results from user defined thresholding of foreground data resulting from superpixels. Here, localisations from connected regions below size and intensity thresholds were assumed to be predominantly from noise. Regions whose properties fell above these were expected to be from multiple unseparated bubbles, and those within were expected to come from spatially isolated single bubbles. Scale bar 1 mm.

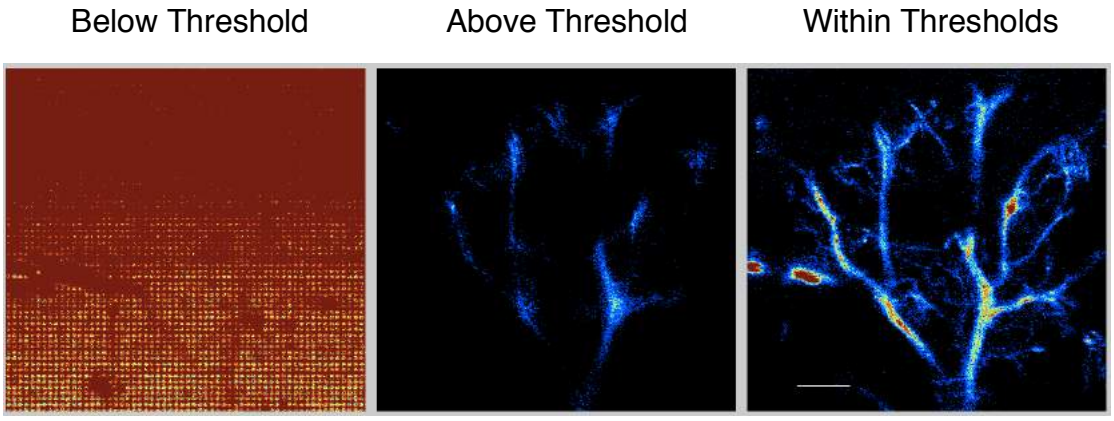

Figure 6.11. *In vivo* results from user defined thresholding of foreground data resulting from superpixels. Scale bar 1 mm.

6.6.3 Classification - K-Means Results and Discussion

In vitro results from k-means clustering shown in Figure 6.12 demonstrate significant variation between different microbubble concentrations. Clusters found within the data using the lowest concentration (C1), do not appear to clearly distinguish bubble signals

(signals originating from within the nominal tube diameter) from those of noise and multiple signals. Additionally, a considerably large number of signals are found spread across the entire image in cluster 3, indicating that this cluster is predominantly noise. With a higher concentration (C2), clusters appear to have better differentiation of bubble signals (cluster 3) from those occurring outside the phantom structure. Furthermore, a cluster is found which contains primarily localisations towards the centre of the crossed structure. However, their exact locations are mostly situated outside of the tube structure, suggesting that these signals are not suitable for super-resolved imaging, i.e. their centre of mass does not correspond to the exact position of the microbubble. Further increase in concentration (C3) shows similar results to those for C2, with an increased number of localisations. Again, cluster 2 contains localisations positioned around the centre of the structure, indicating the increased presence of multiple unseparated bubble signals.

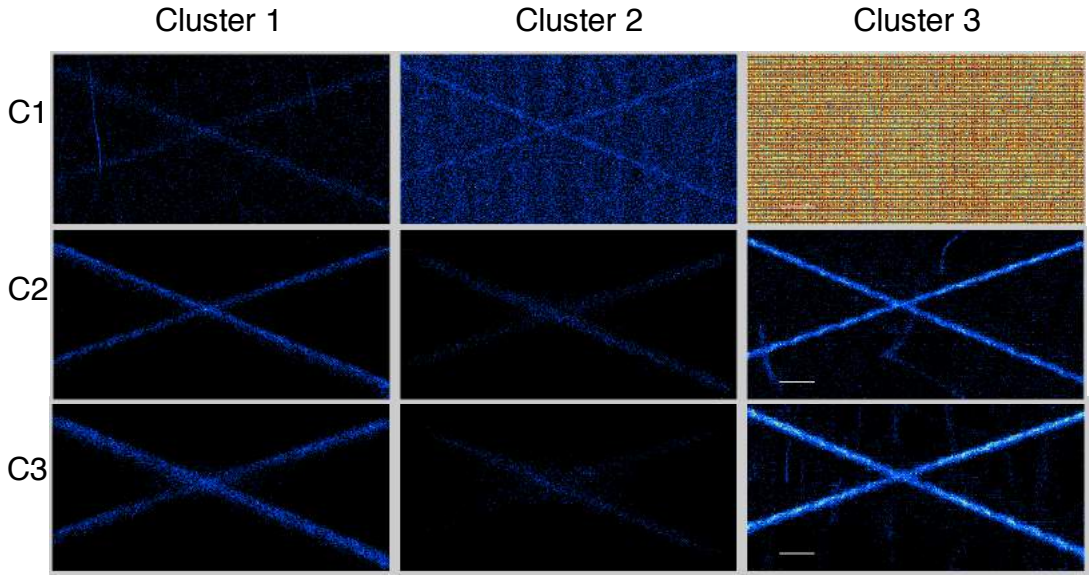

Figure 6.12. *In vitro* results using k-means clustering with k = 3, for three microbubble concentrations C1-C3. Scale bar 1 mm.

Both C2 and C3 show a very low level of noise throughout the clusters. This may be due to elimination of noise during the superpixilation process; a high SNR was observable in the controlled setting of the phantom experiments, which may have caused noise to be classified as background in C2 and C3. Cluster 1 for both C2 and C3 may be an indication that there is another form of signal within the data. These

localisations fall mostly within the tube diameter, however the delineation of the tube diameter and crossed tube centre is less well defined than in cluster 3 (particularly in C3) and the number of detections is considerably lower which may be a result of overlapping scatterer signals.

In vivo results displayed in Figure 6.13 contain a cluster which has a clear dominance of noise signals (cluster 1), while cluster 2 shows a large amount of structure within the mouse ear. This image, however, displays a considerable degradation towards the upper regions of the image, where noise signals are apparent. This is a result of the graduation in intensity in the acquired *in vivo* image data, and demonstrates the sensitivity of k-means to variations in background intensity. The final cluster comprises localisations which again occur predominantly within junctions and areas of high vascular flow similar to those regions seen in Figure 6.11 (above threshold).

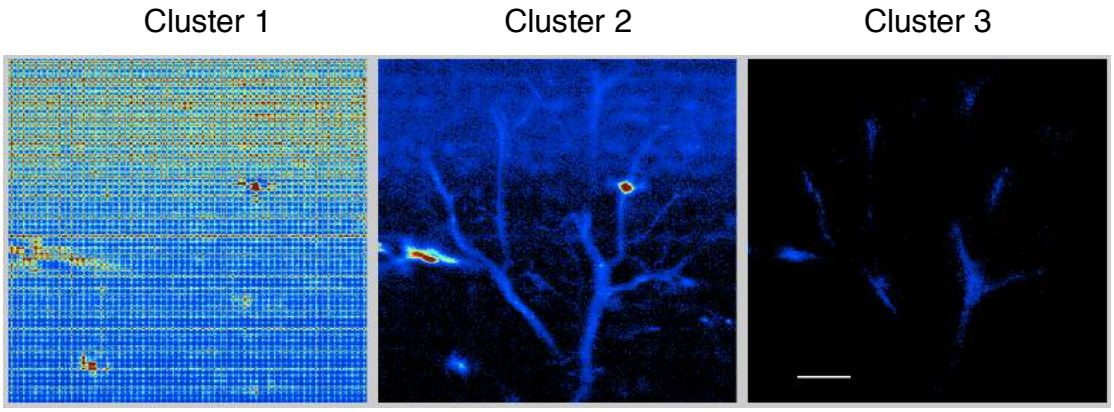

Figure 6.13. *In vivo* results using k-means clustering with k = 3. Scale bar 1 mm.

In order to work effectively, k-means clustering requires the clusters present in the data to have approximately the same size. The results presented in Figure 6.13 indicate that the data may have varying cluster sizes in this application, for example many more signals coming from noise (cluster 1) than multiple bubbles (cluster 3). This may limit the success of the approach presented here.

6.6.4 Classification – GMM Results and Discussion

GMM has the potential to be more reliable than *k*-means clustering if clusters have different numbers of elements (or sizes). Clustering results using GMM, however, did

not show promise for classification of single bubble signals, and instead clusters within each concentration in *vitro* appear to produce similar images (Figure 6.14). Furthermore, *in vivo* results demonstrated a mixture of all signal types across all clusters (Figure 6.15). The approach assumes clusters within the data to be Gaussian distributed in parameter space [315]. Despite parameters showing approximate Gaussian distributions in initial testing, the poor performance of the approach indicates that deviations of parameter distributions from a "true" Gaussian profile may be responsible for the unsatisfactory differentiation between clusters.

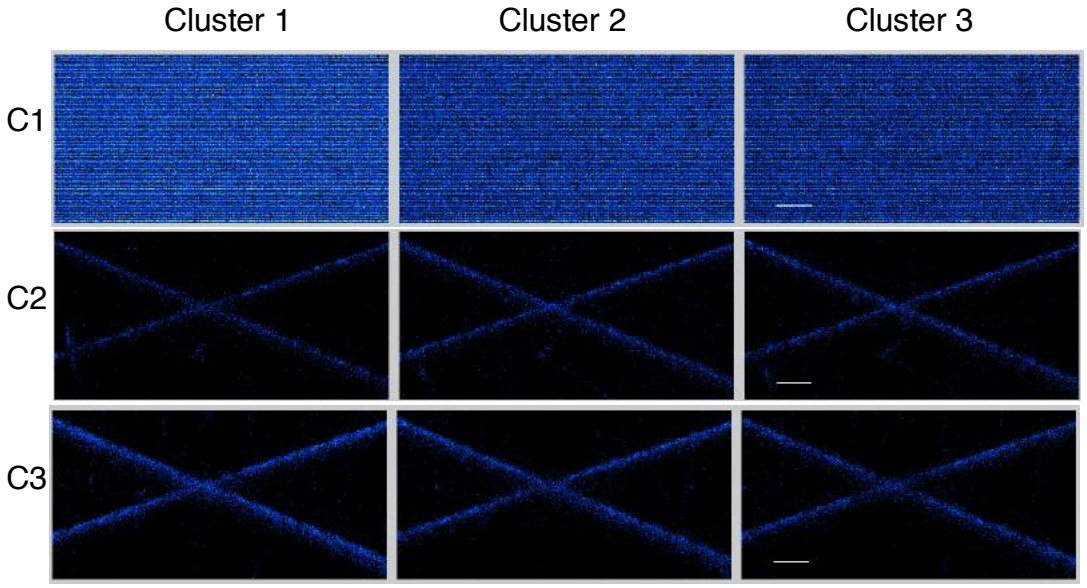

Figure 6.14. *In vitro* results using GMM for three microbubble concentrations C1-C3. Scale bar 1 mm.

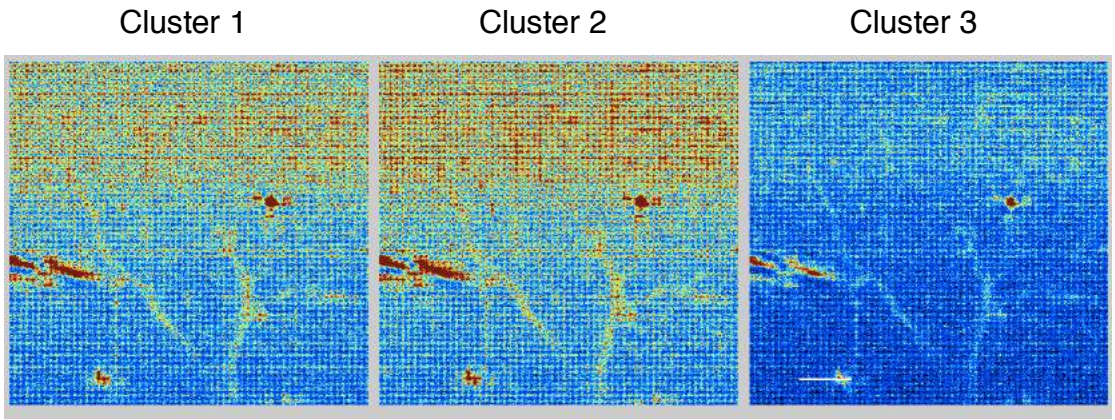

Figure 6.15. *In vivo* results using GMM. Scale bar 1 mm.

6.6.5 CLASSIFICATION – SVM RESULTS AND DISCUSSION

To examine inter-observer variation and the sensitivity of SVM to different training sets, cross-classification was performed. Table 6.1 and Table 6.2 display results of cross-classifying the training sets of both observers. Each row corresponds to the classification results of a given signal class labelled by one of the observers and classified by the other. Diagonal elements show a high number of matching classifications among observers in *in vitro* datasets, except in the case of distinguishing multiple and single bubble signals, where around a quarter of those deemed to be multiple from one observer are labelled as single by the second. These signals may be difficult to differentiate from their appearance if multiple bubbles are close together, i.e. "overlapping" without observable interference effects. They therefore may represent the classification boundary, where the margin between the two classes is small. Classifications among observers in *in vivo* datasets additionally show high values on the diagonal elements, with only a small number of differing cross-classifications.

In Vitro Dataset		Classified by Observer 2		
		Single	Multiple	Noise
Trained by Observer 1	Single	17	8	0
	Multiple	1	24	0
	Noise	0	0	25

In Vitro Dataset		Classified by Observer 1		
		Single	Multiple	Noise
Trained by Observer 2	Single	14	11	0
	Multiple	0	25	0
	Noise	0	0	25

Table 6.1. Results of cross-classification of *in vitro* training data labelled by observer 1 as classified by observer 2, and vice versa. Diagonal elements indicate those that have matching labels.

In Vivo Dataset		Classified by Observer 2		
		Single	Multiple	Noise
Trained by Observer 1	Single	22	0	0
	Multiple	0	25	0
	Noise	2	4	19

In Vivo Dataset		Classified by Observer 1		
		Single	Multiple	Noise
Trained by Observer 2	Single	24	0	1
	Multiple	4	19	1
	Noise	0	0	25

Table 6.2. Results of cross-classification of *in vivo* training data labelled by observer 1 as classified by observer 2, and vice versa. Diagonal elements indicate those that have matching labels.

Despite these variations, the results shown in Figure 6.16 and Figure 6.18 demonstrate qualitatively promising results, and the approach may therefore not be too sensitive to the initial labels assigned in the training set. However, this may also indicate that the classification might benefit from a larger training set.

The noise clusters resulting from the SVM classification algorithm performed on *in vitro* data using both training sets consist of a large number of localisations at the lowest concentration (Figure 6.16, C1). Also evident is a low number of single and multiple bubble detections as expected. At higher concentrations, single bubbles appear to be distinguished owing to their positioning along the tube structure. The multiple bubble clusters display a larger spread over the entire tube position. The number of single bubble localisations classified using SVM is lower (28577 and 30783 localisations) than those found using the thresholding approach (46763 localisations), while considerably more where categorised as coming from multiple unseparated signals (Table 6.3). The potential effect of this can be observed in the intensity profiles taken through a section near the centre of the phantom structure in C3 images shown in Figure 6.17.

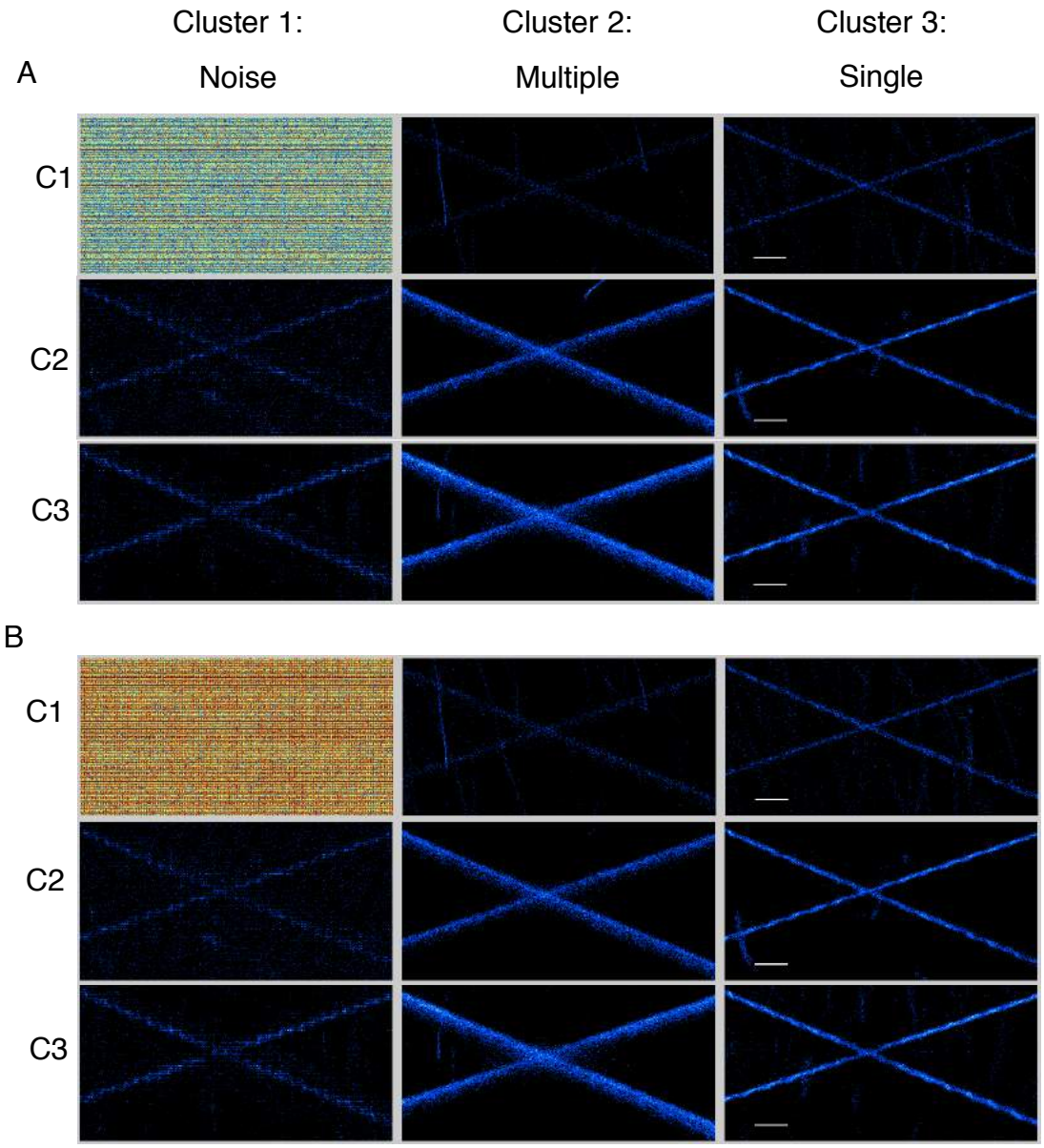

Figure 6.16. *In vitro* SVM results. Figures in (A) display results from the first training set labelled by observer 1, and (B) from observer 2. The three clusters found for each concentration (C1-C3) are displayed in each row. A qualitative comparison between the results of both observers shows good agreement. Scale bar 1 mm.

	SVM-A	SVM-B	Thresholds
Single	31%	33%	60%
Multiple	51%	49%	17%
Noise	18%	18%	23%

Table 6.3. ~~Number~~ Percentage of localisations classified using SVM with training set A and training set B, compared to thresholding technique for *in vitro* experiment (C3). Percentages are rounded to the nearest integer.

A

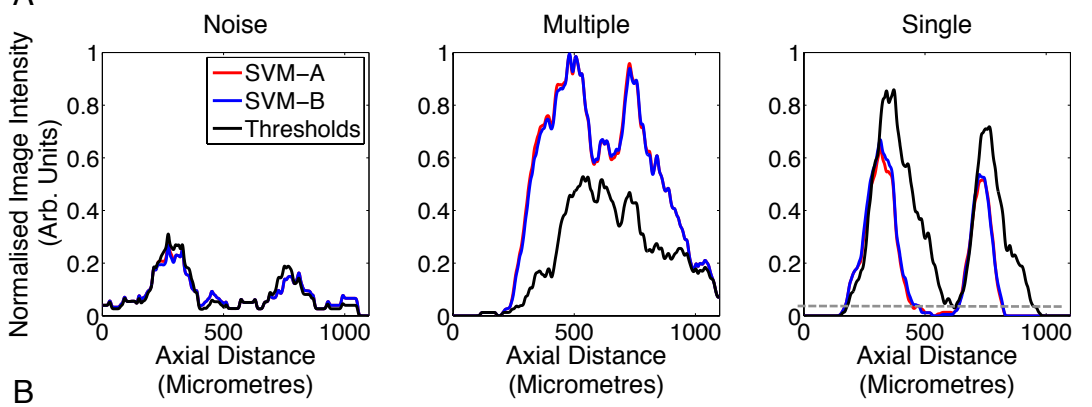

B

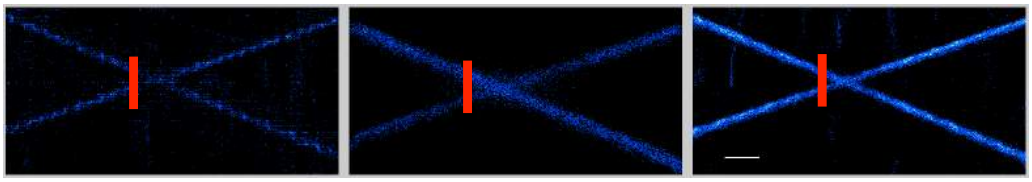

C

Single (μm)	SVM-A	SVM-B	Thresholds
FWHM 1	129	131	181
FWHM 2	100	96	126
S1	305	306	450
S2	212	212	352

Figure 6.17. (A) Average vertical intensity profiles across a 200 μm section of C3 images demonstrated by the red lines in (B), for SVM using two training sets, and thresholding. Profiles were smoothed with a window size of 75 μm (see Chapter 3). The image in (B) was produced using thresholding, shown in Figure 6.10. The table in (C) displays the FWHMs in micrometres of both tube profiles seen in the single bubble localisation image. S1 and S2 are the spatial extents of the profiles, measured as the profile widths at the estimated background level of 0.04 AU (dotted line in graph). Two independent libraries can be observed to result in almost identical profiles, FWHM values and spatial extents.

The intensity profiles of the images, normalised to the maximum amplitude of all techniques (Figure 6.17), display considerably narrower profiles for both SVM single bubble results to that obtained via thresholding. Additionally the spatial coverage of localisations using SVM is more similar to the nominal diameter of the tubes (200 μm); this can be observed in spatial extent values, S1 = 305 μm and S2 = 212 μm (Figure 6.17B, SVM-A), measured as the width of the profiles above the estimated background level (dotted line on the graph at 0.04 AU). The additional localisations seen in the thresholding results broaden the image profiles below the presumed tube positions,

while the profile remains the same at the upper edge (increasing axial direction corresponds to increasing depth). The RMSE of S1 and S2 to the nominal diameter of the tube using SVM-B was 75.4 μm, while for thresholding was 206.9 μm. This has also been observed previously in Chapter 3, where larger and more intense bubble signals were detected predominantly in the lower regions, and were shown to provide localisations outside of the assumed tube dimensions. SVM succeeds in differentiating many of these signals from those which lie within the tube diameter. Furthermore, two completely independent libraries result in almost identical profiles, and subsequently FWHMs and spatial extents. Thresholding resulted in a comparable number of presumed 'noise' localisations to those found using SVM (17510 compared to 16351 and 16106 respectively in Table 6.3), and a similar structure can be observed in both intensity profiles (Figure 6.17A, left). The structure seen within the 'noise' class for both techniques suggests some misclassification of bubble signals assumed to be representative of noise. Multiple bubble profiles show a considerable spread of localisations outside the tube diameters where the two vessel structures cannot be resolved (Figure 6.17A, centre), indicating inaccuracies in the localisation of these bubble signals.

In vivo SVM results displayed in Figure 6.18 also show strong similarities between different training sets. Furthermore, the clusters appear qualitatively more well defined to those obtained using GMM or k-means clustering. Here, the noise clusters have localisations spread over the entire image with little observable structure, while the single bubble cluster reveals a qualitatively similar structure to that seen in Chapter 4, and additionally to thresholding results shown in Figure 6.11. The number of localisations classified as single bubbles is lower than that found in thresholding results (Table 6.4), which can also be observed in average profiles (Figure 6.18C) taken through the vessel shown in Figure 6.18B. A similar trend was previously observed in the *in vitro* experiments. Localisations found within the multiple bubble class show dominance within larger vessel structures and junctions.

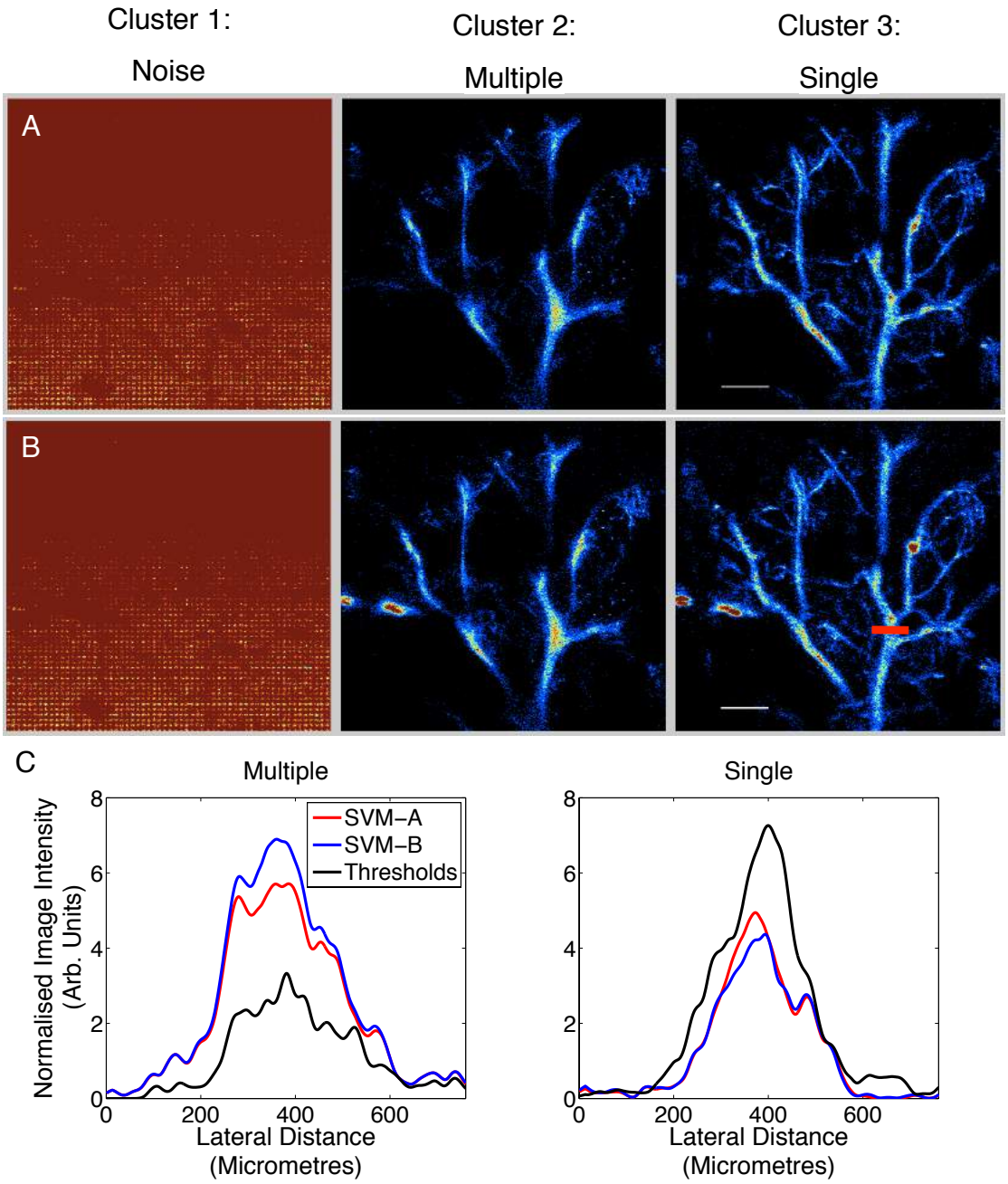

Figure 6.18. *In vivo* SVM results using three classes. Figures in (A) display the three clusters found from the first training set labelled by observer 1 (SVM-A), and (B) from observer 2 (SVM-B). Scale bar 1 mm. Graphs in (C) show average profiles taken through the vessel shown with red line in (B, cluster 3) for both observers and thresholding.

	SVM-A	SVM-B	Thresholds
Single	0.4%	0.6%	0.8%
Multiple	0.2%	0.5%	0.1%
Noise	99.4%	98.9%	99.1%

Table 6.4. Number of localisations classified for the SVM classification algorithm for training set A and training set B, compared to thresholding technique for *in vivo* experiment.

Following these promising results in the differentiation of foreground signals, and in light of the fact that both users noticed two types of 'multiple' bubble signals in the process of creating the training sets, it was further investigated whether it was possible to differentiate subtypes of multiple signals. When 'multiple' bubbles are in close proximity of each other, localisation may become inaccurate because their signals overlap or interfere, thus a single localisation will be found in the presence of multiple bubbles. Here, this situation can be distinguished into two separate instances: microbubble signals which are close enough to be detected as a single region in the foreground, while each underlying signal may be visually identified by the presence of more than one peak; these signals are termed 'separable' bubble signals. Bubble signals which overlap extensively, such that identification of more than one underlying signal is not possible, are termed 'overlapping' bubble signals. Both signal types may present various challenges to the super-resolution algorithm. Separable bubbles, due to the large spatial extent of the signals and the likelihood that centroid calculations will find a point between the underlying signals, may result in large inaccuracies, in particular in the case of branching or parallel vessels. Overlapping bubbles, which are visually more similar to single bubble signals, present challenges due to the inability to separate the multiple underlying scatterers and the potential for interference effects which may be present when bubbles are in such proximity. The differentiation of 'separable' and 'overlapping' bubbles therefore may be important in super-resolution imaging. As the previous multiple bubble category consisted of only separable bubbles, both observers were therefore additionally tasked to find 25 instances of cases where bubbles were overlapping.

Data were subsequently classified into four signal classes (Figure 6.19). The separable bubble clusters (Figure 6.19A and B, cluster 2) appear to consist of localisations

principally in areas dominated by what appears to be larger vessels (larger spatial extent with a higher number of localisations) and at junctions of branching vessels. The localisations in these areas show a wider spread and do not present the same edge definition to those seen in the single bubble clusters (Figure 6.19A and B, cluster 4), as can be observed in the profiles in Figure 6.19C.

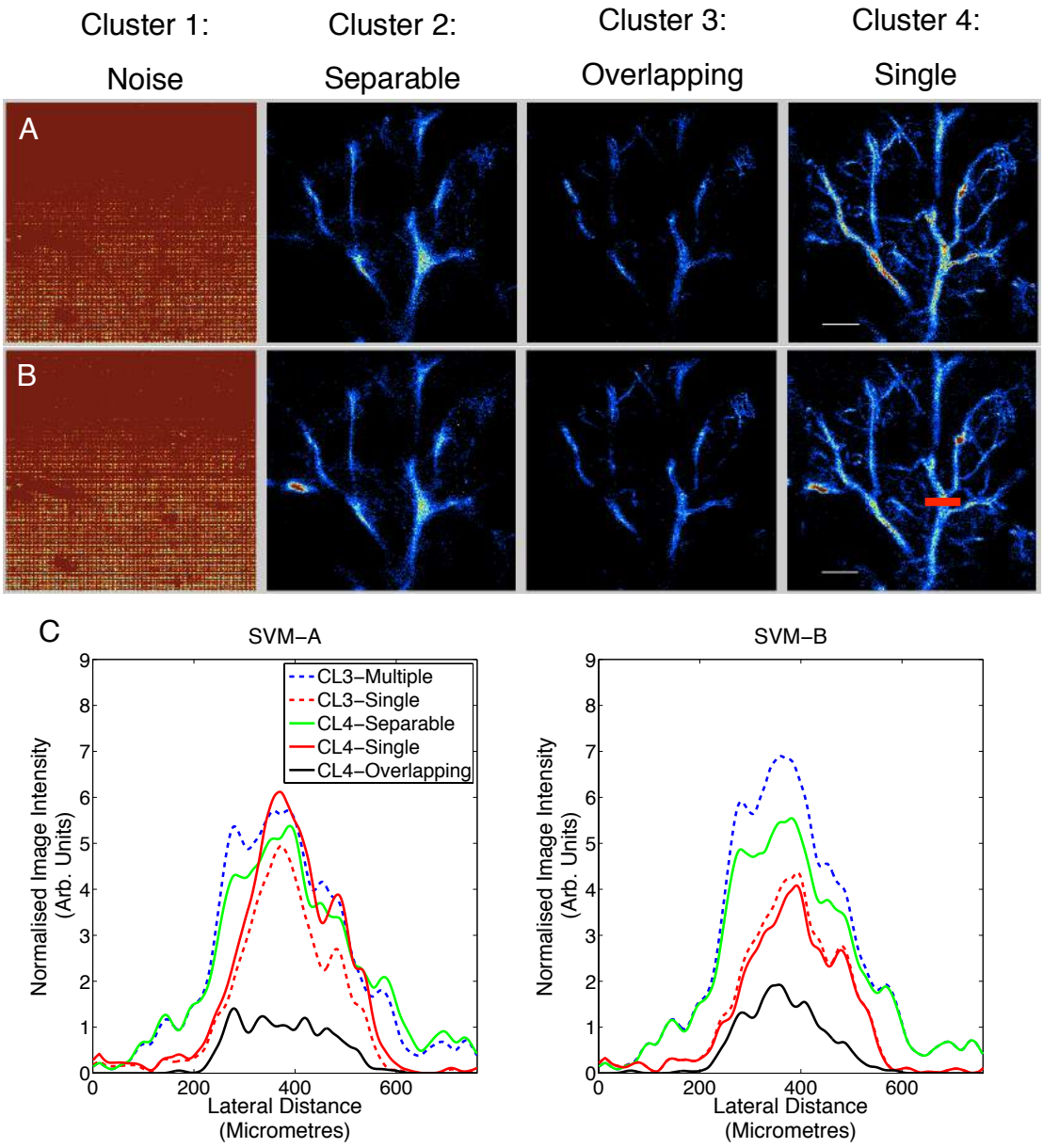

Figure 6.19. *In vivo* SVM results using four classes. Figures in (A) display the four clusters found from the first training set labelled by observer 1 (SVM-A), and (B) from observer 2 (SVM-B). for each training set are displayed in each row. Scale bar 1 mm. The graph in (C) displays the profiles through the same vessel structure shown in Figure 6.18 for three classes (multiple and single, dashed lines) along with the equivalent profiles for separable, overlapping, and single signals for four classification groups.

Similarly, the overlapping signal clusters show a prevalence of localisations at junctions and larger vessels (Figure 6.19A and B, cluster 3), however, in this case, their positions appear to remain within the apparent vessel structure as defined by the single bubble profiles (Figure 6.19C). The large majority of localisations classified as multiple bubble signals in the original results (CL3-Multiple) appear to be identified as separable signals in the four class implementation (CL4-Separable) indicated by the similarity of their profiles in Figure 6.19C. The centre of mass of separable, but spatially connected, signals is likely to exist between the individual bubble positions, this may be a cause of the spreading of localisations seen with these signal types observed in Figure 6.19C: CL4 - Separable, while overlapping signals may be more likely to provide centroids which do not differ significantly from those of a single bubble which may be due to the overlapping signals having a smaller spatial extent than those which are separable. However, effects such as interference may occur due to the presence of multiple scatterers within the resolution cell. In the presence of such events the estimated localisation point could be disturbed to an extent where the difference between overlapping and single bubbles can no longer be ignored.

6.7 DISCUSSION

K-means clustering requires the data to consist of approximately equal cluster sizes to accurately learn the data structure. The presented results, however, indicate that the data in this application does not fulfil this requirement, which may lead to the unsuitable results in signal classification. In contrast, GMM does not necessitate clusters to be of equal size and allows every data point to have a probability of being assigned to a number of Gaussian distributions. It requires, however, that the data or extracted features follow Gaussian distributions in parameter space, which cannot be guaranteed in this setting. Therefore both kmeans and GMM do not show potential for adequate differentiation of signal types in this investigation. When transitioning from unsupervised to supervised, a training set must be created, relying upon the participation of an expert or experienced user. The algorithm then learns from this set of initial data to subsequently perform classification. In contrast to unsupervised approaches, SVM provided good qualitative and quantitative results for signal classification, for both *in vitro* and *in vivo* datasets, and demonstrated better performance compared to thresholding, when applied to phantoms with a known vessel diameter. In comparison

to thresholding, the line profiles through resulting single bubble images using SVM displayed a more well defined outline, and furthermore enabled the identification of an additional signal type (overlapping bubbles) which would be a challenge using thresholding. Separable signals have the potential to be further processed to extract individual bubble information rather than being rejected or incorrectly localised in super-resolution algorithms. Identifying this signal type would therefore enable higher data recall for improved localisation efficiency.

Superpixel segmentation has been demonstrated to vary considerably with different bubble concentrations between C1-C3, where a large number of candidate regions belong to noise signals. This is most likely due to empty frames. In the case of an empty frame, the superpixelation will still attempt to create two superpixels by grouping together image pixels based on k-means clustering, and thus will cluster small regions of similar intensities within the images, which would then belong to noise. This can cause challenges for low concentration experiments, where a high number of empty frames can be expected; this work utilised the previous and following frame to improve the superpixel segmentation and reduce empty frame artefacts. Including more frames before and after the one which is segmented might further improve the utility of this approach in case of low concentration cases, as more data will be used to learn foreground and background. The majority of *in vivo* data frames, however, contained single, and in most cases many bubble signals. Therefore the effect of empty frames was negligible, not necessitating the inclusion of additional dynamic information. Application of superpixel segmentation required the definition of two "parameters", the number of superpixels and the compactness ratio. Here superpixilation is used to separate foreground and background, meaning that the number of superpixels is constant and set as two. The compactness ratio must be defined empirically. However, as shown in Section 6.6.1 investigations showed that this parameter produced stable results across a large range of settings. Additionally, visual assessment over a variety of imaging targets and US scanning parameters suggested that this parameter is stable with respect to such variations as well and therefore does not introduce significant user dependence.

From previous work, regions which appear to contain a considerable number of multiple

bubble signals correlate with structures where multiple vessels exist in close proximity, for example at a branching junction or a coupling of vessels which most likely represent arterioles and venuoles. This can be seen in the *in-vitro* high concentration k-means and SVM results, where an increased number of multiple bubble signals are detected in the region around the centre of the tube. Furthermore, there is a decrease in the single bubble localisation number within this region. This indicates that the proximity of the vessel structures in this area causes a decrease in the likelihood of detecting spatially isolated bubble signals.

In this application, data was considered to consist of noise, single bubbles and signals from more than one bubble. However, there may be a number of other signals present in the data, such as interference patterns, signals resulting from constructive and destructive interference of signals, or ringing effects caused by the continuing oscillation of a bubble at the resonance frequency after the oscillations due to the incident pulse having stopped [104]. Additionally, tissue breakthrough in CEUS imaging modes due to nonlinear propagation could be present and thus may make the classification process more challenging. These additional signals could mean data driven classification becomes less accurate since the predefined number of classes becomes unknown. SVM could address this by manually labelling additional signal classes, however, the increased amount of manual labour with possibly very large number of classes makes this approach difficult, or possibly unfeasible, to implement. However, this would also present a challenge in signal classification using thresholding. The results presented here suggest that these effects may be minor within the experimental models tested here, but should be of consideration for further work.

The presence of localisations within the tube location in SVM noise labelled clusters implies some misclassification of bubble signals assumed to be representative of noise. Weak bubble signals could occur when the vessel is positioned on the edge of the elevational field of view, where the amplitude of signals tails off significantly. These low intensity signals may be more similar to noise and hence wrongly classified. Alternatively, damped responses from bubbles which are close to the tube wall, or bubbles which are off-resonance may also be classed as noise. Including such bubble signals in the training data set may cause noise to be misclassified as single bubble

signals. It is important (in particular in a clinical setting) for super-resolved images to exclude false positives, i.e. noise being classified as single bubble signals, which may result in increased rejection of weak bubble signals. The corresponding trade-off between acquisition time and image SNR should be considered and needs to be guided by the application.

The investigation of alternative echo features than those used in this approach will influence the performance of the results. Preliminary investigation was performed in this study in order to identify features which showed the best potential, however, in the future, a full analysis may further enhance the potential of these techniques.

6.8 CONCLUSION

The presence of multiple bubble signals which are not spatially separated may introduce higher uncertainties in the centroid position due to interference. This reduces the efficacy of super-resolved US imaging. Differentiation of these sources are therefore vital for accuracy of the technique. In addition fully or close to automated processing of the data would drastically increase the clinical viability of acoustic super-resolution.

When analysing data, the first step is the separation of the foreground from the background. Superpixel foreground segmentation allowed close to automated image segmentation. The benefit of this technique, over the commonly used simple intensity thresholding, lies in the fact that superpixelation tries to segment an image into ‘meaningful’ regions and does not involve significant user dependence. In addition, this approach can easily include temporal information, which is a natural extension in the setting of an imaging system that acquires data over time. Superpixelation in combination with SVM classification demonstrated quantitatively improved results for phantom experiments (reduced spatial extent RMSE to the nominal tube diameter) when compared to thresholding classification.

7 SUPER-RESOLUTION IMAGING IN 3D

7.1 INTRODUCTION AND MOTIVATION

Demonstrations of 2D super-resolution both *in vitro* and *in vivo* in previous chapters have shown that fine vascular structures can be visualised using acoustic single bubble localisation. With the exception of work in Chapter 5, these targets possessed limited complexity in the elevational direction. Visualisation of more complex and disordered 3D vasculature, such as that of a tumour, requires an acquisition strategy which can additionally localise bubbles in the elevational plane with high precision. Two-dimensional matrix array transducers are enabling volumetric, real-time imaging to become a reality. However, without state-of-the-art scanners with full 3D imaging capability, an alternative method of 3D localisation is required. Furthermore, a particular challenge lies in the need to provide this level of visualisation with minimal acquisition time. This chapter therefore aims to address two important challenges of this technique: 1) poor spatial resolution in the elevational plane of the existing 2D imaging

---

Aspects of this work were presented at The IEEE International Ultrasonics Symposium 2015 in Taipei, Taiwan under the title: '3D Super-Resolution Ultrasound using Microbubbles.'

set up, and 2) long acquisition times.

The purpose of this chapter is thus to develop a fast, coherent US imaging tool for microbubble localisation in 3D and provide practical demonstration of its potential and limitations. The importance of this step is not only to enable visualisation of 3D structures at high resolution, but with additional 3D velocity mapping, to eventually allow investigation of the complete flow pattern of blood vessels associated with disease. The capability to measure both structure and flow within the microvasculature at depth *in vivo*, would ultimately enable analysis of microvascular morphology, blood flow dynamics and occlusions resulting from disease states.

Translation to 3D imaging often requires a significant increase in image rendering volume, therefore a faster imaging acquisition strategy than that employed in previous chapters is needed. Furthermore, 3D image rendering places particularly demanding requirements on the quality and completeness of the flow data compared to 2D. This chapter will therefore demonstrate a proof of concept of this new acquisition strategy; areas where improvements in data processing, acquisition protocol and duration are most required to provide sufficient information in the final rendering will be discussed.

7.2 STUDY OUTLINE

Translation of super-resolution to 3D was developed using two programmable US imaging systems (Ultrasound Advanced Open Platform (ULA-OP) systems, University of Florence). As discussed in Chapter 2, in general, it is assumed that the scattering from diagnostic microbubbles is dominated by the active emission of sound due to the change of volume of the scatterers [159], and therefore spherically symmetric. This imaging strategy was designed to exploit the spherical scattering from microbubbles to detect scattering effects in a complementary imaging plane.

Conventional US imaging with line-by-line focused pulses, as used in Chapters 3-6, limits the highest achievable time resolution. The use of ultrasonic plane-wave transmissions enables ultrafast frame rates often over 1000 frames per second, each of which insonify a large field of view with each transmission [189]–[191]. Ultrafast plane wave transmission was therefore implemented and adapted for nonlinear imaging to

recover contrast images. The localisation of a moving object in 3D using only 1D probes requires its coincident detection by multiple probes which are able, together, to localise its position in all three dimensions. The imaging strategy therefore involves the transmission and reception of plane wave contrast pulse sequences from a 1D linear array transducer, with simultaneous detection of scattered signals by a second, orthogonal synchronised system, allowing detection of the same scatterer in the elevational plane. In this way, the systems act as an 'active' and 'passive' probe pair, enabling the combination of complementary localisation information. Coincident scatter events from isolated US microbubble signals were identified and localised in 3D.

Thus, this chapter involves four new imaging features compared to that of Chapters 3-6. These are: (1) the use of a new programmable US system, (2) the compounding of data from multiple synchronised systems, (3) the implementation of contrast plane wave transmission and (4) subsequent RF data extraction and processing. These will be described in more detail in the following sections. The initial performance of this system will be characterised using simple *in vitro* phantoms to determine factors including: background noise and sensitivity, synchronisation parameters and the system's suitability for nonlinear imaging. Next, the diffraction limited resolution, and the estimated 3D localisation precision of the system are examined. Lastly, the chapter ends with demonstration of 3D super-resolution *in vitro* using microbubbles.

7.3i ULTRASOUND IMAGING EQUIPMENT AND SET-UP

7.3i.1 ULA-OP SYSTEM

The ULA-OP system (MSD Lab, University of Florence, Italy) is an open platform, programmable US imaging system with 64 independent arbitrary waveform generators able to simultaneously control up to 64 elements of a number of different element array probes [331]. This is integrated in separate analogue and digital boards within the system, as illustrated in Figure 7.1. The ULA-OP system allows programming of user-defined pulse sequences. These include definition of acquisition sequencing, data storage and save parameters, and real-time window display settings. Generation of transmit and receive beams includes the definition of scanning sequences, aperture size, beamforming, focusing and apodisation settings.

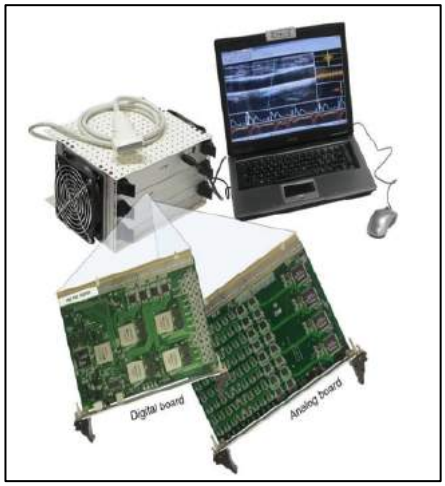

Figure 7.1. ULA-OP System. Image reproduced with permission from [331]

One major feature of the ULA-OP system is the wide availability of raw data [331]. Figure 7.2 displays the flowchart of received raw data, illustrating the key stages of data extraction, for pre-beamformed RF data, post-beamformed RF data, I/Q data and image data. ULA-OP incorporates computer data storage devices of 1 GB and 256 MB which are managed like circular buffers. The larger buffer is reserved for pre-beamformed RF data, consisting of 12-bit sample streams at a rate of 50 MHz (Figure 7.2A) [331]. The second buffer is used for RF beamformed and/or baseband data, illustrated in Figure 7.2B and C respectively. The preceding data accumulated in the circular buffers can be downloaded to a PC file at any point during acquisition. A further saving option concerns typically video data (Figure 7.2D).

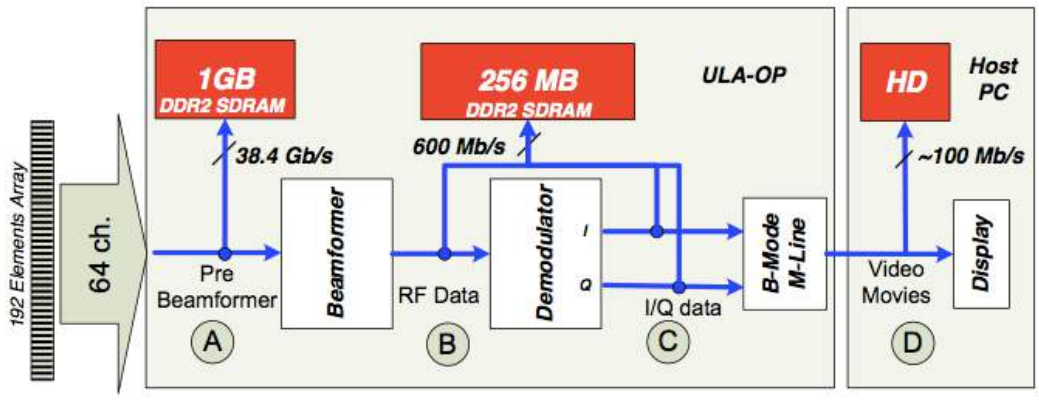

Figure 7.2. Data access schematic. The data are saved as pre-beamformed 8 or 12 bit (A), post-beamformed 16 bit (B), or 24 bit I/Q data (C). Video data is also available, encoded at 8 bits/pixel. Image reproduced with permission from [331].

7.3i.2 IMAGING TRANSDUCERS

Two imaging probes were used in this chapter. The LA533 linear array probe has a 6 dB bandwidth ranging from 3 MHz to 13 MHz (Esaote, Firenze, Italy) and is made of 192 elements, with pitch equal to 0.245 mm. The ULAOP system was also used to drive the LA332 imaging transducer. This 144 element linear array probe has a 6 dB bandwidth ranging from 2 MHz to 7.5 MHz bandwidth and a 0.254 mm pitch. The impulse response and bandwidth of both probes are shown in Figure 7.3. Experimental settings parameters will be defined for each of the following experiments in this chapter.

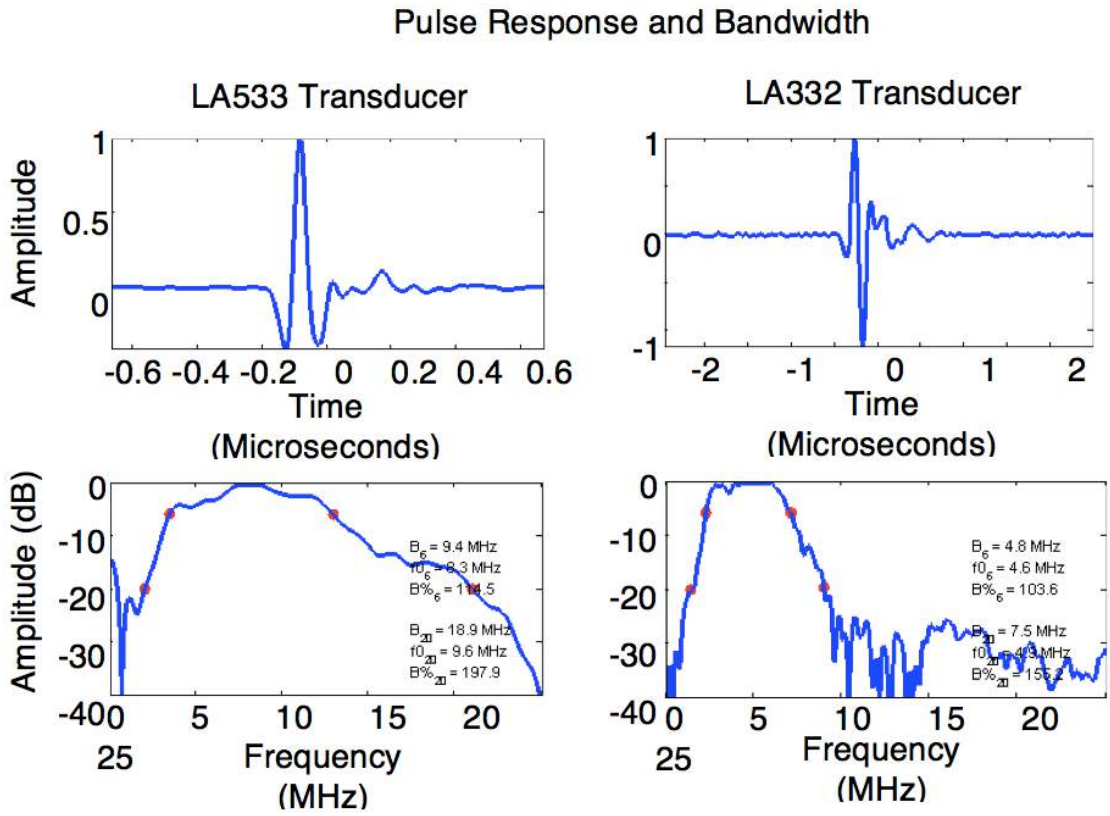

Figure 7.3. Pulse response and bandwidth of LA533 and LA332 probes. Images obtained from ULAOP PC software.

7.3i.3 EXPERIMENTAL EQUIPMENT DESIGN

In order to provide positional accuracy in the imaging set-up, custom-made probe holders were designed. A surface model was created by scanning a single linear array probe using a pre-clincal CT scanner. This model was then segmented and used to create two 3D printed probe holders with perpendicular fixings for accurate

perpendicular or parallel positioning within the experimental set-up. Figure 7.4 demonstrates the use of these probe holders in a simple example set-up. Note: the set-up in Figure 7.4 has been positioned for visualisation and differs from the configuration used in experiments.

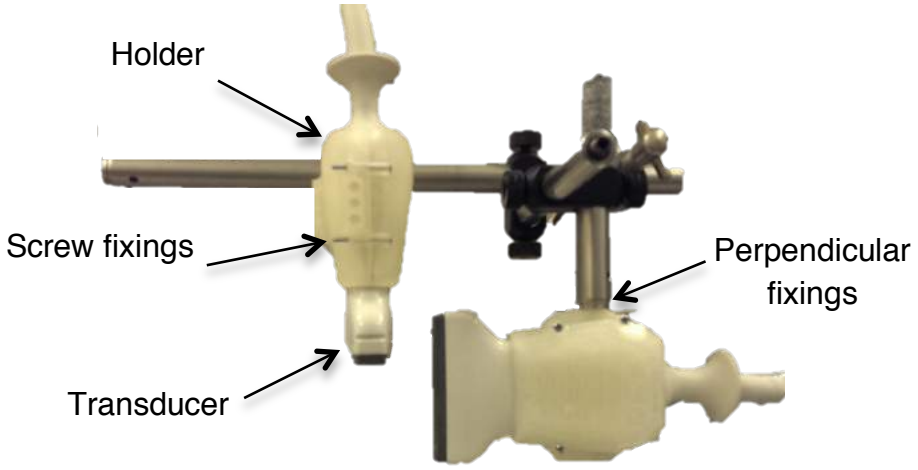

Figure 7.4. Photo of orthogonally positioned transducers and 3D printed holders. Inbuilt fixings within holders enable perpendicular/parallel placement of transducers within experimental set-up.

7.3i.4 PHANTOM CONSTRUCTION

A common issue regarding US phantom development is the rapid degradation of the material, rendering many unsuitable for repeated use. Furthermore the opaqueness often associated with phantom materials such as agar, means that optical validation is difficult. Phantoms developed for 3D US imaging were constructed using medium density paraffin gel wax in order to suspend a point scatterer in 3D space. These phantoms allow transducer positioning without the need to submerge the imaging probes deep into water. This gel is a transparent and soft compound and has the advantage over other phantom materials of longevity [332]. It does not suffer dehydration and therefore is relatively structurally stable over time; phantoms were left for months without degradation. Furthermore, this material is translucent which enables visual assessment of targets, and the potential for optical validation with a microscope.

To create the phantom, firstly, paraffin gel wax was placed into a mould using sterile

gloves in a clean environment to limit the possibility of small fragments and dust particles embedding in the phantom. Rectangular and circular silicone moulds were used to create the phantoms. This allowed easy removal of the phantoms from the mould after melting and subsequent cooling. In order to create small linear scatterers within the phantom, small air bubbles were injected into the paraffin gel wax approximately 10 minutes after removing the phantom from the oven using a micro-pipette. The bubble injection must occur within a time frame that the temperature is high enough to allow re-moulding of the gel after removal of the pipette, while the viscosity is high enough for the bubble to be stable within the gel so as not to float to the top. Optical images of air bubble within the phantom were then acquired using a microscope, see example image Figure 7.5, where this air bubble was estimated to have a diameter of 133 μm.

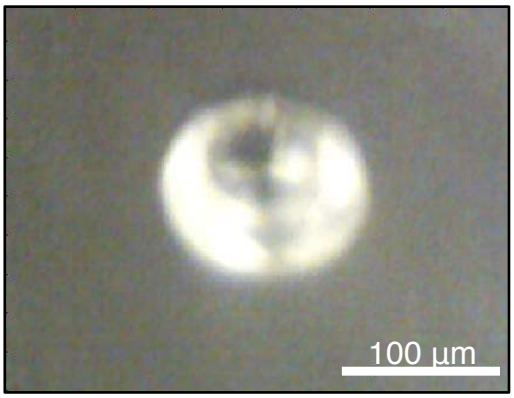

Figure 7.5. Example optical image of air bubble in paraffin gel phantom estimated to have a diameter of 133 μm.

Further phantoms were created in which cellulose tubes were instead embedded into the paraffin after approximately 10 minutes of cooling time, and were held in position until the phantom was stiff enough to hold the tube in place. These were then trimmed and inserted into 25G butterfly winged infusion needles at either end. An epoxy resin was used to secure the connections between the tubes and the needles.

The speed of sound within the phantom was estimated by using a simple reflection substitution technique [16,17]. Ten single cycle, 3 MHz plane wave transmit pulses were sent with and without the phantom sample between a pulse-echo transducer and a

plane reflector, as illustrated in Figure 7.6.

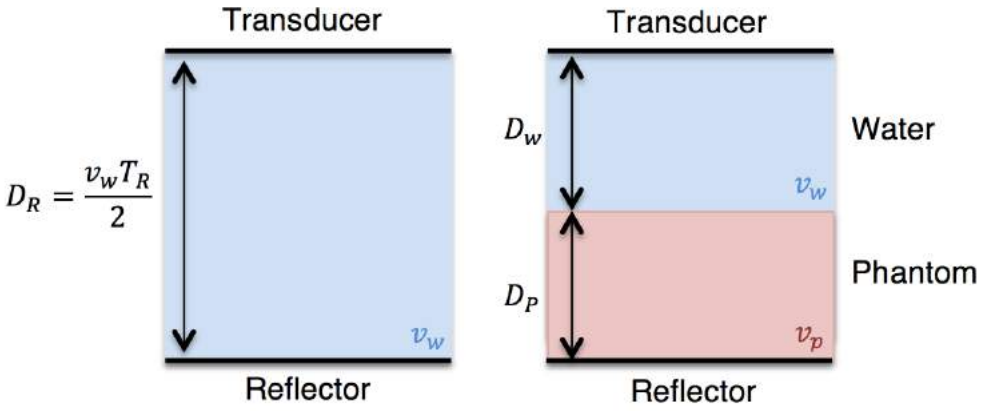

Figure 7.6. Schematic illustration of the reflection substitution technique used to calculate the speed of sound within the phantom material. (A) shows a pulse echo experiment set up in a water bath, where D_R is the distance to the reflector surface, T_R is the backscatter time after pulse transmission and v_w is the velocity of sound in water. (B) displays the substitution of the phantom material within an identical set-up, where D_P and D_w are the distances the sound travels through the phantom material and the water respectively.

The backscatter time through the phantom set-up is given by

$$T = \frac{2D_w}{v_w} + \frac{2D_P}{v_p}, \tag{7.1}$$

$$v_p = \frac{2D_p}{T - \frac{2(D_R - D_p)}{v_w}}, \tag{7.2}$$

where D_R is the distance to the reflector surface, T_R is the backscatter time after pulse transmission, and D_P and D_w are the distances the sound travels through the phantom material and the water respectively. Assuming an ultrasonic velocity in water, v_w, of 1488 m/s at 22°C, Equation (7.2) was then used to estimate a speed of sound in the phantom, v_p, of 1425 ± 3 m/s, which corresponded to values found in literature [332].

7.3i.5 US IMAGING CONFIGURATION

The proposed technique relies upon the detection of signals from spherical scattering of US waves from gas-filled microbubbles using two 2D linear array probes. One system is programmed to operate as a transmitting and receiving US imaging device, termed here an 'active' transducer, with the second running as a 'passive' detector that is temporally synchronised to the first. Utilising an active transducer, and a separate angled passive transducer allows detection of off-axis scattered energy in a complimentary imaging plane. A pulse of US is emitted from the active transducer and insonates a low concentration of microbubbles. If the path of the emitted pulse insonifies a bubble which lies within the imaging plane of the passive imaging transducer, then sufficient information can be obtained to localise the bubble in 3D space. The region defined by the overlapping imaging planes therefore determines the field of view in which 3D localisation is possible, as illustrated in Figure 7.7.

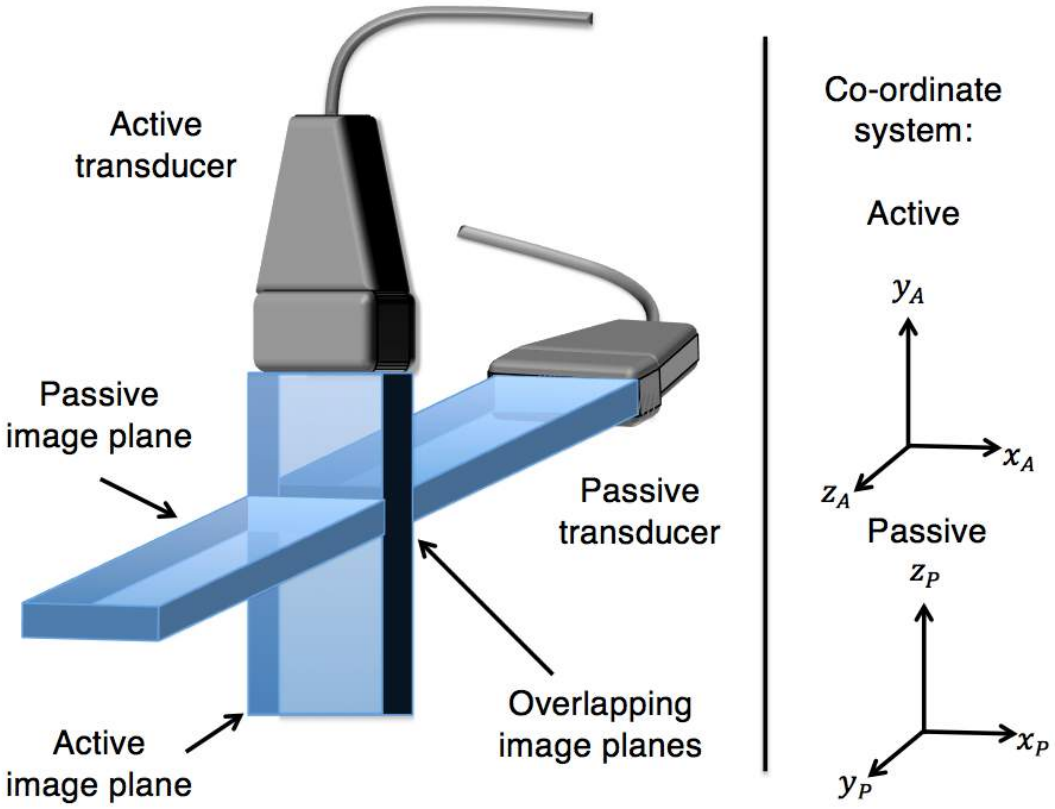

Figure 7.7. Illustration of active and passive transducer configuration when orthogonally positioned. The region defined by the overlapping imaging planes therefore determines the field of view in which 3D localisation is possible. Independent co-ordinate systems are displayed on the right hand side.

Provided that temporal synchronisation of the two imaging systems is achieved, the time of arrival of echoes from moving bubbles recorded at both transducers can be used to locate an object from non-focused US waves. The time before scattered signals arrive at the passive imaging transducer depends on the length of the acoustic path taken (and any system delays due to synchronisation – this will be considered further in section 7.3ii.3). This path length can be estimated by assuming a constant speed of sound in the medium of interest and measuring the time interval between emission and detection of the pulse.

A point-like scatterer positioned at $r_s = (x_s, y_s, z_s)$ will scatter US energy radially assuming a monopole scattering behaviour. If r_i and r_j are the locations of the active and passive transducers T_i and T_j respectively, as illustrated in Figure 7.8, then the arrival times of the echoes from a scatterer within the overlapping imaging region are

$$t_{si} = \frac{2|r_s - r_i|}{c} \tag{7.3}$$

$$t_{sj} = \frac{|r_s - r_i|}{c} + \frac{|r_s - r_j|}{c} \tag{7.4}$$

where c is the speed of sound travelling within the scattering medium. The use of 1D array transducers will provide visualisation of the scatterer in a 2D image plane. Therefore, transducer T_i will enable measurement of coordinates (x_s, y_s) (see co-ordinate system in Figure 7.7). In this conventional imaging system, coordinate z_s can be localised only to within the elevational resolution of the system, which in this case is estimated to be over 1 mm for a 3 MHz 3 cycle pulse (see Section 7.3ii.4). Positioning transducer T_j orthogonally, or at an angle, to T_i allows in plane measurement of (y_s, z_s) or (x_s, z_s), depending on the transducer configuration. Coordinate z_s can be localised to within the axial (as in the case shown in Figure 7.7) or lateral precision of the imaging system, depending on the relative orientations of the transducers, thus enabling higher precision localisation within the elevational imaging plane of transducer T_i. If the point

target is detected in both systems simultaneously, the coordinate y_s can be measured by both transducers, providing a point of registration for the imaging systems.

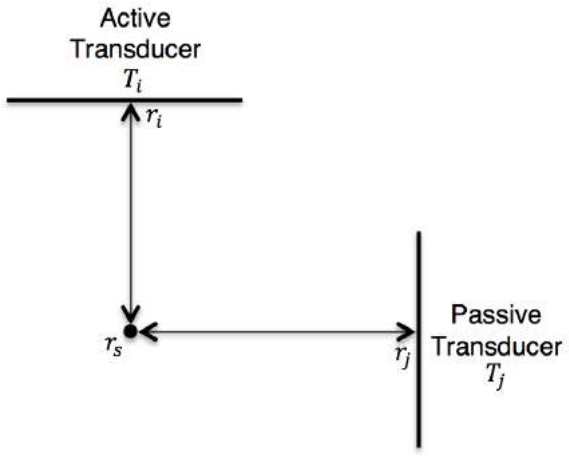

Figure 7.8. Schematic diagram of experimental set-up, where r_s is the position of the point scatterer, and T_i and T_j and the active and passive transducers, positioned at r_i and r_j respectively.

7.3ii ULTRASOUND SYSTEM CHARACTERISATION

In vitro experiments were performed to characterise the ULA-OP system. These will be presented in the following sections as a series of mini investigations. Firstly, the background noise and sensitivity of the system was investigated. Secondly, since the imaging of US contrast agents required implementation of nonlinear imaging strategies, user defined pulsing strategies were developed for use in following *in vitro* microbubble experiments. This involved testing the non-linearity of the system while imaging both linear and non-linear targets with various transmission pulses. Lastly, delays associated with synchronisation of the imaging systems were examined.

7.3ii.1 ELEMENT SENSITIVITY

7.3ii.1.1 AIM

To perform experiments to assess the element or channel sensitivity.

7.3ii.1.2 METHOD

Imaging was performed using two LA533 probes at a frequency of 6 MHz. Plane wave pulse transmission was generated on the central 64 array elements. Here, each LA533

imaging transducer was placed in a beaker of gas-equilibrated water with no target in the field of view in order to visualise variation in background signal. The two parameters investigated were the uniform gain applied, denoted *G* (in dB), and the time gain compensation (TGC) (dB/cm) with values given in Table 7.1. When employed, uniform gain was set to G = 15 dB, TGC was set to TGC = 9 dB/cm. Three measurements were performed by interchanging two ULA-OP systems and two identical transducers in order to investigate the source of variation due to gain related parameters.

Measurement	System 1		System 2	
	Transducer 1	Transducer 2	Transducer 1	Transducer 2
1	Uniform Gain & TGC	Uniform Gain & TGC	Uniform Gain & TGC	Uniform Gain & TGC
2	Uniform Gain	Uniform Gain	Uniform Gain	Uniform Gain
3	No Gain	No Gain	No Gain	No Gain

Table 7.1. Characterisation experiment parameters used to investigate the variation in element/channel sensitivity of the ULA-OP system. If employed, uniform gain was set to G = 15 dB, TGC was set to TGC = 9 dB/cm.

7.3ii.1.3 Results and Discussion

Experimental results performed to assess the variation in RF background signals are shown in Figure 7.9. A variation in amplitude between adjacent element lines was observed in all experimental results. Background intensity variations across RF image lines was observed to be characteristic of each ULA-OP imaging system, rather than the transducer array, as demonstrated by the comparison of system 1 and system 2, where

background signal patterns remain largely the same with interchanging transducer probes.

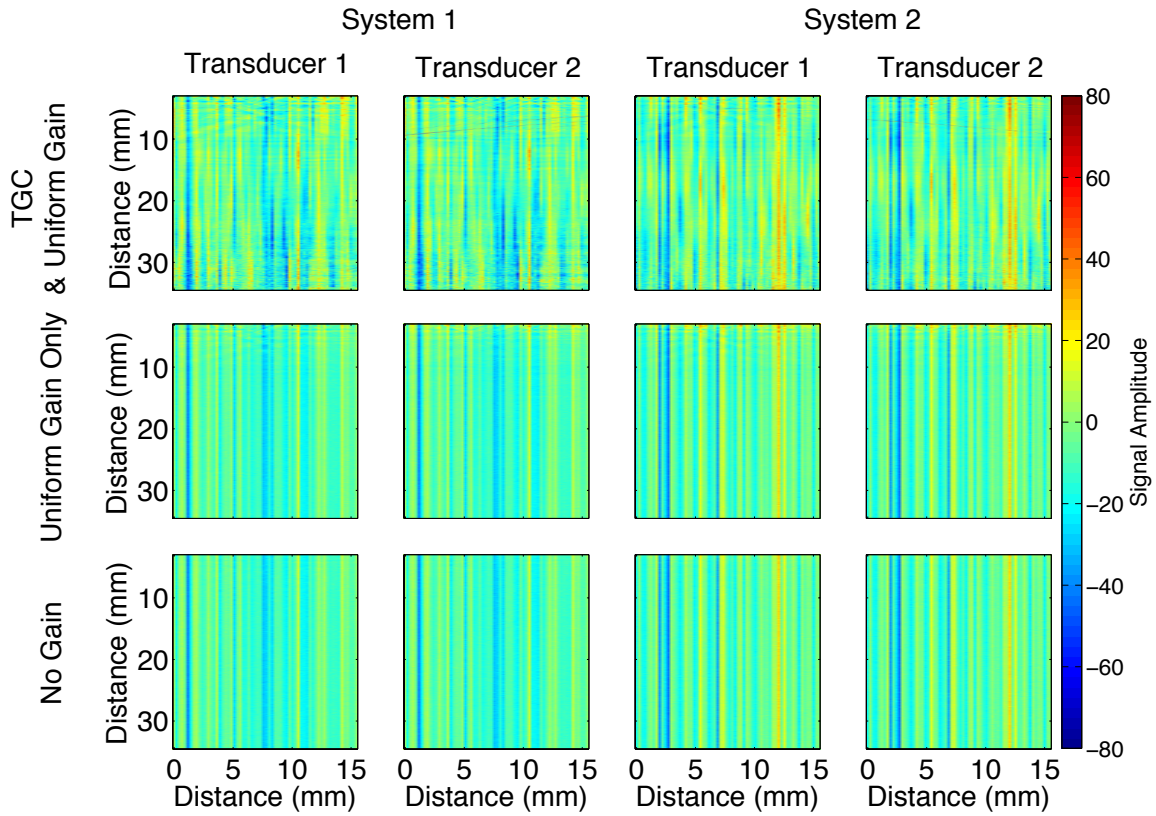

Figure 7.9. Experimental results investigating the source of variations in background image intensity by imaging a gas-equilibrated water bath for visualisation of background signal variation. Background intensity variations across RF image lines show the affect of alternating between two systems and two transducers, as well as the affect of uniform gain and Time Gain Compensation (TGC). Intensity variations appear to be system dependent, and become vertically uniform in the absence of TGC.

Additionally, this can be seen in the line profiles shown in Figure 7.10, where small variations in signals between transducer 1 and 2 using the same system are assumed to be caused by system noise. Furthermore, TGC causes a vertical variation in background intensity, while uniform amplitude gain appears to cause little or no change in background signal. Intensity variations therefore appear to be system dependent rather than transducer dependent and caused by a characteristic channel DC offset. This could be caused by variations in the material and/or manufacturing of each individual element. These variations become vertically uniform in the absence of TGC.

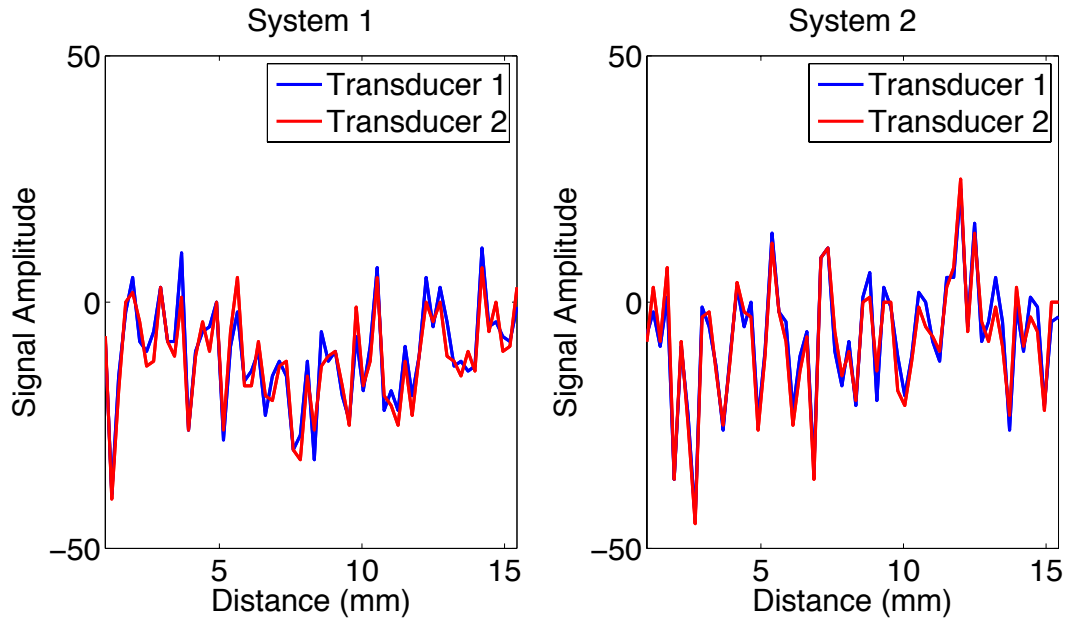

Figure 7.10. Horizontal line profiles at 20 mm across received RF data from plane wave transmission in a gas equilibrated water bath with no TGC or uniform gain. This was performed to assess background signal variation across channels using two ULA-OP imaging systems and interchanging imaging transducers. Background signal patterns remain largely the same with interchanging transducer probes, where small variations in signals between transducer 1 and 2 using the same system are assumed to be caused by system noise.

Quantisation errors caused by analogue-to-digital conversion meant that noise present in RF data had a variation for each element line over 3 quantisation levels, as shown in Figure 7.11. If it is assumed the noise is Gaussian with zero-mean, the mean value of each RF data line is representative of the underlying channel sensitivity offset. This can be visualised in RF data lines from backscatter signals after plane wave transmission to a point scatterer shown in Figure 7.12A. Corresponding mean values are displayed with dotted lines in the figure, where a clear channel offset is visible. Resulting signals after mean subtraction can be seen in Figure 7.12B, showing removal of the individual channel offsets.

7.3ii.1.4 Summary and Comments for Future Work

In all subsequent experiments, each RF line was zero-centred by subtraction of its mean as an initial post-processing step.

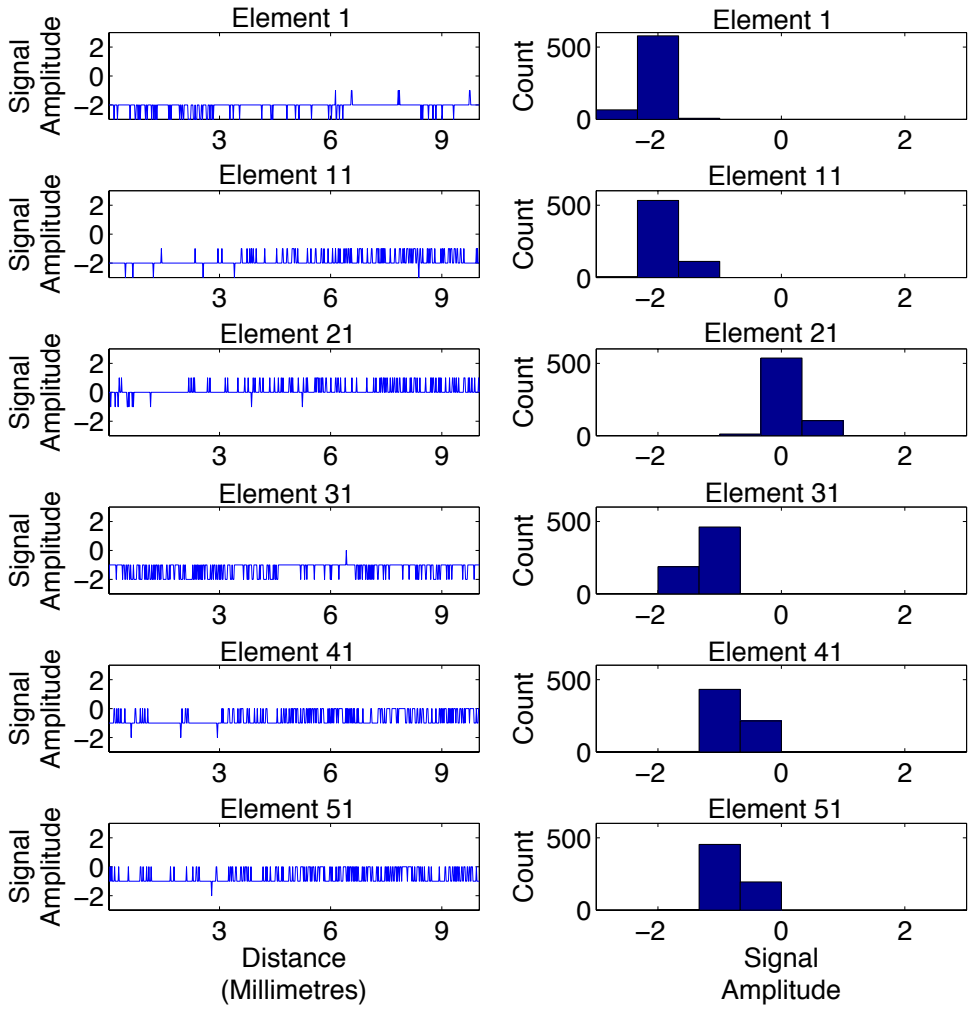

Figure 7.11. Line profiles and corresponding histograms along every 10th element across the aperture of our control experiment.

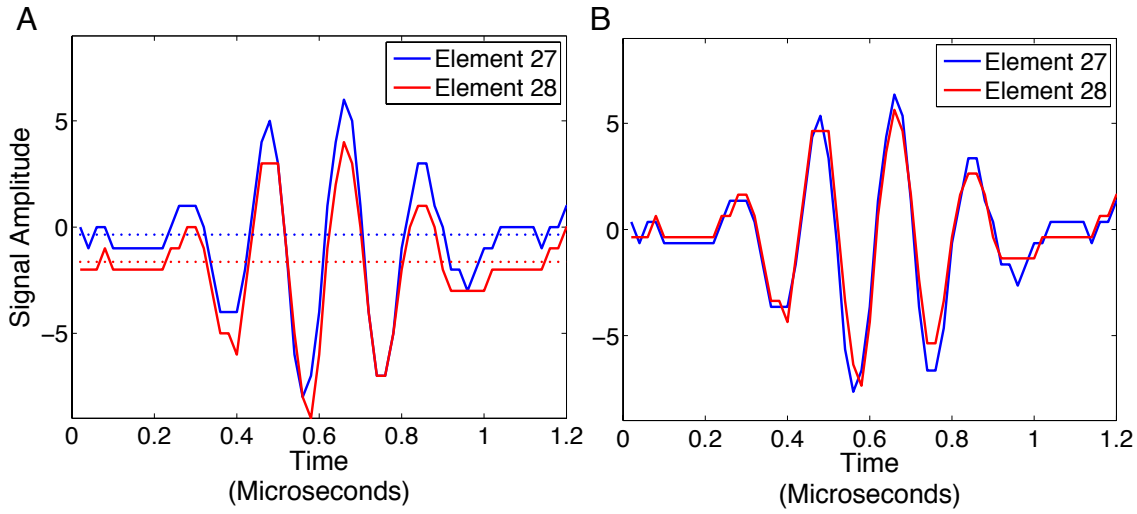

Figure 7.12. RF data lines after plane wave imaging of a point scatterer using no TGC and no uniform gain. (A) displays example RF line profiles through adjacent element channels, where mean values are displayed with dotted lines. (B) displays resulting profiles after mean subtraction.

7.3ii.2 NONLINEAR PLANE WAVE IMAGING AND CHARACTERISATION OF NONLINEARITY

7.3ii.2.1 AIM

To develop and program plane wave, contrast imaging strategies for use with the ULAOP system which can effectively suppress linear scatterers.

7.3ii.2.2 METHOD

Nonlinear plane wave strategies allow fast US imaging of microbubbles through adaptation of contrast imaging techniques such as pulse inversion (PI), amplitude modulation (AM) and associated combinations such as pulse inversion amplitude modulation (PIAM) as discussed in Chapter 1. The non-linearity of the system was explored using plane wave contrast strategies on both linear and nonlinear targets; this was to ensure suppression of signals coming from tissues and other predominantly linear scatterers even at the maximum transmit amplitude of the system was achieved, while signals received from nonlinear targets were enhanced. This also allowed determination of the desired transmit settings for the subsequent *in vitro* experiments involving microbubbles.

A linear imaging target 133 μm in diameter was prepared within a paraffin phantom as discussed in Section 7.3i.4. Its linearity was corroborated by visually checking its suppression using a conventional clinical scanner in CE imaging mode. An LA533 transducer was positioned touching the phantom and coupled with US gel, where the linear target was approximately 12.6 mm from the transducer surface. Additionally, a beaker containing a low concentration of SonoVue™ microbubbles (10 μl SonoVue™ /60 ml water) was prepared as the non-linear imaging target.

The ULA-OP system was programmed to transmit four different imaging pulses in succession. These consisted of a full amplitude wave of zero phase, followed by a full amplitude wave of 180° phase in order to perform PI imaging. Additionally, two half amplitude waves of zero phase are transmitted in order to perform AM and PIAM imaging, and as such we can define an imaging strategy with wave amplitudes proportional to $A = \{0.5, 1, -1, 0.5\}$, where 1 is the maximum amplitude available on the system. To test the nonlinearity of the system, the absolute amplitudes of transmit

signals were varied between $0.1A$ to A, in steps of $0.1A$. All imaging pulses involved the transmission of a 3 cycle, 6 MHz wave at a pulse repetition frequency (PRF) of 4000 Hz using no gain. Received pre-beamformed RF data was then saved to process offline using MATLAB.

Methods to extract, combine and process RF plane wave data for contrast imaging are described in the following section. MATLAB code was written to implement B-Mode, PI, AM, and PIAM processing using single angle combinations of the imaging pulse echoes. The peak-to-peak amplitude, root-mean-square (RMS) amplitude, and the ratio of second harmonic to fundamental component of receive echoes were calculated. Beamforming was additionally performed as described in Chapter 2, Section 2.3.3.1, to reconstruct contrast images from plane wave data. Signals from linear and non-linear targets after PI, AM and PIAM were assessed in resulting images to determine the most suitable imaging procedures for the subsequent experiments.

7.3ii.2.3 Results and Discussion

Figure 7.13 shows example receive RF data along the central aperture element of an echo from a linear scatterer after transmission with the maximum pulse amplitude tested of $A = \{0.5,\ 1, -1, 0.5\}$. Results displayed in Figure 7.14 show an approximately linear increase in both peak-to-peak (Figure 7.14A) and RMS (Figure 7.14B) amplitude measurements with increasing transmit amplitudes from $0.1A$, to A. The second harmonic signal remains below -30 dB throughout amplitude transmissions shown in Figure 7.14C and D. To further test the linearity of these signals, contrast imaging strategies were performed on received RF echoes from both linear scatterers and bubbles to test the ability to suppress linear signals, while preserving those from non-linear targets.

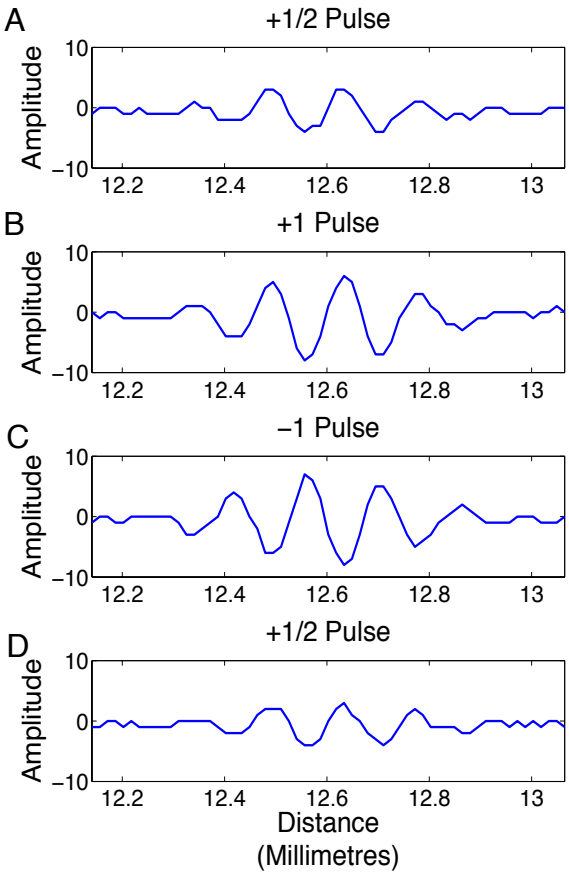

Figure 7.13. Pulse profile of receive RF data along the central aperture element of an echo from a linear scatterer after transmission with pulse amplitudes of $A = \{0.5, 1, -1, 0.5\}$ for (A), (B), (C) and (D) respectively.

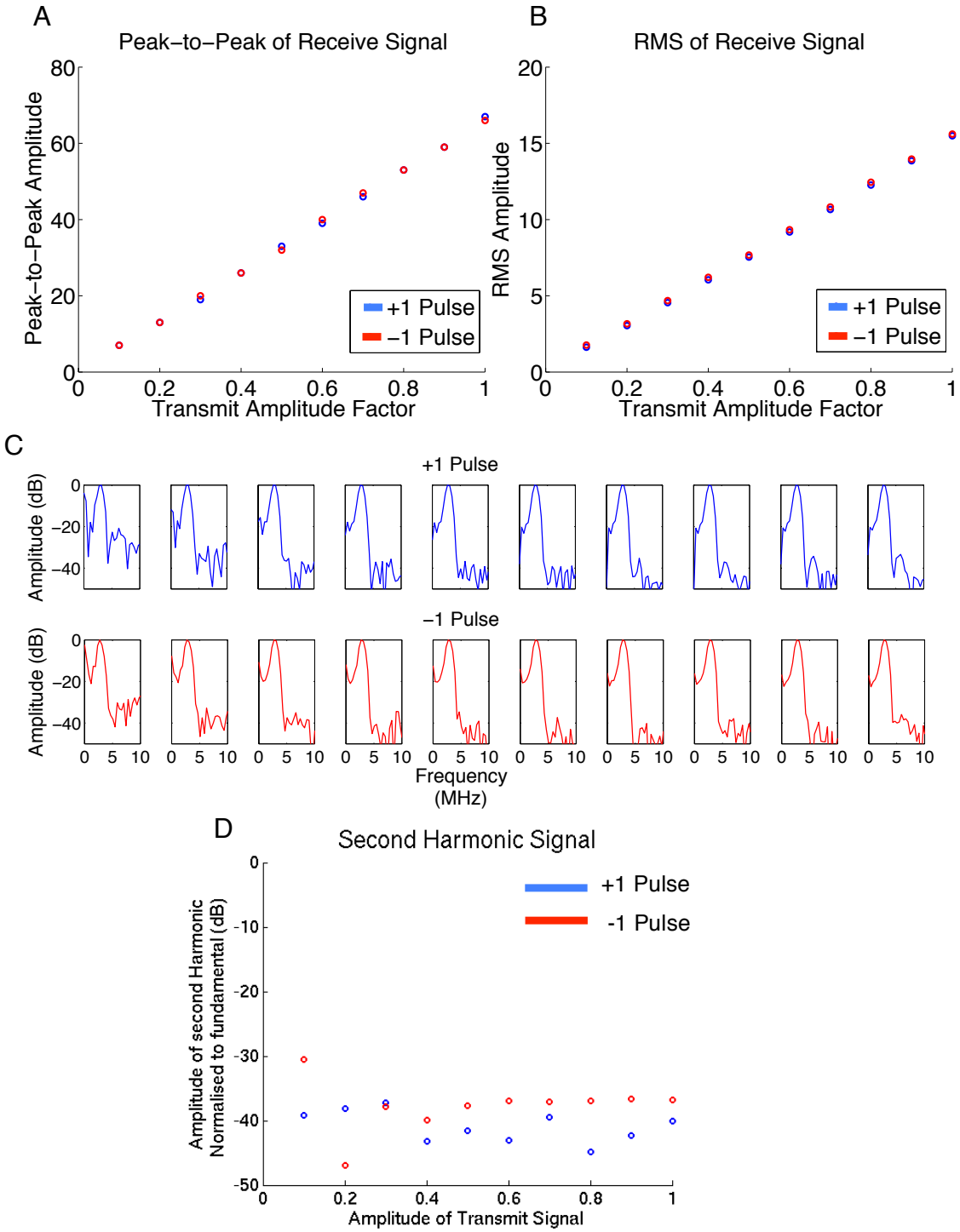

Figure 7.14. Testing the nonlinearity of receive signals when imaging a linear point scatterer. (A) the peak-to-peak, (B) the Root-Mean-Square (RMS), (C) the frequency spectrum and (D) the second harmonic amplitude normalised to fundamental of the echoes from two 180° out of phase signals with varying transmit amplitude from 0.1*A* to *A* at a linear target (transmit amplitude from 0.1 to 1). Results show an approximately linear increase of both peak-to-peak and RMS measurements with increasing amplitude in transmission. The second harmonic signal remains below -30 dB low throughout amplitude transmissions displayed in (C) and (D).

Figure 7.15 displays an example line profile of a linear scatterer echo along the central aperture element after transmission of four pulses with amplitude A, using contrast imaging strategies PI (Figure 7.15A), PIAM (Figure 7.15B), and AM (Figure 7.15C). Figure 7.16 and Figure 7.17 show reconstructed images following beamforming of plane wave echoes from the linear and non-linear targets respectively. The linear signal is largely suppressed in all contrast processing strategies shown here, verifying that negligible nonlinearity is observed over the full range of transmit amplitudes. AM provides the highest level of suppression of linear targets in both instances shown here. Imaging of a dilute suspension of microbubbles in a beaker displays visualisation of nonlinear signals for all contrast imaging strategies tested here (Figure 7.17) with highest contrast-to-tissue ratio (CTR) of 5.2 occurring with the use of AM, compared to 3.1 for PI and 2.3 for PIAM. AM provides conservation of the odd harmonic components of the signal (e.g. fundamental) and it is also less sensitive to harmonics generated from propagation which may be the reason for the greater CTR [79], [106].

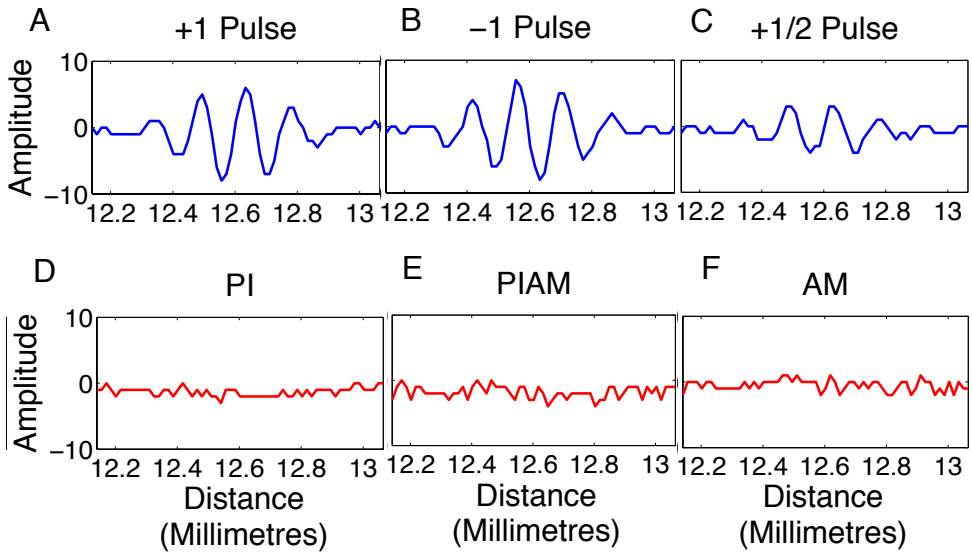

Figure 7.15. Received echoes from a linear scatterer after transmission with pulse amplitude of A, where (A),(B) and (C) correspond to transmit waves of amplitude $1, -1$ and 0.5. Example pulse profiles after RF data processing using contrast imaging strategies PI, PIAM and AM are displayed in (D), (E) and (F) respectively. The linear signal is largely suppressed in all contrast processing strategies shown here.

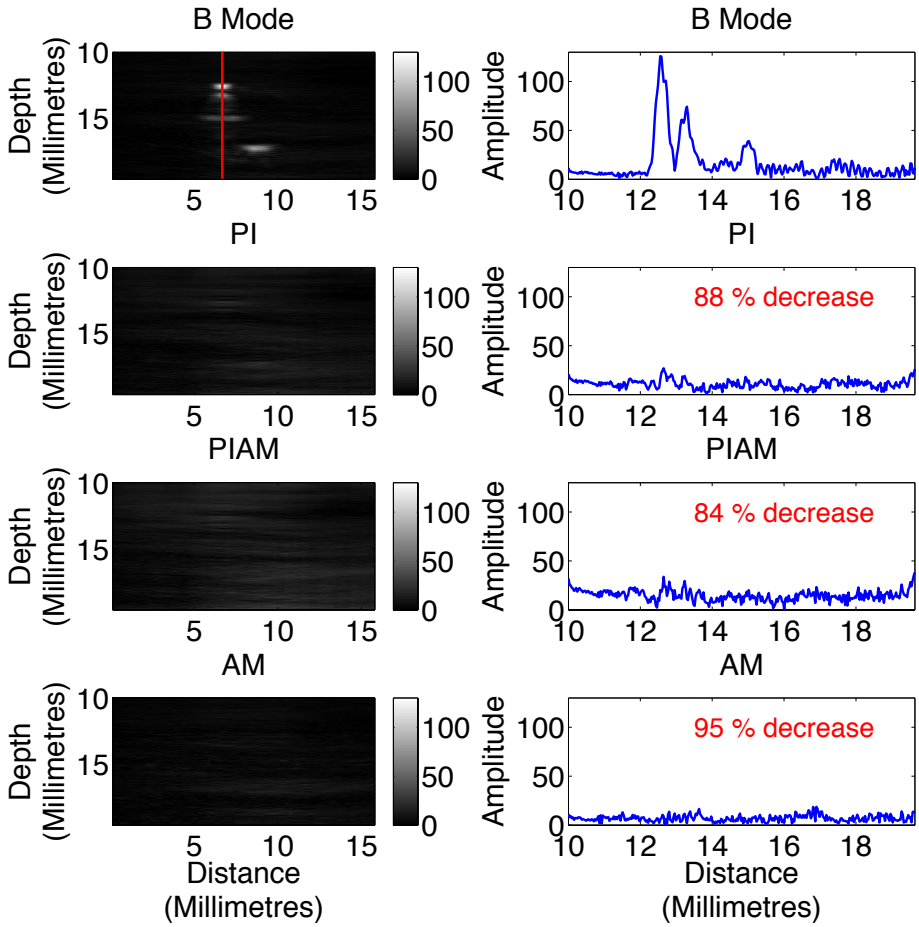

Figure 7.16. Reconstructed images using delay and sum beamforming of RF data echoes from linear scatterers. Percentage decrease in amplitude is measured as the relative change of amplitude around the peak of the measured B-Mode signal along the line of maximum image intensity. AM provides the highest level of suppression of linear targets shown here.

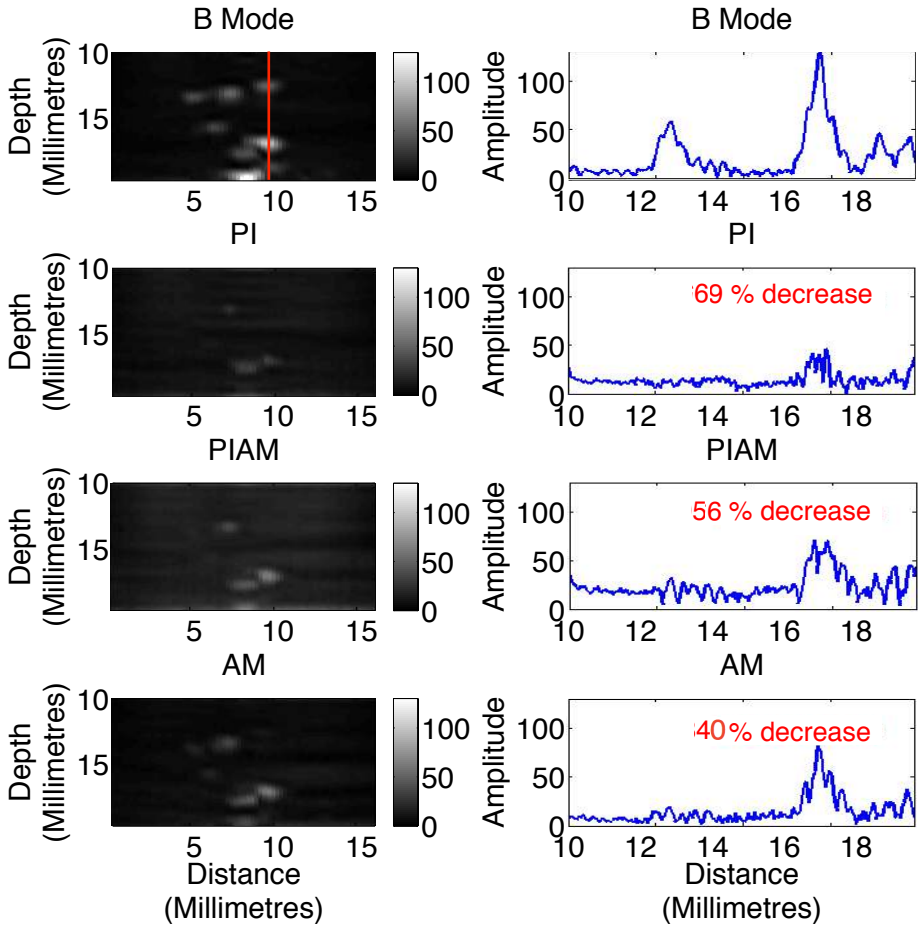

Figure 7.17. Reconstructed images after beamforming of RF echoes from a dilute suspension of microbubbles in a beaker following B Mode, PI, PIAM and AM processing. CTR values are 3.1, 2.3 and 5.2 respectively. In this example, AM provides the lowest suppression of nonlinear bubble signals and the highest CTR.

7.3ii.2.4 Summary and Comments for Future Work

Characterisation experiments allowed investigation of the optimum transmit amplitude for future *in vitro* experiments. Full amplitude pulses of amplitude *A* were employed in the following experiments since these provided the highest transmit power for bubble excitation, while maintaining suppression of linear signals. Furthermore, AM contrast imaging was implemented in future experiments since this provided the greatest CTR.

7.3ii.3 ESTIMATION OF SYNCHRONISATION DELAY

7.3ii.3.1 AIM

To estimate the delays associated with the synchronisation of two ULAOP systems with independent clocks.

7.3ii.3.2 METHOD

Two identical ULA-OP systems were synchronised in order to coincidentally detect signals from moving bubbles in both transducer imaging planes. Each ULA-OP system is able to function as an 'active' system, whereby it transmits a pulse synchronous with the system's internal PRF via a coaxial cable connector. Correspondingly, each system also has the capability of acting in 'passive' mode, where the internal PRF is disabled, and the system instead transmits waveforms when triggered by an external synchronisation pulse applied via the coaxial cable connector.

The trigger received at the passive system is subject to a time delay of approximately 4 μs [331], [334] caused by the time between the rising edge of the external synchronisation pulse and the activation of bit stream generation. Moreover, the synchronisation signal is internally sampled at 12.5 MHz, consequently this delay is additionally affected by a jitter of up to 80 ns. Thus, the delay in the trigger of the passive system, t_d, in addition to the jitter, t_j, associated with the phase delay must be incorporated into the duration between wave transmission and reception. Thus, Equation (7.4) becomes

$$t_{pj} = \frac{|r_p - r_i|}{c} + \frac{|r_p - r_j|}{c} - t_d + t_j \tag{7.5}$$

The time delay associated with this synchronised imaging strategy was measured in the following experiment. The two systems were synchronised as described above using two identical LA533 probes. Active and passive transducers were positioned in a gas-equilibrated water bath, an equal height of 25 mm above a stationary, flat reflector made of polyvinyl chloride plastic. This target was used in order to generate a high amplitude linear reflection of the transmitted signals. The active system was programmed to transmit a 3-cycle plane wave at the maximum system amplitude of 1 at 6 MHz with a

PRF of 4000 Hz. The central 64 elements were used both in transmit and receive. The remaining configuration parameter settings were identical for both systems, including acquisition ordering, and data saving parameters. Pre-beamformed RF data was saved after every 1000 pulse repetitions. The arrival times of the reflections received at both the active and passive systems were measured and used to assess the synchronisation delay time using varying PRFs.

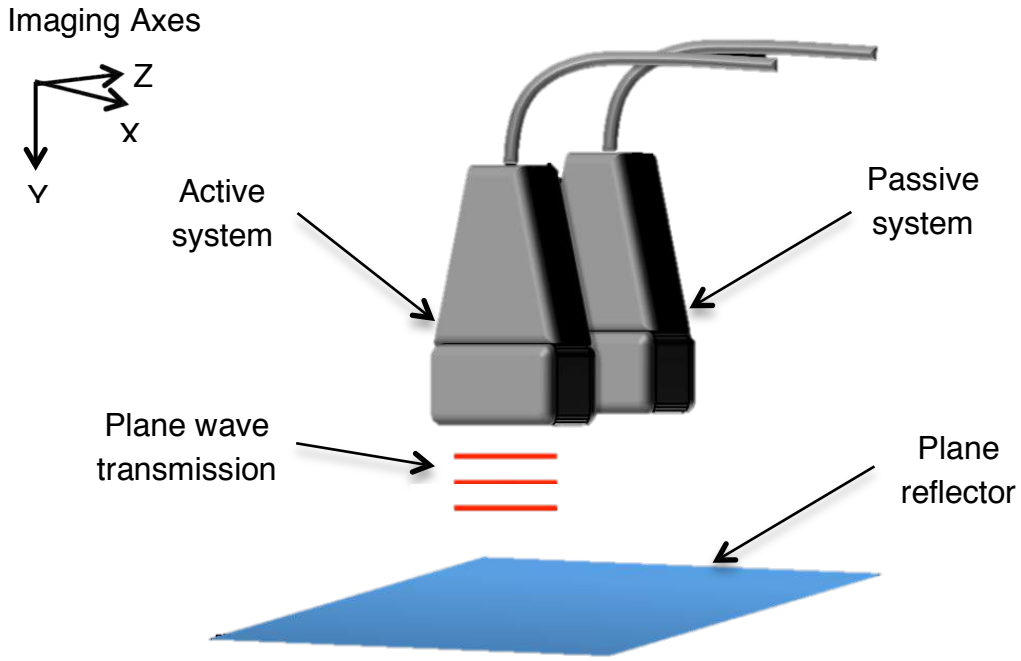

Figure 7.18. Experimental set-up for synchronisation time delay experiment.

7.3ii.3.3 Results and Discussion

Figure 7.19 shows the arrival time of the reflection received at both systems following transmission from the active system. The difference in calculated signal arrival time between the passive and active transducer allowed estimation of the time delay associated with the synchronisation process. Here it is clear that the passive system is subject to a time delay of approximately 4 μs, and is further subject to a sawtooth 'jitter' variation over time. This jitter function can be observed to accumulate a further delay of approximately 80 ns over a time period of approximately 35 ms; this time period remains approximately constant when varying the PRF as displayed in Figure 7.20, which shows the measured backscatter time from a stationary reflector on the passive

system when varying the transmit PRF from 3000 Hz to 17000 Hz in steps of 2000 Hz. These have been displayed in reference to pulse index (x-axis) for comparative purposes.

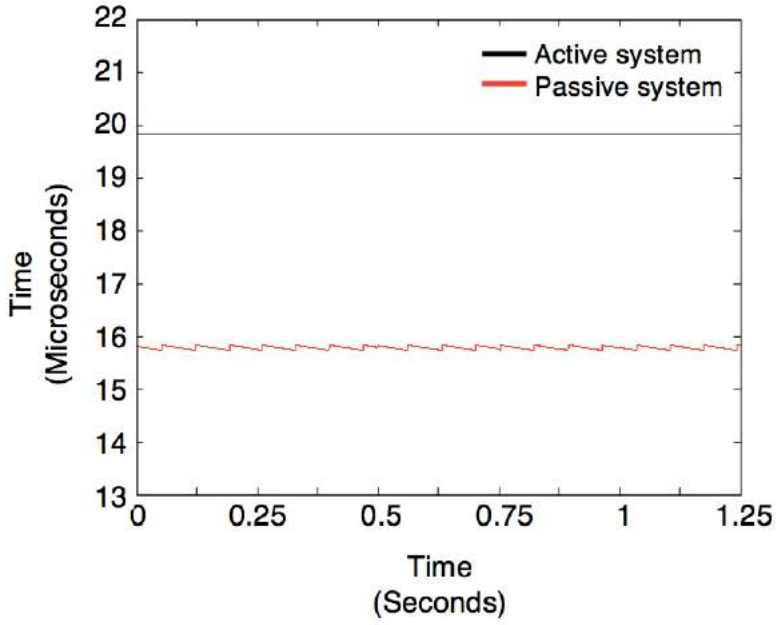

Figure 7.19. Arrival time of flat reflector echo for active and passive systems. The passive system is subject to a time delay caused by the inter-system triggering, which is in turn subject to a saw-tooth variation over time. The difference in calculated signal arrival time between the passive and active transducer allows estimation of the time delay associated with the synchronisation process.

This sliding variation is due to the internal clock in each of the systems running at different speeds. The synchronisation signal is internally sampled at 12.5 MHz, or once every 80 ns. The synchronisation starts when a pulse is initialised from the active system. Since both internal clock sources are assumed to be stable, for every pulse repetition, a new synchronisation pulse is sent, creating a different phase error within ± ½ the sampling clock, where this difference can be visualised as a gradual sliding over time, as seen in Figure 7.19 and Figure 7.20. After a single clock cycle, a single clock period should be added to recover the sliding effect. The difference in speed of the two clocks was investigated by switching the functionality (active/passive) of each of the systems and recording the receive signal for each system when acting passively. In each system this should cause a gradual de-phasing with opposing gradients. This behaviour is evident in Figure 7.21.

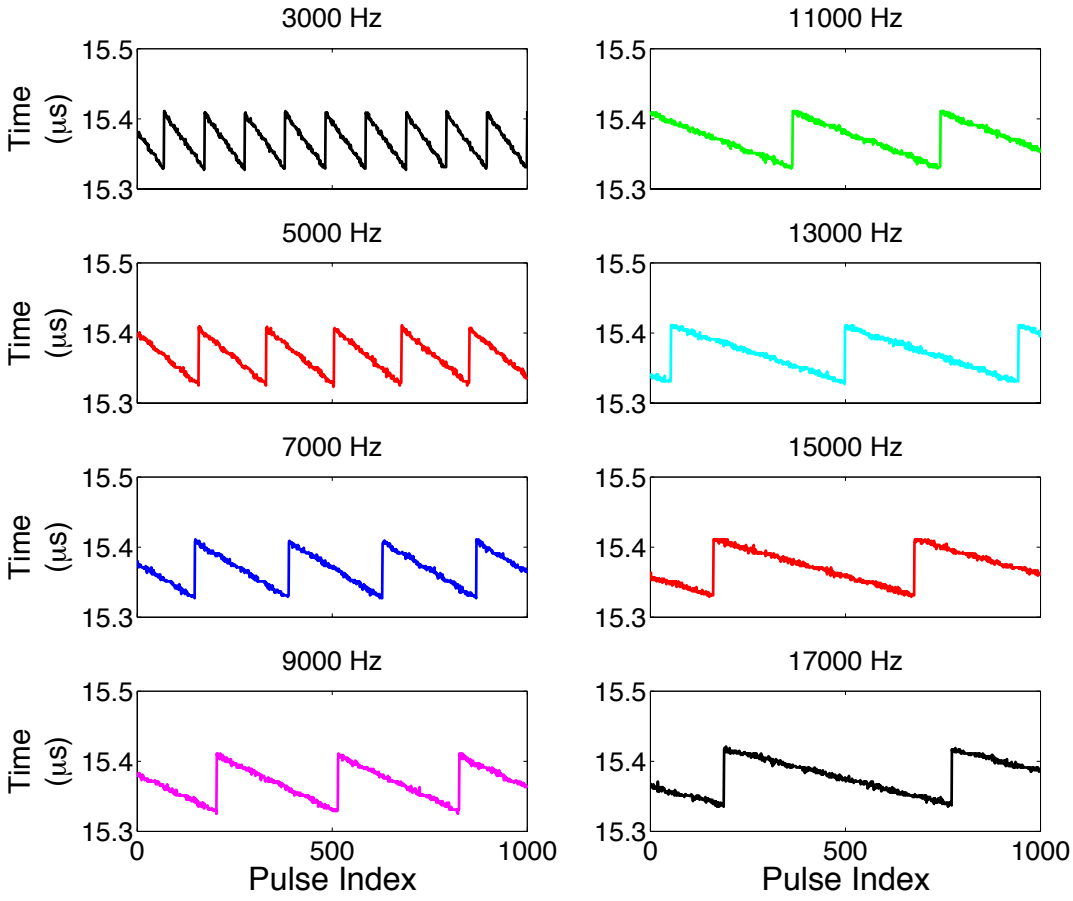

Figure 7.20. Measured backscatter time for an echo from a stationary reflector at passive system for varying PRFs.

It can also be identified that the temporal delay of the initial synchronisation pulse appears randomly within the 80 ns delay. This can be seen by comparing the initial positions of the measured backscatter time for each of the experiments with varying PRFs in Figure 7.20. This not only occurs at the initial synchronisation pulse, but additionally at any point where the system is interrupted, for example for data saving. Since pre-beamformed RF data was saved after every 1000 pulse repetitions in this experiment, this can be seen between pulse 1000 and pulse 1001 in Figure 7.21, where there is a small discontinuity from the gradual delay function most notable in the blue data of System 1, which then continues the same gradient de-phasing as before. A less noticeable, but still evident discontinuity is seen in the red data plot. This means that the exact value of the delay function cannot be known until the position of this initiation point is known, or alternatively if the location of each of the sharp discontinuities which occur approximately every 35 ms can be identified.

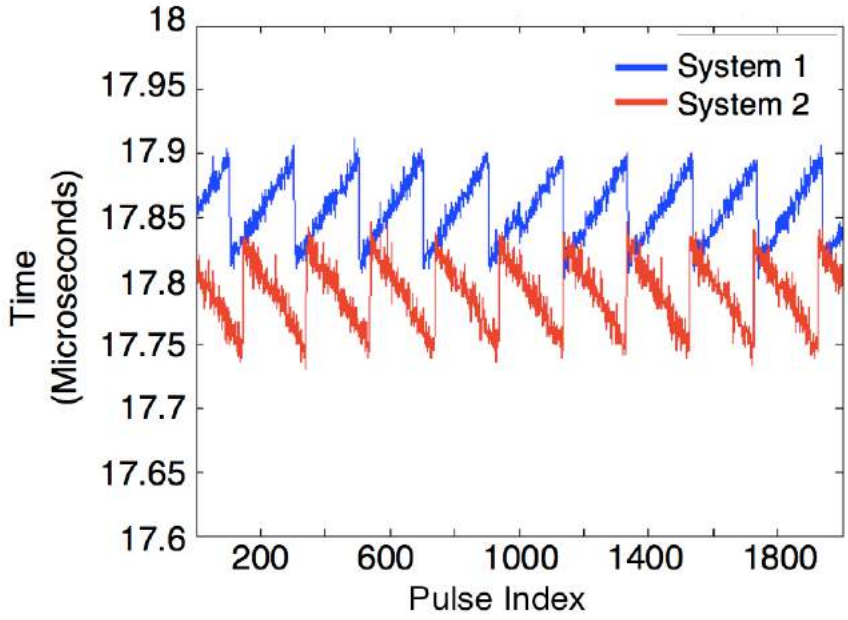

Figure 7.21. Backscatter arrival time from system 1 and 2 when acting as passive systems. This shows the gradual de-phasing of the clock times for each pulse repetition.

Under the assumption that both clock systems have the same precision, with a sampling rate given by $F_c = 50\,MHz$ [331]. The drift between the two clock systems can be estimated by the linear trend

$$t_{drift} = mt - t_d, \tag{7.6}$$

where t is time in the active clock system, t_{drift} is the time difference for the passive clock system. The slope m defines the drift speed of the passive clock system. Over a single clock cycle, T_{Period}, m is given by

$$m = \frac{\Delta t_{drift}}{\mathrm{T}_{Period}}, \tag{7.7}$$

$$= \frac{80 \cdot 10^{-9}\,s}{35 \cdot 10^{-3}\,s} = 2.2857 \cdot 10^{-6}.$$

where Δt_{drift} is the relative change in time in the passive system over a single clock cycle. Therefore, if $m < 0$, the passive system clock is running slower than the active system clock, the opposite is true for $m > 0$, and the clocks are running equal if $m =$

0. The drift rate of the passive system clock is then given by

$$Drift\ rate\ = \frac{m}{\mathrm{T}_{Period}}, \tag{7.8}$$

$$= \frac{2.2857 \cdot 10^{-6}}{35 \cdot 10^{-3}\ s},$$

$$= 6.5306 \cdot 10^{-6}\ \text{Hz}.$$

Subsequently the system rate can be given by its sampling frequency, F_c, with the associated drift,

$$System\ Rate\ =\ F_c \pm\ Drift\ rate, \tag{7.9}$$

$$= 50 \cdot 10^{6}\ \pm\ 6.5306 \cdot 10^{-6}\ Hz;$$

The estimated maximum localisation error over a complete clock cycle, E_{max}^{loc}, caused by this jitter is given by:

$$E_{max}^{loc}\ = \frac{t_{max} \cdot c}{2} \tag{7.10}$$

$$= \frac{80\ \cdot\ 10^{-9}\text{s}\ \cdot 1540\ \text{ms}^{-1}}{2} = 61.6\ \mu m$$

where c is the speed of sound in soft tissue, assumed to be constant at $\mathrm{c} = 1540\ \text{ms}^{-1}$. The variation in adjacent frames will depend on the transmit PRF. At a PRF of 4000 Hz,

$$\mathrm{E}_{\mathrm{frame}}^{\mathrm{loc}} = \frac{\mathrm{E}_{\mathrm{max}}^{\mathrm{loc}}}{\mathrm{N}_{\mathrm{frame}}^{\mathrm{c}}}, \tag{7.11}$$

$$= \frac{\mathrm{E}_{\mathrm{max}}^{\mathrm{loc}}}{\mathrm{PRF} \cdot \mathrm{T}_{\mathrm{Period}}}, \tag{7.12}$$

$$= 0.44\ \mu\mathrm{m\ frame}^{-1}.$$

where N_{frame}^{c} is the number of frames in one cycle. If identification of the discontinuity, E_{max}^{loc}, within the data is possible, then a linear correction can be performed, as demonstrated for the stationary scatterer in Figure 7.22.

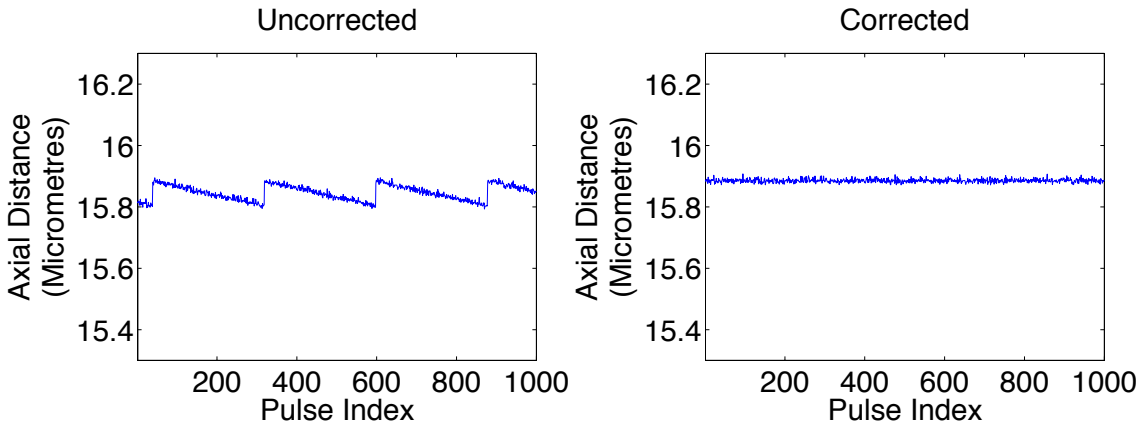

Figure 7.22. Demonstration of delay correction using discontinuity identification and linear correction on signal detected at passive system after reflection from a plane target.

However, this may not always be possible, particularly when imaging *in vivo*, where it may not be possible to verify if scattering targets are truly stationary. The jitter could, however, still be corrected through identification of the discontinuities in the delay function during a standard acquisition. The occurrence of the discontinuity would correspond to an estimated spatial displacement of scatter signals of 61.6 μm between consecutive frames as calculated using Equation (7.10). The average blood speed in capillary networks has been estimated to be 0.3 mm/s (Chapter 1, Table 1.1) [27], [112], [335]. Thus, when utilising frame rates between 100-1000 frames per second, a bubble would have to be moving 20-200 times faster than the average capillary blood speed in the axial direction, i.e. corresponding to 60 μm/frame vertically, in order to create the same spatial translation. Providing that the image acquisition time is longer than one

clock cycle, and that a scatterer can be confirmed to be observed in consecutive frames, the discontinuities in the drift should be identifiable and would provide adequate information to perform a linear correction based on this drift rate characterisation.

7.3ii.3.4 Summary and Comments for Future Work

Synchronisation of the two ULA-OP systems with independent clocks has been demonstrated to cause a slow de-phasing over time. De-phasing has been shown to occur on a designated timescale independent of the PRF. Identification of discontinuities in the jitter delay would allow correction based on the characterisation of drift rate.

7.3ii.4 Estimation of the Diffraction Limited System Resolution

7.3ii.4.1 Aim

To estimate the diffraction limited resolution of the ULA-OP ultrasound system.

7.3ii.4.2 Method

The diffraction limited resolution of the imaging system under ideal conditions was investigated using 3 MHz and 7.5 MHz transmit frequencies with a single ULA-OP system. A 100 μm diameter brass wire was held horizontally between two fixings in a gas equilibrated water bath. The wire was positioned normal to the US image plane so that the cross-section of the wire imitated a point scatterer. Focussed B-Mode pulses were transmitted using a 3 cycle pulse with the maximum amplitude of 1, a PRF of 4000 Hz, and a focus of 18 mm. The PSF of the wire was measured at depths between 13 mm to 23 mm in the axial direction, and across 12 mm laterally. Focussed US data was acquired in IQ format. With the wire at the focus, 100 plane wave pulses were additionally transmitted and saved in pre-beamformed RF format in order to compare the PSF achieved using focussed and beamformed plane wave imaging.

Delay and sum beamforming was applied to reconstruct images of the scatterers from acquired plane wave RF data. Sensitivity maps with varying amplitude weighting factors were additionally generated and used within the beamforming process in order to investigate its affect on reconstructed signals. These aimed to emulate the directional

sensitivity of each transducer element during image reconstruction; maps were constructed for each transducer element, x_1 by defining a Gaussian amplitude weighted profile across each row of the data matrix with the peak positioned at the element of interest; the standard deviation of the Gaussian profile increased with depth according to an angular factor, α ,which determined the narrowness of the weighting map. Examples of sensitivity maps are displayed in the following section.

The resolution of the US system was measured as the FWHM of the signal in the lateral and axial directions. The elevational resolution of the system was estimated by translating a wire target in 0.250 mm steps across the field of view using a micrometre stage and measuring the signal amplitude in the acquired IQ data. To account for the finite size of the wire in the measurement of the PSF, the FWHM value was deconvolved by the wire diameter to obtain new values of the PSF FWHM (see Chapter 3).

7.3ii.4.3 Results and Discussion

An example data frame in which the wire was positioned at a depth of 18 mm using 3 MHz insonation frequency is shown in Figure 7.23. Figure 7.24 displays the FWHMs of the PSF at the focus in the axial and lateral directions respectively, along with the measured elevational amplitude profile for both a transmit frequency of 7.5 MHz using the LA533 imaging probe (Figure 7.24A) and at 3 MHz using the LA332 imaging probe (Figure 7.24B). Variations in the estimated diffraction limited resolutions of the imaging system over a region approximately $10\ mm \times 12\ mm$ in size are displayed in Figure 7.25. Results show variation in the resolution over the field of view, in addition to considerable improvement when using 7.5 MHz over a lower transmit frequency of 3 MHz as expected. Average measured FWHMs over the field of view (or over repeated measurements in the case of the elevational resolution) for 7.5 MHz transmit frequency are 211 ± 36 μm, 680 ± 156 μm and 820 ± 210 μm in the axial, lateral and elevational planes respectively. Corresponding values for the LA332 at a transmit frequency of 3 MHz equate to 534 ± 29 μm, 953 ± 103 μm and 1188 ± 160 μm respectively.

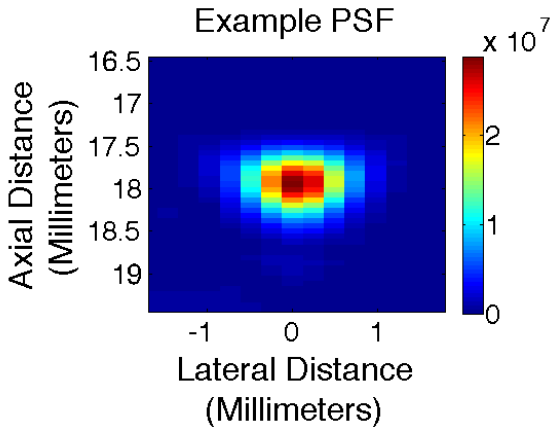

Figure 7.23. Measuring the diffraction limited resolution of the imaging system. (A) displays an example IQ image data frame at the transducer focus of 18 mm at 3 MHz.

Implementation of the aforementioned orthogonal imaging set-up (Figure 7.7) allows replacement of the poorest resolution imaging plane, with the highest resolution of the current imaging system, i.e. objects within the elevational plane can be localised to within the axial resolution of the system. Thus, the 3D resolution can already be significantly improved without super-resolution processing.

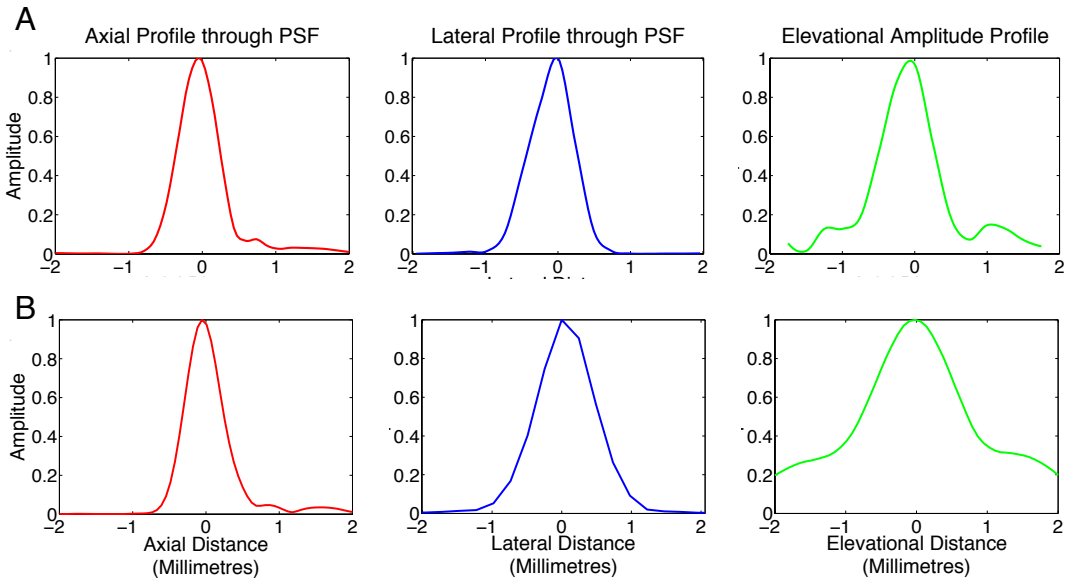

Figure 7.24. Experimental estimation of the system resolution. (A) shows the profiles of the PSF at the focus in the axial and lateral directions respectively, along with the measured elevational amplitude profile for a transmit frequency of 7.5 MHz, and (B) shows the equivalent measurements at a transmit frequency of 3 MHZ using the LA332 probe.

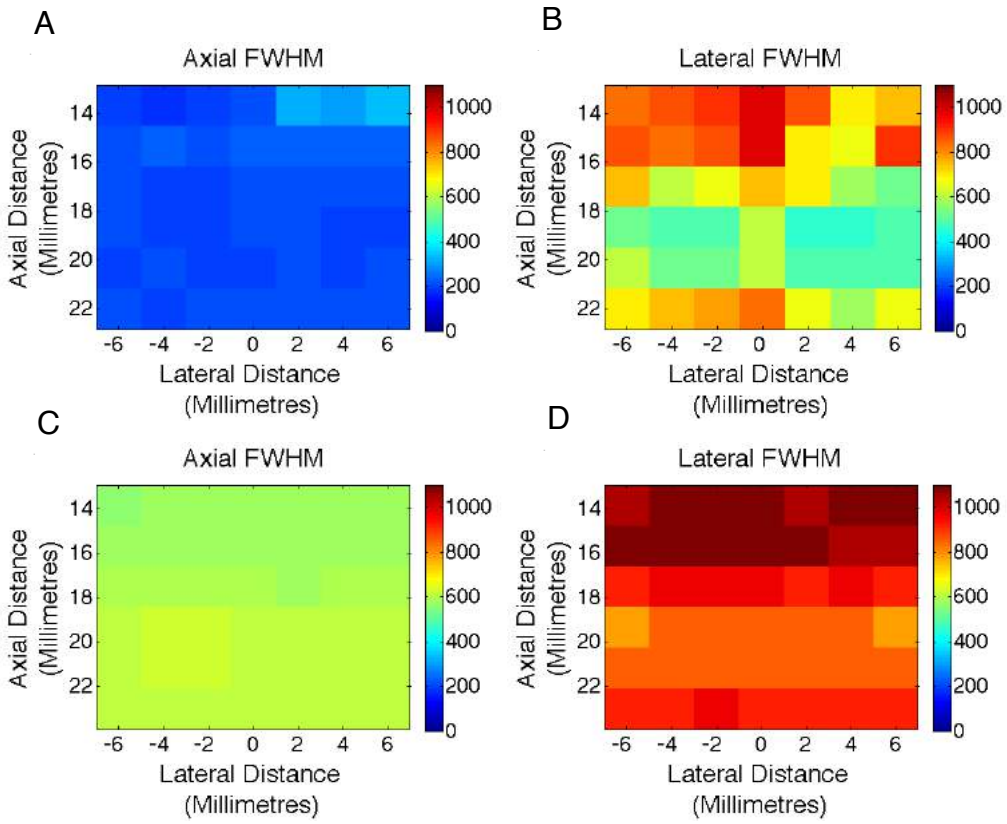

Figure 7.25. Variation of the diffraction limited resolution of the imaging system. (A) and (B) display the axial and lateral FWHMs respectively using a 7.5 MHz transmit frequency from the LA533 probe. (C) and (D) show corresponding axial and lateral FWHMs respectively using a 3 MHz transmit frequency with the LA332 probe. Average resolution estimations over the field of view are 211 ± 36 μm and 680 ± 156 μm respectively at 7.5 MHz. Corresponding results for the LA332 at a transmit frequency of 3 MHz are 534 ± 29 μm and 953 ± 103 μm.

Figure 7.26 compares the resolution of beamformed images from single plane wave echoes from a point scatterer with varying sensitivity maps. This includes a uniform sensitivity map (equivalent to having no sensitivity map) shown in Figure 7.26A and B, along with varying angular factors, α. Estimated axial resolutions for reconstructed plane wave data were found to be better than that of focused imaging at 448 μm, compared to an average of 534 μm. Lateral resolutions were however significantly poorer for beamformed plane wave data in all instances shown in Figure 7.26, where the minimum was 1250 for $\alpha = 100$, compared to that of focused data at an average of 953 μm.

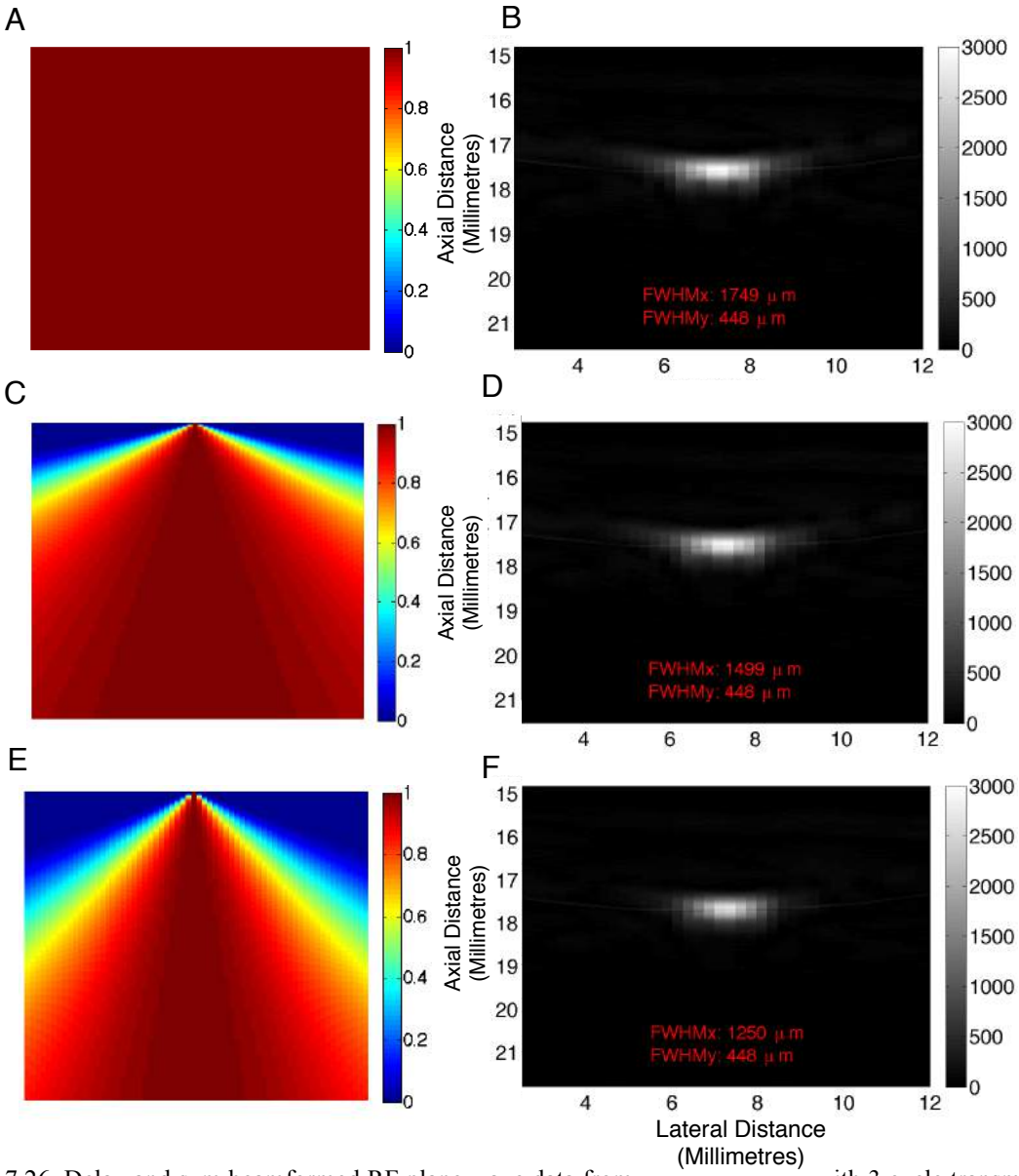

Figure 7.26. Delay and sum beamformed RF plane wave data from a point scatterer with 3 cycle transmit pulse and frequency of 3 MHz. Sensitivity maps are shown here for the central transducer element, where (A) represents no sensitivity map (i.e. weighting is 1 across field of view), and the remaining plots display sensitivity maps with increasing Gaussian standard deviation with depth where α,= 50 in (C), and α = 100 in (E). Resulting images and corresponding FWHMs are displayed in (B), (D) and (F).

7.3ii.4.4 Summary and Comments for Future Work

The diffraction limited resolution was shown to vary over the imaging field of view. At a transmit frequency of 3 MHz, suitable for the imaging of contrast agents such as SonoVue™, the average diffraction limited resolution was estimated to be 534 ± 29 μm,

953 ± 103 μm and 1188 ± 160 μm in the axial, lateral and elevational planes respectively. A slightly higher axial resolution of 488 μm was achieved using plane wave beamforming. These values provide an approximate comparison for measuring the resolution improvement achieved after implementing super-resolution imaging.

7.3ii.5 ESTIMATION OF LOCALISATION PRECISION IN 3D

7.3ii.5.1 AIM

To estimate the localisation precision achievable using super-resolution with the described orthogonal imaging set-up.

7.3ii.5.2 METHOD

The orthogonal setup described in Section 7.3i.5 and illustrated in Figure 7.7 was constructed using two identical LA332 transducers each connected to individual ULA-OP systems. The systems were synchronised.

In order to effectively image a point scatterer in three dimensions, an air bubble was suspended in space in an optically transparent paraffin gel phantom as described in Section 7.3i.4 and shown in Figure 7.5. This was positioned within the overlapping imaging region of the orthogonal transducers (Figure 7.27). Three cycle, single angle plane waves were transmitted from the central 64 elements of the active transducer at 3 MHz with a PRF equal to 4000 Hz and amplitude equal to 1. Coincident echo detections at the passive and active imaging probes were then used for 3D localisation. Additionally, the localisation precision was tested using varying transmit frequencies (3 MHz, 4 MHz and 5 MHz).

In Chapters 3-6, localisation of individual bubble signals involved calculating the centre of mass of an image formed by the microbubble to estimate its location. As discussed previously, when a small scatterer is insonified by a plane wave, it can be assumed to emit a spherical wave. In this chapter, scatterer localisations were estimated using two methods for comparison. In the first method, after reception of plane wave RF data, RF data lines from each element were Hilbert transformed for envelope detection and its peak was calculated. Since a spherical wave emitted by a point scatterer can be approximated as a hyperbole when detected across parallel transducer array elements,

the peaks detected in each channel line were then used to fit a polynomial of order two across the lateral image plane. The position of the minimum in time of this polynomial was estimated to be the location of the insonated point scatterer. Examples of such echo data will be shown in the Results and Discussion section.

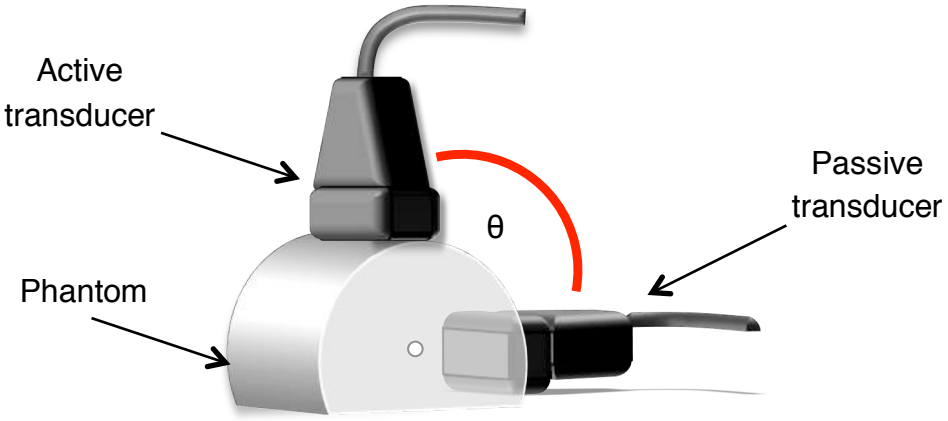

Figure 7.27. Illustration of imaging configuration using suspended point scatterer within a phantom, with the active and passive transducers at 90°.

In the second method, each single plane wave echo was beamformed offline to reconstruct an image of the point scatterer. This was performed with no sensitivity map (equivalent to a uniform sensitivity map shown in Figure 7.26A) since the element sensitivity profile was unknown. The location of the scatterer is then estimated by calculating the centre of mass of the signal as performed in Chapters 3-6.

The localisation precision for each method was measured to be the standard deviation of these localisation positions over 100 frames. Jitter correction was applied to passive localisations through the identification of discontinuities and subsequent linear correction using equations presented in Section 7.3ii.3. The SNR was calculated as the ratio of the average absolute intensity of the detected signal within the field of view, to the average absolute background signal; in this way, signals which occur near the edge of the field of view tend to have a smaller SNR value than those signals occurring in the centre.

7.3ii.5.3 Results and Discussion

Figure 7.28 shows example plane wave RF data from a point scatterer in the field of view of a single transducer. Figure 7.28A displays an echo from the target when positioned close to the transducer focus. The red line shows the fitted second order polynomial, and corresponding green crosses indicate the positions of localisations over 100 plane wave pulses. Figure 7.28B displays a plane wave echo from the same target positioned on the edge of the field of view. The lateral spread of localisations is approximately 10 times larger in (B) than in (A).

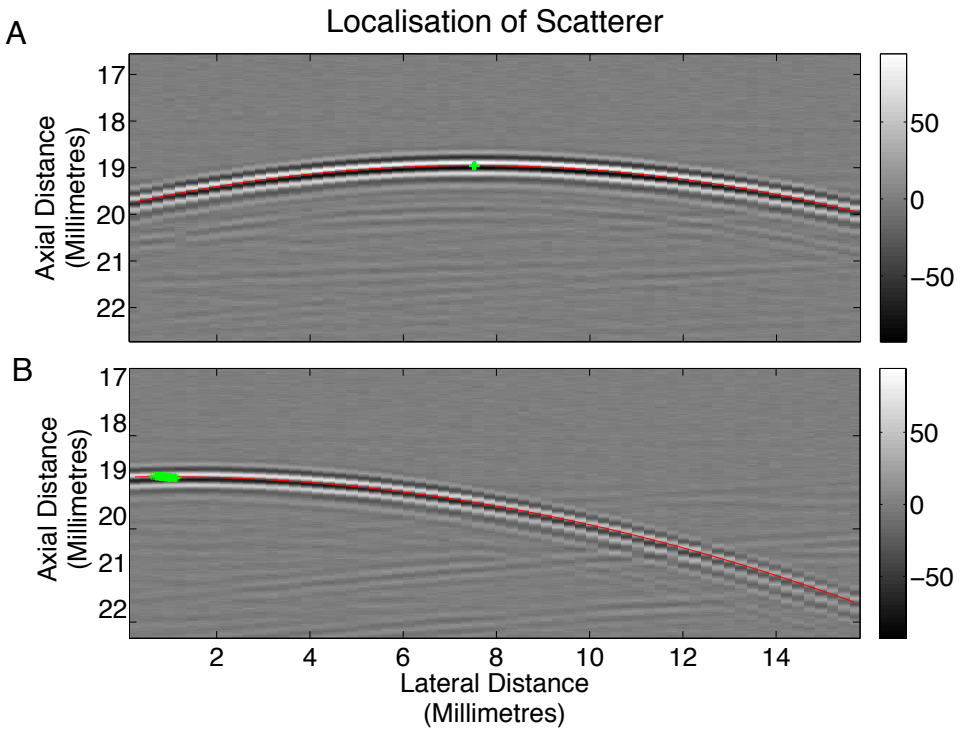

Figure 7.28. Example plane wave RF data from a linear point scatterer. (A) displays a plane wave received from the target positioned close to the transducer focus, (B) displays a plane wave echo from a target positioned on the edge of the field of view. The red lines indicate the polynomial fits, with corresponding localisations over 100 pulse repetitions shown in green. The lateral spread of localisations is approximately 10 times larger in (B) than (A).

Localisation precisions calculated across the entire field of view are displayed in Figure 7.29. The lateral localisation precisions have an average of 11.0 ± 25.0 μm, with a minimum of 6.9 μm and maximum of 101.7 μm. The average axial localisation precision is 1.9 ± 1.6 μm, ranging from 0.7 μm to 9.4 μm at the edge of the field of view

as shown in Figure 7.28. Signal-to-noise (SNR) values are shown in Figure 7.29C. SNR values decrease for target positions near the edge of the imaging plane due to signal cut-off, where additionally an increase in localisation error is seen. SNR values in the rest of the field-of-view do not show a direct correlation to corresponding axial and lateral error values.

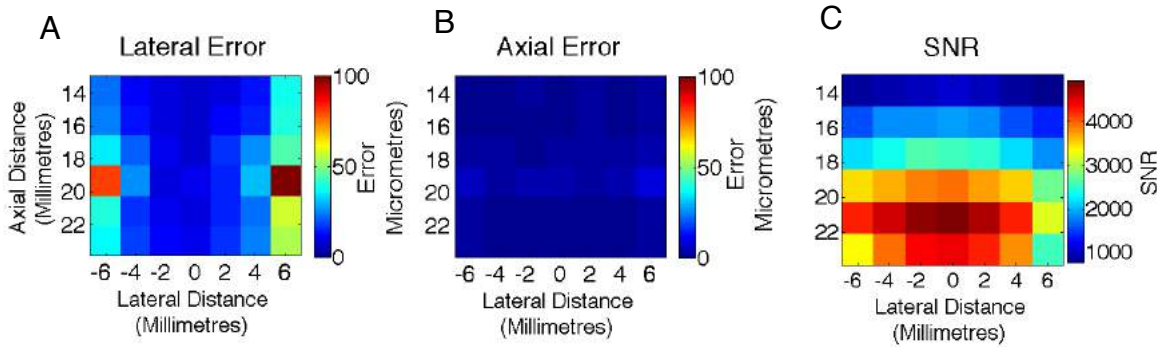

Figure 7.29. Localisation precision estimations using RF plane wave receive signals across the field of view at a transmit frequency of 3 MHz. (A) and (B) show the axial and lateral precisions respectively, and (C) is the estimated signal-to-noise (SNR) of the receive signals.

The localisation error was tested with varying transmit frequencies, measured from RF plane wave data at 3, 4 and 5 MHz at a depth of approximately 18 mm. Results shown in Figure 7.30A display a decrease in error with increasing frequency, which does not appear to correlate to corresponding SNR values for the same signals (Figure 7.30B). Comparison between the localisation precision measured from raw RF data and that of beamformed data were investigated at the same depth with a transmit frequency of 3 MHz. Results shown in Figure 7.31 demonstrate a slight increase in localisation error when implementing super-resolution methods with reconstructed RF data over raw plane wave data.

Simultaneous detection of 500 echoes were detected from a single point scatterer by active and passive transducers. Passive localisations are subject to the jitter delay explored in Section 7.3ii.3, and are thus spread across the axial direction as shown in the black localisations in Figure 7.32. Resulting passive localisations following correction based on discontinuity identification are displayed in red and are used in the following stages.

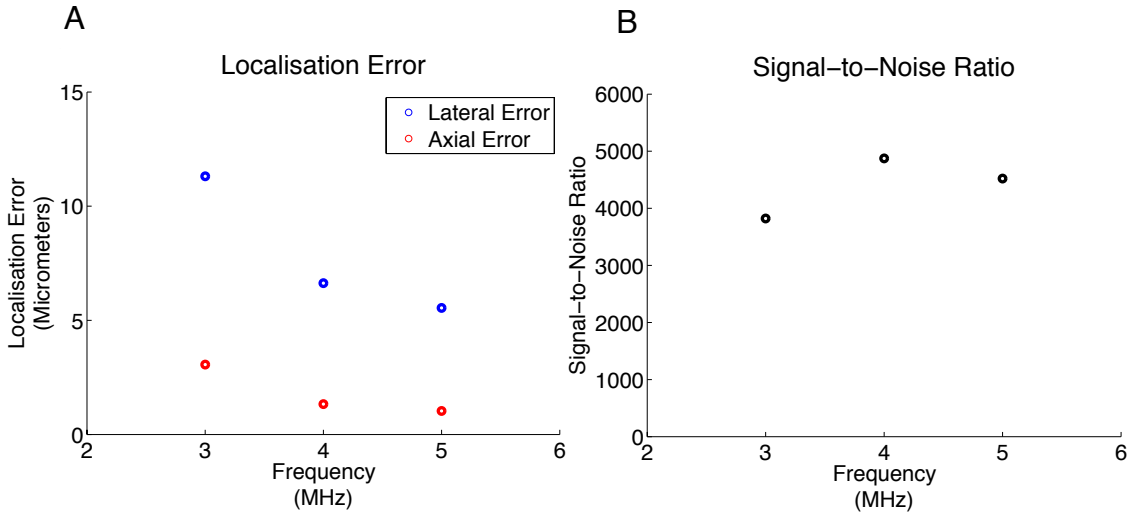

Figure 7.30. Estimation of localisation error from RF plane wave data with transmit frequencies of 3, 4 and 5 MHz. Results shown in (A) display a decrease in localisation error with increasing frequency. Corresponding SNR values for the same signals are displayed in (B).

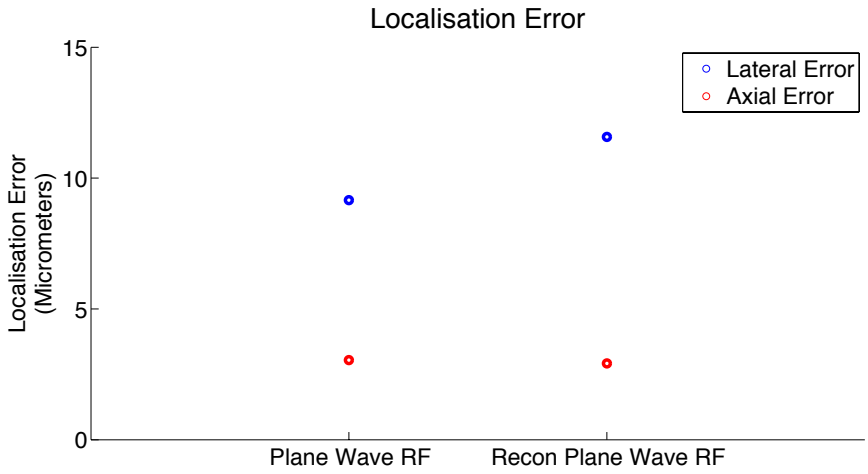

Figure 7.31. Comparison of estimated localisation error from RF plane wave data localisation, and beamformed reconstructed image data using an intensity weighted centre of mass using a transmit frequency of 3 MHz. Results display a small increase in axial and lateral error when using beamformed RF data compared to raw plane wave data.

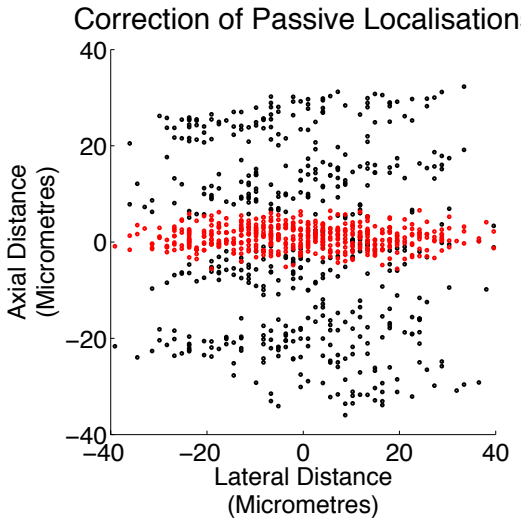

Figure 7.32. Passive localisations are subject to the jitter delay explored in section 7.3ii.3., and are thus spread across the axial direction, shown in black. Resulting localisations following correction based on discontinuity identification are show in red.

Figure 7.33A and B display the coincident localisations within each transducers' own co-ordinate system. The passive localisations enable detection within the active transducer's (x, z) plane; the resulting 3D localisation precision is thus shown in Figure 7.33C. Localisations detected using varying detection angle θ are displayed in Figure 7.34, with corresponding elevational localisation precisions presented in Figure 7.35; this indicates a dependency of the localisation precision on the SNR, where in general higher SNR measurements correlated with higher estimated precision. The difference between the highest and lowest precisions (60° and 75° respectively) was 0.6 μm. Comparative profiles showing the average localisation precision using orthogonal probe acquisition, to the original imaging system resolution are shown in Figure 7.36.

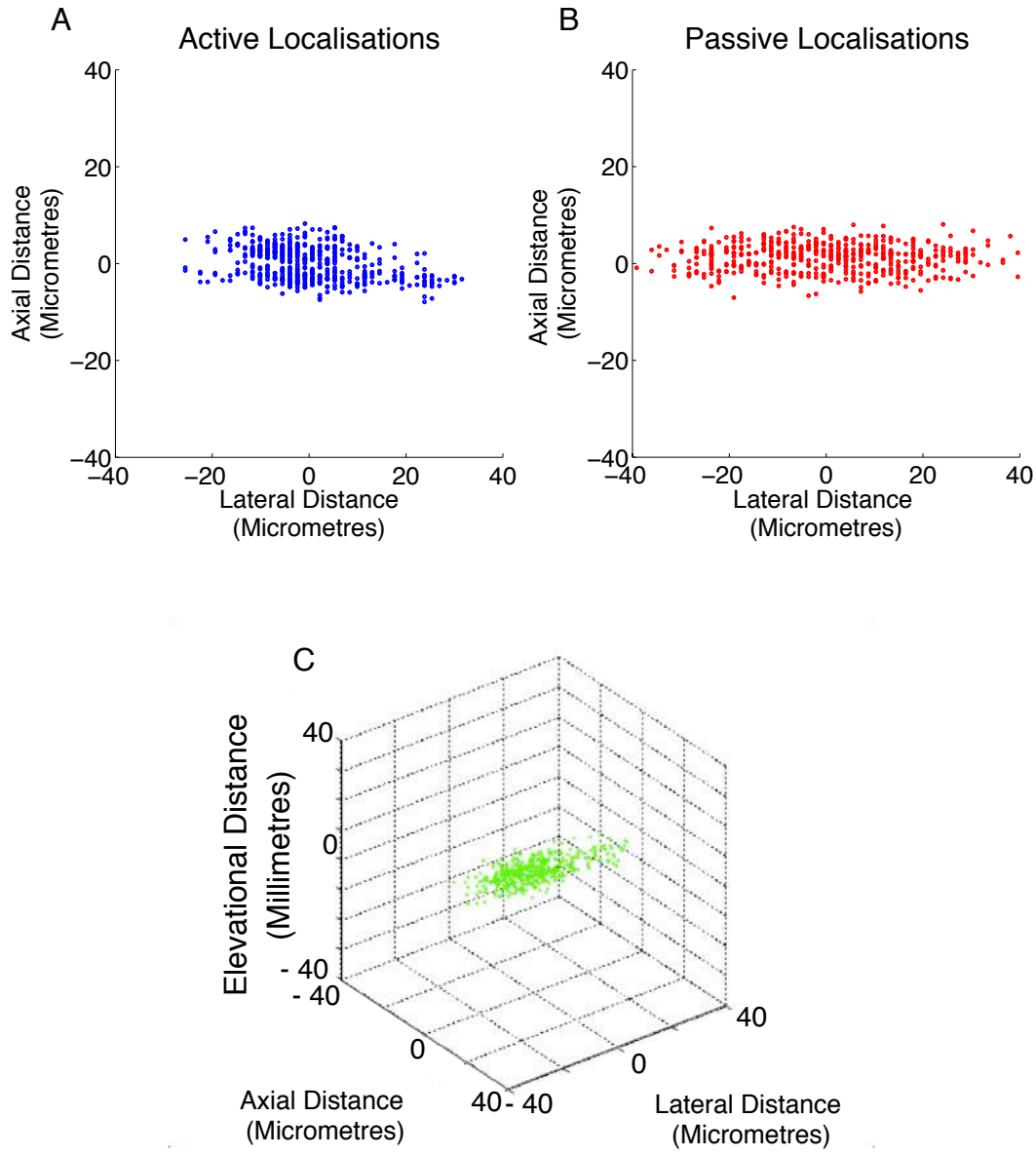

Figure 7.33. 3D localisation precision. Detection by both active and passive transducers provides localisations as displayed in (A) and (B) respectively. These figures display localisations within the transducers own co-ordinate system. When combining localisations in the global orthogonal configuration, the passive localisations enable detection within the active transducer's (x, z) plane. The resulting 3D localisation precision is thus shown in (C).

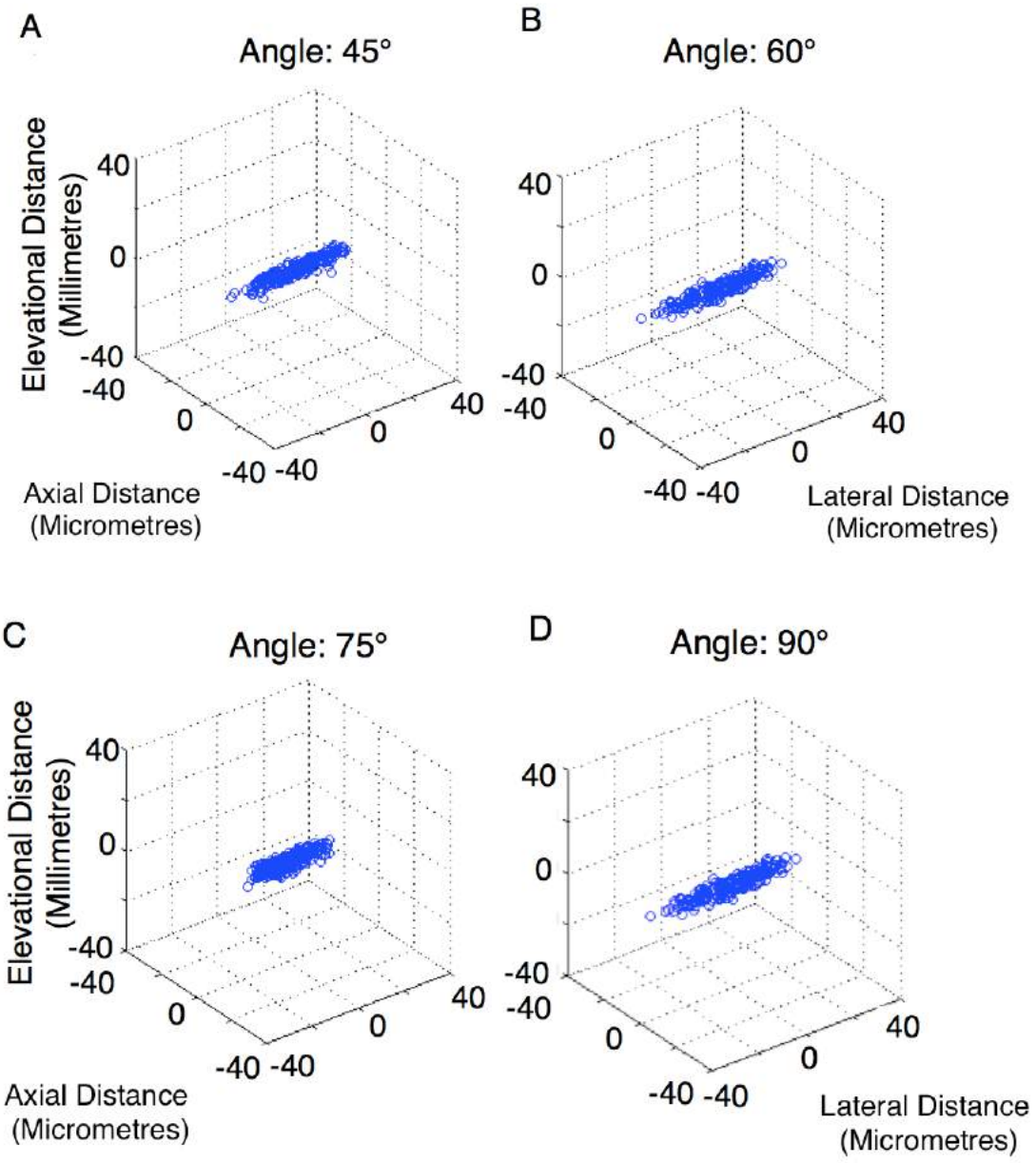

Figure 7.34. 3D localisations for varying passive detection angle θ, for angles (A) 45°, (B) 60°, (C) 75° and (D) 90°.

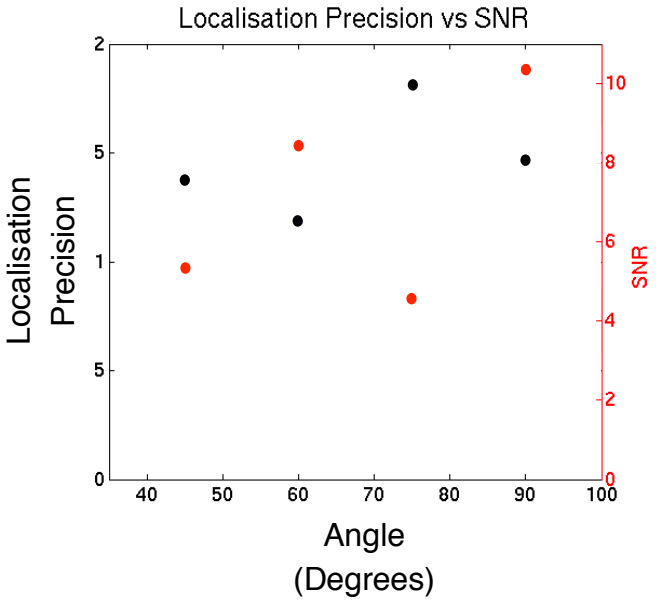

Figure 7.35. Elevational localisation precision estimates and corresponding SNR values for varying angles displayed in Figure 7.34.

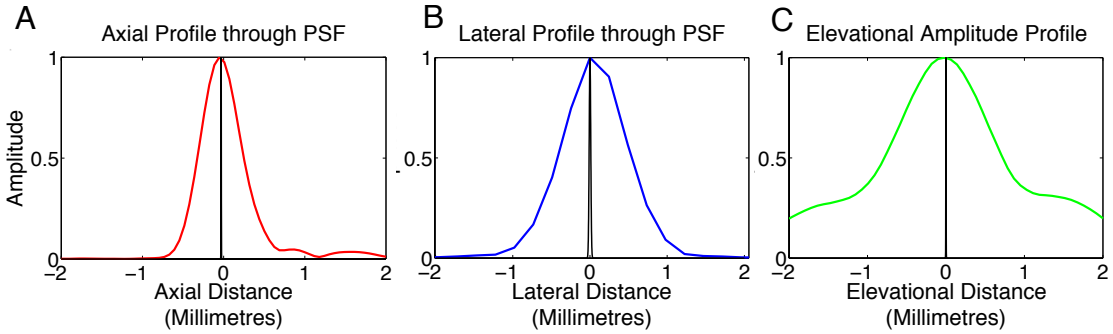

Figure 7.36. Diffraction limited resolution comparison to 3D localisation precision. (A), (B), and (C) display the original diffraction limited resolution of the imaging system using the LA332 imaging transducer in the axial, lateral and elevational directions respectively, along with average localisation precision values in each imaging plane of the new 3D orthogonal imaging configuration displayed in black.

7.3ii.5.4 Summary and Comments for Future Work

3D super-resolution allows detection of point scatterer signals in 3 dimensions with average precision equal to 1.9 μm in axial and elevational planes, and 11 μm in the lateral plane with respect to the active transducer, comparing to 488 μm, 1188 μm and 953 μm as the three dimensions of diffraction limited resolution for the original imaging

system as shown in Figure 7.24 and Figure 7.26. Average estimated localisation precisions at 3 MHz transmit frequency were implemented in rendering procedures in the following experiment.

7.3iii IN VITRO MICROBUBBLE LOCALISATION

7.3iii.1 CAPILLARY TUBE IMAGING

7.3iii.1.1 AIM

To achieve super-resolution in 3D *in vitro* using microbubbles.

7.3iii.1.2 METHOD

Two 200 μm internal diameter cellulose tubes (Hemophan®, Membrana) were held alongside each other within a distance smaller than the active transducer's elevational resolution. The apparatus was placed in a gas-equilibrated water bath in a configuration similar to that illustrated in Figure 3.9, Chapter 3, at a depth of approximately 14 mm. The ULA-OP systems were synchronised in the aforementioned orthogonal set-up (Figure 7.7), with the tubes positioned within the region defined by the overlapping imaging planes. At this point in the project, a hardware improvement meant that multiple ULA-OP systems could run from a single master clock, thus removing the affect of jitter from the passive detections. A low concentration solution of 100 μl SonoVue™/600 ml water was prepared which was found to provide a suitable concentration for imaging spatially isolated microbubbles (equivalent to that used in Chapter 3). The solution was drawn through both tubes at 50 μl/min with opposing flow directions.

Limited data storage meant that the frame rate and duration of acquisition had to be considered in relation to the maximum number of RF data frames that could be stored. Since the microbubble localisation imaging approach requires that the microbubbles sample the entire microvascular structure, a lower PRF to that of previous sections was implemented to enable the passage of many microbubbles through the field of view over a longer acquisition time, as well as ensuring that bubble motion was evident between consecutive frames; these parameters will be further discussed in Section 7.4. The active ULA-OP system was therefore driven at a frame rate of 400 Hz using AM plane

wave transmission at a transmit frequency of 3 MHz. Transmission and reception was performed on all of the 64 active elements in parallel. RF data was saved from both systems simultaneously. A single dataset consisted of a 15 second acquisition corresponding to 6000 individual frames, equivalent to 2000 AM frames once combined. Five datasets were collected and processed for the final visualisation.

Identical post-processing was performed for both active and passive data. Initial frames acquired prior to bubble inflow consisted of water filled tube signals only; these were averaged in order to provide a background subtraction for the remaining frames to reduce the signal from the tube and any other unwanted background signals. Next, an asymmetric median filter of size [2 x 8] was applied; this size was chosen to smooth noise variations across the RF signal frame without significantly blurring the data, which possessed more high frequency detail in the axial direction.

A template-matching algorithm was then used to identify the presence of hyperbole structures in the data by computing the normalised cross-correlation between the RF data and a reference signal, or 'template'. The template was constructed by extracting the scatter signal from previously acquired point scatterer echo in section 7.3ii.5. The position of the maximum cross-correlation identified the approximate position of the scatterer in the data. So as not to bias the bubble localisation by characteristics of the linear scatterer signal, a region of interest surrounding the maximum position of cross-correlation was extracted using a binary mask. The binary mask consisted of a region of pixels with a value of one which extended 4 μs above and below the fitted template position, while the remaining pixels had a value of zero. This allowed extraction of a large axial extent of the detected bubble signals to incorporate phase information in the localisation, while still isolating potential bubble signals from erroneous or noise related signals present in the rest of the data which may decrease the accuracy of the technique. The peaks of each RF data line within the masked frame were then fitted with a second order polynomial; the point on the curve representing the minimum arrival time was estimated to represent the bubble position. Coincident detections of plane wave echoes by both transducers were extracted. Active localisations provided measurement of the axial and lateral bubble positioning, (C_x, C_y) while the passive system enabled localisation within the active transducer's elevational plane, (C_z).

A 3D rendering of the combined localisations was constructed by plotting each estimated bubble location, $C = C_x, C_y, C_z$, as an ellipsoid with semi-axis lengths equal to the previously estimated localisation precisions in the axial, lateral and elevational directions, $\sigma = (\sigma_x, \sigma_y, \sigma_z)$, given by

$$\frac{(x - C_x)^2}{\sigma_x^2} + \frac{(y - C_y)^2}{\sigma_y^2} + \frac{(z - C_z)^2}{\sigma_z^2} = 1,$$

where x , y , and z are the coordinates of any points on the surface of the ellipsoid. Microbubble tracking algorithms developed in our previous work [149] were extended for 3D implementation to determine the flow velocity within the microvessel structure. Intensity cross-correlations between each bubble signal in frame *n* and each of the bubble signals found in frame *n-1* were then calculated and the maximum cross correlation was found for each signal in frame n. A pair of signals were considered to come from the same bubble if the maximum cross-correlation exceeded an empirically determined threshold of 0.4 (significantly lower than that in previous chapters due to the nature of the RF signals compared to beamformed, positive, envelope detected image data). For each pair, a velocity vector was then calculated between $C_x^{\,n}, C_y^{\,n}, C_z^{\,n}$, and $C_x^{\,n-1}, C_y^{\,n-1}, C_z^{\,n-1}$ and assigned to the centroid location $C_x^{\,n}, C_y^{\,n}, C_z^{\,n}$, in frame n.

7.3iii.1.3 RESULTS AND DISCUSSION

Figure 7.37 displays coincident detections of scattered plane waves from microbubbles within a flow phantom, where the peak (white cross) of the fitted curve (black line) is estimated to represent the bubble position. Figure 7.38 displays the combined localisations from all acquired frames corresponding to two adjacent tubes with opposing flow direction. The direction of the detected elevational component of velocity remained relatively constant throughout the data, therefore, the colour of each ellipsoid displayed in the image is defined by the lateral and axial directional components of the velocity vector. Results consist of 3149 localisations assumed to originate from microbubbles coincidentally detected on both systems. The spatial information in the final image appears incomplete. The high localisation precision of the imaging system presents an advantage in that the potential super-resolution accuracy is

high; nevertheless, this puts demanding requirements on the number of localisations required to fully delineate structures in the 3D rendering. Furthermore, the number of localisations per unit area degrades over the field of view; this can be seen by the higher number of localisations detected at the right hand side for one vessel structure, and in the left hand side for the vessel with opposite flow direction. This was visible within the acquired data, as a proportion of the bubbles appeared to dissolve or become destroyed during their movement across the lateral distance. This will be further considered in the Discussion section of this chapter.

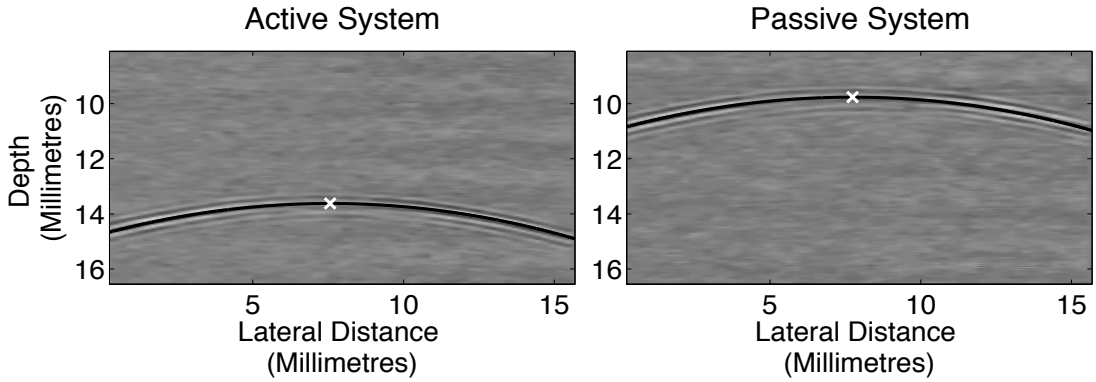

Figure 7.37. Coincident detections of echo from a single microbubble within the flow phantom after background subtraction. A second order polynomial is fitted to the RF echo data (black line) and the peak of this fitted curve is the estimated bubble location (white crosses). These coincident localisations are used in subsequent 3D rendering.

Figure 7.39A shows the projection of the detected localisations along the lateral plane; the capillary tubes are resolved within the diffraction limited elevational resolution (~1188 μm) shown with red dashed lines (Figure 7.39B), where profiles were found to have FWHM of 215 μm and 235 μm, corresponding well to the tube diameter. The elongation of the tube profiles seen in the projection suggests the surface of the tubes may not have been exactly parallel with the transducer face. With micrometre scale target objects such as these, only a small misalignment can cause a noticeable elongation or slanting in the resulting localisations. The FWHM of the profiles are in both cases slightly larger than the nominal diameter of the tubes which may be due to the measurement being performed on the projection of localisations in the axial direction.

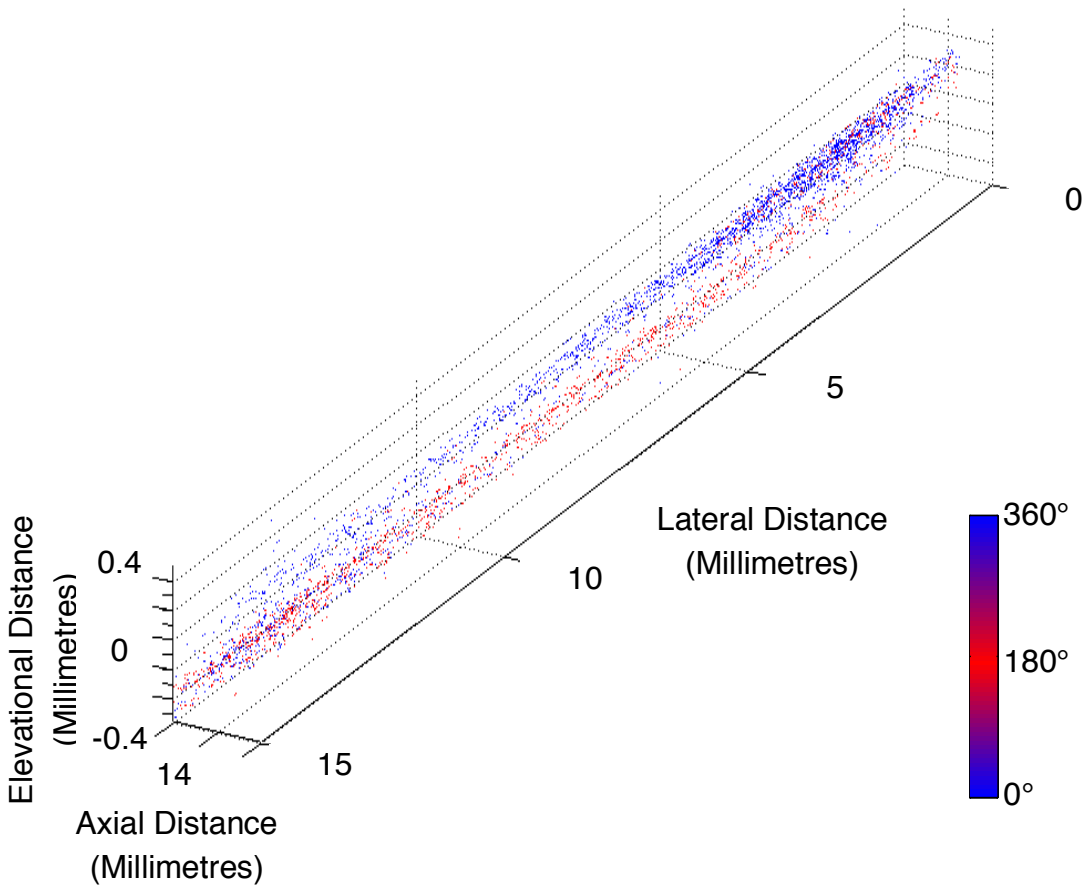

Figure 7.38. Microbubble localisations after coincident detection of plane wave echoes through a flow phantom by active and passive imaging systems. Localisations are plotted as ellipsoids with semi-axis lengths equal to the localisation precision of the system in three dimensions, $\sigma = (\sigma_x, \sigma_x, \sigma_x)$. The color map displays the lateral and axial components of the velocity vector only.

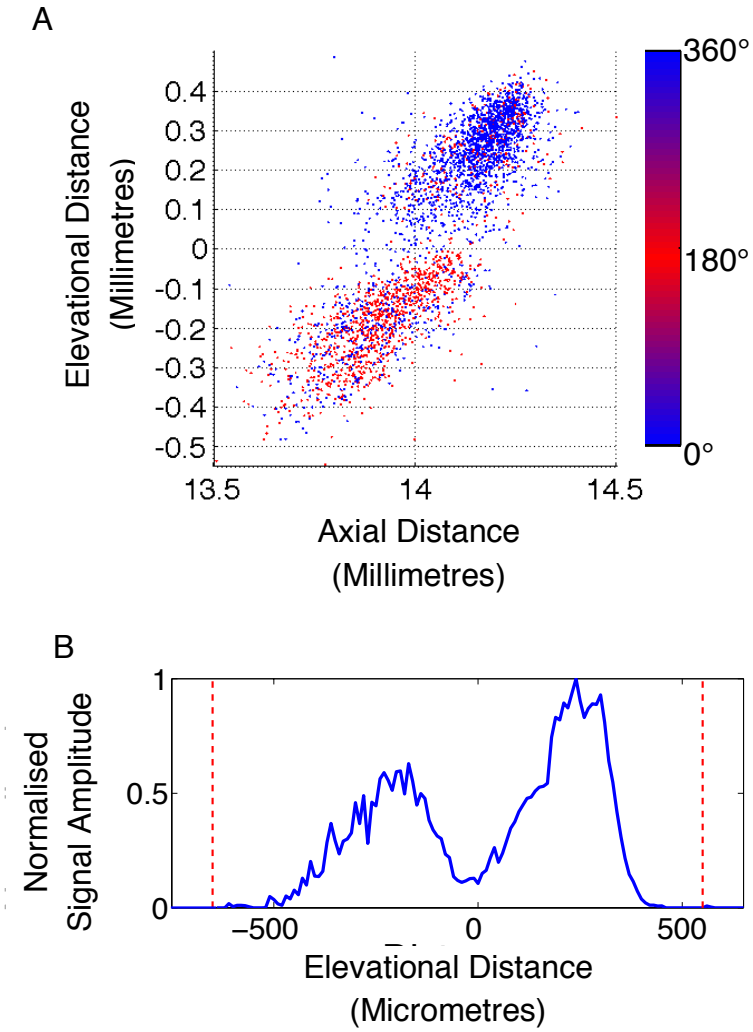

Figure 7.39. (A) The projection of the microbubble localisations along the lateral plane, where colour is used to display tracked direction of the axial and lateral component of velocity. Average profiles show in (B) show the ability to resolve structures within the diffraction limited elevational resolution (~1188 μm – red dashed lines), where profiles were found to have FWHM of 215 μm and 235 μm.

7.3iii.1.4 Summary and Comments

A fast, multi-probe US strategy has been developed for super-resolution imaging in 3D and has demonstrated the ability to distinguish two vessel structures in 3D far beyond the estimated diffraction limited resolution of the system, where image acquisition was performed in under 1.5 minutes. This has addressed two important challenges of the existing 2D imaging set up presented in previous chapters: 1) poor spatial resolution in the elevational plane, and 2) long acquisition times. With additional 3D velocity

mapping, investigation of both structure and flow of microstructures is possible. The relationship between PRF, bubble velocity, and compounding strategies will be discussed in the final section of this chapter.

7.4 DISCUSSION

3D super-resolution using a synchronised, multi-probe imaging configuration allows localisation of bubble signals in 3D with estimated localisation precision approximately two orders of magnitude higher than the original diffraction limited resolution. Plane wave imaging offered the possibility of significant enhancement in time resolution and as such, an opportunity to perform volumetric imaging in more clinically viable acquisition times.

7.4.1 IMAGING CONFIGURATION

With such an acquisition strategy, the elevational slice thickness of each probe governs the potential 3D field of view, in that the poorer the elevational resolution, the larger the potential imaging volume; as such a poor elevational resolution becomes an asset rather than a limitation. To further increase the target region, one or both of the systems can be scanned spatially over a larger 3D region of interest. For example, a mechanical probe can be used as the orthogonally placed passive receiver to detect bubble signals from a wide axial depth range.

The purpose of this chapter was additionally to provide practical demonstration of the challenges associated with this imaging strategy. These include the lack of suitability of the orthogonal imaging set-up for clinical implementation. Indeed, this technique can be performed when aligning the transducers at angles less than 90°, and this is of course the principle implemented in 2D matrix array technology. Nonetheless, this configuration was chosen for the initial proof of concept using the equipment available; an initial exploration into the effect of changing the angle between the transducers displayed no significant effect on the elevational localisation precision (maximum change in localisation precision of 0.6 μm), while higher SNR appeared to have affect on the localisation error, however full implementation with smaller angles could be a topic for further investigation.

7.4.2 PHANTOM DEVELOPMENT

The advantages of paraffin-gel waxes over alternative materials are their longevity and structural rigidity. The phantom acoustic parameters were in accordance with values reported in the literature [332]. For future use of paraffin gel phantoms, carnauba wax can be added to vary the attenuation coefficient, and glass microspheres can be added to act as tissue scatterers [332].

7.4.3 LOCALISATION PRECISION

The localisation precision has been shown to vary with frequency, position in the field of view, and data processing techniques. Thus, an overall localisation precision cannot be defined for the entire imaging procedure, but instead estimates can be gathered to approximate the accuracy of 3D super-resolution.

The localisation precision is no longer affected by pixelation associated with image data as discussed in Chapter 5; instead other imaging parameters such as the sampling rate of the system (the temporal resolution of acquisition is predominantly limited by the system sampling frequency), the number of transducer elements, the echo duration, and the aperture size are likely to have a fundamental effect on the localisation precision of RF plane wave echoes [198]. In 1986, Bobroff defined the limit to which the position of a signal could be estimated for general experimental data analysis to be based on the instrument resolution, the sampling density, and the data SNR [198]. The diffraction limited US axial resolution is proportional to the SPL of the signal, while the lateral resolution improves with aperture length (the width of the combined number of elements used in the transducer), and increasing frequency. Localisation precision measurements display an increase in localisation precision with higher transmit frequencies. This suggests that with increasing depth penetration, and the use of lower insonating frequencies, there may be a compromise in localisation precision in the final super-resolved image, as also indicated in Figure 7.30; precisions were found to change by a few micrometres per 1 MHz decrease in frequency in this experimental set-up. It is expected that as well as an increase in frequency, a larger aperture and higher number of elements will contribute to a higher localisation precision (lower standard deviation σ). In US however, the PSF is highly dependent on the position of the source within the field of view. The impact of the lateral scatterer position within the field of view on the

standard deviation was investigated, and remained relatively stable within the central imaging region (Figure 7.29). However, as the target neared the edge of the field of view, the lateral precision reduced considerably, where the detection of signals from only a single side of the scatterer was possible. Localisation appeared more reliable when the targets are in the centre of the imaging volume. This super-resolution process is therefore spatially varying, and its limit will be determined by a combination of these imaging factors. Although SNR measurements did not provide conclusive results in regards to whether localisation error directly relates to changes in noise levels, it has been indicated that this remains an important factor in determining the precision of the technique (Figure 7.29 and Figure 7.35).

7.4.4 LOCALISATION ACCURACY

The accuracy of localisation will be affected by assumptions involved in the centre of mass approach. This method obtains the intensity weighted centre of the bubble signal, however, the signal obtained from an object contains the time varying reflection of a pressure wave received at the probe. Thus, the actual location of the scatterer may not occur at the centre, but instead may be situated at a location close to the beginning of the returned pressure wave. If this was the case, the centre of mass localisations would be subject to a bias in their actual positions equal to approximately half of the spatial pulse length, and thus of the location of the target vasculature. However, in the case that echoes are asymmetric in the axial direction e.g. due to ringing, a non-Gaussian transmit pulse, or aberration, this could cause variable inaccuracies, and would blur the resulting localisation positions. This is an important topic for future investigation.

7.4.5 MICROBUBBLE IMAGING AND LOCALISATION RATE

An increase in temporal resolution using plane wave imaging not only allows faster 3D image acquisition, but also should provide a higher bubble localisation rate for a given microbubble concentration, and moreover, may improve velocity estimations due to more frequent sampling. Since super-resolution microbubble imaging relies upon the combined contributions of many localisations over time, for a given microbubble concentration, a greater frame rate should therefore result in a decrease in the overall acquisition time. Nevertheless, the super-resolution technique requires that the microbubbles sample the entire microvascular structure during acquisition to provide

full spatial information. This, therefore, places a limit on the minimum imaging time possible for adequate visualisation.

In the case of imaging moving bubbles, two competing factors are at play when thinking about acquisition time; these relate to blood flow velocity and frame rate. Firstly, in order for microbubbles to provide new spatial information in each frame, the bubbles must be moving, and their position in each frame should contribute supplementary spatial information to the final rendering. As such, one can define 'supplementary' information to be the occurrence of a bubble localisation in frame $n+1$ in which the bubble has moved beyond the FWHM of the 2D Gaussian distribution plotted for the same bubble localisation in frame n. In other words, the bubble velocity should be large enough that its movement exceeds the localisation precision of the imaging system (equal to the 2D Gaussian localisation distribution) in each CEUS multi-pulse compounded image. This becomes more important when fast plane wave imaging is implemented in contrast to considerably lower frame rates employed in previous chapters. Thus, for a PRF of 3000 Hz, using multi-pulse imaging where the number of pulses, $N_{pulses} = 3$, and localisation precisions of 1.9 μm axially and 11 μm laterally, the velocity of bubbles in the lateral and axial directions, v_{bx} and v_{by}, which provide new spatial information in each frame can be given by the following relations

$$\begin{aligned} v_{bx} &\geq \sigma_x \cdot Imaging\ Rate \\ &\geq 11\ \mu\text{m} \cdot 1000\ Hz \\ v_{bx} &\geq 11\ \text{mm/s} \end{aligned} \tag{7.13}$$

and

$$\begin{aligned} v_{by} &\geq \sigma_y \cdot Imaging\ Rate \\ &\geq 1.9\ \mu\text{m} \cdot 1000\ Hz \\ v_{by} &\geq 1.9\ mm/\text{s} \end{aligned} \tag{7.14}$$

The required lateral velocity for this condition to be true, v_{bx}, is far higher than the expected velocities within the microcirculation (mostly under 10 mm/s). For the

microbubble experiment shown in section 7.3iii, a PRF of 400 Hz was used, and thus equations (7.13) and (7.14) become

$$v_{bx} \geq 1.5 \text{ mm/s}$$
$$v_{by} \geq 0.25 \text{ mm/s},$$

which is more in line with microvascular blood velocities (Chapter 1, Table 1.1). This can help to define the limit to which increasing the frame rate will no longer gain spatial structure in the image. Nevertheless, as previously mentioned, this condition does not mean increasing the frame rate will not be valuable; above this frame rate, localisations from bubbles below $v_b = (v_{bx}, v_{by})$ will still contribute signal to the final rendering, and thus will enhance SNR in the final image even if they do not provide new spatial information. Indeed, the occurrence of many localisations within a spatial region can importantly indicate the amount of blood flow through an area.

Conversely, the frame rate should be high enough that bubble motion during multi-pulse frames does not drastically affect the result of coherent compounding. The compounding of image data involves sending multiple plane wave transmissions for each nonlinear plane wave pulse, i.e. for each phase inverted or amplitude modulated pulse in PI, AM, or PIAM transmission. Bubble movement between each plane wave transmission may mean the plane waves may not be added coherently, and could result in artefacts, incomplete suppression of linear targets, or a smearing or spreading of nonlinear signals in the direction of motion. It is noted that an axial displacement of approximately half a pulse wavelength, 255 μm in this case, during the time required to acquire a frame will lead to destructive interferences in the compounding operation and as a result image degradations [336]. Higher phase coherence is required to avoid motion artefacts in the axial direction than the lateral since the spatial frequency in the axial direction is much higher, while in the lateral direction the point spread function acts as a spatial low-pass filter [244], [336]. At a speed of 1 mm/s, above average within the capillaries, bubble motion in a single AM frame (3 pulses) at 3000 Hz would equate to 1 μm. This is far below the estimated PSF size, and furthermore is smaller than the axial and lateral localisation precisions of the imaging system and thus should not significantly affect the accuracy of the technique. At a PRF of 400 Hz, bubble

movement during multi-pulses would increase to 7.5 μm. Smearing due to fast bubble movement in compounded images may cause a reduction in localisation accuracy. Nevertheless, this should not cause a problem to the final visualisation if the bubble trajectory remains within the lumen of the vessel, i.e. without sharp change in direction during each pulse sequence.

This study involved the use of single angle plane wave transmission. Multi-angle compounding has previously been demonstrated to provide improved SNR and lateral resolution to that of single angle transmission [189], and therefore its implementation may contribute to an improved localisation precision (reduced $\sigma = \sigma_x, \sigma_y, \sigma_z$) when estimated on a stationary scatterer. However, to provide benefit, the localisation precision should improve by more than the corresponding decrease in precision caused by the effect of bubble motion due to slower imaging rates with the addition of compounding imaging pulses, N_{pulses}. As such, multi-angle compounding in conjunction with multi-pulse contrast imaging must be considered in relation to the time taken to acquire the signal and the relative motion of the bubble. For example, at 1 mm/s, bubble motion in a single AM frame (3 pulses) at 400 Hz with 12 wave multi-angle compounding would increase to 90 μm. Thus the gain in localisation precision must also outweigh the inaccuracy due to target motion in order for this to enhance the technique. Furthermore, the potential for microbubble destruction caused by repeated insonation by successive US pulses across the field of view, as was evident in this experiment, must be considered in relation to transmit pressure and PRF.

7.4.6 MICROBUBBLE DETECTION

The finite dimensions of the US pulse and the detector sensitivity will alter the appearance of the detected signals [337]. The transducers' elevational amplitude profiles could result in variation in receive signals from each of the probes. For example, a bubble within the centre of the elevational field in active transducer may appear as a weak signal in the orthogonal passive receiver if it is located on the edge of the elevational field of view in detection. This may be a reason that slightly more localisations are detected in the active transducer than in the passive. The acceptance of only coincidental detections on the active and passive transducers is an additional noise reduction step, whereby noise or other false positive detections identified on one system

are unlikely to occur simultaneously on the passive system also and hence may lead to a decrease in noise localisations in the final rendering.

In addition, the approach used here relies upon the detection of monopole scattering from spatially isolated scatterers. Aberration effects, caused when sound waves travel through heterogeneous tissue layers with spatially varying mass density ρ, and bulk compressibility χ, result in time-delay differences in the propagating wave. This can degrade the focusing of the US beam, and as such, can affect the appearance of scatterers in the image. Recognition of these isolated, monopole scatterers would thus be difficult, and the centre of mass of the resulting aberrated signals are likely to be inaccurate. Hence, the development of aberration correction procedures will be essential for accurate microbubble detection, particularly for deep tissue imaging.'

7.4.7 RF DATA AVAILABILITY

As discussed in Chapter 1, in conventional US imaging, images are generated by taking the amplitude of the envelope of the RF echo signals received at the US probe. This process does not retain the phase information of the RF signals and is affected by pixelation. The availability of volumes of RF data allows both the amplitude and phase information of the US signals to be utilised. The use of plane wave RF data showed higher localisation precision to that performed on beamformed reconstructed data (offline). The availability of volumes of RF data should allow the more accurate detection and correction of 3D motion effects and may be more robust in the case of overlying, aberrating tissue [151].

7.4.8 MICROBUBBLE SCATTERING

If bubble behaviour is not strictly that of monopole scattering, the received signal may have angular dependency and hence have varying appearances when observed with different detector arrays. There exists possible contributions to the emitted sound pressure from a bubble which have not been included in existing theory discussed in Chapter 2. These include direct or indirect results of bubble shape oscillations [166] causing an orthogonal pressure field term. If the bubble itself is translated by the incident sound, an additional scattering cross-section with a characteristic angular

dependence results [158] [166], as introduced as dipole scattering in Chapter 2. In literature, for the case of a gas bubble in a liquid, this contribution is of the same order of magnitude as the passive contribution solely due to the presence of the bubble, and is assumed to be negligible [166]. However, a study by Ye et al. regarding Albunex bubbles found that under certain situations, scattering may not solely be due to monopole vibrations [338]. In this study, anisotropic scattering was investigated, where differences between forward and backward scattering occurred when the bubble radius was greater than the resonance frequency radius of the bubble, and this relationship was shown to depend on both driving frequency and bubble diameter. Furthermore, if two or more bubbles are in close proximity, they will alter the emitted sound field either by direct secondary scattering, or indirectly by modifying their modes of oscillation for example via secondary Bjerknes forces [339]. Investigation into whether non-spherically symmetric scattering would cause inaccuracies in the centre of mass localisation strategy and to what degree would be a point for further investigation. Since here the technique uses a low bubble concentration designed to image spatially separated bubble signals, and in addition to limit bubble-bubble interactions, these effects have not been incorporated into the post-processing analysis but are restricted to the case of isolated bubbles.

7.4.9 Comparison to Other 3D Super-Resolution Techniques

Three dimensional super-resolution techniques have been reported by two other groups, namely O'Reilly et al. 2013 and Desailly et al. 2013. Both implement the use of specialised transducer technology. In the first, the use of a hemispherical transcranial therapy array where the transmit focus was steered through a volume with 2 mm step size allowed the visualisation of a spiral structure through an *ex vivo* skull [151]. Localisations demonstrated improvement over diffraction limited US data, however the lack of 3D rendering means that analysis of the resolution in all three dimensions is limited, although an average localisation precision of approximately 40 μm in the elevational direction is stated, compared to 1.9 μm in this work. Furthermore, localisations far exceeded the internal diameter of the tube (255 μm), where detected positions were found over 600 μm from the tube centre line. Desailly et al. 2013 imaged a tilted 2D structure using a 2D matrix array transducer [340], however the absence of

3D rendering or analysis of elevational resolution means comparison to this technique is limited.

7.5 CONCLUSION

The use of plane wave imaging in a synchronised, multi-probe imaging configuration allows 3D super-resolution beyond the system diffraction limit with significant enhancement in time resolution. When choosing the imaging frame rate, consideration of the localisation precision, the expected range of microbubble velocities for a given sample, and the density of microbubbles in the field of view will aid efficiency of the technique.

8 CONCLUSION

8.1 SUMMARY

The work in this thesis was motivated by the need to assess details of the microcirculation non-invasively. Acoustic super-resolution is a technique that draws strength from the behaviour of intravascular contrast agents that mimic the dynamics of red blood cells.

To examine the accuracy with which the location of a bubble can be found, one must first consider and account for US system parameters. This thesis therefore began with a demonstration of such parameter effects on the potential localisation precision in a conventional US imaging system (Chapter 3). Moreover, demonstration of *in vitro* acoustic super-resolution imaging was performed down to a depth of 7 cm, allowing visualisation of a number of microvessel phantoms at sub-diffraction scale. This provided an insight into the potential of the method, and introduced some of the challenges involved in the identification and accurate localisation of single bubbles. Furthermore, a temporal tracking algorithm was introduced and tested on phantoms, enabling extraction of dynamic information of the fluid flow at a super-resolved spatial scale.

To the best of our knowledge, Chapter 4 demonstrated the first super-resolution imaging

with super-resolved velocity tracking performed *in vivo*, where visualisation of microvasculature structures with FWHM of under 20 μm at imaging depths of up to 1.5 cm *in vivo* was achieved. This was performed on a mouse ear model using image data from standard equipment routinely used in clinical US scans. Within this chapter, a sub-pixel rigid motion correction algorithm was developed and implemented, and velocity tracking results provided visualisation of microcirculatory dynamics shown to provide further differentiation of already highly resolved coupled vessel structures by distinguishing clearly opposing flow directions associated with paired arterioles and venules. Furthermore, the affect of longer image acquisitions demonstrated the build up of structural detail in the images over time.

The following chapter explored the opportunity for super-resolution imaging to provide quantitative measures. Chapter 5 introduced new methods to assess microvascular perfusion from localisation data. *In vitro* validation demonstrated good correlation of measures to known microbubble concentrations and flow speeds. Furthermore, a new automated method was introduced to remove spatially varying background signals. In the second section of Chapter 5, localisation number and density measures were able to demonstrate a significant relative change between pre- and post exercise scans for healthy patients, and a considerably reduced, insignificant relative change was found for patients with symptomatic PAD. Bubble localisation number was shown to be more repeatable than peak intensity and TTP perfusion parameters derived from destruction replenishment TICs for a sample of subjects within a repeatability study, and has been shown to provide comparable but slightly lower repeatability to that of flow rate.

Chapter 6 explored the use of machine learning techniques for foreground/background detection and single bubble identification in both *in vitro* and *in vivo* data. Superpixel foreground detection allowed close to automated image segmentation. The proposed SVM machine learning method in combination with superpixel foreground segmentation demonstrated the most promising results for single bubble detection with limited user input, while the unsupervised techniques investigated showed unsuitable classification results.

In Chapter 7, the development and implementation of a fast, synchronised, multi-probe compounding strategy allowed 3D super-resolution and flow detection in little over a minute of acquisition time. This was able to resolve tube structures within the diffraction limited elevational resolution evident in existing 2D super-resolution with the use of a secondary passive probe; the average 3D localisation precision of the system was estimated to be approximately 2 orders of magnitude higher than the 3D diffraction limited resolution.

Overall, this technique has been able to overcome a number of limitations of established methods for imaging the microvasculature, and compares favourably to many existing high resolution US techniques, where advantages include:

- No specialised equipment is required: 2D super-resolution can be performed on conventional clinical scanners, using just image data for simple and direct implementation (as demonstrated in Chapters 3-6).

- The technique does not suffer the same depth penetration limitations inherent in many other high resolution US/hybrid techniques: The method has been demonstrated down to 7 cm *in vitro* and 4 cm in humans (Chapters 3 and 5).

- Haemodynamic information can be extracted: An extension of the technique enables the visualisation of blood flow at super-resolved scales within the microcirculation, and has been demonstrated to resolve slow flow speeds under 1 mm/s *in vivo* (Chapter 4).

- 3D super-resolution is possible: Super-resolution imaging will further benefit from advances in US technologies such as 2D matrix arrays with ultrafast plane wave imaging for 3D imaging (initial demonstration shown in Chapter 7).

- Quantification measures may provide additional clinical value: With further development, super-resolution imaging has the potential to provide quantitative information in addition to image rendering through counting and tracking

algorithms (Chapter 5).

Nevertheless, many challenges still remain to be investigated, creating a wealth of possible future work. These will be discussed and proposed in the following two sections.

8.2 DISCUSSION OF KEY FINDINGS AND LIMITATIONS

8.2.1 LOCALISATION PRECISION

The theoretical resolution limit corresponds to the position error of the localisation process. Specifying this is not only of importance to be able to characterise the level of accuracy that is achievable, but it also has significant effect on the choice of imaging target that can be accurately studied using this technique [199]. Imaging targets should have a size larger than the localisation precision of the system in order to accurately delineate their structure; thus, localisation precisions below 5 μm would be desirable for imaging capillary structures.

For single, isolated signals in image data, this is inherently limited by the SNR of the system and pixelation of the image data (Chapter 3-5). Pixelation has been shown to affect the achievable localisation precision due to limitations imposed by reduced data sampling, as discussed in Chapter 5. This indicates that precisions will be reduced with a larger field of view when the final image is constructed with a lower sampling rate. Within RF data, the localisation precision is determined by the number of channels used in receive processing, and the temporal resolution of the acquisition system, which is predominantly limited by the system sampling frequency prior to beamforming (Chapter 7). The inherent system sampling frequency is unaffected by the imaging field of view. Variation of the parameters discussed here, and their effects on localisation precisions achievable with both image and RF data experimentally and in simulation would be beneficial.

Experimentally, a wire imaging target has been demonstrated to provide considerably different signals to those of microbubbles (Chapter 3), and therefore the study of the

localisation precision using stationary bubbles under varying US insonation will be valuable. The fitting of a 2D Gaussian model was shown to be unsuitable for the identification of single bubble echoes. The imaging of single stationary bubbles could improve the understanding of varying bubble echoes for the development of signal models more suitable to bubble echo fitting, and hence accurate localisation. In addition, analytical models could be developed which use the time of flight and imaging system parameters to estimate the achievable localisation precision.

Further analysis of the factors discussed here should uncover the true extent to which US super-resolution can provide improved visualisation and the accuracy to which measurements can be reliable.

8.2.2 Single Bubble Identification and Localisation Methods

Accurate single bubble signal extraction is important to eliminate false or inaccurate localisations, and to ensure efficiency of the method. A fast post-processing technique for single bubble localisation and tracking was implemented in Chapters 3-6; the centre of mass of the single particle image was extracted using an algorithm that firstly used the characterisation of the noise intensity of the system along with thresholds to reject signals deemed to be outside the expected size range of single bubble signals as a simplistic foreground extractor. Unlike many fitting techniques, the position estimator requires little prior information about the shape or characteristics of the tracked particle image and uses only simple arithmetic operations, making it appropriate for future hardware implementation and real-time feedback applications. Nevertheless, a model built upon the physics of single bubble signals, which can reliably identify and reject the existence of multiple, inseparable bubble signals, may be able to enhance the accuracy and reliability of post-processing procedures. Further development in signal processing for analysing dense and complex data may also enable this technique to become more efficient. The development of algorithms that are able to simultaneously fit multiple partially overlapping single bubble models instead of just one may facilitate the imaging of a higher concentration of microbubbles and thus increase localisation rate [230], however caution must be taken that speckle effects do not occur. Furthermore, the

separation limit to which microbubbles can be accurately localised remains to be explored, and consideration of subsequent bubble-bubble interactions will be necessary.

As previously discussed, both the centre of mass approach, and peak finding using Gaussian fitting make the assumption that the intensity weighted centre or peak of the received signal represents the location of the underlying scatterer. In reality, the leading edge of the pressure wave may instead be a more accurate estimate of the actual scatterer location. This could result in a bias in the axial positioning of many such scatterers, or blurring and deterioration of the image in the event of asymmetrical and/or varying scatterer signals. These must be the topic of future work, and the estimation of the quantifiable effect this inaccuracy may have is important.

Chapter 6 introduced the use of a range of learning algorithms to provide semi-automated and automated post-processing. Initial results demonstrated promising results when implementing supervised classification algorithms (SVMs), while the unsupervised techniques investigated appeared unsuitable. Limitations discussed within the chapter indicate there may be potential for the implementation of more complex algorithms. This will be discussed further in the following future work section.

8.2.3 TIME RESOLUTION AND DURATION OF ACQUISITION

Because of the trade-off between acquisition time and spatial information intrinsically involved, super-resolution imaging is in general slower than many conventional US techniques. However, as has been shown, dynamic processes such as bubble velocity can be extracted which could provide significant clinical value in combination with structural information [12], [19]. Nevertheless, time resolution and the duration of acquisition will have impact on the suitability of super-resolution for imaging biological structures and their clinical relevance. Furthermore, minimisation of acquisition time will not only help the technique become practically feasible for the clinician, but will help to reduce motion effects.

The frame rate achievable is reduced for larger propagation depth to allow time for the reception of echoes; this increases the acquisition time of all US imaging, however they

are still able to operate in real time. For super-resolution imaging, there will of course be a resulting increase in acquisition time to accumulate spatial information in the final image. An alternative image display technique could involve the plotting of localisations in each frame, generating the image by gradually accumulating localisations in real time. This could provide dynamic visual display for more immediate feedback, where the acquisition can be performed for as long as necessary for visualisation of the specific application.

In a plane wave imaging system, the imaging rate is no longer lengthened by the requirement to acquire line-by-line focussed pulses as in conventional imaging, but is limited by the time of flight of a single pulse to reach the target and return to the transducer. At a depth of 8 cm, the optimal imaging rate becomes approximately 3000 frames per second when using three multi-pulses for CEUS imaging. Fast plane wave imaging has been demonstrated to achieve localisation precision suitable for imaging microvascular targets (1.9 – 11.0 μm) in *in vitro* work presented in Chapter 7, and provides the opportunity to drastically reduce the acquisition time due to these very high frame rates. However, the requirement remains that the microbubbles should sample the entire target structure to provide full spatial information in the final result. Therefore, there is a limit to which the increase in PRF will no longer reduce the acquisition time, and this will depend upon the blood velocity within the vessel of interest. The imaging of capillary flow travelling at an average of 300 μm/s at a PRF of 3000 Hz (equivalent to an imaging rate of 1000 Hz using three multi-pulses) will require a localisation precision better than 0.3 μm in order to provide new spatial information in each consecutive frame as defined in Chapter 7. Therefore, it may not be beneficial to increase the frame rate further (apart from to increase the image SNR), and may even degrade the technique if bubbles are prone to disruption with repeated insonation (possibly due to high pressure transmit waves or for bubbles which are less stable). Further investigation into these factors, and alternative plane wave acquisition strategies to reduce acquisition times is required.

The relationship between frame rate, contrast agent concentration, localisation precision, and the diffraction limited resolutions are included in a model in Appendix

Section 9.1. As expected, in this model the acquisition time increases with those parameters which tend to increase all CEUS imaging techniques (increased imaging depth, increased number of pulses within multi-pulse CEUS imaging techniques, and a decreased speed of sound in the medium of interest). The super-resolution component demonstrates an inverse relationship between imaging time and localisation error in the super-resolved images. This is due to the increased size of the Gaussian localisation plots in the final image; since the size of the 2D Gaussian profile plotted in the final image compared to the target vessel area governs the quantity of localisations required to create adequate visualisation in the image in this model. In reality, higher precisions are still favourable, and modified image rendering techniques could be developed to create improved visualisation. Additionally, higher diffraction limited resolutions enable increased numbers of spatially isolated signals to be present in a given imaged region, i.e. a higher concentration can be used since the signals will have a higher probability of being spatially separated than with a poorer resolution; this provides the potential for a higher localisation density per frame and hence will lead to reduced acquisition times.

8.2.4 MICROBUBBLE VELOCITY AND VELOCITY TRACKING

The ability to track the micrometre-scale motion of contrast agents in clinical US would greatly improve non-invasive access to micrometre-scale haemodynamics. By tracking the local motion of bubbles over successive frames, estimations of bubble motion could be measured over a large range of velocities, from micrometres per second to centimetres per second, as demonstrated in Chapters 3 and 4, where the exact sensitivity depends on the frame rate and localisation precision. Thus, improvement in the localisation precision discussed in Section 8.2.1 will have a direct impact on the sensitivity and accuracy of velocity estimations. Super-resolved velocity mapping additionally enables the detection of velocity measurements over 360° in plane, or a full 3D velocity vector in 3D acquisition. Full directional analysis may be particularly valuable for assessing the tortuosity of the microvasculature.

Quantitative velocity measures applied in Chapter 5 did not identify significant changes in microvascular blood speeds for healthy patients following exercise as hypothesised.

The error on velocity measurements resulting from poor localisation precision in clinical image data, in addition to the more complex vascular structure (particularly in the elevational plane) and reduced SNR may have contributed to this result. As mentioned previously, more advanced tracking may therefore be required such as Monte Carlo data association algorithms [279]. Furthermore, the use of a smaller ROI, or access to RF data may improve the measure's performance.

8.2.5 MOTION CORRECTION

For *in vivo* implementation, motion or deformation of tissue is inevitable and will become a critical source of error. Target motion was evident in Chapter 4 and 5, in which a rigid sub-pixel motion correction strategy was developed and implemented in post-processing procedures. The occurrence of non-rigid motion however cannot be addressed with this technique. In the future, implementing appropriate motion-correction algorithms incorporating non-rigid image registration techniques such as those developed for the medical image registration toolbox for MATLAB (MIRT) [245], [246] may be useful, however the accuracy of this method for sub-pixel displacement in US images requires investigation. Future work should build upon the extensive work developed within the tissue motion tracking and elastography field [243]–[247]. Motion-correction algorithms exist based on the cross-correlation of RF signals acquired at high frame rates, which have been demonstrated to compensate for motion down to tens of micrometres [244], and have been implemented to detect small displacements in shear-wave elastography. The development of motion correction techniques which can preserve the high precision achieved with super-resolution (in the range of a few microns) is required.

8.2.6 QUANTIFICATION

The study presented in Chapter 5 was performed on a small group of subjects and thus an increased number of both control and symptomatic subjects, along with measures of disease grading and progression, are required to demonstrate diagnostic validation and value. Furthermore, the implementation of a non-rigid motion correction algorithm, such as those discussed in Section 8.2.5, may also generate improved visualisation of microvessels, and furthermore may provide an improvement in results found for tracked

microbubble speed. With further validation and refinement, super-resolution techniques could improve quantification using existing CEUS imaging procedures for both macro- and microvessel imaging. This could be done by reducing infusion rates or injecting lower bubble concentrations and applying localisation algorithms.

Quantification using super-resolution does not necessarily require the superposition of localisation data for visual display, and it may instead be clinically valuable to employ the localisation technique as a bubble counting or tracking method. An additional benefit for the application of super-resolution for quantification analysis therefore may be a reduction in acquisition time. Limiting the imaging duration could still provide enough information to extract useful quantitative measures, and could involve dynamic information using destruction imaging to generate quantitative values such as the number of localisations over time, while the spatial distribution of information in final image would not need to be sufficient for adequate qualitative analysis.

8.2.7 ABERRATION

US imaging is based on the time-of-flight between a probe element and a target. Generally, conventional US scanners model the target medium as homogeneous and therefore assume a constant speed of sound of approximately 1540 m/s. In reality, the human body comprises varying tissue layers with inhomogeneous acoustic velocities, thus beamforming operations are affected by spatial variations in the US propagation velocity. When sound waves travel through heterogeneous tissue layers with spatially varying mass density ρ, and bulk compressibility χ, the resulting time-delay differences in the propagating wave degrades the focusing of the US beam and increases the side lobe level. This can lead to reduced spatial and contrast resolution which reduces the clinical value of the images [341]. This phenomenon is called aberration. Aberration effects are predominantly generated in the human body wall, which is composed of skin, subcutaneous fat, muscle and connective tissue, where typical velocities range from 1478 m/s for fat, 1547 m/s for muscle, and 1614 m/s for skin and connective tissue, and constitute the largest sound speed differences in the human body [341].

The large number of publications concerning US aberration and aberration correction is

an indication of the research requirement and efforts to develop correction methods for US imaging as a whole [342]–[348]. This is an inherent problem common in all US imaging, nevertheless, disparities between US propagation velocities are likely to have a more notable affect on the micrometre scale precisions involved in acoustic super-resolution imaging. With the speed of sound in skull bone varying from 2000 to 4000 m/s [2], aberration correction is a crucial part of any effective transcranial imaging procedure. The correction of aberration effects on the imaging of single bubbles has been demonstrated through the use of phase correction techniques for RF data in O'Reilly et al. 2013 [151]. In this method, the source position was estimated by fitting a Gaussian function based on the experimentally measured PSF of the system to the beamformed RF data without phase or amplitude correction. Geometric delays associated with this point scatterer from this source location were then determined. The difference between estimated geometric delays, and the measured echo delays between each of the RF lines received at each of the transducer elements would then provide the correction delay [151]. As a first step, simulations could be formulated to investigate the implications of aberration on imaging deep target structures; additionally techniques such as this could be tested using phantoms with overlaying aberrating materials. Possible implementation will be described in the following future work section.

8.2.8 US CONTRAST AGENTS

Microbubbles are approved for clinical use worldwide, and although not used routinely for clinical US scans, their use as a contrast imaging agent in diagnostics and therapeutics is continuing to grow. Currently, microbubbles manufactured commercially for diagnostic or therapeutic purposes consist of polydisperse populations. The broad size distribution of SonoVue™ used in this work was illustrated in Chapter 3. As has been observed in *in vitro* work, a large variation in the characteristics of bubble signals exists; these are likely to depend on many properties of the individual bubbles such as its size and composition, and proximity to a boundary [169], [180], [207], [208]. Since super-resolution algorithms currently rely on detection of the expected acoustic response from a bubble, improvements could be facilitated with the use of improved microbubbles.

One possible modification of super-resolution therefore may involve the use of mono-dispersed bubbles, as developed by a number of research groups internationally [349]–[352]. Since interactions of an US wave with microbubbles depend highly on their size and can change drastically with small differences in diameter, utilising a uniformly sized bubble population should result in a more consistent response and, when combined with the optimal excitation frequency, an increased echo response [210]. This may mean that more bubbles could be localised with high precision, resulting in gains in sensitivity, acquisition speed and resolution. However, due to a spatially variant PSF, there will still be some variation in signals across the field of view. This will be discussed further in the following future work Section 8.4.

8.2.9 MICROBUBBLE CONCENTRATION

A suitable bubble concentration is crucial for efficient data acquisition. Too high and the occurrence of multiple, unseparable signals will limit the number of isolated signals detected, too low and the requirement for a large number of frames will mean a long acquisition time. As demonstrated in Chapter 3 and 4, the calculation of the required microbubble concentration prior to imaging based on the imaging sample volume is challenging, and is likely to be unfeasible in a clinical environment. Sustaining a suitable concentration of microbubble scatterers within the image volume may instead require development of an automatic feedback system that regulates the bubble concentration. By automatically monitoring the bubble density per frame during image acquisition according to the optimum predicted by statistical models (such as Poisson statistics), the concentration information could be used to drive an infusion pump delivering adjustable microbubble concentrations.

8.2.10 2D/3D SUPER-RESOLUTION

The implementation of fast, 3D *in vivo* imaging is essential for clinical translation. The majority of the work presented in this project was limited by the underlying 2D acquisition strategy with no super-resolved information in the elevational plane, with the exception of the final chapter. Some of the challenges evident when using traditional US imaging with a 1D transducer included constrained spatial sampling to a single imaging plane at any one time, out of plane motion resulting in an unrecoverable loss of

data, degradation of super-resolution imaging due to poor elevational resolution, and a limited imaging volume which would cause long acquisition times for complete organ or tissue analysis.

Three dimensional super-resolution imaging presented in Chapter 7 demonstrated the ability to localise bubble signals with high precision (1.9-11.0 μm) using only a single angle plane wave. Nevertheless, this chapter highlighted the requirement for a considerably large number of localisations for adequate 3D visualisation. Furthermore, the physical configuration of the acquisition strategy was not ideal. Two-dimensional matrix transducer arrays are now enabling volumetric, real-time contrast imaging to become a reality. Possible super-resolution implementations will be discussed in Section 8.4. Ultrafast US imaging has developed significantly in recent years for non-CEUS clinical applications and is currently revolutionising the role US can play in clinical practice. The generation of 3D velocity mapping at depth *in vivo* would enable analysis of microvascular morphology, blood flow dynamics and occlusions resulting from diseased states in real-life applications.

8.2.11 DEPTH

In vitro demonstrations of acoustic super-resolution in this project have been performed down to 7 cm. Current clinical use of US contrast agents routinely detect signals from microbubbles at over 10 cm depth in the body and thus it is believed this approach has the potential to image at these depths. The effect of depth on localisation precision however is yet to be fully investigated.

8.3 COMPARISON TO OTHER US TECHNIQUES

8.3.1 NON US/HYBRID TECHNIQUES

In reality, each imaging modality has its own strength and limitations depending on the specific clinical application and target location. Acoustic super-resolution is of course limited to structures that can be accessed with US. For example, MRI and CT are capable of penetrating structures such as the skull and lungs, while US is ideal for imaging the soft tissues such as the abdomen, heart and many other organs. In general,

many high resolution *in vivo* imaging techniques suffer from trade-offs between achievable spatial resolution, acquisition times and depth penetration. Micro-CT [353], [354] and high resolution MRI techniques [355], [356] are able to image vessels, at depth, at a resolution of tens of micrometres, but are limited by long acquisition times, as well as issues inherent to each technique including the magnification of vessel sizes (MRI), primarily revealing venous vessels (MRI), expense (MRI), lack of suitability for human imaging (micro-CT) and ionising radiation (micro-CT). As discussed in the literature review, photoacoustic techniques do not require microbubbles and have reported resolutions down to a few micrometres laterally and 15 μm axially (PAM), but with a limit of approximately 0.7 mm penetration depth [357], [358], while UA-PACT provides an increased depth (50 mm) but with a considerable reduction in the achievable resolution to 800 μm laterally and 300 μm axially, comparable to diffraction limited US resolutions [134], [138], [359]. Moreover, translation to the clinic will require specialised equipment [134]. Lastly, acoustic angiography is able to resolve tumour vessels with a diameter of 150 μm, but suffers from the trade-off between penetration and resolution [131], [132].

Safe, low cost, real time imaging at low frequencies using microbubble contrast agents as vascular markers, as well as the possibility of high frame rates, provide technical arguments supporting US based super-resolution imaging of soft tissues.

8.3.2 US SUPER-RESOLUTION TECHNIQUES

Techniques developed in O'Reilly et al. 2013 use the same low bubble concentration strategy as used here, however the technique is predominantly designed for the enhancement of across-skull imaging [360]. A technique known as ultrasound localisation microscopy (uULM) [340] has recently implemented fast imaging frame rates to visualise the transient behaviour of microbubbles and microbubble disruption over short time scales to enable the localisation of bubble signals. The technique has similarities to the one presented in this thesis in that localisations of more than one bubble within the Rayleigh criterion are not performed at the same time. The method relies upon the same principle to that in this project that scattering events are detected and localised individually, requiring the acquisition of many image frames over time,

while the difference lies in the way in which these bubble signals are isolated: transient bubble behaviour versus low bubble concentration. Thus, any advantages in speed of one technique over another remains to be investigated. The acquisition time will be determined by the number of transient events occurring in each image frame in the former technique, and the number of spatially isolated bubble signals in a low concentration bubble frame in the latter. Here, optimisation of the injection concentration based on imaging volume estimations will work to ensure a high localisation rate. Controlling or optimising the number of transient events is less obvious, but may involve the use of bubble disruption techniques and/or transmit pressure changes to enhance the number of single bubble events detected over a distinct timescale determined by the PRF.

8.4 FUTURE DEVELOPMENT

This thesis has demonstrated the development of super-resolution imaging from *in vitro* to *in vivo*, with exploration of quantitative measures for clinical investigations, automated post-processing techniques, as well as the implementation of a 3D multi-probe strategy. Many opportunities remain to significantly improve the performance of acoustic super-resolution as discussed, and these are essential to turn the approach into a practicable clinical imaging modality. Suggestions of possible future work objectives are discussed below, before finally possible future applications of the technique are addressed.

8.4.1 OVERALL FUTURE OBJECTIVE

The primary goal would be to demonstrate that US super-resolution imaging of the microvasculature is possible in 3D, at depth, with clinically useful acquisition times.

8.4.2 AIMS

In the following section, a number of distinct future aims are described which strive to cohesively address this overall objective. These are:

1) Full implementation of 3D super-resolution
    A. Using existing tools
    B. Using dedicated technology

2) Development of simulation and data analysis tools
3) *In vivo* demonstration of 3D super-resolution imaging

8.4.3 PROPOSED WORK

8.4.3.1 FULL IMPLEMENTATION OF 3D SUPER-RESOLUTION

The possibilities and limitations of 3D super-resolution acoustic imaging can be studied by experimenting with different but complementary strategies, which can be categorised into those which involve the use of existing tools, and those which require new dedicated technology. This could involve three strands: the use of existing 3D clinical equipment which has limited control, the use of existing 2D experimental programmable acquisition hardware with greater flexibility (as introduced in Chapter 7), and strategies which involve the use of new 3D prototype matrix array technology with still further flexibility. Many of the findings of the three approaches would be transferable, and the combination allows wide opportunities for discovery, as well as comparison between the different approaches. These strands will be discussed here in more detail.

A. USING EXISTING TOOLS

1) DIRECT TRANSLATION TO 3D USING A COMMERCIAL CLINICAL 2D MATRIX ARRAY

One of the most exciting recent innovations in US is the advance in 3D imaging using 2D matrix array probes. Perhaps the most direct extension of this work is therefore the translation of existing 2D image acquisition and analysis strategies (Chapters 3-6) to 3D using clinical 2D arrays. This will be able to monitor microbubble dynamics in multiple imaging planes simultaneously. By characterising the 3D PSF of the native volume acquisition mode available on such systems using a point scatterer suspended within a phantom, 3D super-resolved image renderings can be acquired of complex vessel structures in a tissue volume. Concern over target motion is additionally reduced provided the region of interest remains within the imaging volume.

These systems, however, will currently not allow control of the beamforming or acquisition ordering. Therefore, the extension of compounded imaging with the

extraction of RF data would additionally be desirable: this is discussed in Section 8.4.3.1B. The 3D localisation precision and localisation rate can then be compared between alternative systems.

2) CONTINUATION OF 2D COMPOUNDING APPROACH FOR 3D LOCALISATION

Chapter 7 provided an initial exploration into the use of multiple probes in a synchronised acquisition mode. Extension of the acquisition volume is possible through the use of a built-in translation stage. This can be scanned linearly through space in the elevational direction (or other imaging planes) to enable larger and more complex 3D vascular phantoms to be imaged. Inbuilt mechanical probes may also be employed which use internal motors to provide an increase in imaging field of view without externally controlled motion. Consequently, the imaging of more complex 3D microvascular phantoms can be imaged (see Section 8.4.3.2A). One will have to consider the balance between the dimensions of each interrogated volume (slice thickness) and the frame rate required to capture the bubble kinetics within the volume. The overlapping acoustic fields could be controlled with appropriate micrometre precision, essential for coherent operation of the two arrays, using an optical bench setup. The impact of multi-angle compounding pulses on the localisation precision for varying PRF and flow velocity can be performed. Additionally, exploration of the effect of varying passive detection angle, and furthermore the point in which the elevational resolution of the probes becomes a limiting factor, is important in the assessment of this strategy for acoustic super-resolution.

B. USING DEDICATED TECHNOLOGY

A further improvement to super-resolution would be to achieve 3D CEUS imaging using dedicated programmable 2D matrix arrays, which provide additional control over beamformers and the transmitted waveforms. Transducers of this kind are available in the US research field, [75], [361], [362], including a 256 element sparse matrix array ULAOP system, an advancement of that used in Chapter 7. Unlike the devices discussed in Section 8.4.3.1, the availability of volumes of RF data allow both the amplitude and phase information of the US signals to be utilised. The benefit of this approach is thus the opportunity to investigate novel acquisition strategies and the

implementation of detection algorithms based on unprocessed echo data, providing potential for higher speed and precision compared with that described in Section 8.4.3.1A, part 1). This is discussed further in Section 8.4.3.2D. The ideal implementation of 3D US to quantify the microvasculature is currently unknown. This technology could be investigated as a controllable and flexible means of generating 3D diffraction-limited bubble signals; these data can be subsequently processed to generate super-resolved 3D maps. In addition, the availability of volumes of RF data should allow the more accurate detection and correction of 3D motion affects.

EXPLORATION OF HIGH SPEED PLANE WAVE VOLUMETRIC IMAGING

Continuing from that performed in Chapter 7, investigation of the use of plane wave imaging at very high imaging rates can be performed in order to increase the volume acquisition rate towards thousands of volumes per second. This would enable high speed volumetric acquisition of 3D microbubble localisation over the entire region. Experiments could be performed to optimise the number of simultaneous transducer elements needed for transmit and receive, and investigate how to distribute the active transducer elements across the 2D array for optimal localisation precision. This work could be guided by the simulations performed in Section 8.4.3.2B and the results may then serve to validate and, if necessary, refine the simulations. This adaptive mode approach could also be used to investigate transient effects in individual bubbles e.g. variations in individual bubble responses and times to bubble destruction. Three dimensional beam steering may also help alleviate distortions due to target motion, allowing real-time target tracking. Additionally, the use of partially focussed waves instead of plane waves could alleviate issues due to attenuation of lower pressure plane waves at depth compared to focused waves.

8.4.3.2 DEVELOPMENT OF SIMULATION AND DATA ANALYSIS TOOLS

This investigation would be multi-faceted. The development of both simulation tools and experimental phantoms to understand, model and test the acquisition strategies discussed in section 1 is vital. The extension of this work would benefit considerably from computer models which can predict outcomes of image acquisition procedures, provide evaluation of optimal bubble concentrations, and potentially assist in the

improvement of detection algorithms.

A. Construction of a 3D vessel phantom test rig

The construction of a combined optical and acoustic rig in which the size, position and motion of the microbubbles could be observed optically, both pre- and post-acoustic insonation could offer valuable insights. This could provide validation for velocity measurements, characterisation of scattered signal changes as individual bubbles become close enough to cause interference, and understanding changes in signal response of single bubbles within capillary tubes due to vessel wall interactions. Furthermore, the effects of size and shape variations of the PSF across the field of view could be investigated using a point scatterer suspended within a phantom. An experimental set-up designed for a combined optical and acoustic rig consisting of a capillary tube within a water tank is illustrated in Figure 8.1. This could consist of a long working distance 40x optical objective lens coupled with a digital camera (Canon Powershot SX240 HS) that can be focused on the flow in an *in vitro* capillary tube phantom aligned such that the fields of view of the two modalities are overlapping. Fibre optic tubing allows underwater illumination of the target for optical imaging. The field of view of the 40x objective will be approximately 0.44 mm; thus using the maximum available frame rate of 240 frames per second will allow detection of bubble velocities up to approximately 105 mm/s along its length and will enable imaging of the entire tube width so the full parabolic flow profile can be observed. This proposed set-up will enable validation of US position and velocity measurements against the optical ground truth, and furthermore investigation of the acoustic response from bubbles of different sizes and in different locations in the tube. Contrast enhanced plane waves will be interleaved with B-Mode imaging using an active and passive synchronised transducer pair for comparison between implementing super-resolution on RF plane wave data and B-Mode image data. The orthogonal receive angles will additionally enable investigation of non-spherical sound scattering.

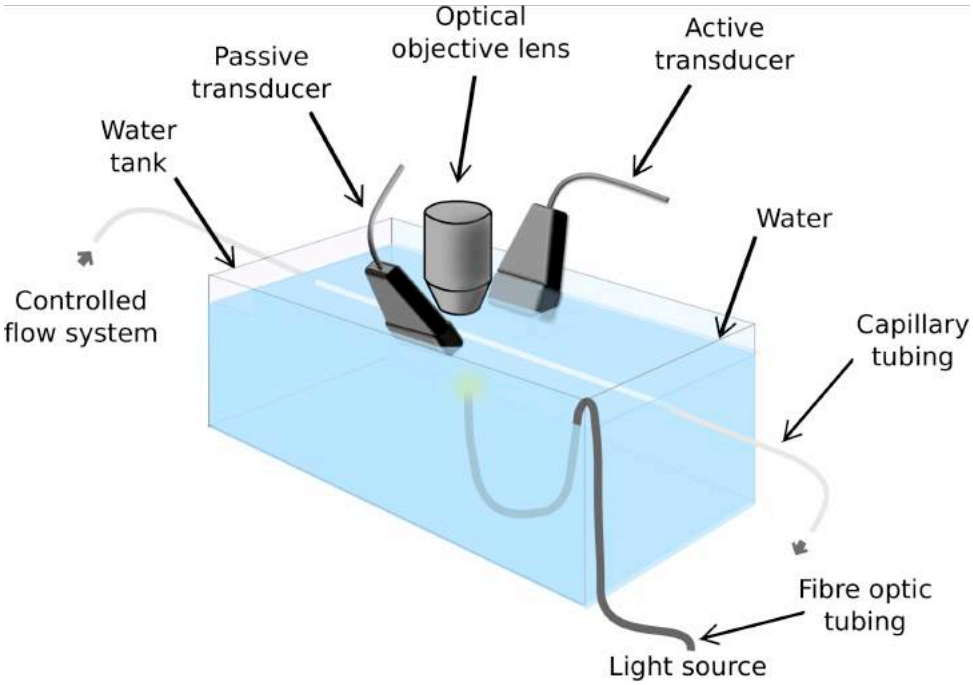

Figure 8.1. An experimental set-up designed for a combined optical and acoustic rig consisting of a capillary tube within a water tank. This could consist of a long working distance optical objective lens coupled with a digital camera that can be focused on the flow in an illuminated capillary tube aligned such that the fields of view of the two modalities are overlapping. The bubbles will be insonated using the active transducer and will be detected simultaneously on the active and passive synchronised systems.

Simple 3D vessel phantoms could additionally be constructed to emulate branching and tortuous structures both in water and paraffin-gel wax based phantoms which can be produced with a range of acoustic properties; an initial simple design could involve a flexible spiral capillary tube set within paraffin wax (Figure 8.2). The effects of depth, attenuation and aberration can also be investigated with the addition of varying tissue-mimicking layers. A proposed imaging set-up could involve the gradual increase in tissue mimicking material overlaying embedded microvessel tubes as illustrated in Figure 8.3. The material could be composed of a combination of paraffin gel, carnuba wax and glass microspheres for attenuation, or alternatively a fat mimicking oil-in-gelatin emulsion to emulate aberration of the abdominal wall as developed in Lacefield et al. 2002 [346]. This would allow analysis of the effect of a continuous increase in the parameter of interest on the level of super-resolution attainable in the phantom, as well as its affect on velocity estimations. As with the experimental demonstrations presented

in this thesis, the flow rate can be carefully controlled by a syringe pump to enable investigation and validation of velocity measurements.

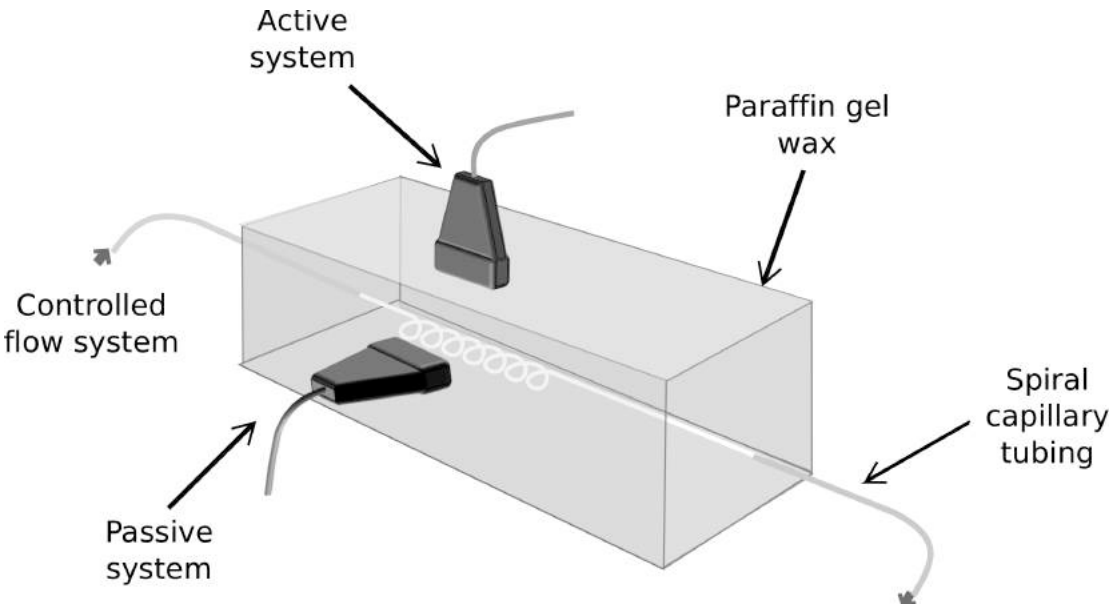

Figure 8.2 .An experimental set up consisting of a flexible spiral capillary tube set within paraffin wax. Note: paraffin gel wax is transparent and is shown here in colour for visualisation.

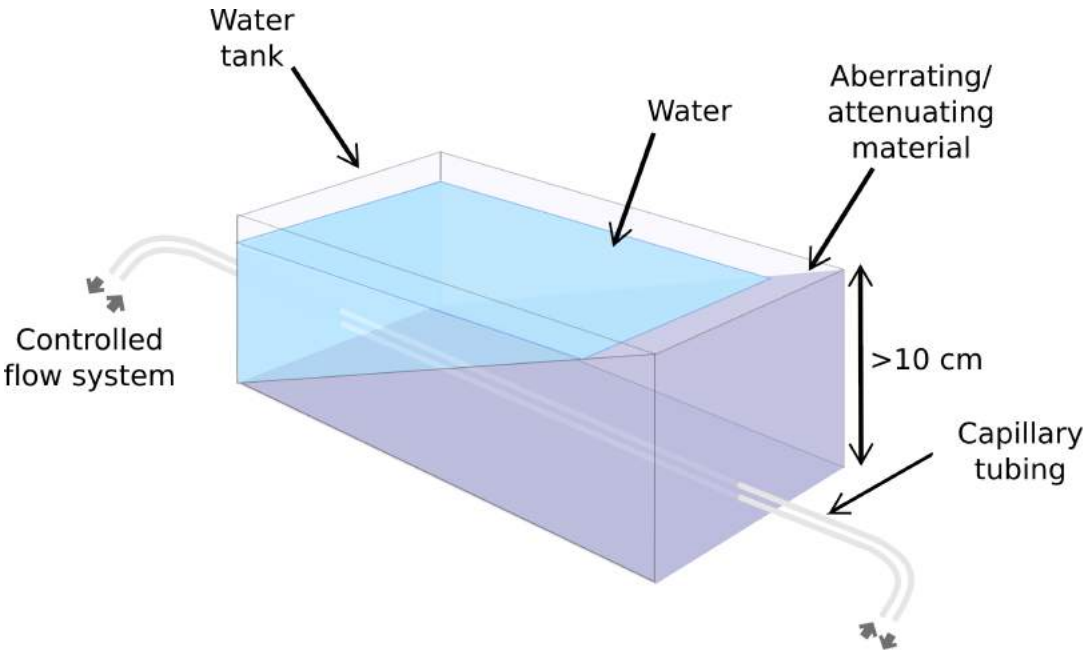

Figure 8.3. Proposed experimental set-up for the investigation of aberration or attenuating effects on super-resolution acoustic imaging, involving the gradual increase in overlaying tissue mimicking material using paraffin gel wax. This could contain carnuba wax and glass microspheres for attenuation, or alternatively oil-in-gelatin emulsion fat mimicking tissue mimicking material with aberrating spheres. Microvessel tubes could be embedded within the phantom near the base and connected to a controlled flow system similar to that demonstrated in this project.

B. Microbubble Localisation Simulation Software

This would involve the development of software to enable each of the proposed experimental geometries to be modelled. Software would incorporate the system noise, variations in PSF, microbubble concentration and effects of transmit frequency and aberration. Single bubble signals have been demonstrated to deviate considerably from that of a 2D Gaussian function (Chapter 3). Results from optical and acoustic experimental analysis (Section 8.4.3.2A) can compliment the development of models for acoustic behaviour and will aid development of more accurate predictions of microbubble signal responses to the acoustic field in capillary vessels. Characteristics of their responses may enable improved direct selective detection of single microbubble signals within dense data. Alternatively, these investigations may enable development of a signal response model with adaptive and flexible parameters to enable the fitting and subsequent accurate localisation of microbubble signals. These simulations would enable testing and subsequent development of single bubble identification algorithms based on fitting error, as well as the opportunity to inform and guide the development of the US hardware and data processing.

C. Study the impact of microbubble acoustic properties on Super-resolution

Firstly, the distribution of acoustic responses of SonoVue™ to the specific pulses developed in the acquisition systems described in Section 8.4.3.1 of future development would be investigated. This could then be used incorporated as prior knowledge into existing signal processing to test for improvements in resolution and SNR, and could be employed in machine learning algorithms (Section 8.4.3.2F).

Furthermore, the use of microbubbles which are designed to exhibit enhanced nonlinear

behaviour and a more consistent acoustic response should improve both resolution and SNR of CEUS imaging. In both cases, gains in SNR can be traded for improvements in acquisition time, thus addressing one of the key objectives for the super-resolution technique presented in this project. Such microbubbles have been developed by a number of research labs [349]–[351], [363] and present an opportunity for future experimental work.

It is not trivial to estimate the localisation precision of the system using single stationary microbubbles rather than a fixed linear scatterer. A key challenge for characterising the acoustic response of single microbubbles is achieving sufficient isolation to observe a scatterer's response in the absence of external influences such as a wall or boundary. More challenging is facilitating control of the proximity of neighbouring bubbles or boundaries that may modify the bubble behaviour. This would involve firstly the isolation of a single microbubble often less than 10 μm in size within a considerably larger volume e.g. the transducer's imaging field of view, the accurate and sustained positioning of the bubble, and the ability to repeat these measurements hundreds of times. The isolation of individual bubbles for repeated measurements has nonetheless been demonstrated by US imaging groups around the world for quantitative analysis of bubble dynamics.

Techniques include using optical tweezers based on Laguerre-Gaussian laser beams to counteract a microbubble's buoyancy [364], [365], [177]; this method has been used with a high speed camera to optically observe and quantitatively compare the affect of introducing a neighbouring bubble on the dynamics of a single bubble [177]. Other methods include the use of a micropipette with a tip size of 0.5 μm attached to a translational stage; this was used in Sijl et al. 2011 to insert a single bubble from a suspension into a capillary tube allowing the comparison of optical and acoustic responses from individual bubbles of varying resting radii [366]; however, it is not stated whether precise stationary positioning of the bubble can be ensured throughout the imaging procedure. The simultaneous observation of both optical and acoustic scatter from individual, yet moving, particles has been simultaneously recorded using a co-axial flow focusing device. This involves the passage of a continuous stream of

unconstrained particles through the combined focal region of an US transducer and a laser and has demonstrated the ability to resolve changes in object radius down to 0.1 μm [363]. This is dissimilar to previously mentioned methods in that the particles are in motion, but are still isolated and unaffected by physical boundaries or neighbouring particles. Instead, by accurately controlling the microbubble flow, the affect of bubble motion during the time to acquire a single frame, and moreover, during plane wave compounding techniques, the precision of localising moving microbubbles could be fully investigated. Furthermore, this could enable validation and refinement of velocity tracking techniques, with investigation of echoes from bubbles of varying resting radii, velocity components, and frequencies, under both plane wave and focussed insonation for quantitative comparison.

D. Investigation of possible improvements by RF access/processing

The experimental systems used in Section 8.4.3.1B will provide the opportunity to use the raw unprocessed received signals, as well as pre-envelope-detected IQ and image data, for microbubble localisation. Measuring the localisation precision of the same target using both image and RF data will allow comparison of the data types for acoustic super-resolution. It is likely that RF data will enable better differentiation of both electronic and clutter noise from signals with the preserved phase information. This will also enable more precise sub-wavelength tracking of tissue motion. These aspects can be investigated using data acquired from *in vitro* vessel phantoms described in part A of this section.

E. Investigation of frequency and tissue depth interaction on the ability to generate super-resolved images

Using a lower US frequency (~2-3 MHz vs. > 6 MHz) decreases the effects of attenuation, but the longer wavelength naturally leads to poorer resolution. In the context of super-resolution imaging, it is important to explore the effect of decreasing SNR with depth on localisation accuracy. Some effects of SNR and depth have been initially reported in Chapter 3. This is an important trade-off for real clinical applications of the microbubble localisation approach. Investigations can be performed using the software developed in Section 8.4.3.2B and experimentally using the phantoms described in Section 8.4.3.2A.

F. LEARNING-BASED METHODS FOR AUTOMATIC AND ROBUST LOCALISATION

The development of more robust learning-based methods employing forward models of the image formation process could provide likelihood estimates for the number, size and location of point scatterers in the field of view. These can be viewed as latent variables underlying the acquired data and techniques such as hidden Markov models, an approach previously demonstrated in microscopy [367], can provide maximum likelihood estimates for these variables in each frame. Temporal information could then be incorporated to refine these estimates, finding consensus among hypotheses across frames. This relies on the ability to estimate motion between frames in a sequence, and this is possible with registration methods such as Optical Flow in 2D [368], or Free-Form Deformations in 3D [369]. Such an automated framework could help to improve precision, accuracy, reproducibility and speed of processing.

8.4.3.3 *IN VIVO* DEMONSTRATION OF 3D SR IMAGING

In all cases, refinement and iterations of developments should be systematically tested using *in vitro* phantoms. However, since many aspects of the imaging process cannot be easily recreated *in vitro*, including tissue motion and acoustic property variation across different tissue types, demonstration and testing of the methods *in vivo* would provide valuable insight. These could be performed at key points throughout further development of acoustic super-resolution in the following ways:

A. PRE-CLINICAL SMALL ANIMALS

The most appropriate and promising imaging methods should be applied to study microvasculature in a mouse model. These experiments could follow a similar experimental design to that presented in Chapter 4, where a relatively superficial structure is utilised such as the vasculature in the ear in order to compare optical and super-resolved US imaging. Following US imaging, optical images of microvasculature could be obtained for blood vessel visualisation (~5 μm resolution) using confocal microscopy of clarified whole tissue samples based on the work of Yang *et al*. [370].

B. DEMONSTRATION IN HUMANS

One would also seek to demonstrate 3D super-resolved images in a clinical setting. The

feasibility of the current 2D approach was demonstrated in Chapter 5, where data from the lower limb of human subjects was acquired in an ethically approved study into the use of microbubbles for assessing perfusion. However, this data does not provide high resolution information in the elevational plane. With the development of 3D image acquisition strategies outlined in Section 8.4.3.1, it is envisaged the performance could greatly surpass that demonstrated in this project. These experiments could be performed initially using commercially available US transducers as described in Section 8.4.3.1. A possible target site could be the acoustical temporal bone window for the imaging of cerebral microvasculature in the human brain.

8.5 FUTURE APPLICATIONS

In the future, the method of super-resolution, and particularly 3D super-resolution, could provide a wide range of tools and potential biomarkers to characterise the microcirculation in tissues and tumours. The technique presented in this thesis has the potential of overcoming some limitations of established methods.

8.5.1 VISUALISATION AND CHARACTERISATION OF VASCULAR IMPAIRMENTS

The potential for super-resolution imaging to provide visualisation of atherosclerosis and other vascular blockages or vessel narrowing is not unreasonable, since the technique provides visualisation of the path of microbubble flow. Providing the localisation precision of the imaging system is in the order of a few micrometres, and that motion effects can be well compensated, delineation of the vessel lumen could be acquired. Sites of atherosclerosis may be able to be detected at source through identification of narrowing or discontinuity of microbubble localisations, in addition to its effect on the blood flow in latter branching levels. This could be performed on smaller vessels not able to be accurately defined with existing techniques. Furthermore, this technique could be used for the detection and quantification of intra-plaque neovascularisation which has recently been demonstrated using CEUS [371]–[373].

8.5.2 Quantitative Measures of Perfusion/Tumour Response

As proposed in Section 8.2.6, individual microbubble localisation performed during CEUS could be used to generate localisation time curves. Functional information could be obtained by parameterisation of localisation curves similar to that performed for TICs acquired during the inflow of contrast agent into a region [14], [374]. This measure, however, has limited spatial information as data are diffraction limited and it is calculated over a region of interest. Many functional indices could be derived from acoustic super-resolution data, including the extraction of blood flow rate, time to peak localisation density, as well as quantitative measures obtained from super-resolved microvascular images such as localisation density measures. Quantitative images of the microbubble perfusion could also be obtained since the microvascular maps not only demonstrate the structure of the vessels, the intensity of the resulting spatial maps represent the number of detected microbubbles passing through each vessel over a fixed time period. This could therefore provide information on the perfusion within the tumour or tissue. This could be useful in targeted imaging, where quantitative results of targeted microbubbles are often normalised by perfusion, to compensate for the number of microbubbles travelling in the target area [375], [376]. Furthermore, parametric maps of vascularity and blood perfusion (blood velocity x vascular cross-section) could aid the detection of small lesions, and thus help distinguish benign from malignant masses [377]. Maps such as these can be used to calculate tumour heterogeneity and other spatially dependent indices of tumour response, and detecting the change in blood volume can also be used to monitor the progression of anti-angiogenic therapy [117]. As introduced in Chapter 5, the contribution from macro-vessels may be able to be removed such that the fraction of blood volume under analysis originates predominantly from small vessel flow. Localisation time curves of each individual pixel, may also allow further analysis of individual haemodynamics and their spatial distribution within the imaging plane.

8.5.3 Tissue and Tumour vascularity

As discussed in the Introduction, tissue vascularity can reflect the metabolic requirements of surrounding tissue; therefore, its absence can indicate regions of

necrosis or damaged tissue, and can thus be used to detect and characterise tissue pathologies in soft tissue regions such as the breast, liver or prostate. Additionally, vascularity can be an important parameter in evaluating the effectiveness of therapeutic treatments such as radiotherapy and drug therapies which rely on the level of tissue oxygenation and sufficient vascular access to their targets, respectively.

Microvascular density (MVD) measures the inter-capillary distance and has been shown to provide quantitative measures of tumour angiogenesis [39]. MVD has been proven to be a useful prognostic indicator in a range of cancers [378], [379] and thus has become a valuable clinical tool for assessing cancer treatment options [380]. Techniques to measure MVD such as using high power microscopes and immuno-histochemical staining require tumour tissue biopsies or operative specimens to provide direct assessment of angiogenesis [39]. This procedure is not only invasive, but is also limited by the inability to provide functional vascular information, especially for assessing response to treatment. Furthermore, the assessment of only a finite number of biopsy samples of a heterogeneous mass can lead to misrepresentation of its geometrical characteristics [381]. Indirect techniques which are quantitative and in which the functional status of a large volume of the vasculature can be assessed are thus required. Assessment of angiogenesis using US imaging has the advantage of being non-invasive, and can be performed on tumours in situ. Vascular morphology can already be depicted using CEUS and MIP images [92], [382], however the resolution of the imaging system typically exceeds microvessel diameters and thus limits the assessment of the microcirculation. The use of super-resolution techniques in this application, therefore, may be able to improve the sensitivity to microvascular changes.

Despite its clinical value, MVD is a relatively simple index, and in reality it cannot always capture the complexity of microvessel shapes, sizes and patterns that differentiate normal, benign and malignant tissue vasculature [383]. Being able to additionally assess the complex architecture of the microvasculature at depth, for example through quantification of the fractal geometry or tortuosity of the tumour vascular network, has been recognised as a useful tool to detect the presence of malignant tumours [383]–[385]. Techniques such as acoustic angiography have

demonstrated the measurement of vascular tortuosity in tumours [386], however the trade-off between resolution and depth will pose a challenge for the assessment of microvascular morphology at depth.

Measures of microvascular morphology surrounding tumours can be quantified from segmentations of vessels structures within, ideally 3D, acoustic super-resolution image renderings. Thus, in the future, acoustic super-resolution maps could enable assessment of microvessel diameters, tortuosity, blood vessel velocity, and fractal dimensions at depth. Maps of vascularity, alongside quantitative measures of blood volume, flow rate and perfused vascular area can potentially improve detection and diagnosis of microvascular related diseases/tumours. A multivariate approach, which considers multiple vascular parameters may provide the most reliable and robust strategy to tackle this challenge.

8.6 FINAL WORDS

Acoustic super-resolution using microbubbles has been demonstrated to allow visualisation of microvessel structures *in vivo* which greatly surpasses that possible with conventional clinical US imaging frequencies. It has advantages in its relative simplicity, ease of implementation and it can be readily integrated using clinical imaging systems, requiring little to no extra technology or equipment. The most significant challenge is its optimisation for clinically viable acquisition times which requires consideration of frame rates, system localisation precision, ~~and~~ target blood flow velocity, as well as tissue and probe motion. Its adoption in a clinical setting is likely to be impeded by the current requirement to acquire long periods of data with limited motion, as well as the requirement for microbubble injection. The topic of super-resolution in US imaging is an exciting, new, but quickly emerging, area of research. Establishing the method clinically will require objective evidence of its performance in 3D *in vivo*, the extraction of quantitative clinical measures, and the development of standardised protocols.

9 APPENDICES

9.1 SUPER-RESOLUTION SIMULATION

9.1.1 INTRODUCTION

The optimisation of microbubble concentration in super-resolution imaging is crucial to time-efficient image acquisition. The following simulation has been developed based on a simplified Poisson statistical model which aims to investigate the combined affects of imaging parameters on localisation rate and image acquisition time.

9.1.2 METHOD

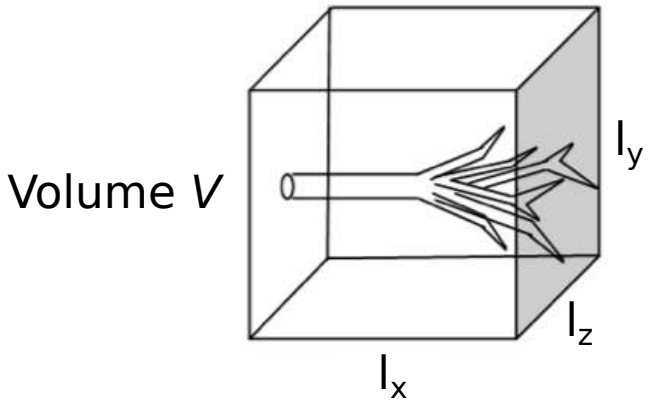

Figure 9.1. Illustration of example simulated imaging volume, where volume V is imaged by the US system, where vascular structures cover an area given by a fraction V/a of the overall volume.

Suppose we are imaging a cubic volume V with sides of length l_x, l_y, l_z, (Figure 9.1) at a depth d. Since only a proportion of the imaging volume will contain blood vessels, we define the vascular volume fraction to be V/a, and the microbubble concentration C is assumed to be constant throughout the vasculature.

A PSF or resolution voxel, is defined here as a cube with sides equal in length to the diffraction limited system resolution in each dimension, illustrated in Figure A9.2, where the original PSF volume, V_{PSF}, can be approximated to be

$$V_{PSF} = \mathrm{FWHM}_x \, \mathrm{FWHM}_y \Delta z, \tag{9.1}$$

where FWHM_x and FWHM_y are the lateral and axial FWHM of the PSF respectively, and Δz is the elevational resolution (slice thickness). For simplicity, isotropic voxels are displayed in diagrams; in reality the in plane components are anisotropic, and these differ greatly to the slice thickness.

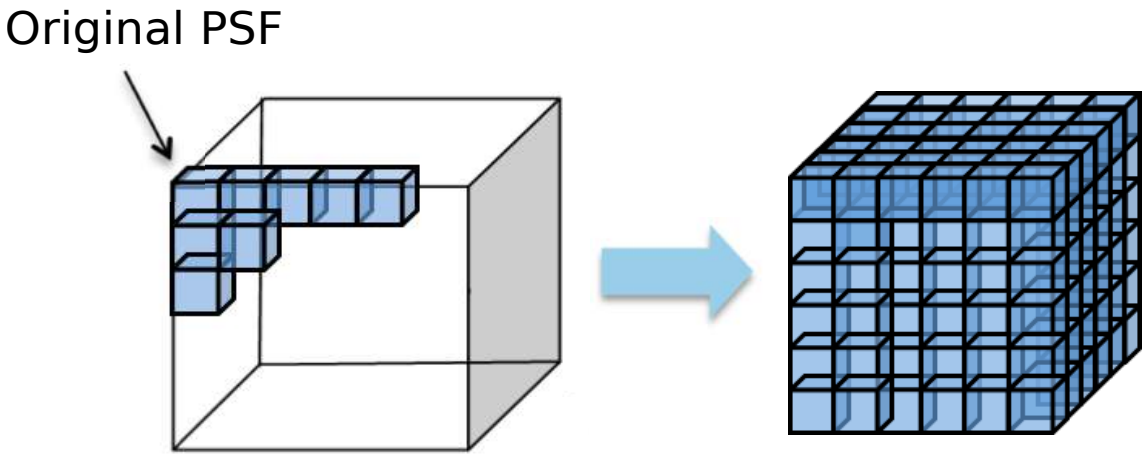

Figure A9.2. The imaging volume V can be divided in approximate PSF sized voxels, corresponding to the three dimensional diffraction limited resolution of the imaging system.

If independent and discrete events occur with a known average rate then Poisson statistics can be used to express the probability of a given number of events occurring within a fixed interval of time or space; in this work, an event is defined as the presence of a bubble, and the fixed spatiotemporal interval of observation is a PSF sized region within an image frame [232], [233]. If the imaging of microbubble flow within vessels is assumed to be stochastic and discrete, such that it involves a randomly determined set of observations, where each observation can be considered as a sample from a probability distribution, then Poisson statistics can be used to examine the probability of imaging single bubbles in a resolution voxel. It must therefore be assumed that the bubbles do not cluster, and therefore bubble events can be defined for a finite set of values of k. In this case, the probability, P_{PSF}, of having k bubbles in a sample volume can be given by the following relation

$$P_{PSF}(k) = \frac{\mu^k e^{-\mu}}{k!}, \tag{9.2}$$

where μ is the Poisson expectation value, found using the known number of events occurring in one sample volume, V_{PSF}, given by

$$\mu = C \cdot V_{PSF}, \tag{9.3}$$

where C is the microbubble concentration [232], [233]. Since there exists a precision associated with the localisation of point scatterers using a US imaging system, a super-resolution (SR) voxel is therefore approximated as a voxel with sides equal in length to the localisation precision in the x, y and z dimensions, denoted by σ_x, σ_y, and σ_z (Figure 9.3), and as such the volume, V_{SR}, is given by

$$V_{SR} = \sigma_x \sigma_y \sigma_z. \tag{9.4}$$

The localisation precision additionally determines the FWHM of the 2D Gaussian localisation profile plotted in the final super-resolution image.

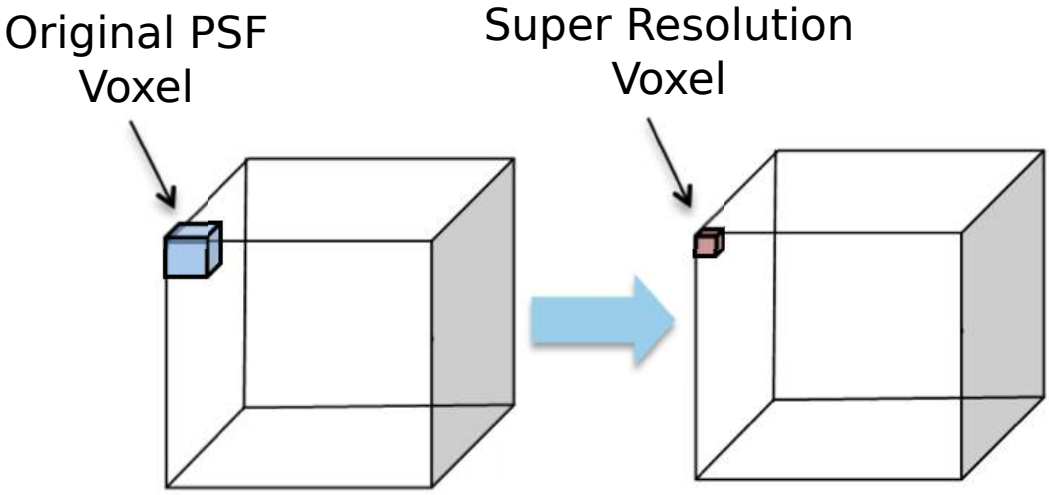

Figure 9.3. Illustration of the change of image resolution represented by a change in PSF voxel size, where the original resolution of the system is the PSF measured of the US imaging system, and the super-resolution PSF is defined as a voxel size equal to the localisation precision in the x, y and z dimensions.

If it can be assumed that the signal analysis algorithm can detect every single bubble and can reject signals from multiple bubbles, then on average the number of PSF volumes, n_{PSF}, needed to acquire a signal from a single bubble is

$$n_{PSF} = \frac{1}{P_{PSF}(1)} \tag{9.5}$$

Where, using equation (9.2) and (3.25),

$$P_{PSF}(1) = C\, V_{PSF} e^{-C \cdot V_{PSF}} \tag{9.6}$$

Alternatively, it is possible to define a specific certainty of acquiring a single microbubble signal using the Binomial formula. To calculate the number of PSF voxels required for X% certainty that there is one microbubble in at least one of them, the Binomial formula gives you the probability of getting s successes in n trials

$$P = \binom{n}{s} p^s (1-p)^{n-s}, \tag{9.7}$$

where parameter definitions are displayed in Table 9.1, where the probability of success, p, is the probability of having one microbubble in a PSF, $P_{PSF}(1)$, and the number of trials, n, is the number of PSFs.

Parameters	Definition
Success	1 microbubble in PSF volume
Failure	0 or > 1 microbubble in PSF volume
Trial	PSF
n	Number of trials = n_{PSF}
s	Number of successes
$n - s$	Number of failures
p	Probability of success in one trial = $P_{PSF}(1)$
$1 - p$	Probability of failure in one trial

Table 9.1. Definition of parameters used in Binomial formula.

For example, in order to be 99% sure at least one PSF contains a single microbubble signal

$$P(s > 0) = 0.99, \tag{9.8}$$

$P(s = 0)$ can be defined as

$$P(s = 0) = 1 - 0.99 = 0.01. \tag{9.9}$$

Thus, the number of PSFs required to reduce the probability of total failure to 1% can be given by

$$P(s = 0) = \binom{n}{0} p^0 (1-p)^{n-0} \tag{9.10}$$

which reduces to

$$P(s = 0) = (1-p)^n \tag{9.11}$$

$$n_{PSF} = \frac{\ln[P(s=0)]}{\ln[1-p]} = \frac{\ln[0.01]}{\ln[1 - P_{PSF}(1)]}. \tag{9.12}$$

In the subsequent derivation, the average number of PSFs required, given in Equation (9.5), is employed, however this can be adjusted to provide a specific level of certainty by instead using Equation (9.12). The effect of using a certainty parameter will be demonstrated in results.

If it is assumed the number of single bubble localisations in each interrogation, N_{loc} will only result from vascular areas then

$$N_{loc} = \frac{Vascular\ Volume}{Volume\ required\ for\ single\ bubble\ detection} \tag{9.13}$$

$$= \frac{V/a}{n_{PSF} \cdot V_{PSF}} = \frac{\mathrm{V}}{an_{PSF}\mathrm{FWHM}_x\ \mathrm{FWHM}_y\Delta z} \tag{9.14}$$

In the super-resolved image, the number of SR voxels, N_{SR}, requiring localisation information will also only be the areas in which vessels are present, thus

$$N_{SR} = \frac{Vascular\ Volume}{Volume\ of\ \mathrm{SR}\ voxel} \tag{9.15}$$

$$= \frac{V/a}{V_{SR}}$$

$$= \frac{\mathrm{V}}{a\ \sigma_x\sigma_y\sigma_z} \tag{9.16}$$

If it is then assumed that to create a meaningful image we need on average $N_{locImage}$ localisations per SR voxel then

$$N_{SRImage} = N_{SR} \cdot N_{locImage}$$

$$= \frac{\mathrm{V}N_{locImage}}{a\ \sigma_x\sigma_y\sigma_z} \tag{9.17}$$

and the number of interrogations required can then be given by

$$N_{Interrogations} = \frac{N_{SRImage}}{N_{loc}} \tag{9.18}$$

Using time-of-flight, the time taken to receive a single echo is given by $t_{ps} = \frac{2d}{c}$, where c is the speed of sound in the medium, assumed to be constant. Using multi-pulse CEUS imaging techniques such as pulse inversion (PI) or Contrast Pulse Sequencing (CPS), a single image frame is composed of the echoes resulting from multiple pulses. Thus, for each interrogation N_{pulses} are transmitted, and the time to acquire each image frame is $t_f = \frac{2d}{c} \cdot N_{pulses}$. When assuming an ideal scenario where a 3D volume can be imaged using one interrogation,

$$Acquisition\ Time = t_f \cdot N_{Interrogations} \tag{9.19}$$

By combining relations from previous equations, an approximate overall relation can be given by

$$Acquisition\ Time = \left(\frac{2dN_{pulses}}{\mathrm{c}}\right)\left(\frac{N_{locImage}\ \mathrm{e}^{C\cdot \mathrm{FWHM}_x\ \mathrm{FWHM}_y \Delta z}}{\mathrm{C}\sigma_x\sigma_y\sigma_z}\right) \tag{9.20}$$

or

$$Acquisition\ Time = \left(\frac{2dN_{pulses}}{\mathrm{c}}\right)\left(\frac{N_{locImage}\ \mathrm{e}^{C\cdot \mathrm{V}_{PSF}}}{\mathrm{C}V_{SR}}\right) \tag{9.21}$$

Thus, as expected acquisition time increases with those parameters which tend to increase all CEUS imaging techniques as shown in the first bracketed term, including increased imaging depth, increased number of pulses within multi-pulse CEUS imaging techniques, and a decreased speed of sound in the medium of interest. The super-resolution component of the model (second bracketed term) demonstrates an inverse relationship between imaging time and localisation error in the super-localisation images; this is due to the increased size of the Gaussian localisation plots in the final image. A reduction in the size of the diffraction limited resolution acts to decrease the acquisition time. The desired number of localisations per super-resolution voxel, $N_{locImage}$, relates to the signal-to-noise (SNR) in the resulting image; hence the higher

SNR desired, the longer the acquisition time required. Changes in concentration will impact the acquisition time with the relation,

$$Acquisition\ Time = t_f \cdot N_{Interrogations} \tag{9.22}$$

which has stationary roots where

$$\frac{\partial}{\partial C}\left(\frac{\mathrm{e}^{C\cdot \mathrm{V}_{PSF}}}{\mathrm{C}}\right) = \frac{\text{PSF Volume}\ \mathrm{e}^{\mathrm{C}\cdot \mathrm{V}_{PSF}}}{C} - \frac{\mathrm{e}^{\mathrm{C}\cdot \mathrm{V}_{PSF}}}{C^2} = 0,$$

$$C = \frac{1}{\mathrm{V}_{PSF}}, \tag{9.23}$$

i.e. where the average number of bubbles in each PSF volume equals one; above or below this value, the acquisition time will be greater.

Currently, imaging the entire volume in one interrogation is not possible with the equipment available, however it is expected that this will be possible in the near future. Current plane wave imaging techniques are able to acquire an entire image slice with one acoustic pulse, where the time required to image the entire volume can be approximated instead by

$$t_f = t_{ps} \cdot N_{slices} \cdot N_{pulses}, \tag{9.24}$$

where

$$N_{slices} = \frac{l_z}{\Delta z} \cdot 2, \tag{9.25}$$

here sampling is performed at twice that defined by the slice thickness. A similar expression can be defined for line-by-line acquisition given by,

$$t_f = t_{ps} \cdot N_{slices} \cdot N_{lines} \cdot N_{pulses}, \tag{9.26}$$

where

$$N_{lines} = \frac{l_x}{FWHM_x} \cdot 2. \tag{9.27}$$

Estimations of the acquisition time of this technique are performed using volumetric, slice-by-slice and conventional line-by-line acquisition.

LOCALISATION RATE

Using multi-pulse imaging techniques, a single image frame is composed of the echoes resulting from N_{pulses}, and thus the imaging rate must be considered as the number of images created per second given by

$$Imaging\ Rate = \frac{1}{t_f} \tag{9.28}$$

During imaging, microbubbles are flowing through the vasculature at a velocity v_b. In order for the microbubbles to provide new spatial information in consecutive frames, the bubble velocity should be large enough that its movement exceeds the localisation precision of the imaging system in each CEUS multi-pulse compounded image (for a full discussion see Chapter 7). Thus, the distance moved by a bubble in each frame, d_b, should be

$$d_b \geq \sigma \tag{9.29}$$

thus

$$v_b \geq \sigma \cdot Imaging\ Rate. \tag{9.30}$$

$$Acquisition\ Time \geq \left(\frac{\sigma}{v_b}\right)\left(\frac{N_{locImage}\ \mathrm{e}^{C \cdot \mathrm{V}_{PSF}}}{\mathrm{C}V_{SR}}\right) \tag{9.31}$$

This does not, however, mean that if velocities are below this speed they are not useful. Below this speed, they will still contribute signal, and thus will enhance SNR in the final image and in addition provide information about the amount of blood flow through the imaged region.

Simulations were performed for an example imaging volume of size 1 cm^3 at 5 cm depth, with an original diffraction limited resolution of $FWHM_x = FWHM_y = \Delta z = 400$ µm using PI. The resulting super-resolution localisation precision is varied and its impact on acquisition time is explored.

9.1.3 RESULTS

Figure 9.4 displays the probability of imaging k bubbles in each PSF volume, where $k = 0,1,$ and > 1 and in this example V_{PSF} is a cube with sides 400 µm and $V = 1\ cm^3$. The probability of imaging no bubbles in a PSF decreases exponentially with increasing concentration, while the probability of imaging single bubbles increases to a maximum as the balance between $P(k = 1)$ and $P(k \neq 1)$ becomes optimal. This occurs at a concentration of 15625 bubbles/ml equivalent to V/V_{PSF} (the number of PSFs sized volumes in V). Further increase in concentration decreases the probability of achieving single bubble signals, while the probability of imaging multiple bubbles within the resolution continually increases and approaches 1.

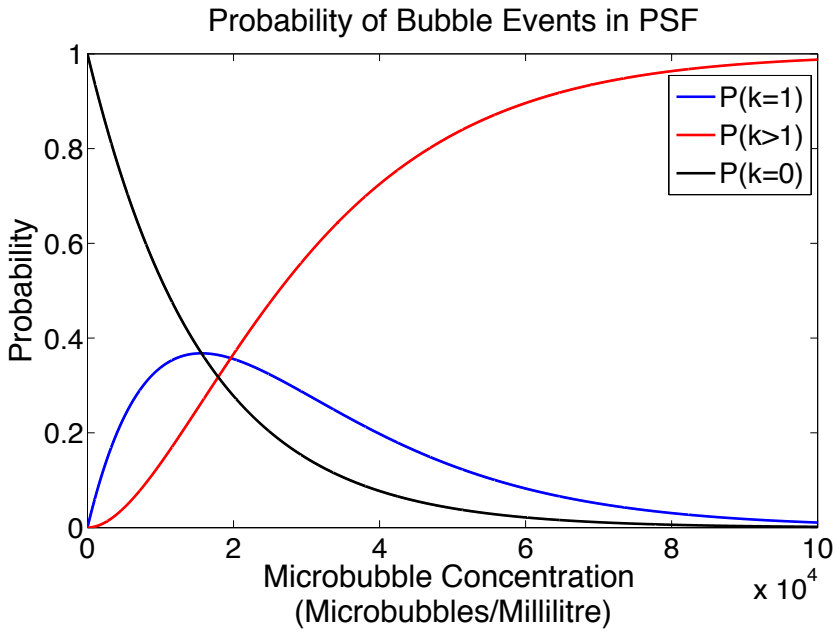

Figure 9.4. Graph to show the probability of bubble events occurring in the PSF of the system when the original system PSF is 400 µm in all dimensions.

Figure 9.5 shows simulated acquisition times required for super-fast imaging of a 1 cm^3 volume at a depth of 5 cm with a diffraction limited isotropic resolution voxel with

sides of 400 μm. For this particular imaging target, the optimal concentration seen in Figure 9.4 can be observed to provide the line of minimum acquisition time across all factors of improvement. The relationship between acquisition time and factor of improvement at this concentration is shown in Figure 9.6. At the optimum concentration, to achieve a factor of 80 improvement in resolution, equivalent to a localisation precision of $\sigma_x = \sigma_y = \sigma_z = 5\,\mu m$, the required acquisition time is 180.7 seconds (approximately 3 minutes). When imaging at a resolution 40 times better than the original, ($\sigma_x = \sigma_y = \sigma_z = 10\,\mu m$), the predicted acquisition time is only 22.6 seconds. At lower concentrations, the probability of empty PSFs ($P(k = 0)$) is dominant, and thus the number of interrogations required to create equivalent images will be increased. As the concentration surpasses the optimum level, the chance of multiple bubbles being present in a single PSF becomes influential and the acquisition time increases once more.

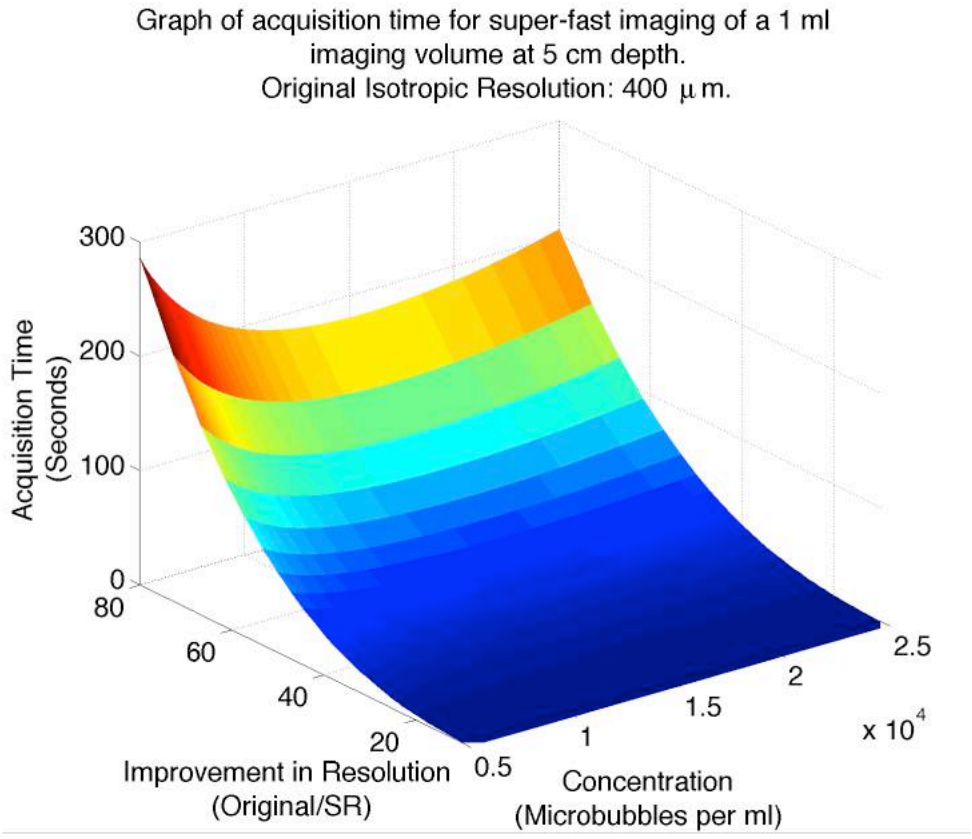

Figure 9.5. Simulated results showing imaging acquisition time to acquire sufficient data as a function of concentration (x-axis) and improvement in resolution (y-axis) for super-fast imaging of a 1 cm³ imaging volume at 5 cm depth where volumetric data can be acquired in two interrogations (PI imaging). The original resolution of the system is 400 μm in all dimensions.

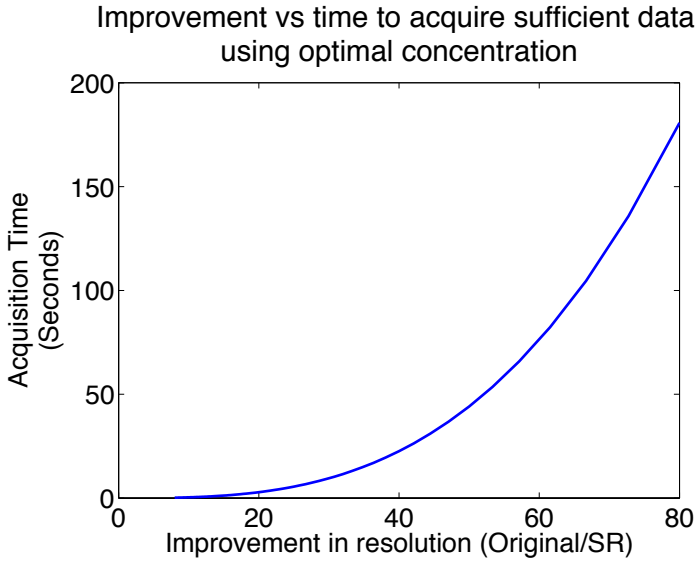

Figure 9.6. Graph to show PI imaging acquisition time to acquire sufficient data according to Equation (9.21) as a function of improvement in resolution (original resolution/SR localisation precision) at the optimum concentration of 15625 microbubble/ml for a 1 ml imaging volume. Here, an factor of 80 improvement corresponds to 400 μm /80 = 5 μm.

A larger range of concentrations tested are displayed in Figure 9.7, where the acquisition time is shown to drastically increase at these extremes; when the bubble concentration is too low, the low localisation per second rate will result in a longer required acquisition time, while too high a concentration would also require a long acquisition time due to the a high number of rejections caused by multiple bubble signals and few single localisations.

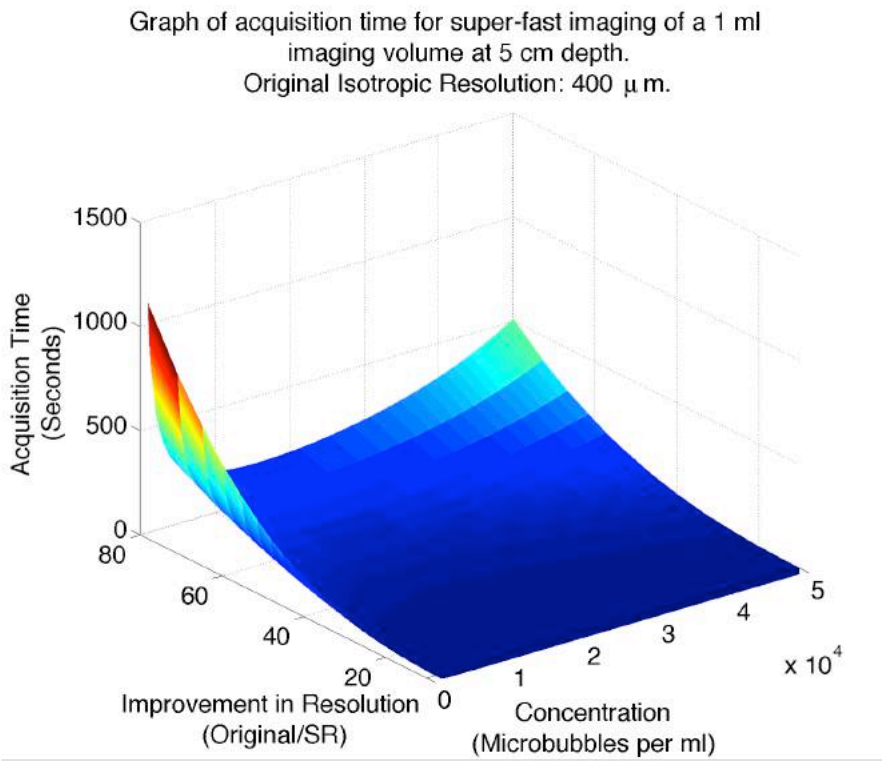

Figure 9.7. Graphical results showing imaging acquisition time to acquire sufficient data as a function of concentration (x-axis) and improvement in resolution (y-axis) for super-fast imaging of a 1 ml imaging volume at 5 cm depth where volumetric data can be acquired in one interrogation. The original resolution of the system is 400 μm

The use of a higher transmit frequency will allow higher potential localisation rates; for a fixed target volume V, a smaller V_{PSF} will result in a larger optimal bubble concentration (equal to V/V_{PSF}), and hence an increased number of bubbles can be localised in each interrogation than at a lower frequency. Simulated results are shown in Figure 9.8.

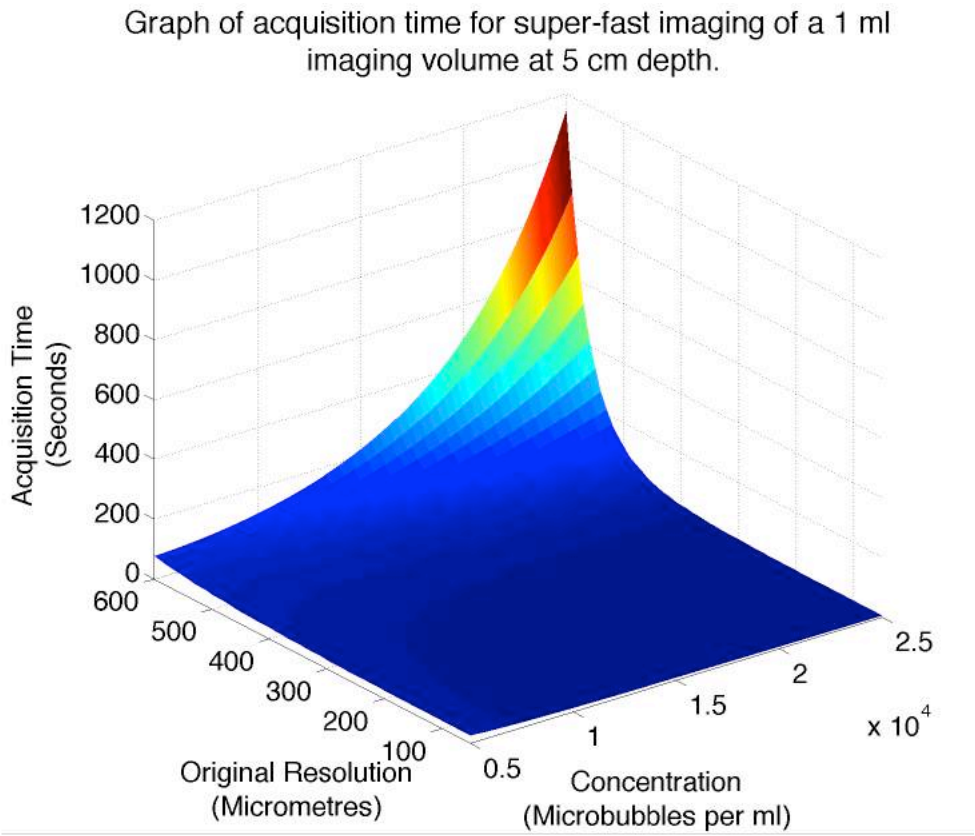

Figure 9.8. Simulated acquisition time required to image a 1 cm^3 target volume at 5 cm depth using PI for microbubble concentrations from 0.5 - 2.5 · 10^4mb/ml, with varying diffraction limited resolution from 50 - 600 μm with localisation precision fixed at 10 μm. The duration required reduces for an increase in diffraction limited resolution and for an increase in bubble concentration.

With a certainty set to 0.9 in the Binomial formula, the acquisition time increases as shown in Figure 9.9 compared to employing an average approach as in Figure 9.7, where at the optimum concentration, the time required to obtain super-resolution images at $\sigma_x = \sigma_y = \sigma_z = 5\ \mu m$ would increase from 180.7 seconds, to 333.8 seconds (almost 6 minutes).

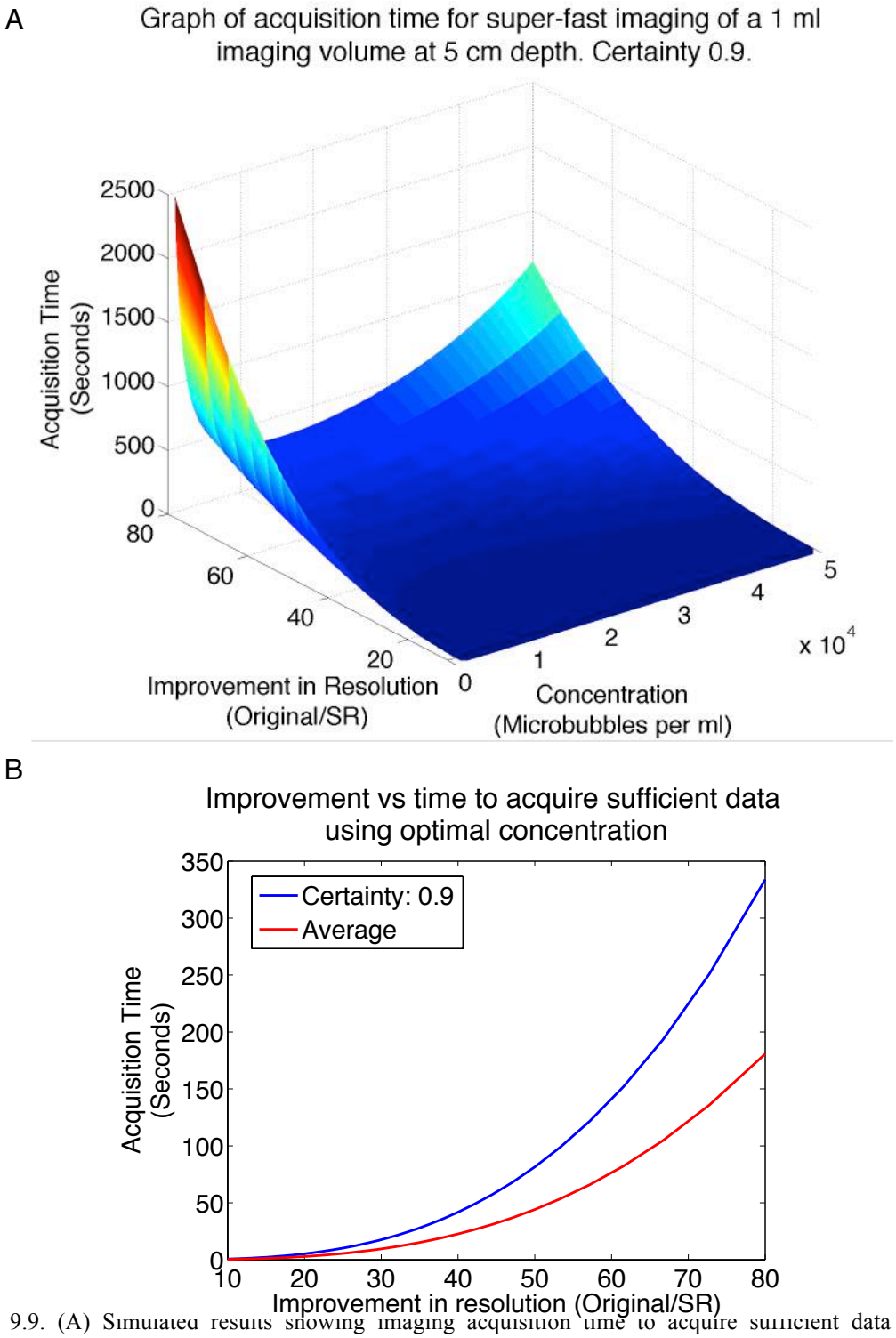

Figure 9.9. (A) Simulated results showing imaging acquisition time to acquire sufficient data as a function of concentration (x-axis) and improvement in resolution (y-axis) for super-fast imaging of a 1 ml imaging volume at 5 cm depth where volumetric data can be acquired in one interrogation. The original resolution of the system is 400 μm and the certainty using the Binomial Theorem has been set to 0.9. (B) displays a comparison of acquisition time at the optimal microbubble concentration between using the average number of PSF volumes and setting the certainty of success to 0.9.

Assuming a single 2D plane wave could be transmitted in each interrogation, and employing a slice-by-slice method, for a localisation precision of 10 μm (improvement factor of 40) the acquisition time would increase from 22.6 seconds to 1162 seconds (approximately 20 minutes), and when acquiring data line by line, this increases to $5.8 \cdot 10^4$ seconds (approximately 16 hours). Acquiring data using US scanner designed for 3D image acquisition would therefore be necessary for the progression of this technique towards clinical application. A reduction in acquisition time would be achieved with a shallower imaging depth, a higher frequency transmit pulse for a higher diffraction limited resolution, a lower super-resolution precision, or a smaller imaging volume.

Using Equation (9.30) and (9.31), if the frame rate were to be restricted to ensure that microbubble flow within the capillaries (v_b = 300 μm/s on average) moved more than the localisation precision in each frame, the acquisition time for super-fast imaging at optimal concentration would be restricted to 5799 seconds (approximately 1.6 hours). However, since the microcirculation is likely to contain vessels ranging from μm/s to several mm/s (Chapter 1, Table 1.1) and since velocities below this value will still contribute to the final rendering, with v_b = 2000 μm/s the acquisition time would be 869.9 seconds or around 14.5 minutes. This increased acquisition time (cf. 22.6 seconds for optimal frame rate) may be beneficial to increase the likelihood that microbubbles have sufficient time to flow through the entire vascular volume.

9.1.4 DISCUSSION

This simulation aimed to provide an insight into the relationship between imaging parameters and microbubble concentration on the localisation rate and acquisition time of super-resolution US imaging. Under the assumptions of a Poisson distribution, this provided estimations of ideal bubble concentrations for minimising acquisition time.

The simulated results showed that the use of an optimal concentration is important in reducing acquisition times, and thus ensuring the technique is clinically feasible. In examples shown for the imaging of a 1 cm^3 imaging volume at 5 cm depth with diffraction limited resolution $\mathrm{FWHM}_x = \mathrm{FWHM}_y = \Delta z$ = 400 μm using superfast

volumetric acquisition and achieving a factor of 80 improvement in resolution, the acquisition time could be as low as 180.7 seconds. However, as stated above, the microbubble signals must be detected throughout the vasculature for the full structure to be visible in the final rendering and may therefore benefit from a longer imaging duration. If we restrict the frame rate to that in which the motion of a microbubble travelling at microvascular blood speeds is likely to provide new spatial information in each image, then the imaging time increases considerably. Additionally, using Equation (9.5) to apply a high level of certainty to the likelihood of imaging spatially isolated bubble signals would ensure a greater level of localisations in the final rendering, however there would be a inherent trade-off with acquisition time even at the optimal concentration.

There are a number of assumptions implemented in this simulation which would lead to discrepancies between simulated and experimental findings. The simulation assumes an ideal super-resolution algorithm which is able to correctly detect single bubbles in all cases, and reject those from multiple bubbles within one PSF sized volume. A more realistic imaging scenario would incorporate noise as well as varying bubble signals such as ringing or interference signals created by clouds of bubbles; these would affect the ability of the algorithm to identify and accurately localise bubbles. In reality, V_{PSF} is generally not isotropic; the elevational resolution is typically much larger than in plane resolutions. This should not affect the predictions of acquisition time within the model.

Additionally, the assumption that events are independent may not always hold; the bubbles may cluster [234], or if the frame rate is high enough that the volume of blood imaged in previous observations is present in those subsequent, the same microbubble will be imaged consecutively. To ensure that for each frame, a entirely new sample volume is imaged,

$$Flow\ Rate\ =\ Imaging\ Rate\ \cdot\ Sample\ Volume,$$

where the sample volume is the volume of the target within each interrogation. This could be calculated for *in vitro* implementation where the flow rate can be controlled

and the sample volume can be estimated, however this would be challenging *in vivo* due to the need for prior knowledge regarding the target blood flow rate.

Since super-resolution imaging is aimed at imaging vessels which are smaller than the diffraction limit, the volume of vessel contained within each PSF volume will additionally need consideration since this will influence the probability of single bubble occurrences. For example, within a single diffraction limited resolution voxel, there may exist an isolated capillary vessel, or the resolution voxel may be positioned fully within a macrovessel, producing a spatially variable expectation value due to an inhomogeneous voxel-based concentration. Furthermore, over long acquisition times, the microbubble concentration may gradually decrease due to dissolution and destruction. In these cases it may be that an inhomogeneous Poisson process could be modelled, in which the expectation value can be given as a spatially or temporally varying parameter [387].

As seen in the experimental procedures in Chapter 3 and Chapter 4, it is not always possible to calculate the optimal concentration prior to imaging due to experimental uncertainties, as well as unknown bubble dissolution and destruction during *in vitro* and in particular *in vivo* circulation. Possible methods for maintaining an optimal concentration have been discussed in Chapter 3, Section 3.2ii.3.4. This simulation could form a basis for the development of more complex and realistic simulations for super-resolution in the future.

Simulated implementation of the super-resolution technique shows considerably larger acquisition time when 2D slice acquisition is used, estimated to be a time of 20 minutes for the case described above at optimal microbubble concentration; this would currently be unfeasible in a clinical setting due to motion effects and the use of both clinician and patient time. Acquiring data with a 3D probe is therefore vital to the progression of this technique towards clinical application.

9.2 CALCULATION OF THE MOVEMENT OF MICROBUBBLES DURING IMAGING USING PARABOLIC FLOW

A parabolic flow profile can be described by the equation for Poiseuille Flow, given by

$$v_z(r) = \frac{\partial P}{\partial z}\frac{r^2 - R^2}{4\eta}, \tag{9.32}$$

$v_z(r) = Laminar\ low\ velocity\ at\ radial\ coodinate\ \ r,$

$\frac{\partial P}{\partial z} = Pressure\ drop\ between\ the\ ends\ of\ the\ tube,$

$r = radial\ position,$

$R = Radius\ of\ tube,$

$\eta = viscosity.$

At the centre of the tube, $r = 0$, and the velocity is at a maximum, given by

$$v_{max} = \frac{\partial P}{\partial z}\frac{R^2}{4\eta}, \tag{9.33}$$

Using the use the Hagen-Poiseuille relation, assuming irrotational flow and steady state, the relationship between pressure and flow rate can be given by

$$\Delta P = \frac{128\eta LQ}{\pi d^4}, \tag{9.34}$$

$\Delta P = Pressure\ change,$

$L = Length\ of\ tube,$

$Q = \ Volumetric\ flow\ rate,$

$d = 2R = Tube\ diameter$

Then,

$$v_{max} = \frac{-2Q}{\pi R^2}, \tag{9.35}$$

The tube internal cross section is given by

$$\pi R^2 = 0.0314\, mm^2. \tag{9.36}$$

Flow rate $Q = 200\, \mu l/min = 3.33\, mm^3/s$, thus,

$$v_{max} = \frac{-2 \cdot 3.33\, mm^3}{0.0314 mm^2}, \tag{9.37}$$

$$v_{max} = -212.3\, mm/s$$

$$v_{mean} = \frac{v_{max}}{2} = -106.2\, \mathrm{mm}/s \tag{9.38}$$

The maximum distance moved by bubble per frame is expected to be

$$d_{frame} = \frac{v_{max}}{Frame\ rate} = 4.32\ \mathrm{mm}.$$

9.3 Calculation of Microbubble Exposure to Ultrasound Acquisition Lines

The time taken to acquire a single pulse line, t_l, at a target depth of $d = 0.07\, m$, where the speed of sound in tissue is taken as c =1540ms^{-1}, can be given by

$$t_l = \frac{2d}{c}, \tag{9.39}$$

$$t_l = \frac{0.14}{1540},$$

$$t_l = 9 \cdot 10^{-5}\, s$$

At a frame rate of 25 Hz, the time taken to acquire a single frame, t_f, can be given by

$$t_f = 1/25 = 0.04\ \mathrm{s}$$

The transmission of three multi-pulses are used for Cadence CPS imaging, therefore the number of lines per frame L_f, can be approximated by,

$$L_f \sim \frac{t_f}{t_l \cdot 3}, \tag{9.40}$$

$$L_f \sim 148\ lines\ per\ frame$$

If the lateral region which is imaged is approximately 3 cm, the line density can be given by

$$Line\ density = \frac{L_f}{3} = \frac{148}{3}, \tag{9.41}$$

$$49\ lines\ per\ cm = 0.0049\ lines\ per\ \mu m$$

The lateral FWHM of bubble signal is 336 μm, corresponding to 4.9 CPS lines. Thus,

$$Time\ bubble\ exposed = 4.9 \cdot 9 \cdot 10^{-5}\ s,$$
$$\approx 4.4 \cdot 10^{-4} s$$
$$Distance\ moved = 4.4 \cdot 10^{-4} s \cdot 106\ mm/s$$
$$\sim 47\ \mu m.$$

9.4 CLINICAL IN VIVO IMAGING

Figure 9.10 shows the destruction replenishment TIC curves for remaining volunteer data with a log-normal perfusion fit.

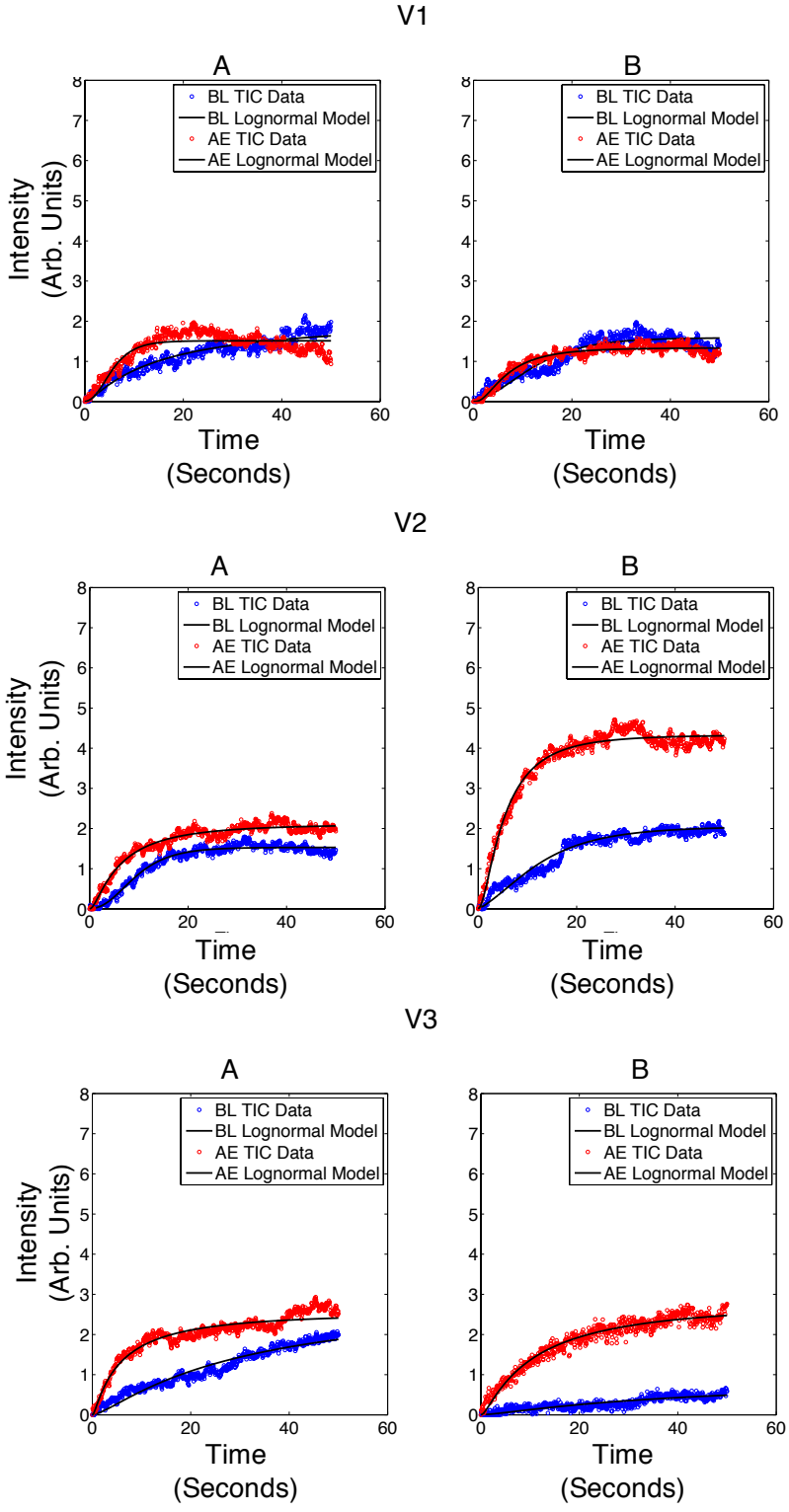

Figure 9.10. Destruction-replenishment TIC curves for Volunteers 1-3 in the following 50 seconds after bubble destruction at baseline (blue) and after exercise (red), with log-normal perfusion model fit

REFERENCES

[1] K. Tuma, Ronald F. , Duran, Walter N. , Ley, *Microcirculation*. Academic Press, 2011.

[2] American Diabetes Association, "Peripheral Arterial Disease in People with Diabetes," *Diabetes Care*, vol. 26, no. 12, pp. 3333–3341, 2003.

[3] N. C. Dolan, K. Liu, M. H. Criqui, P. Greenland, J. M. Guralnik, C. Chan, J. R. Schneider, A. L. Mandapat, G. Martin, and M. M. McDermott, "Peripheral artery disease, diabetes, and reduced lower extremity functioning.," *Diabetes Care*, vol. 25, no. 1, pp. 113–20, Jan. 2002.

[4] R. Zatz and B. M. Brenner, "Pathogenesis of diabetic microangiopathy. The hemodynamic view," *Am. J. Med.*, vol. 80, no. 3, pp. 443–453, Mar. 1986.

[5] M. J. Fowler, "Microvascular and Macrovascular Complications of Diabetes," *Clin. Diabetes*, vol. 26, no. 2, pp. 77–82, Apr. 2008.

[6] P. G. Camici and F. Crea, "Coronary Microvascular Dysfunction," *N. Engl. J. Med.*, vol. 356, no. 8, pp. 830–840, Feb. 2007.

[7] N. Weidner, J. Folkman, F. Pozza, P. Bevilacqua, E. N. Allred, D. H. Moore, S. Meli, and G. Gasparini, “Tumor angiogenesis: a new significant and independent prognostic indicator in early-stage breast carcinoma.,” *J. Natl. Cancer Inst.*, vol. 84, no. 24, pp. 1875–87, Dec. 1992.

[8] D. M. McDonald and P. L. Choyke, “Imaging of angiogenesis: from microscope to clinic.,” *Nat. Med.*, vol. 9, no. 6, pp. 713–25, Jun. 2003.

[9] N. Weidner, “Intratumor microvessel density as a prognostic factor in cancer.,” *Am. J. Pathol.*, vol. 147, no. 1, pp. 9–19, Jul. 1995.

[10] N. Weidner, J. P. Semple, W. R. Welch, and J. Folkman, “Tumor angiogenesis and metastasis--correlation in invasive breast carcinoma.,” *N. Engl. J. Med.*, vol. 324, no. 1, pp. 1–8, Jan. 1991.

[11] D. E. Goertz, D. A. Christopher, J. L. Yu, R. S. Kerbel, P. N. Burns, and F. S. Foster, “High-frequency color flow imaging of the microcirculation.,” *Ultrasound Med. Biol.*, vol. 26, no. 1, pp. 63–71, Jan. 2000.

[12] a R. Padhani and M. Neeman, “Challenges for imaging angiogenesis.,” *Br. J. Radiol.*, vol. 74, no. 886, pp. 886–90, Oct. 2001.

[13] H. Becher and P. N. Burns, *Handbook of contrast echocardiography: left ventricular function and myocardial perfusion*. Springer, 2000.

[14] D. Cosgrove and N. Lassau, “Imaging of perfusion using ultrasound.,” *Eur. J. Nucl. Med. Mol. Imaging*, vol. 37 Suppl 1, pp. S65–85, Aug. 2010.

[15] T. S. Desser and R. B. Jeffrey, “Tissue harmonic imaging techniques: physical principles and clinical applications.,” *Semin. Ultrasound. CT. MR*, vol. 22, no. 1,

pp. 1–10, Feb. 2001.

[16] J. Allen and K. Howell, “Microvascular imaging: techniques and opportunities for clinical physiological measurements.,” *Physiol. Meas.*, vol. 35, no. 7, pp. R91–R141, Jul. 2014.

[17] M. J. Leahy, *Microcirculation Imaging*. John Wiley & Sons, 2012.

[18] S. Delorme and M. V Knopp, “Non-invasive vascular imaging: assessing tumour vascularity.,” *Eur. Radiol.*, vol. 8, no. 4, pp. 517–27, Jan. 1998.

[19] D. M. McDonald and P. L. Choyke, “Imaging of angiogenesis: from microscope to clinic.,” *Nat. Med.*, vol. 9, no. 6, pp. 713–25, Jun. 2003.

[20] M. Greaves, *Cancer: The Evolutionary Legacy*. Oxford University Press, 2001.

[21] F. G. Fowkes, E. Housley, E. H. Cawood, C. C. Macintyre, C. V Ruckley, and R. J. Prescott, “Edinburgh Artery Study: prevalence of asymptomatic and symptomatic peripheral arterial disease in the general population.,” *Int. J. Epidemiol.*, vol. 20, no. 2, pp. 384–92, Jun. 1991.

[22] P. E. Norman, J. W. Eikelboom, and G. J. Hankey, “Peripheral arterial disease: prognostic significance and prevention of atherothrombotic complications.,” *Med. J. Aust.*, vol. 181, no. 3, pp. 150–4, 2004.

[23] E. Selvin and T. P. Erlinger, “Prevalence of and risk factors for peripheral arterial disease in the United States: results from the National Health and Nutrition Examination Survey, 1999-2000.,” *Circulation*, vol. 110, no. 6, pp. 738–43, Aug. 2004.

[24] “Tackling Peripheral Arterial Disease More Effectively: Saving Limbs, Saving Lives.” [Online]. Available: http://appgvascular.org.uk/reports. [Accessed: 04-Sep-2015].

[25] N. Weidner and J. Folkman, “Tumoral vascularity as a prognostic factor in cancer.,” *Important Adv. Oncol.*, pp. 167–90, Jan. 1996.

[26] L. Womack, D. Peters, E. J. Barrett, S. Kaul, W. Price, and J. R. Lindner, “Abnormal Skeletal Muscle Capillary Recruitment During Exercise in Patients With Type 2 Diabetes Mellitus and Microvascular Complications,” *J. Am. Coll. Cardiol.*, vol. 53, no. 23, pp. 2175–2183, 2009.

[27] A. C. Guyton and J. E. Hall, *Textbook of medical physiology*. Saunders, 2000.

[28] K. Rogers, *Blood: Physiology and Circulation*. The Rosen Publishing Group, 2010.

[29] C. G. Caro, *The Mechanics of the Circulation*. Cambridge University Press, 2012.

[30] L. Sherwood, *Human Physiology: From Cells to Systems*. Cengage Learning, 2008.

[31] “Heart & Circulatory System | Revision World.” [Online]. Available: http://revisionworld.com/gcse-revision/biology/human-body/heart-circulatory-system. [Accessed: 11-Sep-2015].

[32] A. Bollinger, P. Butti, J.-P. Barras, H. Trachsler, and W. Siegenthaler, “Red blood cell velocity in nailfold capillaries of man measured by a television microscopy technique,” *Microvasc. Res.*, vol. 7, no. 1, pp. 61–72, Jan. 1974.

[33] M. L. Moya, Y.-H. Hsu, A. P. Lee, C. C. W. Hughes, and S. C. George, “In vitro perfused human capillary networks.,” *Tissue Eng. Part C. Methods*, vol. 19, no. 9, pp. 730–7, Sep. 2013.

[34] P. Vaupel, F. Kallinowski, and P. Okunieff, “Blood flow, oxygen and nutrient supply, and metabolic microenvironment of human tumors: a review,” pp. 6449–6465, 1989.

[35] M. E. Gerritsen, *Microcirculation*. Elsevier, 2008.

[36] D. N. Granger and E. Senchenkova, “Anatomical Considerations.” Morgan & Claypool Life Sciences, 2010.

[37] H. J. Granger and A. P. Shepherd, “Intrinsic microvascular control of tissue oxygen delivery,” *Microvasc. Res.*, vol. 5, no. 1, pp. 49–72, Jan. 1973.

[38] T. Albrecht, M. J. Blomley, D. O. Cosgrove, S. D. Taylor-Robinson, V. Jayaram, R. Eckersley, A. Urbank, J. Butler-Barnes, and N. Patel, “Non-invasive diagnosis of hepatic cirrhosis by transit-time analysis of an ultrasound contrast agent.,” *Lancet (London, England)*, vol. 353, no. 9164, pp. 1579–83, May 1999.

[39] T. Jeswani and A. R. Padhani, “Imaging tumour angiogenesis.,” *Cancer Imaging*, vol. 5, pp. 131–8, Jan. 2005.

[40] J. Folkman, “Circulating precursor endothelial cells,” vol. 6, no. April, pp. 273–286, 2007.

[41] C. Blood, “Tumor interactions with the vasculature: angiogenesis and tumor metastasis,” *Biochim. Biophys. Acta - Rev. Cancer*, vol. 1032, no. 1, pp. 89–118, Jun. 1990.

[42] J. M. Hudson, “QUANTIFICATION OF BLOOD FLOW USING ULTRASOUND CONTRAST AGENTS by : John Monte Hudson Quantification of Blood Flow Using Ultrasound Contrast Agents,” p. 178, 2011.

[43] R. K. Jain, “Normalization of tumor vasculature: an emerging concept in antiangiogenic therapy.,” *Science*, vol. 307, no. 5706, pp. 58–62, Jan. 2005.

[44] D. H. Johnson, L. Fehrenbacher, W. F. Novotny, R. S. Herbst, J. J. Nemunaitis, D. M. Jablons, C. J. Langer, R. F. DeVore, J. Gaudreault, L. A. Damico, E. Holmgren, and F. Kabbinavar, “Randomized phase II trial comparing bevacizumab plus carboplatin and paclitaxel with carboplatin and paclitaxel alone in previously untreated locally advanced or metastatic non-small-cell lung cancer.,” *J. Clin. Oncol.*, vol. 22, no. 11, pp. 2184–91, Jun. 2004.

[45] B. Al-Husein, M. Abdalla, M. Trepte, D. L. Deremer, and P. R. Somanath, “Antiangiogenic therapy for cancer: an update.,” *Pharmacotherapy*, vol. 32, no. 12, pp. 1095–111, Dec. 2012.

[46] K. Ouriel, “Peripheral arterial disease.,” *Lancet (London, England)*, vol. 358, no. 9289, pp. 1257–64, Oct. 2001.

[47] “Peripheral Arterial Disease in People With Diabetes,” *Diabetes Care*, vol. 26, no. 12, pp. 3333–3341, Nov. 2003.

[48] O. W. Brawley, “Prostate carcinoma incidence and patient mortality: the effects of screening and early detection.,” *Cancer*, vol. 80, no. 9, pp. 1857–63, Nov. 1997.

[49] A. W. Griffioen and G. Molema, “Angiogenesis: Potentials for Pharmacologic Intervention in the Treatment of Cancer, Cardiovascular Diseases, and Chronic Inflammation,” *Pharmacol. Rev.*, vol. 52, no. 2, pp. 237–268, Jun. 2000.

[50] S. H. Katsanis and N. Katsanis, “Molecular genetic testing and the future of clinical genomics.,” *Nat. Rev. Genet.*, vol. 14, no. 6, pp. 415–26, Jun. 2013.

[51] W. J. Choi and R. K. Wang, “In vivo imaging of functional microvasculature within tissue beds of oral and nasal cavities by swept-source optical coherence tomography with a forward/side-viewing probe.,” *Biomed. Opt. Express*, vol. 5, no. 8, pp. 2620–34, Aug. 2014.

[52] M. S. Mahmud, D. W. Cadotte, B. Vuong, C. Sun, T. W. H. Luk, A. Mariampillai, and V. X. D. Yang, “Review of speckle and phase variance optical coherence tomography to visualize microvascular networks.,” *J. Biomed. Opt.*, vol. 18, no. 5, p. 50901, May 2013.

[53] Z. Chen, T. E. Milner, S. Srinivas, X. Wang, A. Malekafzali, M. J. C. van Gemert, and J. S. Nelson, “Noninvasive imaging of in vivo blood flow velocity using optical Doppler tomography,” *Opt. Lett.*, vol. 22, no. 14, p. 1119, Jul. 1997.

[54] S. Yazdanfar, A. M. Rollins, and J. A. Izatt, “In vivo imaging of human retinal flow dynamics by color Doppler optical coherence tomography.,” *Arch. Ophthalmol. (Chicago, Ill. 1960)*, vol. 121, no. 2, pp. 235–9, Feb. 2003.

[55] M. Miura, Y.-J. Hong, Y. Yasuno, D. Muramatsu, T. Iwasaki, and H. Goto, “Three-dimensional vascular imaging of proliferative diabetic retinopathy by Doppler optical coherence tomography.,” *Am. J. Ophthalmol.*, vol. 159, no. 3, pp. 528–38.e3, Mar. 2015.

[56] W. Drexler, U. Morgner, R. K. Ghanta, F. X. Kärtner, J. S. Schuman, and J. G. Fujimoto, “Ultrahigh-resolution ophthalmic optical coherence tomography.,” *Nat. Med.*, vol. 7, no. 4, pp. 502–7, Apr. 2001.

[57] P. S. Tofts, G. Brix, D. L. Buckley, J. L. Evelhoch, E. Henderson, M. V Knopp, H. B. Larsson, T. Y. Lee, N. A. Mayr, G. J. Parker, R. E. Port, J. Taylor, and R. M. Weisskoff, "Estimating kinetic parameters from dynamic contrast-enhanced T(1)-weighted MRI of a diffusable tracer: standardized quantities and symbols.," *J. Magn. Reson. Imaging*, vol. 10, no. 3, pp. 223–32, Sep. 1999.

[58] F. Boschi, P. Marzola, M. Sandri, E. Nicolato, M. Galiè, S. Fiorini, F. Merigo, V. Lorusso, L. Chaabane, and A. Sbarbati, "Tumor microvasculature observed using different contrast agents: a comparison between Gd-DTPA-Albumin and B-22956/1 in an experimental model of mammary carcinoma.," *MAGMA*, vol. 21, no. 3, pp. 169–76, May 2008.

[59] P. K. Upputuri, K. Sivasubramanian, C. Seow, K. Mark, and M. Pramanik, "Recent Developments in Vascular Imaging Techniques in Tissue Engineering and Regenerative Medicine," vol. 2015, 2015.

[60] R. Wutke, W. Lang, C. Fellner, R. Janka, C. Denzel, M. Lell, W. Bautz, and F. A. Fellner, "High-Resolution, Contrast-Enhanced Magnetic Resonance Angiography With Elliptical Centric k-Space Ordering of Supra-aortic Arteries Compared With Selective X-Ray Angiography," *Stroke*, vol. 33, no. 6, pp. 1522–1529, Jun. 2002.

[61] M. Beaumont, M. G. DuVal, Y. Loai, W. A. Farhat, G. K. Sándor, and H.-L. M. Cheng, "Monitoring angiogenesis in soft-tissue engineered constructs for calvarium bone regeneration: an in vivo longitudinal DCE-MRI study.," *NMR Biomed.*, vol. 23, no. 1, pp. 48–55, Jan. 2010.

[62] L. M. Brubaker, E. Bullitt, C. Yin, T. Van Dyke, and W. Lin, "Magnetic resonance angiography visualization of abnormal tumor vasculature in genetically engineered mice.," *Cancer Res.*, vol. 65, no. 18, pp. 8218–23, Sep. 2005.

[63] J. R. Dillman, J. H. Ellis, R. H. Cohan, E. M. Caoili, H. K. Hussain, A. D. Campbell, and P. J. Strouse, “Safety of gadolinium-based contrast material in sickle cell disease.,” *J. Magn. Reson. Imaging*, vol. 34, no. 4, pp. 917–20, Oct. 2011.

[64] T. Kanda, T. Fukusato, M. Matsuda, K. Toyoda, H. Oba, J. Kotoku, T. Haruyama, K. Kitajima, and S. Furui, “Gadolinium-based Contrast Agent Accumulates in the Brain Even in Subjects without Severe Renal Dysfunction: Evaluation of Autopsy Brain Specimens with Inductively Coupled Plasma Mass Spectroscopy.,” *Radiology*, vol. 276, no. 1, pp. 228–32, Jul. 2015.

[65] A. Arkudas, J. P. Beier, G. Pryymachuk, T. Hoereth, O. Bleiziffer, E. Polykandriotis, A. Hess, H. Gulle, R. E. Horch, and U. Kneser, “Automatic quantitative micro-computed tomography evaluation of angiogenesis in an axially vascularized tissue-engineered bone construct.,” *Tissue Eng. Part C. Methods*, vol. 16, no. 6, pp. 1503–14, Dec. 2010.

[66] S. J. Schambach, S. Bag, C. Groden, L. Schilling, and M. A. Brockmann, “Vascular imaging in small rodents using micro-CT.,” *Methods*, vol. 50, no. 1, pp. 26–35, Jan. 2010.

[67] T. Engelhorn, I. Y. Eyupoglu, M. A. Schwarz, M. Karolczak, H. Bruenner, T. Struffert, W. Kalender, and A. Doerfler, “In vivo micro-CT imaging of rat brain glioma: a comparison with 3T MRI and histology.,” *Neurosci. Lett.*, vol. 458, no. 1, pp. 28–31, Jul. 2009.

[68] K. Murata, H. Itoh, G. Todo, M. Kanaoka, S. Noma, T. Itoh, M. Furuta, H. Asamoto, and K. Torizuka, “Centrilobular lesions of the lung: demonstration by high-resolution CT and pathologic correlation.,” *Radiology*, vol. 161, no. 3, pp. 641–5, Dec. 1986.

[69] E. A. Kazerooni, “High-resolution CT of the lungs.,” *AJR. Am. J. Roentgenol.*,

vol. 177, no. 3, pp. 501–19, Sep. 2001.

[70] P. N. T. Wells, “Ultrasound imaging.,” *Phys. Med. Biol.*, vol. 51, no. 13, pp. R83–98, Jul. 2006.

[71] C. R. Merritt, F. W. Kremkau, and J. C. Hobbins, “Diagnostic ultrasound: bioeffects and safety.,” *Ultrasound Obstet. Gynecol.*, vol. 2, no. 5, pp. 366–74, Sep. 1992.

[72] J. B. Fowlkes and C. K. Holland, “Mechanical bioeffects from diagnostic ultrasound: AIUM consensus statements. American Institute of Ultrasound in Medicine.,” *J. Ultrasound Med.*, vol. 19, no. 2, pp. 69–72, Feb. 2000.

[73] R. A. Novelline and L. F. Squire, *Squire’s Fundamentals of Radiology*. La Editorial, UPR, 2004.

[74] F. S. Foster, P. N. Burns, D. H. Simpson, S. R. Wilson, D. a Christopher, and D. E. Goertz, “Ultrasound for the visualization and quantification of tumor microcirculation.,” *Cancer Metastasis Rev.*, vol. 19, no. 1–2, pp. 131–8, Jan. 2000.

[75] A. Fenster and D. B. Downey, “3-D ultrasound imaging: a review,” *IEEE Eng. Med. Biol. Mag.*, vol. 15, no. 6, pp. 41–51, 1996.

[76] D. Cosgrove, “Ultrasound contrast agents: an overview.,” *Eur. J. Radiol.*, vol. 60, no. 3, pp. 324–30, Dec. 2006.

[77] V. Gibbs, D. C. TDCR., and A. Sassano, *Ultrasound Physics and Technology: How, Why and When*. Elsevier Health Sciences, 2009.

[78] A. Ng and J. Swanevelder, “Resolution in ultrasound imaging,” *Contin. Educ. Anaesthesia, Crit. Care Pain*, vol. 11, no. 5, pp. 186–192, Aug. 2011.

[79] T. L. Szabó, *Diagnostic Ultrasound Imaging: Inside Out*. Academic Press, 2004.

[80] *The Essential Physics of Medical Imaging*. Lippincott Williams & Wilkins, 2002.

[81] J. T. Bushberg and J. M. Boone, *The Essential Physics of Medical Imaging*. Lippincott Williams & Wilkins, 2011.

[82] M. Ali, D. Magee, and U. Dasgupta, “Signal processing overview of ultrasound systems for medical imaging,” *SPRAB12, Texas ...*, no. November, pp. 1–27, 2008.

[83] M.-X. Tang, H. Mulvana, T. Gauthier, A. K. P. Lim, D. O. Cosgrove, R. J. Eckersley, and E. Stride, “Quantitative contrast-enhanced ultrasound imaging: a review of sources of variability.,” *Interface Focus*, vol. 1, no. 4, pp. 520–39, Aug. 2011.

[84] K. R. Persons, P. M. Palisson, A. Manduca, W. J. Charboneau, E. M. James, N. T. Charboneau, N. J. Hangiandreou, and B. J. Erickson, “Ultrasound grayscale image compression with JPEG and wavelet techniques,” *J. Digit. Imaging*, vol. 13, no. 1, pp. 25–32, Feb. 2000.

[85] D. P. Hurlstone, S. Brown, S. S. Cross, A. J. Shorthouse, and D. S. Sanders, “High magnification chromoscopic colonoscopy or high frequency 20 MHz mini probe endoscopic ultrasound staging for early colorectal neoplasia: a comparative prospective analysis.,” *Gut*, vol. 54, no. 11, pp. 1585–9, Nov. 2005.

[86] Y. Saitoh, T. Obara, K. Einami, M. Nomura, M. Taruishi, T. Ayabe, T. Ashida, Y. Shibata, and Y. Kohgo, “Efficacy of high-frequency ultrasound probes for the

preoperative staging of invasion depth in flat and depressed colorectal tumors," *Gastrointest. Endosc.*, vol. 44, no. 1, pp. 34–39, Jul. 1996.

[87] Y. Xu and L. V. Wang, "Signal processing in scanning thermoacoustic tomography in biological tissues," *Med. Phys.*, vol. 28, no. 7, p. 1519, Jul. 2001.

[88] Olympus Corporation, "Ultrasonic Transducers," 2015.

[89] J. N. Wright, "Image Formation in Diagnostic Utrasound," *Short Course*, 1997.

[90] R. A. Harris, D. H. Follett, M. Halliwell, and P. N. Wells, "Ultimate limits in ultrasonic imaging resolution.," *Ultrasound Med. Biol.*, vol. 17, no. 6, pp. 547–58, Jan. 1991.

[91] J. C. Bamber and R. J. Dickinson, "Ultrasonic B-scanning : a computer simulation," *Phys. Med. Biol.*, vol. 463, no. 3, 1980.

[92] M. A. Pysz, K. Foygel, C. M. Panje, A. Needles, L. Tian, and J. K. Willmann, "Assessment and monitoring tumor vascularity with contrast-enhanced ultrasound maximum intensity persistence imaging.," *Invest. Radiol.*, vol. 46, no. 3, pp. 187–95, Mar. 2011.

[93] A. A. Doinikov and A. Bouakaz, "Review of shell models for contrast agent microbubbles.," *IEEE Trans. Ultrason. Ferroelectr. Freq. Control*, vol. 58, no. 5, pp. 981–93, May 2011.

[94] E. Stride and N. Saffari, "Microbubble ultrasound contrast agents: A review," *Proc. Inst. Mech. Eng. Part H J. Eng. Med.*, vol. 217, no. 6, pp. 429–447, Jun. 2003.

[95] N. de Jong, A. Bouakaz, and P. Frinking, “Basic Acoustic Properties of Microbubbles,” *Echocardiography*, vol. 19, no. 3, pp. 229–240, Apr. 2002.

[96] F. Forsberg, W. T. Shi, C. R. B. Merritt, Q. Dai, M. Solcova, and B. B. Goldberg, “On the usefulness of the mechanical index displayed on clinical ultrasound scanners for predicting contrast microbubble destruction.,” *J. Ultrasound Med.*, vol. 24, no. 4, pp. 443–50, Apr. 2005.

[97] K. Wei, A. R. Jayaweera, S. Firoozan, A. Linka, D. M. Skyba, and S. Kaul, “Quantification of Myocardial Blood Flow With Ultrasound-Induced Destruction of Microbubbles Administered as a Constant Venous Infusion,” *Circulation*, vol. 97, no. 5, pp. 473–483, Feb. 1998.

[98] E. Stride and M. Edirisinghe, “Novel microbubble preparation technologies,” *Soft Matter*, vol. 4, no. 12, p. 2350, Nov. 2008.

[99] J. R. Lindner, “Microbubbles in medical imaging: current applications and future directions.,” *Nat. Rev. Drug Discov.*, vol. 3, no. 6, pp. 527–32, Jun. 2004.

[100] B. B. Goldberg, J.-B. Liu, and F. Forsberg, “Ultrasound contrast agents: A review,” *Ultrasound Med. Biol.*, vol. 20, no. 4, pp. 319–333, Jan. 1994.

[101] P. N. Burns, D. Hope Simpson, and M. A. Averkiou, “Nonlinear imaging.,” *Ultrasound Med. Biol.*, vol. 26 Suppl 1, pp. S19–22, May 2000.

[102] P. N. Burns, S. R. Wilson, and D. H. Simpson, “Pulse inversion imaging of liver blood flow: improved method for characterizing focal masses with microbubble contrast.,” *Invest. Radiol.*, vol. 35, no. 1, pp. 58–71, Jan. 2000.

[103] “Ultrasound imaging system employing phase inversion subtraction to enhance the image.” 27-May-1997.

[104] E. Quaia, *Contrast Media in Ultrasonography: Basic Principles and Clinical Applications*. Springer Science & Business Media, 2006.

[105] A. Hoskins,Peter R., Martin, Kevin., Thrush, *Diagnostic Ultrasound: Physics and Equipment*. Cambridge University Press, 2010.

[106] R. J. Eckersley, C. T. Chin, and P. N. Burns, "Optimising phase and amplitude modulation schemes for imaging microbubble contrast agents at low acoustic power.," *Ultrasound Med. Biol.*, vol. 31, no. 2, pp. 213–9, Feb. 2005.

[107] P. J. Phillips, "Contrast pulse sequences (CPS): imaging nonlinear microbubbles," in *2001 IEEE Ultrasonics Symposium. Proceedings. An International Symposium (Cat. No.01CH37263)*, 2001, vol. 2, pp. 1739–1745.

[108] F. Lin, C. Cachard, R. Mori, F. Varray, F. Guidi, and O. Basset, "Ultrasound contrast imaging: influence of scatterer motion in multi-pulse techniques.," *IEEE Trans. Ultrason. Ferroelectr. Freq. Control*, vol. 60, no. 10, pp. 2065–78, Oct. 2013.

[109] K. Wei, E. Le, J.-P. Bin, M. Coggins, J. Thorpe, and S. Kaul, "Quantification of renal blood flow with contrast-enhanced ultrasound," *J. Am. Coll. Cardiol.*, vol. 37, no. 4, pp. 1135–1140, Mar. 2001.

[110] D. Duerschmied, L. Olson, M. Olschewski, A. Rossknecht, G. Freund, C. Bode, and C. Hehrlein, "Contrast ultrasound perfusion imaging of lower extremities in peripheral arterial disease: a novel diagnostic method.," *Eur. Heart J.*, vol. 27, no. 3, pp. 310–5, Mar. 2006.

[111] J. R. Lindner, L. Womack, E. J. Barrett, J. Weltman, W. Price, N. L. Harthun, S. Kaul, and J. T. Patrie, "Limb stress-rest perfusion imaging with contrast

ultrasound for the assessment of peripheral arterial disease severity.," *JACC. Cardiovasc. Imaging*, vol. 1, no. 3, pp. 343–50, May 2008.

[112] J. A. Jensen, *Estimation of Blood Velocities Using Ultrasound: A Signal Processing Approach*. Cambridge University Press, 1996.

[113] N. C. Nanda, R. Schlief, and B. B. Goldberg, Eds., *Advances in Echo Imaging Using Contrast Enhancement*. Dordrecht: Springer Netherlands, 1997.

[114] J. M. Rubin, R. O. Bude, P. L. Carson, R. L. Bree, and R. S. Adler, "Power Doppler US: a potentially useful alternative to mean frequency-based color Doppler US.," *Radiology*, vol. 190, no. 3, pp. 853–6, Mar. 1994.

[115] J. L. Alcázar, "Tumor angiogenesis assessed by three-dimensional power Doppler ultrasound in early, advanced and metastatic ovarian cancer: A preliminary study.," *Ultrasound Obstet. Gynecol.*, vol. 28, no. 3, pp. 325–9, Sep. 2006.

[116] V. Sboros and M.-X. Tang, "The assessment of microvascular flow and tissue perfusion using ultrasound imaging.," *Proc. Inst. Mech. Eng. H.*, vol. 224, no. 2, pp. 273–90, Jan. 2010.

[117] N. Lassau, L. Chami, M. Chebil, B. Benatsou, S. Bidault, E. Girard, G. Abboud, and A. Roche, "Dynamic contrast-enhanced ultrasonography (DCE-US) and anti-angiogenic treatments.," *Discov. Med.*, vol. 11, no. 56, pp. 18–24, Jan. 2011.

[118] J. Koster, T. Schlosser, C. Pohl, C. Lentz, S. Lohmaier, C. Veltmann, S. Kuntz-Hehner, H. Omran, B. Luderitz, H. Becher, and K. Tiemann, "Blood Flow Assessment by Ultrasound-Induced Destruction of Echocontrast Agents Using Harmonic Power Doppler Imaging: Which Parameters Determine Contrast Replenishment Curves?," *Echocardiography*, vol. 18, no. 1, pp. 1–8, Jan. 2001.

[119] T. Schlosser, C. Pohl, C. Veltmann, S. Lohmaier, J. Goenechea, A. Ehlgen, J. Kšter, D. Bimmel, S. Kuntz-Hehner, H. Becher, and K. Tiemann, “Feasibility of the flash-replenishment concept in renal tissue: which parameters affect the assessment of the contrast replenishment?,” *Ultrasound Med. Biol.*, vol. 27, no. 7, pp. 937–944, Jul. 2001.

[120] E. Stride, M.-X. Tang, R. J. Eckersley, and R. Eckersley, “Physical phenomena affecting quantitative imaging of ultrasound contrast agents,” *Appl. Acoust.*, vol. 70, no. 10, pp. 1352–1362, 2009.

[121] A. Heimdal and H. Torp, “Ultrasound doppler measurements of low velocity blood flow: limitations due to clutter signals from vibrating muscles,” *IEEE Trans. Ultrason. Ferroelectr. Freq. Control*, vol. 44, no. 4, pp. 873–881, Jul. 1997.

[122] F. S. Foster, C. J. Pavlin, K. A. Harasiewicz, D. A. Christopher, and D. H. Turnbull, “Advances in ultrasound biomicroscopy.,” *Ultrasound Med. Biol.*, vol. 26, no. 1, pp. 1–27, Jan. 2000.

[123] M. Berson, F. Patat, Z. Q. Wang, D. Besse, and L. Pourcelot, “Very high frequency pulsed Doppler apparatus.,” *Ultrasound in medicine & biology*, vol. 15, no. 2. pp. 121–31, Jan-1989.

[124] D. Christopher and P. Burns, “A high-frequency continuous-wave Doppler ultrasound system for the detection of blood flow in the microcirculation,” *Ultrasound Med. ...*, vol. 22, no. 9, pp. 1191–1203, 1996.

[125] D. Christopher and P. Burns, “A high-frequency pulsed-wave Doppler ultrasound system for the detection and imaging of blood flow in the microcirculation,” *Ultrasound Med. ...*, vol. 23, no. 7, pp. 997–1015, 1997.

[126] H. ISHIKAWA and J. SCHUMAN, “Anterior segment imaging: ultrasound biomicroscopy,” *Ophthalmol. Clin. North Am.*, vol. 17, no. 1, pp. 7–20, Mar. 2004.

[127] D. E. Goertz, D. A. Christopher, J. L. Yu, R. S. Kerbel, P. N. Burns, and F. S. Foster, “High-frequency color flow imaging of the microcirculation,” *Ultrasound Med. Biol.*, vol. 26, no. 1, pp. 63–71, Jan. 2000.

[128] F. S. Foster, J. Hossack, and S. L. Adamson, “Micro-ultrasound for preclinical imaging.,” *Interface Focus*, vol. 1, no. 4, pp. 576–601, Aug. 2011.

[129] A. Needles, A. Heinmiller, J. Sun, C. Theodoropoulos, D. Bates, D. Hirson, M. Yin, and F. S. Foster, “Development and initial application of a fully integrated photoacoustic micro-ultrasound system.,” *IEEE Trans. Ultrason. Ferroelectr. Freq. Control*, vol. 60, no. 5, pp. 888–97, May 2013.

[130] D. E. Kruse and K. W. Ferrara, “A new imaging strategy using wideband transient response of ultrasound contrast agents.,” *IEEE Trans. Ultrason. Ferroelectr. Freq. Control*, vol. 52, no. 8, pp. 1320–9, Aug. 2005.

[131] R. C. Gessner, C. B. Frederick, F. S. Foster, and P. a. Dayton, “Acoustic angiography: A new imaging modality for assessing microvasculature architecture,” *Int. J. Biomed. Imaging*, vol. 2013, 2013.

[132] P. A. Dayton, R. C. Gessner, L. Phillips, S. E. Shelton, K. Heath Martin, M. Lee, and F. S. Foster, “The implementation of acoustic angiography for microvascular and angiogenesis imaging.,” *Conf. Proc. ... Annu. Int. Conf. IEEE Eng. Med. Biol. Soc. IEEE Eng. Med. Biol. Soc. Annu. Conf.*, vol. 2014, pp. 4283–5, Jan. 2014.

[133] J. Xia, J. Yao, and L. V Wang, “Photoacoustic tomography: principles and advances.,” *Electromagn. waves (Cambridge, Mass.)*, vol. 147, pp. 1–22, Jan. .

[134] S. Hu and L. V Wang, “Photoacoustic imaging and characterization of the microvasculature.,” *J. Biomed. Opt.*, vol. 15, no. 1, p. 011101, Jan. .

[135] J. Laufer, P. Johnson, E. Zhang, B. Treeby, B. Cox, B. Pedley, and P. Beard, “In vivo preclinical photoacoustic imaging of tumor vasculature development and therapy.,” *J. Biomed. Opt.*, vol. 17, no. 5, p. 056016, May 2012.

[136] K. Maslov, H. F. Zhang, S. Hu, and L. V. Wang, “Optical-resolution photoacoustic microscopy for in vivo imaging of single capillaries,” *Opt. Lett.*, vol. 33, no. 9, p. 929, Apr. 2008.

[137] G. Ku and L. V. Wang, “Deeply penetrating photoacoustic tomography in biological tissues enhanced with an optical contrast agent,” *Opt. Lett.*, vol. 30, no. 5, p. 507, Mar. 2005.

[138] L. Song, K. Maslov, R. Bitton, K. K. Shung, and L. V Wang, “Fast 3-D dark-field reflection-mode photoacoustic microscopy in vivo with a 30-MHz ultrasound linear array.,” *J. Biomed. Opt.*, vol. 13, no. 5, p. 054028, 2008.

[139] E. Betzig, G. H. Patterson, R. Sougrat, O. W. Lindwasser, S. Olenych, J. S. Bonifacino, M. W. Davidson, J. Lippincott-Schwartz, and H. F. Hess, “Imaging intracellular fluorescent proteins at nanometer resolution.,” *Science*, vol. 313, no. 5793, pp. 1642–5, Sep. 2006.

[140] M. J. Rust, M. Bates, and X. Zhuang, “Sub-diffraction-limit imaging by stochastic optical reconstruction microscopy (STORM).,” *Nat. Methods*, vol. 3, no. 10, pp. 793–5, Oct. 2006.

[141] M. Bates, B. Huang, G. T. Dempsey, and X. Zhuang, “Multicolor super-resolution imaging with photo-switchable fluorescent probes.,” *Science*, vol. 317, no. 5845, pp. 1749–53, Sep. 2007.

[142] S. T. Hess, T. P. K. Girirajan, and M. D. Mason, “Ultra-high resolution imaging by fluorescence photoactivation localization microscopy.,” *Biophys. J.*, vol. 91, no. 11, pp. 4258–72, Dec. 2006.

[143] B. Huang, M. Bates, and X. Zhuang, “Super-resolution fluorescence microscopy.,” *Annu. Rev. Biochem.*, vol. 78, pp. 993–1016, Jan. 2009.

[144] E. Betzig, G. H. Patterson, R. Sougrat, O. W. Lindwasser, S. Olenych, J. S. Bonifacino, M. W. Davidson, J. Lippincott-Schwartz, and H. F. Hess, “Imaging intracellular fluorescent proteins at nanometer resolution.,” *Science*, vol. 313, no. 5793, pp. 1642–5, Sep. 2006.

[145] B. Huang, W. Wang, M. Bates, and X. Zhuang, “Three-dimensional super-resolution imaging by stochastic optical reconstruction microscopy.,” *Science*, vol. 319, no. 5864, pp. 810–3, Feb. 2008.

[146] S. T. Hess, T. J. Gould, M. V Gudheti, S. A. Maas, K. D. Mills, and J. Zimmerberg, “Dynamic clustered distribution of hemagglutinin resolved at 40 nm in living cell membranes discriminates between raft theories.,” *Proc. Natl. Acad. Sci. U. S. A.*, vol. 104, no. 44, pp. 17370–5, Oct. 2007.

[147] R. Henriques, C. Griffiths, E. Hesper Rego, and M. M. Mhlanga, “PALM and STORM: unlocking live-cell super-resolution.,” *Biopolymers*, vol. 95, no. 5, pp. 322–31, May 2011.

[148] O. M. Viessmann, R. J. Eckersley, K. Christensen-Jeffries, M. X. Tang, and C. Dunsby, “Acoustic super-resolution with ultrasound and microbubbles.,” *Phys.*

Med. Biol., vol. 58, no. 18, pp. 6447–58, Sep. 2013.

[149] K. Christensen-Jeffries, R. J. Browning, M.-X. Tang, C. Dunsby, and R. J. Eckersley, "In Vivo Acoustic Super-Resolution and Super-Resolved Velocity Mapping Using Microbubbles," *IEEE Trans. Med. Imaging*, 2015.

[150] M. Siepmann, G. Schmitz, J. Bzyl, M. Palmowski, and F. Kiessling, "Imaging tumor vascularity by tracing single microbubbles," in *2011 IEEE International Ultrasonics Symposium*, 2011, pp. 1906–1909.

[151] M. a O'Reilly and K. Hynynen, "A super-resolution ultrasound method for brain vascular mapping.," *Med. Phys.*, vol. 40, no. 11, p. 110701, Nov. 2013.

[152] M. T. M. F. O. C. Y. Desailly, "Sono-activated ultrasound localization microscopy," *Applied Physics Letters*, 2013. [Online]. Available: http://scitation.aip.org/docserver/fulltext/aip/journal/apl/103/17/1.4826597.pdf?expires=1385376753&id=id&accname=freeContent&checksum=4ED2C42A758FE3193A35D0B83437B723.

[153] W. Wang, J. Gu, T. He, Y. Shen, S. Xi, L. Tian, F. Li, H. Li, L. Yan, and X. Zhou, "Optical super-resolution microscopy and its applications in nano-catalysis," *Nano Res.*, vol. 8, no. 2, pp. 441–455, Jan. 2015.

[154] A. Neice, *Advances in Imaging and Electron Physics: Optics of Charged Particle Analyzers*. Academic Press, 2010.

[155] J. W. S. B. Rayleigh and R. B. Lindsay, *The Theory of Sound, Volume 1*. Courier Corporation, 1945.

[156] L. Hoff, *Acoustic Characterization of Contrast Agents for Medical Ultrasound Imaging*. Dordrecht: Springer Netherlands, 2001.

[157] Shutilov, *Fundamental Physics of Ultrasound*. CRC Press, 1988.

[158] L. Hoff, *Acoustic Characterization of Contrast Agents for Medical Ultrasound Imaging*. Springer Science & Business Media, 2013.

[159] S. Hilgenfeldt, D. Lohse, and M. Zomack, "Response of bubbles to diagnostic ultrasound: a unifying theoretical approach," *Eur. Phys. J. B*, vol. 4, no. 2, pp. 247–255, Aug. 1998.

[160] A. Herzenberg, K. L. Kwok, and F. Mandl, "Resonance scattering theory," *Proc. Phys. Soc.*, vol. 84, no. 4, pp. 477–497, Oct. 1964.

[161] Lord Rayleigh, "VIII. On the pressure developed in a liquid during the collapse of a spherical cavity," *Philos. Mag. Ser. 6*, vol. 34, no. 200, pp. 94–98, Aug. 1917.

[162] M. S. Plesset, "The Dynamics of Cavitation Bubbles," *Journal of Applied Mechanics*. American Society of Mechanical Engineers, 01-Sep-1949.

[163] T. G. Leighton, "Derivation of the Rayleigh-Plesset equation in terms of volume." Institute of Sound and Vibration Research, University of Southampton, 17-Apr-2007.

[164] C. C. Church, "The effects of an elastic solid surface layer on the radial pulsations of gas bubbles," *J. Acoust. Soc. Am.*, vol. 97, no. 3, p. 1510, Mar. 1995.

[165] P. J. A. Frinking and N. de Jong, "Acoustic Modeling of Shell-Encapsulated Gas Bubbles," *Ultrasound Med. Biol.*, vol. 24, no. 4, pp. 523–533, May 1998.

[166] S. Hilgenfeldt, D. Lohse, and M. Zomack, “Response of bubbles to diagnostic ultrasound: a unifying theoretical approach,” vol. 255, p. 21, 1998.

[167] B. P. Barber, R. A. Hiller, R. Löfstedt, S. J. Putterman, and K. R. Weninger, “Defining the unknowns of sonoluminescence,” *Phys. Rep.*, vol. 281, no. 2, pp. 65–143, Mar. 1997.

[168] T. G. Leighton, *The Acoustic Bubble, Volume 10*. Academic Press, 1997.

[169] N. de Jong and L. Hoff, “Ultrasound scattering properties of Albunex microspheres,” *Ultrasonics*, vol. 31, no. 3, pp. 175–181, May 1993.

[170] N. de Jong, L. Hoff, T. Skotland, and N. Bom, “Absorption and scatter of encapsulated gas filled microspheres: Theoretical considerations and some measurements,” *Ultrasonics*, vol. 30, no. 2, pp. 95–103, Mar. 1992.

[171] S. M. van der Meer, M. Versluis, D. Lohse, C. T. Chin, A. Bouakaz, and N. d. Jong, “The resonance frequency of SonoVue as observed by high-speed optical imaging,” in *IEEE Ultrasonics Symposium, 2004*, 2004, vol. 1, pp. 343–345.

[172] K. E. Morgan, J. S. Allen, P. A. Dayton, J. E. Chomas, A. L. Klibaov, and K. W. Ferrara, “Experimental and theoretical evaluation of microbubble behavior: effect of transmitted phase and bubble size.,” *IEEE Trans. Ultrason. Ferroelectr. Freq. Control*, vol. 47, no. 6, pp. 1494–509, Jan. 2000.

[173] S. Qin and K. W. Ferrara, “Acoustic response of compliable microvessels containing ultrasound contrast agents.,” *Phys. Med. Biol.*, vol. 51, no. 20, pp. 5065–88, Oct. 2006.

[174] K. E. Morgan, J. S. Allen, P. A. Dayton, J. E. Chomas, A. L. Klibaov, and K. W.

Ferrara, “Experimental and theoretical evaluation of microbubble behavior: effect of transmitted phase and bubble size.,” *IEEE Trans. Ultrason. Ferroelectr. Freq. Control*, vol. 47, no. 6, pp. 1494–509, Jan. 2000.

[175] A. Prosperetti, “Nonlinear oscillations of gas bubbles in liquids. Transient solutions and the connection between subharmonic signal and cavitation,” *J. Acoust. Soc. Am.*, vol. 57, no. 4, p. 810, Apr. 1975.

[176] J. S. Allen, D. J. May, and K. W. Ferrara, “Dynamics of therapeutic ultrasound contrast agents.,” *Ultrasound Med. Biol.*, vol. 28, no. 6, pp. 805–16, Jun. 2002.

[177] V. Garbin, D. Cojoc, E. Ferrari, E. Di Fabrizio, M. L. J. Overvelde, S. M. van der Meer, N. de Jong, D. Lohse, and M. Versluis, “Changes in microbubble dynamics near a boundary revealed by combined optical micromanipulation and high-speed imaging,” *Appl. Phys. Lett.*, vol. 90, no. 11, p. 114103, Mar. 2007.

[178] H. J. Vos, B. Dollet, J. G. Bosch, M. Versluis, and N. de Jong, “Nonspherical vibrations of microbubbles in contact with a wall: a pilot study at low mechanical index.,” *Ultrasound Med. Biol.*, vol. 34, no. 4, pp. 685–8, Apr. 2008.

[179] H. N. Oğuz and A. Prosperetti, “The natural frequency of oscillation of gas bubbles in tubes,” *J. Acoust. Soc. Am.*, vol. 103, no. 6, pp. 3301–3308, Jun. 1998.

[180] E. Sassaroli and K. Hynynen, “Resonance frequency of microbubbles in small blood vessels: a numerical study.,” *Phys. Med. Biol.*, vol. 50, no. 22, pp. 5293–305, Nov. 2005.

[181] E. Sassaroli and K. Hynynen, “Forced linear oscillations of microbubbles in blood capillaries.,” *J. Acoust. Soc. Am.*, vol. 115, no. 6, pp. 3235–43, Jun. 2004.

[182] C. F. Caskey, D. E. Kruse, P. A. Dayton, T. K. Kitano, and K. W. Ferrara,

"Microbubble oscillation in tubes with diameters of 12, 25, and 195 microns," *Appl. Phys. Lett.*, vol. 88, no. 3, p. 033902, Jan. 2006.

[183] D. H. Thomas, V. Sboros, M. Emmer, H. Vos, and N. de Jong, "Microbubble oscillations in capillary tubes.," *IEEE Trans. Ultrason. Ferroelectr. Freq. Control*, vol. 60, no. 1, pp. 105–14, Jan. 2013.

[184] M. Butler and A. Dermitzakis, "Single microbubble acoustics in small tubes," *Int. Congr. Acoust.*, no. August, pp. 1–3, 2010.

[185] V. Sboros, "A review of Single Microbubble Acoustics," no. August, pp. 1–5, 2010.

[186] S. Qin and K. W. Ferrara, "The natural frequency of nonlinear oscillation of ultrasound contrast agents in microvessels.," *Ultrasound Med. Biol.*, vol. 33, no. 7, pp. 1140–8, Jul. 2007.

[187] S. H. Bloch, R. E. Short, K. W. Ferrara, and E. R. Wisner, "The effect of size on the acoustic response of polymer-shelled contrast agents.," *Ultrasound Med. Biol.*, vol. 31, no. 3, pp. 439–44, Mar. 2005.

[188] M. Tanter, J. Bercoff, L. Sandrin, and M. Fink, "Ultrafast compound imaging for 2-D motion vector estimation: application to transient elastography," *IEEE Trans. Ultrason. Ferroelectr. Freq. Control*, vol. 49, no. 10, pp. 1363–1374, Oct. 2002.

[189] G. Montaldo, M. Tanter, J. Bercoff, N. Benech, and M. Fink, "Coherent plane-wave compounding for very high frame rate ultrasonography and transient elastography," *IEEE Trans. Ultrason. Ferroelectr. Freq. Control*, 2009.

[190] M. Tanter and M. Fink, "Ultrafast imaging in biomedical ultrasound," *IEEE*

Trans. Ultrason. Ferroelectr. Freq. Control, vol. 61, no. 1, pp. 102–119, Jan. 2014.

[191] O. Couture, S. Bannouf, G. Montaldo, J.-F. Aubry, M. Fink, and M. Tanter, "Ultrafast Imaging of Ultrasound Contrast Agents," *Ultrasound Med. Biol.*, vol. 35, no. 11, pp. 1908–1916, Nov. 2009.

[192] T. K. ; C. Song and J H, "Synthetic aperture focusing method for ultrasound imaging based on planar waves," 18-May-2004.

[193] Medison, "Synthetic aperture focusing method for ultrasound imaging based on planar waves," vol. 2, no. 12, 2004.

[194] J. Y. Lu, "Experimental study of high frame rate imaging with limited diffraction beams.," *IEEE Trans. Ultrason. Ferroelectr. Freq. Control*, vol. 45, no. 1, pp. 84–97, Jan. 1998.

[195] J. Cheng and J.-Y. Lu, "Extended high-frame rate imaging method with limited-diffraction beams," *IEEE Trans. Ultrason. Ferroelectr. Freq. Control*, vol. 53, no. 5, pp. 880–899, May 2006.

[196] O. T. von Ramm, S. W. Smith, and H. R. Pavy, "High-speed ultrasound volumetric imaging system. II. Parallel processing and image display.," *IEEE Trans. Ultrason. Ferroelectr. Freq. Control*, vol. 38, no. 2, pp. 109–15, Jan. 1991.

[197] O. Couture, M. Fink, and M. Tanter, "Ultrasound contrast plane wave imaging," *IEEE Trans. Ultrason. Ferroelectr. Freq. Control*, vol. 59, no. 12, Dec. 2012.

[198] N. Bobroff, "Position measurement with a resolution and noise-limited instrument," *Rev. Sci. Instrum.*, vol. 57, no. 6, p. 1152, Jun. 1986.

[199] R. J. Ober, S. Ram, and E. S. Ward, “Localization accuracy in single-molecule microscopy.,” *Biophys. J.*, vol. 86, no. 2, pp. 1185–200, Feb. 2004.

[200] S. Ismail, A. R. Jayaweera, G. Camarano, L. W. Gimple, E. R. Powers, and S. Kaul, “Relation between air-filled albumin microbubble and red blood cell rheology in the human myocardium. Influence of echocardiographic systems and chest wall attenuation.,” *Circulation*, vol. 94, no. 3, pp. 445–51, Aug. 1996.

[201] M. W. Keller, S. S. Segal, S. Kaul, and B. Duling, “The behavior of sonicated albumin microbubbles within the microcirculation: a basis for their use during myocardial contrast echocardiography.,” *Circ. Res.*, vol. 65, no. 2, pp. 458–67, Aug. 1989.

[202] S. Stallinga and B. Rieger, “Accuracy of the gaussian point spread function model in 2D localization microscopy.,” *Opt. Express*, vol. 18, no. 24, pp. 24461–24476, 2010.

[203] O. Haeberlé, M. Ammar, H. Furukawa, K. Tenjimbayashi, and P. Török, “The point spread function of optical microscopes imaging through stratified media,” *Opt. Express*, vol. 11, no. 22, p. 2964, Nov. 2003.

[204] A. J. Berglund, M. D. McMahon, J. J. McClelland, and J. A. Liddle, “Fast, bias-free algorithm for tracking single particles with variable size and shape.,” *Opt. Express*, vol. 16, no. 18, pp. 14064–75, Sep. 2008.

[205] R. Henriques, M. Lelek, E. F. Fornasiero, F. Valtorta, C. Zimmer, and M. M. Mhlanga, “QuickPALM: 3D real-time photoactivation nanoscopy image processing in ImageJ.,” *Nat. Methods*, vol. 7, no. 5, pp. 339–40, May 2010.

[206] H. Deschout, K. Neyts, and K. Braeckmans, “The influence of movement on the

localization precision of sub-resolution particles in fluorescence microscopy.," *J. Biophotonics*, vol. 5, no. 1, pp. 97–109, Jan. 2012.

[207] N. de Jong, M. Emmer, A. van Wamel, and M. Versluis, "Ultrasonic characterization of ultrasound contrast agents.," *Med. Biol. Eng. Comput.*, vol. 47, no. 8, pp. 861–73, Aug. 2009.

[208] A. A. Doinikov, L. Aired, and A. Bouakaz, "Acoustic scattering from a contrast agent microbubble near an elastic wall of finite thickness.," *Phys. Med. Biol.*, vol. 56, no. 21, pp. 6951–67, Nov. 2011.

[209] P. Marmottant, S. van der Meer, M. Emmer, M. Versluis, N. de Jong, S. Hilgenfeldt, and D. Lohse, "A model for large amplitude oscillations of coated bubbles accounting for buckling and rupture," *J. Acoust. Soc. Am.*, vol. 118, no. 6, p. 3499, Dec. 2005.

[210] M. Kaya, S. Feingold, K. Hettiarachchi, A. P. Lee, and P. A. Dayton, "Acoustic responses of monodisperse lipid-encapsulated microbubble contrast agents produced by flow focusing.," *Bubble Sci. Eng. Technol.*, vol. 2, no. 2, pp. 33–40, Dec. 2010.

[211] J. Jensen, "Field: A program for simulating ultrasound systems," *... Conf. Biomed. IMAGING, VOL. 4, ...*, 1996.

[212] R. E. Thompson, D. R. Larson, and W. W. Webb, "Precise nanometer localization analysis for individual fluorescent probes.," *Biophys. J.*, vol. 82, no. 5, pp. 2775–83, May 2002.

[213] A. Small and S. Stahlheber, "Fluorophore localization algorithms for super-resolution microscopy," *Nat. Methods*, vol. 11, no. 3, pp. 267–279, Feb. 2014.

[214] K. I. Mortensen, L. S. Churchman, J. a Spudich, and H. Flyvbjerg, “Optimized localization analysis for single-molecule tracking and super-resolution microscopy.,” *Nat. Methods*, vol. 7, no. 5, pp. 377–381, 2010.

[215] W. B. Pennebaker and J. L. Mitchell, *JPEG: Still Image Data Compression Standard*. Springer Science & Business Media, 1992.

[216] M. SCHNEIDER, “Characteristics of SonoVue™,” *Echocardiography*, vol. 16, no. s1, pp. 743–746, Oct. 1999.

[217] C. A. Sennoga, V. Mahue, J. Loughran, J. Casey, J. M. Seddon, M. Tang, and R. J. Eckersley, “On sizing and counting of microbubbles using optical microscopy.,” *Ultrasound Med. Biol.*, vol. 36, no. 12, pp. 2093–6, Dec. 2010.

[218] Siemens, “ACUSON S3000™ Ultrasound System - Transducers. Release 1.5.” [Online]. Available: https://www.cee.siemens.com/web/ua/ru/medecine/detection_diagnosis/ultrasaund/OB-GYN/ACUSON_S3000/Documents/ACUSON S3000 Ultrasound System 1.5 Release Transducer Flyer.pdf. [Accessed: 19-Sep-2015].

[219] R. J. Garde, *Fluid Mechanics Through Problems*. New Age International, 1997.

[220] C. F. Caskey, S. M. Stieger, S. Qin, P. A. Dayton, and K. W. Ferrara, “Direct observations of ultrasound microbubble contrast agent interaction with the microvessel wall.,” *J. Acoust. Soc. Am.*, vol. 122, no. 2, pp. 1191–200, Aug. 2007.

[221] J. Owen, P. Grove, P. Rademeyer, and E. Stride, “The influence of blood on targeted microbubbles.,” *J. R. Soc. Interface*, vol. 11, no. 100, p. 20140622, Nov. 2014.

[222] A. D. Michelson, *Platelets*. Academic Press, 2011.

[223] S. Kaul and A. R. Jayaweera, “Determinants of microvascular flow.,” *Eur. Heart J.*, vol. 27, no. 19, pp. 2272–4, Oct. 2006.

[224] A. R. Jayaweera, N. Edwards, W. P. Glasheen, F. S. Villanueva, R. D. Abbott, and S. Kaul, “In vivo myocardial kinetics of air-filled albumin microbubbles during myocardial contrast echocardiography. Comparison with radiolabeled red blood cells.,” *Circ. Res.*, vol. 74, no. 6, pp. 1157–65, Jul. 1994.

[225] D. S. Long, M. L. Smith, A. R. Pries, K. Ley, and E. R. Damiano, “Microviscometry reveals reduced blood viscosity and altered shear rate and shear stress profiles in microvessels after hemodilution.,” *Proc. Natl. Acad. Sci. U. S. A.*, vol. 101, no. 27, pp. 10060–5, Jul. 2004.

[226] P. Hinterdorfer and A. Oijen, Eds., *Handbook of Single-Molecule Biophysics*. New York, NY: Springer US, 2009.

[227] S. J. Holden, S. Uphoff, J. Hohlbein, D. Yadin, L. Le Reste, O. J. Britton, and A. N. Kapanidis, “Defining the limits of single-molecule FRET resolution in TIRF microscopy.,” *Biophys. J.*, vol. 99, no. 9, pp. 3102–11, Dec. 2010.

[228] S. Kvåle, H. A. Jakobsen, O. A. Asbjørnsen, and T. Omtveit, “Size fractionation of gas-filled microspheres by flotation,” *Sep. Technol.*, vol. 6, no. 4, pp. 219–226, Oct. 1996.

[229] M. Kaya, T. S. Gregory, and P. A. Dayton, “Changes in lipid-encapsulated microbubble population during continuous infusion and methods to maintain consistency.,” *Ultrasound Med. Biol.*, vol. 35, no. 10, pp. 1748–55, Oct. 2009.

[230] S. J. Holden, S. Uphoff, and A. N. Kapanidis, “DAOSTORM: an algorithm for

high- density super-resolution microscopy.," *Nat. Methods*, vol. 8, no. 4, pp. 279–280, 2011.

[231] E. Talu, K. Hettiarachchi, S. Zhao, R. L. Powell, A. P. Lee, M. L. Longo, and P. A. Dayton, "Tailoring the size distribution of ultrasound contrast agents: possible method for improving sensitivity in molecular imaging.," *Mol. Imaging*, vol. 6, no. 6, pp. 384–92, Jan. .

[232] R. D. Yates and D. J. Goodman, "Probability and Stochastic Processes: A Friendly Introduction for Electrical and Computer Engineers," p. 496, 2014.

[233] F. A. Haight, "A Handbook of the Poisson Distribution," *J. R. Stat. Soc. Ser. A*, vol. 18, no. 4, Jan. 1967.

[234] F. Dzaharudin, S. A. Suslov, R. Manasseh, and A. Ooi, "Effects of coupling, bubble size, and spatial arrangement on chaotic dynamics of microbubble cluster in ultrasonic fields.," *J. Acoust. Soc. Am.*, vol. 134, no. 5, pp. 3425–34, Nov. 2013.

[235] J. H. Barker, F. Hammersen, I. Bondàr, E. Uhl, T. J. Galla, M. D. Menger, and K. Messmer, "The hairless mouse ear for in vivo studies of skin microcirculation.," *Plast. Reconstr. Surg.*, vol. 83, no. 6, pp. 948–959, Jun. 1989.

[236] H. Ishida, T. Hachiga, T. Andoh, and S. Akiguchi, "In-vivo visualization of melanoma tumor microvessels and blood flow velocity changes accompanying tumor growth," *J. Appl. Phys.*, vol. 112, no. 10, p. 104703, 2012.

[237] P. So, H. Kim, and I. Kochevar, "Two-Photon deep tissue ex vivo imaging of mouse dermal and subcutaneous structures.," *Opt. Express*, vol. 3, no. 9, pp. 339–350, 1998.

[238] R. Keys, “Cubic convolution interpolation for digital image processing,” *IEEE Trans. Acoust.*, vol. 29, no. 6, pp. 1153–1160, Dec. 1981.

[239] M. Akiyama, I., Hayama, A., Nakajima, “Movement analysis of soft tissues by speckle patterns’ fluctuation,” *JSUM Proc.*, pp. 615–616, 1986.

[240] A. A. Morsy and O. T. Von Ramm, “3D ultrasound tissue motion tracking using correlation search.,” *Ultrason. Imaging*, vol. 20, no. 3, pp. 151–9, Jul. 1998.

[241] I. A. Hein and W. R. O’Brien, “Current time-domain methods for assessing tissue motion by analysis from reflected ultrasound echoes-a review.,” *IEEE Trans. Ultrason. Ferroelectr. Freq. Control*, vol. 40, no. 2, pp. 84–102, Jan. 1993.

[242] F. Kober, I. Iltis, P. J. Cozzone, and M. Bernard, “Cine-MRI assessment of cardiac function in mice anesthetized with ketamine/xylazine and isoflurane,” *Magn. Reson. Mater. Physics, Biol. Med.*, vol. 17, no. 3–6, pp. 157–161, 2004.

[243] F. Yeung, S. F. Levinson, D. Fu, and K. J. Parker, “Feature-adaptive motion tracking of ultrasound image sequences using a deformable mesh.,” *IEEE Trans. Med. Imaging*, vol. 17, no. 6, pp. 945–56, Dec. 1998.

[244] B. Denarie, T. A. Tangen, I. K. Ekroll, N. Rolim, H. Torp, T. Bjåstad, and L. Lovstakken, “Coherent plane wave compounding for very high frame rate ultrasonography of rapidly moving targets.,” *IEEE Trans. Med. Imaging*, vol. 32, no. 7, pp. 1265–76, Jul. 2013.

[245] A. Myronenko, “Image registration by minimization of residual complexity,” in *2009 IEEE Conference on Computer Vision and Pattern Recognition*, 2009, pp. 49–56.

[246] A. Myronenko and X. Song, “Intensity-based image registration by minimizing

residual complexity.," *IEEE Trans. Med. Imaging*, vol. 29, no. 11, pp. 1882–91, Nov. 2010.

[247] F. Yeung, S. F. Levinson, and K. J. Parker, "Multilevel and Motion Model-Based Ultrasonic Speckle Tracking Algorithms," *Ultrasound Med. Biol.*, vol. 24, no. 3, pp. 427–441, Mar. 1998.

[248] D. Dawson, M. A. Vincent, E. J. Barrett, S. Kaul, A. Clark, H. Leong-Poi, and J. R. Lindner, "Vascular recruitment in skeletal muscle during exercise and hyperinsulinemia assessed by contrast ultrasound.," *Am. J. Physiol. Endocrinol. Metab.*, vol. 282, no. 3, pp. E714–20, Mar. 2002.

[249] J. Zhang, M. Ding, F. Meng, M. Yuchi, and X. Zhang, "Respiratory motion correction in free-breathing ultrasound image sequence for quantification of hepatic perfusion.," *Med. Phys.*, vol. 38, no. 8, pp. 4737–48, Aug. 2011.

[250] C. Strouthos, M. Lampaskis, V. Sboros, A. McNeilly, and M. Averkiou, "Indicator dilution models for the quantification of microvascular blood flow with bolus administration of ultrasound contrast agents.," *IEEE Trans. Ultrason. Ferroelectr. Freq. Control*, vol. 57, no. 6, pp. 1296–310, Jun. 2010.

[251] J. M. Guralnik, E. M. Simonsick, L. Ferrucci, R. J. Glynn, L. F. Berkman, D. G. Blazer, P. A. Scherr, and R. B. Wallace, "A short physical performance battery assessing lower extremity function: association with self-reported disability and prediction of mortality and nursing home admission.," *J. Gerontol.*, vol. 49, no. 2, pp. M85–94, Mar. 1994.

[252] A. G. MAY, L. VAN DE BERG, J. A. DEWEESE, and C. G. ROB, "Critical arterial stenosis.," *Surgery*, vol. 54, no. 1, pp. 250–9, Jul. 1963.

[253] T. B. Kinney and S. C. Rose, "Intraarterial pressure measurements during

angiographic evaluation of peripheral vascular disease: techniques, interpretation, applications, and limitations.," *AJR. Am. J. Roentgenol.*, vol. 166, no. 2, pp. 277–84, Mar. 1996.

[254] J. C. Wang, "Exertional Leg Pain in Patients With and Without Peripheral Arterial Disease," *Circulation*, vol. 112, no. 22, pp. 3501–3508, Nov. 2005.

[255] M. Krix, H. Krakowski-Roosen, E. Amarteifio, E. Armarteifio, S. Fürstenberger, S. Delorme, H.-U. Kauczor, and M.-A. Weber, "Comparison of transient arterial occlusion and muscle exercise provocation for assessment of perfusion reserve in skeletal muscle with real-time contrast-enhanced ultrasound.," *Eur. J. Radiol.*, vol. 78, no. 3, pp. 419–24, Jun. 2011.

[256] M. Krix, H. Krakowski-Roosen, H.-U. Kauczor, S. Delorme, and M.-A. Weber, "Real-time contrast-enhanced ultrasound for the assessment of perfusion dynamics in skeletal muscle.," *Ultrasound Med. Biol.*, vol. 35, no. 10, pp. 1587–95, Oct. 2009.

[257] E. Amarteifio, S. Wormsbecher, S. Demirel, M. Krix, S. Braun, C. Rehnitz, S. Delorme, H.-U. Kauczor, and M.-A. Weber, "Assessment of skeletal muscle microcirculation in type 2 diabetes mellitus using dynamic contrast-enhanced ultrasound: a pilot study.," *Diab. Vasc. Dis. Res.*, vol. 10, no. 5, pp. 468–70, 2013.

[258] Y. Song, Y. Li, P.-J. Wang, and Y. Gao, "Contrast-enhanced ultrasonography of skeletal muscles for type 2 diabetes mellitus patients with microvascular complications.," *Int. J. Clin. Exp. Med.*, vol. 7, no. 3, pp. 573–9, Jan. 2014.

[259] D. Dawson, M. A. Vincent, E. J. Barrett, S. Kaul, A. Clark, H. Leong-Poi, and J. R. Lindner, "Vascular recruitment in skeletal muscle during exercise and hyperinsulinemia assessed by contrast ultrasound," *Am. J. Physiol. - Endocrinol. Metab.*, vol. 282, no. 3, pp. E714–E720, Mar. 2002.

[260] J. Folkman, “Angiogenesis.,” *Annu. Rev. Med.*, vol. 57, pp. 1–18, Jan. 2006.

[261] D. H. Spodick, P. Raju, R. L. Bishop, and R. D. Rifkin, “Operational definition of normal sinus heart rate,” *Am. J. Cardiol.*, vol. 69, no. 14, pp. 1245–1246, May 1992.

[262] V. Kulkarni and B. R. Ramesh, “A Morphological Study of Dorsalis Pedis Artery and Its Clinical Correlation,” vol. 2, no. 3, pp. 2278–3008, Aug. 2012.

[263] P. Lewis, J. V Psaila, W. T. Davies, K. McCarty, and J. P. Woodcock, “Measurement of volume flow in the human common femoral artery using a duplex ultrasound system.,” *Ultrasound Med. Biol.*, vol. 12, no. 10, pp. 777–84, Oct. 1986.

[264] C. K. Holland, J. M. Brown, L. M. Scoutt, and K. J. Taylor, “Lower extremity volumetric arterial blood flow in normal subjects.,” *Ultrasound Med. Biol.*, vol. 24, no. 8, pp. 1079–86, Oct. 1998.

[265] T. Sandgren, B. Sonesson, Å. R. Ahlgren, and T. Länne, “The diameter of the common femoral artery in healthy human: Influence of sex, age, and body size,” *J. Vasc. Surg.*, vol. 29, no. 3, pp. 503–510, Mar. 1999.

[266] J. E. Chomas, P. Dayton, D. May, and K. Ferrara, “Threshold of fragmentation for ultrasonic contrast agents.,” *J. Biomed. Opt.*, vol. 6, no. 2, pp. 141–50, Apr. 2001.

[267] A. Y. Ammi, R. O. Cleveland, J. Mamou, G. I. Wang, S. L. Bridal, and W. D. O’Brien, “Ultrasonic contrast agent shell rupture detected by inertial cavitation and rebound signals.,” *IEEE Trans. Ultrason. Ferroelectr. Freq. Control*, vol. 53, no. 1, pp. 126–36, Jan. 2006.

[268] J. M. Hudson, K. Leung, and P. N. Burns, “The lognormal perfusion model for disruption replenishment measurements of blood flow: in vivo validation.,” *Ultrasound Med. Biol.*, vol. 37, no. 10, pp. 1571–8, Oct. 2011.

[269] J. T. Belcik, B. P. Davidson, T. Foster, Y. Qi, Y. Zhao, D. Peters, and J. R. Lindner, “Contrast-enhanced ultrasound assessment of impaired adipose tissue and muscle perfusion in insulin-resistant mice.,” *Circ. Cardiovasc. Imaging*, vol. 8, no. 4, p. e002684–, Apr. 2015.

[270] M. Pascotto, H. Leong-Poi, B. Kaufmann, A. Allrogen, D. Charalampidis, E. K. Kerut, S. Kaul, and J. R. Lindner, “Assessment of Ischemia-Induced Microvascular Remodeling Using Contrast-Enhanced Ultrasound Vascular Anatomic Mapping,” *J. Am. Soc. Echocardiogr.*, vol. 20, no. 9, pp. 1100–1108, 2007.

[271] B. S. Hertzberg, M. A. Kliewer, D. M. DeLong, K. J. Lalouche, E. K. Paulson, M. G. Frederick, and B. A. Carroll, “Sonographic assessment of lower limb vein diameters: implications for the diagnosis and characterization of deep venous thrombosis.,” *AJR. Am. J. Roentgenol.*, vol. 168, no. 5, pp. 1253–7, May 1997.

[272] R. R. Sokal and F. J. Rohlf, “Biometry : the principles and practice of statistics in biological research / Robert R. Sokal and F. James Rohlf,” Apr. 2013.

[273] J. M. Hudson, K. Leung, and P. N. Burns, “The Lognormal Perfusion Model for Disruption Replenishment Measurements of Blood Flow: In Vivo Validation,” *Ultrasound Med. Biol.*, vol. 37, no. 10, pp. 1571–1578, 2011.

[274] S. R. Wilson, H.-J. Jang, T. K. Kim, H. Iijima, N. Kamiyama, and P. N. Burns, “Real-time temporal maximum-intensity-projection imaging of hepatic lesions with contrast-enhanced sonography.,” *AJR. Am. J. Roentgenol.*, vol. 190, no. 3, pp. 691–5, Mar. 2008.

[275] T. C. Potdevin, J. B. Fowlkes, A. P. Moskalik, and P. L. Carson, “Analysis of refill curve shape in ultrasound contrast agent studies.,” *Med. Phys.*, vol. 31, no. 3, pp. 623–32, Mar. 2004.

[276] M. Krix, F. Kiessling, S. Vosseler, I. Kiessling, M. Le-Huu, N. E. Fusenig, and S. Delorme, “Comparison of intermittent-bolus contrast imaging with conventional power Doppler sonography: quantification of tumour perfusion in small animals,” *Ultrasound Med. Biol.*, vol. 29, no. 8, pp. 1093–1103, Aug. 2003.

[277] M.-X. Tang and R. J. Eckersley, “Frequency and pressure dependent attenuation and scattering by microbubbles.,” *Ultrasound Med. Biol.*, vol. 33, no. 1, pp. 164–8, Jan. 2007.

[278] M.-X. Tang and R. J. Eckersley, “Nonlinear propagation of ultrasound through microbubble contrast agents and implications for imaging.,” *IEEE Trans. Ultrason. Ferroelectr. Freq. Control*, vol. 53, no. 12, pp. 2406–15, Dec. 2006.

[279] D. Ackermann and G. Schmitz, “Reconstruction of flow velocity inside vessels by tracking single microbubbles with an MCMC data association algorithm,” in *2013 IEEE International Ultrasonics Symposium (IUS)*, 2013, pp. 627–630.

[280] D. T. Williams, K. G. Harding, and P. Price, “An evaluation of the efficacy of methods used in screening for lower-limb arterial disease in diabetes.,” *Diabetes Care*, vol. 28, no. 9, pp. 2206–10, Sep. 2005.

[281] M. Haltmayer, T. Mueller, W. Horvath, C. Luft, W. Poelz, and D. Haidinger, “Impact of atherosclerotic risk factors on the anatomical distribution of peripheral arterial disease.,” *Int. Angiol.*, vol. 20, no. 3, pp. 200–7, Sep. 2001.

[282] S. B. Williams, J. A. Cusco, M. A. Roddy, M. T. Johnstone, and M. A. Creager,

"Impaired nitric oxide-mediated vasodilation in patients with non-insulin-dependent diabetes mellitus.," *J. Am. Coll. Cardiol.*, vol. 27, no. 3, pp. 567–74, Mar. 1996.

[283] X. Ren and J. Malik, "Learning a classification model for segmentation," in *Proceedings Ninth IEEE International Conference on Computer Vision*, 2003, pp. 10–17 vol.1.

[284] R. Achanta, A. Shaji, K. Smith, A. Lucchi, P. Fua, and S. Susstrunk, "SLIC Superpixels," *EPFL Tech. Rep. 149300*, no. June, p. 15, 2010.

[285] J. A. Hartigan and M. A. Wong, "Algorithm AS 136: A K-Means Clustering Algorithm," *Appl. Stat.*, vol. 28, no. 1, p. 100, Jan. 1979.

[286] A. Dempster, N. Laird, and D. Rubin, "Maximum Likelihood from Incomplete Data via the EM Algorithm," *J. R. Stat. Soc. Ser. B*, vol. 39, no. 1, pp. 1 – 38, 1977.

[287] N. Friedman and S. Russell, "Image segmentation in video sequences: a probabilistic approach," pp. 175–181, Aug. 1997.

[288] C. R. Wren, A. Azarbayejani, T. Darrell, and A. P. Pentland, "Pfinder: real-time tracking of the human body," *IEEE Trans. Pattern Anal. Mach. Intell.*, vol. 19, no. 7, pp. 780–785, Jul. 1997.

[289] C. Cortes and V. Vapnik, "Support-Vector Networks," *Mach. Learn.*, vol. 20, no. 3, pp. 273–297.

[290] C. Apté, F. Damerau, and S. M. Weiss, "Automated learning of decision rules for text categorization," *ACM Trans. Inf. Syst.*, vol. 12, no. 3, pp. 233–251, Jul. 1994.

[291] D. H. L. S. D. Thanarat Horprasert, “A statistical approach for real-time robust background subtraction and shadow detection.”

[292] D. Brzakovic, X. M. Luo, and P. Brzakovic, “An approach to automated detection of tumors in mammograms.,” *IEEE Trans. Med. Imaging*, vol. 9, no. 3, pp. 233–41, Jan. 1990.

[293] E. I. Zacharaki, S. Wang, S. Chawla, D. Soo Yoo, R. Wolf, E. R. Melhem, and C. Davatzikos, “Classification of brain tumor type and grade using MRI texture and shape in a machine learning scheme.,” *Magn. Reson. Med.*, vol. 62, no. 6, pp. 1609–18, Dec. 2009.

[294] N. Chenouard, I. Smal, F. de Chaumont, M. Maška, I. F. Sbalzarini, Y. Gong, J. Cardinale, C. Carthel, S. Coraluppi, M. Winter, A. R. Cohen, W. J. Godinez, K. Rohr, Y. Kalaidzidis, L. Liang, J. Duncan, H. Shen, Y. Xu, K. E. G. Magnusson, J. Jaldén, H. M. Blau, P. Paul-Gilloteaux, P. Roudot, C. Kervrann, F. Waharte, J.-Y. Tinevez, S. L. Shorte, J. Willemse, K. Celler, G. P. van Wezel, H.-W. Dan, Y.-S. Tsai, C. Ortiz de Solórzano, J.-C. Olivo-Marin, and E. Meijering, “Objective comparison of particle tracking methods.,” *Nat. Methods*, vol. 11, no. 3, pp. 281–9, Mar. 2014.

[295] C. Stauffer and W. E. L. Grimson, “Learning patterns of activity using real-time tracking,” *IEEE Trans. Pattern Anal. Mach. Intell.*, vol. 22, no. 8, pp. 747–757, 2000.

[296] S. Klöppel, C. M. Stonnington, C. Chu, B. Draganski, R. I. Scahill, J. D. Rohrer, N. C. Fox, C. R. Jack, J. Ashburner, and R. S. J. Frackowiak, “Automatic classification of MR scans in Alzheimer’s disease.,” *Brain*, vol. 131, no. Pt 3, pp. 681–9, Mar. 2008.

[297] M. Eichmann, “Framework for efficient optimal multilevel image thresholding,” *J. Electron. Imaging*, vol. 18, no. 1, p. 013004, Jan. 2009.

[298] P. . Sahoo, S. Soltani, and A. K. . Wong, “A survey of thresholding techniques,” *Comput. Vision, Graph. Image Process.*, vol. 41, no. 2, pp. 233–260, Feb. 1988.

[299] W. van Aarle, K. J. Batenburg, and J. Sijbers, “Optimal threshold selection for segmentation of dense homogeneous objects in tomographic reconstructions.,” *IEEE Trans. Med. Imaging*, vol. 30, no. 4, pp. 980–9, Apr. 2011.

[300] N. R. Pal and S. K. Pal, “A review on image segmentation techniques,” *Pattern Recognit.*, vol. 26, no. 9, pp. 1277–1294, Sep. 1993.

[301] W. D. (Ed) Wertheimer, Max, Ellis, “Laws of organization in perceptual forms.,” in *A source book of Gestalt psychology.*, 1938, pp. 71–88.

[302] K. Koffka, “Why Psychology?: An introductory question,” *Princ. gestalt Psychol.*, pp. 1–14, 1935.

[303] R. Achanta, A. Shaji, K. Smith, A. Lucchi, P. Fua, and S. Süsstrunk, “SLIC superpixels compared to state-of-the-art superpixel methods.,” *IEEE Trans. Pattern Anal. Mach. Intell.*, vol. 34, no. 11, pp. 2274–82, Nov. 2012.

[304] J. Shi and J. Malik, “Normalized cuts and image segmentation,” *IEEE Comput. Soc. Conf. Comput. Vis. Pattern Recognit.*, pp. 731–737, 1997.

[305] B. Fulkerson, A. Vedaldi, and S. Soatto, “Class segmentation and object localization with superpixel neighborhoods,” *Comput. Vision, 2009 IEEE 12th Int. Conf.*, 2009.

[306] R. Cipolla, S. Battiato, and G. M. Farinella, Eds., *Machine Learning for Computer Vision*, vol. 411. Berlin, Heidelberg: Springer Berlin Heidelberg, 2013.

[307] A. Lucchi, K. Smith, R. Achanta, V. Lepetit, and P. Fua, “A Fully Automated Approach to Segmentation of Irregularly Shaped Cellular Structures in EM Images,” *Proc. Med. Image Comput. Comput. Assist. Interv. (MICCAI 2010), Part II*, vol. LNCS 6362, 2010.

[308] B. Fulkerson, A. Vedaldi, and S. Soatto, “Class segmentation and object localization with superpixel neighborhoods,” in *2009 IEEE 12th International Conference on Computer Vision*, 2009, pp. 670–677.

[309] A. Leonardis, H. Bischof, and A. Pinz, Eds., *Computer Vision – ECCV 2006*, vol. 3951. Berlin, Heidelberg: Springer Berlin Heidelberg, 2006.

[310] Y. Li, J. Sun, C.-K. Tang, and H.-Y. Shum, “Lazy snapping,” in *ACM SIGGRAPH 2004 Papers on - SIGGRAPH ’04*, 2004, vol. 23, no. 3, p. 303.

[311] A. Lucchi, K. Smith, R. Achanta, V. Lepetit, and P. Fua, “A fully automated approach to segmentation of irregularly shaped cellular structures in EM images.,” *Med. Image Comput. Comput. Assist. Interv.*, vol. 13, no. Pt 2, pp. 463–71, Jan. 2010.

[312] G. Mori, “Guiding model search using segmentation,” in *Tenth IEEE International Conference on Computer Vision (ICCV’05) Volume 1*, 2005, vol. 2, pp. 1417–1423 Vol. 2.

[313] R. C. D. Anil K. Jain, *Algorithms for Clustering Data*. 1988.

[314] F. Aurenhammer, “Voronoi diagrams---a survey of a fundamental geometric data structure,” *ACM Comput. Surv.*, vol. 23, no. 3, pp. 345–405, Sep. 1991.

[315] J. Bilmes, “A Gentle Tutorial of the EM Algorithm and its Application to

Parameter Estimation for Gaussian Mixture and Hidden Markov Models."

[316] S. Thrun and L. K. Saul, *Advances in Neural Information Processing Systems 16: Proceedings of the 2003 Conference*. MIT Press, 2004.

[317] I. G. Maglogiannis, *Emerging Artificial Intelligence Applications in Computer Engineering: Real Word AI Systems with Applications in EHealth, HCI, Information Retrieval and Pervasive Technologies*. IOS Press, 2007.

[318] J. Zhang, R. Jin, Y. Yang, and A. G. Hauptmann, "Modified Logistic Regression: An Approximation to SVM and Its Applications in Large-Scale Text Categorization," *Proceedings, Twent. Int. Conf. Mach. Learn.*, vol. 2, no. 1999, pp. 888–895, 2003.

[319] C. C. C. L. Chih-wei Hsu, "A practical guide to support vector classification."

[320] S. J. Press and S. Wilson, "Choosing between logistic regression and discriminant analysis." RAND Corporation, 1979.

[321] N. L. M. M. Pochet and J. A. K. Suykens, "Support vector machines versus logistic regression: improving prospective performance in clinical decision-making.," *Ultrasound Obstet. Gynecol.*, vol. 27, no. 6, pp. 607–8, Jun. 2006.

[322] C. J. C. Burges, "A Tutorial on Support Vector Machines for Pattern Recognition," *Data Min. Knowl. Discov.*, vol. 2, no. 2, pp. 121–167.

[323] C. C. N. C. K. Veropoulos, "Controlling the Sensitivity of Support Vector Machines."

[324] J. M. Moguerza and A. Muñoz, "Support Vector Machines with Applications,"

Stat. Sci., vol. 21, no. 3, pp. 322–336, Aug. 2006.

[325] T. Verplancke, S. Van Looy, D. Benoit, S. Vansteelandt, P. Depuydt, F. De Turck, and J. Decruyenaere, "Support vector machine versus logistic regression modeling for prediction of hospital mortality in critically ill patients with haematological malignancies.," *BMC Med. Inform. Decis. Mak.*, vol. 8, no. 1, p. 56, Jan. 2008.

[326] S.-T. Chen, Y.-H. Hsiao, Y.-L. Huang, S.-J. Kuo, H.-S. Tseng, H.-K. Wu, and D.-R. Chen, "Comparative analysis of logistic regression, support vector machine and artificial neural network for the differential diagnosis of benign and malignant solid breast tumors by the use of three-dimensional power Doppler imaging.," *Korean J. Radiol.*, vol. 10, no. 5, pp. 464–71, Jan. .

[327] D. P. H. Pedro F. Felzenszwalb, "Efficiently Computing a Good Segmentation."

[328] P. F. Felzenszwalb and D. P. Huttenlocher, "Efficient Graph-Based Image Segmentation," *Int. J. Comput. Vis.*, vol. 59, no. 2, pp. 167–181, Sep. 2004.

[329] A. Vedaldi and S. Soatto, "Quick shift and kernel methods for mode seeking," *Lect. Notes Comput. Sci. (including Subser. Lect. Notes Artif. Intell. Lect. Notes Bioinformatics)*, vol. 5305 LNCS, no. PART 4, pp. 705–718, 2008.

[330] E. Pedregosa, F. , Varoquaux, G. , Gramfort, A. , Michel, V., Thirion, B. , Grisel, O. , Blondel, M. , Prettenhofer, P., Weiss, R., Dubourg, V. , Vanderplas, J., Passos, A., Cournapeau, D., Brucher, M. , Perrot, M. , Duchesnay, "Scikit-learn: Machine Learning in Python," *J. Mach. Learn. Res.*, vol. 12, pp. 2825–2830, 2011.

[331] P. Tortoli, S. Member, L. Bassi, E. Boni, A. Dallai, F. Guidi, and S. Ricci, "ULA-OP : An Advanced Open Platform for Ultrasound Research," vol. 56, no.

10, pp. 2207–2216, 2009.

[332] S. L. Vieira, T. Z. Pavan, J. E. Junior, and A. a O. Carneiro, “Paraffin-Gel Tissue-Mimicking Material for Ultrasound-Guided Needle Biopsy Phantom,” *Ultrasound Med. Biol.*, vol. 39, no. 12, pp. 2477–2484, 2013.

[333] C. Sun, S. D. Pye, J. E. Browne, A. Janeczko, B. Ellis, M. B. Butler, V. Sboros, A. J. W. Thomson, M. P. Brewin, C. H. Earnshaw, and C. M. Moran, “The speed of sound and attenuation of an IEC agar-based tissue-mimicking material for high frequency ultrasound applications.,” *Ultrasound Med. Biol.*, vol. 38, no. 7, pp. 1262–70, Jul. 2012.

[334] M. Systems, “ULA-OP,” 2014.

[335] W. J. Cliff, *Blood Vessels*. CUP Archive, 1976.

[336] J. Wang and J. Lu, “Motion artifacts of extended high frame rate imaging.,” *IEEE Trans. Ultrason. Ferroelectr. Freq. Control*, vol. 54, no. 7, pp. 1303–1315, 2007.

[337] J. . Shipley, M. Halliwell, and P. N. . Wells, “Localising an ultrasound beam travelling within the scan plane of a diagnostic ultrasound imager,” *Ultrasonics*, vol. 37, no. 2, pp. 123–131, 1999.

[338] Z. Ye, “On sound scattering and attenuation of Albunex® bubbles,” *J. Acoust. Soc. Am.*, vol. 100, no. 4, p. 2011, 1996.

[339] V. Bjerknes, *Die Kraftfelder*. Braunschweig: Druck und Verlag von Friedrich Vieweg, 1909.

[340] Y. Desailly, O. Couture, M. Fink, and M. Tanter, “Sono-activated ultrasound localization microscopy,” *Appl. Phys. Lett.*, vol. 103, no. 17, 2013.

[341] R. S. C. Cobbold, *Foundations of Biomedical Ultrasound*. Oxford University Press, USA, 2006.

[342] D.-L. Liu, “Correction of ultrasonic wavefront distortion using backpropagation and a reference waveform method for time-shift compensation,” *J. Acoust. Soc. Am.*, vol. 96, no. 2, p. 649, Aug. 1994.

[343] S. W. Flax and M. O’Donnell, “Phase-aberration correction using signals from point reflectors and diffuse scatterers: basic principles.,” *IEEE Trans. Ultrason. Ferroelectr. Freq. Control*, vol. 35, no. 6, pp. 758–67, Jan. 1988.

[344] Q. Chen and J. A. Zagzebski, “Simulation study of effects of speed of sound and attenuation on ultrasound lateral resolution.,” *Ultrasound Med. Biol.*, vol. 30, no. 10, pp. 1297–306, Oct. 2004.

[345] L. Nock, G. E. Trahey, and S. W. Smith, “Phase aberration correction in medical ultrasound using speckle brightness as a quality factor.,” *J. Acoust. Soc. Am.*, vol. 85, no. 5, pp. 1819–33, May 1989.

[346] J. C. Lacefield, W. C. Pilkington, and R. C. Waag, “Distributed aberrators for emulation of ultrasonic pulse distortion by abdominal wall,” *Acoust. Res. Lett. Online*, vol. 3, no. 2, p. 47, Dec. 2002.

[347] W. Jiang, J. P. Astheimer, and R. C. Waag, “Aberration compensation of an ultrasound imaging instrument with a reduced number of channels.,” *IEEE Trans. Ultrason. Ferroelectr. Freq. Control*, vol. 59, no. 10, pp. 2210–25, Oct. 2012.

[348] M. E. Anderson, M. S. McKeag, and G. E. Trahey, “The impact of sound speed

errors on medical ultrasound imaging.," *J. Acoust. Soc. Am.*, vol. 107, no. 6, pp. 3540–8, Jun. 2000.

[349] M. R. Kendall, D. Bardin, R. Shih, P. A. Dayton, and A. P. Lee, "Scaled-Up Production of Monodisperse, Dual Layer Microbubbles Using Multi-Array Microfluidic Module for Medical Imaging and Drug Delivery.," *Bubble Sci. Eng. Technol.*, vol. 4, no. 1, pp. 12–20, May 2012.

[350] J. M. Zhang, E. Q. Li, and S. T. Thoroddsen, "A co-flow-focusing monodisperse microbubble generator," *J. Micromechanics Microengineering*, vol. 24, no. 3, p. 035008, Mar. 2014.

[351] M. Parhizkar, E. Stride, and M. Edirisinghe, "Preparation of monodisperse microbubbles using an integrated embedded capillary T-junction with electrohydrodynamic focusing.," *Lab Chip*, vol. 14, no. 14, pp. 2437–46, Jul. 2014.

[352] F. E. Angilè, K. B. Vargo, C. M. Sehgal, D. A. Hammer, and D. Lee, "Recombinant Protein-Stabilized Monodisperse Microbubbles with Tunable Size Using a Valve-Based Microfluidic Device," *Langmuir*, vol. 30, no. 42, pp. 12610–12618, Oct. 2014.

[353] B. P. Chugh, J. P. Lerch, L. X. Yu, M. Pienkowski, R. V Harrison, R. M. Henkelman, and J. G. Sled, "Measurement of cerebral blood volume in mouse brain regions using micro-computed tomography.," *Neuroimage*, vol. 47, no. 4, pp. 1312–8, Oct. 2009.

[354] Z. Starosolski, C. A. Villamizar, D. Rendon, M. J. Paldino, D. M. Milewicz, K. B. Ghaghada, and A. V Annapragada, "Ultra High-Resolution In vivo Computed Tomography Imaging of Mouse Cerebrovasculature Using a Long Circulating Blood Pool Contrast Agent.," *Sci. Rep.*, vol. 5, p. 10178, Jan. 2015.

[355] S.-H. Park, K. Masamoto, K. Hendrich, I. Kanno, and S.-G. Kim, “Imaging brain vasculature with BOLD microscopy: MR detection limits determined by in vivo two-photon microscopy.,” *Magn. Reson. Med.*, vol. 59, no. 4, pp. 855–65, Apr. 2008.

[356] C.-H. Huang, C.-C. V Chen, T.-Y. Siow, S.-H. S. Hsu, Y.-H. Hsu, F.-S. Jaw, and C. Chang, “High-resolution structural and functional assessments of cerebral microvasculature using 3D Gas ΔR2*-mMRA.,” *PLoS One*, vol. 8, no. 11, p. e78186, Jan. 2013.

[357] K. Maslov, H. F. Zhang, S. Hu, and L. V. Wang, “Optical-resolution photoacoustic microscopy for in vivo imaging of single capillaries,” *Opt. Lett.*, vol. 33, no. 9, p. 929, Apr. 2008.

[358] J. Yao, L. Wang, J.-M. Yang, K. I. Maslov, T. T. W. Wong, L. Li, C.-H. Huang, J. Zou, and L. V Wang, “High-speed label-free functional photoacoustic microscopy of mouse brain in action,” *Nat. Methods*, vol. 12, no. 5, p. 407–+, 2015.

[359] G. Ku and L. V. Wang, “Deeply penetrating photoacoustic tomography in biological tissues enhanced with an optical contrast agent,” *Opt. Lett.*, vol. 30, no. 5, p. 507, Mar. 2005.

[360] M. A. O’Reilly and K. Hynynen, “A super-resolution ultrasound method for brain vascular mapping.,” *Med. Phys.*, vol. 40, no. 11, p. 110701, Nov. 2013.

[361] B. Diarra, M. Robini, P. Tortoli, C. Cachard, and H. Liebgott, “Design of optimal 2-D nongrid sparse arrays for medical ultrasound.,” *IEEE Trans. Biomed. Eng.*, vol. 60, no. 11, pp. 3093–102, Nov. 2013.

[362] B. Diarra, H. Liebgott, M. Robini, P. Tortoli, and C. Cachard, “Optimized 2D array design for Ultrasound imaging,” pp. 2718–2722.

[363] P. Rademeyer, D. Carugo, J. Y. Lee, and E. Stride, “Microfluidic system for high throughput characterisation of echogenic particles.,” *Lab Chip*, vol. 15, no. 2, pp. 417–28, Jan. 2015.

[364] V. Garbin, D. Cojoc, E. Ferrari, R. Z. Proietti, S. Cabrini, and E. Di Fabrizio, “Optical Micro-Manipulation Using Laguerre-Gaussian Beams,” *Jpn. J. Appl. Phys.*, vol. 44, no. 7B, pp. 5773–5776, Jul. 2005.

[365] P. A. Prentice, M. P. MacDonald, T. G. Frank, A. Cuschieri, G. C. Spalding, W. Sibbett, P. A. Campbell, and K. Dholakia, “Manipulation and filtration of low index particles with holographic Laguerre-Gaussian optical trap arrays,” *Opt. Express*, vol. 12, no. 4, p. 593, Feb. 2004.

[366] J. Sijl, H. J. Vos, T. Rozendal, N. de Jong, D. Lohse, and M. Versluis, “Combined optical and acoustical detection of single microbubble dynamics.,” *J. Acoust. Soc. Am.*, vol. 130, no. 5, pp. 3271–81, 2011.

[367] S. Cox, E. Rosten, J. Monypenny, T. Jovanovic-Talisman, D. T. Burnette, J. Lippincott-Schwartz, G. E. Jones, and R. Heintzmann, “Bayesian localization microscopy reveals nanoscale podosome dynamics.,” *Nat. Methods*, vol. 9, no. 2, pp. 195–200, Mar. 2012.

[368] B. K. Horn and B. G. Schunck, “Determining Optical Flow,” in *1981 Technical Symposium East*, 1981, pp. 319–331.

[369] D. Rueckert, L. I. Sonoda, C. Hayes, D. L. Hill, M. O. Leach, and D. J. Hawkes, “Nonrigid registration using free-form deformations: application to breast MR images.,” *IEEE Trans. Med. Imaging*, vol. 18, no. 8, pp. 712–21, Aug. 1999.

[370] B. Yang, J. B. Treweek, R. P. Kulkarni, B. E. Deverman, C.-K. Chen, E. Lubeck, S. Shah, L. Cai, and V. Gradinaru, “Single-Cell Phenotyping within Transparent Intact Tissue through Whole-Body Clearing,” *Cell*, vol. 158, no. 4, pp. 945–58, Jul. 2014.

[371] F. Shah, P. Balan, M. Weinberg, V. Reddy, R. Neems, M. Feinstein, J. Dainauskas, P. Meyer, M. Goldin, and S. B. Feinstein, “Contrast-enhanced ultrasound imaging of atherosclerotic carotid plaque neovascularization: a new surrogate marker of atherosclerosis?,” *Vasc. Med.*, vol. 12, no. 4, pp. 291–297, 2007.

[372] N. M. Caplice and K. Martin, “Contrast-Enhanced Ultrasound and the Enigma of Plaque Neovascularization∗∗Editorials published in JACC: Cardiovascular Imaging reflect the views of the authors and do not necessarily represent the views of JACC: Cardiovascular Imaging or the American Coll,” *JACC Cardiovasc. Imaging*, vol. 3, no. 12, pp. 1273–1275, 2010.

[373] P. R. Moreno, K. R. Purushothaman, E. Zias, J. Sanz, and V. Fuster, “Neovascularization in human atherosclerosis.,” *Curr. Mol. Med.*, vol. 6, no. 5, pp. 457–77, Aug. 2006.

[374] M. Palmowski, W. Lederle, J. Gaetjens, M. Socher, P. Hauff, J. Bzyl, W. Semmler, R. W. Günther, and F. Kiessling, “Comparison of conventional time-intensity curves vs. maximum intensity over time for post-processing of dynamic contrast-enhanced ultrasound.,” *Eur. J. Radiol.*, vol. 75, no. 1, pp. e149–53, Jul. 2010.

[375] H. Leong-Poi, “Molecular imaging using contrast-enhanced ultrasound: evaluation of angiogenesis and cell therapy.,” *Cardiovasc. Res.*, vol. 84, no. 2, pp. 190–200, Nov. 2009.

[376] M. Siepmann, G. Schmitz, J. Bzyl, M. Palmowski, and F. Kiessling, “Imaging tumor vascularity by tracing single microbubbles,” *IEEE Int. Ultrason. Symp. IUS*, pp. 1906–1908, 2011.

[377] S. R. Wilson, H.-J. Jang, T. K. Kim, and P. N. Burns, “Diagnosis of focal liver masses on ultrasonography: comparison of unenhanced and contrast-enhanced scans.,” *J. Ultrasound Med.*, vol. 26, no. 6, pp. 775–87; quiz 788–90, Jun. 2007.

[378] A. L. H. Giampietro Gasparini, “Prognostic Significance of Tumor Vascularity,” in *Antiangiogenic Agents in Cancer Therapy*, B. A. Teicher, Ed. Totowa, NJ: Humana Press, 1999, pp. 317–339.

[379] N. Weidner, “Tumoural vascularity as a prognostic factor in cancer patients: the evidence continues to grow.,” *J. Pathol.*, vol. 184, no. 2, pp. 119–22, Feb. 1998.

[380] L. Hlatky, P. Hahnfeldt, and J. Folkman, “Clinical application of antiangiogenic therapy: microvessel density, what it does and doesn’t tell us.,” *J. Natl. Cancer Inst.*, vol. 94, no. 12, pp. 883–893, 2002.

[381] E. R. Christian, “An evaluation of needle biopsy of the liver,” *Am. J. Med.*, vol. 13, no. 6, pp. 689–703, Dec. 1952.

[382] S. R. Wilson, H.-J. Jang, T. K. Kim, H. Iijima, N. Kamiyama, and P. N. Burns, “Real-Time Temporal Maximum-Intensity-Projection Imaging of Hepatic Lesions with Contrast-Enhanced Sonography,” *American Journal of Roentgenology*. American Roentgen Ray Society, 23-Nov-2012.

[383] F. Grizzi, C. Russo, P. Colombo, B. Franceschini, E. E. Frezza, E. Cobos, and M. Chiriva-Internati, “Quantitative evaluation and modeling of two-dimensional neovascular network complexity: the surface fractal dimension.,” *BMC Cancer*, vol. 5, no. 1, p. 14, Feb. 2005.

[384] P. Carmeliet and R. K. Jain, “Angiogenesis in cancer and other diseases.,” *Nature*, vol. 407, no. 6801, pp. 249–57, Sep. 2000.

[385] A. F. Fercher, W. Drexler, C. K. Hitzenberger, and T. Lasser, “Optical coherence tomography - principles and applications,” *Reports Prog. Phys.*, vol. 66, no. 2, pp. 239–303, Feb. 2003.

[386] S. E. Shelton, Y. Z. Lee, M. Lee, E. Cherin, F. S. Foster, S. R. Aylward, and P. A. Dayton, “Quantification of Microvascular Tortuosity during Tumor Evolution Using Acoustic Angiography.,” *Ultrasound Med. Biol.*, vol. 41, no. 7, pp. 1896–904, Jul. 2015.

[387] J. M. Sung Nok Chiu, Dietrich Stoyan, Wilfrid S. Kendall, *Stochastic Geometry and its Applications*. John Wiley & Sons, 2013.

PUBLICATIONS AND SCIENTIFIC COMMUNICATION

PUBLICATIONS

Christensen-Jeffries, K, Schirmer, M. D., Browning, R., Tang, M.-X., Dunsby,, C., Aljabar, P., Eckersley, R. Dec 2014, Super-Resolved Micro-Vascular Imaging Using Microbubbles and Machine Learning, In: IEEE Micro and Nanotechnology in Medicine Conference Proceedings; p.108. Dec 2014.

Christensen-Jeffries, K., Browning, R., Tang, M-X., Dunsby, C. & Eckersley, R., "In Vivo Acoustic Super-Resolution and Super-Resolved Velocity Mapping Using Microbubbles," *IEEE Trans. Med. Imaging*, vol. 34, no. 2, pp 433-40, 23 Sep 2014.

Viessmann, O.M, Eckersley, R., **Christensen-Jeffries, K**., Tang, M. & Dunsby, C., "Acoustic super-resolution with ultrasound and microbubbles.," *Phys. Med. Biol.*, vol. 58, no. 18, pp. 6447–58, Sep. 2013.

Wing Keung Cheung, K.J. Williams, **K. Christensen-Jeffries,** B. Dharmarajah, R.J. Eckersley, A.H. Davies, Meng-Xing Tang. A Temporal and Spatial Analysis Approach

for Automated Segmentation of Microbubble Signals in Contrast Enhanced Ultrasound Images - Application to Quantification of Active Vascular Density in Human Lower Limbs. Investigative Radiology. **Conditionally accepted for publication.**

SCIENCE COMMUNICATION AND PRESENTATIONS

The work presented in this thesis has been shared at the following conferences:

Christensen-Jeffries, K., Browning, R., Tang, M-X., Dunsby, C. & Eckersley, R., 3D Super-Resolution Ultrasound using Microbubbles, Poster, IEEE International Ultrasonics Symposium, Taiwan, Oct 2015.

Christensen-Jeffries, K., Browning, R., Tang, M-X., Dunsby, C. & Eckersley, R. Acoustic Super-Resolution, Oral, Artimino Conference on Medical Ultrasound, Sweden, June 2015.

Christensen-Jeffries, K, Schirmer, M. D., Browning, R., Tang, M.-X., Dunsby,, C., Aljabar, P., Eckersley, R., Super-Resolved Micro-Vascular Imaging Using Microbubbles and Machine Learning, Poster, IEEE Micro and Nanotechnology in Medicine Conference, Hawaii, Dec 2014.

Christensen-Jeffries, K., Browning, R., Tang, M-X., Dunsby, C. & Eckersley, R., Acoustic Single Bubble Tracking for Super-Resolved Velocity Mapping, Poster and short oral, EPSRC CDT in Medical Imaging Launch Event, UK, Oct 2014.

Christensen-Jeffries, K., Browning, R., Tang, M-X., Dunsby, C. & Eckersley, R., Acoustic Single Bubble Tracking at Super-Resolution, Oral, IEEE International Ultrasonics Symposium, Chicago, Sep 2014.

Christensen-Jeffries, K., Browning, R., Tang, M-X., Dunsby, C. & Eckersley, R., Super-Resolution Localisation using Single Bubble Acoustics and Ultrasound, Poster and short oral, The 19th Contrast Symposium Rotterdam, Netherlands, Jan 2014.

ADDITIONAL COLLABORATIVE WORK

Collaborative work outside the scope of this thesis has been presented at the following conferences:

Wing Keung Cheung, K.J. Williams, **K. Christensen-Jeffries**, B. Dharmarajah, R.J.* Eckersley, A.H. Davies, Meng-Xing Tang. Automated quantification of muscle perfusion using contrast enhanced ultrasound: Initial in vitro and in vivo evaluation of lower limb perfusion. Oral, RSNA 101st Scientific Assembly and Annual Meeting, Chicago, Nov– Dec 2015. Presented by *.

Wing Keung Cheung*, K.J. Williams, **K. Christensen-Jeffries,** B. Dharmarajah, R.J. Eckersley, A.H. Davies, Meng-Xing Tang. An automated algorithm for quantification of tissue perfusion in contrast enhanced ultrasound images: initial evaluation in quantification of lower limb perfusion. Oral. The 20th European symposium on Ultrasound Contrast Imaging, Rotterdam, Jan 2015. Presented by *.

List of Tables

List of Figures

List of Abbreviations and Acronyms

ABI	Ankle-brachial index
ADC	Analogue-to-digital converter
AM	Amplitude modulation
ASIC	Application specific integrated circuit
AU	Arbitrary units
AWG	Arbitrary waveform generator
CE	Contrast enhanced
CEUS	Contrast enhanced ultrasound
CPS	Contrast pulse sequencing
CTR	Contrast tissue ratio
CVD	Cardiovascular disease
DCE-MRI	Dynamic contrast enhanced magnetic resonance imaging
DOCT	Doppler optical coherence tomography
FDA	U.S. Food and Drug Administration
FPGA	Field-programmable gate array
FWHM	Full width at half maximum
ICC	Intra-class correlation coefficient
IQ	In-phase and quadrature
LT	Localisation threshold
MB	Microbubble
MI	Mechanical index
MRI	Magnetic resonance imaging
OCT	Optical coherence tomography
OR-PAM	Optical resolution photoacoustic microsopy

PAD	Peripheral arterial disease
PAM	Photoacoustic microscopy
PAT	Photoacoustic tomography
PCC	Pearson cross-correlation
PE	Pulse-echo
PI	Pulse inversion
PNP	Peak negative pressure
PRF	Pulse repetition frequency
PSF	Point spread function
RMSE	Root mean squared error
RP	Rayleigh-Plesset
SH	Sub-harmonic
SNR	Signal-to-noise ratio
SPL	Spatial pulse length
SR	Super-resolution
STD	Standard deviation
SVM	Support vector machine
TGC	Time gain compensation
US	Ultrasound